



Multi-spectrum retrieval of maps of Venus' surface emissivity in the infrared

Publikationsbasierte Dissertation
zur Erlangung des akademischen Grades
“doctor rerum naturalium”
(Dr. rer. nat.)
in der Wissenschaftsdisziplin “Theoretische Physik”

eingereicht an der
Mathematisch-Naturwissenschaftlichen Fakultät
der Universität Potsdam

von
David Kappel

Betreuer: Prof. Dr. Martin Wilkens
Universität Potsdam, Institut für Physik and Astronomie
PD Dr. habil. Gabriele Arnold
Deutsches Zentrum für Luft- und Raumfahrt (DLR), Institut für Planetenforschung

eingereicht am 27.05.2015, verteidigt am 09.11.2015

Published online at the
Institutional Repository of the University of Potsdam:
URN urn:nbn:de:kobv:517-opus4-85301
<http://nbn-resolving.de/urn:nbn:de:kobv:517-opus4-85301>

Abstract

The main goal of this cumulative thesis is the derivation of surface emissivity data from radiance measurements of Venus. Information on surface emissivity in the infrared can contribute to the currently quite limited knowledge of the planet's geology, because it is diagnostic of the chemical composition, texture, and grain size of the surface material. Spectrally resolved images of nightside emissions in the spectral range 1.0–5.1 μm were recently acquired by the InfraRed Mapping channel of the Visible and InfraRed Thermal Imaging Spectrometer (VIRTIS-M-IR) aboard ESA's Venus EXpress (VEX). Surface and deep atmospheric thermal emissions in this spectral range are strongly obscured by the extremely opaque atmosphere, but three narrow spectral windows at 1.02, 1.10, and 1.18 μm allow the sounding of the surface. Some other windows between 1.3 and 2.6 μm provide information on atmospheric parameters that are required to interpret the surface signals. A numerical radiative transfer model can be used to simulate the observable radiation as a function of atmospheric, surface, and instrumental parameters. A retrieval algorithm is then needed to iteratively determine the state vector comprising the wanted parameters from a measured spectrum.

Following the first part of the present work, the introduction, the second part provides important prerequisites to a self-contained understanding of the thesis. It starts with an introduction to the VIRTIS-M-IR instrument. Then, it characterizes the implementation of the utilized radiative transfer model. This is a line-by-line model taking into account thermal emissions by surface and atmosphere as well as absorption and multiple scattering by gases and clouds, and it pays particular attention to the extreme environment close to Venus' surface (735 K, 92 bar). Moreover, the retrieval of state vectors from single spectra is discussed.

In the third part of this thesis, the VIRTIS-M-IR measurements are preprocessed to obtain an optimal data basis for the subsequent steps. For this purpose, a detailed detector responsivity analysis is performed to correct internal and external data inconsistencies. Other preprocessing steps include the removal of straylight, a customization of the geometry data, and the data binning, all with respect to the intended surface and deep atmosphere parameter retrieval ([doi:10.1016/j.asr.2012.03.029](https://doi.org/10.1016/j.asr.2012.03.029)).

The fourth part is dedicated to the development of the new multi-spectrum retrieval algorithm MSR. The VIRTIS-M-IR measurements have a relatively low spectral information content, and different state vectors can parameterize a measured spectrum equally well. A usual measure to regularize the retrieval is to take into account *a priori* mean values and standard deviations of the parameters to be retrieved, which decreases the probability to obtain unlikely parameter values. It proves necessary to additionally consider spatial and temporal *a priori* correlations between retrieval parameters describing different measurements. This approach necessitates a multi-spectrum retrieval, which is here implemented in the form of MSR. Moreover, MSR allows the retrieval of parameters that are common to several measurements. Taking these inter-measurement relations into account decreases the probability to retrieve unlikely spatial-temporal state vector distributions. Neglecting geologic activity, MSR can be applied to retrieve an emissivity map as a parameter vector that is common to several spectrally resolved images that cover the same surface target ([doi:10.1016/j.jqsrt.2013.07.025](https://doi.org/10.1016/j.jqsrt.2013.07.025)).

Even applying MSR, it is difficult to obtain reliable emissivity maps in absolute values. In part five of the thesis, a detailed retrieval error analysis based on synthetic spectra reveals that this is mainly due to interferences from parameters that have to be set to assumed values to enable the radiative transfer simulations, but that cannot be derived from the spectra themselves. It is proposed to retrieve an emissivity map *relative* to a fixed emissivity with MSR to overcome this problem. This approach is predicted to effectively avoid the large emissivity retrieval errors that are due to imperfect or unconsidered parameters ([doi:10.1016/j.pss.2015.01.014](https://doi.org/10.1016/j.pss.2015.01.014)).

In part six of the thesis, the concept of the retrieval relative to a fixed emissivity (0.5) using MSR is further developed. Relative emissivity maps at 1.02, 1.10, and 1.18 μm are finally derived from many VIRTIS-M-IR measurements that cover a surface target at Themis Regio. They are interpreted as spatial variations relative to an assumed emissivity mean of the target. It is verified that the maps are largely independent of the choice of many interfering parameters as well as the utilized measurement data set. The double standard deviation errors of the determined maps amount to 3%, 8%, and 4% for the three surface windows and are largely compatible to error estimates predicted in the previous part. These are the very first Venus IR emissivity map results from a consistent application of a full radiative transfer simulation and a retrieval algorithm respecting *a priori* information. The determined maps are sufficiently reliable for future geologic interpretations ([doi:10.1016/j.icarus.2015.10.014](https://doi.org/10.1016/j.icarus.2015.10.014)). The thesis closes with part seven presenting a discussion, summary, and an outlook.

Kurzfassung

Das Hauptziel dieser publikationsbasierten Dissertation ist die Ableitung von Oberflächenemissivitäts-Daten aus Radianzmessungen der Venus. Informationen über die Oberflächenemissivität im infraroten Spektralbereich können zur Erweiterung des noch sehr begrenzten Wissens über die Geologie des Planeten beitragen. Sie können dazu dienen, die chemische Zusammensetzung, Textur und Korngröße des Oberflächenmaterials zu bestimmen. Spektral aufgelöste Bilder von nachtseitigen Emissionen im Spektralbereich 1.0–5.1 μm wurden kürzlich durch den Infrarot-Kartierungskanal des abbildenden Spektrometers im sichtbaren und infraroten Bereich (VIRTIS-M-IR) an Bord der ESA-Sonde Venus Express (VEX) gewonnen. Die thermischen Emissionen der Oberfläche sowie der tiefen Atmosphäre werden in diesem Spektralbereich stark durch die extrem licht-undurchlässige Atmosphäre verschleiert, aber drei schmale spektrale Fenster bei 1.02, 1.10 und 1.18 μm ermöglichen die Sondierung der Oberfläche. Einige andere Fenster zwischen 1.3 und 2.6 μm liefern Informationen über atmosphärische Parameter, die benötigt werden, um die Oberflächensignale zu interpretieren. Ein numerisches Strahlungstransportmodell kann verwendet werden, um die beobachtbare Strahlung als Funktion von Atmosphären-, Oberflächen-, und Instrumentenparametern zu simulieren. Weiterhin wird ein Retrievalalgorithmus benötigt, der den Zustandsvektor, welcher die gesuchten Parameter beinhaltet, aus einem gemessenen Spektrum iterativ bestimmt.

Nach der Einleitung, dem ersten Teil der vorliegenden Arbeit, werden im zweiten Teil wichtige Grundlagen bereitgestellt, die ein in sich geschlossenes Verständnis der Dissertationsschrift ermöglichen. Zuerst wird das Instrument VIRTIS-M-IR vorgestellt. Als nächstes wird die Implementierung des benutzten Strahlungstransportmodells beschrieben. Dieses ist ein Linie-für-Linie-Modell und berücksichtigt sowohl thermische Emissionen der Oberfläche und Atmosphäre, als auch Absorption und Mehrfachstreuung durch Gase und Wolken. Es trägt insbesondere den extremen Umweltbedingungen nahe der Venusoberfläche (735 K, 92 bar) Rechnung. Weiterhin wird die Bestimmung von Zustandsvektoren aus einzelnen Spektren besprochen.

Im dritten Teil dieser Dissertation werden die VIRTIS-M-IR-Messungen vorverarbeitet, um eine optimale Datenbasis für die nachfolgenden Schritte zu erhalten. Dazu wird eine detaillierte Analyse des Detektoransprechvermögens durchgeführt, um interne und externe Dateninkonsistenzen zu korrigieren. Weitere Schritte der Datenvorverarbeitung beinhalten das Entfernen des Streulichts, eine Anpassung der Geometriedaten und das Daten-Binning. Alle Schritte sind auf die beabsichtigte Ableitung von Parametern der Oberfläche und der tiefen Atmosphäre abgestimmt ([doi:10.1016/j.asr.2012.03.029](https://doi.org/10.1016/j.asr.2012.03.029)).

Der vierte Teil der Arbeit ist der Entwicklung der neuen Multispektrumretrieval-Methode MSR gewidmet. Die VIRTIS-M-IR-Messungen haben einen vergleichsweise geringen spektralen Informationsgehalt, und verschiedene Zustandsvektoren können ein- und dasselbe gemessene Spektrum gleich gut parametrisieren. Eine übliche Maßnahme, das Retrieval zu regularisieren, ist die Berücksichtigung von *a priori*-Mittelwerten und -Standardabweichungen der zu bestimmenden Parameter. Dadurch wird die Wahrscheinlichkeit verringert, unrealistische Parameterwerte zu erhalten. Es erweist sich als notwendig, zusätzlich räumliche und zeitliche *a priori*-Korrelationen zwischen Retrievalparametern, die verschiedene Messungen beschreiben, einzubeziehen. Diese Herangehensweise erfordert ein Multispektrumretrieval, welches hier durch MSR implementiert wird. Zusätzlich erlaubt MSR die Bestimmung von Parametern, die mehreren Messungen gemeinsam sind. Die Berücksichtigung solcher Relationen, die mehrere Messungen in Beziehung zueinander setzen, verringert die Wahrscheinlichkeit, unrealistische räumlich-zeitliche Zustandsvektor-Verteilungen zu erhalten. Vernachlässigt man geologische Aktivität, so kann man mit Hilfe von MSR eine Emissivitätskarte in Form eines Parametervektors bestimmen, der verschiedenen spektral aufgelösten Bildern gemeinsam ist, die denselben Oberflächenbereich überdecken ([doi:10.1016/j.jqsrt.2013.07.025](https://doi.org/10.1016/j.jqsrt.2013.07.025)).

Selbst bei Anwendung von MSR ist es schwierig, verlässliche Karten für die Absolutwerte der Emissivität zu erhalten. Im fünften Teil der Dissertation zeigt eine detaillierte Retrieval-Fehleranalyse, die auf synthetischen Spektren beruht, dass dies hauptsächlich an Interferenzen von Parametern liegt, die nicht aus den Spektren selbst hergeleitet werden können. Um dennoch die Strahlungstransportsimulationen zu ermöglichen, müssen sie auf angenommene Werte gesetzt werden. Als Lösung dieses Problems wird vorgeschlagen, mit MSR eine Emissivitätskarte *relativ* zu einer festen Emissivität zu bestimmen. Es wird prognostiziert, dass durch diese Herangehensweise die großen Fehler bei der Emissivitätsbestimmung, die durch unvollkommene oder unberücksichtigte Parameter verursacht werden, effizient vermieden werden ([doi:10.1016/j.pss.2015.01.014](https://doi.org/10.1016/j.pss.2015.01.014)).

Im sechsten Teil der Dissertation wird das Konzept weiterentwickelt, Karten relativ zu einer festen Emissivität (0.5) mit Hilfe von MSR abzuleiten. Aus vielen VIRTIS-M-IR-Messungen, die einen Oberflächenbereich in der Themis Regio überdecken, werden damit schließlich relative Emissivitätskarten bei 1.02, 1.10, und 1.18 μm bestimmt. Sie werden als räumliche Variationen relativ zu einer angenommenen mittleren Emissivität des Oberflächenbereichs interpretiert. Es wird nachgewiesen, dass die Karten von der Wahl vieler interferierender Parameter sowie der Auswahl der zugrunde liegenden Messungen weitgehend unabhängig sind. Die Fehler der ermittelten Karten (doppelte Standardabweichung) betragen für die drei Oberflächenfenster 3%, 8% und 4% und sind weitgehend mit den Fehlerabschätzungen des vorhergehenden Kapitels vereinbar. Dieses sind die ersten Ergebnisse bezüglich Emissivitätskarten der Venus im Infrarotbereich, die auf einer konsistenten Anwendung einer umfassenden Strahlungstransportsimulation und eines Retrievalalgorithmus, der *a priori* Informationen berücksichtigt, basieren. Die ermittelten Karten sind hinreichend zuverlässig für zukünftige geologische Interpretationen ([doi:10.1016/j.icarus.2015.10.014](https://doi.org/10.1016/j.icarus.2015.10.014)). Die Dissertation schließt mit dem siebenten Teil, in dem eine Diskussion, Zusammenfassung und ein Ausblick dargelegt werden.

Contributions to accumulated manuscripts

The candidate's contributions to the four accumulated manuscripts included in the present thesis are clarified here.

The general topic of the present thesis, the determination of Venus surface information from VIRTIS-M-IR measurements, was defined by Dr. habil. Gabriele Arnold. She was the subject-specific supervisor of this thesis and the consultant with respect to everything related to the surface. Dr. Rainer Haus was the consultant with respect to the atmospheric part, in particular for the radiative transfer. Many discussions with both of them provided important impulses with regard to possible directions of the candidate's studies as well as recommendations on publishing strategy including both international research journals and presentations at international conferences and VIRTIS/VEX team meetings.

The candidate's own implementation of a radiative transfer simulation model (excluding the radiative transfer equation solver subroutines DISORT / LIDORT) was written from scratch for the present thesis in order to better learn the details of radiative transfer, to be able to independently develop required modifications to the model, and to create own implementations of the data structures needed for Bayesian retrieval and later MSR retrieval. The radiative transfer model was implemented in close cooperation with Rainer Haus. Algorithms and simulated results were closely compared to those of him for mutual improvements in each development stage. The corresponding background on radiative transfer is presented in Chapter II.

Chapter III: Refinements in the Data Analysis of VIRTIS-M-IR Venus Nightside Spectra

David Kappel, Gabriele Arnold, Rainer Haus, Giuseppe Piccioni, Pierre Drossart
Advances in Space Research, 50(2):228–255, 2012, [doi:10.1016/j.asr.2012.03.029](https://doi.org/10.1016/j.asr.2012.03.029).

Dr. Giuseppe Piccioni (INAF-IAPS, Rome) and Prof. Dr. Pierre Drossart (CNRS/LESIA, Paris) are the coPIs of the VIRTIS/VEX instrument. They made the measurement data, whose calibration refinements and pre-processings are the topic of this paper, available before public data access was granted. Moreover, they provided important insights into the instrument's properties, performance, and difficulties. They recommended the inclusion of the description and first results of an early version of MSR to make the article more relevant to the wider public. The candidate conceptualized the algorithms for the calibration refinements and the pre-processings. However, three issues were pointed out at VIRTIS team meetings by other scientists: Dr. Nikolay Ignatiev noticed the detector responsivity issue at 1.0–1.3 μm and the sample inhomogeneity. Dr. Nils Müller made the candidate aware of the problems and the solutions in connection with the surface topography except for the motion blurring (see the Acknowledgements Section of this paper). The candidate accomplished all other work including the writing of the manuscript. Discussions with Gabriele Arnold and Rainer Haus additionally supported the candidate to define amount and choice of the material covered in the article. Both of them worked through the manuscripts in each stage, pointed out the possible shortcomings, and suggested improvements until the final version was ready for submission.

Chapter IV: MSR, a multi-spectrum retrieval technique for spatially-temporally correlated or common Venus surface and atmosphere parameters

David Kappel
Journal of Quantitative Spectroscopy and Radiative Transfer, 133:153–176, 2014,
[doi:10.1016/j.jqsrt.2013.07.025](https://doi.org/10.1016/j.jqsrt.2013.07.025).

The candidate accomplished all work. This included the required research, the conceptual and mathematical development of MSR, its computer implementation, testing and application to the different problems connected with the scientific goal of this thesis as well as the writing of the manuscript. Gabriele Arnold and Rainer Haus worked through the different versions of the manuscript and suggested possible improvements.

Chapter V: Error analysis for retrieval of Venus' IR surface emissivity from VIRTIS/VEX measurements

David Kappel, Rainer Haus, Gabriele Arnold

Planetary and Space Science, 113–114: 49–65, 2015, doi:[10.1016/j.pss.2015.01.014](https://doi.org/10.1016/j.pss.2015.01.014).

The candidate accomplished all work including the definition of required investigations and the writing of the manuscript. Discussions with Gabriele Arnold and Rainer Haus were again very helpful in each stage of compiling the paper.

Chapter VI: Multi-spectrum retrieval of Venus IR surface emissivity maps from VIRTIS/VEX nightside measurements at Themis Regio

David Kappel, Gabriele Arnold, Rainer Haus

Icarus, 265:42–62, 2016, doi:[10.1016/j.icarus.2015.10.014](https://doi.org/10.1016/j.icarus.2015.10.014).

The choice of the surface target, based on its geologic relevance, and the preliminary geologic interpretation of the results were done by Gabriele Arnold. The candidate accomplished all other work including the writing of the manuscript. Both Gabriele Arnold and Rainer Haus gave valuable impulses and made recommendations for improvements of the final manuscript.

David Kappel
(doctoral candidate)

Prof. Dr. Martin Wilkens
(supervisor)

Dr. habil. Gabriele Arnold
(supervisor and co-author)

Dr. Rainer Haus
(co-author)

Dr. Giuseppe Piccioni
(co-author)

Prof. Dr. Pierre Drossart
(co-author)

Danksagung

Ich danke Herrn Prof. Dr. Martin Wilkens für seine Betreuung von Seiten der Universität. Seine wertvollen Ratschläge und sein Enthusiasmus haben mir viele Male weitergeholfen.

Mein besonderer Dank gilt meiner fachspezifischen Betreuerin am DLR, Frau PD Dr. habil. Gabriele Arnold. Sie ermöglichte mir den Einstieg in diesen Fachbereich und gab die allgemeine Richtung der Arbeit vor. Gleichzeitig hat sie mir immer genügend Freiraum gelassen, um meine Ideen zu verfolgen. Ihr Vertrauen in mich, ihr fachlicher und strategischer Rat und ihre Erfahrung haben maßgeblich dazu beigetragen, dass die vorliegende Arbeit entstehen konnte. Weiterhin habe ich von ihr vieles über den Forschungsbetrieb im Allgemeinen gelernt. Sie machte mich mit der internationalen Community, insbesondere dem VIRTIS/VEX-Team bekannt, und gab mir frühzeitig die Chance, die Ergebnisse der Arbeitsgruppe auf Konferenzen zu präsentieren. Zu guter Letzt danke ich ihr dafür, dass sie immer einen Weg fand, Finanzierungsmöglichkeiten zu finden. Ohne Frau Dr. Arnold wäre diese Arbeit nicht möglich gewesen.

Mein herzlicher Dank gebührt Dr. Rainer Haus. Ohne ihn und seine Erfahrung wäre mein Einstieg in die Strahlungstransportmodellierung undenkbar gewesen. Der Austausch mit ihm über physikalische und andere Themen ist immer wieder anregend, und es macht mir großen Spaß, mit ihm zusammenzuarbeiten. Außerdem möchte ich ihm für die endlosen Stunden danken, die er damit verbracht hat, sowohl die Artikel als auch den Rest dieser Arbeit durchzuarbeiten. Es ist immer wieder erstaunlich, wie passgenau er für inhaltlich und verbal schwer zu formulierende Passagen genau die richtigen Wendungen findet. Die Zusammenarbeit mit ihm ist ein Privileg.

I would like to thank Dr. Giuseppe Piccioni (INAF-IAPS, Rome) and Prof. Dr. Pierre Drossart (CNRS/LESIA, Paris) for their advice on everything related to the VIRTIS/VEX instrument. They provided important insights into the instrument's properties, performance, and difficulties. Moreover, I would like to express my gratitude to all members of the VIRTIS/VEX team for the interesting discussion forum they provided and for the insights into many other fields connected to VIRTIS/VEX they have given to me.

Ich möchte auch Prof. Dr. Thomas Trautmann und Dr. Franz Schreier für ihr frühzeitiges Feedback zu MSR danken, für die Organisation meines Besuches in Oberpfaffenhofen, sowie die Anmerkungen zum zweiten und dritten Paper.

Weiterhin bedanke ich mich bei Kathrin Markus und Nils Müller für die guten fachlichen und nichtfachlichen Gespräche, sowie bei Barbara Haupt und Philipp Gast für die gemeinsame Zeit im Büro.

Furthermore, I thank the DLR Adlershof and the people working there for the excellent research environment.

Als nächstes möchte ich mich bei meinen Freunden Nicole, Markus und Stephan für ihr Interesse an meiner Arbeit bedanken.

Mein ganz persönlicher Dank gilt meinen Eltern, Petra und Jörg-Peter, sowie meinem Bruder, Marcel, für ihre Ermutigung und Unterstützung und einfach für alles.

Ramona, Dir danke ich für das Korrekturlesen (Copyedit...) und die vielen kleinen und großen Dinge mit denen Du mir bei dieser Arbeit geholfen hast. Und ich danke Dir für so viel mehr.

Abschließend möchte ich mich beim Deutschen Zentrum für Luft- und Raumfahrt, der Deutschen Forschungsgemeinschaft und der Universität Münster/Institut für Planetologie für die finanzielle Unterstützung während der letzten Jahre bedanken.

Table of contents

Abstract	iii
Kurzfassung	iv
Contributions to accumulated manuscripts	vi
Danksagung	ix
Table of contents	xi
List of Figures	xv
List of Tables	xvii
Nomenclature	xix
I Introduction	1
I.1 Surface emissivity in the infrared	2
I.2 State of research	3
I.2.1 Radiative transfer in Venus' atmosphere	3
I.2.2 Determination of surface information	4
I.2.3 Venus' geology	6
I.2.4 Multi-spectrum retrieval algorithms	8
I.3 Main goal of thesis	8
I.4 Outline of accumulated manuscripts and their interrelation	9
I.4.1 Chapter II - Forward model simulation and single-spectrum retrieval algorithm	10
I.4.2 Chapter III - Refinements in the Data Analysis	11
I.4.3 Chapter IV - Multi-spectrum retrieval algorithm	14
I.4.4 Chapter V - Retrieval error analysis	17
I.4.5 Chapter VI - Multi-spectrum retrieval of Venus IR surface emissivity maps	20
II VIRTIS-M-IR, radiative transfer, and single-spectrum retrieval	25
II.1 VIRTIS-M-IR	25
II.2 Forward model	27
II.2.1 The equation of radiative transfer	27
II.2.2 Numerical solution of the radiative transfer equation	31
II.2.3 Gaseous absorption	35
II.2.3.1 Idealized model	35
II.2.3.2 General cases	36
II.2.3.3 Line shapes	37
II.2.3.4 Continuum absorption	39
II.2.3.5 Line-by-line procedure	41
II.2.4 Clouds	44

II.2.4.1	Mie theory	44
II.2.4.2	Standard cloud model	46
II.2.4.3	Cloud optical properties	49
II.2.5	Rayleigh scattering	51
II.2.6	Input to RTE solver	53
II.2.7	Synthetic spectrum and Jacobians	57
II.3	Single-spectrum retrieval algorithm	60
II.3.1	Gauss-Newton algorithm	62
II.3.2	Levenberg-Marquardt algorithm	63
II.3.3	Trust region algorithm	63
II.3.4	Bayesian probability and cost function	64
III	Refinements in the Data Analysis	67
III.1	Introduction	68
III.2	Forward model and retrieval algorithm	69
III.3	Data calibration	70
III.3.1	Calibration baseline	71
III.3.2	Detector responsivity analysis	71
III.3.2.1	Even-odd pattern in the instrument transfer function	72
III.3.2.2	Sample homogenization	75
III.3.2.3	Responsivity adjustment at 1.0–1.3 μm	77
III.3.2.4	Even-odd effect of measurements	79
III.3.3	New despiking and destriping	84
III.4	Data preprocessing for retrieval	84
III.4.1	Straylight	85
III.4.1.1	Straylight sources	85
III.4.1.2	Straylight removal	85
III.4.2	Geometry and topography data update	87
III.4.2.1	Geometry data update	87
III.4.2.2	Re-evaluation of the topography data	88
III.4.2.3	Referencing	88
III.4.2.4	Atmospheric blurring	88
III.4.2.5	Motion blurring	89
III.4.3	Data binning	90
III.4.4	Wavelength shift and uncertainty of the full width at half maximum	91
III.5	Results	91
III.5.1	Impact of retrieval algorithm improvements on retrieval results	91
III.5.1.1	Spatial-temporal correlations	92
III.5.1.2	Common parameters in the retrieval	93
III.5.2	Impact of calibration refinement and preprocessing on the measurement data base	94
III.5.2.1	General impact on spectra	94
III.5.2.2	Topography update	95
III.5.2.3	Binning schemes	96
III.5.3	Impact of calibration refinement and preprocessing on retrieval results	96
III.5.3.1	Clouds	96
III.5.3.2	Minor gases	97
III.5.3.3	Common parameters	97
III.5.3.4	Surface emissivity	98
III.6	Conclusions and outlook	100
	Acknowledgements	102

IV	Multi-spectrum retrieval algorithm	103
IV.1	Introduction	104
IV.2	Multi-spectrum retrieval algorithm (MSR)	105
IV.3	<i>A priori</i> covariance matrix	107
IV.3.1	<i>A priori</i> correlation matrix	108
IV.3.2	Single-parameter problem for several spectra	109
IV.3.2.1	Positive definite functions	109
IV.3.2.2	Spherical planetary surface	112
IV.3.2.3	Spatial-temporal and other separations	112
IV.3.3	Single-spectrum problem for several parameters	113
IV.3.4	Full covariance matrix for correlated retrievals	113
IV.3.5	Retrieval of common parameters	116
IV.4	Parameters for Venus retrieval problems	116
IV.4.1	Forward model	116
IV.4.2	Local parameters	118
IV.4.3	Common parameters	119
IV.5	Examples and discussion	120
IV.6	Conclusions and outlook	124
IV.A	Appendix	126
IV.A.1	Cost function as least squares norm	126
IV.A.2	Inverse square root of <i>a priori</i> covariance matrix	127
IV.A.3	Limit for perfect spatial-temporal coupling	129
IV.A.4	Sparse matrix formulation	133
IV.A.5	Further notes on implementation	134
	Acknowledgements	134
V	Retrieval error analysis	135
V.1	Introduction	136
V.2	Notation and strategy of retrieval error analysis	138
V.2.1	Basic terminology	138
V.2.2	Error measures for single-spectrum retrieval	139
V.2.3	Scaling properties of error measures for multi-spectrum retrieval	142
V.3	Parameters and reference spectra	143
V.3.1	Forward model	145
V.3.2	Surface emissivity	145
V.3.3	Deep atmospheric temperature field	146
V.3.4	Minor gases	147
V.3.5	Clouds	147
V.3.6	CO ₂ opacity correction	148
V.3.7	Surface elevation	149
V.3.8	Reference spectra	150
V.4	Results	150
V.4.1	Spectral ranges and auxiliary parameters	150
V.4.2	Total cloud factor from 1.31 μm peak	151
V.4.3	Three cloud modes from 1.295–2.300 μm	153
V.4.4	Cloud modes 2' and 3 as auxiliary parameters	153
V.4.5	Cloud modes 2, 2', and 3 from 1.00–2.30 μm	153
V.4.6	Other reference spectra	156
V.5	Summary and conclusion	158
	Acknowledgements	160

VI	Multi-spectrum retrieval of Venus IR surface emissivity maps	161
VI.1	Introduction	162
VI.2	Data selection, forward model, and multi-spectrum retrieval	165
VI.2.1	Data selection, calibration, and preprocessing	165
VI.2.2	Forward model	167
VI.2.3	General remarks on multi-spectrum retrieval and renormalization	169
VI.2.4	Retrieval pipeline	172
VI.3	Renormalized emissivity maps at Themis Regio	174
VI.4	Retrieval errors and reference emissivity	176
VI.4.1	Retrieval errors determined from synthetic spectra	176
VI.4.2	Measurement Selection Tests and Parameter Modification Tests	178
VI.4.3	Measurement Selection Tests	179
VI.4.4	Parameter Modification Tests	180
VI.4.5	Reference emissivity	184
VI.5	Discussion	186
VI.6	Summary and conclusion	189
VI.A	Appendix - Supplementary material	192
VI.A.1	Utilized data cubes	192
VI.A.2	Mathematical model	192
VI.A.2.1	Renormalization and variance	192
VI.A.2.2	First order model	194
VI.A.2.3	Measurement Selection Tests	195
VI.A.2.4	Parameter Modification Tests	197
VI.A.3	Wavelength of first spectral band and spectral FWHM	199
VI.A.4	Additional figures	200
	Acknowledgements	202
VII	Discussion, summary, and outlook	203
VII.1	Discussion	203
VII.2	Summary	209
VII.3	Outlook	210
	Bibliography	213
	Selbstständigkeitserklärung	227

List of Figures

II.1	Measured VIRTIS-M-IR day- and nightside spectra.	26
II.2	Nightside spectra from Fig. II.1 in the spectral range studied in this work.	26
II.3	Images of VIRTIS-M-IR cube VI0320_02.	27
II.4	Wavenumbers and lines strengths of allowed transitions of CO ₂	36
II.5	Line shapes.	38
II.6	Line shapes in the far wings.	39
II.7	Temperature and pressure altitude profiles at various latitudes.	42
II.8	Weighted absorption cross sections for gaseous constituents.	42
II.9	Initial altitude distributions of gaseous constituents.	43
II.10	Wavelength dependence of complex refractive index for different solutions of H ₂ SO ₄	46
II.11	Wavelength dependencies of extinction and scattering efficiencies and first phase function moment for two examples of a single spherical droplet.	46
II.12	Particle size distributions for the four cloud modes.	47
II.13	Altitude profiles of the standard model cloud particle densities for the four cloud modes.	48
II.14	Optical properties for cloud mode 3 at 75% H ₂ SO ₄ concentration.	50
II.15	Further cloud optical properties.	51
II.16	Altitude profiles of various optical parameters for standard gas and cloud model.	54
II.17	Venus' surface topography map and usable VIRTIS-M-IR data coverage.	56
II.18	Monochromatic synthetic nightside and dayside spectra and convolution with VIRTIS-M-IR instrumental response function.	57
II.19	Zoom of the nightside spectrum shown in Fig. II.18. Synthetic nightside radiance spectrum when different atmospheric properties are not taken into account.	58
II.20	Monochromatic Jacobians in the 1.74 μm window. Temperature weighting functions.	58
II.21	Temperature weighting function spectrum.	60
II.22	Weighting function spectra for minor gases.	61
II.23	Weighting function spectra for cloud modes.	62
II.24	Example nightside VIRTIS-M-IR measurements and best MSR fits.	66
III.1	Flow of the detector responsivity analysis.	72
III.2	Instrument transfer function for two different samples.	74
III.3	Even-odd effect for a dayside spectrum.	74
III.4	Sample homogenization: sample direction.	77
III.5	Sample homogenization: band direction.	77
III.6	Responsivity adjustment at 1.0–1.3 μm.	78
III.7	The EO scatterplots and the derived reference curves.	82
III.8	Even-odd effect for a nightside spectrum.	83
III.9	Straylight removal.	87
III.10	SO ₂ and cloud column factor for different spatial-temporal correlations.	92
III.11	Constant and non-constant continuum and resulting simulations in the 2.3 μm window.	94
III.12	Comparison of new and old data calibration and preprocessing on the resulting spectral structure.	95

III.13	Surface topography for the old and new (unblurred and blurred) database.	95
III.14	Relative column densities of CO and SO ₂ and the impact of the new calibration and pre-processing pipeline on the retrieval results.	98
III.15	Surface emissivity at 1.02 μm and the impact of the new calibration and preprocessing pipeline on the retrieval result.	100
IV.1	Comparison of various correlation functions.	111
IV.2	Synthetic radiance spectrum and Jacobians (1.0–2.5 μm) at VIRTIS-M-IR resolution. . .	118
IV.3	Comparison of 'true' cloud mode column factors with retrieved values for different <i>a priori</i> correlation lengths.	120
IV.4	Comparison of 'true' 1.02 μm-surface emissivities with retrieved values for different regularization models.	122
IV.5	Detector sample dependence of 'true' and retrieved values for FWHM of instrumental response function, 1.18 μm continuum parameter, and least-squares norms of residuals. . .	122
V.1	Correlation function f_d in comparison to a simple exponential correlation function. . . .	140
V.2	Synthetic radiance spectrum and various Jacobians.	144
V.3	Modified deep atmospheric temperature altitude profiles.	146
V.4	Synthetic reference spectra for different scenarios.	150
V.5	Retrieved surface emissivities for variation of selected external parameters.	154
VI.1	Removal of trends with topography and latitude for the retrieved 1.02 μm emissivity map of Themis Regio.	175
VI.2	Scatterplots illustrating the trends with topography and latitude in the raw retrieved emissivity maps.	175
VI.3	Renormalized emissivity maps of Themis Regio.	176
VI.4	Example maps for MSTs and PMTs at 1.02 μm.	180
VI.5	Dependence of emissivity fluctuations on their raw mean value.	185
VI.6	Renormalized emissivities and double standard deviation errors at 280.26°E, 42.44°S. . .	188
VI.A.1	Dependence of wavelength λ_1^s of first spectral band on detector sample and temperature. .	199
VI.A.2	Dependence of spectral FWHM on detector sample and temperature.	199
VI.A.3	Removal of trends with topography and latitude for the retrieved 1.10 μm emissivity map of Themis Regio.	200
VI.A.4	Removal of trends with topography and latitude for the retrieved 1.18 μm emissivity map of Themis Regio.	201
VI.A.5	Example maps for MSTs and PMTs at 1.10 μm.	201
VI.A.6	Example maps for MSTs and PMTs at 1.18 μm.	202

List of Tables

II.1	Identification and properties of the measurements depicted in Fig. II.1.	26
II.2	Properties of the images depicted in Fig. II.3.	27
II.3	Parameters for the standard cloud model.	48
II.4	Identification and properties of the measurements and MSR fits depicted in Fig. II.24	66
V.1	Summary of discussed external parameters.	144
V.2	Cloud parameters for default reference model.	147
V.3	Surface emissivity retrieval error and noise measures, when the total cloud factor is retrieved as auxiliary parameter from the 1.31 μm peak.	152
V.4	Surface emissivity error and noise measures for the pipeline in Section V.4.5. Scenario 1, 100 noise repetitions.	155
V.5	Emissivity error and noise measures for different scenarios for the pipeline in Section V.4.5 .	157
VI.1	Initial cloud parameters.	169
VI.2	<i>A priori</i> data for retrieval parameters.	173
VI.3	Results from error analysis with synthetic spectra.	178
VI.4	Results of MSTs and PMTs.	181
VI.5	Summary of MST and PMT results.	185

Nomenclature

CCS	Compressed column format
CDSDB	Carbon dioxide spectroscopic databank
CIA	Collisional induced absorption
COO	Coordinate list format
DISORT	Discrete ordinate radiative transfer
DLR	Deutsches Zentrum für Luft- und Raumfahrt (German Aerospace center)
EO	Even-odd
ESA	European Space Agency
FWHM	Full width at half maximum
HITEMP	High-temperature molecular spectroscopic database
HITRAN	High-resolution transmission molecular absorption database
IR	Infrared part of the electromagnetic spectrum
ITF	Instrument transfer function
lbl	Line-by-line
LIDORT	Linearized discrete ordinate radiative transfer
linear	May also mean 'affinely linear'
log	Natural logarithm, inverse to exp
LTE	Local thermodynamic equilibrium
\mathbf{M}^{-T}	Inverse of transpose of matrix \mathbf{M} , $(\mathbf{M}^{-1})^T = (\mathbf{M}^T)^{-1} =: \mathbf{M}^{-T}$
MSR	Multi-spectrum retrieval algorithm
MST	Measurement selection test
PCA	Principal component analysis
<i>pdf</i>	Probability distribution function
PMT	Parameter modification test
rhs.	Right hand side (of an equation)
RMSD	Root mean square deviation
RTE	Radiative transfer equation
SRMSD	Scaled root mean square deviation
T_{exp}	Exposure time of a single VIRTIS-M frame
VEX	Venus Express (ESA mission, name of corresponding space probe)
VIRA	Venus international reference atmosphere
VIRTIS	Visible and infrared thermal imaging spectrometer
VIRTIS-H	High resolution channel of VIRTIS
VIRTIS-M	Mapping channel of VIRTIS
VIRTIS-M-IR	Infrared mapping channel of VIRTIS
VIRTIS-M-VIS	Visible mapping channel of VIRTIS
VIS	Visible part of the electromagnetic spectrum

Note: Vectors and matrices are typed in bold in contrast to scalars

Chapter I

Introduction

Venus is often called the 'sister planet' of Earth. It is the closest planet to Earth, and it is in many respects the most Earth-like planet in the solar system. Both planets are mainly composed of silicate rock and metal, have a solid surface, and possess a significant atmosphere. A comparison of some of the most apparent key data ([Williams, 2013](#)) shows that the two planets have similar equatorial radii (Venus: 6051.8 km vs. Earth: 6378.1 km) and masses ($4.87 \cdot 10^{24}$ vs. $5.97 \cdot 10^{24}$ kg) and, therefore, mean densities (5.24 vs. 5.51 g/cm^3) and equatorial surface gravities (surface accelerations not including rotational effects, 8.87 vs. 9.80 m/s^2). On the other hand, the distances from Sun (semimajor axis $108.2 \cdot 10^6$ vs. $149.6 \cdot 10^6$ km) and the sidereal rotation periods (5832.5 h retrograde vs. 23.9 h prograde) are quite different.

However, Mars is currently much better studied than Earth's sister planet. One reason is that Venus' atmosphere at its surface is so dense, hot, and hostile to any scientific equipment that exploration is very difficult to perform. The surface temperature corresponds to about 735 K (462 °C), and the atmospheric pressure at the surface amounts to about 9.2 MPa (92 bar) according to the Venus International Reference Atmosphere VIRA ([Seiff et al., 1985](#)) and referred to an elevation¹ of 0 km. On Earth, this corresponds to a water pressure at almost 1 km below sea level and translates via the Ideal Gas Law to a Venusian atmospheric density at the surface of about 6.5% of the density of water. Venus' atmosphere mainly consists of CO₂ (96.5% by weight), N₂ (3.5%), and a number of trace gases. Moreover, thick sulfuric acid clouds shroud the deeper atmospheric levels and the surface from an extra-planetary observer in the visible range of the electromagnetic spectrum.

Nevertheless, Venus is a very interesting object of research. It is the most obvious candidate for comparative studies of geologic and atmospheric properties of Earth-like planets and their evolution, and there are many open questions and exciting mysteries. For instance, a runaway greenhouse effect can be observed with all its implications. Moreover, the atmosphere near the cloud top rotates much faster around the planet (≈ 4 Earth-days) than the planet itself (≈ 243 Earth-days), which is called 'atmospheric super-rotation' and is yet to be understood ([Lebonnois et al., 2010b](#)). A still unknown constituent in the upper cloud region leads to distinct absorption features in the ultraviolet spectral range ('unknown UV absorber', [Markiewicz et al., 2014](#)). Furthermore, although Venus' bulk data are very similar to Earth's, the internal processes seem to be very different. For example, there seems to be no significant intrinsic magnetic field ([Russell et al., 1980](#)). Moreover, plate tectonics seems to be absent, but almost the entire surface underwent a catastrophic event, which led to an almost complete surface re-formation in the order of half a billion years ago ('global re-surfacing event', [Basilevsky et al., 1997](#)). There are signs of ongoing volcanism ([Smrekar et al., 2010](#)), and it is conceivable that Venus had oceans once ([Donahue et al., 1982](#)). Improved insights into such phenomena can even yield a better understanding of Earth and can contribute to explain, whether or why Earth is a special terrestrial planet, or how likely it could be to discover a truly Earth-like extrasolar planet.

This work intends to smooth the way that can lead to answers to those questions. Venus' surface composition and texture are not well known. A rudimentary categorization of them could greatly help to better understand the planet's geology and its evolution and thus even the global re-surfacing event. It has been speculated that some of the original surface survived the re-surfacing ([Basilevsky et al., 1997](#)). Identification of such areas is therefore pivotal to the target selection for future lander missions to Venus, because *in situ* measurements at these sites offer the opportunity to find out, what Venus was like before this unique event.

¹For Venus, surface elevations and altitudes within the atmosphere always refer to the planetary mean radius of 6051.8 km.

I.1 Surface emissivity in the infrared

This section motivates the importance of surface emissivity data in the infrared.

There are different approaches to obtain information about composition, texture, and grain size of Venus' surface material. The most direct method is to acquire *in situ* measurements. But this is difficult in view of the extreme environmental conditions on Venus. The first attempts to land probes on the surface failed, because these harsh conditions could not be anticipated, and the probes succumbed to the atmospheric pressure and temperature (e.g. Venera 4–6, Williams, 2015). Later missions (Venera 8–10, 13, 14, and Vega 1 and 2) succeeded to measure the surface composition at seven different landing sites, and the respective elemental compositions were interpreted to correspond to surface materials like granite, rhyolite, alkali basalt, tholeiitic basalt, olivine, and others (see overview by Abdrakhimov and Basilevsky, 2002).

However, *in situ* measurements can only provide quite localized information. To obtain a more global picture, Venus' surface has to be explored by remote sensing techniques. These are indirect methods that do not rely on a physical contact between target and measuring instrument. Rather, they require an intermediate information carrier that has to be able to traverse the medium between target and measuring instrument. One widely used example is remote sensing by sound waves traveling in gaseous, liquid, or solid media. In case of Venus, most remote sensing so far was based on electromagnetic waves as information carrier with the measuring instrument located in space or on Earth.

But this method faces the difficulty that Venus' atmosphere is extremely opaque over wide ranges of the electromagnetic spectrum. The radar instrument aboard the Magellan spacecraft relied on microwave radiation (wavelength 12.6 cm, Pettengill et al., 1991) to penetrate the atmospheric gases and clouds. The surface was observed by both passive and active remote sensing. In passive mode, the instrument recorded radiation that was emitted by the target, whereas in active mode, the radiation was first emitted from the instrument, and the radiation reflected at the target was measured. The Magellan mission provided nearly-global high resolution maps of surface topography and slope as well as of microwave emissivity and reflectivity (Pettengill et al., 1991; Ford and Pettengill, 1992; Rappaport et al., 1999) and the gravity field (Konopliv et al., 1999). These data revealed a strongly increased microwave reflectivity and decreased emissivity, respectively, of surface areas primarily located at high elevations (above 4–5 km) and point to a different surface texture there (Pettengill et al., 1992). It is unclear, whether this effect is also connected to a corresponding variation of the surface composition.

Unfortunately, microwave data alone do not suffice to constrain the surface composition, and measurements at other spectral ranges that are more diagnostic in this respect are needed in addition. Chemical composition, texture, and grain size of the surface material can affect the surface emissivity in the infrared (IR) range (see overview by Haus and Arnold, 2010). One way to improve the knowledge about surface properties is to study spatial maps of the IR surface emissivity, therefore. The wavelength at which the surface emissivity is determined is also a rough measure for the spatial scale (e.g. of penetration depth into soil) on which the measured radiation is most sensitive to surface properties. For instance, surface roughness variations observed in the infrared at 1 μm or by Magellan's radar instrument have a very different meaning and refer to scales in the order of 1 μm and 12.6 cm, respectively.

In contrast to the ultraviolet and visible ranges, where Venus' atmosphere is quite opaque, the infrared range exhibits a few narrow spectral transparency windows on Venus' nightside that probe the deep atmosphere (i.e. the atmosphere below the cloud deck, ≤ 48 km) and even the surface, compare Fig. II.1 (p. 26). Their existence was revealed by ground based observations (i.e. from Earth's surface). They are located at 1.74 and 2.3 μm (Allen and Crawford, 1984; Allen, 1987) and at 1.10, 1.18, 1.27, and 1.31 μm (Crisp et al., 1991). Additional windows were detected during spacecraft flybys and are located at 1.01 μm (Galileo NIMS, Carlson et al., 1991) and at 0.85 and 0.9 μm (Cassini VIMS, Baines et al., 2000).²

ESA's Venus Express (VEX) spacecraft (Titov et al., 2006; Svedhem et al., 2007), launched in November 2005 from Baikonur, entered a Venus orbit in April 2006. This probe was planned to explore the planet at least until October 2007, but it was only lost in January 2015. VEX was the most sophisticated mission to the planet so far. It carried seven instruments named Venus Monitoring Camera (VMC), Spectroscopy

²The windows at 1.01 and 1.27 μm are often also referred to as 1.02 and 1.28 μm windows, respectively, which is also the convention used in this work.

for Investigation of Characteristics of the Atmosphere of Venus (SPICAV), Venus Radio Science Experiment (VeRa), Analyzer of Space Plasma and Energetic Atoms (ASPERA), Magnetometer (MAG), Planetary Fourier Spectrometer (PFS, malfunctioned due to pointing mirror stuck in close position), and Visible and Infrared Thermal Imaging Spectrometer (VIRTIS). This mission was planned to enable a comprehensive investigation of Venus' atmosphere, surface, and plasma environment and proved very successful at that. The present work utilizes spectra of Venus that were acquired by the InfraRed Mapping channel of VIRTIS (VIRTIS-M-IR, 1.0–5.1 μm , [Drossart et al., 2007](#); [Piccioni et al., 2007](#)). An overview of scientific results was given by [Arnold et al. \(2012c\)](#). The instrument is introduced in Section II.1 (p. 25). VIRTIS-M-IR provided the currently only data with high spectral, spatial, and temporal resolution and coverage that are suitable for the determination of reliable IR surface emissivity information.

The Japanese Akatsuki spacecraft ([Nakamura et al., 2007](#)) failed to enter Venus orbit in 2010. If the new attempt in December 2015 proves successful, its IR1 and IR2 cameras can provide multispectral images at 0.90, 0.97, 1.01, 1.73, 2.26, and 2.32 μm that are urgently needed for surface science.

Even though on Venus' dayside, a tiny fraction of incoming infrared sunlight reaches the surface and is reflected there, the imprinted surface information is almost totally lost in the sunlight that is scattered in higher atmospheric layers. Thus, surface reflections cannot be used to derive surface data. However, on the dayside, also surface emissions are far outweighed by scattered sunlight. Hence, this work focuses on Venus' nightside. In the VIRTIS-M-IR spectral range, the nightside windows at 1.02, 1.10, and 1.18 μm allow the sounding of the surface. They are called 'surface windows', therefore. But the information is strongly obscured by the thick clouds and the atmospheric gases, and it is difficult to extract it from the measured spectra. A large part of the measured radiances at these windows originates from the thermal emissions of the surface, which depend on both surface temperature and surface emissivity. Most of the radiance variation is therefore caused by the spatially varying topography (like on Earth, it is colder in the mountains than on surrounding plains) and the absorption due to the spatially and temporally strongly varying cloud abundance. The influence of the latter can be estimated, for instance, on the basis of the spectral radiance peaks between 1.3 and 2.6 μm that originate in the deep atmosphere. One possibility to derive surface information is to use a computer program that numerically simulates the radiative transfer in Venus' atmosphere. A retrieval algorithm then identifies atmospheric and surface parameters that allow the simulation program to reproduce the measured spectra.

Only the nightside spectral IR windows located at 1.02, 1.10, 1.18 μm seem to have sufficient surface information content, given the currently available measured data. Further known IR surface windows are not sufficiently covered by measurements with a satisfactory signal to noise ratio (0.85 and 0.9 μm , this also applies to nightside VIRTIS-M-VIS/VEX measurements in the range 0.3–1.0 μm) or are not usable due to other reasons (1.28 μm , only marginally sensitive to surface emissivity, contaminated by non-LTE O_2 nightglow at 1.27 μm), and are thereby much more difficult to evaluate and not relevant for the present work.

I.2 State of research

First, since the numerical simulation of the radiative transfer in Venus' atmosphere is of special importance for the present thesis, a number of recent key contributions to this and related topics are reported. The section continues by reciting previous efforts to determine Venus surface emissivity data. Next, some background with regard to Venus' geology is recited. Finally, an account of other works that involve a multi-spectrum retrieval is given. Note that an extended introduction into radiative transfer and retrieval techniques as well as the VIRTIS-M-IR instrument is presented in Chapter II (p. 25).

I.2.1 Radiative transfer in Venus' atmosphere

Radiative transfer simulations in Venus' atmosphere have a long tradition, but it was the discovery of the IR nightside spectral windows that enabled sub-cloud remote sensing as performed by [Allen and Crawford \(1984\)](#); [Allen \(1987\)](#); [Kamp and Taylor \(1990\)](#); [Bézard et al. \(1990\)](#); [Crisp et al. \(1991\)](#); [Lecacheux et al. \(1993\)](#). The paper by [Pollack et al. \(1993\)](#) discusses many of the issues that are important for the radiative transfer simulation of Venus' nightside IR spectra. On the basis of moderate and high resolution spectra of the nightside windows at 1.10, 1.18, 1.28, 1.31, 1.74, and 2.3 μm acquired by Earth based telescopes, the

authors studied the suitability of spectral line databases available at that time. They presented cloud and gas models that are still often cited in recent papers, including the present thesis. Spectra measured from space probes augmented the possibilities of radiative transfer studies in the nightside windows that until then relied on ground based observations (Carlson et al., 1991; Baines et al., 2000).

Further ground based high resolution spectra and VIRTIS-H measurements in the 2.3 μm window were used by Marcq et al. (2005); Marcq et al. (2006, 2008) to improve the knowledge on minor gas abundances in dependence on latitude and altitude. Tsang et al. (2008a); Tsang et al. (2008b); Tsang et al. (2009); Tsang et al. (2010) used VIRTIS-M-IR/VEX spectra at 2.3 μm to derive CO abundances in dependence on latitude and also identified a possible anti-correlation between cloud thickness and sub-cloud water abundance. They applied the correlated- k method (see for instance Liou, 2002) instead of a line-by-line radiative transfer. Wilson et al. (2008) described the occurrence of anomalous clouds at the poles of Venus, which is also an obstacle in the present thesis for a potential surface emissivity retrieval in the polar regions. Wilson et al. (2009) presented the first radiative transfer analysis of two small radiance peaks (two orders of magnitude less bright than the 1.74 and 2.3 μm peaks) located at 1.51 and 1.55 μm and mainly originating at around 20–35 km. Along with two other subsidiary peaks at 1.78 and 1.82 μm , these peaks were discovered by Erard et al. (2009) in the frame of a multivariate statistical analysis (an independent component analysis) of VIRTIS-M-IR measurements. Barstow et al. (2012) derived cloud properties from VIRTIS-M-IR data in the 1.74 and 2.3 μm windows and found a systematic latitudinal variation of the cloud base altitude as well as an increased sulfuric acid concentration of the cloud droplets in regions of thicker clouds. Bézard et al. (2009) used VIRTIS-M-IR measurements of the 1.18 μm peak to constrain the H₂O abundance near the surface. A subsequent study by Bézard et al. (2011) on the basis of the spectrally high resolution measurements of the 1.10 and the 1.18 μm peaks by SPICAV/VEX refined these results, revealed missing spectral lines in the CDS database (Tashkun and Perevalov, 2008), and led to a new estimate of the continuum opacity for these windows. Their results provided strong evidence for a uniform H₂O altitude profile below 40 km. Ignatiev et al. (2009) retrieved the altitude of dayside cloud tops from the (dayside) CO₂ absorption band at 1.6 μm . Initially using a relaxation method (Twomey et al., 1977) and later a Bayesian retrieval, Grassi et al. (2008); Grassi et al. (2010, 2014) derived, as Haus et al. (2013, 2014) also did, mesospheric temperature altitude profiles from VIRTIS-M-IR nightside measurements of the 4.3 μm CO₂ absorption band, and also confirmed earlier results with respect to cloud top altitude and CO abundance. Using VIRTIS-M-IR and PMV/Venera-15 (Moroz et al., 1985) measurements, Haus et al. (2013, 2014, 2015a) additionally derived cloud and minor gas abundances in dependence on latitude, time, and local time for both hemispheres, applying the full radiative transfer model for Venus studies described in detail by Haus and Arnold (2010).

A sophisticated numerical general circulation model of Venus' atmosphere was used by Lebonnois et al. (2010b) to study the atmospheric superrotation, which is reproduced above roughly 40 km but not at lower altitudes. Haus et al. (2015b) computed detailed radiative heating and cooling rates in the middle and lower atmosphere of Venus, the results of which can help to improve general circulation models. Tran et al. (2011); Stefani et al. (2013); Snels et al. (2014) were able to directly measure CO₂ absorption properties relevant for Venus' surface windows by using the cavity ring down technique. The experimental conditions do not yet quite reach surface pressures and temperatures, but this line of research is very promising and relevant for possible future retrievals of absolute values of surface emissivities.

I.2.2 Determination of surface information

The already mentioned multivariate statistical analysis by Erard et al. (2009), which did not include radiative transfer simulations, clearly isolated the radiance variations that were due to surface topography. The variations were, in cases of exceptionally good conditions, consistent with an achievable horizontal surface resolution of only 35 km, whereas in more generic cases a horizontal full-width-at-half-maximum (FWHM) of about 100 km can be expected (Hashimoto and Imamura, 2001; Moroz, 2002; Basilevsky et al., 2012). Moreover, there were indications of an occasional layer of high opacity close to the surface in the low lying regions of the planet. This corroborated the findings by Grieger et al. (2004) who analyzed data from the Venera 13 and 14 descent measurements and observed a pronounced layer of increased extinction at an altitude of 1–2 km above the surface. This effect is reencountered in the fourth paper of this thesis.

As it was recited by [Kappel et al. \(2016\)](#), it was demonstrated by [Helbert et al. \(2008\)](#); [Müller et al. \(2008\)](#) that surface information at $1.02\ \mu\text{m}$ can be extracted to some extent from VIRTIS-M-IR measurements in the form of the time averaged so-called thermal flux anomaly. This is the thermal flux from Venus' surface that is not due to topography related surface temperature. It is correlated to surface emissivity. The VIRTIS-M-IR measurements were preprocessed by removing the straylight, and the influence of the viewing geometry (limb-darkening) was removed by a semi-empirical relation. The authors applied further semi-empirical approaches to de-cloud the $1.02\ \mu\text{m}$ VIRTIS-M-IR radiances, with the small surface-unaffected $1.31\ \mu\text{m}$ radiance peak as reference for cloud absorption, and to remove the influence of surface topography. The de-clouding strategy was based on the two-stream approximation of radiative transfer that was used by [Hashimoto and Sugita \(2003\)](#) to estimate the visibility of emissivity contrasts from space and who aimed at simplifying an analogous approach by [Moroz \(2002\)](#). The method by [Helbert et al. \(2008\)](#); [Müller et al. \(2008\)](#) utilizes only two spectral bands and is computationally very fast. The authors were therefore able to process all suitable VIRTIS-M-IR nightside spectra. Based on these results and on gravity field data, [Smrekar et al. \(2010\)](#) were able to identify candidates for recent hotspot volcanism. By correlating the thermal flux anomalies and topography data, [Müller et al. \(2012b\)](#) have also identified a possible variation in Venus' rotation period that may be due to long-term changes in the atmospheric circulation. Furthermore, constraints on the planet's volcanism rate ([Müller et al., 2012a](#)) were derived. However, the meaning of the semi-empirical flux anomaly map at $1.02\ \mu\text{m}$ with respect to surface emissivity as well as its reliability are not entirely clear in this otherwise very successful approach, and data at 1.10 and $1.18\ \mu\text{m}$ were not provided.

A different line of research utilized measurements by the VMC instrument aboard VEX. VMC took images of Venus in four narrow band filters centered at 365, 513, 965, and 1000 nm, respectively ([Markiewicz et al., 2007](#)). The images at $1\ \mu\text{m}$ were used by [Shalygin et al. \(2012\)](#); [Basilevsky et al. \(2012\)](#) to search for surface emissivity anomalies. The authors identified images that are relatively free from cloud opacity variations by observing the ratio of images from two consecutive VEX orbits, i.e. separated by about one Earth day. For this purpose, the images were transformed into the same map projection. The absence of contrast in the ratio indicated an absence of cloud opacity changes from one orbit to another. This absence of temporal cloud variations on the scale of 24 h was in turn interpreted to translate to an absence of spatial cloud variations on the scale of 1000 km, motivated by the strong winds in Venus' atmosphere. Remaining localized variations in the ratios were interpreted as spatial or temporal emissivity variations. The authors estimated the surface emissivities that correspond to the observed ratio variations according to a two-stream approximation and gave an emissivity error estimate of 10%–20% based on observed cloud opacity variations of about 10%. They also simulated the atmospheric blurring effect using the Monte Carlo method, taking into account multiple scattering by gases and clouds. This way, they estimated the detectability of artificially placed lava flows exhibiting different surface temperatures and areas with the result that a flow at 1000 K covering an area of 4–5 km² should be visible from space at $1\ \mu\text{m}$, regardless of surface elevation.

[Meadows and Crisp \(1996\)](#) acquired ground based spectrally resolved Venus nightside images in the range 0.9–1.33 μm . To remove the influence of the spatially varying cloud abundance, they divided the images at given wavelengths by the images at $1.31\ \mu\text{m}$. A full radiative transfer simulation model was then applied to compute synthetic radiance maps on the basis of the surface topography determined by the radar altimeter aboard the Pioneer Venus Orbiter ([Pettengill et al., 1980](#)). At $1.18\ \mu\text{m}$, they finally formed the ratio of the de-clouded ground based radiance maps and the synthetic maps to infer surface emissivity data, but they did not succeed in detecting emissivity variations in excess of 10%.

By using a full radiative transfer model, [Hashimoto et al. \(2008\)](#) analyzed a spectrally resolved image of Venus' nightside that was recorded by Galileo NIMS ([Carlson et al., 1991](#)). First, they preprocessed the spectra by removing the straylight and the effect of limb-darkening. They then determined the cloud mode 2' and 3 abundances (see Chapter II (p. 25) for a description of the cloud modes) using the 1.74 and $2.3\ \mu\text{m}$ peaks. Taking these mode abundances into account, they simulated the radiances at $1.18\ \mu\text{m}$ for different surface emissivities. This relation was used to infer the surface emissivities from the preprocessed measured radiances. They pointed out that this method was prone to large errors and in fact obtained values far outside the physically valid emissivity domain (the interval $[0, 1]$), and their inferred emissivity map showed residual correlations to the cloud mode abundances. Their results suggested that the majority of lowlands likely has higher emissivity at $1.18\ \mu\text{m}$ compared to the majority of highlands. The authors stated that the emissivity difference between low- and highlands would disappear, when the temperature lapse rate of the lowermost atmosphere

were increased by about 1 K/km, but this would imply a statically unstable atmospheric stratification. They also argued that the results indicated that horizontal deep atmospheric temperature variations were in the order of less than 2 K.

To identify surface emissivity anomalies, [Arnold et al. \(2008\)](#) developed a quick-look method based on radiance ratios that was corroborated by radiative transfer simulations. A subsequent paper presented a detailed description of a radiative transfer simulation model developed for Venus studies and reported first retrieved surface emissivities at 1.02 μm ([Haus and Arnold, 2010](#)). The authors noted that these emissivities tended to decrease with increasing surface elevation in agreement with [Hashimoto et al. \(2008\)](#), but the results were mentioned to have a preliminary character. It follows from the present work that these retrieved emissivities were not sufficiently reliable to allow geologic interpretation due to strong interferences from other parameters.

At this point, it was an open question whether surface emissivity data at all three relevant surface windows (1.02, 1.10, and 1.18 μm) can be determined on the basis of a full radiative transfer simulation program in combination with a retrieval algorithm that treats surface emissivities as intrinsic retrieval parameters, exploits a large part of the VIRTIS-M-IR spectra's information content, and respects *a priori* information and physical constraints. Moreover, a stringent quantification of the result's reliability was desirable.

I.2.3 Venus' geology

[Ivanov and Head \(2011\)](#) gave a detailed description of the geologic units into which the surface of Venus can be divided. Their work was mostly based on Magellan radar image and altimetry data. Apart from impact craters and crater outflows, twelve geologic units were defined, exclusively based on their morphology: tessera, densely lineated plains, ridged plains, mountain belts, groove belts, shield plains, lower and upper regional plains, shield clusters, smooth plains, lobate plains, and rift zones. For each unit, a hypsogram, i.e. a histogram of the surface elevation, was shown as well as the areal distribution, and the covered surface area was given. A global map of the geologic units was presented. By globally correlating the stratigraphic relationships (embayment, superposition, crosscutting) between the units, the authors proposed a relative age scenario among the units constructing the stratigraphic column. This relative chronology shows for instance that the tessera, one of the most tectonically deformed type of terrain on Venus, is possibly the oldest unit. It may be the relic of an old plate tectonics preceding the already mentioned global resurfacing event and therefore forms, as the authors put it, a "probable 'window' into the geological past of Venus". Tesserae cover about 7.3% of the mapped area, their surface elevation is distinctly above average. To shortly cite the conclusions (3–5) of this paper, the observable geologic history of Venus is subdivided into three distinctive phases. The earliest phase involved intense deformation and building of regions of thicker crust (tessera). This was followed by the Guineverian Period. Tectonized materials characterize the first part of the Guineverian. The second part involved global emplacement of vast plains. A period of global wrinkle ridge formation largely followed the emplacement of these plains. The third phase (Atlian Period) involved formation of prominent rift zones and fields of lava flows unmodified by wrinkle ridges. In places, the Atlian volcanic activity, which may continue to the present, formed small occurrences of smooth plains and clusters of small volcanoes. About 70% of the exposed surface of Venus was resurfaced during the Guineverian Period and only about 16% during the Atlian Period. Estimates of model absolute ages suggest that the Atlian Period was about twice as long as the Guineverian. [Basilevsky and Head \(1998, 2000\)](#) and [Basilevsky et al. \(1997\)](#) proposed that the major geologic units are generally globally time-correlative over the entire planet. On the other hand, [Guest and Stofan \(1999\)](#) proposed that geological units are diachronous and not time-correlative, forming locally as a series of units representing a sort of 'Wilson Cycle' of activity that occurred at different times in different places around the globe. [Ivanov and Head \(2011\)](#) argue in favor of the former hypothesis, as they found the stratigraphic sequence to be synchronous all over the planet.

The following paragraph cites the review article by [Basilevsky and Head \(2003\)](#). The authors discussed that there is much evidence against plate tectonics operating on Venus within the observed morphological record. The hypsogram of Venus is unimodal, thus being distinctly different from the bimodal distribution of the Earth. The latter is considered to be due to the presence of two types of crustal material: basaltic crust of the oceanic floor and granitic crust of the continents. The unimodal histogram of Venus is considered by some researchers as an indication of the predominance of one type of crustal material, basalt ([Sharpton and Head, 1985](#)). The surface morphology of Venus is dominated by the signatures of basaltic, mostly plains-forming

volcanism and globally widespread compressional and extensional tectonic deformation. Several hundred distinctive specific volcanic-tectonic structures, oval to circular features typically 100–300 km in diameter, called 'coronae' were observed on the surface of Venus (Barsukov et al., 1986). They are considered to form as a result of the rising of hot material in the mantle (Stofan et al., 1997). For many coronae, there is evidence that they started to form in early pre-regional-plains time and continued their activity during and after the emplacement of regional plains. More than 960 impact craters from 1.5 to 270 km in diameter have been identified (Schaber et al., 1992; Herrick et al., 1997). Their size frequency distribution is controlled by the screening effect of the massive Venusian atmosphere, and their spatial distribution is indistinguishable from a random one. The crater size distribution can be used to estimate the mean absolute age of the surface, which was discussed to be about 500–800 million years (McKinnon et al., 1997). Signatures of aeolian erosion and deposition are common on Venus. They include radar-dark parabolas (thought to be mantles of fine debris, primarily originating from impact crater ejecta whose deposition was strongly controlled by wind) and wind streaks (typically originating from accumulation or erosion of material on the lee side of topographic features). The data from Soviet Venera and Vega spacecraft proved that the surface material of Venus is basaltic (tholeiitic at the Venera 9, 10, 14 and Vega 1, 2 landing sites, alkaline at the Venera 8 and 13 sites, Barsukov et al., 1992; Surkov, 1997), so basalts are considered the major component of the crust of Venus although the presence of geochemically weathered materials can be expected (Fegley et al., 1997). The composition of tessera terrain material is unknown. Some researchers suggest it has a basaltic composition. Others believe that tesserae may be made of more feldsparic material resembling Moon's anorthosites or granites of Earth (Nikolaeva et al., 1992). The mineral composition of the surface material has not yet been determined by any conclusive technique. Thermodynamic calculations show that basaltic materials of Venus' surface should react with atmospheric gases to form magnetite, haematite (mostly in the lowlands), quartz, magnesite, anhydrite, pyrite (mostly in the highlands), enstatite and albite (Zolotov and Volkov, 1992; Fegley et al., 1997).

Basilevsky et al. (2012) have discussed the 1 μm emissivity of materials that are potentially present at Venus' surface based on reflectance spectra from the ASTER spectral library (Baldrige et al., 2009) and the Brown University Keck/NASA RELAB Spectra catalog (Pieters et al., 2015). They used Kirchhoff's law to estimate the 1 μm emissivity e from the 1 μm reflectivity r as $e = 1 - r$, regardless of the geometry type (bidirectional, hemispherical, biconical). The authors pointed out that, hence, their quantitative statements should be treated with caution, but trends are qualitatively reliable. They discussed that 1 μm emissivity is a function of a number of parameters including particle size and surface texture at micron to millimeter scale, temperature, and mineralogical composition. The latter is interesting for a search for geological features and terrains whose chemical/mineralogical composition may be different from that of dominating basalts. Surface materials on Venus are most likely involved in possibly strong altitude-dependent chemical interaction with atmospheric gases, leading to chemical weathering. A degree of possible chemical weathering on Venus is unknown, but its effect should be most prominent for the uppermost surface layer and thus potentially could influence the near-infrared emission. For silicates and common rocks, whose optical properties at 1 μm are controlled by volume scattering, emissivities at 1 μm typically decrease with decreasing particle size. The opposite trend or the lack of particle size dependence are typical of highly absorbing materials, e.g., magnetite and sulfides. The average particle size at a given surface target can change due to near-surface winds. On higher elevations, wind velocity should be higher.

Based on VMC images at 1 μm , Basilevsky et al. (2012) found that the 1 μm emissivity of tessera surface material in a certain example area is lower than that of relatively fresh supposedly basaltic lavas of plains and volcanic edifices. They argued that this is consistent with the hypothesis that the tessera material is not basaltic and may be felsic, and that these results are in agreement with the results of Helbert et al. (2008); Müller et al. (2008); Hashimoto et al. (2008); Gilmore et al. (2011) and with early suggestions of Nikolaeva et al. (1992). Basilevsky et al. (2012) concluded that, if the felsic nature of Venusian tesserae were confirmed by further studies, this might have important implications for geochemical environments in the early history of Venus, indirectly supporting a hypothesis of a water-rich early Venus (e.g. Kasting et al., 1984; Kasting, 1988; Grinspoon and Bullock, 2003).

Smrekar et al. (2010) studied lava flows at so-called hot spots on Venus, defined as areas with volcanism, broad topographic rises, and large positive gravity anomalies suggesting mantle plumes at depth. At these hot spots, they investigated thermal flux anomalies of up to 12% at 1 μm that were identified by Müller et al. (2008); Helbert et al. (2008) on the base of VIRTIS-M-IR data. The anomalies were interpreted as a lack of

surface weathering. The authors estimated the flows to be younger than 2.5 million years and probably much younger, likely 250,000 years or less, indicating that Venus is actively resurfacing.

I.2.4 Multi-spectrum retrieval algorithms

The multi-spectrum retrieval algorithm MSR was developed by Kappel et al. (2010a,b, 2012b,c); Arnold et al. (2012a,b, 2013); Kappel (2014); Kappel et al. (2015, 2016) (announced by Haus and Arnold, 2010) for the retrieval of atmospheric, surface, and instrumental data from a set of spectra that is regarded as a single meta-measurement of these parameters. This way, not only error information on the spectra and *a priori* mean values and standard deviations of the retrieval parameters can be taken into account, but also inter-measurement *a priori* information like spatial-temporal correlations between the retrieval parameters. One aspect of this approach is the retrieval of parameters that are common to the utilized set of spectra.

Certain forms of a multi-spectrum retrieval have been described in the literature, however with other aims and capabilities. Carlotti (1988) developed the 'global-fit' algorithm for the retrieval of concentration profiles of atmospheric constituents from a sequence of spectra that scan the limb of Earth's atmosphere. For this purpose, the algorithm minimizes the sum of the squared Euclidean norms of the residuals between the utilized measurements and the corresponding simulations. It considers neither *a priori* nor error information. Hence, the retrieval cost function corresponds to the one in Eq. (IV.1) (p. 107) for MSR but without the term that contains \mathbf{S}_A^{-1} , and where \mathbf{S}_E^{-1} is the identity matrix. The same cost function was used by Benner et al. (1995) to determine spectroscopic parameters from high resolution infrared laboratory molecular spectra and also by others (Plateaux et al., 2001). An improved method was used for instance by Carlotti and Carli (1994); Dinelli et al. (2004); Carlotti et al. (2006); Niro et al. (2007) who explicitly considered \mathbf{S}_E^{-1} in comparison to the global-fit cost function. With respect to the retrieval regularization, these methods can therefore be regarded as special cases of MSR.

The algorithm of Ungermann et al. (2010a,b, 2011) has a different character. The authors treated three-dimensional tomographic retrieval problems where the lines of sight of the airborne measuring instrument repeatedly scan a certain atmospheric volume from many different directions. The aim was to retrieve three-dimensional atmospheric parameter fields in that volume. Their retrieval cost function was the same as in Eq. (IV.1) (p. 107), but there were formally no common parameters, i.e. $\mathbf{X} = (\mathbf{x}_1, \dots, \mathbf{x}_r)$ (without \mathbf{x}_C). They did (in their final version) not construct the *a priori* covariance matrix \mathbf{S}_A but directly the matrix \mathbf{S}_A^{-1} . This matrix was such that, together with the *a priori* mean value vector, it regularized deviations of the retrieved data from that vector as well as deviations of the first order partial derivatives of the retrieved data from the first order partial derivatives of the *a priori* mean value data. This way, the authors had no control over explicit correlation lengths or times or local correlations in contrast to MSR, and \mathbf{S}_A^{-1} had the character of a mere tuning parameter. They used a variant of the Levenberg-Marquardt algorithm in combination with the conjugate gradient method to minimize the cost function and formulated their retrieval algorithm in terms of sparse matrices, which allowed for retrievals of several hundred thousands of measurements and atmospheric constituents. MSR is also formulated in terms of sparse matrices. An early version of MSR used Levenberg-Marquardt (see Section II.3.2 (p. 63)), too, but the advantages of the trust region method (see Section II.3.3 (p. 63)) convinced the present author to switch to that method. In the future, the performance of MSR might be improved for extremely large retrieval problems by switching back to Levenberg-Marquardt in combination with the conjugate gradient method, but it has to be tested whether this outweighs the advantages of the trust region algorithm. However, due to its use of the Kronecker product construction, the overhead of MSR currently is small compared to the radiative transfer simulations, and this switch makes sense only when the problem sizes seriously increase.

I.3 Main goal of thesis

The main goal of the present thesis is the derivation of IR surface emissivity data maps at the three accessible spectral transparency windows located at 1.02, 1.10, and 1.18 μm from Venus nightside radiance spectra acquired by VIRTIS-M-IR.

From the beginning, it was the ambition to solve this task on the basis of a numerical radiative transfer simulation by applying a suitable retrieval algorithm that respects appropriate *a priori* information on the parameters to be retrieved. However, already the first attempts revealed that a single-spectrum regularization that takes into account *a priori* mean values and standard deviations of the retrieval parameters would not be sufficient to obtain useful results. It was therefore planned to develop a multi-spectrum retrieval algorithm that would allow for a better retrieval regularization. But this algorithm was first contrived to only regularize spatial and temporal distributions of the abundances of clouds and trace gases as well as to retrieve a wavelength dependent CO₂ opacity correction as parameter vector that is common to many spectra. This plan did not yet foresee the retrieval of a surface emissivity map as parameter vector that is common to several spectrally resolved images covering the same surface target. The main obstacle in achieving the thesis' goal was suspected in the lacking knowledge on CO₂ opacity, and thus, the focus was set on possible improvements to the quantum-mechanical description of the CO₂ opacity, for instance in the direction of far wing theory of the spectral line shapes, collisional induced absorption, line mixing, etc. On the basis of possible improvements in theory and in combination with the application of the multi-spectrum retrieval algorithm in practice, it was presumed to finally obtain useful surface emissivity results.

But then it was realized that the main problems lay elsewhere. Even before any of the planned quantum-mechanical work commenced, a manifest improvement of the radiative transfer simulations was achieved by utilizing preliminary CO₂ opacity corrections retrieved with an early version of the multi-spectrum retrieval algorithm. But the determination of surface data did not sufficiently improve by that. Apparently, the retrieval of reliable surface emissivity data was much more difficult than expected. The thesis then proceeded into an entirely different direction that could not be anticipated. Even though a retrieval error analysis was planned early in this thesis, it was not foreseen that the errors would be so large that the determination of useful results would necessitate several dedicated papers and a retrieval that had to be completely oriented around the topic of the result's reliability.

Over the course of this work, it became clear that the main goal of this thesis can be accomplished in the following way. For the best available data archive suitable for the determination of Venus IR emissivity information, i.e. the VIRTIS-M-IR archive, the best possible data calibration and preprocessing have to be ensured. The spectral information content has to be exploited to a large extent, and the measured spectra have to be understood as far as possible, in order to achieve the maximum quality of the derived results. For this purpose, the formation of the measured radiances has to be explained by using a detailed description of the radiative transfer taking into account the extreme environmental conditions in Venus' atmosphere and every relevant effect that affected the recorded spectra, such as thermal emissions, absorption and multiple scattering by gases and clouds, the observation geometry, and the properties of the measuring instrument. The retrieved maps have to respect all available *a priori* knowledge, even inter-measurement relations. In particular, the surface emissivity map has to be retrieved as parameter vector that is common to several spectrally resolved images covering the same surface target. Since there are strong interferences between emissivity data and other surface, atmospheric, and, in case of VIRTIS-M-IR, even instrumental parameters, it is of utmost importance to quantify the reliability of any determined map. The maps have to be sufficiently reliable for geologic interpretation, even if this means that the derived emissivity data do not represent absolute emissivity values but only spatial emissivity variations, as long as the physical meaning of the result remains clear. This is the general course established in the manuscripts accumulated in this thesis.

I.4 Outline of accumulated manuscripts and their interrelation

Since many sources are cited in more than one of the presented accumulated articles, an accumulated bibliography is given at the end of this work. References used within the articles (sections, equations, figures, tables) are adapted to the chapter and section divisions of the entire thesis, and when the referred object is not in the vicinity of the respective current page, the page number of the referred target is given in addition. In the published papers, a very few obvious spelling mistakes are corrected (loosing vs. losing, extend vs. extent). In all cases where wording or content are corrected, this is described in footnotes. Comments are also given as footnotes. With the improvement of the understanding of the underlying mechanisms, the terminology evolved between the papers in a few cases.

I.4.1 Chapter II - Forward model simulation and single-spectrum retrieval algorithm

Chapter II (p. 25) is not intended to be published as a paper in a scientific journal. However, it is an integral part of this thesis. It represents a significant portion of the extensive preparatory work that was required to enable the results of the subsequent chapters, i.e. the published papers, in terms of both a detailed study of the underlying principles of radiative transfer and retrieval, as well as the necessary computer implementation. At the same time, this chapter provides important prerequisites to a self-contained understanding of this thesis and serves as an extended subject-specific introduction.

The chapter starts with an introduction of the VIRTIS-M-IR instrument in Section II.1 (p. 25), where also a few typical measured spectra and images are shown.

The largest part of the chapter (Section II.2 (p. 27)) discusses the radiative transfer in Venus' atmosphere and its numerical simulation. It was explained in Section I.1 (p. 2) that surface information can only be determined from Venus' nightside emissions, because on the dayside, surface reflections and emissions are far outweighed by scattered sunlight. To extract surface information from VIRTIS-M-IR nightside spectra, it must first be understood, how surface properties affect the radiance that can be observed from space. Neglecting geologic activity and assuming thermodynamic equilibrium between the surface and the bottom of the atmosphere, the surface temperature decreases with increasing surface elevation according to the Venus International Reference Atmosphere (VIRA, Seiff et al., 1985). The hot surface (735 K at 0 km) emits radiation that depends on both surface temperature and surface emissivity. But the surface information carried by the measured top-of-atmosphere radiances is strongly attenuated and distorted, because the upwelling photons are multiply scattered and partly absorbed by atmospheric gases and clouds (Pollack et al., 1993; Meadows and Crisp, 1996). This also leads to a partial information loss of the radiation's spatial origin according to an approximate horizontal Gaussian blurring with full-width-at-half-maximum (FWHM) in the order of 100 km (Moroz, 2002). Since broad spectral regions of the nightside infrared emissions are completely blacked out by Venus' high-density hot carbon dioxide atmosphere and the thick sulfuric acid clouds, only a few narrow spectral transparency windows between 0.8 and 1.3 μm remain to sound the surface in the infrared, therefore usually called the 'surface windows'. Three of these windows located at 1.02, 1.10, and 1.18 μm were covered by the VIRTIS-M-IR spectral range. Additional windows between 1.3 and 2.6 μm probe the deep atmosphere below the cloud deck.

The fundamental carriers of the surface information, the observed photons emitted from the surface, have to travel through the entire atmospheric column of Venus. Many atmospheric parameters along the photons' paths are spatially and temporally varying, in particular the cloud abundance. Even for constant surface emissivity, such variations strongly affect the observable radiation. Surface emissivity can therefore not be directly deduced from a measured spectrum without a certain knowledge of interfering atmospheric parameters, also to be derived from the measured spectrum. This can be achieved by determining a certain parameter set that allows the numerical simulation of a radiance spectrum that well fits this measurement. These parameters can then be regarded as estimates of the corresponding actual states of atmosphere and surface that led to this measured spectrum.

As a consequence, the task to derive parameters, including the surface emissivity, from a measured spectrum consists of two parts. First, a computer program has to be developed that is able to simulate the radiative transfer in the atmosphere of Venus, taking into account all the just described effects. The fundamental principles of the radiative transfer simulation program utilized for this work are presented in Section II.2 (p. 27). This program computes a synthetic radiance spectrum as it would be detected by the measuring instrument, given

- the state of the surface (elevation, temperature, spectral emissivity),
- the state of the atmosphere (altitude profiles of gas volume mixing ratios, cloud particle densities, temperature, pressure),
- the state of the measuring instrument (wavelength grid, spectral instrumental response function),
- the optical properties of the gases and clouds,
- the observational geometry,
- if necessary the illuminational geometry and the solar spectrum.

Second, an algorithm (called 'retrieval algorithm') has to be developed that is suitable to derive parameters (the 'retrieval parameters') from a given measured spectrum based on the radiative transfer simulation program. This problem is inverse to the task of simulating a spectrum for a set of given parameters. The simulation program is therefore often called the 'radiative transfer forward model', or short 'forward model'. However, different parameter combinations may describe the same spectrum equally well. Thus, the derivation of parameters from a measured spectrum is mathematically an ill-posed problem. A usual way to treat such problems is the Tikhonov regularization (Tikhonov, 1995), where the parameters themselves have to fulfill additional conditions.

Thus, the retrieval algorithm has to determine parameter values that respect the regularization conditions and allow the simulation of a spectrum that well fits the measurement. Starting from an initial guess for the parameters that shall be retrieved, it has to iteratively estimate corrections to the parameter values that reduce the difference between simulated and measured spectrum until the 'best fit' (in the least-squares sense) is found. This requires the retrieval algorithm to repeatedly call the forward model with more and more refined parameter values. Consequently, the retrieved parameters must then always be interpreted within the frame of the utilized forward model and are not well-defined without knowledge of it. For instance, if knowledge of a certain property of the atmosphere would be improved by a future mission to the planet, and the forward model would be correspondingly adapted, the newly retrieved parameter values might differ from the old ones. In the same way, the details of the retrieval regularization should be known in order to be able to understand the meaning of the retrieved results. However, when the retrieved parameters too strongly depend on the details of the regularization, then the parameters are probably more determined by the regularization than by the measurements and therefore meaningless. To avoid this situation, it must always be checked that reasonable modifications of the regularization lead to only small changes of the retrieved results.

The Tikhonov regularization of the ill-posed retrieval problem is here implemented in the form of a Bayesian regularization (Rodgers, 2000). As it is recited by Kappel et al. (2015), this means that prior to the knowledge of the measurement outcome, the retrieval parameters are assumed to follow an *a priori* probability distribution, a Gaussian with certain mean value vector and standard deviations. In addition, measurement and simulation errors of the radiance spectrum are assumed to follow a Gaussian with certain standard deviations and zero mean value vector. Given now the measured spectrum, these probability distributions define the Bayesian *a posteriori* probability distribution of the parameter vector. The location of the global maximum thereof is then the parameter vector that is the most consistent with the measurement and the *a priori* information. An iterative algorithm like the trust region formulation of the Levenberg-Marquardt algorithm (Moré, 1978) can be used to locate local maxima of the *a posteriori* probability distribution. However, the algorithm may possibly converge to just a subsidiary maximum. The *a posteriori* covariance matrix (essentially the 'width' of the *a posteriori* probability distribution around the location of its maximum) can be regarded as a first measure for the uncertainties of and the correlations between the retrieved parameters. Basically, the incorporation of *a priori* mean values and standard deviations decreases the probability to find unreasonable parameter values, whereas the radiance spectrum error distribution defines, technically speaking, the weighting with which the retrieved parameters can deviate from their *a priori* mean values at the cost of a possibly higher deviation of the best-fit simulated spectrum from the measured spectrum. Since this regularization considers only independent single spectra, it shall be called 'single-spectrum regularization'. It is recited in Section II.3 (p. 60) and represents the starting point for the multi-spectrum retrieval algorithm MSR developed in Chapter IV (p. 103) (Kappel, 2014). The radiative transfer simulation program presented in Chapter II (p. 25), in combination with MSR, is able to produce very good fits to the VIRTIS-M-IR measurements and is the foundation of the numerical part of this thesis.

I.4.2 Chapter III - Refinements in the Data Analysis

Chapter III (p. 67) presents the article titled 'Refinements in the Data Analysis of VIRTIS-M-IR Venus Night-side Spectra' (Kappel et al., 2012b).

For each exposure, VIRTIS-M-IR yielded at 256 spatial samples a spectrum of 432 spectral bands dividing the range³ 1.0–5.1 μm equidistantly with wavelength. A series of several exposures scanning a certain target

³The exact interval boundaries were subject to ever-changing instrumental conditions, and so, sometimes 1.0–5.2 μm is stated.

area resulted in a 'data cube', a spectrally resolved two-dimensional image of that target. Different exposure times were needed to acquire useful spectra for the diversity of target conditions that ranged from dayside to nightside. At each exposure, the incoming light was detected at each spectral band and spatial sample on the detector in form of a certain number of counts. This 'net count' depended (in the first order) on the spectral radiance, the responsivity of the detector at that spectral band and spatial sample, and the exposure time. In addition, there was a thermal dark current that accumulated over the course of each exposure to yield the 'dark count' and that was present even when there was no incoming radiation. The starting point of the original calibration pipeline (Cardesin-Moinelo et al., 2010) is the removal of the dark counts that were measured at regular intervals. Next, the net counts are converted into spectral radiances by dividing them by the exposure time and the responsivity that was determined during ground calibration. Then, a despiking to remove the effects of, for instance, cosmic rays is performed among other steps. Finally, the spectral band-to-wavelength mapping is computed. In addition, geometry information is provided for each sample and exposure, for instance the observation angle and the footprint coordinates on the planet along with the corresponding surface elevation.

Already during the first approaches to retrieving surface emissivities in the frame of this thesis, it became clear that single-spectrum retrieval would not be sufficient to derive quantitative surface information from VIRTIS-M-IR spectra, because many different parameter vectors were able to reproduce a measured spectrum equally well, and single-spectrum regularization was not at all able to yield reliable results. This is discussed in detail in Chapter V (p. 135) (Kappel et al., 2015). This insight initiated the development of the multi-spectrum retrieval algorithm MSR discussed in Chapter IV (p. 103) (Kappel, 2014). An overview of MSR is given in Section I.4.3 (p. 14). This algorithm forms the mathematical core of this thesis. In short, MSR does not treat single measurements independently of each other, but it regards a whole set of measurements as a single 'meta-measurement'. This way, inter-measurement *a priori* information like spatial or temporal *a priori* correlations between atmospheric parameters can be incorporated in the retrieval regularization in addition to the usual single-spectrum *a priori* data. Moreover, MSR can retrieve parameters that are common to a selection of measurements, a capability that turned out to be crucial for surface emissivity retrieval in the subsequent papers. The application of MSR leads to retrieval results that are more reliable than corresponding single-spectrum retrieval results.

However, the early development version of MSR was not yet capable of systematically retrieving a surface emissivity map as parameter vector that is common to several VIRTIS-M-IR cubes covering the same surface target. But it was already possible to retrieve parameters that are common to a selection of spectra, mainly with a spectrally resolved correction to the CO₂ opacity in mind. An outline of this early version was presented by Kappel et al. (2012b, Section 2). Even though only up to about 400 spectra could be considered at that time ($\geq 20,000$ in the final version of MSR), it soon became clear that, apparently, certain aspects of the measured spectra were inconsistent. The MSR retrieval of a wavelength dependent CO₂ opacity correction in the 2.3 μm deep atmospheric spectral transparency window yielded a completely unreasonable runaway fine structure that was obviously correlated with the number of the spectral band on the detector. When a band had an even index, the determined opacity correction was huge and of similar size but opposite to that at odd bands. This regular, clearly artificial pattern extended over the entire transparency window (2.2–2.5 μm) and was quite independent of the details of the forward model simulation and the choice of retrieval *a priori* data. Such a regular pattern that was bound to the detector geometry could not be explained by simulation errors, as extensive tests showed. This was rather a manifest hint that the measured radiances had a regular even-odd pattern systematically superimposed onto the true radiances, and thus, that a systematic calibration error might exist. This insight initiated a detailed analysis of the quality of the data calibration and preprocessing, where problems that had been noticed by colleagues in the VIRTIS team were also investigated (see acknowledgements at the end of Chapter III (p. 67)). For instance, observations of the same target at different spatial samples on the detector yielded different spectra. This artificial spatial inhomogeneity of the spectra represented a clear inconsistency within the measured data. Surface emissivities and CO₂ opacity corrections can be retrieved with MSR (final version) as parameters that are common to certain sets of VIRTIS-M-IR spectra. But for this purpose, it is extremely important that the data archive is internally (among the spectra themselves) and externally (with respect to other data sources) consistent.

As it was argued by Kappel et al. (2012b), no measurement apparatus is perfect, and an ever-so detailed ground calibration cannot foresee and capture all facets of the demands of a real-world space mission. In

addition, the launch, cruise, and orbit insertion phases exert extreme stresses onto the instruments, which consequently might shift some of their characteristics. But even slight miscalibrations can lead to systematic measurement errors and corresponding systematic errors of parameters derived from these measurements. However, the VIRTIS-M-IR data archive is unique. VIRTIS-M-IR measurements form at present the only available global data source with high spectral, spatial, and temporal resolution and coverage to derive infrared surface data. Thus, there was no other option than to refine the data calibration and to develop a suitable preprocessing. This step was totally unexpected. A detailed account thereof is presented in Chapter III (p. 67) (Kappel et al., 2012b). This study also includes investigations of the impact of these improvements onto the measurement data base and corresponding retrieved results, as well as of the effect of MSR on retrieved results.

The refinement of the data calibration necessitates a detailed detector responsivity analysis which reveals several different problems whose corrections are described in detail in the cited chapter. Based on the required internal data consistency, the data archive itself can be used as a reference for calibration refinements. Moreover, in absence of conclusive reference measurements, theoretical considerations and model predictions may be used in limited ways to bring the calibration closer to the intended accuracy.

To begin with, the above mentioned even-odd pattern in the $2.3\ \mu\text{m}$ window radiances turns out to be only one aspect of a detector characteristic that has been coined the 'even-odd effect' and affects the entire VIRTIS-M-IR spectral range. In general, the even spectral bands alone yield a spectrum that does not exhibit such pattern. The same is true for the odd bands. Only both combined yield a spectrum where, compared to measurements by other instruments and simulated spectra, a regular sawtooth-like pattern seems to be superimposed on the resulting spectrum. At fixed spatial sample, the magnitude of the effect depends on the spectral range, the measured radiance itself, exposure time, and detector temperature. Errors in the linear calibration (wrong dark counts or responsivities) are excluded as possible causes. It is proposed that this effect could be caused by slight non-linearities in the count-to-radiance mapping that differently affect the even and the odd bands. This can be justified by the independent readout electronics for the even and the odd bands. This working hypothesis can in a natural way even explain the dependence on the measured radiance and the exposure time. The situation is complicated by the fact that the even-odd effect likely had also been present during ground calibration. Here, the linear component of the count-to-radiance mapping (the 'detector responsivity') had been determined, which itself clearly exhibits an even-odd pattern. The latter is corrected first, in order to simplify the study of the actual even-odd effect. Note that even slight non-linearities in the count-to-radiance mapping can lead, through relative differences in the deviation from linearity, to artifacts like the even-odd effect, although the deviations from linearity themselves lie well within the calibration uncertainty. In absence of detailed data describing the non-linearities, an empirical scheme for the correction of the even-odd effect in the wavelength range between 1.0 and $2.6\ \mu\text{m}$ is developed. For nightside spectra acquired at exposure times typical for surface studies, this leads to a correction of the radiance in the spectral nightside peaks of up to 5%.

The next issue with the detector responsivity is the above mentioned spatial inhomogeneity. Pericenter cubes of Venus' dayside with footprints that are sufficiently small to ensure the absence of spatial features are taken as reference here. A wavelength dependent correction is derived that leads to an increase of the radiances of typically 15% in the outer region of the detector in spatial direction, compared to radiances before the correction is applied.

Finally, compared to longer wavelengths, measured *dayside* spectra exhibit too low radiances shortward of $1.3\ \mu\text{m}$. A corresponding correction to the detector responsivity is determined that in turn affects the calibration of *nightside* radiances, which are now increased by up to 35% at $1.0\ \mu\text{m}$. Note that this correction cannot be derived from nightside spectra, as they are valid both with or without it within the frame of the forward model, which is not the case for dayside spectra. A cause of the responsivity issues with the exception of the even-odd effect might be a possible thermal gradient on the detector itself that was naturally not present during ground calibration.

The newly calibrated spectra have to be preprocessed for the retrieval. This includes a removal of straylight, where a principal component analysis of deep space spectra yields the most important principal components that describe the statistical variety of straylight spectra. These components are used to determine for each nightside measurement the approximate straylight spectrum, which can then be removed. The original geom-

etry data (Erard and Garceran, 2008) comprises two data sets. One refers to the surface, the other to an assumed cloud top altitude of 60 km. The effective altitude of the measurement footprints, clearly an important parameter for a slant observation geometry, is the cloud top. But in fact, the cloud top exhibits a latitudinal trend between about 71 km at the equator and 61 km at the poles (Haus et al., 2013, 2014). In order to take this into account, the entire geometry data have to be correspondingly extrapolated. Next, a revised surface topography is determined, as the topography in the VIRTIS geometry data files is based on a superseded Venus topography model that can be wrong by up to several hundred meters (Müller et al., 2008). In addition, it is necessary to preprocess the topography to incorporate the atmospheric blurring of the observed radiances (Müller et al., 2008; for a description of the current implementation see Kappel et al., 2012b) as well as motion blurring. Note that a topography error of 100 m typically translates to a surface emissivity error of about 5% at 1.02 μm . Finally, all data are spatially binned to increase the signal-to-noise ratio and to decrease the amount of redundant data for the retrieval. The binning has to take into account the intended retrieval of surface emissivities as parameters that are common to repeated observations of surface bins (see detailed description of surface bins in Section VI.2.1 (p. 165), Kappel et al., 2016). Note that the spectral band-to-wavelength mapping and the FWHM of the spectral instrumental response function are not sufficiently well predictable by the original calibration pipeline. They have to be retrieved from the spectra themselves.

A comparison between parameters retrieved from the refined vs. the original data archive shows that, for instance, CO can display a column density change in the order of 10%. When retrieving the surface emissivity at 1.02 μm from a single VIRTIS-M-IR cube (not as common parameter vector), a similar comparison shows that it can exhibit changes in the order of 0.2 and up to 0.36 in an example. The application of the early version of MSR leads to an increased stability of the retrieved results and a better avoidance of subsidiary solutions that is noticeable by the smaller residuals between measurements and fits on average. The capability of MSR to determine parameters common to a set of spectra provides a systematic approach to determine CO₂ opacity corrections compatible with the measurements and the forward model. The CO₂ opacity correction for the 2.3 μm window that initiated the development of the discussed calibration and preprocessing refinements is shown in Fig. III.11 (p. 94) (Kappel et al., 2012b). It allows for a good simulation of the newly calibrated and preprocessed radiances in this window. Moreover, it is free from the runaway even-odd pattern that was necessary to simulate the original spectra. Rather, it exhibits a smooth and reasonable wavelength dependence that is not correlated to the number of the spectral band. Usage of the early version of MSR did not yet allow for the systematic retrieval of a surface emissivity map as a parameter vector common to several VIRTIS-M-IR cubes that cover the same target area, but the idea emerged at this point and was already stated in that paper. Note that at this stage, retrieval errors were just taken from the *a posteriori* covariance matrix. Only later it became clear that most retrieval errors are due to a different effect (see Chapter V (p. 135), Kappel et al., 2015). The proposed refinements in calibration, preprocessing, and retrieval represent an important first step to enhance the reliability of retrieved atmospheric and surface parameters of Venus.

I.4.3 Chapter IV - Multi-spectrum retrieval algorithm

Chapter IV (p. 103) presents the article titled 'MSR, a multi-spectrum retrieval technique for spatially-temporally correlated or common Venus surface and atmosphere parameters' (Kappel, 2014).

As it was already mentioned, Venus surface emissivities retrieved from single VIRTIS-M-IR spectra are unreliable. They have such wide uncertainty margins that they cannot be considered useful at all. But VIRTIS-M-IR data are unique and urgently needed. A possible remedy is to use more than one measurement to determine the surface emissivity at a given surface target.

The VIRTIS-M-IR measurements are not isolated soundings in space or time. A set of measurements that is spatially or temporally contiguous is unlikely to originate from completely unrelated single-spectrum state vectors, since the physical drive to balance thermodynamic disequilibria leads to a certain continuity of atmospheric parameters. The underlying parameters of nearby measurements should in this sense be more similar than those of widely separated measurements. Some parameters (e.g. the horizontal temperature distribution in the deep atmosphere) may be more slowly varying than others (e.g. the cloud abundance). There are even parameters that do not vary in space or in time at all, and whose values are not known and shall be retrieved from measured spectra. This applies, for instance, to the above discussed CO₂ opacity correction. Furthermore, neglecting geologic activity (including active volcanism and aeolian processes), the spatially varying

surface emissivity does not change with time and is thus common to all measurements that cover the same surface spot.

This kind of information relating properties of several spectra, even though its presence is rather the regular case, cannot be used in conventional single-spectrum retrievals. This *de facto* neglect corresponds to an only rough approximation of reality and can cause the effect that parameters retrieved from contiguous measurements show unreasonable jumps although a certain spatial or temporal continuity could be expected. Such jumps can be caused by the existence of several retrieval parameters with very similar Jacobians in conjunction with the ill-posed nature of the retrieval problem and the existence of subsidiary minima of the cost function. It can be seen from an example in the chapter that also a smoothing or an averaging, respectively, of single-spectrum retrieval results in a post-processing step can fail to produce useful data. Especially when the single-spectrum information content is low, as it is the case for VIRTIS-M-IR spectra, it is important to incorporate inter-measurement relations. A natural way to do this is the application of MSR, the multi-spectrum retrieval algorithm developed by Kappel (2014). Here, the entirety of a set of measured spectra is regarded as a meta-measurement of all involved single-spectrum state vectors. For each retrieval parameter, correlation lengths and times can then be introduced. The expected correlation length of a spatially slowly varying parameter is larger than that of a faster varying parameter. MSR allows the incorporation of such correlation data from the outset as additional *a priori* data to better regularize the retrieval problem. In the same way as the incorporation of *a priori* mean values and standard deviations in single-spectrum retrievals decreases the probability to find unreasonable parameter *values*, this 'multi-spectrum regularization' decreases the probability to retrieve unreasonable spatial-temporal parameter *distributions*, like unphysical jumps of atmospheric parameters or temporal variations of surface emissivities.

The chapter starts with the mathematical formulation of the Bayesian multi-spectrum regularization. For this purpose, an *a priori* covariance matrix is required that allows for the encoding of *a priori* single-spectrum standard deviations and correlations, as well as of spatial-temporal correlations. It is not a trivial problem to find such a covariance matrix, because it must be positive definite⁴ for an *arbitrary* distribution of distinct footprints, and ideally so by construction already. In addition, for extensive retrieval problems, the matrix can become quite large, and thus it must be efficient to construct and to work with. A large part of the chapter is devoted to the construction of an easily parameterizable suitable matrix. The key is the Kronecker product between matrices that preserves positive definiteness. The factors are the *a priori* covariance matrix of the single-spectrum problem and the matrix of the *a priori* spatial-temporal correlations. The latter is essentially constructed by way of a so-called correlation function that has special properties and is applied to the entries of the matrix of all spatial-temporal distances⁵ between the measurement footprints. The use of a correlation function guarantees that, for spatially-temporally distinct footprints, the resulting matrix is always a proper positive definite correlation matrix. A correlation function is chosen for this purpose that respects the observation that widely⁶ separated footprints experience no correlations anymore and that very close footprints perceive only slowly changing correlations when their distances vary. So far, this construction assumes that the spatial-temporal correlation data are the same for the involved retrieval parameters. When there are several parameter groups with different group-specific correlation data, an *a priori* covariance matrix can still be constructed that combines the matrices of the various parameter groups in a special way. This only works when there are no correlations between the parameter groups, a requirement that is shown to be no serious limitation for Venus problems.

In an appendix, a special-case treatment is derived for parameters where correlation length or time have the limit infinity. Here, the *a posteriori* probability distribution function is mathematically regarded as tempered distribution⁷, because the *a priori* covariance matrix degenerates in the limit. It is shown that such a parameter can be retrieved as parameter that is common to a set of measurements. This requires the corresponding single-spectrum *a priori* data for such a parameter to be the same for each included measurement, an assumption that is quite reasonable in view of the limited *a priori* knowledge for Venus problems. It is not clear from the outset, whether there is a statistical \sqrt{r} -like relative weighting factor between the common and the other parameters that reflects the influence of a common parameter on r spectra. However, it is shown

⁴Semi-definiteness is excluded to allow for the proper definition of the involved probability distributions and is also not needed.

⁵The notion of a spatial-temporal distance becomes clear in Eq. (IV.7) (p. 112).

⁶The lengths scales are defined by the parameter's correlation length and correlation time.

⁷A certain generalization of a function.

that this weighting is exactly 1. It is important to mention that it is the said Kronecker product structure that enables the clean derivation of the retrieval of common parameters in the first place.

The appendix also presents the derivation of a few mathematical shortcuts that can drastically improve the numerical efficiency of MSR. First, the retrieval cost function is reformulated in terms of a least-squares residual norm, because this special structure can be exploited by existing efficient iterative algorithms that search for local minima thereof, like by the trust region formulation of the Levenberg-Marquardt algorithm (Moré, 1978). This requires the computation of the inverse of the matrix square root of the *a priori* covariance matrix. The Kronecker product structure is ideally suited for this purpose, as it allows a very efficient shortcut where the inverse square root must never be computed of the entire high-dimensional matrix, but only of the low-dimensional factors before Kronecker multiplication. For extensive retrieval problems with more than 10,000 spectra, only a few percent of the entries of the resource dominating largest matrix, the Jacobian of the residual between meta-measurement and corresponding simulation, are different from zero. Therefore, the entire matrix algebra is formulated in terms of sparse matrices, which enables the storage and required factorization of the said Jacobian for extensive problems in the first place, as well as the efficient computation of selected *a posteriori* covariance matrix entries. Critical parts of the computer program are parallelized in order to take advantage of multi-core computer hardware. All these improvements were not yet available with the early MSR version presented by Kappel et al. (2012b). In addition, the final version of MSR can systematically prevent violations of domain boundaries of the parameters⁸ in the retrieval iterations by using a variant of the logarithmic barrier method where a penalty is added to the retrieval cost function for each parameter that approaches one of its domain boundaries. The retrieval of parameters whose impacts on the simulated spectra can be separated, can be arranged into several retrieval stages to decrease the maximum required computer resources. The mentioned trust region algorithm is used instead of the plain Levenberg-Marquardt algorithm, and analytic Jacobians can be computed. The numerical and algorithmic optimizations now allow the MSR retrieval from $\geq 20,000$ spectra compared with ≤ 400 spectra in the early version.

In contrast to the early version of MSR, a surface emissivity map can now be retrieved as parameter vector that is common to several VIRTIS-M-IR cubes of the same surface target, neglecting geologic activity. Here, the surface emissivity map can also be regarded as parameter vector with infinite *a priori* correlation time. As already mentioned, it also proves necessary to determine a wavelength dependent correction to the calculated opacity of CO₂ in the extreme environmental conditions in the deep atmosphere of Venus to allow for the simulation of reasonable synthetic spectra in the first place. This opacity correction can be regarded as parameter vector with both infinite *a priori* correlation length and time. A vector that is compatible with (nearly) all VIRTIS-M-IR nightside measurements can be found by retrieving it as common parameter vector from as many and diverse as possible measurements of Venus' nightside emissions. Knowledge gain from single-spectrum retrievals with respect to emissivities and the CO₂ opacity correction is very limited due to interfering atmospheric variations. In an example with a synthetic VIRTIS-M-IR cube, their single-spectrum retrievals are shown to statistically fail, although the spectra are sensitive to these parameters.

It is also exemplarily shown that MSR is especially useful to disentangle retrieval parameters with similar Jacobians and strongly differing correlation data. In particular, this is true for parameters with infinite vs. finite correlation lengths or times. So it is demonstrated that MSR leads to a better disentanglement of CO₂ opacity corrections from spatially-temporally varying atmospheric parameters and of emissivities from CO₂ opacity corrections. This is an important result with regard to the intended emissivity retrieval and justifies the application of MSR.

The stronger constraints that result from the incorporation of inter-measurement relations decrease the number of potential retrieval solutions. However, MSR does on average not lead to larger but to smaller residuals between measurements and fits, and thus to more reliable retrieval results than corresponding single-spectrum retrievals. This is demonstrated for synthetic measurements in the discussed chapter as well as for actual measurements in Chapter III (p. 67) (Kappel et al., 2012b) and indicates the avoidance of subsidiary solutions.

A priori spatial-temporal correlations can be regarded as 'elastic bands' forcing the parameters to stay close to self-establishing general spatial-temporal trends. Their incorporation decreases the probability to find unreasonable spatial-temporal parameter distributions, attenuates the impact of noise, and decreases the

⁸Cloud and gas abundances are ≥ 0 , emissivities lie in the interval $[0, 1]$, the FWHM of the spectral instrumental response function is >0 nm, etc.

probability to find uninteresting subsidiary solutions. The MSR retrieval of a surface emissivity map may be compared to the determination of unchanging properties in a movie of a target that is veiled by wafts of mist.

It is far better to increase the probability of finding a smooth retrieval solution than to post-process single-spectrum retrieval results by smoothing. The latter would in general not lead to a consistent parameter set describing the measurements, in particular when there are unphysical jumps between different subsidiary solutions or parameters close to their domain boundaries. From a mathematical point of view, MSR allows the parameterization of all considered measurements by a fully consistent set of atmospheric, surface, and instrumental parameters that respects all available *a priori* data as well as the measurement and simulation error distributions and that does not neglect the context between adjacent measurements.

As always when regularizing ill-posed problems, it must be checked that retrieved results do not significantly change for reasonable *a priori* data modifications. Note that common parameters retrieved from real-world measured spectra have to be carefully interpreted, since systematic measurement and simulation errors are also common to the spectra. First tests revealed that in presence of such errors, knowledge of the CO₂ opacity corrections is crucial to reliably retrieve absolute emissivity values, and it may be necessary to first assume initial mean surface emissivities to determine such corrections as it is proposed in Chapter V (p. 135) (Kappel et al., 2015).

In conjunction with a refined consistent data calibration and preprocessing (Chapter III (p. 67), Kappel et al., 2012b), retrieval reliability and accuracy can be pushed to their limits using MSR. However, while the processing time overhead of MSR compared to corresponding single-spectrum retrievals is negligible for up to a few thousand spectra, any retrieval based on full radiative transfer simulations requires considerable computational resources. Thus, MSR is selectively applied at first to localized targets that are beforehand identified to be of special geological interest.

I.4.4 Chapter V - Retrieval error analysis

Chapter V (p. 135) presents the article titled 'Error analysis for retrieval of Venus' IR surface emissivity from VIRTIS/VEX measurements' (Kappel et al., 2015).

Once MSR was fully operational, first retrievals from real VIRTIS-M-IR measurements were performed. They yielded reasonable surface emissivity maps, and these results were originally planned to conclude this thesis. However, additional tests were performed, in order to verify the reproducibility of the results using different measurement data sets. These tests ended with a catastrophic failure. Maps from the same target but retrieved from disjoint selections of spectra exhibited large differences, even though the fits well matched the measured spectra. It even seemed possible that the retrieved maps showed just random spatial variations that had nothing to do with reality and were thus useless. Based on these results, the surface emissivity retrieval from VIRTIS-M-IR data seemed to be impossible, the information buried too deep in the measurements. This still could have been a conclusion of this thesis, although a very unsatisfactory one.

However, it had been demonstrated by Müller et al. (2008) that surface information can be extracted to some extent from VIRTIS-M-IR data by applying semi-empirical methods to determine thermal flux anomalies at 1.02 μm that are correlated with surface emissivity. But in view of the just discussed failure, it was not clear, whether surface data extraction would be possible using a full radiative transfer simulation and a retrieval algorithm. Compared to the semi-empirical approach, a higher number of degrees of freedom (in form of the involved retrieval parameters) is required, because acceptable fits to the measured spectra have to be achieved. It was conceivable, therefore, that the retrieval problem could be too strongly underconstrained, even when using MSR, or that the emissivity signal could be systematically annihilated by a compensation from the involved retrieval parameters, in short, that the retrieval errors could be too large to allow useful results. These considerations initiated a search for the reasons of this failure. Chapter V (p. 135) (Kappel et al., 2015) is the product of these efforts.

Obviously, it is difficult to retrieve surface emissivities from VIRTIS-M-IR measurements, and results are prone to errors. This is quantified in the chapter. Especially in such difficult cases, it is important to know the reliability of physical values that are determined from measured data. To begin with, the *a posteriori* covariance matrix encodes, how well surface emissivity could be determined from the utilized measurements, and how well it could be disentangled from the other retrieved parameters. But there are errors that are not

reflected in the *a posteriori* covariance matrix. For instance, the latter is completely local and does not reflect errors that are caused by a convergence to subsidiary solutions. Also, the accuracy of the forward model and the measurements, and the choice of the retrieval parameters, of the spectral ranges that are utilized in the retrieval, and of the *a priori* data can influence emissivity retrieval results. In addition, the information content of a single VIRTIS-M-IR spectrum is quite limited. Therefore, there are always a number of parameters that cannot be derived from the spectra themselves and that are not sufficiently well known to be accurately set in the simulation of the synthetic spectra. They are usually set to certain reasonable values that are compatible with current knowledge on atmospheric and surface conditions and allow the generation of realistic synthetic spectra. When these assumptions deviate from the true physical values, this may cause emissivity retrieval errors, even though the simulations well fit the measured spectra.

In order to determine the impact that wrong assumptions on such interfering parameters may have on surface emissivities retrieved from a *single* spectrum, the true values of both the interfering parameters and the surface emissivity must be known for a certain spectrum. There are only few *in situ* data of surface properties and no *in situ* measurements of the interfering atmospheric parameters at all that were sampled simultaneously with VIRTIS-M-IR measurements of Venus' nightside emissions. Thus, the only spectra with known true underlying parameters are here synthetic spectra. Therefore, a reference spectrum that represents a typical state of atmosphere and surface is first computed by using the forward model. The true underlying parameters are now known by construction. Information losses due to random measurement errors are emulated by adding realistic Gaussian noise to the reference spectrum. To keep the number of interfering parameters to a minimum, only the smallest possible part of the VIRTIS-M-IR spectral range is considered that still has a sufficient spectral information content. As explained in the chapter, this comprises the range 1.0–2.3 μm .

To study the impact of an interfering parameter on the retrieved emissivity, the parameter is set to a value that is different from its true value. The remaining interfering parameters are set to their true values, and the surface emissivity is retrieved from the unmodified reference spectrum. To allow for useful fits at all, certain auxiliary parameters (e.g. cloud abundance) have to be always retrieved in addition. This is repeated for 100 different realizations of the Gaussian noise and for all interfering parameters that shall be studied, whereby each of those parameters is varied over the range that it is physically expected to typically cover. Whenever the quality of the fit is satisfactory, the retrieved emissivity is compared to its true underlying value. Deviations provide a measure for the retrieval error introduced by wrong assumptions on the interfering parameters and the measurement noise.

To allow for a simple characterization of the surface emissivity retrieval errors in terms of a few typical values, a number of error and noise measures are defined. The most important of these, the 'global error measure' defined in the chapter, is the maximum relative deviation of the retrieved from the true emissivity, when an interfering parameter varies over its full expected range. It indicates the typical error range that can be expected due to uncertainties of the interfering parameter. Note that the actual emissivity errors may be even larger, because among other things, not every imaginable interfering parameter can be studied, the interfering parameters may not always lie in the considered ranges, and simulation and measurement errors are not included here. On the other hand, a too wide parameter range can lead to overestimated emissivity errors. Next, the 'color dispersion' specifies the disparity in the deviation of the retrieved from the true emissivities in dependence on the surface window. A low value (compared to the global error measures) indicates that all retrieved emissivities, even if strongly deviating from their true values, experience roughly the same retrieval error. The 'relative error measure' can be used to evaluate the uncertainty of the spatial fine structure of a retrieved emissivity map. Finally, the 'noise measure' enables the estimation of the emissivity error that is due to the actual measurement noise. These error and noise measures are always monitored to allow for a categorization of the success of the surface emissivity retrieval.

Several retrieval pipelines are tested to find out, which auxiliary parameters should be retrieved along with the emissivities from which spectral range to achieve the lowest error and noise measures. Furthermore, retrieval errors may depend on environmental and observational conditions. For instance, when all other parameters are unchanged, observations of targets with few clouds should lead to smaller errors than observations of very cloudy regions. Thus, a number of additional synthetic reference spectra are investigated that represent further key environmental and observational scenarios that may affect the retrieval errors.

But even in the most favorable situations, the retrieved surface emissivities have such wide uncertainty margins that acceptably reliable surface emissivity data cannot be obtained from single VIRTIS-M-IR spectra at all. However, no other suitable data source exists up to now from which infrared surface emissivity on global scale can be extracted with reasonable reliability.⁹

Ultimately, this is the reason for applying MSR. Since the single-spectrum information content is too low, more than one spectrum has to be utilized. But although the application of MSR partly leads to improved error measures, errors due to uncertainties of temporally constant interfering parameters as well as due to deviations of assumed values of interfering parameters from their true time averages remain extremely large. To still obtain some kind of information on the surface emissivities, a possible workaround is proposed: The information content carried by the retrieval parameter that encodes emissivity data has to be weakened. The ambition to retrieve absolute emissivity values has to be dropped for this purpose, and only the spatial variation of the emissivity relative to an initial emissivity value is retrieved with MSR. This approach is implemented as follows. First, MSR is used to pre-determine a wavelength dependent CO₂ opacity correction as parameter vector that is common to as many and diverse as possible measured spectra. But this retrieval problem is strongly underconstrained, which is why it requires a fixed initial emissivity value to be set. Based on this CO₂ opacity correction, MSR is then applied to retrieve a surface emissivity map of the actual surface target. Its emissivity median may not coincide with the initial emissivity, since the measurement sets utilized to determine the opacity correction and the map do not necessarily coincide. For instance, the spatial distributions of time averages of interfering parameters over their respective measurement data set can depend on the measurement data set, and they can be different from their long-term averages. However, this deviation is expected to be spatially slowly varying. When the spatial extension of the surface target is small enough, its impact can be removed by an additive renormalization. The latter is performed by adding a certain constant value to the retrieved map, such that the map's new emissivity median attains the initial emissivity value. The map then shows spatial variations relative to the initial emissivity. This way, the extremely high emissivity retrieval errors due to systematically wrong assumptions on interfering parameters can be largely avoided.

A full multi-spectrum retrieval error analysis is very complex and requires considerable computer resources. But it is possible to roughly estimate global error measures and noise measures for temporally varying interfering parameters by simply scaling single-spectrum error and noise measures with $1/\sqrt{N_r}$ to emulate the statistical impact when each surface bin is covered by N_r repeated measurements. Other parameters and error measures have to be treated differently. Note that the scaling rules are justified in Chapter VI (p. 161) (Kappel et al., 2016). In the following, these estimates are listed for $N_r = 25$ measurement repetitions and the best of the studied single-spectrum retrieval pipelines. Global error measures due to uncertainties of temporally varying interfering parameters like cloud parameters and minor gas abundances can add up to 3%–10% of the true emissivity value, depending on the surface window and the reference spectrum. Temporally constant interfering parameters with a spatial fine structure on a scale of 100 km (surface elevation, interfering emissivities) contribute another 9%–16%. Measurement noise with a standard deviation of 10^{-4} W/(m² sr μ m) leads to additional 1%–4%. The most suitable spectra for emissivity retrieval tend to be the ones with a small cloud opacity, high surface elevation, high true surface emissivity, and small observation angle, but this depends on the emissivity window, retrieval pipeline, and measurement repetition number. The impact of *a priori* data modifications is shown to be negligible. The spatial fine structure of a retrieved emissivity map is more reliable than large-scale trends are. Systematic and unsystematic calibration and preprocessing errors of the measured spectra and forward model errors can lead to further errors for the determined surface emissivities, as can additional interfering parameters.

The approach to retrieve surface emissivity relative to an initial emissivity value from many VIRTIS-M-IR measurements covering the target spot using MSR is thus predicted to yield reasonable error and noise measures. Although it cannot provide absolute emissivity values, it constitutes a first working basis for the quantitative extraction of surface information using full radiative transfer and retrieval. However, in each case, it should be verified that emissivity maps of the same target area derived from different selections of

⁹The IR1 (radiances at 0.90, 0.97, and 1.01 μ m useful for nightside studies) and IR2 (radiances at 1.73, 2.26, and 2.32 μ m useful for nightside studies) cameras aboard Akatsuki (Nakamura et al., 2007) may provide required data (although not hyperspectral), if the second attempt to enter a Venus orbit in December 2015 proves successful. Other than that, it appears that the data situation is not likely to change any time soon, according to current plannings of future space missions to Venus (Limaye and Smrekar, 2010; Zasova, 2012).

measurements reasonably agree ('repeatability'). In retrospect, the failure in the attempt to verify repeatability described at the beginning of this section is not surprising anymore. The retrieval was not yet performed relative to an initial emissivity. The average (and possibly the latitudinal trends, as will be explained in the next section) of the cloud abundance and other temporally varying interfering parameters (cloud bottom altitude, H₂O abundance, etc.) was too different between the utilized disjoint measurement data sets. Moreover, the emissivity median (or mean) of the map before the additive renormalization was too different from the initial emissivity and depended on the measurement data set with side effects explained in the next section, and the number of measurement repetitions was too low.

I.4.5 Chapter VI - Multi-spectrum retrieval of Venus IR surface emissivity maps

Chapter VI (p. 161) presents the article titled 'Multi-spectrum retrieval of Venus IR surface emissivity maps from VIRTIS/VEX nightside measurements at Themis Regio' (Kappel et al., 2016).

Chapter V (p. 135) predicted that emissivity retrieval should be possible after all, and how one has to proceed to obtain useful results. But these predictions were entirely based on synthetic spectra, and retrieval errors were estimated according to scaling rules that were only argued in words to be plausible. Moreover, an actual emissivity map was not studied, but only a few separate reference spectra. In short, now it had to be demonstrated that relative emissivity maps can be retrieved with acceptable reliability from actual measurements. This is addressed in Chapter VI (p. 161).

The first retrievals based on the insights from Chapter V (p. 135) showed that the determined relative emissivity maps were still subject to latitudinal trends. In addition, they exhibited an approximately linear trend with surface elevation below about 2 km. Both trends seem to be unrealistic from a geologic point of view, at least if they should turn out as global phenomena that occur regardless of geologic context. Moreover, the trends were dependent on the choice of the assumed interfering parameters and the utilized measurement data set. The latitudinal trend can be explained, similar to the above discussion of the retrieval relative to an initial emissivity, by the spatial distributions of the time averaged true values of interfering parameters like the cloud bottom altitude or the H₂SO₄ concentration of the cloud droplets. Motivated by the symmetries and spatial scales of the global atmospheric circulation, and provided that the measurements of the surface target are not in the vicinity of the terminators or the polar regions, these distributions are expected to be spatially slowly varying, and only in latitude direction. Moreover, they can depend on the utilized measurement data set. The respective parameters utilized in the forward model simulation are, in absence of detailed knowledge, mostly set to constant values. These spatially slowly varying deviations between time averaged true and assumed parameters lead to corresponding artificial latitudinal trends in the retrieved emissivity map. In the same way, the trend with surface elevation can be explained by unexpected absorption properties close to the surface in the low-lying regions of the planet, for instance due to errors in the CO₂ absorption or to a kind of haze close to the surface. It is assumed here that both emissivity trends with latitude and surface elevation are not real and are only retrieval artifacts due to imperfect or unconsidered forward model parameters. Thus, they have to be removed, the more so because they can depend on the utilized measurement data set. But it should be kept in mind that actual trends with latitude or surface elevation may possibly exist.

The occurrence of the topography trend in the relative emissivity maps was not anticipated at the time of the development of the retrieval relative to an initial emissivity in the preceding paper, and the trend with latitude was assumed to be negligible. The severity of both trends was only discovered when the algorithm was applied to real measurements. The concept of the retrieval of a relative emissivity map had to be modified, therefore. As long as the measurements of the surface target are not in the vicinity of the terminators or the polar regions, and as long as the latitudinal extension of the target is not too wide and the surface elevation and the surface elevation range are not too high, all this to stay in the linear regime, both trends can be removed from the raw retrieved map (i.e. the retrieved map before any post-processing steps are applied) with the help of a multiple linear regression. At this point, the mean value¹⁰ of the raw map is not changed by this de-trending. This mean value does not necessarily coincide with the initial emissivity as already explained, and it is uncontrollable to a certain degree.

¹⁰Since additional statistical parameters like the standard deviation are analyzed in the discussed chapter, the mean value is now used instead of the median proposed by Kappel et al. (2015).

This effect in conjunction with the artificial emissivity trends with latitude and topography before de-trending can cause the retrieved emissivities to be cut off at their domain boundaries 0 or 1. In such a case, a subsequent de-trending makes no sense. To avoid this situation, the CO₂ opacity corrections for the three surface windows are now retrieved each time anew with the emissivity map. The resulting continua differ only slightly. They now take on the character of fine-tuning parameters that shall prevent the raw emissivity maps to approach the boundaries 0 or 1 from the outset.

It can now be observed that the magnitude of the de-trended spatial emissivity fluctuations around their mean value increases with increasing mean value. This is because the radiance response to small emissivity perturbations around an emissivity base value decreases for increasing emissivity base value. The fluctuations are small compared to the emissivity mean. Since different maps have to be compared, for example to verify the repeatability of the results when utilizing different measurement data sets, the uncontrollability of the fluctuation amplitudes that is due to the uncontrollability of the raw emissivity mean values has to be avoided. It is shown that the fluctuations of the de-trended map can be transformed to other emissivity mean values (investigated in the paper for values greater than about 0.5 and not close to 1) according to an affinely linear transformation. In order to represent all maps according to the same standard, each map is transformed to have the same defined mean value called reference emissivity, here 0.5. This transformation replaces the simple adding of a constant value proposed by Kappel et al. (2015) to make the emissivity median value coincide with the initial emissivity. A de-trended map that is referred to the reference emissivity 0.5 is called 'renormalized emissivity map', and the process leading to this map as 'renormalized retrieval'. The results can be later transformed to other reference emissivities if needed. A mathematical appendix formulates the de-trending in terms of an orthogonal projection operator, and the renormalized map as the result of the de-trending and the subsequent transformation to the reference emissivity. This formulation is used to justify the error scaling rules proposed in the preceding paper, thereby discussing the assumptions required to derive them. It is shown that renormalized retrieval is the correct tool to avoid the impacts of spatially slowly varying deviations between time averaged true and assumed parameters as well as of linear trends with surface elevation. The underlying mechanisms of retrieval error origination intuitively realized in the preceding paper are shown to apply.

After these discussions, the chapter presents the complete MSR retrieval pipeline and lists the utilized *a priori* mean values, standard deviations, correlation lengths, and correlation times. Note that the wavelength of the first spectral band and the FWHM of the spectral instrumental response function have to be retrieved for each spectrum, which introduces some complications into the retrieval pipeline. The data calibration and preprocessing (in particular the binning) are shortly described. It is also explained, which VIRTIS-M-IR measurements are considered to be usable for emissivity retrieval. A geologically interesting surface area, Themis Regio, where each surface bin is covered by at least 64 usable binned VIRTIS-M-IR measurements, is selected as surface target to demonstrate the new approach. It comprises 219 surface bins with an area of $91.5 \times 91.5 \text{ km}^2$ each. For this target, the renormalized retrieved emissivity maps at the three surface windows (1.02, 1.10, and 1.18 μm) referred to the reference emissivity 0.5 are computed with MSR using 64 measurement repetitions (i.e. 14016 spectra) and displayed along with the corresponding Magellan radar topography map (Ford and Pettengill, 1992; Rappaport et al., 1999). It is explained, how the maps as well as retrieval errors can be referred to other reference emissivities. The utilized VIRTIS-M-IR cubes are listed in an appendix. Note that, to decrease the expectable error levels, the number of measurement repetitions is increased in comparison to the hypothetical case with 25 repetitions used for the synthetic MSR retrieval error estimation in the preceding paper.

It now has to be verified whether the new retrieval and renormalization approaches suffice to obtain useful emissivity data, or whether further modifications might be required. Independently from the synthetic retrieval error estimation performed in the preceding paper, the presently discussed chapter determines errors based on a statistical evaluation of renormalized emissivity maps derived from real measurements and compares results from both analyses. Two types of tests are designed for this purpose, the 'Measurement Selection Test' (MST) and the 'Parameter Modification Test' (PMT). An MST computes renormalized emissivity maps from a set of S disjoint measurement data sets, each of which covers the same surface target N_r times. N_r has to be smaller than 64, because the number of usable measurement repetitions is limited. At a fixed surface window, the S different maps should be reasonably similar among each other. Additionally fixing the bin, the scatter of the S renormalized emissivities around their mean value at this bin provides a measure of the emissivity

accuracy that is achievable at N_r repetitions. An appendix motivates a measure by which the dissimilarity of the different maps can be quantified and that is at the same time closely related to this scatter. This measure can be scaled according to the appendix, in order to estimate the uncertainty of the map obtained from 64 measurement repetitions with respect to the selection of the utilized measurement data set. Note that only temporally varying parameters lead to significant differences between the S maps (at first order). Three MSTs are performed ($N_r \in \{32, 16, 8\}$), such that in each case $SN_r = 64$.

For the PMTs, the other type of tests, a reference map is first determined from a certain measurement data set. Based on this reference scenario, each PMT modifies an interfering parameter by a reasonable amount and compares the resulting renormalized emissivity map to the reference map according to a measure motivated in an appendix. This way, it is studied, whether the maps are reasonably independent of such modifications, and thus, independent of uncertainties of the respective parameters. The comparison measure is computed for modifications of the initial emissivity (and thus the raw emissivity mean) and the CO₂ opacity corrections as well as for modifications of many other parameters that describe properties of surface, instrument, atmosphere, retrieval pipeline, data calibration, and data preprocessing. To save computer resources, all PMT maps are determined from a fixed measurement data set with only 25 measurement repetitions. An appendix explains, how the comparison measure is statistically scaled to allow interpretation of the $N_r = 64$ -case. It explains furthermore that some of the scaled PMT comparison measures can (and must) also be regarded as contributions to the emissivity errors and have to be quadratically added (square root of sum of squares) to the errors estimated with the MSTs, therefore.

Each MST and PMT and their purpose are described in detail, and the respective comparison measures along with the renormalization coefficients are listed in a table. It is found that the renormalized maps for the MSTs and PMTs agree to a satisfying degree. They show that emissivity errors due to unconsidered time dependent latitudinal trends or offsets of underlying atmospheric parameters are effectively removed by the renormalization. MSTs with different N_r scaled to 64 repetitions also verify that the error scaling rules approximately apply and the estimation of the errors for 64 repetitions using these rules seems to be valid. However, it should be expected that the MST errors, even when they are scaled to 64 repetitions, decrease with increasing N_r due to MSR's usage of more context data from measurements adjacent in time or space. This is indeed the case for scaled $N_r = 32$ -errors, but scaled $N_r = 16$ -errors are not consistently smaller than those for $N_r = 8$. The high uncertainties for the MST error estimates do not yet allow a conclusion based on present results. This must be studied with further surface targets and, if possible, with higher repetition numbers by relaxing the demands on the usability of VIRTIS-M-IR measurements for emissivity retrieval.

MST double standard deviation error estimates are compared to the synthetic error analysis from the preceding paper, but a new evaluation is performed for the latter that better matches the conditions of the present work (revised parameter ranges, inclusion of straylight effects, 64 instead of 25 repetitions, reference emissivity 0.5 instead of 0.65). The revised synthetic errors are compatible with the hypothesis that MST errors are mainly caused by unconsidered time variations of interfering atmospheric parameters. Uncertainties of the CO₂ opacity correction at 1.74 μm , of the H₂O abundance, topography, and of the removed straylight are significant PMT error sources. Special care must be given to these parameters for optimal retrieval results. The synthetic errors determined in the preceding paper due to topography uncertainties are probably overestimated according to the PMTs. The combined scaled MST and PMT results now estimate total double standard deviation errors for the three surface windows of 3%, 8%, and 4%, referred to the reference emissivity 0.5.

Deviations from the mean renormalized emissivity of the target, i.e. from the reference emissivity, that exceed these error levels can, with double standard deviation significance, be considered as emissivity anomalies. Anomalies of up to 8% are detected at both 1.02 and 1.18 μm . At present $N_r = 64$ -sensitivity, no anomalies are identified at 1.10 μm , but anomalies exceeding the determined error level can be ruled out. With single standard deviation significance, all three maps show interesting spatial emissivity variations. A geologic analysis of the target is planned in order to assess the relevance of these variations.

Spatial variations of surface emissivity of 20% that would correspond to the difference between unweathered granitic and basaltic rocks would be easily detectable already at $N_r = 8$ in case of the 1.02 μm window. The present work suggests that such large variations do not occur in the studied target area, but note that contrasts for weathered material might be smaller. According to present results, about 400 repetitions would be needed for MST errors at 1.02 μm to fall below 1%. By excessive extrapolation, this would happen only at

4000 repetitions for all surface windows. The contributing PMT errors are predicted to only slightly improve with increasing N_r .

In conclusion of Chapter VI (p. 161) (Kappel et al., 2016), the issues raised at the beginning of the present subsection have all been successfully addressed. Moreover, the MSTs demonstrate that renormalized emissivity maps determined with MSR from disjoint selections of spectra reasonably agree, in contrast to the failure of the repeatability tests with absolute maps that was described at the beginning of the previous section. The renormalized maps do not show just random spatial variations and most likely represent real surface features. Retrieval errors are sufficiently small to allow geologic interpretation, but note that true emissivities may exhibit real trends with topography or latitude, which cannot be reflected by renormalized maps. The results of the MSTs and PMTs suggest that no further modifications to the approach of the renormalized retrieval are required to obtain first reasonably reliable emissivity data maps. But of course, algorithmic improvements are conceivable that help to further reduce error levels and to interpret the determined maps, in particular with regard to possible real trends with latitude and topography. This is outlined in more detail in Chapter VII (p. 203) that includes an outlook with respect to future work. For the time being, the renormalized emissivities are interpreted as spatial variations relative to the reference emissivity. If the absolute emissivity at a given bin of the target were known, for instance in the form of ground truth data, the absolute emissivity map of the entire target could be computed according to the above mentioned transformation. These are the very first precisely quantified and reliable Venus IR emissivity results from full radiative transfer and retrieval algorithm application and represent an important step toward the retrieval of absolute emissivities.

Chapter II

VIRTIS-M-IR, radiative transfer simulation model, and single-spectrum retrieval algorithm

This chapter recites, how atmospheric and surface parameters can be derived from a spectrum of Venus' nightside as acquired by the VIRTIS-M-IR instrument aboard the Venus Express space probe. First, the instrument is introduced. Next, the radiative transfer model is presented, and simulated radiances and Jacobians are shown. Finally, the retrieval of information from single spectra is discussed. These are important prerequisites to a self-contained understanding of the subsequent chapters. For better readability and an easier overview and navigation, the themes of most paragraphs are emphasized in bold.

II.1 VIRTIS-M-IR

ESA's Venus EXpress space probe (VEX, [Titov et al., 2006](#); [Svedhem et al., 2007](#)) was launched in November 2005 from Baikonur. It was orbiting Venus between April 2006 and January 2015 on a highly elliptical polar orbit. Most of this time, a single orbit lasted 24 Earth-hours, the pericenter was approximately located 250 km above the North Pole, and the apocenter 66000 km above the South Pole. The Visible and InfraRed Thermal Imaging Spectrometer (VIRTIS) aboard VEX was devoted to the study of Venus' atmosphere and surface ([Drossart et al., 2007](#)). It was composed of the aperture High spectral resolution channel VIRTIS-H (2–5 μm), the VISible Mapping channel VIRTIS-M-VIS (0.3–1.0 μm), and the InfraRed Mapping channel **VIRTIS-M-IR** (1.0–5.1 μm). Only the measurements of the latter are suitable for the extraction of surface information, because they provide data at three spectral nightside windows (1.02, 1.10, and 1.18 μm) that probe down to the surface. At each exposure with its HgCdTe detector, VIRTIS-M-IR acquired a frame of 256 spatial pixels ('samples') times 432 spectral bands. The latter divided the range 1.0 – 5.1 μm equidistantly with wavelength. The field of view of a single sample was 250 μrad \times 250 μrad . A series of spatially consecutive frames yielded spectrally resolved two-dimensional images of targets on Venus. Data recorded with VEX in the apocenter region yielded maps of Venus' southern hemisphere by way of a scanning mirror. When VEX was located nearer to the pericenter, the speed relative to the ground was too high for mapping, and the data were recorded in pushbroom mode, approximately resulting in latitudinal profiles of the northern hemisphere. The data acquired during each VEX orbit are divided into a number of subsessions, stored as data cubes. Each VIRTIS-M-IR cube (prefix 'VI') can be uniquely identified by the orbit number, followed by an underscore and the number of the subsession at that orbit, see e.g. Table II.1. The data are calibrated according to [Cardesin-Moinelo et al. \(2010\)](#) and can be accessed at ESA's Planetary Science Archive (PSA, [Drossart et al., 2013](#)). Chapter III (p. 67) ([Kappel et al., 2012b](#)) describes calibration refinements and data preprocessings required for the determination of surface information. An overview of scientific results was given by [Arnold et al. \(2012c\)](#). Having acquired about 5000 data cubes, VIRTIS-M-IR stopped measuring science data in October 2008 when its cryocooler failed.

Fig. II.1 depicts a selection of Venus day- and nightside radiance spectra that are identified in Table II.1. It is typical that, due to reflected sunlight, dayside radiances around 1 μm are more than three orders of magnitudes higher than nightside radiances which originate from thermal emissions by the surface and the deep atmosphere. **VIRTIS-M-IR nightside spectra** at short exposure times like 0.36 s are very noisy at the surface

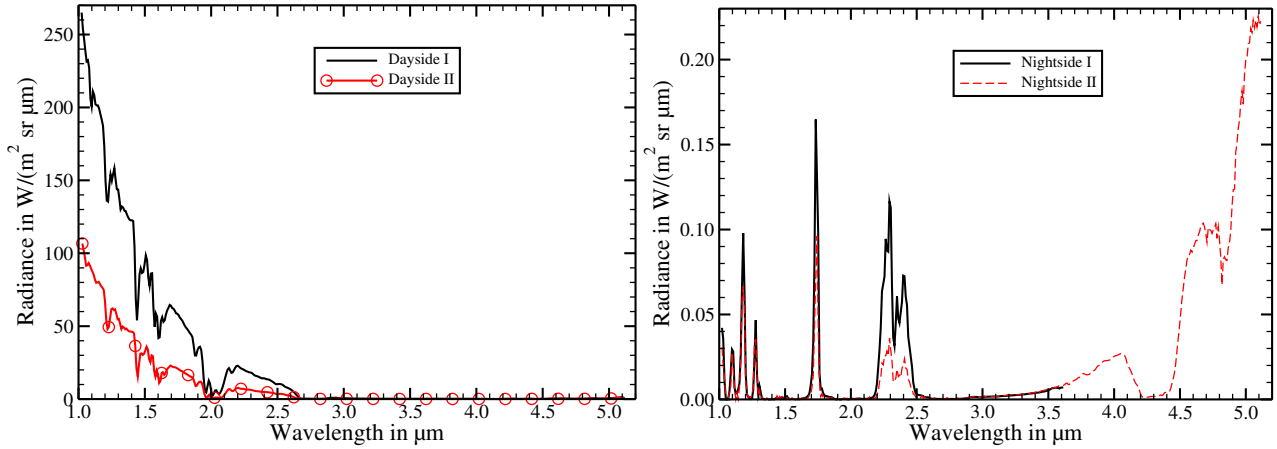


FIGURE II.1: Measured VIRTIS-M-IR day- and nightside spectra. Identification and properties of measurements are listed in Table II.1. Calibration refinements and preprocessings according to Chapter III (p. 67) (Kappel et al., 2012b) have already been applied.

windows. For the determination of surface information, measurements with long exposure times like 3.0 s are utilized, therefore. In this case, the detector is saturated at wavelengths longward of around 4 μm from accumulated detector dark current alone, and radiances cannot be determined there anymore. At the longest exposure time in the VIRTIS-M-IR data archive (18.0 s), only radiances shortward of about 3.5 μm can be measured, see Fig. II.1. Note that this does not affect surface and deep atmosphere studies, but retrievals of temperature profiles above ≈ 60 km that are usually performed in the 4.3 μm CO_2 absorption band range would require short exposure time data to be used (Haus et al., 2013, 2014). This work exclusively utilizes radiances

Spectrum	Cube	t_{exp}	Longitude	Latitude	ϕ_{obs}	ϕ_{Sun}	ϕ_{ph}	Surface elevation
Dayside I	VI0219_00	0.02 s	82.5 °E	-38.4 °N	50.2 °	49.0 °	89.7 °	-422 m
Dayside II	VI0240_00	0.02 s	152.2 °E	-62.8 °N	19.0 °	70.4 °	69.2 °	-826 m
Nightside I	VI0320_01	18.00 s	240.5 °E	-31.1 °N	39.3 °	116.5 °	103.9 °	-181 m
Nightside II	VI0327_02	0.36 s	240.5 °E	-38.4 °N	26.0 °	128.3 °	109.5 °	-54 m

TABLE II.1: Identification and properties of the measurements depicted in Fig. II.1. t_{exp} : single-frame exposure time, ϕ_{obs} : observation angle (also called emergence angle), ϕ_{Sun} : Sun angle (also called incidence angle), ϕ_{ph} : phase angle. The geometric data refer to the respective pixel footprints.

in the spectral range 1.0–2.6 μm that is visualized in Fig. II.2. This figure illustrates that increased absorption of thermal emissions due to thicker clouds leads to smaller radiances in all spectral windows in this range. In principle, the deep atmospheric windows (originating at about 20–40 km altitude) at 1.74 and 2.3 μm are used to derive atmospheric parameters that are required to extract surface information from the surface windows. The formation of the radiance spectra and their numerical simulation is explained in Section II.2, and the retrieval of quantitative information from single measured spectra is discussed in Section II.3 (p. 60). Fig. II.3 illustrates the spatial aspect of the imaging spectrometer.

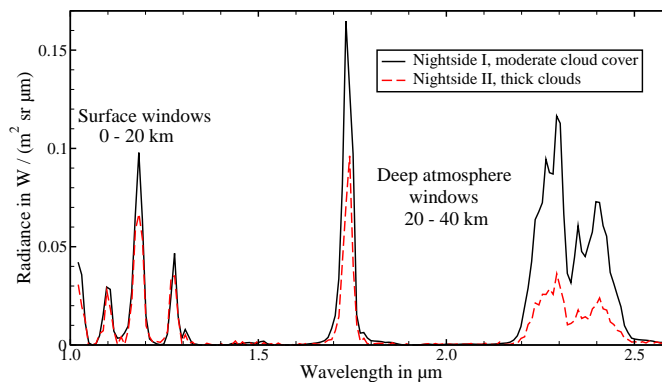


FIGURE II.2: Measured VIRTIS-M-IR nightside spectra from Fig. II.1 in the spectral range studied in this work.

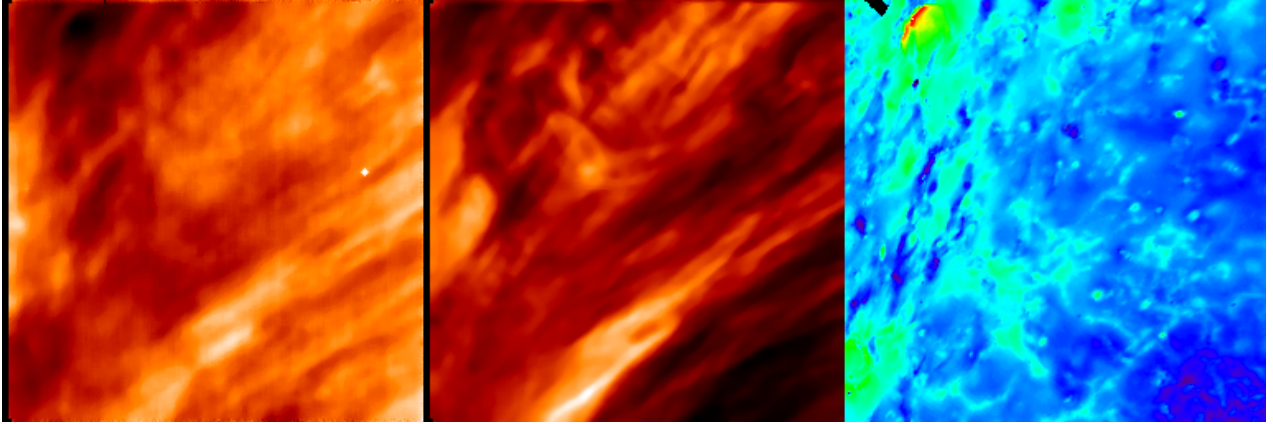


FIGURE II.3: Images of VIRTIS-M-IR cube VI0320_02, calibration refinements and preprocessing as described by Kappel et al. (2012b). Horizontal axis for each image: sample 1 (left) to 255. Vertical axis: line 1 (bottom) to 256. Radiance images were median smoothed (5×5 pixels) and show nightside emissions that were attenuated by clouds with spatially varying opacity. Left: image at $1.028 \mu\text{m}$, black= $0.023 \text{ W}/(\text{m}^2 \text{ sr } \mu\text{m})$, white= $0.047 \text{ W}/(\text{m}^2 \text{ sr } \mu\text{m})$. Center: image at $2.291 \mu\text{m}$, black= $0.006 \text{ W}/(\text{m}^2 \text{ sr } \mu\text{m})$, white= $0.113 \text{ W}/(\text{m}^2 \text{ sr } \mu\text{m})$. Right: (unblurred) surface topography according to Rappaport et al. (1999), black= -2015 m , red= 3986 m . More details are given in Table II.2.

Corner	Longitude	Latitude	ϕ_{Sun}	ϕ_{obs}
Lower left	248.3 °E	-17.8 °N	112.6 °	49.8 °
Lower right	223.3 °E	0.2 °N	139.1 °	60.5 °
Upper left	227.3 °E	-47.7 °N	118.2 °	14.9 °
Upper right	206.6 °E	-23.3 °N	146.7 °	39.8 °

TABLE II.2: Properties of the corner footprints of the images depicted in Fig. II.3. $t_{\text{exp}}=18.0 \text{ s}$. Phase angles are irrelevant for nightside measurements and are not listed here.

II.2 Forward model

A measured spectrum can be simulated using a radiative transfer simulation model, which numerically computes for a given parameter vector the radiance spectrum that the measuring instrument should detect. The parameter vector includes atmospheric parameters (altitude profiles of temperature, gaseous and particulate constituents), surface parameters (elevation, temperature, emissivity), and instrumental parameters (e.g. full width at half maximum (FWHM) of the spectral instrumental response function). The utilized radiative transfer simulation model is a line-by-line code taking into account illumination and observation geometry, thermal emissions by surface and atmosphere, as well as absorption and multiple scattering by gases and clouds. It is valid for plane-parallel geometry and local thermodynamic equilibrium (LTE) conditions. Since the determination of parameters from a measured spectrum is the inversion of the radiative transfer simulation, a radiative transfer simulation model is often called a **forward model**. This section recites the fundamental concepts of radiative transfer as required for this work. It follows, except when stated otherwise, the text book by Liou (2002, Chapters 1–6) with some re-orderings, notational adaptations, and elaborations. The focus is here not so much on algebra but more on the involved physical and numerical concepts and the introduction of quantities that are used in the subsequent chapters. In some places, these concepts are already adapted to the special situations required for this work, and not the complete generality of literature sources is presented. To obtain more details, the interested reader is referred to the respective sources pointed out in these cases.

II.2.1 The equation of radiative transfer

This section first introduces the required physical quantities and then formulates the radiative transfer equation.

Let E be the amount of energy that is transported by light rays passing through the surface A and at each point $a \in A$ being confined to the solid angle $\Omega(a)$ over the course of a time interval $t \in [t_1, t_2]$ and in a wavelength range $\lambda \in [\lambda_1, \lambda_2]$. ϑ denotes the angle between the surface normal at a and the directions that

are confined by the solid angle $\Omega(a)$. Then E can be written as

$$E = \int_{A, \Omega, [t_1, t_2], [\lambda_1, \lambda_2]} R \cos \vartheta \, dA \, d\Omega \, dt \, d\lambda. \quad (\text{II.1})$$

This equation holds for arbitrary open integration domains with piecewise differentiable boundaries and thereby defines the quantity R , called **spectral radiance**. The spectral radiance can also be expressed in the often used wavenumber domain as $R_\nu = R/\nu^2$ with wavenumber $\nu := 1/\lambda$, when considering that $\int_{\lambda_1}^{\lambda_2} R \, d\lambda =: \int_{\nu_2}^{\nu_1} R_\nu \, d\nu$ for arbitrary wavenumbers $\nu_i := 1/\lambda_i$.¹ The frequency f of the light relates to the wavenumber as $f = c\nu$, where c is the speed of light in the medium. It is R (in the wavelength domain) that is measured by the VIRTIS-M-IR instrument in units of $\text{W}/(\text{m}^2 \text{sr } \mu\text{m})$. R is often shortly called 'radiance'. Note that VIRTIS-M-IR cannot discriminate the polarization properties of the measured light. Therefore, polarization is neglected here, and R is simply a scalar quantity.² Note that the nightside emissions are unpolarized.

The totality of **interactions between radiation and matter** can be classified as either extinction (radiance decreases through interaction) or emission (radiance increases), where both can also occur simultaneously (Goody and Yung, 1989, Section 2.1.2). For light traveling along a path with covered distance s , this can be described by $dR/ds = -A + B$. Here, A parameterizes the extinction and B the emission. Both depend on wavelength, material properties, and the radiance field itself.

With respect to A , the radiance decrease in absence of emission is described by the Beer-Bouguer-Lambert Law as $dR/ds = -k_e \rho R = -\beta_e R$. k_e is the wavelength dependent extinction cross section for the radiation per gas molecule and aerosol particle, respectively, where for simplicity, both are referred to as particles in the following. ρ is the (wavelength independent) number density of the particles that cause the extinction. The extinction coefficient $\beta_e := k_e \rho$ represents the extinction cross section density. Deviations from this law in form of non-linearities can be neglected here, since they require photon densities that far exceed those normally occurring in planetary atmospheres. In the same way, B follows from the radiance increase in absence of extinction, which can be described by $dR/ds = +k_e \rho J$. The quantity J is called 'source function' and can in particular depend on wavelength and the radiation field. It is scaled here for convenience to allow the formulation of the now resulting general **radiative transfer equation** (RTE) as $dR/ds = k_e \rho (-R + J)$. This rather generic equation will be specified in the following to describe the situation for VIRTIS-M-IR measurements.

For the problems discussed in this work, it suffices to assume that the atmosphere is plane-parallel in the portion that is permeated by the light measured by a single spatial pixel of VIRTIS-M-IR. This means that in such a portion, light and atmospheric and surface parameters are permitted to only vary in the direction normal to the plane that is perpendicular to the direction of gravity at the measurement's surface footprint. The light and the parameters are, however, allowed to be different for other measurements, but they must again be locally plane-parallel, possibly with respect to a different plane. Note that a spherical geometry for a single measurement as would be required to describe limb observations is hereby excluded. Let then z be the altitude referred to the planetary mean radius of 6051.8 km, θ the inclination to the upward vertical direction, and ϕ the azimuthal angle in reference to the x axis. Introducing $\tau(z) := \int_z^\infty k_e(z') \rho(z') \, dz'$, the 'normal optical depth' at z measured from the top of the atmosphere, and observing that $s = z/\mu$ with the widely used abbreviation $\cos \theta =: \mu$, the general **equation of plane-parallel radiative transfer** can then be written

$$\mu \frac{dR(\tau, \mu, \phi)}{d\tau} = R(\tau, \mu, \phi) - J(\tau, \mu, \phi), \quad (\text{II.2})$$

where the functional dependencies of R and J had to be redefined. Note that τ is usually wavelength dependent. It is assumed that, for each single wavelength, there are no contributions from other wavelengths from any of the terms in the equation, i.e. this equation holds independently for each single wavelength. This behavior is called 'monochromaticity'. Moreover, all involved quantities as well as the equation are assumed to be time independent over the course of a single VIRTIS-M-IR exposure. In addition, variations of the direction of the spatial light propagation due to variations of the index of refraction along the light path are assumed to be negligible. All assumptions in this paragraph are physically well justified for the scope of this work.

¹Here and in the following, ' $:=$ ' symbolizes a defining equality.

²Polarization can be treated by introducing the four dimensional Stokes vector, which reads $(R, 0, 0, 0)^T$ when only unpolarized light is present.

In the following, the contributions to extinction and emission are specified in more detail. The processes that remove energy from a beam of light and thus cause the extinction are absorption and scattering. **Absorption** occurs when some energy of the incoming light is converted into other forms than light, and it is characterized by k_a , the absorption cross section per particle (or molecule). One can also introduce the absorption cross section density, or short absorption coefficient $\beta_a := k_a \rho$, where ρ is the particle number density. **Scattering** is the redistribution of radiance by a particle from an incoming direction into outgoing directions. The part of the radiance $R(\tau, \mu', \phi')$ that is incoming from direction (μ', ϕ') and that arrives at direction (μ, ϕ) due to scattering at a single particle can be written as $R(\tau, \mu', \phi') \cdot k_s P(\mu', \phi'; \mu, \phi) / (4\pi)$. Here, $P(\mu', \phi'; \mu, \phi)$ is the phase function, i.e. the angular dependence of this redistribution. It is normalized such that $\int_{\phi=0}^{2\pi} \int_{\mu=-1}^1 P(\mu', \phi'; \mu, \phi) / (4\pi) d\mu d\phi = 1$. The attenuation of the incoming radiance due to scattering according to the Beer-Bouguer-Lambert Law follows as the sum of the losses into all outgoing³ directions $\int_{\phi=0}^{2\pi} \int_{\mu=-1}^1 R(\tau, \mu', \phi') \cdot k_s P(\mu', \phi'; \mu, \phi) / (4\pi) d\mu d\phi = k_s R(\tau, \mu', \phi')$. Here, k_s is the scattering cross section per particle. In analogy to the absorption coefficient β_a , the scattering coefficient is defined as $\beta_s := k_s \rho$. The extinction cross section is the sum of the absorption and the scattering cross sections, $k_e = k_a + k_s$. In the same way, the extinction coefficient $\beta_e = k_e \rho$ can be written as $\beta_e = \beta_a + \beta_s$. For this work, it is assumed that scattering does not change the wavelength of light ('coherent scattering', also recall monochromaticity assumption for the RTE), and that scattering sources are separated widely enough so that each particle scatters light independently from each other ('independent scattering'). When the density of the scattering sources is high, then light that has already been scattered can be scattered again ('multiple scattering', an important mechanism in Venus' atmosphere). For a spherical particle with radius a , the size parameter $x = 2\pi a / \lambda$ determines the character of the scattering of radiance with a wavelength λ . For $x \ll 1$ the scattering is called Rayleigh scattering (Section II.2.5 (p. 51)), for larger particles Mie scattering (Section II.2.4 (p. 44)).

Light can also be emitted. Relevant for this work is emission in the form of **blackbody radiation**. A blackbody is a configuration of material where the absorption of incoming light is complete. It can be approximated by the entrance hole of a large cavity. The hole is small enough to make the escape of incoming light back through the hole extremely unlikely. Incoming light passing this entrance is repeatedly reflected inside the cavity until it is completely absorbed by the cavity wall. It appears as if the hole is a perfect absorber for light. In the same way, light emitted by the cavity wall is repeatedly reflected inside the cavity. It is weakened by absorption and strengthened by new emission at the wall, until absorption and emission reach an equilibrium with respect to the wall temperature. According to Planck's Law, the spectral radiance emitted by a blackbody with temperature T in thermal equilibrium is

$$B(\lambda, T) = \frac{2hc^2\lambda^{-5}}{e^{hc/(\lambda k_B T)} - 1}, \quad (\text{II.3})$$

where $k_B = 1.3806 \cdot 10^{-23}$ J/K is the Boltzmann constant, $c = 299792458$ m/s is the speed of light, and $h = 6.626 \cdot 10^{-34}$ Js is the Planck constant. Blackbody radiation is homogeneous, unpolarized, and isotropic (Goody and Yung, 1989, Section 2.2.1).

Light absorption and emission by real objects in thermodynamic equilibrium can be expressed as fractions of that by the idealized blackbody by introducing the spectral absorptivity a and spectral emissivity ε , often shortly called 'absorptivity' and 'emissivity'. For instance, the radiation emitted by a surface or gas of temperature T is then $\varepsilon B(\lambda, T)$. Both a and ε may be direction and wavelength dependent, but for this work, directional dependence can safely be assumed to be isotropic at the moment, even for surfaces. An equilibrium argumentation similar to that for the blackbody shows that absorption and emission by real objects are equal, i.e. $\varepsilon = a$ (**Kirchhoff's law of thermal radiation**). Conservation of energy implies that incident energy E_0 equals absorbed (aE_0) plus transmitted (tE_0) plus reflected (rE_0) energy for radiation that hits a surface. By Kirchhoff's law and the fact that there is no transmitted radiation ($t = 0$) at solid planetary surfaces, it follows that $\varepsilon = 1 - r$, which is often also called Kirchhoff's law.

In real planetary atmospheres, thermodynamic equilibrium holds only in localized volumes being sufficiently small to allow the assignment of a uniform temperature at all, a situation called **local thermodynamic**

³ P does not include unscattered light. The amount of radiation that is scattered into direction (μ', ϕ') is assumed to be of measure zero in the integral.

equilibrium (LTE). In other words, in such a volume, there must be an equilibrium between all thermodynamic degrees of freedom, including the molecular energy levels. The latter can be achieved when there are sufficient collisions between molecules where energy can be exchanged. The rate of collisions is determined by a relaxation time that is proportional to the local pressure. When there are too few molecular collisions, and the energy transitions are governed by spontaneous or induced emissions of photons, the LTE can break down. This condition becomes important in Venus' atmosphere only at higher altitudes. For instance, non-LTE O₂ nightside emissions ('O₂ nightglow') can be observed at 1.27 μm from an altitude region around 100 km (Piccioni et al., 2009). However, to avoid complex non-LTE computations, the spectral range 1.235–1.295 μm of the 1.28 μm nightside emission peak that is contaminated by the O₂ nightglow is not considered in this work. This is no disadvantage, because the spectral resolution is not sufficient to disentangle O₂ nightglow from any other spectral information content that is useful for this work. For all other altitudes that are sounded by VIRTIS-M-IR measurements at the considered wavelengths, it is safe to assume LTE, and thermal emission by one particle of the atmospheric gas ($a = k_a$) at temperature T can be written as $k_a B(\lambda, T)$. The density of the thermal emission ($a = \beta_a$) is then $\beta_a B(\lambda, T)$.

Returning to the RTE (Eq. (II.2) (p. 28)), consider light that propagates into direction (μ, ϕ) at an altitude z that corresponds to the normal optical depth τ . The radiance is decreased due to absorption and scattering of a part of it, which corresponds to the first term on the rhs. of the equation. The other term, the **source function** J , can now be specified in more detail. The radiance is increased by thermal emission. Also, light scattered from other directions into direction (μ, ϕ) leads to an increase. It is useful to separate the contribution from the direct (unscattered) incoming sunlight from other contributions. This sunlight can be modeled by an unpolarized parallel beam that is different from zero only for an infinitesimal solid angle around the incoming direction, but its integral over the full solid angle is finite (Goody and Yung, 1989, Section 2.3.4). It has thus the character of a δ -distribution in angular direction in contrast to the remaining 'diffuse' light field. R is now redefined to only include the diffuse light, and the direct sunlight is treated independently of R . The direct sunlight from incoming direction $(-\mu_0, \phi_0)$ (note the minus sign implying $\mu_0 > 0$ for an incoming direction) has the radiance F_0 before undergoing extinction along its path down to altitude z where it is partly redirected into direction (μ, ϕ) by a single scattering process. The extinction along the path can be computed according to Eq. (II.2) (p. 28) by setting $J = 0$ and follows as an attenuation by a factor of $e^{-\tau/\mu_0}$. The contribution into direction (μ, ϕ) can thus be written $F_0 e^{-\tau/\mu_0} \cdot \beta_s P(-\mu_0, \phi_0; \mu, \phi)/(4\pi)$. The diffuse light R originates from multiple scattering and thermal emissions. By scattering of a part of itself into direction (μ, ϕ) , it increases the radiance in this direction. The contribution at the point of scattering from direction (μ', ϕ') can be quantified by the term $R(\tau, \mu', \phi') \cdot \beta_s P(\mu', \phi'; \mu, \phi)/(4\pi)$, and the total contribution from all directions into direction (μ, ϕ) follows as $\int_{\phi=0}^{2\pi} \int_{\mu=-1}^1 R(\tau, \mu', \phi') \cdot \beta_s P(\mu', \phi'; \mu, \phi)/(4\pi) d\mu' d\phi'$. In summary, the radiance in direction (μ, ϕ) is increased by the contributions from single-scattering of diffuse light, single-scattering of direct sunlight, and thermal emission. Recall the scaled definition of the source function J where the radiance increase in absence of extinction is written as $dR/ds = +k_e \rho J$. The source function J in Eq. (II.2) (p. 28) is thus the sum of the just listed contributions, divided by $k_e \rho = \beta_e$.

Based on the above given definitions, Eq. (II.4) describes the **plane-parallel RTE for the diffuse light field** R ,

$$\begin{aligned} \mu \frac{dR(\tau, \mu, \phi)}{d\tau} = & R(\tau, \mu, \phi) - \sigma \int_{\phi'=0}^{2\pi} \int_{\mu'=-1}^1 R(\tau, \mu', \phi') \cdot P(\mu', \phi'; \mu, \phi)/(4\pi) d\mu' d\phi' \\ & - \sigma \cdot F_0 e^{-\tau/\mu_0} \cdot P(-\mu_0, \phi_0; \mu, \phi)/(4\pi) - (1 - \sigma) \cdot B[T(\tau)]. \end{aligned} \quad (\text{II.4})$$

Here, the single-scattering albedo $\sigma := \beta_s/\beta_e$ is used. It is the fraction of the extinction that is due to scattering and implies $\beta_a/\beta_e = 1 - \sigma$. Note that R , τ , σ , P , F_0 , and B depend on λ , and that R , σ , P , and B depend on τ , but these (partly implicit) dependencies are not in each case explicitly written here for simplicity. Eq. (II.4) is a first-order inhomogeneous linear integro-differential equation for R , where the inhomogeneity corresponds to the terms in the second line. Any two solutions differ by a solution of the homogeneous equation. The occurrence of the integral term calls for a numerical solution of the equation, since analytic solutions can only be expected for special cases.

Boundary conditions exist for the top of the atmosphere ($\tau = 0$) and the surface ($\tau = \tau_s$), and in absence

of more detailed knowledge, they are chosen to be of the simplest possible but still reasonable type. The upper boundary condition $R(0, \mu, \phi) = 0$ for $\mu < 0$ reflects that there is no incoming ($\mu < 0$) diffuse radiation from outer space (Goody and Yung, 1989, Section 2.3.4). The surface is modeled as a Lambertian, i.e. perfectly diffuse reflector where the reflectivity r is independent of incoming and outgoing directions. A surface that is rough at all spatial scales relevant for the wavelengths of the incoming radiation can be well approximated by a Lambertian reflector. By Kirchhoff's law, the surface emissivity $\varepsilon = 1 - r$ is also directionally independent. A blackbody is an example of a Lambertian emitter. The lower boundary condition (see for instance Stamnes et al., 1988, Eq. (12), but here for directionally independent 'bidirectional reflectivity'),

$$R(\tau_s, \mu, \phi) = \int_{\phi'=0}^{2\pi} \int_{\mu'=0}^1 \frac{r}{\pi} R(\tau_s, -\mu', \phi') \mu' d\mu' d\phi' + \frac{r}{\pi} F_0 e^{-\tau_s/\mu_0} \mu_0 + \varepsilon B[T(\tau_s)] \quad \text{for } \mu > 0, \quad (\text{II.5})$$

then states that, on the one hand, the diffuse and the direct radiation components are diffusely reflected, and on the other hand, the surface emits a fraction ε of the Planck blackbody radiation (Eq. (II.3) (p. 29)). The structure of the first term on the rhs. of Eq. (II.5) follows from Lambertian reflection of the spectral power flux of single incoming light rays at a unit surface area, compare Eq. (II.1) (p. 28) quantifying the energy transported by light rays. The normalization $1/\pi$ of the first term on the rhs. of Eq. (II.5) follows from the spectral power integration of the equation for $F_0 = 0$ and $B = 0$ over μ and ϕ ($\mu \geq 0$) while observing that the rhs. of the equation is independent of μ and ϕ , and the fact that the total outgoing power flux is equal to r times the total incoming power flux. The direct beam term inherits this structure. Note that, excluding thermal emissions and the direct beam source, it can be shown that the boundary value problem has a unique solution, if one exists (cf. Knyazikhin and Myneni, 2004, Uniqueness Theorem, who cite Germogenova, 1986). Eq. (II.4) ensures by construction that radiative energy is conserved (Knyazikhin and Myneni, 2004, Section I.6).

II.2.2 Numerical solution of the radiative transfer equation

It does not lie in the focus of this work to fully recite the discretization of the RTE that is required to solve it numerically. This subject is extensively described in the literature, see for instance Goody and Yung (1989, Section 8) or Liou (2002, Chapter 6). But to still provide a certain background, the main ideas are stated here. For this work, the **discrete ordinate method** originally developed by Chandrasekhar (1950) is employed. A numerical implementation is readily available in the form of the widely used 'DIScrete Ordinate Radiative Transfer' code (DISORT, Stamnes et al. (1988)), which is well proven for a wide variety of applications (Stamnes et al., 2000). However, not DISORT, but the 'LInearized Discrete Ordinate Radiative Transfer' code (LIDORT, Spurr (2001, 2008)) is used here. It can be regarded as an extension to DISORT and was also tested against it. Together with the solution of the RTE, it can provide *analytic* derivatives with respect to a variety of parameters, which is preferable to the computation of *perturbative* derivatives. The derivatives are required for the computation of the Jacobians of the forward model simulations, which are needed in the retrieval algorithm, see Section II.3 (p. 60). Both DISORT and LIDORT are implemented in the programming language Fortran 77. Many other required numerical tools (matrix algebra, numerical integration, interpolation, etc.) are readily available in Fortran, the code can be extremely well optimized by the compiler, and the processing time is a deciding factor for this work. Therefore, Fortran was chosen for the implementation of the entire computer program for this work. However, since Fortran 95 is better scalable (in particular because arrays are allocatable during run-time) for problem sizes that are unknown at compilation time (e.g. number of considered spectra) Fortran 95 was finally chosen. Note that compiled Fortran 77 subroutines can be linked to a Fortran 95 program without any modification. The current section follows, except when stated otherwise, the paper by Stamnes et al. (1988) with some re-orderings and slight notational adaptations.

For a fixed wavelength λ , the single-scattering albedo σ , the scattering phase function P , and the temperature T must be known for nightside radiance simulations, all in dependence on the normal optical depth τ that essentially is a re-parameterized altitude. The computation of these parameters is discussed starting from Section II.2.3 (p. 35). In addition, the radiance F_0 of the incoming sunlight before extinction by the atmosphere must be known for dayside radiance simulations. A solar spectrum was provided by Kurucz (1995), but note that it has to be rescaled from Earth's to Venus' distance from Sun. Given these parameters, the task is to compute the radiance R that has to respect Eq. (II.4) and the boundary conditions.

First, a **Fourier expansion** helps to reduce the integro-differential equation Eq. (II.4) (p. 30) in the variables (τ, μ, ϕ) to a set of *uncoupled* integro-differential equations in the variables (τ, μ) . In atmospheric radiative transfer, the phase function P is generally assumed to be a function of the scattering angle Θ only. Using the notation $\mu := \cos \theta$ and $\mu' := \cos \theta'$ as before, $\cos \Theta$ can be determined as the scalar product between the vectors $v(\phi, \theta) := (\cos \phi \sin \theta, \sin \phi \sin \theta, \cos \theta)^T$ and $v(\phi', \theta')$ that point from the coordinate origin to the unit sphere,

$$\cos \Theta = \mu\mu' + \sqrt{1 - \mu^2}\sqrt{1 - \mu'^2} \cos(\phi - \phi'). \quad (\text{II.6})$$

Hence, the phase function, now redefined in its functional dependence in form of $P(\cos \Theta)$, can be approximated by a series expansion in terms of Legendre polynomials $P_l(\omega) = 1/(2^l l!) (d/d\omega)^l (\omega^2 - 1)^l$ (correcting Liou (2002, Eq. (E.2)), see Abramowitz and Stegun (1972, p. 22.11)) with the abbreviation $\omega := \cos \Theta$. The Legendre polynomials are orthogonal polynomials with $\int_{-1}^1 P_k(\omega) P_l(\omega) d\omega = 2/(2l+1) \delta_{kl}$ (Abramowitz and Stegun, 1972, p. 22.2), where the Kronecker delta δ_{kl} is 1 when $k = l$ and otherwise 0. The $(2N - 1)$ -th partial sum of the phase function reads $\sum_{l=0}^{2N-1} (2l+1) p_l P_l(\omega)$ with expansion coefficients p_l that are also called 'phase function moments' and are computed according to the orthogonality relation as $p_l = 1/2 \cdot \int_{-1}^1 P(\omega) P_l(\omega) d\omega$. Note that Stamnes et al. (1988) and Spurr (2001) (in agreement with the below cited work of Wiscombe, 1980) and thus this work use normalizations for the phase function moments p_l that slightly differ from the convention used by Liou (2002), where they are defined as $p_l^{\text{Liou}} := (2l+1)p_l$. In order to return to the variables $\mu, \phi, \mu',$ and ϕ' , Eq. (II.6) is substituted into the phase function expansion, and using the addition theorem for spherical harmonics (Liou, 2002, Appendix E), the approximation for $P(\mu', \phi'; \mu, \phi)$ can be rewritten in terms of associated Legendre polynomials $P_l^m(\omega) = (1 - \omega^2)^{m/2} (d/d\omega)^m P_l(\omega)$ (Liou, 2002, Eq. (E.3)) as partial sum of a Fourier cosine series with respect to $\cos[m(\phi - \phi')]$ for $m \in \{0, \dots, 2N-1\}$. This Fourier expansion is substituted into Eq. (II.4) (p. 30) for both occurrences of the phase function. Now, also $R(\tau, \mu, \phi)$ is approximated by the corresponding Fourier cosine expansion $\sum_{m=0}^{2N-1} R_m(\tau, \mu) \cos[m(\phi - \phi_0)]$. Note that B is isotropic, and its Fourier cosine expansion consists only of the zeroth term. As already mentioned, this work assumes Lambertian boundary conditions, which is a special case of isotropic boundary conditions (reflectivity depends only on difference between incoming and outgoing azimuthal angles). When the boundary conditions are not isotropic, a Fourier cosine expansion of R does not suffice, and also Fourier sine terms are required (Barichello et al., 1996). In the isotropic case, there follow $2N$ uncoupled equations for the $2N$ Fourier coefficients $R_m(\tau, \mu)$

$$\mu \frac{dR_m(\tau, \mu)}{d\tau} = R_m(\tau, \mu) - \int_{-1}^1 D_m(\tau, \mu, \mu') R_m(\tau, \mu') d\mu' - Q_m(\tau, \mu), \quad (\text{II.7})$$

where

$$D_m(\tau, \mu, \mu') = \frac{\sigma}{2} \sum_{l=m}^{2N-1} (2l+1) g_l^m P_l^m(\mu) P_l^m(\mu'), \quad g_l^m = \frac{(l-m)!}{(l+m)!} \cdot \frac{1}{2} \int_{-1}^1 P(\mu) P_l(\mu) d\mu, \quad (\text{II.8})$$

$$Q_m(\tau, \mu) = \frac{\sigma F_0}{4\pi} (2 - \delta_{m0}) \sum_{l=0}^{2N-1} (-1)^{l+m} (2l+1) g_l^m P_l^m(\mu) P_l^m(\mu_0) e^{-\tau/\mu_0} + \delta_{m0} (1 - \sigma) B[T(\tau)]. \quad (\text{II.9})$$

Note that the τ -dependencies of $\sigma, P,$ and g_l^m are not explicitly written here. Once the $R_m(\tau, \mu)$ are known, the (approximate) solution of the RTE follows from the sum of the terms in the Fourier cosine expansion of $R(\tau, \mu, \phi)$.

For a numerical solution, the integral in Eq. (II.7) has now to be discretized. It can be approximately evaluated by applying the very accurate **Gaussian quadrature**. For a function q that can be well approximated by polynomials, $\int_{-1}^1 q(\mu) d\mu$ can be well approximated by $\sum_{0 \neq j = -N'}^{N'} w_j q(\mu_j)$. The μ_j are the roots of the Legendre polynomial $P_{2N'}$, and the summation weights are $w_j = 1/P_{2N'}'(\mu_j) \cdot \int_{-1}^1 P_{2N'}(\mu)/(\mu - \mu_j) d\mu$ with $P_{2N'}'$ the derivative of $P_{2N'}$ (Liou, 2002, Section 6.5.2). For given N' , DISORT (and LIDORT) compute the numerical values for μ_i and w_i (Stamnes et al., 2000, Section 3.3.1). Tabulated values are given by Abramowitz and Stegun (1972, Table 25.4). This 'double-Gauss' (Stamnes et al., 1988, Section II.c) approximation is exact for polynomials of order less than $4N'$ (Goody and Yung, 1989, Section 8.2.2), compare also to Stoer and Burlirsch (1993, Theorem 3.6.12). It has proved sufficient for the number of azimuthal components to not exceed

the number of terms of the sum in the Gaussian quadrature. Usually both are set to coincide, $2N = 2N'$ (Stamnes et al., 2000, p. 2.1.1), a practice which is also implemented here. Eq. (II.7) is now considered only at the quadrature angles $\mu := \mu_i$, and the integration over μ' is discretized by Gaussian quadrature, giving rise to the name 'discrete ordinate method'. Thus, each of the $2N$ independent azimuthal components R_m of the diffuse radiation field yields a system of $2N$ coupled inhomogeneous linear ordinary differential equations with coefficients that are nonconstant, because the atmosphere is not homogeneous. R_m can later be evaluated at arbitrary μ by an RTE-compatible interpolation (Stamnes, 1982) of the solutions at the quadrature angles, $R_m(\tau, \mu_i)$. The $R_m(\tau, \mu_i)$ are called 'stream components' or short 'streams'. In the double-Gauss scheme with $2N$ quadrature angles, there are N upward pointing and N downward pointing streams. It turns out that the restriction to $N = 4$ (eight streams) is sufficient for satisfactory simulations of Venus' nightside emissions, i.e. the $N = 4$ -radiances were tested to be only marginally different from $N = 16$ -radiances (relative error $< 2 \cdot 10^{-5}$). However, for dayside simulations, relative errors for $N = 12$ -radiances referred to $N = 16$ -radiances can still reach $2 \cdot 10^{-4}$.

To numerically solve the differential equation system for fixed m , **the atmosphere is divided into layers** thin enough that each layer is nearly homogeneous with respect to τ , σ , and P . This can often be achieved when a sufficient number of layer boundaries are uniformly distributed with respect to the logarithm of the atmospheric pressure or with altitude. For this work, the layer boundaries below 100 km are defined by a grid with step size 1 km, whereas a step size of 10 km suffices above 100 km, and the top of the atmosphere is set to 140 km. The lowest layer is defined by the surface elevation. For each of the layers, the layer averages of σ and P are computed, as well as the optical depth $\Delta\tau$ of the layer. These values are assigned to the layers as constant single-scattering albedos and phase functions, as well as layer optical depths. The Planck radiation term $B[T(\tau)]$ in each layer is modeled as a first order polynomial in τ , which was found in practice to be sufficient (Stamnes et al., 2000, Section 2.5). Each layer gives thus rise to a system of $2N$ coupled linear ordinary differential equations with constant coefficients and inhomogeneities of the form $Q_1 e^{-\tau/\mu_0} + Q_2 \tau + Q_3$, where the Q_i follow for each m , each quadrature angle, and each layer from Eq. (II.9) after Gaussian quadrature of Eq. (II.7) for the current layer and azimuthal component.

Such differential equation systems can be solved by applying standard calculus and linear algebra methods. The general solution can be found as linear combination of the **solution of the homogeneous system** and of a **particular solution of the inhomogeneous system**. The homogeneous solution is at each quadrature angle a linear combination of terms of the form $Q'_j e^{-k_j \tau}$, where the k_j and Q'_j follow from the eigenvalue and eigenvector problem associated to the homogeneous differential equation system. The form of the inhomogeneity inspires that of a particular solution $Q''_1 e^{-\tau/\mu_0} + Q''_2 \tau + Q''_3$.

The solution of a linear ordinary differential equation system is continuous for piecewise continuous coefficients and inhomogeneities. Thus, **the layer solutions have to be pieced together** such that for each azimuthal component and each quadrature angle, the complete solution over all $\tau \in [0, \tau_s]$ is continuous and satisfies the corresponding Fourier decomposed boundary conditions at $\tau = 0$ and $\tau = \tau_s$ at the respective quadrature angle. These conditions are used to determine the coefficients in the aforementioned linear combinations. Finally, the (approximate) solution to the RTE Eq. (II.4) (p. 30) is obtained by adding the azimuthal components of the Fourier cosine expansion $\sum_{m=0}^{2N-1} R_m(\tau, \mu) \cos[m(\phi - \phi_0)]$, where the $R_m(\tau, \mu)$ follow as mentioned from an RTE-compatible interpolation (Stamnes, 1982) of the $2N$ stream solutions.

The details of the numerical implementation in DISORT (and LIDORT) are fine tuned to achieve a numerically accurate, robust, and efficient code. All the required algebra, such as matrix multiplication or inversion, eigenvalue and eigenvector determination, etc., is performed by using well tested and efficient standard numerical subroutines.

An **analytic differentiation** of the complete discrete ordinate solution with respect to the layer optical depths, layer single-scattering albedos, layer phase functions, and a selection of typical surface reflectance functions (here only surface albedo for Lambertian reflection needed, equals $1 - \varepsilon$ with Lambertian surface emissivity ε according to Kirchoffs' law) was carried out in the form of LIDORT by Spurr (2001, 2008) through a consequent application of the product and chain rules of differentiation. However, differentiation with respect to the layer black body temperatures is not yet available as of LIDORT Version 3.3 and has to be performed perturbatively, see below.

The **input to DISORT and LIDORT** aside from boundary conditions and direct beam source descriptions includes for each layer its layer optical depth, single-scattering albedo, and phase function moments (the Legendre coefficients p_l of the phase function, see paragraph following Eq. (II.6) (p. 32)), as well as the temperatures at the layer boundaries. A large part of the custom forward model implementation required to simulate VIRTIS-M-IR spectra is devoted to the computation of these quantities based on the altitude distributions of the considered atmospheric gases and clouds and their optical properties. As additional input data, LIDORT requires the derivatives of the surface reflectance function and for each layer the derivatives of the layer optical depth, single-scattering albedo, and phase function moments, all with respect to the retrieval parameters. The computation of these data by analytic differentiation represents another large part of the custom forward model implementation.

The **output** of both DISORT and LIDORT includes the synthetic monochromatic radiance. LIDORT yields in addition the radiance derivatives with respect to the retrieval parameters. Note that LIDORT's capability of computing derivatives with respect to atmospheric properties for all layers at once ('profile Jacobians') is not employed here, because altitude profiles of gas or cloud abundances cannot be retrieved from VIRTIS-M-IR spectra due to the spectra's low information content. In contrast, certain parameters that act on the total atmospheric column (e.g. a factor that scales the entire altitude profile of the H₂O density) can be retrieved. LIDORT is also capable of computing derivatives with respect to such parameters ('total column Jacobians').

The entire procedure of computing the monochromatic radiance and its derivatives is repeated for many wavelengths. The wavelength resolution should be fine enough to resolve each spectral feature of the absorption and scattering properties of the atmospheric gases and clouds as well as of the solar spectrum. The simulated radiance that would be recorded by the VIRTIS-M-IR instrument at a single spatial pixel is obtained by convolving the monochromatic radiance spectrum with the **spectral instrumental response function**. Based on ground calibration results of the instrument, the spectral instrumental response function K is modeled as a Gaussian with zero mean value and a full-width-at-half-maximum (FWHM) in the order of 17 nm, $K(\lambda) = \exp[-\lambda^2/(2\zeta^2)]/(\zeta\sqrt{2\pi})$, where $\zeta = \text{FWHM}/(2\sqrt{2\log 2})$. The radiance at a single spectral band i corresponding to the nominal wavelength λ_i is thus the integral of the monochromatic spectrum times $K(\lambda_i - \lambda)$ over λ , and the radiance spectrum then follows by computing this integral for all λ_i that form the grid of the nominal wavelengths of all spectral bands. This grid comprises 432 spectral bands dividing the range 1.0–5.1 μm equidistantly with wavelength, and hence $\lambda_i = \lambda_I + (i - 1)\Delta\lambda$ with $i \in \{1, \dots, 432\}$. But the corresponding spectral-band-to-wavelength mapping and the FWHM are not entirely predictable by the VIRTIS-M-IR calibration, compare Section III.4.4 (p. 91). It turns out that they vary with detector temperature and spatial pixel on the detector. The intercept λ_I and slope $\Delta\lambda$ of the band-to-wavelength mapping and the FWHM are thus treated as additional retrieval parameters in this work. All partial derivatives that form the monochromatic Jacobian are convolved in the same way to yield the Jacobian at VIRTIS-M-IR resolution. Note that the derivatives with respect to intercept and slope of the band-to-wavelength mapping and the FWHM can be computed based only on the monochromatic radiance spectrum itself. This can be achieved by integrating the monochromatic radiance spectrum times the easily computable analytic derivatives of the $K(\lambda_i - \lambda)$ with respect to these parameters. To improve numerical efficiency, it is already sufficient to evaluate the monochromatic radiative transfer on a wavelength grid that is just fine enough that the instrumental response function convolutions yield synthetic VIRTIS-M-IR spectra that exhibit no significant differences compared with the synthetic spectra resulting from the evaluation at high wavelength resolution. In the spectral range 1.0–2.6 μm utilized for this work, the monochromatic wavelength (not wavenumber!) grid has a step size of 0.3–1 nm for nightside simulations. A maximum step size of 0.1 nm is recommended near 5 μm or for dayside simulations. To further increase numerical efficiency, certain uninteresting wavelength ranges can be blacked out automatically (initial radiances or Jacobians in the retrieval iterations below certain thresholds) or manually.

The forward model is capable of providing synthetic VIRTIS-M-IR spectra as well as analytic derivatives with respect to certain atmospheric, surface, and instrumental parameters. For any parameter where no analytic derivative can be computed with LIDORT (mainly temperature variables), **perturbative derivatives** with respect to this parameter can be evaluated as difference quotients. But in this case, the parameter perturbation must neither be set too small to avoid noisy derivatives resulting from simulated radiance perturbations close to numerical precision, nor must it exceed the retrieval iteration step lengths or the magnitude that ensures a well approximation of the derivatives by difference quotients. To evade this situation, analytic derivatives are

utilized whenever possible, especially as they are faster to evaluate. However, any newly implemented analytic Jacobian is checked to coincide with its corresponding perturbatively computed Jacobian.

The **following sections** provide some background on the computation of the input parameters to the DISORT (and LIDORT) subroutines in the custom forward model implementation. Aside from the boundary conditions, the temperatures at the layer boundaries, and the direct beam parameterization, the input parameters include for each considered monochromatic wavelength and each atmospheric layer the layer averages of the phase function moments p_l , the single-scattering albedo σ , and the layer optical depth $\Delta\tau$. For this work, the custom forward model was implemented from scratch in Fortran 95 in order to better learn the details of radiative transfer, to be able to independently develop required modifications to the model, and to create own implementations of the data structures needed for Bayesian retrieval (Section II.3 (p. 60)) and later MSR retrieval (Chapter IV (p. 103)). However, this was done in close cooperation with Haus and Arnold (2010), and algorithms and simulated results were in each development stage closely compared to those by the DISORT-based Fortran 77 code by Haus and Arnold (2010) for mutual improvements. Results were also partially checked against results from earlier routines entirely self-implemented by R. Haus (Arnold et al., 2000; Haus and Titov, 2000) that were developed for Mars science and are based on the Successive Orders of Scattering Approximation (see Liou, 2002, Section 6.5.1). Use of the Successive Order technique, however, is for Venus conditions not as efficient and accurate as discrete ordinate based approaches are.

II.2.3 Gaseous absorption

This section discusses the computation of gaseous absorption cross sections k_a and follows, except when stated otherwise, the text book by Liou (2002, Chapter 1.3).

Atmospheric molecules can move in space, rotate, vibrate, and have an electronic energy state. Correspondingly, they can store among others translational, rotational, vibrational, and electronic energy, the last three of them are quantized. Absorption and emission of radiation takes place when the molecules undergo quantum theoretically **allowed transitions** between energy states with energy level difference $E_2 - E_1$. This difference corresponds to the energy hf of an absorbed or emitted photon of frequency f . Purely rotational transitions can typically be observed in the microwave to far infrared, purely vibrational transitions in the infrared, and purely electronic transitions in the visible to ultraviolet spectral ranges. Simultaneous rotational and vibrational transitions are the most important for infrared spectroscopy.

The exact absorption cross sections are difficult to derive from quantum theory, and laboratory data are insufficient to describe absorption at all kinds of pressure and temperature conditions, wavelengths, and compositions of the atmosphere. Therefore, certain **empirical or semi-empirical approaches** are used in practice to provide the gaseous opacities required as input to the RTE. These include rules to estimate the wavenumber dependence and scaling laws in dependence on pressure and temperature, where certain parameter sets at reference conditions are used as initial values and are listed in line databases for various molecules.

II.2.3.1 Idealized model

To start with a simple scenario, a diatomic molecule with non-vanishing electric dipole that can be modeled as a **rigid rotator and harmonic oscillator** has the quantized rotational and vibrational energy $E_{J,n} = hK_r J(J+1) + hK_v(n+1/2)$ according to the time-independent Schrödinger equation. Here, the non-negative integers J and n are the rotational and vibrational quantum numbers, respectively. K_r is a constant that depends on the molecule's moment of inertia, and K_v ($K_v \gg K_r$) is a constant that depends on the force constant of the vibration and the masses of the molecule's atoms. The number of distinct energy states with energy level $E_{J,n}$ is $2J+1$, called the degeneracy of this state (Goody and Yung, 1989, Section 3.2.3).

Allowed rotational-vibrational transitions of this idealized quantum mechanical system are characterized by differences $\Delta J = \pm 1$ of the rotational and $\Delta n = \pm 1$ of the vibrational quantum number. Such statements are called **selection rules**. When there are many photons with all kinds of energies (such as generated by Planck blackbody emission) that cross the atmospheric medium, those can be absorbed that have frequencies corresponding to the energy differences of allowed transitions. This leads to a decreased number of photons at these frequencies, noticeable as absorption lines in an observed radiance spectrum.

Consider the transition from the ground to the first excited vibrational state ($n = 0, \Delta n = +1$) that is due to the absorption of a photon. J and n are the rotational and vibrational quantum numbers before the transition. Then the **frequency of the absorbed photon** follows as $K_v + K_r(\pm 2J \pm 1 + 1)$, depending on the rotational transition. J before the transition can attain an arbitrary positive integer for $\Delta J = -1$ and in addition can be zero in case of $\Delta J = +1$. In presence of a large number of molecules, many states with different J can be occupied for different molecules before and after transitions, and thus, many absorption lines occur. Since $K_v \gg K_r$, the absorption lines are grouped with spacing $2K_r$ on both sides of the frequency K_v . The low frequency group is called 'P-branch', the high frequency group 'R-branch'. Transitions at the frequency K_v ('Q-branch') do not occur here.

In an ensemble of molecules in LTE at temperature T , the energy states with energy E_j are populated with a probability proportional to $g_j e^{-E_j/(k_B T)} / Z(T)$ according to the Boltzmann distribution, where g_j is the degeneracy of the energy states that have energy E_j . The normalization $Z(T) := \sum_j g_j e^{-E_j/(k_B T)}$ is called 'partition function'. The **line strengths** (or 'intensities') of the absorption lines in the P- and R-branches of the transition from the ground to the first excited vibrational state depend on the population of the states before transition and are thus proportional to $(2J + 1) e^{-E_{J,0}/(k_B T)}$ for the discussed idealized system and also depend on the partition function.

II.2.3.2 General cases

Now turning to more general cases, atmospheric molecules can be composed of more than two atoms (e.g. CO₂, H₂O), allowing for more vibrational and rotational modes. In practice, the molecules are neither harmonic oscillators, nor rigid rotators. Therefore, degeneracies of the discussed idealized quantum system may be removed, leading to splittings of degenerate energy levels. In addition, several isotopologues may occur, i.e. a molecule type may differ in its isotopic composition. All this can lead to a much more complicated distribution of molecular energy levels. In addition, the selection rules for not idealized systems allow not just transitions with $\Delta J = \pm 1$ and $\Delta n = \pm 1$. Thus, the line frequencies and strengths cannot be computed in a simple way anymore. For many molecules, these and other line parameters along with the partition functions are given in **line databases** like HITRAN (Rothman et al., 2009) and result from measurements as well as quantum mechanical computations. For CO₂ as an example, parameters of more than 11 million lines are listed in the 'CDS Venus' line database (Tashkun et al., 2003; Tashkun and Perevalov, 2008) between 14 and 12790 cm⁻¹ (see Fig. II.4).

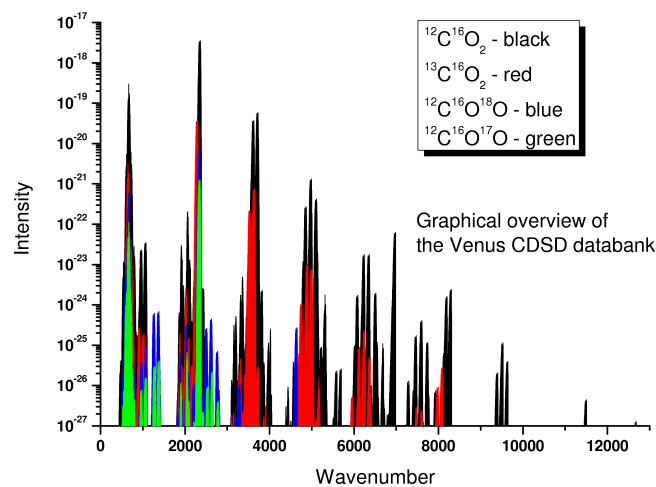


FIGURE II.4: Wavenumbers (in cm⁻¹) and lines strengths ('Intensity', in cm⁻¹/(molecule cm⁻²)) of allowed transitions of CO₂ according to the 'CDS Venus' line database for different isotopologues. Diagram by Tashkun and Perevalov (2008).

The absorption **line strength** of a transition at frequency f depends on the population of the energy state before the transition, but incoming photons of this frequency can, with a probability proportional to $e^{-hf/(k_B T)}$,

also induce a stimulated emission of another photon with exactly the same properties as the absorbed photons, such that it appears as if the probability of photon absorption is somewhat decreased by a factor of $1 - e^{-hf/(k_B T)}$ (Thomas and Stamnes, 2002, Section 4.4). Taking the ratio of the line strengths at a temperature T and a reference temperature T_0 , it follows (Thomas and Stamnes, 2002, Section 4.5) that the line strength scales with temperature as

$$S(T) = S(T_0) \frac{e^{-E_0/(k_B T)} (1 - e^{-hf/(k_B T)}) / Z(T)}{e^{-E_0/(k_B T_0)} (1 - e^{-hf/(k_B T_0)}) / Z(T_0)}, \quad (\text{II.10})$$

where the energy E_0 of the state before transition as well as the line strength $S(T_0)$ at reference temperature $T_0 = 296$ K are listed in line databases (e.g. Rothman et al., 2009). The description of line databases include a tool to compute the (line independent) partition function Z at a given temperature.

II.2.3.3 Line shapes

For a single fixed absorption line, photon absorption is not only possible at the exact wavenumber ν_0 given by the energy difference of the molecular state transition, but also in a certain vicinity, although at smaller efficiency. There are several mechanisms that contribute to this 'line broadening'. Define the shape f of the single spectral line with the wavenumber dependent absorption cross section $k_a(\nu)$ and with intensity $S := \int k_a(\nu) d\nu$ such that $k_a(\nu) = S f(\nu - \nu_0)$. As mentioned, the line intensity can be computed from the partition function, temperature, and others, and is listed in line databases (Rothman et al., 2009). The line shapes are discussed in the following.

First, an excited molecule has a finite average life time τ_n and will decay spontaneously to a lower state by emission of a photon, leading to the 'natural' line shape $f(\nu) = f_L^{\alpha'}(\nu) := \alpha' / \pi \cdot 1 / (\nu^2 + \alpha'^2)$ that follows from a solution to Schrödinger's equation and is also valid for absorption lines, where $\alpha' = 1 / (2\pi c \tau_n)$ (Goody and Yung, 1989, Section 3.3). $f_L^{\alpha'}$ is the Lorentz profile with half FWHM ('line width') α' . However, this **natural broadening** is practically negligible as compared to other broadening mechanisms, since τ_n ranges from about 10^{-1} to 10^1 s (Thomas and Stamnes, 2002, Section 3.3.4), and thus, α' is smaller than about 10^{-10} cm^{-1} .

Next, collisions of other molecules with the emitting (or absorbing) molecule can cause state transitions, leading to the so-called **collisional broadening** or **pressure broadening** of the lines. The corresponding line shape can be motivated by assuming the molecule to emit (or absorb) a harmonic electromagnetic wave and the state transitions to take place instantaneously ('impact approximation'). In the frequency domain, the distribution of the amplitude is represented by the Fourier transform of the harmonic wave times the characteristic function⁴ of a time interval $[-t/2, t/2]$. The time span t of the undisturbed existence of the harmonic wave is Poisson distributed with probability density $e^{-t/t_0} / t_0$ and mean time t_0 . Neglecting terms that are irrelevant in the IR, the average of the intensity distributions (the squared amplitude distributions) for $t \in [0, \infty)$ with respect to the Poisson distribution yields again the Lorentz line shape f_L^α , but now with an $\alpha = 1 / (2\pi c t_0)$ that results from the (pressure dependent) mean time t_0 between collisions. α can be estimated from the kinetic theory of gases to scale according to $\alpha = \alpha_0 (p/p_0) (T_0/T)^n$ for pressure p and temperature T . Here, α_0 is the line width at standard pressure $p_0 = 101.325$ kPa and temperature $T_0 = 296$ K, and the coefficient n ($1/2 \leq n \leq 1$) is listed in line databases (Rothman et al., 2009). Fig. II.5 illustrates the line shape for pressure broadening, in the following often just called Lorentz shape or Lorentz profile. The line databases also list the half FWHM values α_0^s and α_0^f for self- and for foreign broadening (i.e. for collisions with the same and with other molecule types, respectively). α_0 results as $\alpha_0 = (1 - q)\alpha_0^f + q\alpha_0^s$, where q is the volume mixing ratio of the considered molecule type. α_0 ranges typically from 0.01 to 0.1 cm^{-1} . Note that foreign broadening data are mostly listed only in the form of air broadening under Earth conditions, and depending on the missing availability of additional data, these values are carried over to, for instance, Venus conditions. For H_2O and CO , special case treatments are used in this work that are valid at high temperatures for the pressure broadening by CO_2 , the dominating gas in Venus' atmosphere (Delays et al., 1989; Hartmann et al., 1988).

Finally, due to random thermal motion at temperature T , the molecules have a certain velocity component v in the direction of light propagation. This velocity component is for molecules with molecular mass

⁴The characteristic function of a certain set attains the values 1 when the argument is element of this set and 0 elsewhere.

m randomly distributed according to the Maxwell-Boltzmann distribution $P_v(v) = N_v e^{-m/2 \cdot v^2 / (k_B T)}$ with normalization N_v . Incoming light of wavenumber ν has in the reference frame of the moving molecule the wavenumber ν_0 required for absorption, when the velocity component of the molecule leads to a Doppler shift $|\nu - \nu_0| = \nu_0 |v| / c$ for $|v| \ll c$. This translates to the line shape of the **Doppler broadening** $f_D(\nu - \nu_0) := 1 / (\alpha_D \sqrt{\pi}) \cdot e^{-(\nu - \nu_0)^2 / \alpha_D^2}$, where $\alpha_D := \nu_0 / c \cdot \sqrt{2k_B T / m}$. Hence, the Doppler line width $\alpha_D \sqrt{\log 2}$ (half FWHM) depends only on the local temperature and the known molecular mass for a fixed transition and, compared to pressure broadening, becomes important only at high altitudes (in Venus' atmosphere in the infrared above ≈ 60 km, compare Fig. II.5).

In a broad transition region above that altitude, both pressure and Doppler broadening mechanisms have to be taken into account. When pressure and Doppler broadening are treated as independent of each other, the pressure broadened line shape is shifted by the Doppler shift for molecules with velocity component v , and the result is averaged according to the Maxwell-Boltzmann distribution in v , i.e. $f_V(\nu - \nu_0) := \int f_L^\alpha(\nu - \nu_0 - \nu_0 v / c) N_v e^{-m/2 \cdot v^2 / (k_B T)} dv$ (Goody and Yung, 1989, Section 3.3.6). By substituting $\nu' := \nu - \nu_0 v / c$, this function can be written as $f_V(\nu - \nu_0) = \int f_L^\alpha(\nu' - \nu_0) f_D(\nu - \nu') d\nu'$ and is already normalized by construction as convolution of two normalized functions. Another set of substitutions, $t := (\nu - \nu') / \alpha_D$, $a := \alpha / \alpha_D$, and $x := (\nu - \nu_0) / \alpha_D$, leads to the formulation $f_V(\nu - \nu_0) = \frac{1}{\alpha_D \sqrt{\pi}} K(\frac{\nu - \nu_0}{\alpha_D}, \frac{\alpha}{\alpha_D})$ in terms of the Voigt function $K(x, a) := a / \pi \cdot \int e^{-t^2} / [a^2 + (x - t)^2] dt$. This line shape is called **Voigt profile**, and in the limits $\alpha \rightarrow 0$ or $\alpha_D \rightarrow 0$, it reduces to the Doppler or Lorentz profile, respectively. The Voigt profile resembles the Doppler profile in the core region and the Lorentz profile in the far wings. In this work, the Voigt function is calculated by using the Humlíček algorithm (Humlíček, 1982) that makes use of efficiently computable rational approximations. Fig. II.5 illustrates the Lorentz, Doppler, and Voigt profiles.

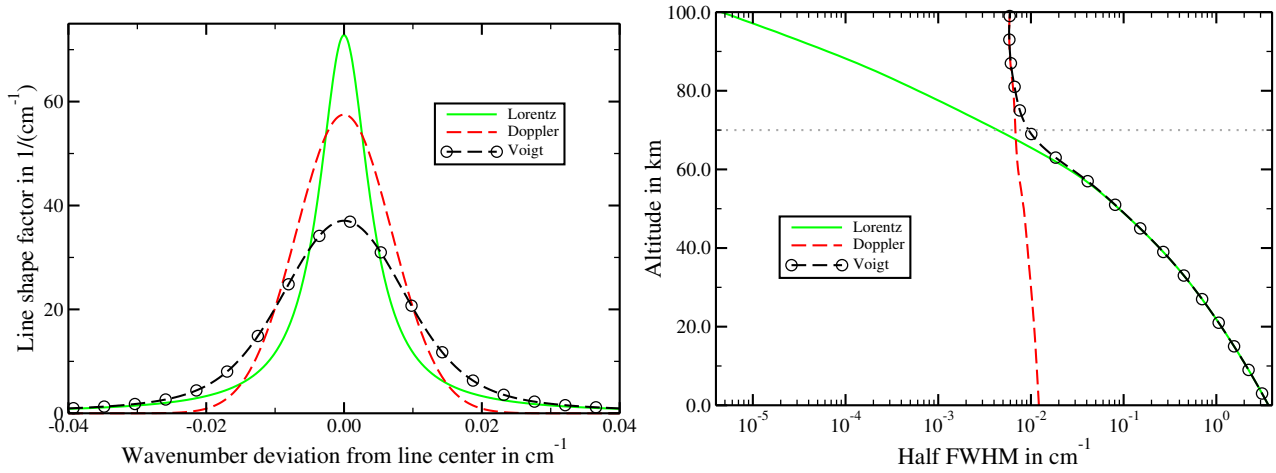


FIGURE II.5: Line shapes for equatorial Venus conditions according to Fig. II.7 (p. 42). The Lorentz shape is here computed for $\alpha_0 = 0.1 \text{ cm}^{-1}$ and $n = 1$. The Doppler shape is depicted for $\nu_0 = 10000 \text{ cm}^{-1}$ (corresponding to $1 \mu\text{m}$) and the molecular mass m for CO_2 that corresponds to a molar mass of 44.0095 g/mol . Left: wavenumber dependence of line shapes at 70 km altitude. Right: line widths in dependence on altitude. The Voigt line width is computed from the Lorentz and the Doppler widths according to Olivero and Longbothum (1977). The dotted gray line indicates the altitude at which the line shapes in the left panel are valid.

In practice, it turns out that, although the Voigt profile well describes the line core region, the **far wings** can strongly deviate from it and exhibit a sub-Lorentzian behavior. This is a result of oversimplifications in the motivation of the Lorentz profile as the line shape of the collisional broadening. On the one hand, the lines were treated as isolated from each other. When the line widths are so large as to be comparable with the distances between neighboring lines, energy perturbations leading to the line broadening in the first place can, as long as quantum-theoretically allowed, bridge the energy gaps between rotational energy levels (Goody and Yung, 1989, Section 3.3.5). This effect is called 'line mixing'. For CO_2 it turns out that photons that could be absorbed without this effect can then not be absorbed anymore, leading to a sub-Lorentzian line shape in the far line wings. On the other hand, the collisions with other molecules were assumed to be instantaneous. A finite duration of the collisions (1 ps for CO_2 at standard temperature and pressure) results in a smoother cutoff of the harmonic electromagnetic wave train and in turn to a faster asymptotic decay of the Fourier transform and thus

also to sub-Lorentzian line wings. Note, however, that the H₂O mid wings can be super-Lorentzian according to the discussions by [Wang and Sirota \(2002\)](#), [De Souza-Machado et al. \(2002, Section 9\)](#), and [Hartmann et al. \(2008, Chapters IV and V\)](#). The resulting line shape is usually modeled by multiplying the Lorentz profile (or Voigt profile, which is almost Lorentzian in the far wings) with a so-called χ -factor. Without consideration of the sub-Lorentzian behavior of CO₂, the main IR absorber in Venus' atmosphere, it is not possible to simulate realistic Venus nightside spectra at all. In some cases and wavenumber ranges, the χ -factor can be inferred from laboratory measurements, and in absence of more detailed information, it is common practice to carry such results over to other situations as long as the simulated radiances are realistic. Like in the forward model described by [Haus and Arnold \(2010\)](#), the χ -factor for CO₂ is here defined according to [Bézar et al. \(2009\)](#) (χ_B) shortward of 1.5 μm (6667 cm^{-1}) and according to [Tonkov et al. \(1996\)](#) (χ_T) longward of 1.5 μm with

$$\chi_B(\nu) = \begin{cases} 1, & \Delta\nu \leq 3 \\ 1.051 \exp(-\Delta\nu/60), & 3 < \Delta\nu \leq 60 \\ 0.6671 \exp(-\Delta\nu/110), & 60 < \Delta\nu \leq 350 \\ 0, & 350 < \Delta\nu \end{cases}, \quad \chi_T(\nu) = \begin{cases} 1, & \Delta\nu \leq 3 \\ 1.084 \exp(-0.027\Delta\nu), & 3 < \Delta\nu \leq 125 \\ 0, & 125 < \Delta\nu \end{cases}, \quad (\text{II.11})$$

where $\Delta\nu := |\nu - \nu_0|/\text{cm}^{-1}$ for a line with line center wavenumber ν_0 . The function χ (and thus the line shape) is continuous except at the cutoff wavenumber (350 cm^{-1} for χ_B , 125 cm^{-1} for χ_T) beyond which the contribution from the respective line is set to zero. Note that the cutoff for χ_T has been chosen smaller here than originally proposed by [Tonkov et al. \(1996\)](#). Fig. II.6 illustrates one example of a basic Voigt profile in comparison to the results of the multiplication with the Bezar and the Tonkov χ -factors, respectively. For the other gaseous components, the χ -factor is set to 1 with a cutoff at 125 cm^{-1} . Reasonable modifications of the cutoff wavenumber have only marginal influence on simulated radiance spectra.

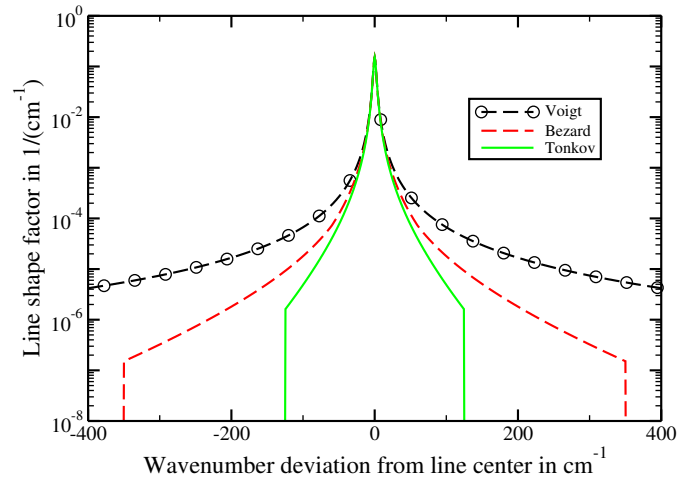


FIGURE II.6: Line shapes in the far wings for different χ -factors applied to the Voigt profile that are valid for the same conditions as described in the caption of Fig. II.5 but at 10 km altitude. The Lorentz profile would be indistinguishable from the Voigt profile in this diagram.

II.2.3.4 Continuum absorption

An additional significant contribution to the CO₂ opacity results from continuum absorption. Radiance spectra simulations are not satisfactory when it is neglected. In contrast to the absorption cross section of the allowed transitions that rapidly change with wavenumber, it has a rather smooth wavenumber dependence (hence the name). The CO₂ continuum is not very well computable, and measurements are difficult to perform (high densities and long path lengths are required) and partly contradict each other (cf. [Pollack et al., 1993, Section 2.3](#)). It is therefore common practice to determine a continuum from the measured spectra themselves that allows one to simulate the measured Venus nightside spectra reasonably well, see below. Note that the continuum is not observable at dayside conditions, since it becomes significant only at the pressure and temperature conditions in the lower atmosphere, and dayside spectra mainly probe altitudes only above the clouds (cf. [Haus](#)

et al., 2013). Possible **causes of the continuum absorption** include accumulated residual contributions from the far wings of all allowed lines (see discussions by Hartmann et al., 2008, Chapter V; for the H₂O vapor continuum, which is also considered in the present work, see Mlawer et al., 2003; Clough et al., 2005, 1989). Furthermore, collision induced absorption (CIA) can contribute to the continuum, where a transient dipole moment for the molecule is created by collisions from other molecules, and photons can thus interact with the molecule that would normally not do so, leading to additional absorption (Hartmann et al., 2008, Chapter V). For H₂O, finally, there is evidence that water dimer (H₂O·H₂O) contributes to the continuum by providing additional capacity for photon absorption (Hartmann et al., 2008, Chapter V).

Far wing contributions and CIA originate from collisions of the absorbing with other molecules and depend on the types of the participating molecules. The **self-continuum** results when absorbing and colliding molecules are of the same type. It must be distinguished from the **foreign-continuum** where the types differ. The continuum absorption is proportional to the collision rate and thus to the density of the perturbing molecule type, but it is also proportional to the density of the absorbing molecule type. Hence, the self-continuum absorption scales with density squared of the absorbing molecule type, and the foreign-continuum with the product of the densities of the absorbing and the perturbing molecule types (Clough et al., 1989), see also De Souza-Machado et al. (2002, Section 8); Pollack et al. (1993). Most important in Venus' atmosphere are collisions with CO₂ molecules that constitute 96.5% of the gaseous atmospheric mass density. For H₂O (volume mixing ratio ≤ 50 ppm) absorption, the foreign-continuum due to CO₂ must thus be taken into account, whereas foreign-continua due to other molecule types and the self-continuum are completely negligible. For this work, H₂O foreign continuum is taken into account according to Mlawer et al. (2003); Clough et al. (2005, 1989) resulting in additional absorption with impacts mainly in the spectral range between the 1.10 and 1.18 μm nightside radiance peaks. Except for CO₂, no continuum is considered for the remaining gaseous components due to lack of both data and significant impact.

The CO₂ self-continuum absorption is modeled here as $\alpha^{\text{s.cont CO}_2} \rho^{\text{mol CO}_2} \rho^{\text{mol CO}_2}$ with the particle number density $\rho^{\text{mol CO}_2}$ of CO₂, and the foreign continuum due to collisions from the other gaseous constituents with combined particle number density ρ^{f} as $\alpha^{\text{f.cont CO}_2} \rho^{\text{mol CO}_2} \rho^{\text{f}}$. Here, $\alpha^{\text{s.cont CO}_2}$ denotes the self- and $\alpha^{\text{f.cont CO}_2}$ the foreign-continuum parameter for CO₂. In absence of more detailed data, $\alpha^{\text{f.cont CO}_2}$ is treated to have the same value as $\alpha^{\text{s.cont CO}_2} =: \alpha^{\text{cont CO}_2}$, such that the CO₂ continuum absorption can be written $\alpha^{\text{cont CO}_2} \cdot q^{\text{mol CO}_2} \cdot \rho^2$, where $q^{\text{mol CO}_2} = 0.965$ is the volume mixing ratio of CO₂ and $\rho = p/(k_B T)$ the particle number density of the ideal gas at temperature T and pressure p . The wavelength dependent quantity $\alpha^{\text{cont CO}_2}$ is the **CO₂ continuum parameter**. Values for the continuum parameter are often not given for $\alpha^{\text{cont CO}_2}$ in the literature, but for $\alpha^{\text{cont CO}_2}/\rho_0^2$, which is expressed in units of $\text{cm}^{-1} \text{amagat}^{-2}$. Here, the Loschmidt constant $\rho_0 = 1$ amagat is the number of particles per cm^3 in an ideal gas of temperature $T_0 = 273.15$ K and pressure $p_0 = 101.325$ kPa, i.e. $\rho_0 = p_0/k_B T_0 = 2.687 \cdot 10^{19} \text{ cm}^{-3}$. Sometimes the value $\alpha^{\text{cont CO}_2}/\rho_0$ is given in the literature, which is measured in units of cm^2 .

But how can the CO₂ continuum be determined from the measurements themselves? The VIRTIS-M-IR spectra can be regarded as measurements of the continuum but with the locally varying parameters (e.g. atmospheric composition and structure) as interfering factors. It is important to understand that the continuum is always the same for all VIRTIS-M-IR nightside measurement. Any continuum determined from the measured spectra must thus be compatible with *all* measured spectra. The multi-spectrum retrieval algorithm MSR developed in the frame of this work is able to retrieve parameters that are common to a selection of measured spectra. Kappel (2014) has demonstrated that MSR allows the **retrieval of continua** from VIRTIS-M-IR measurements, when random measurement errors are assumed to be the only error sources. However, results must be interpreted carefully, since for instance systematic measurement and simulation errors exist that are also common to all spectra. But note that the opacity correction cannot be interpreted as the result of arbitrary kinds of systematic measurement and simulation errors, since its functional dependence complies with that of a continuum absorption. In practice, a wavelength dependent gaseous opacity correction can be retrieved with MSR as parameter vector that is common to as many and as diverse as possible measurements. The main unknown relevant factor in the radiative transfer simulations of Venus IR nightside spectra is the CO₂ self-continuum, and thus, the opacity correction may be attributed to it. Preliminary retrieved continuum parameters that are specific to the spectral transparency windows and constant over the spectral ranges of the respective windows were shown by Haus, Kappel, and Arnold (2013, Table 4). Fig. III.11 (p. 94) (Kappel et al., 2012b) shows a retrieved wavelength resolved continuum parameter for the 2.3 μm spectral radiance

window. The latest best estimate for the opacity correction is presented in Section VI.2.2 (p. 167) (Kappel et al., 2016). Note that these values have always to be referred to the utilized respective line databases and line shapes. Unfortunately, this is not in each case done in the literature. The retrieved continuum has proved to be indeed very successful for (almost⁵) all other VIRTIS-M-IR spectra analyzed so far and is a good candidate for a correction that is compatible with all measured spectra. The opacity correction globally facilitates better fits of the simulated to the measured spectra and has partly the character of a compensation of other not well understood opacity effects. This includes wrong assumptions on line shapes and errors in the line databases, which are kinds of simulation errors. Line database errors present serious problems for the simulation of Venus nightside spectra (Haus and Arnold, 2010; Bézard et al., 2011). Line databases are partly or fully based on theoretical models and not on measurements (Tonkov et al., 1996; Tashkun et al., 2003; Rothman et al., 2009) and may not always be sufficiently verified by experiments, in particular at the extreme environmental conditions close to Venus' surface.

II.2.3.5 Line-by-line procedure

In the custom forward model implementation, the computation of gaseous absorption due to allowed transitions proceeds as described below. Some parts of the present section have already been discussed by Kappel et al. (2015) and Haus et al. (2013) with Haus and Arnold (2010) as the primary source for the details of the forward model implementation.

CO₂ is the main constituent of Venus' atmosphere (96.5% by volume). Considered minor gaseous constituents are H₂O, CO, SO₂, OCS, HCl, and HF. HDO is treated such that the D/H ratio corresponds to 150 times the corresponding ratio for Earth. Other values used in the literature are 95±15 at 74 km (Krasnopolsky et al., 2013), 120±40 below the clouds (de Bergh et al., 1991), and 157±15 at 72 km (Bjoraker et al., 1992). A HDO/H₂O ratio of 240±25 between 70 and 95 km was reported by Fedorova et al. (2008). Monochromatic absorption cross sections of gases due to allowed molecular transitions are computed from the **spectral line databases** CSDS and HITEMP-Venus in case of CO₂ (CSDS for 7500–8000 cm⁻¹ and 11100–25000 cm⁻¹, Tashkun et al., 2003, HITEMP-Venus for 10–7500 cm⁻¹ and 8000–11100 cm⁻¹, Pollack et al., 1993). Data on CO and H₂O isotopologues 161, 181, 171 are taken from HITEMP-Earth (Rothman et al., 1995). HITRAN08 (Rothman et al., 2009) is used for H₂O isotopologues 162, 182, 172, and for the other minor constituents SO₂, OCS, HCl, and HF. To be in line with Haus and Arnold (2010), the more recent high-temperature database HITEMP2010 (Rothman et al., 2010) is not yet considered here.

To calculate gaseous absorption cross sections, information on temperature and pressure conditions is required. The Venus International Reference Atmosphere (VIRA) provides latitude dependent temperature and pressure altitude profiles. For this work, corresponding data are adapted from Haus et al. (2013). These data comprise both VIRA-1 (Seiff et al., 1985) and VIRA-2 (Zasova et al., 2006b) profiles. Although VIRA-2 is based on more recent measurements and is more detailed, it only covers altitudes between 55 and 100 km. Fig. II.7 shows temperature and pressure altitude profiles for different latitudes.

Look-up tables of **gaseous absorption cross sections for allowed transitions** are computed at first. For this purpose, a pressure grid is defined between -5 and 140 km with grid points corresponding to the equatorial VIRA pressures at step 5 km resolution. Three temperatures (equatorial VIRA temperature at this altitude, 30 K higher, 30 K lower) are chosen at each pressure grid point. The so-defined temperature-pressure grid suffices to encompass via quadratic interpolation (and possibly moderate extrapolation) all expected variations of the temperature and pressure conditions between the surface and the top of the model atmosphere at 140 km. As already discussed, a wavelength (or wavenumber) grid is defined on which the monochromatic absorption cross sections are computed. At each wavelength grid point and for each temperature-pressure grid point, the contributions from all lines of a molecule type (line strengths times line shapes) are summed up, yielding a look-up table of the absorption cross sections. Such a look-up table is computed for each molecule type and needs only be recomputed when line shapes or wavelength resolutions or wavelength ranges shall be modified. Two optimizations proposed by Letchworth and Benner (2007, Section 6) are implemented. Spectral lines are not considered at all when they are estimated to yield a negligible contribution to the absorption at

⁵The clouds in the polar regions seem to have anomalous properties (cf. Wilson et al., 2008) and do not always allow for satisfactory fits in the frame of the forward model utilized for the present work. In these cases it cannot be verified at the moment, whether the retrieved continua are compatible with the measurements.

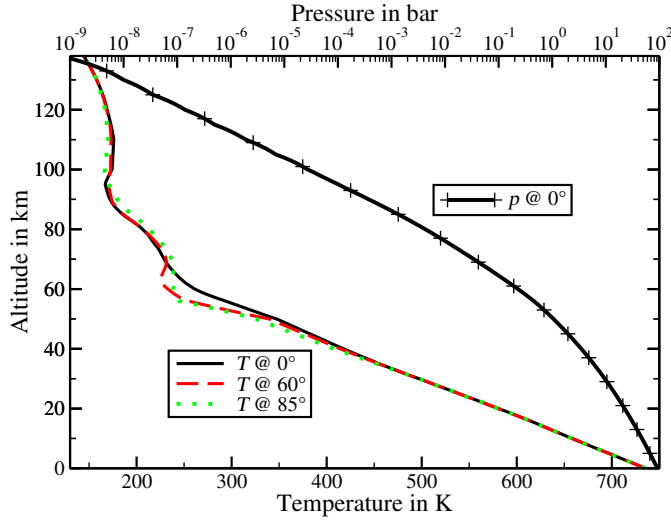


FIGURE II.7: Temperature (T) and pressure (p) altitude profiles at various latitudes according to VIRA and Haus et al. (2013).

the respective temperature and pressure conditions. When contributions far from the line center become negligible, they are also not included in the computation. Fig. II.8 shows for the relevant molecule types weighted monochromatic absorption cross sections per molecule, which are usually represented in the wavenumber domain. Here, they are instead shown in dependence on wavelength for better comparison to the nightside spectra themselves (Fig. II.1 (p. 26)). The weighting shall illustrate the relative importance of the different molecule types and was performed by a multiplication with the mixing ratios of the respective gases at the respective altitudes, see Fig. II.9. In this range, the surface can only be probed through the surface windows (1.02, 1.10,

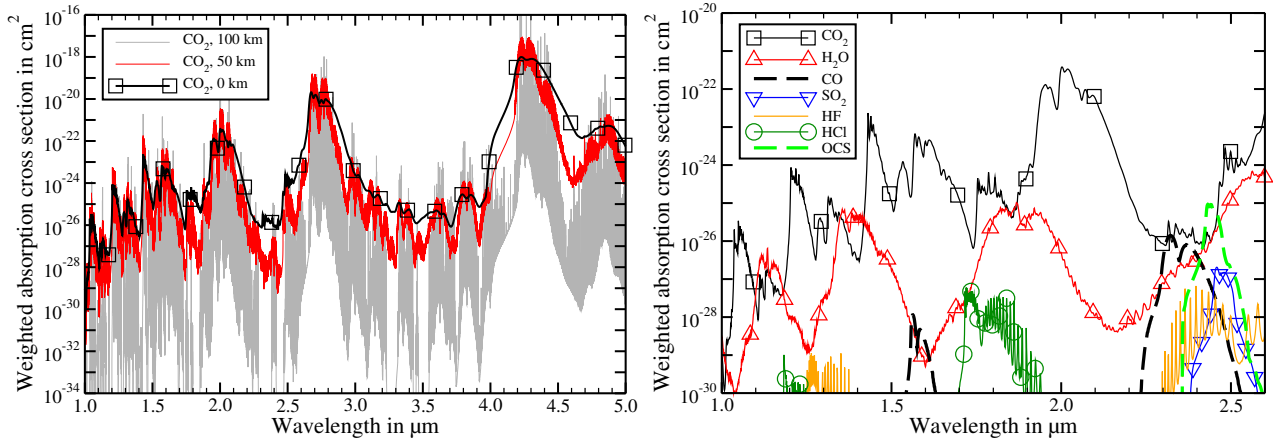


FIGURE II.8: Weighted absorption cross sections per molecule for gaseous constituents. Left: For CO_2 at equatorial VIRA conditions at different altitudes in the approximate VIRTIS-M-IR spectral range. Right: For all relevant molecule types at surface conditions (0 km) in the spectral range most important for this work (1.0–2.6 μm).

and 1.18 μm), but the weighting with the mixing ratios for the representation in Fig. II.8 is still valid at 25 km (cf. Fig. II.9), the altitude probed by the spectral windows in the range 1.7–2.5 μm , as will be shown below. In the right panel of Fig. II.8, surface conditions are chosen for better representation, since the wavelength dependencies are smoother than at higher altitudes. This is due to the less severe line broadening at higher altitude conditions, as it is illustrated in the left panel. The spectral range around the strong CO_2 absorption band at 4.3 μm can be used to retrieve atmospheric temperature altitude profiles between 58 and 84 km from VIRTIS-M-IR nightside spectra (Haus et al., 2013, 2014). Note that most of the gaseous absorption is due to the main gaseous atmospheric constituent CO_2 (Fig. II.8, right panel). The spectral transparency windows at 1.02, 1.10, 1.18, 1.28, 1.31, 1.74, and 2.3 μm result from the corresponding local minima of CO_2 absorption, while H_2O appears as the most important minor gas. Most minor gases have impacts near 2.4 μm . But note

that the conditions at other altitudes as well as other mechanisms are also important to the formation of the observable spectrum.

For the computation of a synthetic radiance spectrum, the actual temperature and pressure altitude profiles may differ for different latitudes (Fig. II.7) and local times. They may even differ from VIRA when determined from actual measurement retrievals. But T and p are not independent of each other. Given the temperature profile $T(z)$ for altitudes z , the corresponding **pressure altitude profile** $p(z)$ is computed by numerically integrating the hydrostatic equation $dp(z)/dz = -g(z)\rho(z)$, where g is the gravitational acceleration and ρ the atmospheric mass density. The initial value is set to the VIRA pressure at the surface. The hydrostatic equation follows from the observation that the pressure difference $p(z_2) - p(z_1)$ between altitudes z_i results from the force exerted by the mass $\int_{z_1}^{z_2} \rho A dz$ onto the area A , i.e. $p(z_2) - p(z_1) = -\int_{z_1}^{z_2} g\rho A dz/A$. $g(z)$ follows from Newton's law of gravitation as $g(z) = \gamma M/(R+z)^2$ with the gravitational constant $\gamma = 6.674 \cdot 10^{-11} \text{ Nm}^2/\text{kg}^2$. $R = 6051.8 \text{ km}$ and $M = 4.87 \cdot 10^{24} \text{ kg}$ are the mean radius and the mass of Venus, respectively. The mass density $\rho(z)$ follows from the ideal gas law $p(z) = \rho(z)k_B T(z)$, where ρ is the particle number density and k_B Boltzmann's constant, and $\rho = \bar{\mu}\rho$ with the mean molecular weight $\bar{\mu}$. Usually, the temperature profile is the retrieved quantity, and the pressure profile is computed as described, because T has a more linear behavior than p which can vary over many orders of magnitude (Fig. II.7).

The **altitude profiles of volume mixing ratios of gaseous components** are modeled according to Fig. II.9, which displays data used by Haus and Arnold (2010) that are based on profiles described by Pollack et al. (1993). Note that N_2 , although with a mixing ratio of 3.5% the second most abundant gas in Venus' atmo-

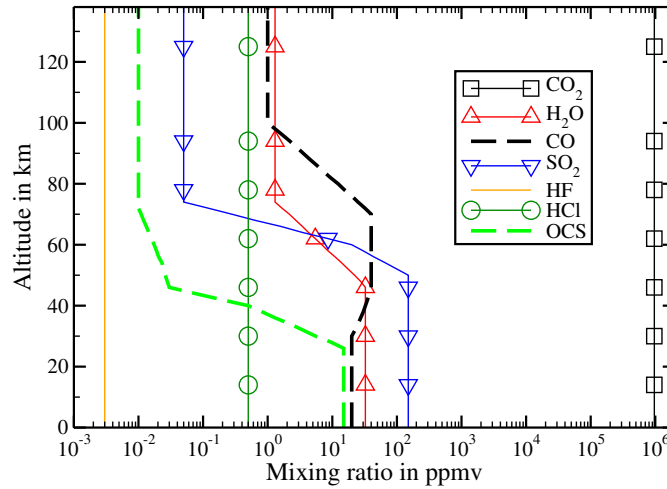


FIGURE II.9: Initial altitude distributions of gaseous constituents.

sphere after CO_2 , is not active in the studied spectral range and is not considered, therefore. The information content of VIRTIS-M-IR spectra is too low to retrieve details of the gaseous altitude profiles, but the abundance can be retrieved in certain altitude ranges for some gases. It is common practice to parameterize such abundance variations for a molecule type by a column scaling, that is, by multiplying the corresponding initial mixing ratio altitude profile by an altitude independent factor, the *column factor* for this molecule type.

As already discussed, the atmosphere is divided into sufficiently thin layers that can be regarded as homogeneous for the solution of the RTE, in this case into layers with a step size between 1 and 10 km. At a certain wavelength, the absorption by a molecule type m due to allowed transitions contributes to the **optical depth of a layer**. This contribution is computed by numerically integrating the product of the corresponding molecular absorption cross section $k_a^{\text{mol } m}$ and the particle number density $\rho^{\text{mol } m}$ over the altitude range $[z_i, z_{i+1}]$ of the layer i , $\Delta\tau_i^{\text{mol } m} = \int_{z_i}^{z_{i+1}} k_a^{\text{mol } m}(z')\rho^{\text{mol } m}(z') dz'$. The particle number density of a molecule type at a certain altitude is the product $\rho^{\text{mol } m} = q^{\text{mol } m} \cdot \rho$ of the respective volume mixing ratio $q^{\text{mol } m}$ and the particle number density $\rho = p/(k_B T)$ of the ideal gas at the respective temperature T and pressure p . Hence, the computation of $\Delta\tau_i^{\text{mol } m}$ requires the knowledge of $k_a^{\text{mol } m}$, p , T , and $q^{\text{mol } m}$ at arbitrary altitudes in the range $[z_i, z_{i+1}]$, but these values are given only at certain grid points. The T profile is known at a number of latitudes and is first linearly interpolated to the current latitude with respect to $\cos(\text{latitude})$ of the latitude grid points. Then the p profile is constructed by integrating the hydrostatic equation for the current T profile as discussed

above. The current T profile is then known at certain altitude grid points and can be linearly interpolated to the current altitude. The p profile is known at the same altitude grid as T , but it is preferable to not evaluate the current p by linear interpolation but by logarithmic interpolation, i.e. the current $\log p$ is linearly interpolated between the logarithms of the pressures at the altitude grid points. $k_a^{\text{mol } m}$ is known on a certain T - p grid and can be logarithmically interpolated to the current T and $\log p$ conditions. The volume mixing ratio $q^{\text{mol } m}$ can be linearly interpolated between the altitude grid points at which it is given. When the $\Delta\tau_i^{\text{mol } m}$ for layer i have been computed for all molecule types m at a certain wavelength, the layer optical depth $\Delta\tau_i^{\text{mol}}$ at that wavelength due to allowed transitions results as the sum of the $\Delta\tau_i^{\text{mol } m}$ over all considered molecule types. Note that the optical depth at a certain layer boundary is the sum of the layer optical depths from the top of the atmosphere down to this layer boundary. It is sometimes denoted as 'cumulative optical depth', therefore.

As already discussed, molecule type m may contribute to the gaseous layer optical depth by its **continuum absorption**. Such a contribution $\Delta\tau_i^{\text{cont } m}$, if it can be quantified at all, is computed by numerically integrating the continuum absorption of the molecule type over the i -th layer. For instance for CO_2 , the continuum contribution at wavelength λ is computed as $\Delta\tau_i^{\text{cont CO}_2}(\lambda) = \int_{z_i}^{z_{i+1}} \alpha^{\text{cont CO}_2}(\lambda) \cdot q^{\text{mol CO}_2}(z') \cdot \rho(z')^2 dz'$, where $q^{\text{mol CO}_2}(z') = 0.965$ is the volume mixing ratio of CO_2 at altitude z' , $\rho(z') = p(z')/[k_B T(z')]$ is the particle number density of the ideal gas at temperature $T(z')$ and pressure $p(z')$, and $\alpha^{\text{cont CO}_2}(\lambda)$ is the wavelength dependent CO_2 continuum parameter at wavelength λ .

II.2.4 Clouds

Absorption and scattering by clouds are important aspects for the radiative transfer in Venus' atmosphere. In order to describe these effects, it is required to understand the absorption and scattering of light in presence of a time independent single spherical cloud droplet of radius a . This situation is approached by **Mie theory**, when the size parameter $x := 2\pi a/\lambda$ for incident light of wavelength λ is neither very small, nor very large. The case $x \ll 1$ can already be well described by Rayleigh scattering (Section II.2.5 (p. 51)), whereas the case $x \gg 1$ (not relevant for this work) is better described by geometric optics due to slow convergence in Mie calculations. The total effect of all cloud particles can be derived from that of the single droplet by assuming the earlier mentioned 'independent scattering', i.e. the scattering sources are separated widely enough so that each particle scatters light in the same way as if all other particles were not present. The description of Mie theory in this section follows, except when stated otherwise, the text book by Liou (2002, Chapter 5.2), but the algebra is largely omitted, and only the underlying ideas are distilled from this text. This is done, because, on the one hand, listing the equations of the results without reproducing the intermediate steps is not so helpful here, and the details are extensively described in many text books and already implemented in well proven computer routines like that of Wiscombe (1980). On the other hand, it is useful to understand the physical and mathematical key arguments, for instance in order to be aware of the assumptions and underlying mechanisms and to be able to evaluate the limitations of the method.

II.2.4.1 Mie theory

Without loss of generality, the coordinate origin is placed at the center of the spherical cloud droplet, a homogeneous and isotropic sphere of radius a and with the complex index of refraction m . The embedding atmospheric medium in absence of the droplet can well be modeled as homogeneous and isotropic with refractive index 1. The incident light is modeled as a plane wave propagating along the direction of the positive z axis. The situation is described by the (so-called macroscopic) **Maxwell differential equations**⁶ in absence of electric charge and current densities. First, the time dependence of the resulting wave equations for \mathbf{E} and \mathbf{H} is separated, leading to the Helmholtz equation $\Delta\mathbf{A} + k^2 m^2 \mathbf{A} = 0$, where $\Delta = \nabla \cdot \nabla$ is the Laplace operator, $k = 2\pi/\lambda$ (not to be confused with wavenumber $\nu = 1/\lambda$), and \mathbf{A} can be either \mathbf{E} or \mathbf{H} .

⁶ $\nabla \cdot \mathbf{D} = \rho$, $\nabla \cdot \mathbf{B} = 0$, $\nabla \times \mathbf{E} = -\partial_t \mathbf{B}$, $\nabla \times \mathbf{H} = \mathbf{j} + \partial_t \mathbf{D}$ with constitutive relations for a linear isotropic medium $\mathbf{j} = \sigma \mathbf{E}$, $\mathbf{D} = \varepsilon_0 \varepsilon_r \mathbf{E}$, $\mathbf{B} = \mu_0 \mu_r \mathbf{H}$ and electric and magnetic fields \mathbf{E} and \mathbf{H} , electric and magnetic flux densities \mathbf{D} and \mathbf{B} , electric charge and current densities ρ and \mathbf{j} , specific conductivity σ , vacuum and relative permittivity ε_0 and ε_r , vacuum and relative magnetic permeability μ_0 and μ_r , refractive index $m = \sqrt{\varepsilon_r \mu_r}$, speed of light in vacuum $c = 1/\sqrt{\varepsilon_0 \mu_0}$, and phase velocity of light in medium $v = c/m$ for real m .

In view of the spherical symmetry of the droplet, the Helmholtz equation is formulated in spherical coordinates (r, θ, ϕ) in terms of the radial distance r , polar angle θ , and azimuthal angle ϕ . The general solution of this homogeneous linear second order partial differential equation is then formulated in terms of spherical harmonics and Bessel and second kind Hankel functions of half-integral orders with still unspecified coefficients. The coefficients are determined by **boundary and continuity conditions**. Inside the droplet, \mathbf{E} and \mathbf{H} are solutions of the Helmholtz equation with refractive index m , whereas outside, they are solutions with respect to refractive index 1. The total outside \mathbf{E} -field can be represented as the sum of the \mathbf{E} -fields of the incident plane wave and the scattered wave. The same applies to \mathbf{H} . On the one hand, the (known) incident plane wave outside the sphere solves the Maxwell and thus the Helmholtz equations and can thus be rewritten in the spherical coordinate representation of the general solution to specify the corresponding coefficients. On the other hand, the solution inside the sphere must be finite, and the scattered wave outside the sphere must vanish at infinity. Furthermore, the bounding surface of the droplet constitutes a surface of discontinuity with respect to the material properties in the Maxwell equations, since ε and μ are spatially continuous except at that surface. At each point of this surface, \mathbf{E} , \mathbf{D} , \mathbf{B} , and \mathbf{H} can be decomposed into components that are tangential and that are normal to the surface. It can be shown⁷ that the normal components of \mathbf{B} and \mathbf{D} , as well as the (for this discussion relevant) tangential components of \mathbf{E} and \mathbf{H} must be continuous across this surface, because there are no source terms in the Maxwell equations ($\rho = 0$, $\mathbf{j} = 0$). Note that, when the tangential components of \mathbf{E} are continuous at this surface, those of \mathbf{D} have a discontinuity there when ε_r differs between the droplet and the embedding medium. The same applies to \mathbf{H} vs. \mathbf{B} with respect to μ_r . All these boundary and continuity conditions suffice to determine all coefficients in the spherical coordinate representation of the global solution of the Helmholtz equation. The internal and the scattered waves are thereby fully specified.

In practice, this scattering process is observed only from large distances ($r \gg 1/k$). Therefore, it suffices to analyze only the **far field asymptotic** of the scattered wave to derive the extinction and scattering cross sections and the scattering phase function. To obtain results for unpolarized incident light, the scattered wave has to be computed independently for two incident light beams with the same direction of propagation, where each beam is linearly polarized, the polarization directions of both beams are perpendicular to each other, the phase relations between them are random, the electric fields have the same amplitudes, and the magnetic fields have the same amplitudes. The scattered radiances (not the electric fields!) of both beams have then to be added to arrive at the scattered wave of the unpolarized incident light. The reduction of the incident energy due to absorption and scattering by the droplet is evaluated by observing the superimposed incident and scattered waves in the region that lies, with respect to the propagation of the incident wave, behind the droplet. The extinction cross section is computed as the (perpendicular) area over which the incident light would have to be totally blocked to achieve the same energy reduction. The scattering cross section results as the area that had to be totally blocked to achieve an energy reduction that corresponds to the total energy transported by the scattered wave through a sphere around the droplet with infinite radius. The phase function results as the normalized angular distribution of the energy transported by the scattered wave. The extinction and scattering cross sections k_e and k_s and the scattering phase function moments p_l can be represented in terms of the now known coefficients in the spherical coordinate representation of the global solution of the Helmholtz equation.

The **computation** of k_e , k_s , and the p_l for a given droplet size parameter $2\pi a/\lambda$ and the complex refractive index m is implemented in well tested Fortran routines like that by [Wiscombe \(1980\)](#). λ is the wavelength of the incident light, and a is the radius of the spherical droplet. The wavelength dependent refractive index is taken from [Palmer and Williams \(1975\)](#) who list the real and imaginary parts between 0.36 and 25 μm for 25, 38, 50, 75, 84.5, and 95.6 weight-% H_2SO_4 solutions in water at 300 K. Only concentrations $\geq 50\%$ are realistic for Venus' cloud droplets ([James et al., 1997](#)) and are considered here. The imaginary parts of the [Palmer and Williams \(1975\)](#) data unrealistically drop to zero between 1.78 and 2.69 μm at 50% and in different concentration dependent intervals lying in the range 2.56–2.84 μm at higher concentrations. This situation is

⁷Consider a small 'pillbox' enclosing a part of the surface of discontinuity with its bottom and lid aligned 'parallel' to the surface. In the limit of zero height, apply to this pillbox and the Maxwell equations containing ' $\nabla \cdot$ ' Gauss's theorem for converting volume into surface integrals to prove the assertion for the normal components. Analogously, consider a small rectangular loop circumscribing a part of the surface with the long sides aligned 'parallel' to the surface. In the limit of zero length of the rectangle's sides normal to the surface, apply to this rectangle and the Maxwell equations containing ' $\nabla \times$ ' Stokes's theorem for converting surface into line integrals to prove the assertion for the tangential components ([Jackson, 1975](#)).

treated according to Haus et al. (2013) where these gaps are filled with inter- and extrapolated data given by Carlson and Anderson (2011) who list imaginary indices for 68, 72, 76, 84, 88, 92, and 96 weight-% between 1.7 and 2.8 μm at a comparable temperature of 295 K. Note that the temperatures in the clouds ($\approx 200\text{--}400$ K between 45 and 75 km where the clouds mainly reside, cf. Figs. II.7 (p. 42) and II.13 (p. 48)) are not extremely different from this temperature, and that refractive indices for these solutions and wavelength ranges but at other temperatures are difficult to find in the literature. Fig. II.10 shows the wavelength dependencies of the real and imaginary parts of m for two different H_2SO_4 concentrations. It is useful to define the extinction and

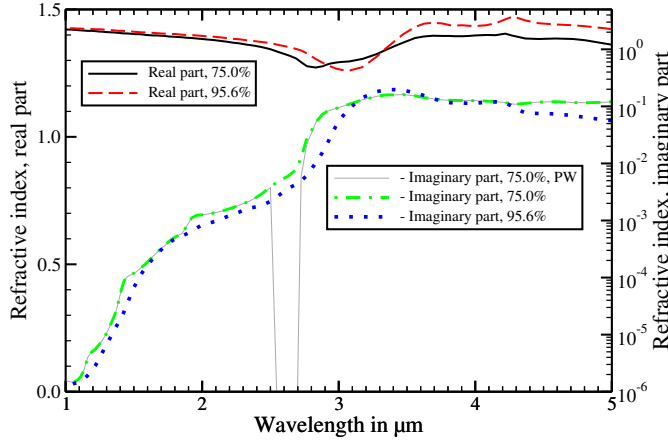


FIGURE II.10: Wavelength dependence of complex refractive index for different solutions of H_2SO_4 (Palmer and Williams, 1975; Carlson and Anderson, 2011) in the approximate VIRTIS-M-IR spectral range. Note that the imaginary parts are represented on a logarithmic scale for better representation. The minus sign before the imaginary parts is by convention. PW: original Palmer and Williams (1975) data.

the scattering efficiencies $Q_e := k_e/(\pi a^2)$ and $Q_s := k_s/(\pi a^2)$ as the respective cross sections relative to the 'cross section area' πa^2 of the droplet. Fig. II.11 illustrates the wavelength dependencies of Q_e , Q_s , and the first phase function moment p_1 for two droplets with different (fixed) radii. The zeroth moment p_0 is always 1.

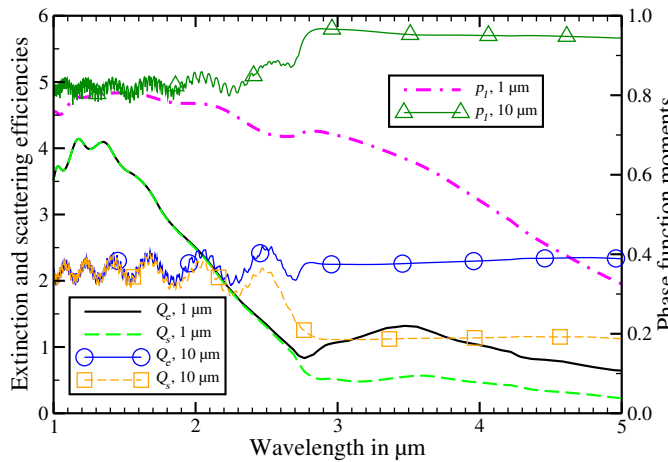


FIGURE II.11: Wavelength dependencies of (unitless) extinction and scattering efficiencies Q_e and Q_s and first phase function moments p_1 for one spherical droplet of radius $a=1 \mu\text{m}$ and one of radius $a=10 \mu\text{m}$, both consisting of 75 weight-% H_2SO_4 /water solution with refractive indices according to Palmer and Williams (1975); Carlson and Anderson (2011).

II.2.4.2 Standard cloud model

In practice, the clouds consist of droplets that do not all have the same radius. The particle size spectrometer experiment on the Pioneer Venus sounder probe showed that the cloud particles followed certain size distributions that depended on altitude (Knollenberg and Hunten, 1980). Together with the insight that at least some of

the droplets consist of an H_2SO_4 /water solution (Hansen and Hovenier, 1974) and further refinements based on new observations and analyses (Crisp, 1986; Pollack et al., 1993; Ignatiev et al., 2009; Barstow et al., 2012; Haus et al., 2013, 2014), cloud models emerged that allow one to simulate VIRTIS-M-IR measurements extremely well, as will be shown later on. In the following, one such model is presented, which corresponds to the model of Haus et al. (2013, 2014) and shall be called **standard cloud model** henceforth. It allows for an easy adjustment of some of its parameters like the cloud bottom altitude or the droplet number densities, but these modifications that are required in the later parts of this work refer to this standard model parameterization.

The cloud droplets occur in several modes, dependent on altitude, where each mode corresponds to a droplet population with a certain size distribution. The **radius distributions of the droplets** for the different cloud modes are taken from Pollack et al. (1993), who model the clouds to comprise four modes, denoted by 1, 2, 2', and 3, each of which consists of spherical droplets of 75 weight-% H_2SO_4 /water solution with log-normally distributed droplet radii. For cloud mode j , the droplet radii a are distributed according to

$$n_j(a) = \frac{1}{a \bar{\sigma}_j \sqrt{2\pi}} \exp\left(-\frac{\log^2(a/\bar{a}_j)}{2\bar{\sigma}_j^2}\right), \quad \text{for } a > 0, \quad (\text{II.12})$$

where the modal radius \bar{a}_j and the unitless scale parameter $\bar{\sigma}_j$ are listed in Table II.3. Note that $\int_0^\infty n_j(a) da = 1$, and that the mean radius is not given by \bar{a}_j but by $\int_0^\infty a n_j(a) da = \bar{a}_j \exp(\bar{\sigma}_j^2/2)$ as can be seen by substituting $y := \log(a/\bar{a}_j)$, completing the square in the exponent, and recalling that $\int_{-\infty}^\infty \exp[-(y - y_0)^2/(2\bar{\sigma}_j^2)] dy = \sqrt{2\pi} \bar{\sigma}_j$. The radius where n_j attains its maximum can be found by zeroing the derivative of n_j with respect to a and amounts to $\bar{a}_j \exp(-\bar{\sigma}_j^2)$. Fig. II.12 depicts the cloud droplet radius distributions for the four cloud modes. The log-normal distribution is well suited to describe particle

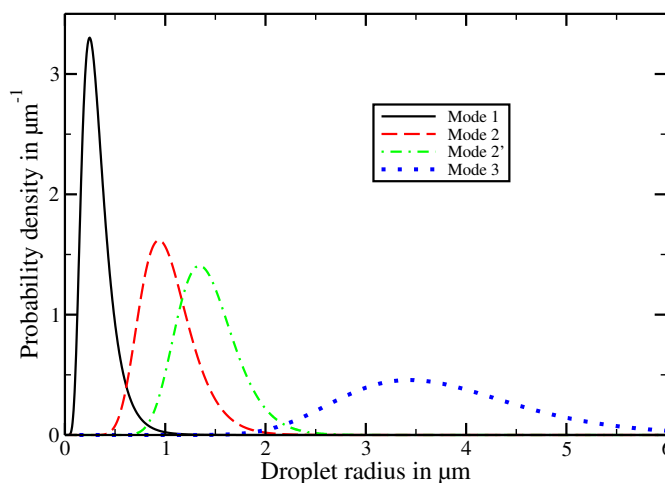


FIGURE II.12: Particle size distributions for the four cloud modes according to Pollack et al. (1993). The functional description is given by Eq. (II.12) with values from Table II.3.

distributions that arise from vapor growth processes (Söderlund et al., 1998). Note that it results as the approximate probability distribution of the *product* of many independent *positive* random variables, where in comparison, the probability distribution of the *sums* of many independent random variables is approximately the normal (or Gauss) distribution (Papoulis, 1991, Section 8.4, central limit theorem). Also note that some of the cloud modes may not consist of H_2SO_4 /water solution or not even of liquid or spherical particles. For instance, the famous unknown UV absorber in Venus' mesosphere might fall into these categories (Markiewicz et al., 2014). But in absence of detailed knowledge, it has proven to be convenient and sufficient, at least in the near IR, to model the cloud droplets as described.

For the standard cloud model, the **altitude profiles** of the particle number densities for each of the four cloud modes are taken from Haus et al. (2013). These profiles represent simplifications of measured profiles that still allow one to well simulate VIRTIS-M-IR spectra but that are easily analytically re-parameterizable.

The particle number density $N_j(z)$ for mode j at altitude z is given by

$$N(z) = \begin{cases} 0 & z > 85 \text{ km} \\ N_0 \exp(- (z - z_t)/s_t) & z_t < z \leq 85 \text{ km} \\ N_0 & z_b \leq z \leq z_t \\ N_0 \exp(- (z_b - z)/s_b) & z < z_b, \end{cases} \quad (\text{II.13})$$

where the index j is always omitted for better readability. Mode-specific values are listed in Table II.3. Fig. II.13 shows a graphical representation of the standard model altitude profiles of the cloud particle number densities. This standard cloud model can be customized to fit the actual cloud conditions by introducing cloud mode factors m_1 , m_2 , $m_{2'}$, and m_3 that scale these number densities for always the entire column, $m_j N_j(z)$. The number of mode j cloud droplets per horizontal unit area with radius between a_1 and a_2 and altitudes between z_1 and z_2 can thus be computed as $\int_{z_1}^{z_2} \int_{a_1}^{a_2} n_j(a) m_j N_j(z) da dz$ which factorizes to $(m_j \int_{z_1}^{z_2} N_j(z) dz) (\int_{a_1}^{a_2} n_j(a) da)$. Recall that $\int_0^\infty n_j(a) da = 1$, such that the total number of cloud mode j particles per horizontal unit area between z_1 and z_2 results simply as $m_j \int_{z_1}^{z_2} N_j(z) dz$. For fixed m_j , variations of z_b , z_t , s_b , or s_t for cloud mode j re-parameterize the altitude distribution of the respective cloud mode, but in order to separate variations of altitude distribution and total particle abundance, N_0 for mode j is accordingly rescaled to keep the total number of mode j particles per horizontal unit area constant. It has

Cloud mode	1	2	2'	3
Modal radius, \bar{a} in μm	0.30	1.0	1.40	3.65
Scale parameter, $\bar{\sigma}$, unitless	$\log 1.56$	$\log 1.29$	$\log 1.23$	$\log 1.28$
Top of peak density, z_t in km	65	66	60	57
Base of peak density, z_b in km	49	65	49	49
Upper scale height, s_t in km	5	3.5	1	1
Lower scale height, s_b in km	1	3	0.1	0.5
PND at z_b , N_0 in cm^{-3}	181	100	50	14

TABLE II.3: Parameters for the standard cloud model as given by Eqs. (II.12) and (II.13) and with values taken from Pollack et al. (1993) and Haus et al. (2013). PND is the particle number density.

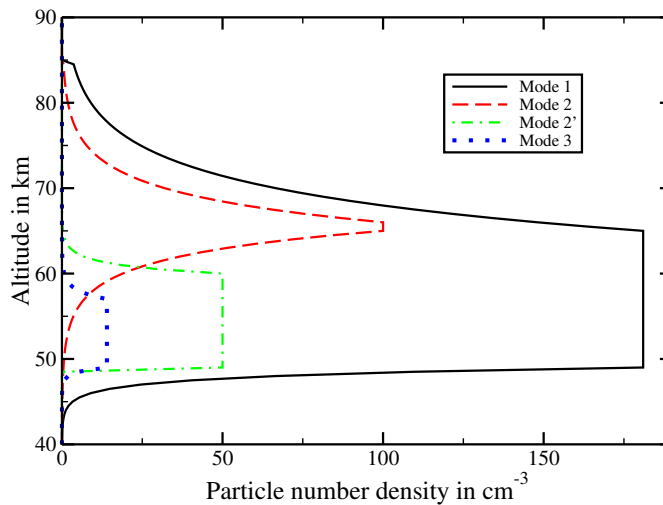


FIGURE II.13: Altitude profiles of the standard model cloud particle densities for the four cloud modes according to Haus et al. (2013). The functional description is given by Eq. (II.13) with values from Table II.3.

been found by several authors (Zasova et al., 1999, 2006a, 2007; Titov et al., 2008; Ignatiev et al., 2009; Lee et al., 2012; Haus et al., 2013, 2014) that the cloud top altitude varies with latitude. It is defined as the altitude where the cumulative cloud optical depth (i.e. counted from the top of the atmosphere) reaches 1 ('unity optical depth'). Since optical depths depend on wavelength, the cloud top altitude has to be referenced to a certain wavelength ($1 \mu\text{m}$ in this work). On average, it is fairly constant between 72 and 74 km equatorward of $50\text{--}60^\circ$ latitude. Poleward, it gradually descends to 63–64 km. This can be crudely reflected by adjusting z_t

for cloud modes 1 and 2 and z_b for mode 2 in dependence on latitude, such that they correspond to Table II.3 equatorward of 55° , are decreased by 10 km poleward of 80° , and are linearly interpolated in between (cf. Haus et al., 2013, Fig. 32, but note that these authors denote the cloud top altitude by z_t). These modifications are included in the latitude dependent standard cloud model. Compare also to Section III.4.2.1 (p. 87) (with slightly different values), where it is described that the geometry data of the measurements have to be referenced to the local cloud top altitude, where the effective source of the measured radiation is expected.

The **cloud microphysical properties** and the acid concentration of the aerosol particles were modeled by James et al. (1997), who considered the vertical transport of sulfuric acid solution aerosols, their nucleation, growth and evaporation, coagulation, and sedimentation. Their results were able to well explain measurements acquired by several missions to Venus. The simulation results of these authors, although not to be taken as absolute truth, shall be summarized here, as they can serve to provide some interesting background and justification to the cloud model employed for this work. The authors found that the lower Venus cloud is formed by an upward flux of sulfuric acid vapor from an evaporation region below the cloud base, and the mechanism of lower cloud formation is heterogeneous nucleation of sulfuric acid and water vapor on soluble nuclei. Further citing from the conclusions of these authors, water and sulfuric acid vapor abundances are controlled by condensation/evaporation in the cloud. The saturation pressures of sulfuric acid vapor and water vapor are determined by temperature and the composition of cloud droplets. The vertical profile of sulfuric acid vapor closely follows the saturation curve. The altitude of the base of the Venus cloud is determined by the abundance of sulfuric acid vapor below the clouds and the temperature profile which defines the saturation pressure curve of sulfuric acid vapor. The size distribution of cloud particles is approximately bimodal in the middle cloud and trimodal in the lower cloud.⁸ The smallest particle mode is formed by solid condensational nuclei diffused from below the cloud. The largest mode is formed by cloud droplets nucleated near the top of the cloud. The droplets continue to grow while sedimenting; thus, the mean size of this mode increases toward the bottom of the cloud. The middle mode, present in the lower cloud, appears as a result of heterogeneous nucleation on soluble cores. The aerosols that contain enough soluble material to reduce the vapor pressure significantly are activated to become cloud droplets and form this mode. Those containing less soluble material remain behind as aerosols of the smallest mode. The sulfuric acid concentration of the cloud droplets declines with increasing altitude, varying from $\approx 97\text{--}99\%$ near the cloud base to $\approx 80\%$ near 58 km altitude. The temperature profile is the main factor controlling cloud particle composition.

Note that tests are performed for this work with **altitude dependent H_2SO_4 concentrations** according to James et al. (1997). The concentration altitude profile is in these cases approximated by a linear function that attains a concentration of 88% at an altitude of 55 km and decreases with increasing altitude with a slope of -2.5% /km (these values can be modified if needed, for instance when they are treated as retrieval parameters). Wherever this linear function exceeds the maximum (95.6%) or falls below the minimum (50%) of the H_2SO_4 concentrations actually utilized in the present work, the concentration is set to this maximum or minimum, respectively. Note, however, that the altitude dependence of the H_2SO_4 concentration proposed by James et al. (1997) is not verified by measurements, and most authors successfully use just a constant concentration, e.g. 75% (Pollack et al., 1993; Haus et al., 2013, 2014). Moreover, the varying concentration profile was implemented late in this work, and it is thus not utilized in all chapters, since some of them had already been published. Thus, the constant 75% concentration model is chosen for the standard cloud model throughout this work except when stated otherwise, for instance when the impact of changes to the cloud model on retrieved emissivities is tested (Chapters V (p. 135) and VI (p. 161)).

II.2.4.3 Cloud optical properties

Now, the optical properties of the clouds can be computed, that is, the extinction and scattering coefficients, single-scattering albedo, and phase function moments that are required as inputs to the RTE solvers DISORT or LIDORT. As already discussed above, **independent scattering** is assumed. Consequently, the radiance scattered by an ensemble of cloud particles can be computed by adding the radiances scattered by the single droplets, without regard of the phase relations between the scattered waves (Liou, 2002, Section 5.2.4).

⁸Compare to Fig. II.13 to relate the mode assignments in this work to the authors' explanations. Transition from lower to middle and upper cloud is here at ≈ 60 km. Altitude assignments vary between authors, see overview by Barstow et al. (2012, Fig. 3).

For the computation of the total scattering cross section, this translates to adding the individual scattering cross sections. Recall the definition of the scattering coefficient $\beta_s := k_s \rho$ in the paragraphs following Eq. (II.2) (p. 28), where k_s is the droplet radius dependent scattering cross section and ρ the number density of the particles that cause the scattering. ρ for cloud mode j follows from Section II.2.4.2 (p. 46) as $m_j N_j(z) n_j(a)$, where n_j is the cloud mode j droplet size distribution according to Eq. (II.12) (p. 47) and $m_j N_j$ the altitude distribution of the cloud mode j particles, see Eq. (II.13) (p. 48) and its subsequent paragraph. It follows that $\beta_s^{\text{cloud } j}(z) := \int_0^\infty k_s(a) n_j(a) da \cdot m_j N_j(z)$, compare Liou (2002, Eq. (5.2.116)) who used an unspecified particle size distribution that includes both the a - and the z -dependent part from the outset. $\beta_s^{\text{cloud } j}$ is the altitude dependent scattering coefficient for cloud mode j particles which already takes the scattering from all occurring droplet sizes into account. For a fixed droplet size distribution and droplet H_2SO_4 concentration, the part $\int_0^\infty k_s(a) n_j(a) da =: \bar{\beta}_s^{\text{cloud } j}$ is independent of the cloud particle altitude distribution and thus needs only be computed once. This is done by numerical integration, which requires the computation of k_s on a fine a -grid (here with 20000 grid points that sample the corresponding log-normal distribution), such that interference phenomena are fully considered. However, $\bar{\beta}_s^{\text{cloud } j}$ depends on wavelength and on the H_2SO_4 concentration of the cloud droplets. The wavelength grid where $\bar{\beta}_s^{\text{cloud } j}$ has to be computed, does not need to be very fine, and a resolution of 10 nm was found to be sufficient (see for instance Figs. II.11 (p. 46) and II.14). These values are computed for each of the four cloud modes and for each of the four H_2SO_4 concentrations $\geq 50\%$ that are available through the refractive index data by Palmer and Williams (1975) and Carlson and Anderson (2011). These data are then stored in a look-up table for cloud optical properties. Figs. II.14 and II.15 illustrate the wavelength dependence of $\bar{\beta}_s^{\text{cloud } j}$. For the actual use

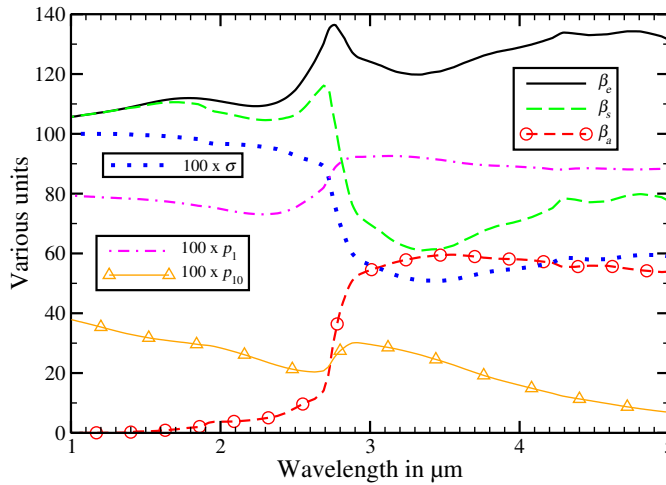


FIGURE II.14: Optical properties for cloud mode 3 at 75% H_2SO_4 concentration in the approximate VIRTIS-M-IR spectral range. The altitude independent parts of the cloud extinction, scattering, and absorption coefficients $\bar{\beta}_e^{\text{cloud } 3}$, $\bar{\beta}_s^{\text{cloud } 3}$, and $\bar{\beta}_a^{\text{cloud } 3} = \bar{\beta}_e^{\text{cloud } 3} - \bar{\beta}_s^{\text{cloud } 3}$ are given in units of μm^2 . The corresponding cloud single-scattering albedo $\bar{\sigma}^{\text{cloud } 3} = \bar{\beta}_s^{\text{cloud } 3} / \bar{\beta}_e^{\text{cloud } 3}$ and the cloud phase function moments $\bar{p}_1^{\text{cloud } 3}$ and $\bar{p}_{10}^{\text{cloud } 3}$ are unitless. $\bar{p}_0^{\text{cloud } 3}$ is always 1. A simplified notation is used in the legends.

in the forward model, $\bar{\beta}_s^{\text{cloud } j}$ is interpolated, on the one hand, to the (finer) wavelength grid utilized by the line-by-line computation of the gaseous absorption (Section II.2.3.5 (p. 41)). On the other hand, it is also interpolated to the possibly altitude dependent H_2SO_4 concentration assumed for the cloud droplets, see for instance James et al. (1997) or Section II.2.4.2 (p. 46). The layer average of the **cloud scattering coefficient** $\beta_{s,i}^{\text{cloud } j}$ for cloud mode j and the atmospheric layer i with layer altitude boundaries z_i and z_{i+1} finally results as $\beta_{s,i}^{\text{cloud } j}(\lambda) = \int_{z_i}^{z_{i+1}} \tilde{\beta}_s^{\text{cloud } j}(\lambda, z') \cdot m_j N_j(z') dz' / (z_{i+1} - z_i)$, where $\tilde{\beta}_s^{\text{cloud } j}(\lambda, z')$ is the interpolation of $\bar{\beta}_s^{\text{cloud } j}$ to the wavelength λ and the cloud droplets' H_2SO_4 concentration at altitude z' .

Next, recall the definition of the extinction coefficient $\beta_e := k_e \rho$ in the two paragraphs before Eq. (II.2) (p. 28), where k_e is the droplet radius dependent extinction cross section and ρ the number density of the particles that cause the extinction. In the same way as for the scattering coefficient, the altitude independent part (for a fixed H_2SO_4 concentration) of the extinction coefficient, $\bar{\beta}_e^{\text{cloud } j} := \int_0^\infty k_e(a) n_j(a) da$, is

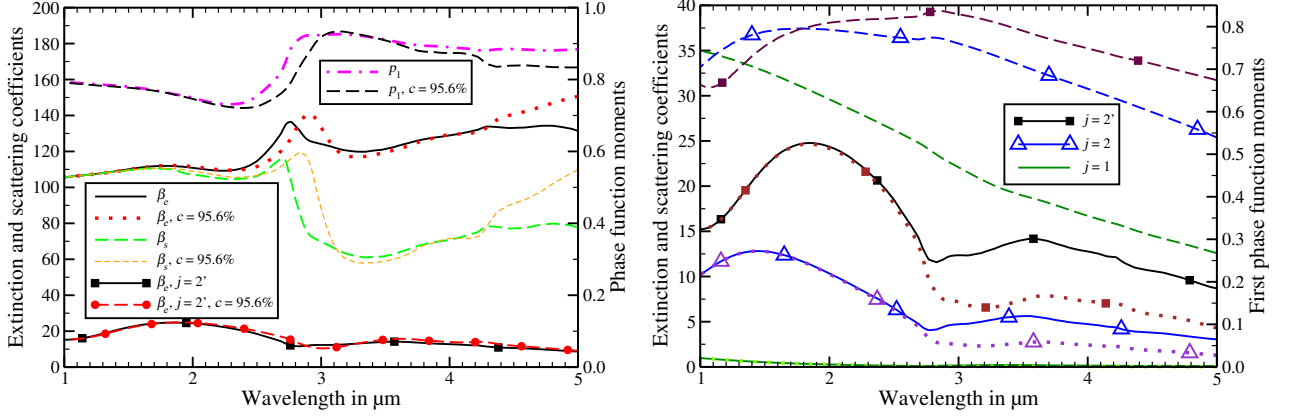


FIGURE II.15: Further cloud optical properties for cloud mode $j = 3$ at H_2SO_4 concentration $c = 75\%$, except when legend indicates otherwise. Left: Impact of modification to H_2SO_4 concentration on various quantities. Right: $\bar{\beta}_e^{\text{cloud } j}$ (continuous lines), $\bar{\beta}_s^{\text{cloud } j}$ (dotted), and $\bar{p}_1^{\text{cloud } j}$ (dashed) for cloud modes 1 (greenish, no symbols), 2 (bluish, empty triangles), and 2' (brownish, filled boxes). Note that phase function moments are assigned to axes on the right. For units and more detailed definitions of depicted quantities, see caption to Fig. II.14.

stored in the look-up table for cloud optical properties in dependence on wavelength, H_2SO_4 concentration, and cloud mode, see again Figs. II.14 and II.15 for an illustration. The layer average of the **cloud extinction coefficient** $\beta_{e,i}^{\text{cloud } j}$ for cloud mode j and atmospheric layer i is then computed in complete analogy to $\beta_{s,i}^{\text{cloud } j}$.

The cloud phase function moments are also not added directly. Recall that in the independent scattering approximation, the radiance scattered by a cloud droplet ensemble is computed by adding the radiances scattered by the single droplets. The radiance scattered by one single droplet is proportional to the product of the corresponding k_s and the corresponding phase function, see paragraph following Eq. (II.2) (p. 28). Hence, the l -th phase function moment of the cloud mode j droplet ensemble is computed as the product of $m_j N_j(z)$ and $\int_0^\infty p_l(a) k_s(a) n_j(a) da / \int_0^\infty k_s(a) n_j(a) da =: \bar{p}_l^{\text{cloud } j}$, where the denominator ensures proper normalization of the phase function moments and is exactly the same as $\bar{\beta}_s^{\text{cloud } j}$. The $\bar{p}_l^{\text{cloud } j}$, for this work computed up to the 32nd moment, are again stored in the look-up table for cloud optical properties in dependence on wavelength, H_2SO_4 concentration, and cloud mode. See again Figs. II.14 and II.15 for an illustration. In order to compute the layer averages of the **cloud phase function moments** $p_{l,i}^{\text{cloud } j}$ for cloud mode j and atmospheric layer i , note that *not* the $\bar{p}_l^{\text{cloud } j}$ are interpolated and then averaged as for the cloud scattering and extinction coefficients. Instead, the unnormalized (radiance-proportional) $\bar{p}_l^{\text{cloud } j} \cdot \bar{\beta}_s^{\text{cloud } j}$ have to be interpolated and averaged. The resulting quantities can only be normalized after that, with respect to $\int_{z_i}^{z_{i+1}} \bar{\beta}_s^{\text{cloud } j}(\lambda, z') \cdot m_j N_j(z') dz' / (z_{i+1} - z_i)$, which is exactly the same as $\beta_{s,i}^{\text{cloud } j}$. It follows that $p_{l,i}^{\text{cloud } j}(\lambda) = \int_{z_i}^{z_{i+1}} \bar{p}_l^{\text{cloud } j}(\lambda, z') \cdot m_j N_j(z') dz' / (z_{i+1} - z_i) / \beta_{s,i}^{\text{cloud } j}$, where $\bar{p}_l^{\text{cloud } j}(\lambda, z')$ is the interpolation of $\bar{p}_l^{\text{cloud } j} \cdot \bar{\beta}_s^{\text{cloud } j}$ to the wavelength λ and the cloud droplets' H_2SO_4 concentration at altitude z' .

II.2.5 Rayleigh scattering

The atmospheric molecules do not only cause absorption but also scattering of light. The present discussion of this **molecular Rayleigh scattering** is based on Liou (2002, Chapter 3.3.1), and the specialization to Venus' CO_2 atmosphere is treated according to Hansen and Travis (1974, Section 2.2).

The scattering molecules are assumed to be homogeneous, isotropic, and spherical with radii that are much smaller than the wavelength λ of the incident light. Because of this smallness, the incident light's electric field $\mathbf{E}_0 e^{ikct}$ at a certain molecule's location appears to the molecule as homogeneous and induces an electric dipole moment $\mathbf{p} = \alpha \mathbf{E}_0 e^{ikct}$, where α is the molecule's polarizability (assumed to be scalar), t the time, c the speed of light, and $k = 2\pi/\lambda$ (again not to be confused with wavenumber $\nu = 1/\lambda$). The oscillating electric field of the incident wave induces **oscillations of the dipole**, which in turn generate a plane-polarized electromagnetic wave, the scattered wave. According to the classical electromagnetic solution for an accelerated dipole given by Heinrich Hertz, the scattered wave has in the far field regime (distance of observer from

scatterer $r \gg 1/k$) the electric field $\mathbf{E} = \sin(\gamma)/(c^2 r) \partial_t^2 \mathbf{p}$, where γ is the angle between \mathbf{p} and the direction of observation. Hence, $\mathbf{E} = -\mathbf{E}_0 e^{ikct} k^2 \alpha \sin(\gamma)/r$.

To obtain results for unpolarized incident light, the scattered radiances for two independent incident light beams with perpendicular linear polarization directions, random phase relations, and same amplitudes and directions have to be added. For this purpose, the incident light is orthogonally decomposed into components with electric fields that are perpendicular and parallel, respectively, to the plane of scattering and have amplitudes E_{0r} and E_{0l} . The plane of scattering is defined by the directions of the incident and the scattered waves. The perpendicular and parallel electric field amplitudes E_r and E_l of the scattered wave follow as $E_r = -E_{0r} k^2 \alpha \sin(\gamma_r)/r$ and $E_l = -E_{0l} k^2 \alpha \sin(\gamma_l)/r$, respectively. For the perpendicular component, the angle γ_r between the direction of the correspondingly induced dipole oscillation (orthogonal to the plane of scattering) and the plane of scattering is by construction $\pi/2$. The parallel component induces a dipole oscillation that lies in the plane of scattering and is orthogonal to the incident light's direction of propagation. The scattering angle Θ is defined as the angle between the incident wave and the scattered wave at the observer's viewpoint. Therefore, $\gamma_l = \pi/2 - \Theta$, and thus, $\sin \gamma_l = \cos \Theta$, whereas $\sin \gamma_r = 1$. It follows for the perpendicular and the parallel components of the scattered radiance R that $R_r = R_{0r} k^4 \alpha^2 / r^2$ and $R_l = R_{0l} k^4 \alpha^2 \cos^2 \Theta / r^2$, where R_{0r} and R_{0l} are the perpendicular and the parallel components of the incident radiance R_0 . For unpolarized incident light, $R_{0r} = R_{0l} = R_0/2$, and thus, the **scattered radiance for molecular Rayleigh scattering** reads

$$R = \frac{R_0}{r^2} \alpha^2 \left(\frac{2\pi}{\lambda} \right)^4 \frac{1 + \cos^2 \Theta}{2}. \quad (\text{II.14})$$

Choosing a spherical coordinate system with polar angle Θ and azimuthal angle Φ , the integral of R over the full unit sphere around the scattering source reads $\int_{\Phi=0}^{2\pi} \int_{\Theta=0}^{\pi} R \cdot \sin \Theta \, d\Theta \, d\Phi = R_0 / r^2 \alpha^2 \left(\frac{2\pi}{\lambda} \right)^4 \cdot 2\pi \cdot \frac{4}{3}$. Thus, R defines a normalized phase function (see second paragraph after Eq. (II.2) (p. 28) and paragraph before Eq. (II.6) (p. 32)) $P^{\text{Rayl}}(\cos \Theta) = \frac{3}{4}(1 + \cos^2 \Theta)$. The scattered radiance can therefore be written as $R = R_0 / r^2 k_s^{\text{Rayl}} P^{\text{Rayl}}(\cos \Theta) / (4\pi)$, where $k_s^{\text{Rayl}} = \alpha^2 \left(\frac{2\pi}{\lambda} \right)^4 \cdot \frac{2}{3} \cdot 4\pi$. The quantity k_s^{Rayl} can be identified with the scattering cross section for the scattering molecule, and P^{Rayl} with the corresponding scattering phase function, when considering that the sum of the radiance losses into all outgoing directions due to the scattering can be computed as the spectral power flux $\int_{\Phi=0}^{2\pi} \int_{\Theta=0}^{\pi} R \cdot r^2 \sin \Theta \, d\Theta \, d\Phi$ that passes the spherical surface with radius r around the scatterer. This flux is (still referred to the far field approximation) independent of r and reads $k_s^{\text{Rayl}} R_0$, which corresponds to the definition of k_s^{Rayl} as the scattering cross section of the scattering molecule (see second paragraph after Eq. (II.2) (p. 28)). Applying the definitions of the Legendre polynomials $P_l(\omega)$ and the phase function moments p_l subsequent to Eq. (II.6) (p. 32) to the just presented Rayleigh scattering phase function $P^{\text{Rayl}}(\omega) = \frac{3}{4}(1 + \omega^2)$, the Rayleigh scattering phase function moments follow as $p_0^{\text{Rayl}} = 1$, $p_1^{\text{Rayl}} = 0$, $p_2^{\text{Rayl}} = 1/10$, and $p_l^{\text{Rayl}} = 0$ for $l \geq 3$. Since they are independent of altitude (and wavelength), their layer averages $p_{l,i}^{\text{Rayl}}$ over the atmospheric layer i with altitude boundaries z_i and z_{i+1} are exactly p_l^{Rayl} .

According to the Lorentz-Lorenz formula (see Liou, 2002, Appendix D), the polarizability is given by $\alpha = \frac{3}{4\pi\rho} \frac{m^2 - 1}{m^2 + 2}$, where ρ is the number density of the scattering molecules as in Section II.2.1 (p. 27). m is the refractive index of the gas, which is effectively real and very close to 1 in the solar visible (and conjecturally also in the infrared) spectrum, such that $m^2 + 2$ can be approximated by 3. This also implies that the Rayleigh absorption cross section effectively vanishes, $k_a^{\text{Rayl}} = 0$, and that the Rayleigh extinction cross section k_e^{Rayl} equals k_s^{Rayl} . Note that this does not apply to molecular absorption that has already been discussed in Section II.2.3 (p. 35). The **Rayleigh scattering cross section** k_s^{Rayl} follows as

$$k_s^{\text{Rayl}} = \frac{8\pi^3}{3} \frac{(m^2 - 1)^2}{\lambda^4 \rho^2} \frac{6 + 3\delta}{6 - 7\delta}, \quad (\text{II.15})$$

where the last factor arises from possibly anisotropic properties of randomly orientated molecules. The 'anisotropic factor' δ depends on the molecule type and amounts to 0.09 for Venus' predominantly CO_2 atmosphere (Hansen and Travis, 1974, Section 2.2).

Hansen and Travis (1974, Section 2.2) derived a **relation between the atmospheric pressure and the optical thickness due to molecular Rayleigh scattering** by assuming hydrostatic equilibrium (see Section II.2.3.5 (p. 41), paragraph 'pressure altitude profile') and altitude independence of the acceleration of gravity g and $\kappa_s^{\text{Rayl}} := \beta_s^{\text{Rayl}}/\rho$, i.e. the scattering coefficient $\beta_s^{\text{Rayl}} = k_s^{\text{Rayl}}\rho$ referred to the atmospheric mass density ρ . These assumptions are applicable here, since molecular Rayleigh scattering is of only secondary importance in the VIRTIS-M-IR spectral range, as corresponding calculations show. Note that these authors use a different notation for these variables, for instance k_{sca} for the scattering coefficient and N for the number density of the scattering molecules. The Rayleigh optical depth above altitude z is given by $\tau^{\text{Rayl}}(z) = \int_z^\infty k_e^{\text{Rayl}}\rho dz' = \int_z^\infty k_s^{\text{Rayl}}\rho dz' = \int_z^\infty \kappa_s^{\text{Rayl}} dz' = \kappa_s^{\text{Rayl}} \int_z^\infty dz'$ (compare Section II.2.1 (p. 27), paragraph 'equation of plane-parallel radiative transfer'). The pressure at z amounts to $p(z) = \int_z^\infty g\rho dz' = g \int_z^\infty \rho dz'$ according to the hydrostatic equation (see Section II.2.3.5 (p. 41), paragraph 'pressure altitude profile'). By comparing these equations, it follows that $\tau^{\text{Rayl}} = \kappa_s^{\text{Rayl}} p/g = k_s^{\text{Rayl}} p/(g\bar{\mu})$, where $\bar{\mu} = \rho/\rho \approx 44 \cdot 1.66 \cdot 10^{-27} \text{ kg}$ is the mean molecular mass of Venus' CO₂ atmosphere. It also follows that $\tau^{\text{Rayl}}(z)/\tau^{\text{Rayl}}(z_0) = p(z)/p(z_0)$, or $\Delta\tau_i^{\text{Rayl}} = \tau^{\text{Rayl}}(z_0) \cdot \Delta p_i/p(z_0)$ for the Rayleigh optical depth $\Delta\tau_i^{\text{Rayl}}$ of layer i between altitudes z_i and z_{i+1} with layer boundary pressure difference $\Delta p_i = p(z_i) - p(z_{i+1})$. The reference Rayleigh optical depth $\tau^{\text{Rayl}}(z_0)$ at the surface ($z_0 = 0 \text{ km}$, $p(z_0) \approx 93 \text{ bar} = 9.3 \text{ MPa}$) amounts to $1.527(\lambda/\mu\text{m})^{-4}(1 + 0.013(\lambda/\mu\text{m})^{-2})$ according to Hansen and Travis (1974, Eq. (2.32)). These authors use constants from Allen (1963, pp. 87, 114) and $p(z_0) = 93 \text{ bar}$ instead of the VIRA value 92.1 bar multiplied by the CO₂ concentration 96.5%. On the other hand, they also do not include the $\approx 3.5\%$ N₂ contribution. To stay in accordance with this source and other publications and because of the secondary importance of IR Rayleigh scattering, this formula is used as stated. Note that $\Delta\tau_i^{\text{Rayl}}/(z_{i+1} - z_i)$ is the average Rayleigh scattering coefficient $\beta_{s,i}^{\text{Rayl}}$ for layer i .

In view of the approximate λ^{-4} dependence of τ^{Rayl} that is also used to explain the blue sky under Earth conditions, Rayleigh scattering is more important in the visible than in the infrared spectral range. In the VIRTIS-M-IR spectral range, molecular Rayleigh scattering is **most important near 1 μm** , where it contributes an optical depth of about 1.5 between surface and top of atmosphere. But already at the important 2.3 μm nightside spectral window, this contribution reduces to 0.05. Comparing these values to the planetary average of the cloud optical depth of ≈ 35 at 1 μm (Haus et al., 2013, 2014), it becomes clear that Rayleigh scattering is of only secondary importance in the VIRTIS-M-IR spectral range.

II.2.6 Input to RTE solver

Now, all parameters are available that are required as **input to the RTE solver** (DISORT or LIDORT). First, the temperatures at the layer boundaries (and the wavelength in order to compute the corresponding Planck emissions), the observation geometry, and, in case of dayside simulations, the incoming spectral radiance of the Sun and the illumination geometry can be provided straightforwardly as already discussed.

Then, for each monochromatic wavelength λ and **for each atmospheric layer** i with layer boundaries at altitudes z_i and z_{i+1} and thickness $\Delta z_i = z_{i+1} - z_i$, the layer optical depth $\Delta\tau_i$, single scattering albedo σ_i , and phase function moments $p_{l,i}$ are needed. They are discussed in the following.

The **optical depth** $\Delta\tau_i$ of layer i results as the sum of all terms that contribute to the extinction of radiance, which here comprise:

- the sum of the layer optical depths due to allowed molecular transitions over all considered molecule types m (Section II.2.3.5 (p. 41)): $\sum_m \Delta\tau_i^{\text{mol } m} =: \Delta\tau_i^{\text{mol}}$
- the sum of continuum absorptions over all molecule types m (when a continuum is considered), here CO₂ (Section II.2.3.5 (p. 41)) and H₂O (foreign continuum, see Section II.2.3.4 (p. 39)): $\sum_m \Delta\tau_i^{\text{cont } m}$
- the sum of the layer averages of the cloud extinction coefficients times the layer thickness Δz_i over the four cloud modes j (Section II.2.4.3 (p. 49)): $\sum_j \beta_{e,i}^{\text{cloud } j} \Delta z_i =: \Delta\tau_i^{\text{cloud}}$
- the layer optical depth due to molecular Rayleigh scattering (Section II.2.5 (p. 51)): $\Delta\tau_i^{\text{Rayl}}$.

The layer **single scattering albedo** σ_i of layer i results as the ratio $\beta_{s,i}\Delta z_i/\Delta\tau_i$, where $\Delta\tau_i$ is the sum of all terms that contribute to extinction (i.e. the just discussed layer optical depth), and $\beta_{s,i}\Delta z_i$ is the sum of all terms that contribute to scattering, which here comprise:

- the sum of the layer averages of the cloud scattering coefficients times the layer thickness Δz_i over the four cloud modes j (Section II.2.4.3 (p. 49)): $\sum_j \beta_{s,i}^{\text{cloud } j} \Delta z_i$
- the layer average of the molecular Rayleigh scattering coefficient times the layer thickness Δz_i (Section II.2.5 (p. 51)): $\beta_{s,i}^{\text{Rayl}} \Delta z_i = \Delta \tau_i^{\text{Rayl}}$.

Note that, if $\Delta \tau_i$ happens to vanish for layer i and a certain λ , σ_i is correspondingly defined to be 0, since zero optical depth also indicates absence of scatterers.

The layer averages of the **phase function moments** $p_{l,i}$ of layer i can be computed as the ratio $\widehat{p}_{l,i}/(\beta_{s,i}\Delta z_i)$, where $\beta_{s,i}\Delta z_i$ was just discussed in connection with the layer single scattering albedo, and $\widehat{p}_{l,i}$ is the sum of all unnormalized (radiance-proportional) phase function moment terms, which here comprise:

- the sum of the unnormalized layer averages of the cloud phase function moments times the layer thickness Δz_i over the four cloud modes j (Section II.2.4.3 (p. 49)): $\sum_j p_{l,i}^{\text{cloud } j} \cdot \beta_{s,i}^{\text{cloud } j} \Delta z_i$
- the layer average of the unnormalized molecular Rayleigh phase function moments times the layer thickness Δz_i (Section II.2.5 (p. 51)): $p_{l,i}^{\text{Rayl}} \cdot \beta_{s,i}^{\text{Rayl}} \Delta z_i$.

$p_{l,i}$ is defined to be 0 in case of vanishing $\beta_{s,i}\Delta z_i$ indicating absent scatterers. In this case, the phase function for this layer and wavelength is not needed for the solution of the RTE, but from a mathematical point of view, proper normalization of the phase function requires $p_{0,i}$ to be set to 1.

Fig. II.16 illustrates the **altitude profiles** for a selection of optical parameters at 1.00 and 2.35 μm . To get an impression of the wavelength dependence of some of these quantities, compare also the parameters shown in Figs. II.8 (p. 42), II.14 (p. 50), and II.15 (p. 51) that are closely related to them.

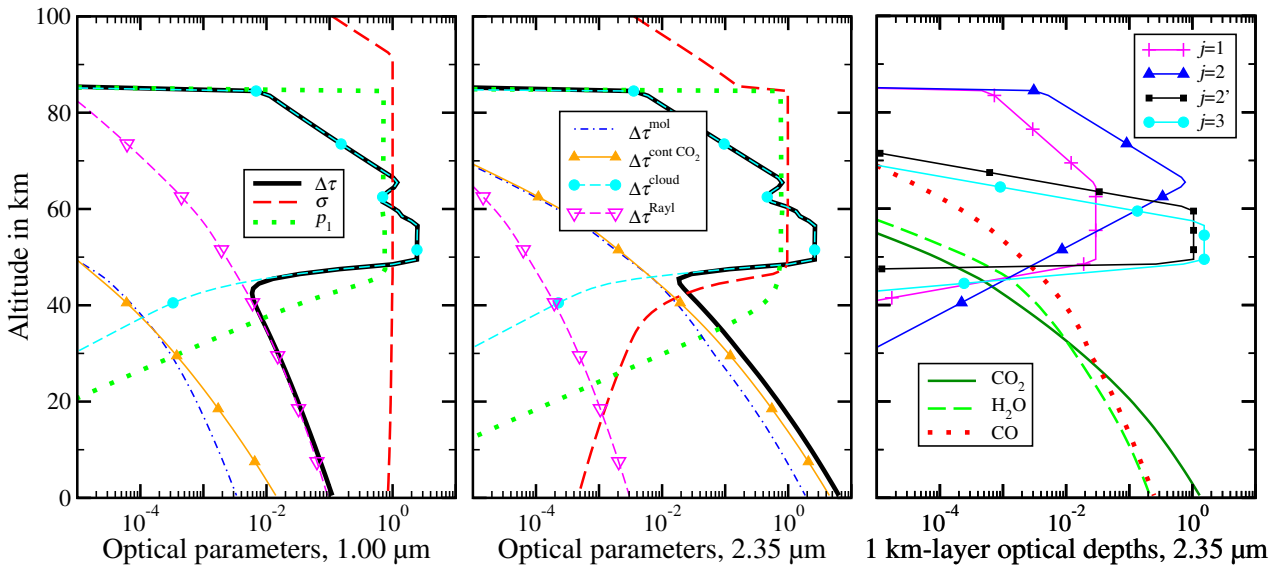


FIGURE II.16: Altitude profiles of various optical parameters for standard gas and cloud model. The atmosphere is divided into layers i with thickness 1 km. All quantities are referred to these layers, while the index i is always omitted in the legends. Left and center diagrams (with shared legends): layer optical depth $\Delta \tau_i$, single scattering albedo σ_i , first phase function moment $p_{1,i}$, and the contributions to $\Delta \tau_i$ (due to allowed molecular transitions $\Delta \tau_i^{\text{mol}}$, CO_2 continuum absorption $\Delta \tau_i^{\text{cont CO}_2}$, cloud extinction $\Delta \tau_i^{\text{cloud}}$, and molecular Rayleigh extinction $\Delta \tau_i^{\text{Rayl}}$) at 1.00 μm (left) and 2.35 μm (center). Right diagram: details of contributions to $\Delta \tau_i^{\text{mol}}$ (due to CO_2 , H_2O , and CO) and $\Delta \tau_i^{\text{cloud}}$ (due to cloud modes j) at 2.35 μm .

It will turn out (see Section VI.2.3 (p. 169)) (Kappel et al., 2016) that there might be an additional absorber in the deep atmosphere close to the surface. According to Section VI.4.4 (p. 180) and due to lacking more detailed information, this **surface haze** is actually modeled as a gaseous constituent with a wavelength independent absorption cross section of $k_a^{\text{mol srf haze}} = 10^{-20} \text{ cm}^2$ and a mixing ratio in the order of $q^{\text{mol srf haze}} = 0.1 \text{ ppmv}$ between the surface and an altitude of 2 km and zero elsewhere. This leads to a weighted absorption cross section of about $k_a^{\text{mol srf haze}} \cdot q^{\text{mol srf haze}} = 10^{-27} \text{ cm}^2$ at 0 km (cf. Fig. II.8 (p. 42)). Note that only this product has any meaning at the moment, and different values could have been assigned to

the factors. This surface haze contributes an optical depth of $\Delta\tau_{i0}^{\text{mol srf haze}}=8.8\cdot 10^{-2}$ in an atmospheric layer $i0$ between 0 and 1 km altitude. At $1.00\ \mu\text{m}$ this amounts to almost the same contribution as from Rayleigh extinction ($\Delta\tau_{i0}^{\text{Rayl}}=9.3\cdot 10^{-2}$, compare Fig. II.16, left diagram) and scales in a similar way with respect to altitude, since both are modeled with an altitude independent mixing ratio, as long as $q^{\text{mol srf haze}}=0.1$ ppmv.

In practice, the $1.28\ \mu\text{m}$ nightside radiance peak ($1.225\text{--}1.295\ \mu\text{m}$) is often contaminated by spatially and temporally varying non-LTE O_2 emissions at $1.27\ \mu\text{m}$ that originate from an altitude region around 100 km (Piccioni et al., 2009). This O_2 nightglow is outside the focus of this work and has the character of an interfering parameter here that cannot be controlled. Note that in a few cases, the O_2 nightglow is so strong that even the $1.31\ \mu\text{m}$ radiance peak is affected. The $1.28\ \mu\text{m}$ nightside radiance depends only very weakly on surface emissivity, and no significant knowledge gain can be expected even in absence of O_2 nightglow. When information is extracted from a measured spectrum in the following, this window will thus be blacked out. But it is desirable to still obtain fits to the measured spectra in the *entire* considered spectral range. Therefore, after all other parameters have been retrieved from the remaining spectral range, the $1.28\ \mu\text{m}$ peak is simulated by using these parameters and an assumed surface emissivity of 0.75 (choice of value not important). A radiance of $c^{\text{O}_2 \text{glow}}\cdot 10^{-3}\ \text{W}/(\text{m}^2\ \text{sr}\ \mu\text{m})$ is then added to the monochromatic radiance in the range $(1.26887\pm 0.00500)\ \mu\text{m}$, and the constant $c^{\text{O}_2 \text{glow}}$ is retrieved from the measured spectrum. This approach was described by Haus and Arnold (2010). It avoids complex non-LTE computations in the radiative transfer simulation and is still able to yield very good fits at VIRTIS-M-IR spectral resolution and an estimate of the strength of the O_2 nightglow.

The **spectral surface emissivity** $\varepsilon_s(\lambda) \in [0, 1]$ is the primary target of this entire work and must be set as (lower) boundary condition in the forward model simulation before it can be retrieved from measured spectra. It is wavelength dependent, and in the considered spectral range, it is only observable in three spectral night-side transparency windows located at 1.02 , 1.10 , and $1.18\ \mu\text{m}$. When in the loop over the wavelengths of the monochromatic wavelength grid, the current wavelength λ is in the range of one of the respective windows ($1.02\text{--}1.055\ \mu\text{m}$, $1.055\text{--}1.125\ \mu\text{m}$, $1.125\text{--}1.225\ \mu\text{m}$), $\varepsilon_s(\lambda)$ is set to the emissivity value assigned to this window. $\varepsilon_s(\lambda)$ is therefore modeled as constant within the range of the respective window, but it can differ for different windows. When λ is outside of these ranges, $\varepsilon_s(\lambda)$ must also be set to a certain value (e.g. 0.5), but the simulated radiance spectrum does not depend on that value.

The **surface temperature** T_s must also be provided as boundary condition. The (known) surface elevation at the measurement footprint coordinates (but see also discussion of atmospheric and motion blurring in Section III.4.2 (p. 87)) defines the bottom altitude of the atmosphere, and thus, that of the lowest atmospheric layer. T_s is here set to the temperature of the bottom of the atmosphere and can be computed by interpolating the temperature profile to the surface elevation. If necessary, T_s can also be set to a different value to estimate for instance the impact of a fresh lava flow on a radiance spectrum. The (un-blurred) surface topography map is depicted in Fig. II.17.

The bottom part of this figure also shows, how often the different parts of Venus' surface are covered by the **VIRTIS-M-IR measurements that are the most suited to extract surface information from.**⁹ They were empirically found to comprise nightside measurements (angle zenith-sun exceeding 98° to also exclude dawn and dusk straylight) with an observation angle less than 60° to avoid significant spherical effects in the radiative transfer that is modeled here as plane-parallel. The (blurred) Magellan surface elevation must be available, too. Furthermore, the spectrally averaged radiance between 2.15 and $2.30\ \mu\text{m}$ shall exceed $0.003\ \text{W}/(\text{m}^2\ \text{sr}\ \mu\text{m})$, since smaller radiances in the short-wavelength flank of the $2.3\ \mu\text{m}$ window (corresponding to very thick clouds) make it difficult to disentangle any cloud mode information and to obtain any useful surface information. The detector exposure time shall be at least 3 s to exclude spectra with very low signal-to-noise ratios in the surface windows. Spectra are also excluded where the data preprocessing (see Chapter III (p. 67)) leads to large corrections exceeding $0.004\ \text{W}/(\text{m}^2\ \text{sr}\ \mu\text{m})$ on spectral average in the range $1.0\text{--}2.6\ \mu\text{m}$, for instance due to the removal of straylight. The larger such a correction is, the larger will be the uncertainty of this correction and thus of the preprocessed spectrum. Later in this work, the emissivity of a surface target will be retrieved as parameter that is common to a number of VIRTIS-M-IR spectra that all cover the same surface target. But because of the different spacecraft orientations and distances to the surface target, the footprints of the single measurements do not coincide for repeated measurements of the same target. To improve the spectra's signal-to-noise ratio, to reduce the amount of data to be processed, to obtain spectra that are referred to the same

⁹Parts of this paragraph are from the manuscript by Kappel et al. (2016, Section 3).

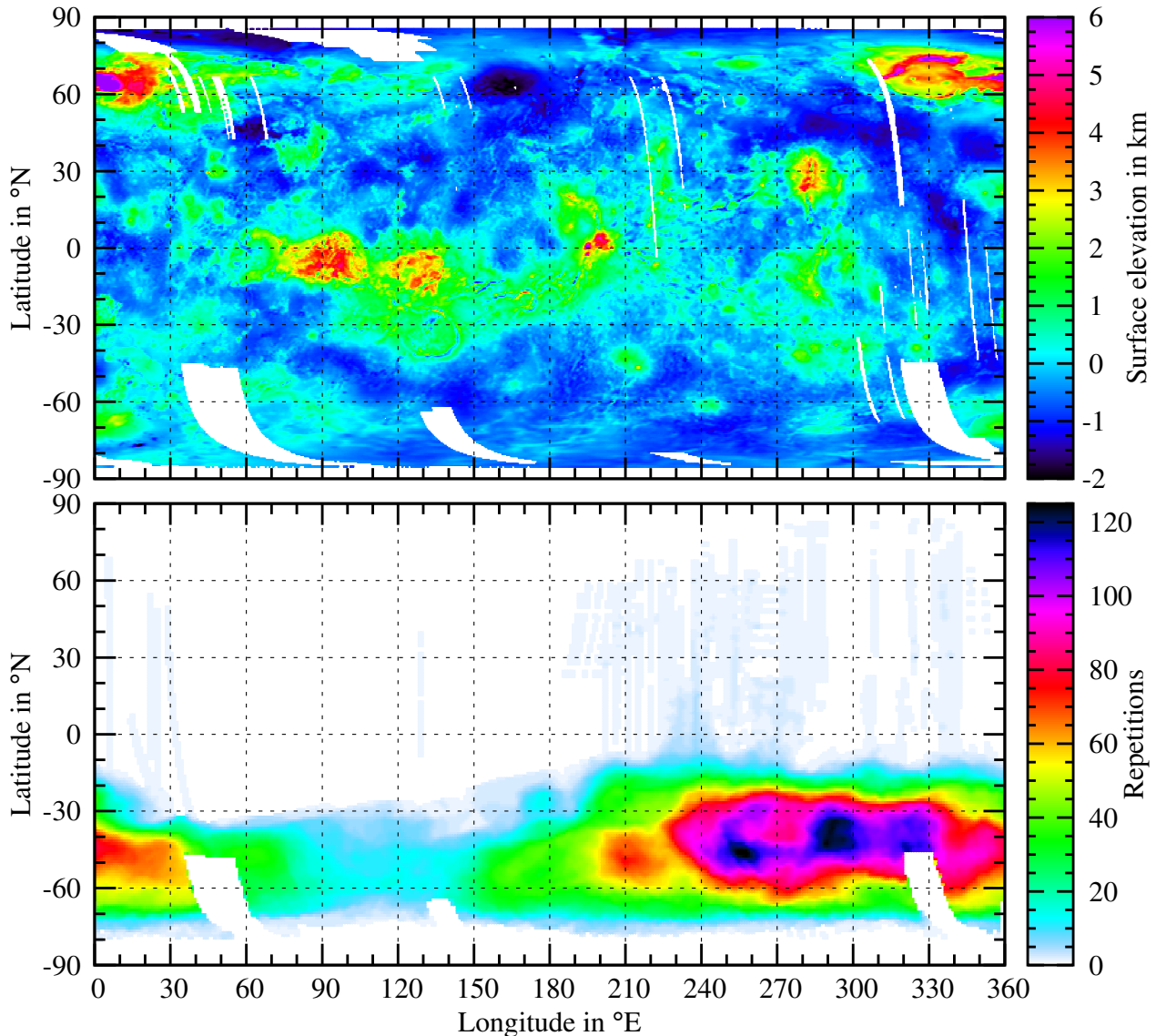


FIGURE II.17: Top: Venus' surface topography map according to Magellan radar measurements (Pettengill et al., 1991; Ford and Pettengill, 1992; Rappaport et al., 1999). White indicates missing data. Bottom: number of VIRTIS-M-IR coverages that can be used for surface emissivity retrieval as explained in the text.

surface target, and since the achievable spatial resolution of surface information derived at $1\ \mu\text{m}$ is expected to be limited to about $100\ \text{km}$ by atmospheric blurring (Moroz, 2002), the surface is here divided into bins that all have the same area of about $100 \times 100\ \text{km}^2$ ($91.5 \times 91.5\ \text{km}^2$ to be exact, see below), and the measurements are binned accordingly for each VIRTIS-M-IR data cube. The binning is performed with respect to Lambert equal area projections (Bugayevskiy and Snyder, 1995). To minimize the deviations of the bins' aspect ratios from unity, spectra with footprint latitudes $\leq 38.68^\circ$ are binned with respect to the Lambert cylindrical projection with standard parallel 30° . At the standard parallel, there is no local distortion due to the map projection. To allow for 360 bins in longitude direction, each surface bin has to cover an area of $91.5 \times 91.5\ \text{km}^2$. Spectra with footprints north or south of 38.68° latitude are binned with respect to the Lambert azimuthal projection centered around the North and the South Pole, respectively. Typically, 30 spectra contribute to each binned spectrum, but to ensure a sufficient statistical weight and improvement of the signal-to-noise ratio of the binned spectra, only those are used for surface data extraction where at least ten (unbinned) measurements contribute. Finally, note that the strongly eccentric orbit of the VEX spacecraft prevented the mapping of more than a small portion of the northern hemisphere, since the spacecraft's pericenter was located roughly above the North Pole where the velocity of the spacecraft was highest, and at the same time, the field of view allowed only narrow swaths of the surface to be observed. These regions were only measured in pushbroom mode, and essentially no part of the surface was covered more than once. Thus, for this work, only the apocenter mapping

data of the southern hemisphere can be used to derive surface emissivity. For some VIRTIS-M-IR data cubes, the full spatial resolution of 256 spatial samples was binned down to 64 samples already aboard the spacecraft before data transmission to Earth. These cubes are also excluded here to avoid an unnecessary coarse assignment of the individual spectra to the surface bins. However, in order to allow in Fig. II.17 an indication of the nature of the northern hemisphere pushbroom data that are mainly only available in the 64-sample mode, this last selection criterion was not applied to the pushbroom swaths. As it will turn out (Chapter V (p. 135)), *at least* 16–25 repetitions are required for a reliable retrieval of the emissivity of a surface bin, and areas with higher surface elevations are preferable over those with lower elevations. Fig. II.17 can thus be used as a first indicator of suitable target areas for the retrieval of surface emissivity maps.

The RTE solver **LIDORT** needs in addition to the DISORT input the derivatives of $\Delta\tau_i$, σ_i , $p_{l,i}$, and of the spectral surface reflectance $1 - \varepsilon_s$, all with respect to each of the retrieval parameters (that do not yield trivially zero derivatives), see Section II.2.2 (p. 31), paragraph ‘input to DISORT and LIDORT’. Recall that LIDORT (at the moment) does not compute analytic derivatives with respect to temperature related parameters, and that these derivatives have to be computed perturbatively, see Section II.2.2 (p. 31), paragraph ‘perturbative derivatives’.

This completes the discussion of the input required to compute the monochromatic synthetic spectra. Additional discussions of certain forward model details and the reasons why they are required can also be found in Haus and Arnold (2010).

II.2.7 Synthetic spectrum and Jacobians

In order to obtain the **synthetic radiance spectrum that would be detected by the VIRTIS-M-IR instrument**, $\mathbf{f} \in \mathbb{R}^m$, the synthetic monochromatic spectrum is convolved with the VIRTIS-M-IR spectral instrumental response function. The latter is for each of m spectral bands a Gaussian with a detector temperature dependent FWHM that ranges from about 14 nm on the left side of the detector to about 20 nm on the right side, see Section II.2.2 (p. 31), paragraph ‘spectral instrumental response function’. These FWHM values were retrieved from measured spectra, compare Fig. VI.A.2 (p. 199). Fig. II.18 shows a comparison between monochromatic synthetic nightside and dayside spectra at standard conditions and the corresponding convolution with the VIRTIS-M-IR instrumental response function. Fig. II.19 (left) shows a zoom of the nightside

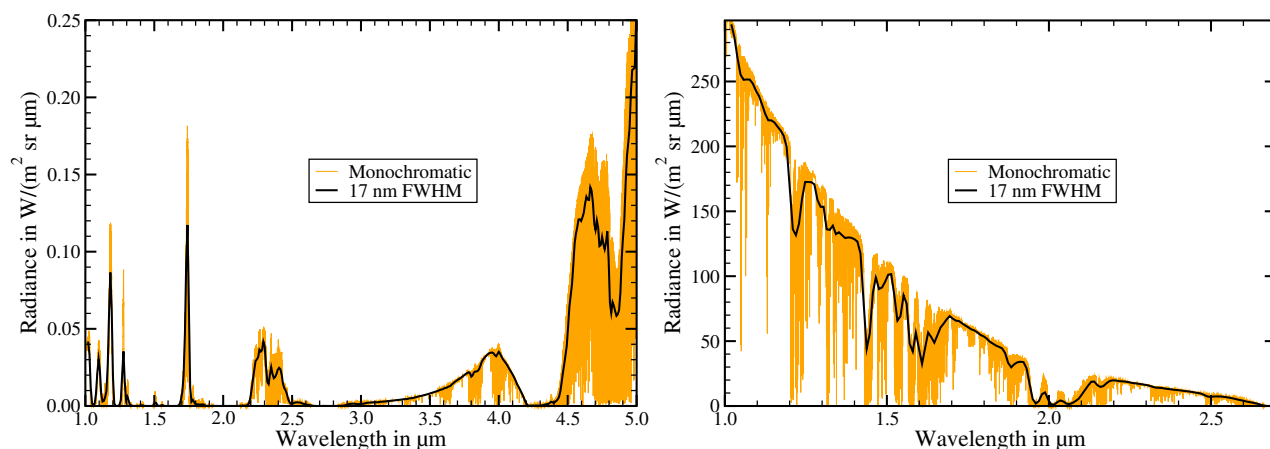


FIGURE II.18: Left: the monochromatic (0.1 nm resolution) synthetic nightside spectrum at standard conditions as presented in the previous sections and at zero observation angle in the approximate VIRTIS-M-IR spectral range and the convolution with the standard VIRTIS-M-IR instrumental response function (17 nm FWHM, gridpoints at $(1.02 + b \cdot 0.00949) \mu\text{m}$ with spectral bands $b \in \{0, \dots, 431\}$). Right: the same for the dayside spectrum at standard conditions, zero observation angle, 45° zenith-sun angle, and 45° phase angle in the wavelength range where the radiance appears as non-vanishing at this radiance axis scaling.

spectrum from Fig. II.18 to the 1.0, 1.74, and 2.3 μm window complexes that are relevant for this work.

Fig. II.19 (right) illustrates synthetic radiances, when certain atmospheric properties are not taken into account in the simulation algorithm. When neither atmospheric gases nor clouds are included, the spectrum is determined by the Planck radiation at the respective surface temperature, multiplied by the spectral surface

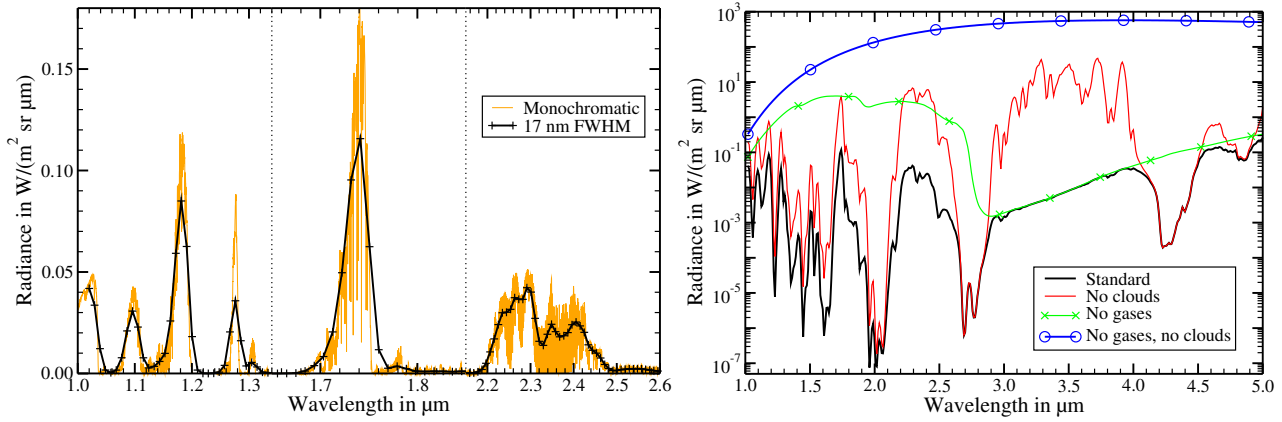


FIGURE II.19: Left: zoom of the nightside spectrum shown in Fig. II.18 to the relevant nightside window complexes. Note the non-uniform wavelength axis. The symbols indicate the synthetic radiances at the VIRTIS-M-IR spectral gridpoints. Right: Synthetic nightside radiance spectrum when different atmospheric properties are not taken into account. Note the logarithmic scale.

emissivity, here assumed to be constant with wavelength. Inclusion of the clouds leads to a decrease of the radiances. The same is observed when including the gases. Both radiance spectra for excluded gases and for excluded clouds constitute **upper envelopes** of the standard spectrum. Obviously, there are spectral ranges where the standard spectrum is dominated by cloud extinction (e.g. 3.0–3.9 μm), and other ranges where gases dominate (e.g. 4.1–4.5 μm). The surface and the deep atmosphere peaks between 1.0 and 2.6 μm require both clouds and gases to be taken into account.

Another aspect of the ability to compute a synthetic radiance spectrum $\mathbf{f}(p_1, \dots, p_n)$ is the opportunity to study the influences of the different parameters p_i on the spectrum. As an example, Fig. II.20 (left) compares the monochromatic standard radiance spectrum in the 1.74 μm window and the radiance derivatives with respect to the HCl and the H₂O column factors, see Section II.2.3.5 (p. 41), paragraph ‘altitude profiles of the volume mixing ratios of the gaseous components’. The matrix of all first-order partial derivatives of \mathbf{f} at

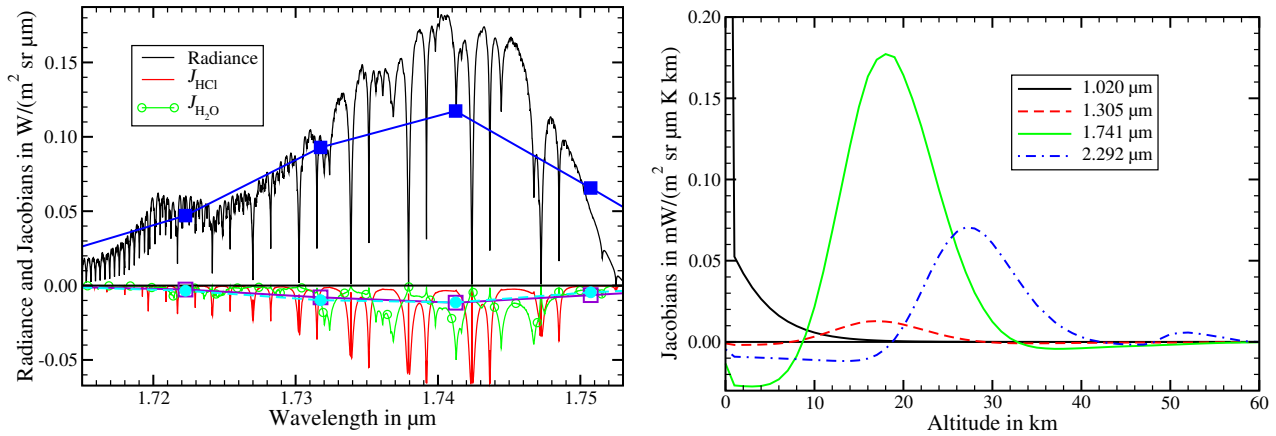


FIGURE II.20: Left: monochromatic (0.005 nm resolution) radiance and corresponding minor-gas-column Jacobians in the 1.74 μm nightside window. Corresponding curves at VIRTIS-M-IR resolution: radiance (blue line, filled squares), and HCl-Jacobian (violet line, empty squares) and the very similar H₂O-Jacobian (cyan dashed line, filled circles). Right: Temperature weighting functions at selected wavelengths, compare Fig. II.19 (left). The 1.02 μm value at 0 km amounts to 0.84 $\text{mW}/(\text{m}^2 \text{sr } \mu\text{m K km})$ and is cut off for better representation.

(p_1, \dots, p_n) is called **the Jacobian** at (p_1, \dots, p_n) . Its i -th column $\mathbf{J}_i(p_1, \dots, p_n)$, also (somewhat sloppily) called ‘Jacobian’, is defined as the differential quotient $\partial \mathbf{f}(p_1, \dots, p_n) / \partial p_i \in \mathbb{R}^m$. The monochromatic Jacobians shown in Fig. II.20 (left) are defined accordingly. The Jacobian with respect to p_i can be regarded as the perturbation of the radiance spectrum caused by a small perturbation δp_i of the parameter p_i , divided by δp_i , $\mathbf{J}_i(p_1, \dots, p_n) = \partial \mathbf{f}(p_1, \dots, p_n) / \partial p_i \approx (\mathbf{f}(p_1, \dots, p_i + \delta p_i, \dots, p_n) - \mathbf{f}(p_1, \dots, p_i, \dots, p_n)) / \delta p_i$. The increase of, for instance, the H₂O abundance leads to more absorption and thus a decrease of the radiance

at certain wavelengths, which is the reason, why the minor-gas-column Jacobians in the figure are at each wavelength $\leq 0 \text{ W}/(\text{m}^2 \text{ sr } \mu\text{m})$. The unit of a Jacobian results as the ratio of the unit of the radiance and the unit of the respective parameter. At the high spectral resolution depicted in Fig. II.20 (left), it is clearly discernible, which spectral features originate from which parameter. For instance, the triple downward pointing radiance structure between 1.7355 and 1.7370 μm is clearly associated to the H_2O column, but not to HCl , whereas the single radiance bottom at 1.738 μm is associated to HCl , but not to H_2O . The Jacobians with respect to the retrieval parameters are needed for the efficient retrieval of these parameters, as will be explained in Section II.3. When retrieving parameters from a given spectrum, the high spectral resolution in Fig. II.20 (left) suffices to disentangle the H_2O and the HCl abundances. However, the 1.74 μm peak at VIRTIS-M-IR spectral resolution (also depicted in the figure) does not allow one to disentangle these two gases (for actually measured spectra), and they can also not be disentangled from the cloud mode column factors that have Jacobians that are very similar to the H_2O and HCl Jacobians. Fig. V.2 (p. 144) shows Jacobians at VIRTIS-M-IR resolution with respect to many relevant parameters. Note that even parameters with Jacobians that have very different magnitudes cannot be disentangled, as long as their 'shapes' do not differ significantly. In this sense, the dissimilarity of the Jacobians \mathbf{J}_i and \mathbf{J}_j may be quantified by the 'angle' $\phi_{i,j}$ between them, where $\cos \phi_{i,j} := \langle \mathbf{J}_i, \mathbf{J}_j \rangle / (\|\mathbf{J}_i\|_2 \cdot \|\mathbf{J}_j\|_2)$. Here, $\|\mathbf{J}_i\|_2$ denotes the Euclidean norm of \mathbf{J}_i , which is computed as $\sqrt{\langle \mathbf{J}_i, \mathbf{J}_i \rangle}$ by using the standard Euclidean scalar product $\langle \cdot, \cdot \rangle$. Referred to Fig. II.20 (left), the angle between the HCl and the H_2O Jacobians in the depicted spectral range corresponds to 67.8° (monochromatic), or to 10.1° (VIRTIS-M-IR resolution), respectively. Parameters with parallel Jacobians ($\phi_{i,j}=0^\circ$) cannot be disentangled at all, whereas orthogonal Jacobians ($\phi_{i,j}=90^\circ$) indicate parameters that can be disentangled best, provided all other conditions are equal.

It is also possible to determine the altitude ranges in which different atmospheric parameters like the altitude profiles of the minor gases, cloud modes, and temperature affect the spectra. For this purpose, Jacobians can be computed with respect to small perturbations of the respective parameter altitude profile at localized altitude ranges. Let the altitude boundaries of an atmospheric layer i be z_i and z_{i+1} . Here, the layer thicknesses Δz_i are all equal to 1 km. A parameter altitude profile is then defined by the values p_i at the z_i , and the p_i can be compiled into the vector \mathbf{p} . The radiance Jacobian with respect to p_i is then computed as perturbative derivative $\mathbf{J}_i := (\mathbf{f}[\mathbf{p} + \Delta p \delta_i] - \mathbf{f}[\mathbf{p}]) / (\Delta p \Delta z_i)$ for a small Δp (see paragraph 'perturbative derivative' of Section II.2.2 (p. 31) for the meaning of 'small' in this context). All entries of the vector δ_i are zero, except for the i -th entry that has the value 1. The \mathbf{J}_i can be compiled into a matrix \mathbf{J} with columns \mathbf{J}_i . A row of \mathbf{J} is the **weighting function** at the respective wavelength for this parameter. Fig. II.20 (right) shows temperature altitude profile weighting functions (or short 'temperature weighting functions') at selected wavelengths. The unit of the entries of \mathbf{J} results as the radiance unit divided by the unit of Δp (e.g. K for temperature weighting functions) and the unit of the thickness of a layer (km). The temperature weighting functions indicate the altitude ranges that are probed at the respective wavelengths. At 1.02 μm , most of the radiance originates at the surface (here 0 km). The small 1.31 μm peak originates at about 17 km, and so on. Note that the temperature weighting functions can attain negative values, because, to ensure consistent atmospheric profiles, the temperature perturbation leads to a changed pressure altitude profile according to hydrostaticity and the ideal gas law, see paragraph 'pressure altitude profile' in Section II.2.3.5 (p. 41). For instance, the radiance at the 1.74 μm window should be expected to be unresponsive to a localized temperature increase in the lowest layers. But this increase accordingly leads to a localized expansion of the atmosphere and thus a shift of the overlying pressure profile toward higher altitudes. This results in an increased optical path and consequently a lesser radiation at the top of the atmosphere. On the other hand, when the temperature increase is located around 18 km, the increased emissions outweigh this pressure effect in case of the 1.74 μm window. Structurally, \mathbf{f} is really a functional of the (continuous) altitude profile $p(z)$, and \mathbf{J}_i is the approximation of the directional derivative $\frac{d}{d\Delta p} \mathbf{f}[p + \Delta p \delta_i]$ in direction of a localized perturbation $\delta_i(z)$. \mathbf{J} is therefore often called a functional derivative. The weighting functions are required to efficiently retrieve the respective altitude profile from a measured spectrum. However, information can essentially be only obtained from altitude ranges where the weighting functions indicate significant contributions to the radiances. Fig. II.21 (left) depicts the temperature- \mathbf{J} for the wavelength range used in this work. The temperature weighting function spectrum in the range 1.0–5.0 μm can be divided by the radiance spectrum to compensate the large variability of the spectrum over this range (see Fig. II.18 (p. 57), left), and thus to obtain the relative temperature weighting function spectrum. Fig. II.21 (right) shows this ratio normalized with respect to its maximum value 0.021 / (K km)

for better representation and comparison to the subsequent figures. The altitudes probed by the radiances at

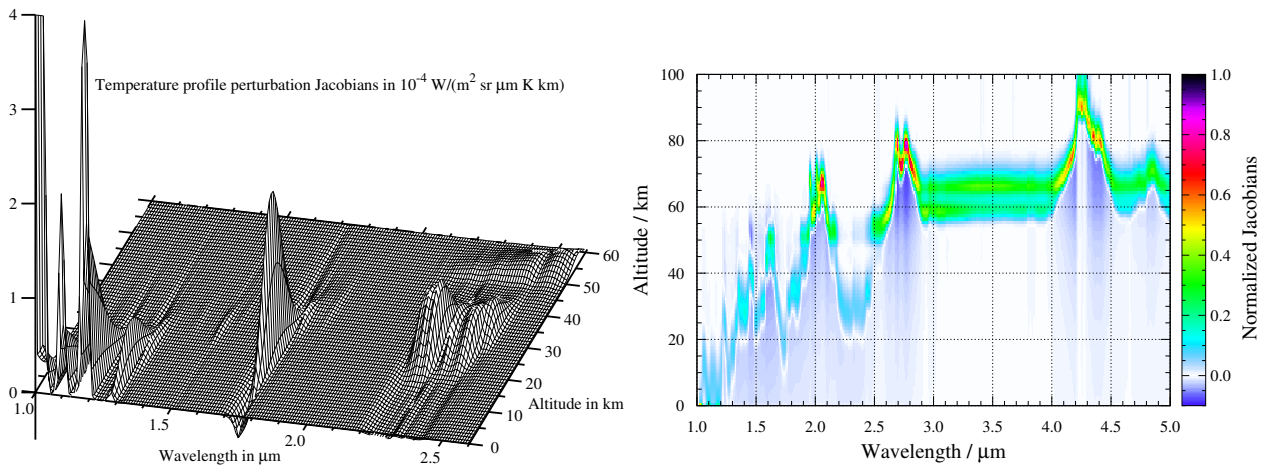


FIGURE II.21: Left: temperature weighting function spectrum in the spectral range used in this work. Right: temperature weighting function spectrum in the range 1.0–5.0 μm , normalized with respect to the radiance spectrum and with respect to the maximum of this ratio.

the different wavelengths are clearly discernible, but note that wavelengths with radiances that are close to the measurement noise level cannot yield useful information.

The weighting functions also indicate, for which altitude ranges retrieved column factors for certain parameters are valid. For instance, a CO column factor can be retrieved from the long-wavelength flank of the 2.3 μm peak (2.3–2.4 μm). This factor does not yield any information about the CO abundance at the surface or at 70 km. It only informs about the altitude around 30 km. This is illustrated by Fig. II.22, which presents the weighting function spectra with respect to the **minor gases** considered in this work. Again, they are divided by the radiance spectrum, but now these ratios are normalized with respect to their minimum values for better representation, since an increased minor gas abundance leads to an increased absorption and (in general) a decreased radiance. The minimum values amount to -0.0050 (H_2O), -0.00036 (HDO), -0.0017 (CO), -0.0011 (SO_2), -0.23 (HF), -0.0098 (HCl), and -0.21 (OCS) in units of $(\text{ppmv km})^{-1}$. Note that these values do not indicate the 'importance' of the gases in the formation of the radiance spectrum (the amount of radiance they have absorbed), since the volume mixing ratios of the gases are very different (Fig. II.9 (p. 43)), and for the computation of the weighting functions, the response to a certain volume mixing ratio perturbation is always divided by the perturbation.

In the same way, Fig. II.23 (p. 62) depicts the weighting function spectra for the **cloud modes**, divided by the radiance spectrum, and normalized with respect to the minimum values of these ratios. These minimum values amount to -0.00019 (mode 1), -0.0037 (mode 2), -0.0082 (mode 2'), and -0.065 (mode 3) in units of $(\text{cm}^{-3} \text{ km})^{-1}$. Note that for various applications in the subsequent chapters, the altitude profiles of the cloud mode particle densities are always rescaled, such that the total number of particles per horizontal unit area for a cloud mode remains unchanged by altitude profile changes. This is done to disentangle variations of altitude distributions and variations of total column particle abundances. This rescaling is not performed for the computation of the weighting functions shown in Fig. II.23 (p. 62) in order to avoid non-local effects. The figure demonstrates, for example, that additional clouds near the surface (although they do not exist at these temperature and pressure conditions) would only affect the surface windows. In general, there are only responses to perturbations in atmospheric layers that lie within or above the respective line forming regions, compare Fig. II.21. Furthermore, the relative impact moves towards longer wavelengths for the cloud modes with larger modal radii of the respective droplet radius distributions, compare Table II.3 (p. 48), as should be expected.

II.3 Single-spectrum retrieval algorithm

The forward model discussed so far (Section II.2 (p. 27)) simulates a spectrum for a given parameter vector. The problem of finding a suitable parameter vector that describes a given measurement according to the for-

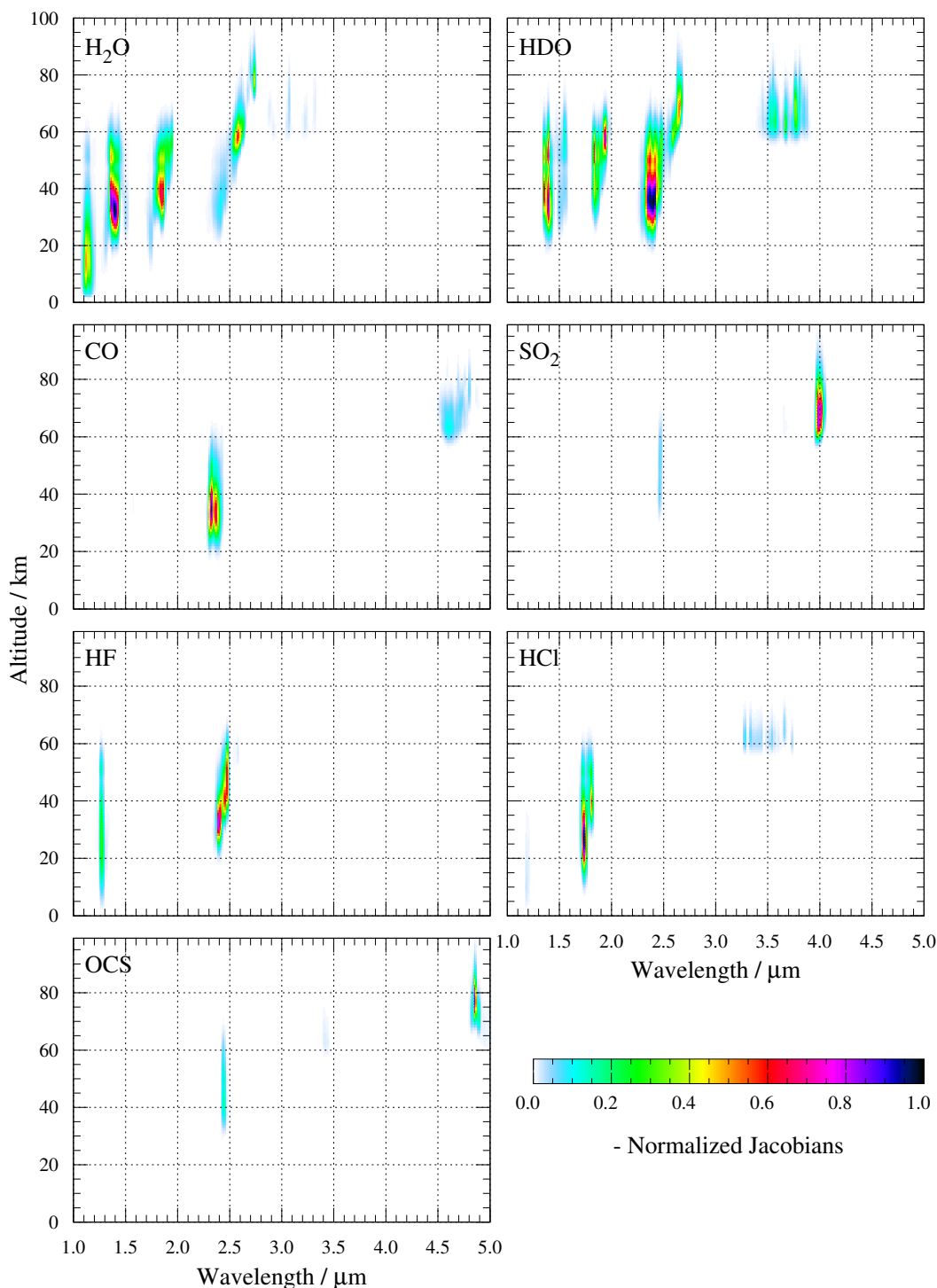


FIGURE II.22: Weighting function spectra for minor gases in the range 1.0–5.0 μm , normalized with respect to the radiance spectrum and with respect to the minimum of this ratio.

ward model is the inversion of the forward model. This operation is called **retrieval**. Within the frame of the forward model, the measured spectrum can then be adequately parameterized by the retrieved parameter vector, which is interpreted as the description of the state of the atmosphere, surface, and instrument that led to the measured spectrum and thus yields the wanted quantitative information. The inversion of the forward model can be formulated as a numerical optimization problem. The solution is determined by an iterative algorithm that improves the approximation of the wanted parameter vector at each iteration step, starting from an initial guess. Chapter IV (p. 103) (Kappel, 2014) will introduce multi-spectrum retrieval, but for a better understanding of that chapter, this section presents the basic concepts of retrieval from a single spectrum.

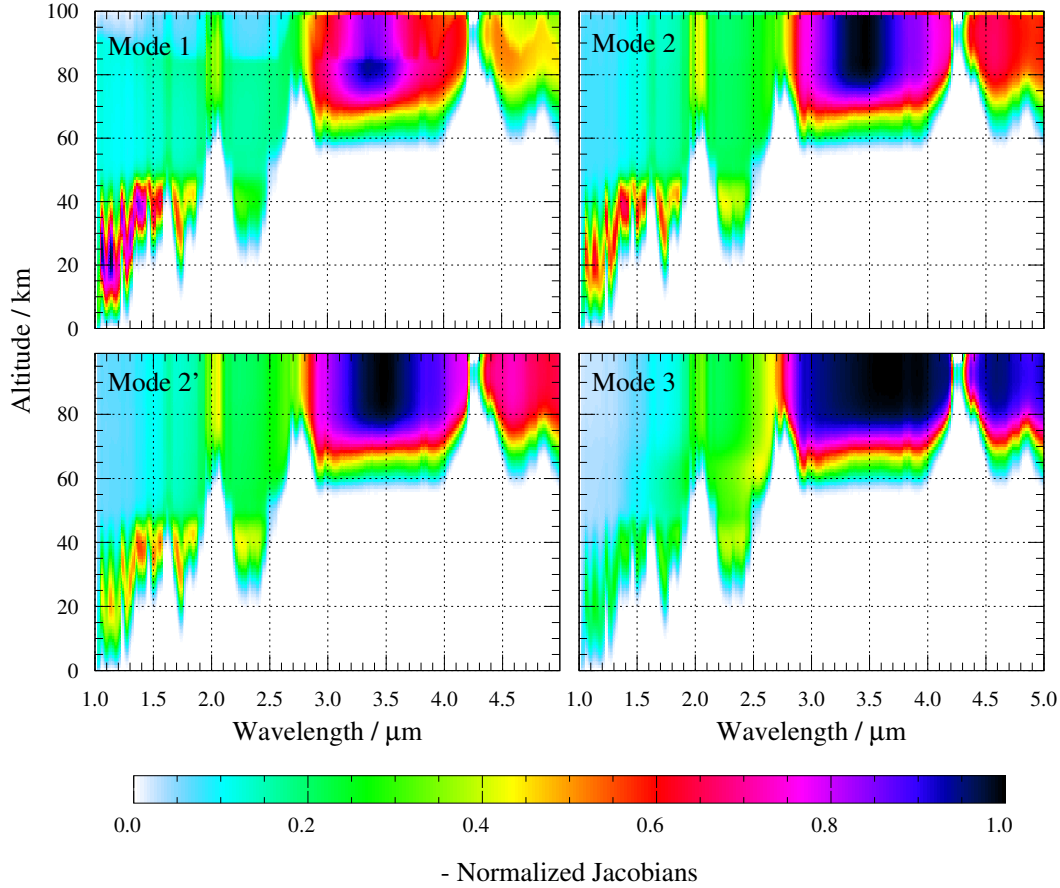


FIGURE II.23: Weighting function spectra for cloud modes in the range 1.0–5.0 μm , normalized with respect to the radiance spectrum and with respect to the minimum of this ratio.

II.3.1 Gauss-Newton algorithm

As a short motivation and introduction, a **simple iterative algorithm** for solving non-linear optimization problems, the Gauss-Newton algorithm, is outlined here. It is analogous to the well-known one dimensional Newton algorithm for solving non-linear equations. Let \mathbf{y} be the m -dimensional vector comprising a calibrated and preprocessed VIRTIS-M-IR radiance spectrum, that is, the list of radiances at m different wavelengths. $\mathbf{f}(\mathbf{x})$ shall be the vector of simulated radiances at the same wavelengths. \mathbf{f} is here a differentiable function of the n -dimensional parameter vector \mathbf{x} . \mathbf{x} is also called 'state vector', and the single entries 'retrieval parameters'. The task is to find an optimal state vector $\hat{\mathbf{x}}$ such that $\mathbf{f}(\hat{\mathbf{x}})$ is a good approximation of \mathbf{y} in the least squares sense. $\mathbf{f}(\hat{\mathbf{x}})$ is called the 'best fit' (or short 'fit'), i.e. the simulated spectrum that best fits the measured one. For this purpose, the Euclidean norm $\|\mathbf{y} - \mathbf{f}(\mathbf{x})\|_2$ of the residual between measurement and simulation shall be minimized (that is, the quality of the fit shall be maximized) by varying the state vector \mathbf{x} . To solve this problem, $\mathbf{f}(\mathbf{x})$ is approximated by an affinely linear function in the vicinity of a certain guess \mathbf{x}_j of the optimal solution $\hat{\mathbf{x}}$: $\mathbf{f}(\mathbf{x}) \approx \mathbf{f}_j + \mathbf{J}_j(\mathbf{x} - \mathbf{x}_j)$. Thereby, \mathbf{f}_j and \mathbf{J}_j denote the evaluation and the Jacobian of \mathbf{f} at \mathbf{x}_j , respectively (as they are discussed in Section II.2.7 (p. 57)). A necessary requirement to minimize the residual norm is the vanishing of the derivative of its square with respect to \mathbf{x} , i.e. $D[(\mathbf{y} - \mathbf{f}(\mathbf{x}))^T(\mathbf{y} - \mathbf{f}(\mathbf{x}))] \stackrel{!}{=} 0 \Leftrightarrow 0 = -D(\mathbf{f}(\mathbf{x}))^T(\mathbf{y} - \mathbf{f}(\mathbf{x})) \approx -\mathbf{J}_j^T(\mathbf{y} - \mathbf{f}_j - \mathbf{J}_j(\mathbf{x} - \mathbf{x}_j)) \Leftrightarrow \mathbf{x} \approx \mathbf{x}_j + (\mathbf{J}_j^T \mathbf{J}_j)^{-1} \mathbf{J}_j^T(\mathbf{y} - \mathbf{f}_j) =: \mathbf{x}_{j+1}$, where D computes the derivative with respect to \mathbf{x} . \mathbf{x}_{j+1} is an (in a favorable case) improved guess of $\hat{\mathbf{x}}$. The algorithm starts with an initial guess \mathbf{x}_0 , which shall be iteratively improved by the respective iteration steps from \mathbf{x}_j to \mathbf{x}_{j+1} . But it should be noted that it is neither guaranteed that the iteration converges, nor that the limit of the iteration is $\hat{\mathbf{x}}$. This simple algorithm demonstrates that iterative approaches may be used to solve the retrieval problem, that it is possible to simultaneously determine the single parameters comprising the state vector, and that the numerical computation may involve Jacobians of the simulated spectra. However, such an algorithm does not necessarily yield the 'best' or even the 'true' state vector. If the iteration converges,

then the limit is locally an optimal solution, but it may be a subsidiary solution, that is, it could be different from the location of the smallest local minimum of the residual norm or from the global solution. Note that the function of \mathbf{x} that has to be minimized in order to identify $\hat{\mathbf{x}}$ is called the 'cost function' of the retrieval problem. Here, this role is played by the squared residual norm.

This **simple retrieval algorithm can be improved** in a number of ways. First, it should be possible to take information about measurement and simulation errors into account. For example, radiance residuals in a spectral range where the signal-to-noise ratio is high should have a higher weight than those in other ranges. Next, it is also useful to incorporate available *a priori* information on the retrieval parameters. For instance, a parameter may be expected to be close to a certain value and to vary according to a certain probability distribution function. This information can help to rule out unlikely parameter values from the outset and thus to avoid subsidiary solutions. Then, the algorithm should also be able to give an estimate of the uncertainty of the retrieved parameters. Finally, an iterative algorithm with robust convergence properties is preferred, but it should still be efficient. This last issue is addressed in the next two sections.

II.3.2 Levenberg-Marquardt algorithm

The Gauss-Newton algorithm rapidly converges to a stationary point when the initial guess is close to this point and the cost function is approximately quadratic in the vicinity. But in general, it can happen that the cost function at \mathbf{x}_{j+1} is not improved compared to the one at \mathbf{x}_j , that the convergence is not robust, or that there is no convergence at all, as can be seen already for one-dimensional problems. An improved algorithm is the **Levenberg-Marquardt method** (Marquardt, 1963). Here, the Gauss-Newton step is replaced by $\mathbf{x}_{j+1} = \mathbf{x}_j + (\mathbf{J}_j^T \mathbf{J}_j + \lambda \mathbb{1})^{-1} \mathbf{J}_j^T (\mathbf{y} - \mathbf{f}_j)$, with a free parameter λ . When λ is chosen small (compared with the squared column norms of \mathbf{J}_j), this nearly coincides with the Gauss-Newton step. But when this step proves unfavorable (i.e. the cost function increases), the step can be rejected, and an alternative step is computed with an increased λ . In the extreme case for a large λ , the difference between \mathbf{x}_{j+1} and \mathbf{x}_j tends to the gradient-descent direction of the squared residual norm, $\gamma \cdot 2\mathbf{J}_j^T (\mathbf{y} - \mathbf{f}_j)$, where $\gamma > 0$. A step into this direction for a sufficiently small γ *guarantees* by construction a reduction of the squared residual norm, and thus in this case the cost function, but with a possibly small (i.e. inefficient) step size. The Levenberg-Marquardt step is thereby a combination of the Gauss-Newton step (rapid convergence but not robust) and a gradient-descent step (robust convergence but slow). A further improvement is the replacement of the identity matrix $\mathbb{1}$ by a diagonal matrix with suitable scaling factors on the diagonal (e.g. the squared column norms of \mathbf{J}_j) to allow for a more appropriate scaling of problems with large differences between the gradients in different directions. For more details see Marquardt (1963). The parameter λ is often chosen according to a heuristic line search method: As mentioned, if the cost function increases due to the iteration step, the step is not performed, λ is increased, and the step is recomputed. On the other hand, if the cost function decreases, the step is performed and λ is decreased, see also Rodgers (2000, Section 5.7).

II.3.3 Trust region algorithm

The plain Levenberg-Marquardt algorithm can lead to unwantedly large iteration steps, thereby impeding the robustness of the convergence. A different way of approaching the non-linear optimization problem is a trust region algorithm. The idea is to model the cost function as a quadratic function (by way of the Jacobian) within the trust region, a certain elliptical region around a point in the parameter space. It is assumed that within that region, the quadratic model function is a good prediction of the cost function. The minimum of the model function defined on the trust region is attained either within the interior or on the boundary of the trust region. When this minimum has been determined, the reduction predicted by the model function is compared to the actual reduction of the cost function. If the cost function is not reduced at all, the step is rejected and the size of the trust region is reduced. If the cost function decreases but the predicted reduction is too small, the step is performed, but the model function cannot be 'trusted' on the trust region, and the size of the trust region for the next step is reduced. In each other case, the step is performed, and the trust region for the next step is enlarged. For details, see Moré (1978). This trust region algorithm is a **robust and efficient version of the plain Levenberg-Marquardt algorithm**, incorporating a refined scaling of the parameter space dimensions and a refined choice of λ (described in Section II.3.2 but now based on the trust region size). The step size is

automatically bounded by the trust region, and unwantedly large iteration steps are avoided, yielding a robust convergence. The convergence rate close to a local minimum of the cost function is as good as for Gauss-Newton. Far away from a local minimum, the iteration is more stable than the plain Levenberg-Marquardt algorithm (see also Plesa (2008) for a discussion of the performance of the trust region algorithm).

These properties favor the trust region algorithm as the **method of choice** for this work, because here, the parameter space for the retrieval can be quite high-dimensional and the cost function quite complicated, with potentially many subsidiary minima and saddle points. In addition, the computational resources for the evaluation of the Jacobians and thus the cost function can be very high. The number of iteration steps required for convergence shall be as small as possible, therefore, but not at the cost of an unstable convergence. There are freely available computer subroutine libraries that provide well tested implementations of the trust region algorithm, for instance *dnls1.f* from the SLATEC library (Vandevender and Haskell, 1982), which is used as the starting point for the implementation of the retrieval algorithm in this work. Note that, even though they would allow for a more precise approximation of the cost function, algorithms involving second derivatives (like the plain Newton algorithm) are not used here, because the computational resources for the determination of the Hessian scale quadratically with the dimension of the parameter space (for Jacobians only linearly).

II.3.4 Bayesian probability and cost function

As was recited by Kappel et al. (2012b, Section 2), retrieval is mathematically an ill-posed problem, since the results may not be unique. Simulations with different parameter vectors can reproduce a measured spectrum equally well in the least squares sense. This is particularly true for the sparse spectral signatures of the Venus nightside spectra at VIRTIS-M-IR resolution. In the simplest form, the retrieval algorithm looks for local minima of least squares residuals between measurement and simulations. But this is an optimization problem in a possibly high-dimensional space, and possibly many subsidiary minima impede the locating of the global minimum. To improve this situation, the retrieval problem has to be **regularized**. Not each parameter vector that can well describe the measurement is equally likely to be the closest to the true one. To single out the most likely parameter vector, reasonable demands are imposed on the parameter vector itself. One way of doing this is to take Bayesian *a priori* information on the parameters into account (Rodgers, 2000). Gaussian *a priori* probability distributions for the parameters are incorporated in the retrieval process in form of expected mean values and standard deviations of the parameters to be retrieved. These *a priori* data can be obtained, for instance, from *in situ* data, from different spaceborne experiments, and from ground based data. A measure for the errors of measurement, calibration, and simulation can also be taken into account in this framework. The location of the maximum of the Bayesian *a posteriori* probability distribution is iteratively determined and is the best estimate of the parameter vector, that is, the ‘retrieval result’. The covariance of this distribution is a measure of the uncertainty of the retrieved parameters. This technique ensures that completely improbable parameter situations can be ruled out, which would be otherwise allowed when not using these *a priori* data.

Mathematically, this approach is implemented by replacing the cost function, which was set to the squared residual norm in the previous sections, by a different function. Its formulation is here based on Sections 2.3 and 5.2 in Rodgers (2000). Let P_P be the probability distribution function (*pdf*) describing the *a priori* knowledge of the state vector, i.e. $\int_V P_P(\mathbf{x}) d\mathbf{x}$ is the probability of the state vector \mathbf{x} to lie in the Volume V of the parameter space before knowledge of the outcome of the measurement. For this work, P_P is assumed to be a Gauss function. Similarly, P_M denotes the *pdf* of the measurement vector \mathbf{y} before the measurement is made. P_J is the joint prior *pdf* on the Cartesian product of the parameter space \mathcal{P} and the measurement space \mathcal{M} with $P_P(\mathbf{x}) = \int_{\mathcal{M}} P_J(\mathbf{x}, \mathbf{y}) d\mathbf{y}$ and $P_M(\mathbf{y}) = \int_{\mathcal{P}} P_J(\mathbf{x}, \mathbf{y}) d\mathbf{x}$. Finally, the conditional probability of the measurement vector, given that the state vector is \mathbf{x} , is $P_m(\mathbf{y}|\mathbf{x}) = P_J(\mathbf{x}, \mathbf{y}) / \int_{\mathcal{M}} P_J(\mathbf{x}, \mathbf{y}) d\mathbf{y}$, and the conditional probability of the state vector, given that the measurement vector is \mathbf{y} , is $P_p(\mathbf{x}|\mathbf{y}) = P_J(\mathbf{x}, \mathbf{y}) / \int_{\mathcal{P}} P_J(\mathbf{x}, \mathbf{y}) d\mathbf{x}$. Thus, when the measurement outcome is known to be \mathbf{y} , the resulting posterior *pdf* of the state vector is $P_p(\mathbf{x}|\mathbf{y})$. This is the quantity of interest in the retrieval. It follows **Bayes’ theorem** that $P_p(\mathbf{x}|\mathbf{y}) = P_m(\mathbf{y}|\mathbf{x})P_P(\mathbf{x})/P_M(\mathbf{y})$.

$P_m(\mathbf{y}|\mathbf{x})$ is the statistical description of the residual $\mathbf{R}(\mathbf{x}) := \mathbf{y} - \mathbf{f}(\mathbf{x})$ between the measurement \mathbf{y} and the simulated outcome $\mathbf{f}(\mathbf{x})$ of the measurement given the state vector \mathbf{x} . It describes **measurement and simulation errors**. A Gaussian distribution is usually a good approximation for real-world errors and is simple enough to derive useful formulas. Thus, if the errors are assumed to follow a Gaussian distribution in the

residual \mathbf{R} with the error covariance matrix \mathbf{S}_ϵ , then $P_m(\mathbf{y}|\mathbf{x})$ can be written as

$$P_m(\mathbf{y}|\mathbf{x}) = \frac{1}{N_1} \exp\left(-\frac{1}{2}\mathbf{R}^T(\mathbf{x})\mathbf{S}_\epsilon^{-1}\mathbf{R}(\mathbf{x})\right),$$

where $1/N_1$ is a normalization factor. If \mathbf{S}_ϵ is chosen to be diagonal, there will be no coupling between the errors at different wavelengths. In this case, the entries on the diagonal are the variances of the errors at the respective wavelengths, i.e. the squares of the standard deviations.

The *a priori* knowledge of the state vector \mathbf{x} was assumed to be a Gaussian and can be written as

$$P_P(\mathbf{x}) = \frac{1}{N_2} \exp\left(-\frac{1}{2}(\mathbf{x} - \mathbf{a})^T \mathbf{S}_a^{-1}(\mathbf{x} - \mathbf{a})\right),$$

where $1/N_2$ is a normalization factor, \mathbf{a} is the *a priori* mean value of the state vector, and \mathbf{S}_a is the *a priori* covariance matrix. Note that both \mathbf{S}_ϵ and \mathbf{S}_a as covariance matrices have to be real, symmetric, and positive semi-definite, and they have to be positive definite to allow for the above definitions of P_m and P_P . If no statistical correlations between the single retrieval parameters are expected, then \mathbf{S}_a is a diagonal matrix, and the diagonal entries denote the individual *a priori* variances of the retrieval parameters. The better the knowledge of a certain parameter is, the smaller is the corresponding variance. The construction of suitable covariance matrices is not trivial and is discussed in detail in Section IV.3 (p. 107) (Kappel, 2014).

By applying Bayes' theorem, it follows

$$-2 \log P_p(\mathbf{x}|\mathbf{y}) = (\mathbf{x} - \mathbf{a})^T \mathbf{S}_a^{-1}(\mathbf{x} - \mathbf{a}) + \mathbf{R}^T(\mathbf{x})\mathbf{S}_\epsilon^{-1}\mathbf{R}(\mathbf{x}) + N. \quad (\text{II.16})$$

The logarithms of the normalization factors $1/N_1$ and $1/N_2$ as well as of the \mathbf{x} -independent $P_M(\mathbf{y})$ have been absorbed into N . P_p is the *a posteriori pdf of the state vector*. To describe this *pdf* in terms of a few characteristic parameters, it is useful to determine the location of its maximum and a quantity describing the width of the *pdf* in the vicinity of this location. Note that \mathbf{R} can be a complicated function due to the properties of the forward model \mathbf{f} and measurement noise. Thus, there can be more than one local maximum of P_p , but it is the location of the global maximum which is the best estimate of the state vector. It can be difficult or even impossible to identify. The utilization of the *a priori* information in the form of a Gaussian damping of P_P improves this situation. For instance, when the *a priori* variances are small enough, this can lead to the elimination of subsidiary maxima, at least in the extreme case where the standard deviations tend to zero and the solution follows as the vector of the *a priori* mean values. But in practice, it must be kept in mind that the retrieved state vector could be just a subsidiary solution, and as it turns out, this is indeed often the case. In absence of a fast and reliable global maximizer, the retrieval algorithm will determine the locations of local maxima of P_p , and as a rough test, it should be checked whether different initial guesses lead to the same solution.

To determine a local maximum of P_p is equivalent to the task of finding a local minimum of the rhs. of Eq. (II.16). The *retrieval cost function* f_c to be minimized can therefore be defined as

$$f_c(\mathbf{x}) := (\mathbf{x} - \mathbf{a})^T \mathbf{S}_a^{-1}(\mathbf{x} - \mathbf{a}) + \mathbf{R}^T(\mathbf{x})\mathbf{S}_\epsilon^{-1}\mathbf{R}(\mathbf{x}), \quad (\text{II.17})$$

which is a non-linear function of \mathbf{x} . Its values are non-negative, since \mathbf{S}_a and \mathbf{S}_ϵ and thereby their inverses are positive definite matrices. The location of a local minimum can be iteratively determined by applying the discussed trust region algorithm (Section II.3.3 (p. 63)) to f_c , once it has been reformulated as a squared residual norm as it is discussed in detail in Section IV.A.1 (p. 126) (Kappel, 2014).

An expression for the width of the *a posteriori pdf*, and thus a measure for the *retrieval uncertainty*, is obtained from the quadratic term in the Taylor expansion of f_c at $\hat{\mathbf{x}}$. By neglecting the derivative of the Jacobian in comparison to the other terms, one arrives at

$$\hat{\mathbf{S}}^{-1} = \mathbf{S}_a^{-1} + \mathbf{K}(\hat{\mathbf{x}})^T \mathbf{S}_\epsilon^{-1} \mathbf{K}(\hat{\mathbf{x}}), \quad (\text{II.18})$$

where $-\mathbf{DR}(\mathbf{x}) = \mathbf{Df}(\mathbf{x}) =: \mathbf{K}(\mathbf{x})$ is the Jacobian of the forward model at \mathbf{x} . $\hat{\mathbf{S}}$ will be interpreted as the covariance of the retrieval solution. On the diagonal, the variances provide a measure for the uncertainty of a

retrieved state vector, and the off-diagonal values bear information on the interdependence of the parameters. But note that $\hat{\mathbf{S}}$ does not bear information on retrieval errors due to errors in assumptions on other interfering forward model parameters. This is discussed in Chapter V (p. 135) (Kappel et al., 2015).

When only the mean value $\hat{\mathbf{x}}$ and the covariance $\hat{\mathbf{S}}$ of a *pdf* P are given, then a Gaussian distribution with these properties is the *pdf* with the least information content, or, equivalently, with the maximum entropy $S[P] = - \int P \log P$. This can be shown by a simple argument using calculus of variations under constraints, see also Rodgers (2000, p. 41). The unique *pdf* compatible with just these two quantities and without implying further knowledge is therefore this Gaussian. Once $\hat{\mathbf{x}}$ and $\hat{\mathbf{S}}$ have been determined from f_c , an **appropriate approximation of the a posteriori pdf** has thus been found, and the retrieval problem is solved. This retrieval algorithm meets all demands listed in the last paragraph of Section II.3.1 (p. 62). Example measurements and respective best (MSR) fits are shown in Fig. II.24. The small residuals demonstrate the capabilities of the forward model simulation model and the retrieval algorithm.

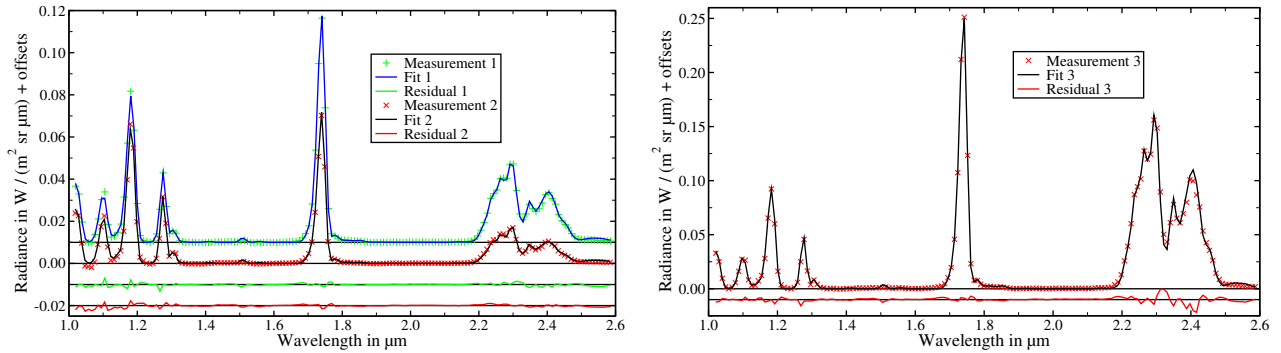


FIGURE II.24: Example nightside VIRTIS-M-IR measurements and best MSR fits. Left: moderate cloud opacity, respective best fit slightly worse for measurement 2 than for measurement 1. Right: small cloud opacity. Offsets in units of $W/(m^2 \text{ sr } \mu\text{m})$ (Measurement, Fit, Residual): measurement 1 (0.01, 0.01, -0.01), measurement 2 (0, 0, -0.02), measurement 3 (0, 0, -0.01). Details are listed in Table II.4.

Spectrum	Cube	t_{exp}	ϕ_{obs}	ϕ_{Sun}	ϕ_{ph}	m_1	m_2	m_2'	m_3	CO	H_2O^b	OCS	FWHM	QF
Measurement 1	VI0368_03	3.3 s	33.7°	116.2°	102.1°	0.6	0.8	1.0	1.1	1.2	1.0	0.7	18.2 nm	3.8%
Measurement 2	VI0333_05	8.0 s	27.2°	112.4°	120.4°	1.0	0.4	1.4	1.3	1.0	1.0	0.6	16.3 nm	5.4%
Measurement 3	VI0571_13	3.0 s	34.6°	120.2°	112.0°	1.1	1.3	0.0	0.8	1.3	1.2	1.2	16.7 nm	4.9%

TABLE II.4: Identification and properties of the measurements and MSR fits depicted in Fig. II.24. All are located at 280.26°E, -42.44°N (at Shivanokia Corona in the Themis Regio) and belong to the 64 measurement repetition data set in Kappel et al. (2016), see explanations therein and Fig. VI.3 (p. 176). Surface elevation (blurred with 100 km FWHM): 1784 m, t_{exp} : single-frame exposure time, ϕ_{obs} : observation angle, ϕ_{Sun} : Sun angle, ϕ_{ph} : phase angle. Retrieved parameters: (unrenormalized) common surface emissivities: 0.48 (1.02 μm), 0.56 (1.10 μm), 0.61 (1.18 μm), m_i : cloud mode column factors, CO: CO column factor, H_2O^b : H_2O column factor below 26 km, OCS: OCS column factor, FWHM: FWHM of spectral instrumental response function, QF : quality of fit ($\|y - f(\hat{x})\|_2$ in percent of $\|y\|_2$). All other parameters are as in the cited source. O_2 nightglow at 1.27 μm is treated as in Section II.2.6 (p. 53), paragraph 'O₂ nightglow'.

Chapter III

Refinements in the Data Analysis of VIRTIS-M-IR Venus Nightside Spectra

David Kappel^{1,2}, Gabriele Arnold^{1,2}, Rainer Haus¹, Giuseppe Piccioni³, Pierre Drossart⁴

¹*Institute for Planetology, Westfälische Wilhelms-Universität Münster, Wilhelm-Klemm-Straße 10, 48149 Münster, Germany*

²*German Aerospace Center (DLR), Institute of Planetary Research, Rutherfordstrasse 2, 12489 Berlin, Germany*

³*Instituto di Astrofisica Spaziale e Fisica Cosmica, Rome*

⁴*LESIA, Observatoire de Paris, CNRS, UPMC, Université Paris-Diderot, Meudon*

A copyedited version of this article was published in:

Advances in Space Research, 50(2):228–255, 2012.

Received 25.01.2011; received in revised form 30.01.2012; accepted 24.03.2012.

Available online 03.04.2012. doi:[10.1016/j.asr.2012.03.029](https://doi.org/10.1016/j.asr.2012.03.029)

Copyright: 2012 COSPAR. Published by Elsevier Ltd. All rights reserved.

Abstract

The successful long-duration radiation measurements performed by the VIRTIS instrument aboard ESA's Venus Express spacecraft have provided an excellent collection of atmospheric and surface data that stand out due to their high temporal and spatial coverage of the planet and due to a high diversity of measurement and environmental conditions.

A detailed investigation of the VIRTIS-M-IR data archive is described and possible improvements in the analysis of Venus night and dayside spectra are discussed. These improvements are both based on the application of new retrieval algorithms and on some calibration and data preprocessing refinements including a detector sensitivity investigation, an advanced straylight removal technique, and the allocation of a revised surface topography model customized to the intended surface and deep atmosphere parameter retrieval. Different data binning schemes are investigated and recommendations for their use, based on scientific objectives, are given.

While the precise impacts on the retrieved parameters are difficult to summarize in a few numbers due to the sophisticated relations between the measurement space and the high dimensional parameter space, some general or exemplary trends are presented. Compared to retrieval results from spectra based on the earlier calibration and preprocessing pipeline, for instance CO and SO₂ can display a column density change in the order of 10%, and the surface emissivity at 1.02 μm can exhibit changes in the order of 0.2 and up to 0.36 in an example. Such changes can lead to different interpretations concerning atmospheric and geologic properties of Venus.

The proposed refinements and the corresponding mathematical tools exploit the limits of what can be achieved with the available data. They enhance the retrieval reliability of atmospheric and surface parameters of Venus.

Some of the tools described in the paper are not only very useful for VIRTIS data analyses, but should also provide interesting suggestions for a handling of data from other spaceborne experiments.

III.1 Introduction

Little is known about the composition of the surface of Venus and the weathering processes that take place under extreme environmental conditions on the planet leading to surface emissivity variations which are difficult to predict. The determination of absolute values of surface emissivity from spaceborne remote sensing measurements remains a great challenge in general.

Venus Express (VEX) is a space probe orbiting Venus on a highly elliptical orbit since 2006 (Drossart et al., 2007). The Visible and Infrared Thermal Imaging Spectrometer (VIRTIS) aboard VEX is an experiment dedicated to spectrally resolved observations of Venus' atmosphere and surface. The infrared imaging channel VIRTIS-M-IR yields a spectrum of 432 spectral bands in the range between 1.0 μm and 5.2 μm at 256 spatial pixels for each exposure (Cardesin-Moinelo et al., 2010). A series of several exposures scanning a certain target area results in a data cube, which obtains a two dimensional image of the target area for each spectral band at a certain wavelength, and for each pixel of the image a spectrum of the pixel target, respectively. The data acquired during each Venus Express orbit is divided into a number of subsets, the data cubes. Each data cube can be uniquely identified by the orbit number during which it was acquired in conjunction with the index of the subset. Data cube 113_15 is thus the 15th subset acquired during orbit 113. Sometimes the data cube identification is abbreviated by just the orbit number when there are no ambiguities. Data cube 113_15 is thus often denoted as orbit 113 in this work. This is the notation also used by Arnold et al. (2008) and Haus and Arnold (2010). Different exposure times are needed to acquire useful spectra for the diversity of target conditions that range from the dayside to the nightside. Currently, the nightside emissions from Venus are the only data source to obtain Venus surface and deep atmosphere information in the infrared on a global scale. Due to the high gas and cloud opacity in the spectral range covered by VIRTIS-M-IR, most emissions originating from below the cloud deck are totally blacked out, and only a few narrow spectral windows probe this domain. But the VIRTIS nightside measurements provide an excellent resource of data due to their high temporal and spatial coverage of the planet and due to a high diversity of measurement and environmental conditions.

A detailed investigation of physical parameters that determine the retrieval accuracy of atmospheric and surface features of Venus has been published by Haus and Arnold (2010). It was shown that new radiative transfer simulation tools are well suited to fit the VIRTIS measurements and to retrieve the desired parameters, but a number of open questions remained. Local surface anomalies were identified over the northern hemisphere and possible origins like emissivity variations were discussed. The authors reported that the surface emissivity in the highlands seems to be smaller compared with lowlands. But they also concluded that more extensive analyses of the data archive and further improvements of radiative transfer simulation and retrieval techniques are required to enhance the retrieval accuracy and reliability.

The accuracy of the retrieval of atmospheric and surface parameters on the basis of radiance simulations using a so-called forward model depends on the success of the regularization of this inverse problem as well as on the accuracies of the forward model and the data calibration quality. Especially the extraction of surface information is very sensitive and requires a sophisticated data preprocessing. Improved retrieval techniques and improvements in the evaluation of the VIRTIS data archive due to increased insights into the detailed measurement characteristics of the instrument will seriously enhance the possibilities of full exploitation of measurement information content. This will eventually lead to a higher reliability of retrieval results and slightly different values compared to earlier analyses as it is demonstrated in this paper.

The present paper describes methods and results of detailed investigations of the VIRTIS-M-IR data archive with respect to possible improvements in the analysis of Venus night and dayside spectra. These improvements are both based on the application of new retrieval algorithms and on some calibration and data preprocessing refinements. The latter includes a detailed detector responsivity analysis, an advanced straylight removal technique, and the determination of a revised surface topography model customized to the intended retrieval of surface and deep atmosphere parameters. Different data binning schemes will be discussed and recommendations for their use in dependence on the scientific objective will be given.

The use of new retrieval algorithms that have been specially developed with the difficulties for the VIRTIS-M-IR Venus night side parameter retrieval in mind (Kappel et al., 2010a,b) is an essential part of work to enhance the reliability of atmospheric and surface parameter retrievals on Venus, and it should also be useful in other situations. But the present paper will not focus on the utilized retrieval algorithms, since the description of the mathematical framework and its application to the VIRTIS measurements is rather complex and is beyond the scope of this paper. This matter will be discussed in detail in a subsequent paper. But a short description of the approach and its capabilities is given in Section III.2.

Section III.2 gives a short overview on the utilized forward model and retrieval algorithm. A detailed account on the data calibration is presented in Section III.3, whereas the data preprocessing for the retrieval is described in Section III.4. The impacts of the improved retrieval algorithm and of the calibration and preprocessing refinements are discussed in Section III.5.

III.2 Forward model and retrieval algorithm

The measured spectra can be simulated by using a forward model, which computes for a given parameter set the radiance that the measuring instrument should detect. The parameter set includes atmospheric parameters (altitude profiles of temperature, gaseous and particulate constituents), surface parameters (elevation, temperature, emissivity), and instrumental parameters (e.g. full width at half maximum (FWHM) of the instrumental response function). The utilized forward model was described in detail by Haus and Arnold (2010). It is a line-by-line code taking into account thermal emission, absorption, and multiple scattering by gases and clouds.

Retrieval, that is in this case the inversion of the radiative transfer equation, is a mathematically ill-posed problem in the Hadamard sense, since the results are not unique. There are many different parameter sets for the simulation of the synthetic spectra that can reproduce the measured spectra equally well in the least squares sense, especially for the sparse spectral signatures of the Venus nightside spectra at VIRTIS-M-IR resolution. The retrieval algorithm looks for local minima of least squares residuals between measurement and simulations, but this is an optimization problem in a possibly high dimensional space, and possibly many subsidiary minima impede the locating of the global minimum. To improve this situation, the problem has to be regularized. Therefore, Bayesian *a priori* information on the parameters is used in the present approach (Rodgers, 2000). Gaussian *a priori* probability distributions for the parameters are incorporated in the retrieval process in the form of expected mean values and standard deviations of the parameters to be retrieved. This *a priori* data is based on former observational *in situ* results gathered during the VENERA missions (Avduevskii et al., 1983) and from the analysis of earlier ground based high-resolution data (Marcq et al., 2006; de Bergh et al., 1995; Pollack et al., 1993; Meadows and Crisp, 1996) as well as from other spaceborne experiments (limb observations, de Kok et al., 2011, radio science, Tellmann et al., 2009). A measure for the error of the measurement, the calibration, and the simulation can also be utilized in this framework. The maximum of the Bayesian *a posteriori* probability distribution is iteratively determined by minimizing the cost function $(\mathbf{x} - \mathbf{a})^T \mathbf{S}_a^{-1} (\mathbf{x} - \mathbf{a}) + (\mathbf{y} - \mathbf{f}(\mathbf{x}))^T \mathbf{S}_\epsilon^{-1} (\mathbf{y} - \mathbf{f}(\mathbf{x}))$, where \mathbf{x} is the parameter vector, \mathbf{a} the *a priori* mean value vector, \mathbf{y} the measurement vector, $\mathbf{f}(\mathbf{x})$ the forward model at the parameter vector \mathbf{x} , \mathbf{S}_a the *a priori* covariance matrix, and \mathbf{S}_ϵ the error covariance matrix (Rodgers, 2000).¹ The location of the minimum is the best estimate of the parameters, that is, the retrieval result. The covariance matrix of the *a posteriori* probability distribution yields a measure for the uncertainty of the retrieved parameters. This technique ensures that completely improbable parameter situations can be ruled out, which are otherwise allowed when not using these *a priori* data.

But there is still further *a priori* information, since contiguous measurements are not expected to originate from completely unrelated parameters. Correlation lengths and times can be set to describe the spatial-temporal correlations between parameters of different acquisitions. Moreover, local correlations can be set, for instance for temperature profiles of individual measurements. The retrieval of the parameters of each of such related spectra can be accomplished by a simultaneous coupled retrieval of several spectra. An

¹Vectors and matrices were not typed in bold in the published paper. For consistency with the other papers that constitute the present thesis, they are typed in bold here. Corrected: In the last two clauses, \mathbf{S}_a^{-1} and \mathbf{S}_ϵ^{-1} were mistakenly stated in the published paper to be the respective covariance matrices.

extended measurement vector \mathbf{Y} is therefore defined as the concatenation of several measurement vectors, $\mathbf{Y}^T = (\mathbf{y}_1^T, \dots, \mathbf{y}_n^T)$, and the corresponding parameter vectors form an extended parameter vector \mathbf{X} . Similarly, an extended *a priori* mean value vector \mathbf{A} , an extended forward model vector $\mathbf{F}(\mathbf{X})$, and a corresponding extended error covariance matrix \mathbf{S}_E are defined. A matching extended *a priori* covariance matrix \mathbf{S}_A encoding the local and the spatial-temporal *a priori* correlations as well as the *a priori* covariances has to be constructed. Then the cost function to be minimized reads $(\mathbf{X} - \mathbf{A})^T \mathbf{S}_A^{-1} (\mathbf{X} - \mathbf{A}) + (\mathbf{Y} - \mathbf{F}(\mathbf{X}))^T \mathbf{S}_E^{-1} (\mathbf{Y} - \mathbf{F}(\mathbf{X}))$. The adaption of the retrieval algorithm to this multi-spectrum retrieval is a procedure which is too complex to present within the framework of this paper and will be described in a subsequent paper.

It has to be emphasized, that the result of a correlated retrieval is not just a smoothing of the spatial-temporal distribution of the results of an uncorrelated retrieval, but the probability of running into subsidiary solutions can be decreased by forcing the parameters being close to a self-establishing general spatial-temporal trend. A correlated retrieval uses stronger constraints compared with an uncorrelated retrieval, but it actually provides smaller least squares residuals of the fits in many cases. This fact confirms that subsidiary solutions can be avoided. The impact of measurement noise can be additionally attenuated using this approach.

Finally, the new algorithm allows a retrieval of parameters that are common to all spectra. For instance, the broad band CO_2 continuum and the spectral line shapes of the allowed transitions are independent of measurement acquisition time and observational geometry. They also do not depend on the atmospheric state or other locally varying environmental parameters and are thus common to all spectra. Each measurement can now also be interpreted as a probing of these parameters, but now with the atmospheric composition and the surface properties as interfering factors. The common parameters can be determined in the framework of the described multi-spectrum retrieval by performing a simultaneous retrieval of the common parameters and all other parameters, but for many, highly diverse spectra to disentangle the varying and the common parameters. The corresponding cost function is $(\mathbf{X}_C - \mathbf{A}_C)^T \mathbf{S}_C^{-1} (\mathbf{X}_C - \mathbf{A}_C) + (\mathbf{X} - \mathbf{A})^T \mathbf{S}_A^{-1} (\mathbf{X} - \mathbf{A}) + (\mathbf{Y} - \mathbf{F}(\mathbf{X}))^T \mathbf{S}_E^{-1} (\mathbf{Y} - \mathbf{F}(\mathbf{X}))$, where \mathbf{X}_C is the concatenation of the common parameters, \mathbf{A}_C the corresponding *a priori* mean value vector, and \mathbf{S}_C the *a priori* covariance matrix of the common parameters. In the situation of measurements with overlapping footprints, the surface properties can be treated as common parameters to these spectra, too.

The retrieval of common parameters can be used to increase the knowledge of parameters with lacking laboratory data, like the broad band CO_2 continuum or spectral line shapes. Also simulation problems due to imperfect line data bases can be partially compensated, which can be a major issue especially in the high temperature and high pressure environment close to the surface of Venus. But the results have to be carefully interpreted, since systematic measurement errors and simulation errors are also common to all spectra. Nevertheless, an improved overall fit contributes to an enhanced convergence behavior of the iterative retrieval process by better avoiding subsidiary solutions.

III.3 Data calibration

No measurement apparatus is perfect, and an ever-so detailed ground calibration cannot foresee and capture all facets of the demands of a real-world space mission. In addition, the launch, cruise and orbit insertion phases exert extreme stresses onto the instruments which might shift some characteristics. But even slight miscalibrations can lead to systematic measurement errors and corresponding systematic retrieval errors. The retrieved results can only be as good as the calibration.

Based on requirements in the data consistency, the data collected during the mission can itself be used as a reference for a calibration refinement. Also, in absence of conclusive reference measurements, theoretical considerations and model predictions may be used in limited ways to bring the calibration closer to the intended accuracy. In this way, the already very good VIRTIS-M-IR data can still be somewhat improved to push the surface data evaluation possibilities to the limit of what can be achieved with this instrument.

The data preprocessing in preparation for the retrieval is presented in Section III.4 (p. 84).

III.3.1 Calibration baseline

This section shortly recites the main steps of the calibration pipeline that was also used in an earlier work (Arnold et al., 2008). The full pipeline is described in detail by Cardesin-Moinelo et al. (2010).

At first, there is an onboard removal of the dark counts measured at regular intervals (often every 20th frame) by simply not opening the shutter when acquiring these dark frames. The dark count can drift over the course of an observational sequence and is for that on ground corrected by utilizing the linearly interpolated dark frames. Dead and saturated spectels are identified and flagged by special values. The spectral registration, that is, the spectral band-to-wavelength mapping, is computed. The net counts are converted into physical units of spectral radiance by dividing by the exposure time and the instrument transfer function (ITF), a two dimensional matrix containing the values of (linear) responsivity of the sensor frame for each spectel. A despiking is performed subsequently to remove the effects of cosmic rays or single outliers, among others. Finally, the images corresponding to each fixed spectral band are destriped, which is necessary, since there are samples that have a different responsivity with respect to the other ones along the slit, without being reflected in the ITF. The provided geometrical information for each pixel includes pixel footprint coordinates and corresponding surface topography as well as observation, sun, phase angles, local time, and others (Erard and Garceran, 2008).

The calibration refinements and data preprocessings discussed in Sections III.3 and III.4 (p. 84) introduce new steps into the pipeline. Instead of the plain conversion of the net counts into the spectral radiance by using the original ITF, a corrected ITF is used (determined in Sections III.3.2.1, III.3.2.2 (p. 75), and III.3.2.3 (p. 77)), and an additional partial correction of nonlinearities of the detector responsivity is performed (Section III.3.2.4 (p. 79)) before the despiking and destriping (Section III.3.3 (p. 84)). The steps in Section III.3.2 have to be performed only once, to determine the corrected ITF and the data required for the nonlinearity correction, except for Section III.3.2.4 (p. 79), which also describes the actual nonlinearity correction procedure which has to be applied every time a spectrum has to be calibrated.

The data preprocessing for the retrieval (Section III.4 (p. 84)), performed only after all calibration steps (i.e. Section III.3), describes the removal of the straylight affecting the night emissions (Section III.4.1 (p. 85)), the update of the geometry (Section III.4.2 (p. 87)), and subsequent to all other preprocessing steps the rebinning of all spatially and temporally resolved data (Section III.4.3 (p. 90)). Finally, the preprocessed data serves as the input to the retrieval algorithm, which extracts a refined spectral registration (compare Section III.4.4 (p. 91)) and the sought atmospheric and surface parameters (Section III.5 (p. 91)).

III.3.2 Detector responsivity analysis

This section describes the processing steps that lead to an adjustment of the instrument transfer function. Furthermore, an algorithm is characterized, which is able to partially compensate slight detector nonlinearities that affect the even versus the odd spectral bands on the detector in a different way (EO effect).

It is important to abide a certain order for these steps to avoid the reintroduction of previously already solved issues. Fig. III.1 depicts the flow of the detector responsivity analysis. The original ITF is cleaned from a so-called even-odd (EO) pattern (see Section III.3.2.1 and Fig. III.2 (p. 74)). Then the science data (science raw data, dark frames, housekeeping (HK) data) is radiometrically calibrated ('RC') using this EO corrected ITF. The radiometric calibration is performed as described by Cardesin-Moinelo et al. (2010). This leads to a set of radiances ('Rad.') which is used to apply the sample homogenization procedure ('S. hom', see Section III.3.2.2 (p. 75)) to ensure that the radiances for homogeneous targets are actually homogeneous, resulting in a further modified ITF. This 'ITF hom.' is again used for a radiometric calibration of the science data, yielding sample homogenized radiances ('Rad. hom.'). A simple EO removal ('Day EO') is then applied to day spectra, which are then analyzed by the retrieval algorithm ('RT') to determine the final modification to the ITF ('ITF fin.') by adjusting the responsivity near 1 μm in order to improve the registration of dayside spectra (Section III.3.2.3 (p. 77)). This ITF is used in a radiometric calibration to arrive at a data set of radiances that is still affected by the EO effect ('Rad. EO'). The data reduction of EO scatterplots ('EO red.'), a procedure to extract data necessary for the correction of the EO effect, is then the final step to determine the EO reference curves ('EO ref.', see Section III.3.2.4 (p. 79)). Once determined, the final ITF and the EO reference curves are needed for the new calibration pipeline. The details are discussed in the remainder of this

section. At several points of this detector responsivity analysis, the geometry of the measurements has to be used. But before using it, the original geometry data ('Orig. geometry') has to be updated to yield the 'Upd. geometry' (Section III.4.2 (p. 87)).

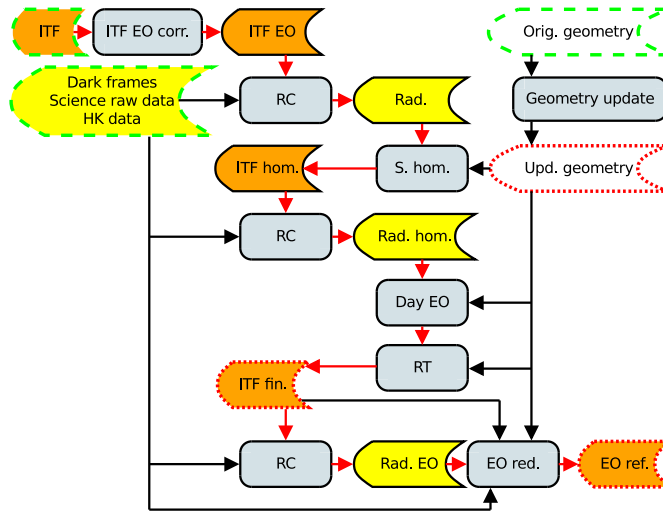


FIGURE III.1: Flow of the detector responsivity analysis. Operations are denoted by straight boxes, data sets by bended boxes. Points of origin are marked by dashed green framing, results by dotted red framing. Bended boxes with white filling are related to geometry data, with orange (darker) filling to data needed for radiometric calibrations, with yellow (lighter) filling to other data. The arrows related to the conceptual thread are highlighted in red.

III.3.2.1 Even-odd pattern in the instrument transfer function

Compared to ground based and earlier space probe based Venus spectra and also compared to the high-resolution VIRTIS-H measurements, it seems that a regular, sawtooth-like pattern is superimposed on the VIRTIS-M-IR spectra. It depends on the spectral range, the measured radiance and the exposure time (see Fig. III.3 (p. 74)). Synthetic spectra also do not reproduce this pattern, which has been denoted as 'even-odd effect' ('EO effect'). The even spectral bands alone do not show such a pattern, nor do the odd bands, but only both combined.

In the VIRTIS-M-IR data, the EO effect can be observed to decrease for longer exposure times, but with some notable exceptions. The most prominent exception is the spectral range from 2.2 to 2.6 μm (see Fig. III.3 (p. 74), bands 124–160). A closer inspection reveals that the instrument transfer function (ITF) itself in this range is affected by an even-odd pattern. In the following discussion it is assumed that this originates from the even-odd effect being present during the ITF ground calibration. This ITF even-odd pattern makes it difficult to identify the cause of the EO effect of the measurements, since the EO effect is reversed in this range and for short exposure times also less pronounced. Therefore, to simplify the study of the EO effect causes, at first the ITF is cleaned from its EO pattern by applying a controlled smoothing to the ITF.

Even-odd annihilating convolution kernels

For the study of the even-odd effect, a method to quantify EO patterns is needed. The EO residual of a spectrum, that is, the difference between the original spectrum and the spectrum with the EO pattern removed, will be that spectrum's measure for the EO effect. The removal of the EO pattern is an operation that resembles a smoothing. Therefore, it seems to be a good starting point to convolve the spectrum in question with a certain kernel c of length n .

For $n = 3$ the condition to leave an affinely linear function invariant against c and thereby annihilating a 'regular even-odd effect', $f = ((-1)^j)$, uniquely determines c as $ker_1 = (1, 2, 1)/4$. ker_1 works quite well for actually measured spectra, as long as they are, aside from the even-odd effect, 'almost affinely linear', see Fig. III.3 (p. 74), ker_1 residual outside the day spectrum valleys. With real world spectral features present,

ker_1 acts almost like a convolution with a Gaussian, leading to a FWHM increase of peaks or valleys and thus a broadening and thereby strong modification of the spectral features. But it is possible to improve this procedure by allowing longer convolution kernels.

In general, one can ask for kernels, mapping polynomials of degree p , affected by EO patterns varying according to polynomial envelopes of degree q , to the original polynomials. This gives rise to

$$\sum_{j=-(n-1)/2}^{(n-1)/2} \left(\sum_{l=0}^p a_l (i-j)^l + \sum_{l=0}^q b_l (i-j)^l (-1)^{i-j} \right) c_j \stackrel{!}{=} \sum_{l=0}^p a_l i^l. \quad (\text{III.1})$$

Eq. (III.1) can easily be solved for c_j , given n, p, q , by forming an equation system by recursively setting the otherwise arbitrary a_l and b_l to the special value 0. This leads to $ker_{p,q}$ with a minimal required odd n . For the ease of use, $q = 0$ -kernels may be abbreviated by ker_p , justifying the notation ker_1 for $ker_{1,0}$. Choosing a too high p or q has some disadvantages, since the region of influence of the convolution gets too wide, and since actual spectral features of a certain pattern may be detected as even-odd effects and will be removed, or an actual even-odd pattern may be detected as a polynomial of a high degree and will thus not be removed. Some tests suggest $ker_{5,0}$ to be a good compromise, having a minimal length of $n = 7$, and coincidentally also fulfilling the $ker_{6,1}$ -condition, thereby annihilating linearly varying even-odd patterns, which is very useful, as will be seen later, since the even-odd effect does not have a constant envelope in general. Leaving polynomials of sixth degree invariant is especially useful in sharp peak or valley situations, as well as in the bases of the flanks of the nightside peaks, all resulting in a great improvement over ker_1 . Solving the corresponding linear equation system, $ker_{5,0}$ is found as $(1, -6, 15, 44, 15, -6, 1)/64$ and will be abbreviated as ker_5 . Compared to ker_1 , this kernel works remarkably well for actual EO pattern affected measurements. This can be also verified by convolving synthetic spectra that include artificially added EO patterns. ker_5 convolution only slightly modifies even sharp peaks or valleys unaffected by EO patterns (also compare ker_5 residual to ker_1 residual near bands 21 and 44 corresponding to major day spectrum valleys in Fig. III.3). Thus, for less problematic spectral ranges, ker_5 should be appropriate to quantify the EO effect. In the following, all EO effect related considerations are studied by using ker_5 .

Reduction of even-odd pattern in the instrument transfer function

Based on the net detector count DN , the measured radiance I is computed as $I(b, s) = \frac{DN(b,s)}{T_{exp} F(b,s)}$, where F is the instrument transfer function. b denotes the band and s the sample on the detector. T_{exp} is the exposure time. Since the basic quantity is the incoming radiance, every operation on the ITF has to be performed with $1/F$, the reciprocal of the ITF. Each even-odd pattern affected spectral band of $1/F$ will be replaced by the ker_5 -smoothing of $1/F$, for each sample. To identify a band i as EO pattern affected, the following criteria are applied:

- The fractional EO residual² $R = \frac{1/F}{(1/F)*ker_5} - 1$ must change the sign from band to band: $(R(i-1)R(i) < 0$ and $R(i)R(i+1) < 0)$.
- The fractional even-odd amplitude $|R|$ must vary slowly, that is, the ratio for neighboring bands must not differ much from 1 to ensure an identification only when there is a certain regularity of the effect: $|\log_{10} |R(i+1)/R(i-1)| < 0.5$.
- $|R|$ must be smaller than an empirically determined value of 0.3 to exclude larger spikes in the ITF from this procedure, since these do not belong to the EO pattern category.
- Special cases have to be handled individually: at band 124 (starting with band 0) there is for all samples an abrupt change from an unaffected to an affected range.

It is assumed for reasons that are explained later that the EO effect affects both, the even as well as the odd bands. Thus, both sets of bands have to be corrected, and not just for instance the odd bands (with then twice

²Convolution is denoted by '*' in the following. This is mentioned in the published paper only in Section III.3.2.4 (p. 79).

the correction amplitude) while leaving the even bands uncorrected. The examination of potential deviations from this is postponed to a possible improvement of the absolute calibration using for instance stars as reference sources.

Fig. III.2 depicts the correction of the EO pattern in the ITF for two different samples. The impact on the

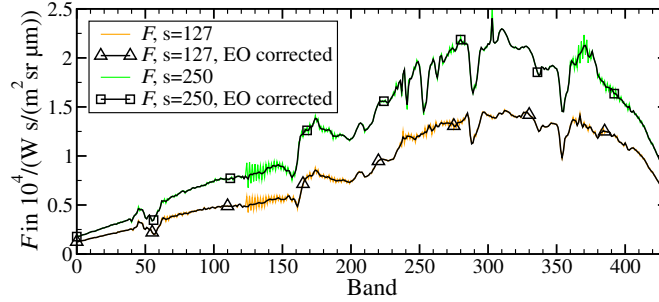


FIGURE III.2: Instrument transfer function F for two different samples s . $s=127$ is located near the center of the detector, and $s=250$ near its right edge. The EO pattern in the original ITF is clearly visible. The corrected curves follow the trends and even the small scale structure of the original ITF very closely and do not longer exhibit the EO pattern. The bands from 124 to 160 are most affected corresponding to about $2.2\text{--}2.5\ \mu\text{m}$.

spectra is visualized in Fig. III.3. It shows that the measurement with the ITF EO pattern uncorrected does

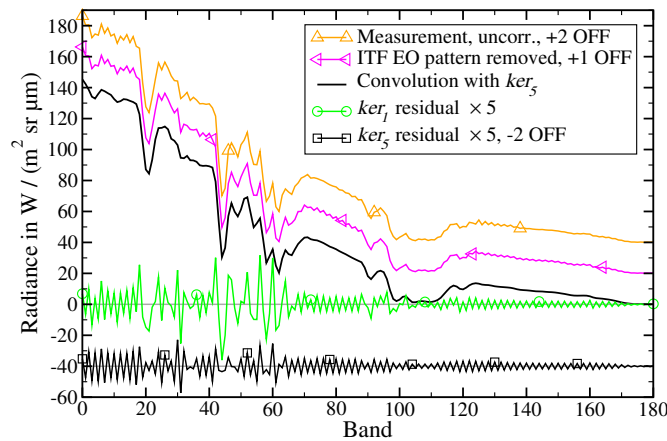


FIGURE III.3: Even-odd effect for a dayside spectrum (data cube 113_16, average over all samples of line 100) in the wavelength range $1.0\text{--}2.7\ \mu\text{m}$. Certain offsets in units of $\text{OFF}=20\ \text{W}/(\text{m}^2\ \text{sr}\ \mu\text{m})$ were added to the various curves and the residuals were scaled for better representation.

not exhibit a clearly discernible regular EO pattern, while the same measurement with that pattern removed obviously displays a regular EO pattern (compare bands 70–90 and 120–170 for these curves). This is not an artificial introduction of an EO pattern to the measurements, but the unmasking of an underlying regularity in the detector nonlinearity (see Section III.3.2.4 (p. 79)). The ker_5 convolution is also depicted together with the scaled ker_1 and ker_5 residuals. ker_5 produces a much higher regularity in the residuals than does ker_1 . There is a larger EO effect for bands with higher radiances. Also compare to Fig. III.6 (p. 78) in Section III.3.2.3 (p. 77) to see that the simulations are smooth and do not exhibit an EO pattern. In the range $1.4\text{--}2.7\ \mu\text{m}$ not covered by Fig. III.6 (p. 78), the simulations look almost exactly like and are as smooth as the ker_5 -smoothed measurement in Fig. III.3, bands 41–180.

This controlled removal leads to the identification of a clear trend in the even-odd effect of the measured spectra across the whole detector both for night and dayside spectra. It is almost completely regular across the samples and the bands. It is reproducible, it seems to increase for higher radiances in most cases (see Fig. III.3), and it is smaller for higher exposure times. These findings suggest the EO effect to be predictable and thus correctable. This will be addressed in Section III.3.2.4 (p. 79).

III.3.2.2 Sample homogenization

During the launch, cruise, or orbit insertion phase of VEX, some instrumental characteristics of VIRTIS-M-IR seem to have slightly shifted. There are indications of an inhomogeneous detector temperature field which naturally had not been present during ground calibration and now requires a subsequent calibration adjustment. The flatfield for a fixed band of VIRTIS-M-IR now appears to have a somewhat different profile than during ground calibration. This can be seen in several situations, where a quite homogeneous measured radiance along the sample direction is expected. To improve the consistency of the measurements, a sample homogenization attempt is outlined in the following. Note, that this procedure has to be performed after the reduction of even-odd pattern in the ITF (Section III.3.2.1 (p. 73)), since the EO pattern removal of the homogenized ITF reintroduces slight inhomogeneities. On the other hand, a reintroduced EO pattern in the ITF by the sample homogenization procedure, as well as the EO effect of the measurements in general will be corrected in any case through the procedure for the correction of the even-odd effect of the measurements (Section III.3.2.4 (p. 79)), which consequently has to succeed the sample homogenization.

Introducing a homogenization factor $h(b, s)$ for the uncorrected ITF $F(b, s)$, both quantities depending on the band b and sample s on the detector, the corrected radiance I computes as $I(b, s) = \frac{DN(b, s)}{T_{exp} h(b, s) F(b, s)}$, where T_{exp} is the exposure time and DN the net detector count. When using the uncorrected radiance I_u , it follows that $h = I_u/I$. The expected homogeneity translates to I being independent of the sample. But I is not known as long as no absolute calibration sources like stars can be analyzed. But to have a point to start with, it will be assumed that the 48 central samples of all 256 samples are not very much influenced by the described flatfield modification. For homogeneous targets, these central samples also detect the highest radiances for most bands. This suggests a slight defocusing with a responsiveness decrease towards the detector edges or a temperature gradient between detector center and edges as possible causes of the flatfield modification. This would mean that the center is to be taken as the reference and the samples close to the detector edge have to be corrected. Additionally, when studying the normalized standard deviation of the correction factor for each band and each sample as a function of a certain number of central reference samples (c) and averaging this rather stable function of band and sample over all bands and samples, a c value of about 50 minimizes this mean standard deviation. Since some measurements were taken in a mode that bins four samples each time and leads to a 64-sample measurement instead of a 256 one, a c value divisible by 4 is preferred. A c value of 48 is chosen therefore for a stronger weighting of the center of the detector. But it should be kept in mind that an absolute calibration should be the reference, once available.

Sample homogenization using lateral cubes

There are two data cubes for VIRTIS-M-IR that were acquired in a lateral detector orientation geometry where the attitude of the spacecraft was adjusted to align the slit of the detector collinearly with the direction of motion of the nadir-pointing spacecraft with VIRTIS-M-IR measuring in push-broom mode, data cube 284_12 for the dayside, 284_13 for the nightside. Neglecting the atmospheric dynamics, each sample on the detector was probing the same spot on the planet after a certain sample-dependent time lag. Thus, each sample should have received the same incoming photon flux, and the flatfield calibration has to ensure that the measured radiance reads the same for each sample. Deviations require the introduction and enable the determination of the correction factor h .

First, a regular latitudinal binning of these polar orbit data acquired essentially on just a single meridian is performed to define the reference spots of the measurements. The bins must neither be too large to avoid a strong blurring of information, nor too small to avoid a noisy binning (strong variations in the number of contributing data points for different bins). A value of 0.3° seems to be an appropriate choice here. Then, for each bin, the radiance that each sample has measured from this fixed spot is known. This is normalized with respect to the 48 central samples for each bin and for each band. This way, each bin yields an estimation of the homogenization factor $h(b, s)$, and to decrease the noise, the average of these estimates is taken.

Measurement noise and atmospheric motion impede this otherwise very straightforward approach to re-gauge the flatfields. Moreover, a significant photon flux is also needed to get a reliable homogenization. One of the two lateral data cubes contains nightside spectra while the other one consists of dayside spectra. Thus, both cubes are somewhat complementary in the spectral ranges where a useful homogenization factor can be

acquired. These factors, when computed separately for day and night, are mostly consistent for overlapping low-noise spectral ranges, hinting at the actual universality of the homogenization factor. The standard deviation of h as a function of the spectral band clearly reflects the spectral characteristics of the nightside and the dayside spectra, respectively. It has minima for the highest detector counts, confirming the validity of this method for only the spectral ranges with significant detector counts.

Remaining issues are the noisiness of h , especially beyond $2.6\ \mu\text{m}$, where almost no signal is measured in the lateral dayside cube. Furthermore, only two lateral cubes can be evaluated, both acquired within 24 h, and a possible evolution during the course of the entire mission cannot be assessed this way. Also, this is a quite small data base, and a slight uncertainty due to the non-instantaneous nature of the lateral cubes as well as straylight biases cannot be excluded. Therefore, it is useful to consider an additional approach as it is outlined in the next section.

Sample homogenization using pericenter data

The idea is that observations, which were performed from measurement positions close to the planet, essentially show the same radiance for all samples, since the correlation lengths of atmospheric features range in excess of several hundred kilometers, and surface features are only observable with an expected FWHM of about 50–100 km. Straylight is however correlated with the observational geometry provided that close-to-terminator footprints are not considered. Thus, when observations are restricted to where the footprints of all samples within a single frame do not exceed approximately 50 km in distance, direct measurements of the inhomogeneity should be possible. Neither lateral observation geometry nor a binning procedure is necessary for this purpose. The advantage of this approach is the availability of about the order of 10,000 frames that satisfy this condition over the course of the entire mission and under a large variety of observational conditions and that include very low noise long exposure measurements.

Only spectra with a certain minimum detector count are taken into consideration to avoid noisy data from the outset. Detector counts close to saturation are also precluded. For each band and for each frame, the radiances are normalized again with respect to the 48 central reference samples. Then, the mean over all frames is calculated after having verified that the shape of the homogenization factor remains indeed stable under nearly all conditions along the course of the entire mission. Only for some nightside spectra there are deviations. A closer inspection reveals that in situations where the frame footprint covers a cloud flank, an additional gradient of the radiances is superimposed on h . These measurements are excluded. Comparison to the lateral cube method shows, that the pericenter homogenized ITF is less noisy, and the flatfield trends mostly agree between 1.0 and $2.6\ \mu\text{m}$. Some differences become apparent at the $2\ \mu\text{m}$ day spectrum valleys, and beyond $2.6\ \mu\text{m}$, underlining the problems of either method. To guarantee a self-contained continuous data set, the factor derived from the pericenter data is used. There may also be a sample dependent bias of the correction factor due to the sample dependent wavelength shift (Section III.4.4 (p. 91)). This shift has systematic deviations from the mean value in sample direction of about $0.5\ \text{nm}$. On the flanks of the dayside valleys (1.195 , 1.225 , 1.425 , and $1.450\ \mu\text{m}$, corresponding to about bands 19, 22, 43, and 45) this estimates to a potential 1%, 1%, 3%, and 3% error in the factor, but elsewhere to typically less than 0.5%, which is small compared to the correction itself. For nightside spectra, this is therefore only an issue in the long wavelength flank of the $1.18\ \mu\text{m}$ peak. Nevertheless, the homogenization improves the consistency of the measurements and should be applied when quantitatively assessing the spectra.

Figs. III.4 and III.5 serve to illustrate the sample homogenization in sample and band direction, respectively. In Fig. III.4, the radiance for dayside measurements across the samples (data cube 113_16, line 50, band $b=76$ corresponding to about the nightside peak at $1.74\ \mu\text{m}$) is shown before and after the homogenization procedure is applied.³ These are measurements from close to the pericenter, the leftmost and rightmost pixel footprints

³Corrected: The 'Radiance day, uncorrected' curve in Fig. III.4 was wrong in the published paper. It was depicted to lie above the 'Radiance day, corrected' curve, almost mirrored at the corrected curve. A new inspection of the data revealed that, for representation in this diagram, the uncorrected curve was reconstructed from a data file containing the corrected curve and the homogenization factor, but it was mistakenly divided by that factor when it should have been multiplied with it. Consequently, in the published paper, some statements in the following mistakenly referred to a radiance decrease in the outer parts of the detector due to the homogenization, when it is actually an increase.

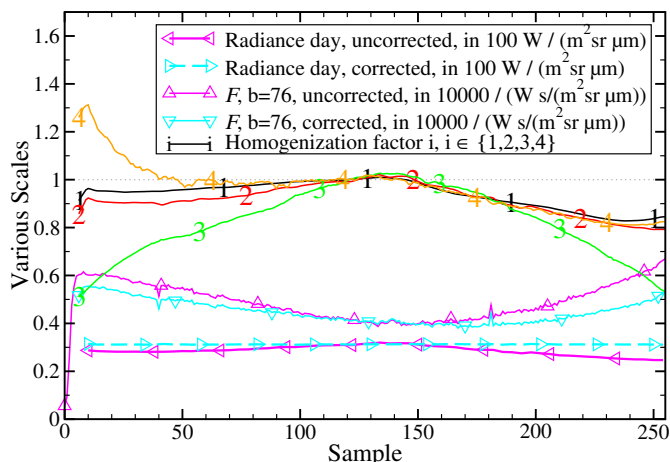


FIGURE III.4: Sample homogenization: sample direction. Radiances and the ITF are depicted at band $b=76$ before and after homogenization, along with a selection of four different homogenization factors in different colors with numbers 1–4 as symbols i , $i=1$ (black) at band 0 ($1.02 \mu\text{m}$), $i=2$ (red) at band 76 ($1.74 \mu\text{m}$), $i=3$ (green) at band 180 ($2.73 \mu\text{m}$), and $i=4$ (orange) at band 251 ($3.40 \mu\text{m}$).

at the cloud tops are 30 km apart. Therefore, the radiance should be nearly constant. The effect of the homogenization is clearly discernible. The radiance has been recorded in the 64 sample mode, but scaled to be comparable to the 256 sample mode the other curves are represented in. Four different homogenization factors are also shown, to illustrate the various shapes of the homogenization factors (also compare to Fig. III.5). Finally, the ITF F is depicted at band $b=76$ across the samples before and after the homogenization to show the impact on the shape of the ITF in sample direction.

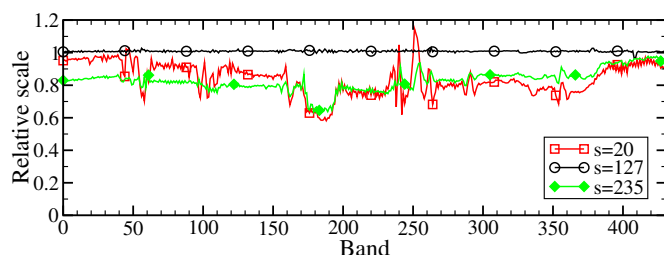


FIGURE III.5: Sample homogenization: band direction. Homogenization factors at three different samples are depicted. The samples are chosen at the center of the detector (sample $s=127$ of 256 total, starting with 0) and near the edges ($s=20$ and $s=235$).

In Fig. III.5, the homogenization factors for three different samples across the 432 bands are shown to illustrate the magnitude of the homogenization for the different bands. The samples are chosen at the center of the detector and near the edges. The center is almost unaffected (factor approximately 1), since the 48 central samples serve as the reference, while near the edges the deviation is largest and the factor is usually smaller than 1. Also compare to Fig. III.4 for the shapes in sample direction.

III.3.2.3 Responsivity adjustment at 1.0–1.3 μm

The attempt to fit VIRTIS-M-IR dayside spectra in the whole range 1.0–2.7 μm is not entirely satisfactory. Using the EO corrected dayside spectra (here a simple ker_5 smoothing, see Section III.3.2.1 (p. 72)), a quite good fit is possible starting from about 1.25 μm , but lowering this boundary increases the difficulties to fit the whole range and drastically decreases the probability of the retrieved parameters. Using the retrieved parameters from a fit in the range 1.25–2.7 μm to simulate the spectrum in the range 1.0–2.7 μm yields a systematic deviation of the simulated radiances from the observed radiances in the range 1.0–1.3 μm that increases from about zero at 1.3 μm to about +35% at 1.0 μm . It might be possible that the ITF derived from the ground calibration has to be slightly modified. As there seems to be no significant systematic change of that deviation with mission time or other parameters, either the ground calibration was biased, or events in the launch, cruise,

or orbit insertion phase may have altered some instrumental characteristics, similar to the issues discussed in Section III.3.2.2 (p. 75) regarding the homogenization. The uncertainty of the absolute radiance calibration for this instrument is difficult to estimate and has a typical value of 15–20% (Cardesin-Moinelo et al., 2010). If the simulations were true, the uncorrected radiances were 26% too low at 1.02 μm and already at 1.07 μm the mentioned 20% margin applied. The deviation is thus still within plausible limits and may well originate from a ground calibration bias caused by a weak reference black body near 1 μm .

One can try to find a correction curve to the ITF which depends only on the band (not the sample) to achieve improved day spectra fits. A set of 69 dayside spectra from all mission phases under different sun, observation, and phase angle conditions as well as from different latitudes and local times was retrieved in the spectral range 1.25–2.7 μm to find parameters which can be used to simulate the spectra in the range 1.0–1.25 μm . The ratio of the simulations and the measurements is averaged to yield a first correction curve candidate. To ensure reliable high-quality dayside spectrum retrievals in the 1.25–2.7 μm range, and to obtain EO effect unaffected ratios of the simulations and measurements, the measured dayside spectra have to be cleaned from their EO patterns by a simple ker_5 smoothing. But the correction curve candidate still shows some spectral features. It has been decided to correct only the trend of the ITF to avoid the introduction of false spectral features from possible simulation or retrieval errors. Therefore, it is better to use a polynomial fit to this candidate as a correction curve. A polynomial of fifth degree has proven to be a good compromise between too much loss of curvature information of this curve and the introduction of too much fine structure. The standard deviation of the averaging of the 69 ratios as function of the band is used as the error measure in the fit of the fifth-degree polynomial to this mean ratio curve in the range 1.0–1.3 μm . Here 1.3 μm is used as the upper boundary, since at about this wavelength the fifth degree polynomial attains the value one.

Fig. III.6 shows the results. The averages over the spectra (uncorrected and corrected measurements, simu-

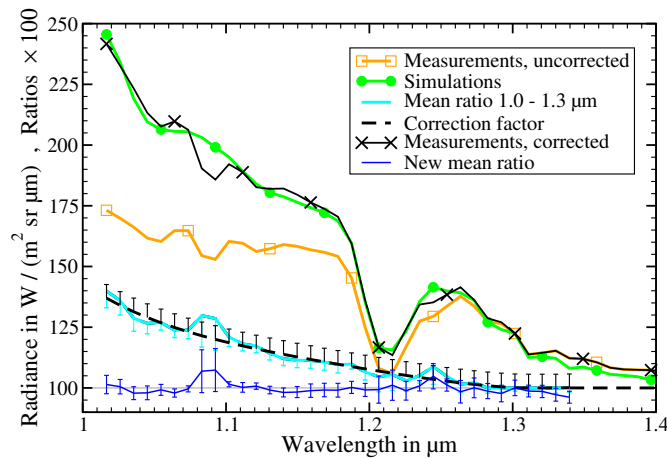


FIGURE III.6: Responsivity adjustment at 1.0–1.3 μm , corresponding to about bands 0–30 on the detector. All curves are the averages over 69 dayside spectra or ratios, respectively.

lations) are not weighted and only meant to demonstrate the functionality of the correction factor in the figure. As explained, the simulations in the full range are performed using parameters retrieved from the uncorrected measurements in the range 1.25–2.7 μm . Two times the standard deviation of the averaging of the ratios is depicted as down pointing error bars. The resulting uncertainty of the correction factor is symbolized by the up pointing error bars. The new fits to the now corrected spectra over the full range are virtually identical to the original full range simulations based on the 1.25–2.7 μm retrievals and are not shown here. Their averaged ratio to the corrected measurements is shown with accompanying double standard deviation error bars up and down, together with an indicated ideal value of 1. The wavelength range between 1.4 and 2.7 μm is not depicted, since here the spectra are not affected by the responsivity adjustment and also because the simulation average agrees very well with the measurement average, and thus these three curves nearly coincide, see Fig. III.3 (p. 74), bands 39–176, 'Convolution with ker_5 ' for the general shape in this range.

It has been verified, that this smooth correction factor enables very good fits of the dayside spectra in the entire range. When this factor is also used to fit nightside spectra, very good fits with entirely probable retrieved parameters are produced. But the same holds true without applying a correction factor to the nightside spectra.

Consequently, there are no constraints to any kind of correction factor that can be derived from the analogous analysis of night side spectra. But without this correction, an increased continuum parameter is needed around 1 μm . And on the other hand, there should be no continuum in this range, because of the absence of strong CO_2 bands in the vicinity.

Only an actual measurement of a known reference like a star or a blackbody could decide, whether this correction is justified, but at the moment the improvement in the general consistency of the data hints at the usefulness of this correction.

III.3.2.4 Even-odd effect of measurements

Following the steps described in Section III.3.2.1 (p. 73) (reduction of ITF even-odd pattern) and in Section III.3.2.2 (p. 75) (sample homogenization), it is easier to identify the even-odd effect as systematic trends in the measurements. First, the dayside spectra will be studied, since there are less pronounced spectral features compared to the nightside spectra, and ker_5 from Section III.3.2.1 (p. 72) should be quite adequate to quantify the even-odd effect for most spectral ranges.

The basic assumption used in the following section is, that the even-odd effect is reproducible and not random. This means, that the same EO pattern emerges for equal conditions. Thus, for a fixed spectel on the detector and with the detector temperature, the exposure time, the dark count, the electronic offset, the incoming radiance, the radiances of the adjacent spectels, etc. being equal for different measurements, the even-odd effect should be the same, apart from the measurement noise.

Due to the finite data pool, it is not possible to study all imaginable influences on the EO effect, and some simplifying assumptions are used, which have proven practicable: the EO effect of a spectel is independent of the adjacent spectels. When all other parameters are equal (in particular the dark count), the detector should not discriminate between long exposure times and small radiances vs. short exposure times and high radiances. This means, that only the incoming photon flux is decisive. But it is unknown, except for the measurement of the digital counts on the detector, which is not the same. The fundamental quantity to work with is chosen to be the absolute detector count, including dark count, electronic offset and net count (the photon flux induced part).

The EO effect, on the other hand, is defined as a deviation in the radiance. It has to be computed from the radiance I , therefore. But the fundamental detector quantities are the counts again, and the EO effect, as a relative radiance deviation, should be represented as relative count deviation, to be, for example, comparable across different exposure times. This is simply done by multiplying the EO residual $EO(b, s) := I(b, s) - (I(\cdot, s) * ker_5)(b)$ by the exposure time and the ITF, where '*' denotes the convolution. This EO count is mostly positive for even bands (starting with band 0) and negative for odd bands due to the alternating character of the EO effect. For simplicity, exclusively the even bands are discussed in the following. The odd bands behave analogously but with reversed sign.

Scatterplots and interpretation

The investigation of the scatterplot of the EO residual as function of the absolute detector count reveals a very peculiar curve (for all other parameters equal) (see Fig. III.7 (p. 82), top panel, 0.36 s, $b=150$). Starting with measurements of almost no radiance, the EO residual for increasing absolute counts is at first steeply increasing from 0 almost affinely linear. Then the curve bends towards a lower slope quite abruptly (in the example in the figure at about 8500 absolute counts), only to show an affinely linear behavior again. Finally, there is a second bend (in the example at about 11,800 absolute counts), again decreasing the slope of the adjoining again affinely linear function, which can then show a negative slope and eventually can even attain negative values, thereby reversing the EO effect. This general shape is reproducible for the different bands, samples, exposure times, and temperatures, but with different slopes and different locations of the bends.

This shape is not an artifact of the earlier corrections, since it also emerges from the uncorrected data, but with different slopes and locations of the bends. Also, this seems not to be a statistical effect, which would probably display a more definite shape like that of a square root, and should not abruptly change slopes and

even signs for increasing absolute count. Furthermore, this shape does not result from incorrect ITF or dark current calibration, since these are linear or simple offset operations.

The cause of this shape rather seems to be founded in a slight nonlinearity of the detector responsivity. The detector responsivities for the even bands are assumed to be quite uniform, but slightly different from an also uniform odd band responsivity. The differences then result in an EO pattern. The factual separation into an even and an odd detector is justifiable due to the independent readout electronics for the even and the odd bands. The approximate shapes of the nonlinearities can be deduced from the outlined EO scatterplot: Bends in the scatterplot hint at bends in the otherwise linear detector responsivity. It is conceivable that both detectors feature both bends at the same locations, but it is more likely that each detector has only one bend and the different locations of the bends causes the two bends in the difference.

The general trends of the EO effect can be explained by starting from the premise that the absolute count C as a function of the incoming photon flux R is a continuous function made up of two affinely linear functions with different slopes:

$$C(R) := \begin{cases} a(R - R_0) + C_0, & R \leq R_1 \\ b(R - R_1) + C_0 + a(R_1 - R_0), & R > R_1 \end{cases}, \quad (\text{III.2})$$

with a quite uniform distribution of a , b , R_0 , R_1 , and C_0 for the even bands (thereby defining $C_{\text{even}}(R)$), and an analogous but different distribution for the odd bands (defining $C_{\text{odd}}(R)$). Now, half the difference of $C_{\text{even}}(R)$ and $C_{\text{odd}}(R)$ as a function of the mean of $C_{\text{even}}(R)$ and $C_{\text{odd}}(R)$ results in a shape exactly as described for the EO effect, except for a slight rounding of the abrupt bends.

When comparing the scatterplots for increasing exposure times under otherwise equal conditions, a seemingly systematic trend towards smaller EO amplitudes emerges. This seems to contradict the assumption that the detector should not discriminate between long exposure times and small radiances vs. short exposure times and high radiances, for all other parameters equal. But, in fact, the counts accumulated due to the dark current are higher for longer exposure times. A higher dark count leads to a higher absolute count for the zero radiance level. Assuming the zero radiance level to lie below the bend level, a higher dark count means a lower net count needed to reach the bend, provided that the bends in the detector responsivities are really fixed at an absolute count level. Thus, the zero radiance level is already closer to the first bend in the EO scatterplot, effectively translating the EO scatterplot towards smaller EO amplitudes during the dark count removal in the calibration pipeline, while the shape of the scatterplot remains invariant. This results in a decrease of the maximum absolute EO difference for the spectel in question and in a smaller EO effect, as it is observed for the scatterplots for higher exposure times, see Fig. III.7 (p. 82), top panel, 3.3 s, $b=150$.

Different detector temperatures also lead to differences in the scatterplot, independent from any temperature related dark current modifications. An explanation could be a possible temperature dependence of the detector responsivity, i.e. of the slopes and of the location of the bend. There is a clear trend between the EO effect and the detector temperature for a fixed absolute count and all other parameters being equal. But this trend is dependent on the absolute count and possibly other parameters, and the data coverage seems to be too small to study this effect in detail to obtain reliable assertions. At the current stage, this temperature effect is neglected. The error caused by this neglect is hard to estimate due to the lack of data but seems to be no larger than twice the scatter error measure indicated by the error margins in Fig. III.7 (p. 82). It is also not random and is similar in absolute value when comparing nearby even and odd bands. Thus, a detector temperature related misestimation of the EO counts would result in EO corrected radiance spectra still displaying EO patterns which they approximately do not, as will be seen in the next section. But this temperature effect implies an at least slight temperature dependence of the detector responsivity itself, which should be kept in mind.

Construction of reference curves

The behavior, as described in the previous section, may provide clues as to the possible causes of the EO effect. Also, it becomes obvious that both the even and the odd bands should be corrected and not just only one of them. But it is possible to remove the general trends of the EO effect, as outlined in the following. The quality of the retrieval fits increases and the retrieved parameters are more reliable. It is also an improvement

compared to the retrieval of the spectra from the even and from the odd detector separately (thereby losing information), since really both have to be corrected. When the even and the odd results are then in disagreement, a simple mean is not the same as the retrieval result of the complete corrected spectrum due to the nonlinearity of the problem. Especially for parameters which are observable in just a few spectral bands, this correction should be performed.

At the moment it seems to be impossible to reconstruct the absolute detector responsivity curves $C(R)$, since always at least one parameter is missing. Which one, depends on the elimination process of auxiliary parameters. Therefore it is assumed that the mean (in the ker_5 -sense) of the even and the odd bands is the true measured incoming radiance, and this will be the starting point.

Nightside measurements with an exposure time of 0.36 s and shorter were decided to be discarded for the retrieval analysis, since in the wavelength range of interest for this work (1.0–2.6 μm) only very few counts contribute to the net measurement, namely of the order of 20 in the peaks. For comparison, the zero radiance count including dark count and electronic offset amounts to about 7500–8000. Exposure times of 3 s and longer allow for a better overall reliability of the signal in this range (by avoiding to have to take the difference of two large similar quantities, when subtracting the zero radiance count), and also for a larger signal-to-noise ratio. The survey of the EO effect is ideally realized using dayside spectra, since the spectral features have less contrast when compared to the night spectra, and the ker_5 convolution has a lower impact on the underlying (even-odd unaffected) true spectra. Furthermore, the most interesting information for this work is encoded in the wavelength ranges around the night spectra peaks. Here, the spectra have to be corrected most precisely and, if possible, independently from the night spectra themselves. Fortunately, the day spectral features with the strongest contrasts lie largely in other than the interesting night spectra wavelength ranges. The day spectra are thus suited quite well for the ker_5 survey of the EO effect with the night spectra correction in mind. The day spectra should have an exposure time of no longer than that of the nightside spectra to be corrected, since a too long exposure time implies a higher dark count and thus a higher zero radiance count than suitable for the night spectra absolute count, such that the needed information would be missing. It has proven most practical to use 0.36 s exposure time measurements for the dayside spectra, since shorter times like 0.02 s yield too few counts to be useful as reference for high night spectra peaks at longer exposure times. Longer dayside exposure times like 3.3 s, on the other hand, lead to counts, which are even at comparatively very low dayside radiances in the saturated region of the detector and no longer usable. This constraint also decreases the number of available measurements for the scatterplots. To avoid saturated measurements for the 0.36 s dayside spectra, only measurements relatively close to the terminator are taken as valid data.

To decrease the interference of noise in the EO effect quantification, the day data is binned with a bin size of four lines and $s/64$ samples, where s is the number of samples, either 256 or 64, depending on the mode of the data acquisition. This reduction to 64 bins in sample direction (in the following again called 'samples') is entirely sufficient for the purposes of this work, because the nightside data for the retrieval will also be binned for noise and data amount reduction.

First, the day spectra scatterplots are restricted to measurements with a detector temperature close (± 2 K) to the median detector temperature and a zero radiance count close to the median zero radiance count (± 5 counts) to avoid interferences from the aforementioned detector temperature effect and to have a defined zero radiance count level, thereby avoiding uncontrolled translations of the EO effect, as described. Then the spectra are ker_5 smoothed and the resulting EO residuals are converted to counts using the ITF and the exposure time. Now, the scatterplot of the EO counts as functions of the absolute counts is constructed. This scatterplot has to be reduced to a reference curve to be usable for the even-odd correction. To this effect, the EO counts are binned to a suitable absolute count grid, and for each bin the median of the absolute counts and the median of the EO counts yield the wanted support point in the reference curve. A measure for the error of the reference curve can be constructed as the mean modulus of the deviation from the median of the EO count for each bin, or as quantiles.

In Fig. III.7, top panel, the peculiar shape of the scatterplots (in the legend 's.plot') at band $b=150$ between about 7500 and 20,000 absolute counts is clearly visible. Also depicted are the reference curves from the reduction of the scatterplots (in the legend 'red.') as well as the error measures as dashed margins. The zero radiance count level for 0.36 s at $b=150$ and $s=31$ (out of 64 bins in sample direction) amounts to about 7700, while the first and second bend are located in the vicinity of 8500 and 11,800 absolute counts, respectively.

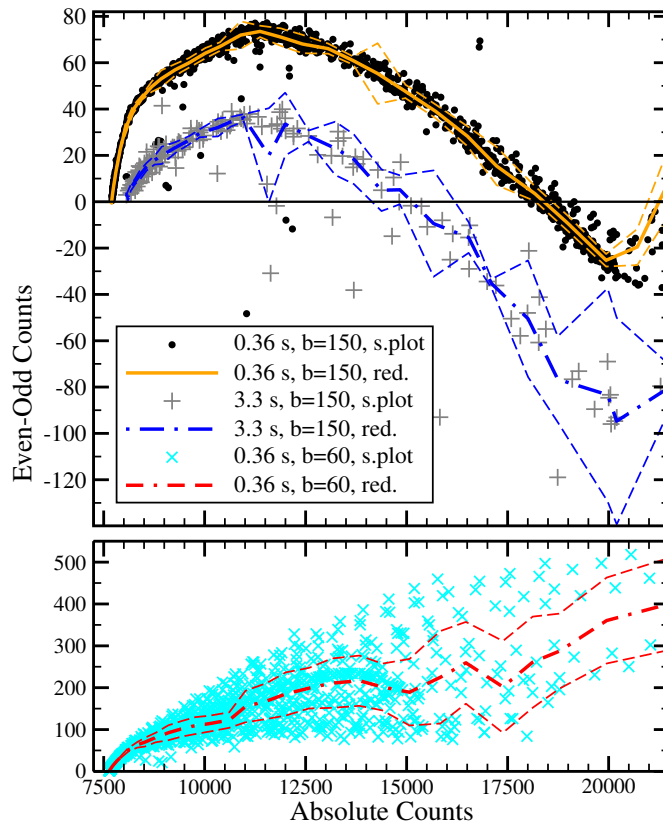


FIGURE III.7: The EO scatterplots ('s.plot') and the derived reference curves ('red.') for 0.36 and 3.3 s measurements at band $b=150$ (top panel) as well as for 0.36 s at $b=60$ (bottom panel) are depicted for sample 31 (out of 64 bins in sample direction). Also displayed are the binwise mean moduli of the deviations from the reference curves as dashed error margins.

For absolute counts above 20,000, the curve drifts up to higher EO counts due to the saturation in the odd bands while the even band measurements are still below the saturation level. The analogous curve for 3.3 s will not be used for the EO correction and is only shown here to demonstrate the impact of different exposure times. It is almost a translation of the 0.36 s curve towards lower EO counts with only slight deviations at higher absolute counts. To obtain enough points for the 3.3 s scatterplot, the zero radiance count level is not so tightly restricted (median ± 100 counts) as for the 0.36 s curve. Still, the statistics is not as stable as in the 0.36 s case due to the few points. The zero radiance count level corresponds to about 8070 for 3.3 s at $b=150$, the first bend is hard to locate due to its vicinity to the zero radiance count level, while the second bend is located close to the second bend of the 0.36 s curve at $b=150$. Additionally, the 0.36 s scatterplot is shown in Fig. III.7, bottom panel, for band $b=60$ as a scatterplot with a worst case spread of the points. This is due to the underlying spectral features in the dayside spectra in this spectral region (compare $b=150$ and $b=60$ in Fig. III.3 (p. 74)). For individual spectra, the ker_5 convolution does not clearly disentangle the EO pattern and the spectral features at $b=60$, but thanks to the statistical variation of the spectral features the reduced curve is expected to reasonably predict the EO pattern, although at the cost of larger error margins, as discernible in the figure. But also note that $b=60$ is of less importance for nightside spectra (Fig. III.8, 'EO pattern removed' and 'EO error'). The zero radiance count level corresponds to about 7630 for 0.36 s at $b=60$, while the bends are hardly determinable due to the high spread of the data points. Also note that due to the different location on the detector, the bends and slopes are probably different from the $b=150$, $s=31$ curves, and that 90% of the scatterplots at the different bands and samples show a much smaller spread with most of the remaining high-spread scatterplots irrelevant for night spectra.

Correction of the even-odd effect of the measurements

Once the reference curves for each band and each sample are established, they can be used to look up the EO residual for the nightside spectra to be processed. The ker_5 smoothed nightside spectrum in question is con-

verted to counts which are then added to the zero radiance counts. This quantity, the count of the ker_5 -mean of the even and the odd bands, serves as the reference point to be looked up in the corresponding reference curve (corresponding band and sample of the acquisition). The obtained EO count is converted back to radiance and subtracted from the original radiance spectrum. The measure of error for this operation is computed using the same reference point, but looking up in the error curve, and is then again converted to radiance. The thus corrected spectrum now agrees in its fine structure much better with measurements performed by other instruments and also with synthetic spectra. But the measure for the error should be closely observed. If it becomes too large, the EO correction should be discarded for the corresponding spectrum.

For testing reasons, the 0.02 s reference curves are also constructed and applied to dayside spectra. The improvement to the spectra is immediately visible and largely agrees with a simple ker_5 smoothing as expected. But it is more trustworthy, since a simple smoothing affects noise and other fine structure deviations, whereas the outlined correction does not. Additionally, a rough error estimate of the correction becomes available.

For the 3.3 s nightside measurements, the derived EO correction is quite significant in the peaks (in the order of up to 5%), which carry the most information for this work (see Fig. III.8). Even for the long exposure times spectra (8 and 18 s, respectively), a correction in the order of 1% still occurs in the peaks.

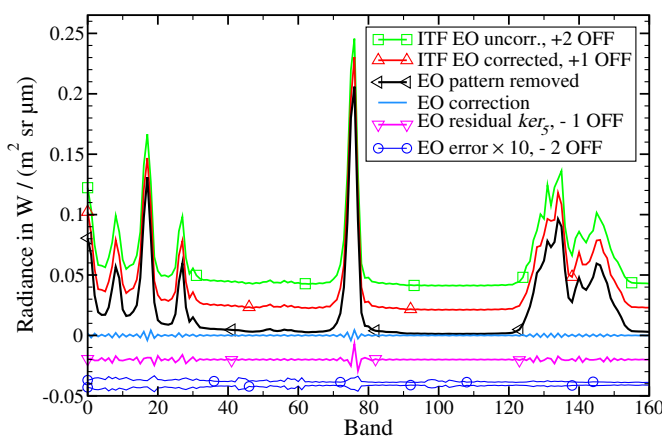


FIGURE III.8: Even-odd effect for a nightside spectrum (data cube 148_15, average over all samples of line 250, exposure time 3.3 s). Certain offsets in units of OFF=0.02 W/(m² sr μm) were added to the various curves for better representation.

The measurement with the ITF EO pattern uncorrected is depicted in Fig. III.8 for comparison to the same measurement with the ITF EO pattern corrected (Section III.3.2.1 (p. 73)). The latter is then also shown with the EO effect of the measurements removed, according to the explanations in Section III.3.2.4. The EO correction curve is subtracted from the ITF EO corrected curve for this purpose. The ker_5 residual of the ITF EO corrected curve is also depicted to demonstrate the difference, and thus the superiority and necessity of the reference curve approach. In the wavelength ranges where there are few spectral features (offside the peaks), the reference-curve based correction largely agrees with a simple ker_5 smoothing. But in some of the peak ranges, clear deviations between the two approaches appear, resulting from the ker_5 impact on the underlying EO unaffected spectra. Finally, the estimated error margins of the EO correction are shown, scaled by a factor of 10 for better representation. The error for the shown spectrum is of the order of 10-20% of the EO correction in the peaks. In case of the EO corrected curve, the shape of the 2.3 μm peak (bands 122–155) agrees very well with the convolution of high-resolution ground based observations to VIRTIS-M-IR-resolution and to simulations. The uncorrected curves, especially the curve with the uncorrected ITF EO pattern, show deviations from the expected shape (spikes and dents in the left flank). The overall EO pattern in the EO corrected curve is reduced to a satisfying degree.

The EO correction is only applied in the 1.0–2.6 μm range, since the dark current beyond this range becomes much stronger and varies over larger ranges, especially starting from about 4 μm longwards, so that the construction of the reference curves becomes more difficult due to the sparseness of the points in the scatterplots. For 3.3 s exposure time, the bands with 4.5 μm and beyond are already saturated from the dark counts alone. Dayside spectra become very small above 2.7 μm and provide a too low count level to be usable as reference points. It could be possible to use 3.3 s dayside spectra to achieve a higher count level. But in this case many

bands are already saturated in the range 1.0–2.7 μm due to the high net count and starting from 4.5 μm due to the dark count. This would possibly also disturb the valid data through strong in-frame scattering and CCD-related problems like blooming. It is also imaginable to derive the reference curves from nightside spectra in this range, but this is already quite close to a circular argumentation, similar to the correction of day spectra using day spectra reference curves. At least at the moment, this attempt was dropped, and no EO correction is performed for bands with wavelengths longer than 2.6 μm . This lack of the EO correction is not an urgent issue, since most of the retrieval analyses to investigate deep atmosphere and surface parameters will be based on the range 1.0–2.6 μm .

The above outlined EO correction procedure is only a zero-order correction. It neglects the detector temperature dependence and the residual detector nonlinearity among others. Furthermore, it is only a working hypothesis at the moment. But nevertheless, a correction towards the right direction is still better than no correction at all, and the resulting improvements in the retrievals seem to justify this approach. Also, it is very much better to apply the EO correction than to apply just the ker_5 -smoothing to night spectra which would result in large radiance errors (compare Fig. III.8, 'EO correction' vs. 'EO residual ker_5 '), or even worse, ker_1 . As discussed in the first paragraph of 'Construction of reference curves' of Section III.3.2.4 (p. 79), the EO correction should be strongly preferred to the separate analysis of the odd and even spectra, too. But the decisive argument can only be an absolute calibration with respect to a known reference like a star or a black body.

III.3.3 New despiking and destripping

It cannot be excluded that the previous steps have introduced new spikes or stripes, see Section III.3.1 (p. 71). Therefore, a new despiking and destripping procedure has to be performed following all of these previous steps.

Due to potential imperfections in the sample homogenization procedure (Section III.3.2.2 (p. 75)), it is reasonable to perform a despiking in sample direction for each band of each frame at first. Otherwise some systematic spikes common to all frames will not be identified in the subsequent general despiking. The five sample median smoothing is applied to each band of each frame, and a measure is estimated for the oscillation of the data (upper and lower quartile of the smoothing residual, that is the difference between the unsmoothed and smoothed data). Where the smoothing residual is out of the bounds defined by the oscillation multiplied by an appropriate threshold, the unsmoothed data is replaced by the smoothed data. The subsequent additional general despiking follows the same procedure as in the original calibration pipeline (Cardesin-Moinelo et al., 2010).

The destripping should not be performed, if the data will be binned at a later step (Section III.4.3 (p. 90)). The destripping is a smoothing in sample direction for each band of each frame. The average of smoothed data should ideally not be different from the average of unsmoothed data. However, to minimize the number of implemented operations on the data, binning of the non-destriped data is preferred. If no binning was desired, because the full resolution data is needed, the new destripping procedure follows the same procedure as in the original calibration pipeline (Cardesin-Moinelo et al., 2010), which effectively removes the stripes without critically affecting the spectral information. The cause of the striping could not be identified by Cardesin-Moinelo et al. (2010). However, based on the new insights described in Section III.3.2.4 (p. 79), it seems plausible that it may be due to a nonlinear detector response differently affecting different samples, although not following such a regular pattern as observed in the case of the spectral bands' EO effect.

III.4 Data preprocessing for retrieval

To prepare the data for the retrieval algorithm, a number of preprocessing steps has to be performed. This includes the removal of interfering straylight and the determination of the surface topography corresponding to the pixel footprints and customized to the intended surface and deep atmosphere parameter retrieval. To increase the signal-to-noise ratio, a certain data binning can be performed.

III.4.1 Straylight

Several different sources of straylight overlay the nightside emissions. In some wavelength ranges and under certain observational conditions, the straylight can even outweigh the nightside emissions. It is important to note that from the physical standpoint the removal of the straylight has to be done only after all data calibration steps have been performed. The latter determine the incoming radiance, while straylight really is incoming radiance, unwanted or not. Either the straylight is included in the modeling, and the retrieval procedure discriminates the nightside emissions from the straylight, or the straylight is removed before the retrieval. The lack of an adequate modeling of the straylight due to its complex nature, physical as well as geometrical (a spherical version of the radiance transfer code would have to be incorporated, thus complicating also other matters), and the feasibility of a quite straightforward removal as outlined in the following, leads to the preference of the second option.

III.4.1.1 Straylight sources

Before the new straylight removal procedure is presented, the most important straylight sources for the nightside measurements will be shortly discussed.

(1) Near-terminator straylight: Light from the dayside is scattered into the atmosphere of the geometrical nightside (dusk and dawn). This situation can be easily avoided by restricting to measurements with a solar angle larger than 98° (empirically determined).

(2) Direct sunlight outside but close to the VIRTIS field of view: Some direct sunlight is scattered by the instrument itself into the field of view. This is mostly an issue for some northern hemisphere push broom observations and can be avoided through restricting to measurements with an angle between boresight and the vector pointing from the spacecraft to Sun of greater than about 40° (empirically determined). In some situations this restriction is not necessary, because Sun is eclipsed by Venus from the spacecraft's point of view.

(3) Venus dayside outside but close to the VIRTIS field of view: This is quite the same issue as (2), but with the bright dayside as radiation source. Since apocenter observations always have the terminator and thus the dayside nearby the field of view, this is a severe problem which cannot be avoided without losing a substantial part of the total amount of acquisitions for the southern hemisphere. The straylight spectrum is different from that of the direct sunlight issue.

(4a) Spectral in-frame straylight: When the spacecraft is close to the planet and above the nightside, there are situations where the terminator and near terminator regions are completely eclipsed by the planet itself and radiation sources of the types (1)–(3) are definitely not present. Even in these situations, straylight can be detected. Its intensity is correlated to the intensity of nightside peaks, which are mainly determined by the cloud cover and the surface elevation. This suggests that light of a certain wavelength can be scattered onto parts of the detector responsible for other wavelengths. A slight adaptation of the instrumental response function from pure Gaussian to include also a possibly Lorentz-like component could help to describe this phenomenon.

(4b) Spatial in-frame straylight: For dayside and nightside (or deep space) measurements in the same frame, nightside (or deep space) spectra can be strongly disturbed. This situation should be avoided for quantitative nightside analyses, since the nightside emissions may not be recoverable reliably by a correction procedure. The amount of data affected by this situation is not critical. The cause of this issue is similar to that of (4a), only that the scatter path has components in sample direction. This suggests that there may be also spatial in-frame straylight for pure nightside as well as for pure dayside frames, which corresponds to a slight smearing of the information in the spatial dimension.

Both in-frame issues, (4a) and (4b), have not yet been studied in detail for this work.

III.4.1.2 Straylight removal

In order to remove the straylight, its spectrum has to be known. The best way to obtain the straylight spectrum is a direct measurement. Deep space observations are a good source of straylight measurements. But different

conditions (observational and other) yield different straylight spectra. A search for all deep space observations without straylight situation (2) and also excluding spatial in-frame straylight from the dayside returns a wealth of spectra from all mission phases and under most diverse conditions. Only those spectra are included that have a certain minimum mean net count (100) in bands 0–4 to exclude noisy data and that belong to frames with at most 2 *NaN*-values or saturated spectels in the bands 0–50 per spectrum on average. Some not generic spectra are also excluded. The corresponding data cubes are despiked and binned to four samples and four lines per bin to decrease noise interferences. The spectra from the about 50,000 so-obtained bins form the straylight data base, after they were normalized with respect to the first 12 bands.

The average of the straylight spectra resembles a (normalized) dayside spectrum. This is not surprising, since the dayside is the main source of straylight (see source type (3)). But the average is not simply a scaled dayside spectrum, since it is a superposition of dayside spectra under different conditions, distorted by some instrumental scatter characteristics. In fact, it also resembles a λ^{-4} curve often associated with scattering processes, but with superimposed spectral characteristics of dayside spectra. The λ^{-4} trend is incidentally a consequence of the responsivity adjustment at 1.0–1.3 μm (Section III.3.2.3 (p. 77)), without which the deviation from the λ^{-4} trend would be much larger. The average of the deep space straylight spectra alone is not suited to represent the straylight spectrum for a given nightside measurement (see Fig. III.9, 'Simple straylight spectrum'). This is the reason for introducing the following approach.

The idea is to find an easy parameterization of the statistical variety of the straylight data base. A principal component analysis (PCA, see Jolliffe (2002)) is carried out for this purpose. A single spectrum of 432 bands can be regarded as a point in a 432-dimensional space. The set of all spectra of the straylight data base is then a point cloud in this space with the mean spectrum being a single point in this space. When projecting the data to a line through the mean spectrum, the variance of the projected data can be computed for each line. The direction of the line with the greatest variance is then the direction of the first principal component. Now the data are projected to lines orthogonal to the direction of the first principal component. The greatest variance then yields the direction of the second principal component, and so forth. The variability of each principal component is consequently also a result of the PCA. A few of the largest principal components can already describe the variability of the data set quite accurately when the variances of the other principal components are small enough.

The mean straylight spectrum and the first few principal components can now be used as reference curves to estimate the straylight spectrum of straylight affected nightside spectra. The reference curves are fitted to the corresponding nightside spectrum in the spectral ranges lacking the pure nightside emissions. It turns out, that this can lead to disproportional high fitting coefficients in relation to the PCA results, thereby overemphasizing the lesser important principal components. To avoid this, the spectra are split into two overlapping ranges from 1.0 to 1.4 μm and from 1.35 to 3.0 μm , respectively. The PCA is performed for both ranges. Beyond 3 μm , the straylight can be neglected. In the first spectral range, the variabilities coming from the first three principal components amount to about 59%, 16%, and 8%, whereas for the second range, the variabilities are about 54%, 16%, and 7%. This time, the mean straylight spectrum and just the first principal component for each range are used. For the range 1.0–1.4 μm , these two components are fitted at band 4 ($\sim 1.06 \mu\text{m}$) and at the bands 34–39 (~ 1.35 – $1.40 \mu\text{m}$) to the measured spectrum in the mean sense by solving the corresponding system of two equations. For the range 1.35–3.0 μm , the corresponding 'dark' ranges are the bands 34–39 again and the bands 91–94 (~ 1.89 – $1.92 \mu\text{m}$). The straylight spectrum in the overlapping range (bands 34–39) of the two straylight ranges is defined in the first half (bands 34–36) through the solution for the first range, and in the second half through the solution for the second range. Hence, four degrees of freedom are used to estimate the straylight spectrum for each measured spectrum without the occurrence of disproportionately high coefficients for the principal components when using only one, unified range. Finally, these estimated straylight spectra are subtracted from the measured spectra to obtain the straylight corrected spectra.

Fig. III.9 visualizes the straylight removal procedure for a nightside measurement example exhibiting a very high straylight intensity to illustrate the functionality of the algorithm. It shows the (otherwise corrected) measurement including straylight, the straylight spectrum according to the above given explanations, and the measurement with that straylight spectrum removed. At 1.21 and 1.55 μm , the removal is not perfect, but the straylight intensity is much smaller for most other measurements. When using just the mean straylight spectrum in the full range, the resulting 'Simple straylight spectrum' (Fig. III.9) is not suited due to its mis-

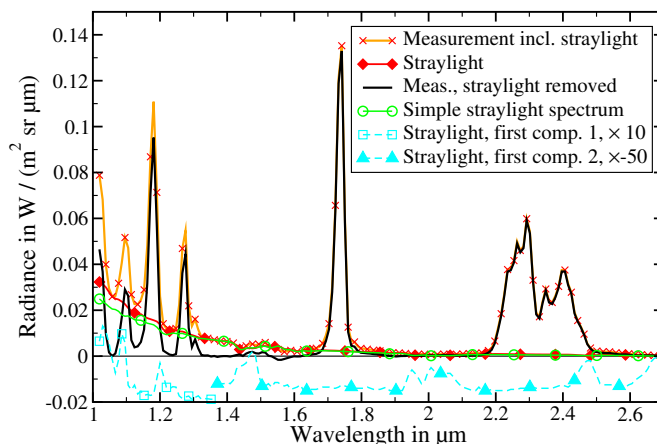


FIGURE III.9: Straylight removal for data cube 320_00, sample 127, line 150, at 18 s exposure time. It is a very low noise spectrum even without binning.

match to the lower envelope of 'Measurement incl. straylight' between 1.0 and 1.4 μm , thereby justifying the PCA-approach. The mean and first principal components are fitted to the depicted measurement in the range '1' between 1.0 and 1.36 μm and in the range '2' between 1.36 and 2.7 μm . The sum of the fitted mean and first components for '1' yields the straylight spectrum in range '1', and analogous for '2'. The fitted mean components are not depicted, since by a suitable scaling, they yield exactly the 'Simple straylight spectrum' in the respective ranges. The first components for both ranges are depicted in the figure scaled with 10 or -50 , respectively, for a better graphical representation.

The described straylight removal technique seems to be quite effective in the straylight situation (3), but may not be ideal for situation (4a) and for the pure night case of situation (4b), which remain the most serious uncorrected types at the moment. Measurements with straylight types (1) and (2) and the day-night case of type (4) are generally excluded from the correction scheme.

III.4.2 Geometry and topography data update

The geometry data has to be extrapolated and updated to suit as input for the retrieval algorithm. The topography in the VIRTIS geometry data is based on a superseded Venus topography model and is not referenced with respect to the correct coordinate system. In addition, it is necessary to preprocess the topography data to incorporate the atmospheric blurring of the observed radiances (Moroz, 2002) as well as a motion blurring. Sections III.4.2.2 to III.4.2.4 are mostly based on Müller et al. (2008); Müller et al. (2012b, and personal communication) and are included here in preparation to Sections III.4.2.5 (p. 89) and III.4.3 (p. 90) and to make the discussions on the topography more self-contained.

III.4.2.1 Geometry data update

The geometry data files accompanying the VIRTIS data (Erard and Garceran, 2008) includes the surface topography for each pixel footprint center and corner, referred to both the surface itself and to the 60 km level above the mean planetary radius (6051.8 km). The latter roughly corresponds to the cloud tops, where the effective source of the VIRTIS observable radiation is expected. The actual cloud top altitude (unity cloud optical depth at 1 μm , altitudes from dayside retrievals) is slightly higher, between about 74 km at low and middle latitudes up to 50° poleward and decreasing to 63–69 km in the polar regions (Ignatiev et al., 2009). The topography vertically below the cloud top footprint is needed as a boundary condition in the simulations. Therefore, all geometry data, except for the topography, has to be extrapolated to the expected cloud top altitude, with the surface and the 60 km level data as support points, and the cloud top level based surface topography has to be referred with respect to the new cloud top footprint corner and center coordinates (Erard and Garceran, 2008, personal communication). There is no difference between the surface and the cloud top data sets when the observation angle is zero, that is, when the line of sight is orthogonal to the mean planetary surface. But at other observation angles, the cloud top data set must be used. Of course, this is a very

simplified model, but it is still much more accurate than to use just the footprint on the planetary surface or the 60 km based geometry.

III.4.2.2 Re-evaluation of the topography data

The Venus surface topography model that is used as reference for VIRTIS geometry data files (Erard and Garceran, 2008) is the Global Topography Data Record (GTDR) obtained through the evaluation of data acquired by the Magellan probe (Ford and Pettengill, 1992). But this is based on preliminary knowledge of the gravity field of Venus, which has been re-evaluated using a refined Magellan ephemeris. Based on this improvement, an updated topography model has been computed (Rappaport et al., 1999), which has not yet been taken into account in the VIRTIS geometry data files. Since a main target of this work is the retrieval of surface information, the most precise topography data available has to be incorporated in the analysis. Therefore, the surface topography referred to the cloud top level footprints has been computed from the updated GTDR. To check the algorithms, this data has also been computed using the older GTDR and compared to the VIRTIS geometry data files. There are discrepancies of less than a few meters due to rounding issues. The difference between the original and the updated topography, on the other hand, can amount to 500 m and more. It is particularly large in certain extended swaths reaching from pole to pole as well as in the mountain regions on Venus. The updated topography is the base for all following considerations (see also discussion by Müller et al., 2008).

III.4.2.3 Referencing

The Magellan topography data (Ford and Pettengill, 1992) in the VIRTIS geometry files is referenced to a coordinate system according to IAU 2000 (Erard and Garceran, 2008; Seidelmann et al., 2002). Although the reprocessed Magellan topography (Rappaport et al., 1999) is described to be referenced according to IAU 1991 (Davies et al., 1992), which provides the same parameters as IAU 2000 for Venus, it is in fact referenced according to IAU 1985 (Davies et al., 1986), (Müller et al., 2012b). To correct for this, the re-evaluated topography data (Section III.4.2.2) has to be rotated to the reference frame where VIRTIS pointing data is referenced in (IAU 2000). However, the impact is almost neglectable.

Additionally, there seems to be a slight misestimation of the Venus mean rotational period given by Seidelmann et al. (2002) owing to the neglect of a slight variation of the Venus rotation rate, see discussion by Müller et al. (2012b). This leads to a longitudinal offset of 0.165° at the median time of the VIRTIS data acquisition between the coordinate systems the Magellan topography and the VIRTIS geometry are referenced in, translating to roughly 17 km at the equator. The cause is still under consideration (Müller et al., 2012b) but the offset is incorporated in the topography data update.

III.4.2.4 Atmospheric blurring

An individual photon emitted from the surface is very unlikely to be detected directly from space. It will be rather repeatedly absorbed and re-emitted as well as scattered by the molecules of the thick atmosphere and the aerosol particles comprising the thick clouds and the haze. This leads to a loss of the exact location where the initial emission took place and thereby to a loss of the exact surface topography and emissivity information. Consequently, the observable radiance at a certain cloud top footprint results from many photons emitted from different surface locations with different surface elevations and emissivities. Theoretical estimations (Moroz, 2002) suggest a blurring of the upwelling surface emissions which can be approximated by a Gaussian blurring function of approximately 50–100 km FWHM. The natural distance measure is thereby given as the spherical distance on a sphere with a radius corresponding to the expected cloud top altitude, i.e. $6051.8 \text{ km} + 74 \text{ km}$ for most of the planet. The effective surface elevation and emissivity to be used as boundary conditions in the simulations is thus a weighted mean of the actual surface data, the blurred surface topography and emissivity. The weighting measure has to be computed from the fundamental radiation quantity to be averaged, i.e. the radiance. The radiance contributing to the Gaussian average and emitted at a certain surface spot can be approximated by the Planck radiation $B(T)$ emitted by this surface spot of temperature T , multiplied by

the surface emissivity at that spot, and attenuated by the atmosphere. By assuming thermodynamic equilibrium between surface and atmosphere, the temperature of the surface at a certain elevation h is given by the temperature of the atmosphere at that altitude according to the Venus International Reference Atmosphere (VIRA, [Zasova et al. \(2006b\)](#)). The attenuation is accounted for by using not the actual VIRA temperature, but an effective temperature T_e , an approximation used by [Müller et al. \(2008, personal communication\)](#) and also obtained from simulations using the forward model in Section III.2 (p. 69) and checked against VIRTIS measurements:

$$T_e = 710 \text{ K} - 5 \text{ K/km} \cdot h. \quad (\text{III.3})$$

The effective lapse rate -5 K/km and the reference temperature 710 K at $h = 0 \text{ km}$ are dependent on wavelength, atmospheric composition, cloud depth, surface elevation and emissivity, and other parameters. But these uncertainties are checked to be of only minor importance for the final result (blurred surface information and derived radiance simulations) and are therefore neglected.

The blurring algorithm for the surface topography is based on the assumption that the surface emissivity, as parameter to be determined in the retrieval, is constant. The surface elevation h at surface longitude and latitude (φ, ϑ) is converted to the effective Planck emission I using the temperature from Eq. (III.3). The resulting mean radiance $\langle I \rangle$ at the observation coordinates (φ_m, ϑ_m) is given by

$$\langle I \rangle_{|(\varphi_m, \vartheta_m)} = \int I(h(\varphi, \vartheta)) R^2 \cos(\vartheta) b(d(\varphi, \vartheta; \varphi_m, \vartheta_m)) d\varphi d\vartheta \quad (\text{III.4})$$

with the Gaussian blurring weight

$$b(d) = N \exp\left(\frac{-d^2 4 \log 2}{FWHM^2}\right) \quad (\text{III.5})$$

and the spherical distance $d(\varphi, \vartheta; \varphi_m, \vartheta_m)$ between (φ, ϑ) and (φ_m, ϑ_m) . The effective surface elevation $\langle h \rangle$ at (φ_m, ϑ_m) is computed from the resulting mean radiance $\langle I \rangle_{|(\varphi_m, \vartheta_m)}$ using the the Planck equation and Eq. (III.3). N is a normalization factor such that the integral in Eq. (III.4) for constant I yields I again.⁴

This averaging is performed for each point on a regular longitude-latitude grid covering the whole planet with 4096×2048 grid points to yield a reference data base for the blurred topographies of the cloud top level pixel footprint projections to the surface.

The use of just 100 km as the FWHM is again a simple model, which is needed to approximate reality. For thinner clouds, the FWHM may be smaller possibly down to 30 km . For future studies of the FWHM impact, the topography is also blurred with respect to 65 km and 30 km , respectively. The unblurred data is additionally provided.

The artificial blurring of the topography data is especially important in the mountain regions. Neglect of this effect can amount to 500 m difference and more on the mountain slopes, whereas lowland planes are less affected. For areas where the Magellan topography is missing (gaps in the topography mapping), it has to be ensured that the blurred topography is also marked as missing regardless of the capability of the algorithm to produce results that extend into these areas.

III.4.2.5 Motion blurring

For the northern hemisphere pushbroom mode observations, the ground speed of the spacecraft can reach high values near the North Pole, which is close to the pericenter. This is a consequence of the highly elliptic orbit of the probe and Kepler's second law. The pixel footprints are moving in the course of the exposure. Hence, photons are collected that originate not only from the instantaneous footprint at the nominal exposure point in time, but also from some areas before and after the central point on the track, the forward and backward extensions. This motion blurring is especially important above the slopes of the mountains close to the pole, in particular Ishtar Terra, where this effect can add up to 100 m difference.

⁴Corrected: In the published paper, \sin instead of \cos was mistakenly written in Eq. (III.4). However, the computer implementation was correct. Moreover, $4 \log 2 / (\pi \cdot FWHM^2)$ was mistakenly given instead of the normalization factor N in Eq. (III.5), whereas in the computer implementation, N is numerically determined according to the (newly included) last sentence of this paragraph.

To include the motion blurring into the topography determination, the effective radiances are utilized again in the averaging as described in the atmospheric blurring procedure (using Eq. (III.3)). The footprint corners at the beginning of the exposure and the footprint corners at the end of the exposure are computed for each pixel taking into account that the geometry data for the dark frames is missing. For this operation, not only the exposure duration is needed, but also the repetition time, i.e. the time span between consecutive exposures. Finally, the effective topography for each pixel is determined from the weighted mean of the effective radiances using the corresponding weights w , where $w = 1$ for each of the four instantaneous footprint corners, $w = 4$ for the instantaneous footprint center, $w = 1/2$ for each of the four forward extension corners, and $w = 1/2$ for each of the four backward extension corners.

The effect of motion blurring can be neglected above the southern hemisphere, since the ground speed of the spacecraft is comparatively small. But it cannot harm either, and thus, to keep the algorithm simple and the results consistent, the motion blurring is considered for each pixel everywhere.

An example of the overall impact of the topography update is shown later on in Fig. III.13 (p. 95).

III.4.3 Data binning

To increase the signal-noise-ratio and to decrease the amount of data to be analyzed by the retrieval procedure, it is useful to decrease the spatial resolution by data binning. There is not too much information loss if this is done appropriately, since the expected observable spatial resolution of the surface information is about 50–100 km FWHM (Moroz, 2002), the correlation length of the clouds is of the order of some hundred kilometers, and the correlation length of the gaseous constituents and atmospheric temperature is expected to be even longer.

This data reduction is the last step of the data preprocessing for the retrieval. All other preprocessing has to be finished at this point. Not only the radiance data has to be binned, but also geometrical parameters (for instance topography, distances, observational angles, footprint geometry, spacecraft time, etc.) and other auxiliary parameters (error measures, housekeeping parameters like detector temperature). Special attention has to be paid to the binning of cyclic parameters, like longitude or local time, to properly handle the behavior at the cut (0° vs. 360° , 0 h vs. 24 h).

Before the data is binned, it has to be filtered according to geometrical and other parameters, if needed. Two times the standard deviation of each band and bin is added to the error measure for each band and bin. The surface topography is not binned directly, but similar to the topography averaging described in Section III.4.2.4 (p. 88), the effective brightness temperature is binned and transformed back to the topography. Because the main intention of this work is the retrieval of parameters from spectral data, the full spectral information should be preserved, and only the spatial information should be binned.

In the following, two different approaches are presented that describe how the data is binned. Both of them have their benefits, depending on what kind of information is sought.

The first binning method is a 'regular' binning taking into account the detector geometry and the data structure in general. Most of the data is archived in cubes with 432 bands, 256 or 64 samples, and a certain number of lines. It is straightforward to bin the spatial information into blocks of a certain number of new samples and lines. For mapping of the southern hemisphere, a moderate data reduction is achieved by a binning resulting in 64 bins in sample direction. For the northern hemisphere pushbroom mode data, which resembles more a cross section structure, a binning which results in 16 bins in sample direction has proven sufficient, since the spacecraft is closer to the planet here and the resulting spatial resolution is absolutely sufficient for this work. For both cases, it is reasonable if four lines contribute to each bin in the downtrack direction.

A definite disadvantage of the 'regular' binning method is the varying spatial resolution that is inherited from the unbinned data and caused by the varying observation angle and distance from spacecraft to footprint. Moreover, repeated measurements of the same surface region on the planet will probably not have the same footprint geometry, but a possibly slightly shifted, scaled, or rotated one. Since the atmosphere is perpetually changing anyway, this is not a disadvantage for atmospheric targets.

When surface information is the primary target, and several measurements of the same spot on the surface are to be compared among each other, a binning with respect to the planetocentric longitude-latitude grid is preferred. In this case, the data is sorted into bins bounded by lines of longitudes and latitudes, or according

to an equal-area map projection, such that each bin corresponds to a surface coverage of about $100 \times 100 \text{ km}^2$, matching the expected achievable resolution for surface studies.

For the northern hemisphere pushbroom mode data, very few surface areas are probed even only twice, and the primary argument for using this surface targeted binning type does not apply. Nevertheless, the swaths, which resemble latitudinal cross sections, might be binned into a regular latitudinal grid of 1° resolution, ignoring the nearly constant longitudes for each data cube. This scheme has been used in [Arnold et al. \(2008\)](#). But the standard deviations of the individual spectra of each bin can be quite large (up to 20% of the signal itself). Here, the regular binning restricted to a single new sample bin should be used instead to achieve cross-sectional results.

III.4.4 Wavelength shift and uncertainty of the full width at half maximum

The band-to-wavelength mapping and the full width at half maximum (FWHM) of the instrumental response function seem to have slightly changed during the cruise phase, as can be verified when comparing VIRTIS-M-IR measurements to simulations and older measurements. Both parameters are temperature dependent (VIRTIS spectrometer temperature). The ground calibration was conducted under conditions that underestimated the operational temperature ranges of the VIRTIS instrument while operating in Venus orbit. This mainly results in a slight misestimation of the FWHM and of the temperature dependent slope and intercept of the band-to-wavelength mapping, which is indicated by a temperature and band depending wavelength shift ranging from about -2 to 13 nm . Additionally, there is a sample dependence of the band-to-wavelength mapping (order of 1 nm) and the FWHM (up to 4 nm), which cannot be stored in the archive at the moment. Finally, there is evidence of a slight band dependence of the FWHM.

There are ongoing efforts to improve the temperature dependency issues and to revise the data structure of the archive to allow for the storing of the sample dependence. They are based on the analysis of an on-board calibration source (polystyrene), but due to the spectral characteristics of the calibration source, only a limited spectral range at about $3 \mu\text{m}$ can be used. Therefore, no definite results for the scaling of the band-to-wavelength mapping and for the band dependence of the FWHM are expected. Moreover, residual uncertainties of the order of 1 nm are expected.

This is the reason why for this work auxiliary parameters were introduced in the retrieval, allowing at least for the retrieval of the intercept and slope of the band-to-wavelength mapping. This hardly interferes with the retrieval of other parameters, since their Jacobians are almost orthogonal to the Jacobians of these auxiliary parameters. The FWHM as auxiliary parameter is more difficult to retrieve, since there are interferences with the cloud factors and the atmospheric temperature. But once the trends are studied in more detail, these parameters can be externally parameterized and their retrieval can be dropped.

III.5 Results

To demonstrate the advances in the data analysis compared to earlier works by the authors ([Arnold et al., 2008](#)), all conditions are set to the earlier conditions. For instance, the latitudinal binning scheme used by [Arnold et al. \(2008\)](#) will still be used in the current section, although in planned subsequent papers the other binning schemes discussed in Section III.4.3 will be preferred. Also, the selection of data to be analyzed is restricted to the data selected by [Arnold et al. \(2008\)](#). Any amounts of gaseous or particulate atmospheric components depicted in the following diagrams, are represented on a relative scale with respect to the profiles used by [Haus and Arnold \(2010\)](#), which are based on [Pollack et al. \(1993\)](#).

III.5.1 Impact of retrieval algorithm improvements on retrieval results

The improvements in the retrieval algorithm outlined in Section III.2 (p. 69) lead to different retrieval results when comparing to the original retrieval algorithm applied by [Arnold et al. \(2008\)](#) and [Haus and Arnold \(2010\)](#). In order to demonstrate the impact of the retrieval algorithm alone, the same data set according to the new calibration and preprocessing is analyzed by both retrieval algorithms.

III.5.1.1 Spatial-temporal correlations

The introduction of spatial-temporal correlations of the parameters indeed proves beneficial on the retrieval. An example is presented in Fig. III.10, where the retrieved SO₂ column factor for data cube 113_15, or short

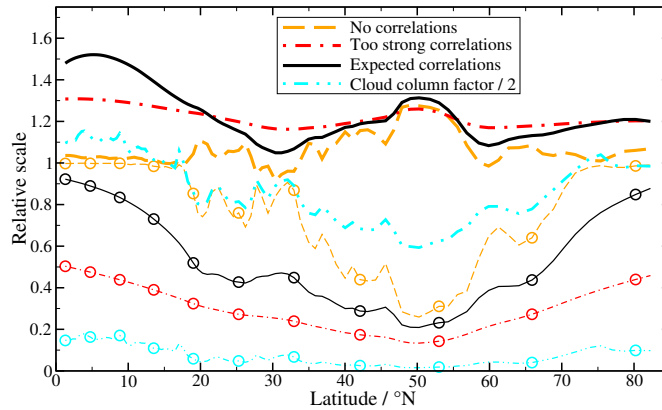


FIGURE III.10: SO₂ and cloud column factor as a function of northern latitude for different spatial-temporal correlations for orbit 113, new calibration and preprocessing. The corresponding thin lines with circles depict the retrieval uncertainties (two times standard deviation), for the clouds scaled with 10 for better representation. Here, the regular binning scheme with 16 bins in sample direction is used and the fourth bin is selected to extract the results for the three cases shown.

orbit 113, in the new calibration and preprocessing is shown as a function of latitude for different *a priori* spatial-temporal correlations for CO, OCS, SO₂, and the surface emissivity. The cases for missing correlation and too strong correlation (ten times the expected values) are compared to the profile for an expected correlation (2,000 km correlation length and 12 h correlation time for minor gases, 500 km and 3.6 h for clouds, 100 km and 10⁶ h for surface emissivity). For each case, the *a priori* means and standard deviations for each of the retrieved parameters and the *a priori* spatial-temporal correlations for the remaining parameters are the expected *a priori* values. The correlated profiles are smoother than the uncorrelated profile as expected. The stronger the correlation, the smoother is the profile with a perhaps too smooth result for the too-strong-correlation-case. The retrieval uncertainties are smaller for thinner clouds and smaller for stronger spatial-temporal correlations. In the too-strong-correlation-case, the retrieval uncertainty is underestimated due to the deliberately wrong chosen *a priori* correlation data. But in the expected-correlation-case, the decreased retrieval uncertainty compared to the uncorrelated case clearly shows the beneficial impact of the increased information content in the context of the adjoining measurements. The CO, OCS, and surface emissivity profiles exhibit a similar behavior. Nevertheless, since only a very small spectral region carries information on the SO₂ column (essentially one spectral band at 2.46 μm), the thus still high retrieval uncertainties in the expected-correlation-case obstruct a significant SO₂ information gain. Unexpected are the different trends for the uncorrelated and the correlated retrieval results. While the profiles for the too-strong and the expected correlation seem to share the same trend with different smoothness, the uncorrelated profile follows a different trend. Also unexpected is the smaller residual norm for the correlated retrievals in spite of the stronger constraints on the parameters. This is a clear indication that the uncorrelated retrieval converged to subsidiary solutions between about 0 and 20 °N and 70 and 85 °N. Thus, it has to be emphasized, that the incorporation of spatial-temporal correlations of the parameters is not equivalent to a simple smoothing of the results of an uncorrelated retrieval, the more, because a simple smoothing does not have to yield a consistent parameter set suitable for the accurate simulation of each individual spectrum.

This discussion underlines the usefulness of the correlated retrieval. The more similarity (in the Euclidean angle sense) there is between the Jacobians of the parameters, the more detailed *a priori* knowledge has to be incorporated in the retrieval to get useful results, with the zero correlation length and time implicitly presumed in the non-multi-spectrum retrieval as a very crude approximation of the reality. A detailed discussion of the multi-spectrum retrieval algorithm and its application to the VIRTIS-M-IR data of the Venus nightside will be presented in subsequent paper.

III.5.1.2 Common parameters in the retrieval

The utilized multi-spectrum retrieval algorithm allows for the determination of parameters common to all spectra. Currently, the most critical and not-well-known quantity for the simulation of the spectra is the optical thickness of CO₂. The ambiguity between different spectral line data bases (compare the discussion by Haus and Arnold, 2010), spectral line shapes, and the broad band CO₂ continuum is a serious obstacle to reliable retrievals of surface and deep atmosphere information. But all these parameters are common to all Venus nightside emission spectra. While they are far less observable in the dayside spectra (Haus and Arnold, 2010) and basically cannot be extracted from dayside measurements, they can strongly influence the shape of the nightside spectra that can consequently be used to determine them. Whereas random errors are of decreasing importance for an increasing number of utilized spectra in the multi-spectrum retrieval, systematic measurement, calibration, or preprocessing errors as well as simulation errors can certainly affect the results, since they are also common to the data set to be analyzed. But it should still be possible to constrain some general properties. For instance, a CO₂ line shape retrieval in the vicinity of the peak at 1.10 μm shows that there is no realistic line shape to arrive at satisfactory fits without using an artificial continuum. The latter is not easily justifiable from physical considerations. But it is entirely possible that the CO₂ line data bases have imperfections for the extreme environmental conditions near the Venus surface, since they are mostly not based on measurements, but mainly on numerical computations (Tashkun et al., 2003).

While for the earlier works, a trial-and-error method was used to determine acceptable CO₂ continuum parameters for the different atmospheric windows, it is now possible to determine them systematically as common parameters, which are thereby compatible with all utilized measurements under the most diverse conditions. Currently, it is common practice to use continuum parameters which are constant throughout the entire range of a spectral window.

A high continuum for the 1.74 μm window, for instance, acts similar to a high cloud opacity, so these parameters cannot be disentangled. Of course, the remaining observed spectral windows constrain the cloud amount, but in these windows the continuum is also not exactly known. Different cloud modes are also allowed to vary in the retrieval, and the optical depth for one window only constrains the optical depth for another window to a certain limited extent. The use of the wrong continuum parameters can still reproduce very good fits for certain spectra with coincidentally matching cloud mode abundances, while for other spectra the fits can be unsatisfactory for each cloud mode combination. The retrieval of the continuum parameters as common parameters for a representative selection of spectra under highly diverse conditions allows to determine these parameters in an automatic way, and indeed the convergence is quite robust for different *a priori* parameter selections and different representative selections of spectra, thereby hinting at the universality of the retrieved parameters.

As an example, the retrieved continuum for the 2.3 μm window is $4 \cdot 10^{-8} \text{ cm}^{-1} \text{ amagat}^{-2}$ compared to the values $10\text{--}16 \cdot 10^{-8} \text{ cm}^{-1} \text{ amagat}^{-2}$ determined by Brodbeck et al. (1991) or $4 \cdot 10^{-8} \text{ cm}^{-1} \text{ amagat}^{-2}$ applied by Tonkov et al. (1996) and de Bergh et al. (1995). For the 1.74 μm window, the retrieved value is $0.4 \cdot 10^{-8} \text{ cm}^{-1} \text{ amagat}^{-2}$, whereas in the literature one finds $0.5 \cdot 10^{-8} \text{ cm}^{-1} \text{ amagat}^{-2}$ (de Bergh et al., 1995).

It is even possible to define a wavelength dependent continuum parameter for each window with a wavelength resolution comparable to the VIRTIS-M-IR resolution, a 'non-constant continuum'. An example is shown in Fig. III.11 for the 2.3 μm window. To regularize the deviation from the previously retrieved constant continuum, the non-constant continuum is treated as a non-constant offset from the constant continuum with an *a priori* mean value of 0 and a standard deviation of the order of the retrieved constant continuum. Also *a priori* correlations between the continuum values corresponding to different wavelengths are imposed to ensure a smoother continuum, which is needed as a countermeasure against effects from possible small residual even-odd patterns of the spectra.

The continuum parameter is strongly affected by spectrally dependent systematic measurement, calibration, or preprocessing errors and simulation errors. Therefore, this parameter has to be carefully interpreted and, if possible, verified, refined, or falsified by experiment, also compare Tran et al. (2011), before declaring it as an actual continuum parameter. At least it still has an entirely technical benefit, since the overall fit to the measurements can be improved. As can be seen in Fig. III.11, the fit using a constant continuum has a different shape than the measurement near 2.4 μm probably due to an imperfection in the computation of the

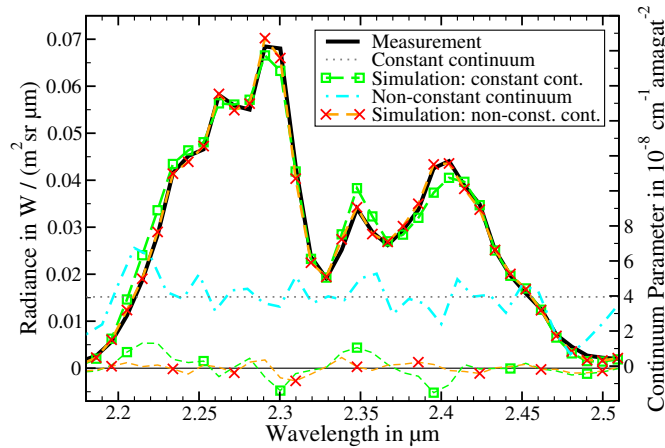


FIGURE III.11: Constant and non-constant continuum (right hand side axis) and resulting simulations in comparison with a measurement (left hand side axis) in the 2.3 μm window. Differences of simulations to measurement are depicted as corresponding thin lines in the bottom part.

CO_2 opacity. Provided that the line data base discussed by Haus and Arnold (2010) is used and line mixing or collisional induced absorptions are neglected, it is not possible to obtain a good fit in this spectral range by merely using a constant continuum. There are also situations when the residual norm is very similar to the constant-continuum-case shown in Fig. III.11, but the shape of the fit is even more distorted. This happens, because an improbable composition of the minor gases was retrieved despite the utilized *a priori* data. Obviously, subsidiary solutions far away from the true solutions were found in that case. When using the non-constant continuum, this situation did not occur and the fits for these very cases are satisfactory. Thus, the probability of locking to subsidiary solutions in the course of the iterative retrieval process can be decreased by using the non-constant continuum parameter. Therewith, the convergence behavior can be greatly improved.

Systematic simulation errors, like the neglect of line mixing or collisional induced absorptions, imperfect line data bases, line shapes, and continua, etc. can be compensated by this method, thereby decreasing their impact on the retrieved surface and deep atmosphere parameters.

III.5.2 Impact of calibration refinement and preprocessing on the measurement data base

III.5.2.1 General impact on spectra

Fig. III.12 illustrates the impact of the data calibration and preprocessing on a selected spectrum for a latitudinal bin (see Section III.4.3 (p. 90)) for orbit 113 (3.3 s exposure time) comparing the new and the old calibration and preprocessing pipeline. The old one was used by Arnold et al. (2008). The main differences appear in the range 1.0–1.3 μm . The new radiance is larger in the peaks, gradually increasing from 1.3 μm to 1.0 μm which is mainly a consequence of the responsivity adjustment (Section III.3.2.3 (p. 77)). The shape of the valleys is also somewhat changed owing to the new straylight removal approach (Section III.4.1.2 (p. 85)).

The shape of the 2.3 μm window complex is now less jagged because of the reduction of the EO pattern in the ITF (Section III.3.2.1 (p. 73)) and the correction of the EO effect of the measurements (Section III.3.2.4 (p. 82)). The other windows also undergo slight modifications of the peak and valley shape due to the EO correction.

The radiances are now generally slightly higher across all wavelengths as a consequence of the sample homogenization (Section III.3.2.2 (p. 75)), since for the latitudinal binning used here, additional radiance contributions measured at the detector edges are incorporated in the binning. When the regular binning scheme is used, measurements recorded near the center of the sample direction of the detector are hardly affected by the sample homogenization, but the closer they are to the detector edges in sample direction, the stronger the impact will be in general resulting in higher radiances according to the new pipeline.

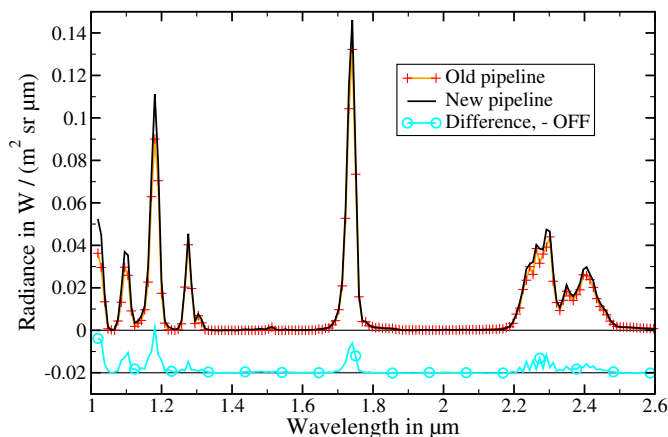


FIGURE III.12: Comparison of new and old data calibration and preprocessing on the resulting spectral structure for latitudinal bin covering 64–65 °N for orbit 113. The difference between the new and the old spectrum is displayed with an offset of $OFF=0.02 \text{ W}/(\text{m}^2 \text{ sr } \mu\text{m})$.

III.5.2.2 Topography update

Topography and geometry data changes (Section III.4.2 (p. 87)) do not affect atmospheric and surface parameter retrievals in a systematic way. Nevertheless, the topography changes can produce large changes in the results and should be explicitly investigated here.

The difference between the old topography data without blurring and the updated topography is dependent on the location on the planetary surface. It is at some places quite small and at other places very large with up to more than 1000 m in single spots in rough terrain. This is a consequence of the new Magellan data evaluation. But even when comparing both data sets blurred, large deviations can be found, especially in some extended swaths reaching from pole to pole.

Fig. III.13 shows the surface topography as a function of northern latitude for orbit 113 for the old (unblurred) and new (blurred and unblurred) database. Latitudinal binning was used in this example. The old data set ('Old') is the unblurred surface topography according to the accompanying geometry data file based on the superseded Magellan data evaluation. The surface topography based on the new Magellan data evaluation ('New') does not exhibit the above mentioned large systematic deviations from the old data for this example orbit, but in the mountain regions there are differences of up to several hundred meters. The blurred version of the 'New' data set ('New_{blur}') exhibits the largest deviations in the mountain regions, too. This is the updated topography to be utilized in this and future works. The surface topography differences with respect to the 'New_{blur}' data set are also depicted in Fig. III.13 and can amount to up to 600 m in absolute value for this orbit.

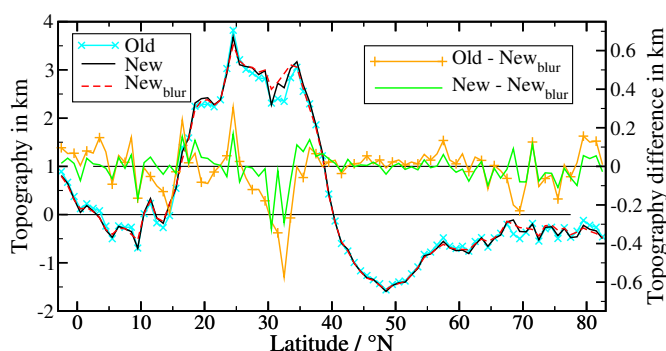


FIGURE III.13: Surface topography as a function of northern latitude (thick lines, left hand side axis) for orbit 113 (latitudinal binning) for the old and new (unblurred and blurred) database. Thin lines show the deviation between different data sets (right hand side axis).

It is very important to mention here, that a topographic uncertainty of 100 m translates roughly to a surface emissivity uncertainty of about 5% at mid-level emissivities (see also Fig. 18 by Haus and Arnold, 2010).

This fact underlines the importance of using as accurate as possible topography data sets for surface emissivity retrieval. The new topography data still suffers from uncertainties, especially with respect to the value of the FWHM for the artificial blurring, but it is presumed, that the accuracy is reasonable for the majority of the surface. Some preliminary tests similar to [Arnold et al. \(2008, Fig. 11\)](#) show the 100 km FWHM to be more suited than 65 km or less.

III.5.2.3 Binning schemes

The planetocentric (latitudinal) binning scheme (Section [III.4.3 \(p. 90\)](#)) utilized for the comparisons to earlier work was found to be unsuitable for the analysis of the northern hemisphere pushbroom mode data. The variability of the spectra within a single bin as well as the drift of the FWHM and the spectral registration as function of the location on the detector is too large, thereby blurring the spectral resolution of the averaged spectra. Instead, the regular binning is now preferred for this purpose. To extract a single swath on the northern hemisphere from a pushbroom observational sequence, only one sample of the binned data is selected for further analysis. In sample direction, it will be chosen from left of the center, since the FWHM is smaller there, yielding spectrally higher resolved information.

Contrary to pushbroom analyses, the planetocentric binning scheme will be chosen for future surface emissivity retrievals with the surface emissivity of a certain small area as common parameter of measurements repeatedly sampling this area. Thus, the binning scheme has to be selected in dependence on the pursued scientific goal, since it has a significant impact on retrieval results.

As one example, compare the SO₂-curve from the new calibration and preprocessing in [Fig. III.14 \(p. 98\)](#) (latitudinal binning) to the SO₂-curve for the expected correlations in [Fig. III.10 \(p. 92\)](#) (regular binning) to see the impact of the latitudinal versus the regular binning scheme on the retrieved SO₂-column factor, but keep in mind the high retrieval uncertainty for SO₂ as well as the high standard deviation of the spectra in the latitudinal bins.

III.5.3 Impact of calibration refinement and preprocessing on retrieval results

Compared to the earlier ([Arnold et al., 2008](#)) utilized data, the calibration refinement and the new data preprocessing cause some mostly systematic changes to the spectra. While the new multi-spectrum retrieval algorithm affects the retrieval results due to an improved extraction of information from a set of spectra by incorporating *a priori* knowledge and the possibility to determine systematic parameters, the updated calibration and preprocessing procedure improves the measurement data base upon which the retrievals are based. To demonstrate the sole impact of the latter, both the old and the new data base are analyzed in the following by the new multi-spectrum retrieval algorithm utilizing the same *a priori* data. Because of the mostly systematic nature of the spectral modifications, some general impacts on the retrieved parameters can be stated.

III.5.3.1 Clouds

Clouds attenuate the nightside emissions. The four different cloud modes utilized in the atmospheric model, have different impacts in different spectral ranges ([Haus and Arnold, 2010](#)). When using invariant column profiles for these modes, one can either try to retrieve a single factor acting on all four columns equally, or to retrieve a single factor acting on just one of the modes. Neither approach yields satisfying fits in general. On the other hand, in practice the four modes are hard to disentangle in the retrievals, and the retrieval of four individual cloud mode factors is mainly governed by the *a priori* data. One could try to vary just two modes and leave the others fixed, which already yields satisfying fits, or one could also try to retrieve all four cloud mode factors with equally well fits compared to the two mode variation. For this work, it was decided to first determine a single cloud factor, acting on all four columns equally, as a rough estimation of the cloud amount. Then, as a fine tuning, all four modes are retrieved as correcting factors, treating the cloud mode factors as parameters describing an envelope, needed to obtain good fits, and not as parameters with a certain real meaning. The reason for that is the general lack of knowledge of the clouds and the cloud modes. Nearly nothing is known of the *a priori* means and standard deviations of the single cloud modes, or any correlations between them. Not even the composition of the clouds is known within reasonable limits. All modes are assumed

to consist of 75% H_2SO_4 watery solution, but the H_2SO_4 concentration is not well known, and some modes could also have a completely different composition, like sulfur crystals or other. These are therefore mainly assumptions, based on a few *in situ* measurements during the VENERA missions, just as the column profiles and the modal model itself (droplet radii follow lognormal distributions with certain modal radii and dispersions). Therefore, the cloud mode factors rather serve as an auxiliary parameterization of how the cloud modes can possibly affect the shape of the spectra within a reasonable cloud model, until more definite knowledge emerges.

As long as no definite meaning is assigned to the modal factors, the impact of the new calibration and preprocessing is not so important. The main conclusion at the moment is that a slightly different composition results from the new data calibration and preprocessing. This emerges not so much for the trends or small scale structure of the retrieved spatial distributions, but rather for the offsets. The most notable difference to earlier work is due to the multi-spectrum retrieval that now suppresses discontinuities in the results, ensures a reasonable smoothness, and stabilizes the solutions by preventing an otherwise certain erratic behavior resulting from jumps between different subsidiary solutions.

III.5.3.2 Minor gases

The minor gaseous constituents of the atmosphere which are observable in the utilized spectral range of the nightside emissions measured by VIRTIS-M-IR are H_2O and HDO, CO, SO_2 , HF, HCl, and OCS (see overview by Haus and Arnold, 2010). H_2O exhibits absorption bands in the vicinity of the 1.15 μm valley, in the 1.74 μm peak, and in the right hand side of the 2.3 μm window. HCl absorbs in the center of the 1.74 μm window. All the other minor gases have fingerprints in the right hand side of the 2.3 μm window. HDO, HF, and HCl are not retrieved at the moment, since the resulting uncertainty margins are too wide to derive meaningful results.

The modifications of the spectra with respect to the earlier calibration and preprocessing in the 2.3 μm window range can cause changes of the retrieved absorber amount (column density). But other spectral ranges are also indirectly contributing, since for instance a different cloud modal composition or amount, which is derived according to the modifications within the whole spectral range, may also change the general shape of the cloud-based envelope of this window. Nevertheless, some gas column factors experience only small impacts, for instance CO, as it is shown in Fig. III.14, where the results from the new calibration and preprocessing are essentially just the old values scaled by about 0.9. This invariance of the relative behavior is a consequence of the spectral position of the CO absorption feature close to the left flank of the 2.3 μm window. This left flank is free from minor constituent influences. In addition, it is a consequence of the relatively broad CO absorption feature located between 2.30 μm and 2.40 μm that averages small scale changes from the even-odd effect correction over about ten spectral bands on the detector. Only in the case of very thick clouds (in Fig. III.14 discernible as the latitude range with the widest uncertainty margins, compare also cloud column factor for regular binning and new calibration and preprocessing in Fig. III.10 (p. 92)) there are some non-negligible differences, which are due to the ambiguities arising from the then relatively small radiance over the whole window range. On the other hand, the scaling by about 0.9 results from a difference in the continuum parameters which were derived using the different calibrations and preprocessings, and the corresponding difference in the retrieved cloud parameters.

But the narrower the absorbing range of the gas is, the stronger can be the impact of the even-odd effect correction. SO_2 presents the other extreme case, since it is observable in essentially one spectral band only, namely at 2.46 μm . Aside from a near the retrieval uncertainty minimum similar scaling factor as in the CO-case, the relative impact of the even-odd correction compared to the radiance itself is very strong in case of small radiances (below 20°N, above 75°N for orbit 113). This can result in a large difference between the retrieved parameter magnitudes and trends with respect to the two data calibration and preprocessing sets, as it is illustrated in Fig. III.14.

III.5.3.3 Common parameters

Currently, the most important common parameters in the multi-spectrum retrieval are the continua for the different spectral windows. It is theoretically and experimentally difficult to derive these parameters. In order to

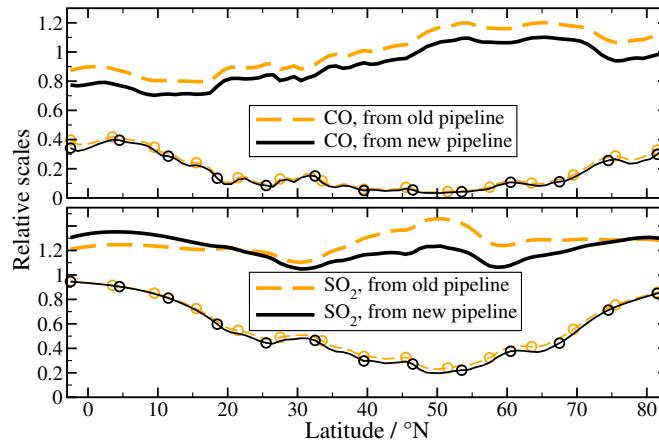


FIGURE III.14: Relative column densities of CO and SO₂ as functions of northern latitude and the impact of the new calibration and preprocessing pipeline on the retrieval results for orbit 113. The corresponding thin lines with circles depict the retrieval uncertainties (two times standard deviation).

enable the simulations to fit the measurements nonetheless, in the Venus radiative transfer community the continua are usually treated as auxiliary opacity correction parameters. As long as their physical meaning is not better understood, they should be treated as the smallest possible opacity corrections that cannot be explained by better understood opacity sources such as clouds. For the retrieval of the continua, their *a priori* means are therefore set to zero. Once they are retrieved as parameters common to a representative set of spectra, they are used as fixed external parameters for the regular spectral fits. Further studies are needed to put a definite physical meaning to the continuum parameters.

A higher continuum means lower simulated radiances and decreased radiance contrasts provided all other parameters remain unchanged. The new calibration and preprocessing results in an increase of the spectra in the 1.0–1.3 μm range relative to the remaining range due to the responsivity adjustment in this range, see Section III.3.2.3 (p. 77). This has the effect, that now a much smaller continuum is needed for the spectral windows in this range. This is in contrast to the earlier calibration and preprocessing, where much higher continua were retrieved to compensate for the too small measured radiance relative to the remaining spectral range. From a physical standpoint it is hard to justify a significant continuum in the 1.0–1.3 μm range, because of the absence of strong CO₂ bands in the vicinity. In this respect, the new calibration and preprocessing proves a significant advantage over the earlier one.

The continua in the other spectral windows are not so much affected by the new calibration and preprocessing, since there is only a general increase of the radiances that can be mainly compensated by smaller cloud factors, while in the range from 1.3 μm to 1.0 μm , the radiance is gradually increasing with respect to the remaining range (see Figs. III.6 (p. 78) and III.12 (p. 95)).

When using non-constant continua for the windows (see Section III.5.1.2 (p. 93)), the even-odd effect of the earlier data resulted in an even-odd patterned runaway continuum at the wavelength grid points. In retrospect this resulted as the attempt of the retrieval algorithm to explain the radiance even-odd pattern that was superimposed on the underlying spectrum, and this was also common to all spectra of a fixed exposure time. In fact, this has been the trigger for the development of the new data calibration and preprocessing. When applying the retrieval algorithm to the newly calibrated and preprocessed spectra, this even-odd pattern in the non-constant continuum disappears, and the simulations utilizing a rather smooth non-constant continuum can reproduce the measurements very well (see Fig. III.11 (p. 94)).

III.5.3.4 Surface emissivity

The surface emissivity is determined separately for the three surface windows with peaks at 1.02, 1.10, and 1.18 μm , respectively (see Fig. III.12 (p. 95)). The non-LTE O₂ glow at 1.27 μm interferes with the surface and deep atmosphere emissions in the 1.28 μm peak, and is therefore excluded from the surface emissivity determination. An independent additive auxiliary parameter is used to make the simulations fit the measurements in the 1.28 μm peak and can straightforwardly be interpreted as the intensity of the O₂ glow (Haus and

Arnold, 2010). This purely mathematical trick in the simulations enables the retrieval algorithm to include this window and to avoid complex non-LTE calculations in the code. The subsidiary peak at $1.31\ \mu\text{m}$ does not carry any significant information on the surface, the maximum information originates already well above the surface near an altitude of about 17 km.

The values of the retrieved surface emissivity in the three windows are affected by almost every other parameter in the retrieval. Emissivity is one of the most difficult parameters to be determined. Its magnitude is directly affected by the continua in this spectral range. A lower radiance can either be explained by a stronger atmospheric continuum or by a smaller surface emissivity, provided other parameters are not changed. But it is very important to note, that this correlation has its limits, since the surface emissivity cannot exceed 1 nor be negative, while at the same time the continuum must be common to all spectra. In fact, the emissivities are probably not very close to either 0 or 1, and further constraints arise from this. The multi-spectrum retrieval algorithm can determine a continuum that is compatible with this restriction, and the retrieved surface emissivity is a consequence of the remaining spatial radiance variation. For this work, the expected surface emissivity is set to vary around 0.75, but further studies are required to refine this value. All this requires the surface temperature and near-surface temperature profile to be known, as well as a known cloud optical depth. The former are at the moment set to follow the VIRA temperature profile assuming thermodynamic equilibrium of the surface and the adjoining atmosphere, while the latter is determined at the same time from the whole spectral range together with all other retrieval parameters.

An annotation should be given at this point. It may seem that all the mentioned retrieval parameters are underdetermined by the available spectral information content, and in fact, this may well be when not using *a priori* data. But the retrieval algorithm intrinsically works with probability distributions, and a narrower tolerance region for a certain parameter decouples it from otherwise closely correlated parameters, that are, parameters with a scalar product between their normalized Jacobians⁵ close to 1. The retrieval results are also probability distributions. For closely correlated parameters with wide mutually compatible tolerance regions, the uncertainties of these parameters are high.

The new calibration and preprocessing of the measurement data results in much smaller constant continua for the surface windows and higher retrieved surface emissivities as it is shown in Fig. III.15. Only the $1.02\ \mu\text{m}$ surface emissivity is depicted here, since it is more reliable than the values that result from the other windows and have wider uncertainty margins.

It was explained by Haus and Arnold (2010) in Figs. 4 and 5 that the maximum contribution to the measured radiance at the top of the Venus atmosphere originates at the surface and in the very close-to-surface atmospheric layers, but with different weights. 96% of the measured nightside emissions at $1.02\ \mu\text{m}$ result from the surface, while the windows at $1.10\ \mu\text{m}$ and $1.18\ \mu\text{m}$ yield 57% and 48% surface contribution, respectively. Moreover, these two windows are partly contaminated by water vapor and this fact introduces an additional unknown parameter into the emissivity retrieval procedures. As a consequence, they carry less surface information and the retrieval of emissivity values becomes much more difficult.

Note, that the latitudinal trends of surface emissivity and their small scale structure show similar features for the old and the new data calibration and preprocessing. The absolute values are still a matter of further research, because of the presented difficulties. Also note that the anomaly at 68.5°N on orbit 113 discussed by Arnold et al. (2008) and Haus and Arnold (2010) is still discernible, while the topography trend represented by Haus and Arnold (2010), Fig. 28, seems to have vanished. This is a consequence of the now different continua resulting from the multi-spectrum retrieval as common parameters and the new data calibration and preprocessing. A too high continuum in the surface windows leads to an ever increasing excess of gaseous opacity for decreasing surface topography, which is compensated by the retrieval algorithm through the gradual increasing excess of surface emissivity discernible in Haus and Arnold (2010), Fig. 28. Compare also the continuum discussion by Bézard et al. (2009) for the $1.18\ \mu\text{m}$ peak. Further studies are planned to verify or falsify a possible topography trend of the surface emissivity.

⁵Corrected: In the published paper, the term 'normalized' (referring to the Euclidean norm) was mistakenly omitted.

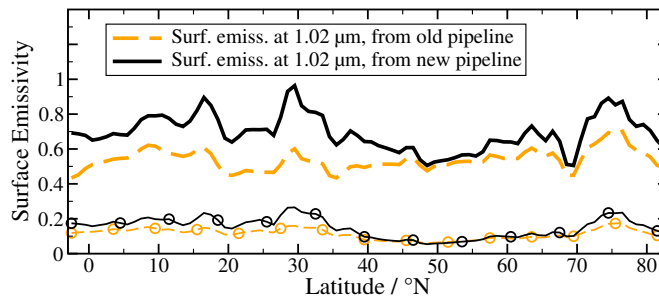


FIGURE III.15: Surface emissivity at $1.02\ \mu\text{m}$ as a function of northern latitude and the impact of the new calibration and preprocessing pipeline on the retrieval result for orbit 113. The corresponding thin lines with circles depict the retrieval uncertainties (two times standard deviation).

III.6 Conclusions and outlook

In order to achieve high-quality retrievals of VIRTIS-M-IR spectra, the spectral data base as well as the retrieval algorithm had to be adapted and improved. This is of special importance for the extraction of surface data. The improvement of the spectral data base included a detailed detector responsivity analysis which revealed, that the instrument transfer function (ITF), needed to compute radiances from detector counts, had to be adjusted in several ways. First, an even-odd pattern in the original ITF, a result from the so-called even-odd effect being present during the ground calibration, had to be removed. Then a factor improving the spatial homogeneity of the detector was derived. This so-called sample homogenization factor, when using the central region of the detector as a reference, leads to a wavelength dependent increase⁶ of the radiance in the outer region of the detector in sample direction in the order of about 15%. Furthermore, to allow for a satisfying retrieval of day spectra, it proved necessary to adjust the ITF near the low-wavelength end of the detector. This correction results in an increase of the radiance of between 0% at $1.3\ \mu\text{m}$ and of up to 35% at $1.0\ \mu\text{m}$. The detector responsivity analysis also revealed a temperature dependent possible nonlinearity of the detector-count-to-radiance mapping. The even bands of the detector probably suffer a bend in this otherwise possibly quite linear mapping. When restricted to the even bands, the bend characteristics are quite homogeneous in band direction, but they vary in sample direction. The same behavior exists for the odd bands, but with differing bend locations and angles from that of the adjacent even bands. This differing piece-wise linearity between the even and odd detectors is the probable cause of the even-odd effect. This working hypothesis can also explain the decrease of the even-odd pattern for increased detector exposure time. In absence of detailed data describing this nonlinearity, an empirical scheme for the correction of the even-odd effect in the wavelength range between 1.0 and $2.6\ \mu\text{m}$ was developed, with day spectra as reference for night spectra. For night spectra acquired at an exposure time of 3.3 s, this leads to a correction of the radiance in the night side peaks of up to 5%. For the longer exposure times 8 or 18 s still a correction of up to 1% is predicted.

The newly calibrated spectra have to be preprocessed for the retrieval. This includes a removal of the straylight, an update of the geometry and topography data, and a rebinning adapted to the intended retrieval task. The new straylight removal algorithm, when compared to the old straylight removal algorithm, leads to modified shapes of the night side spectral peaks and valleys affecting mainly the quality of the retrieved best fit, and to possibly different radiance peak heights, depending on the straylight situation of up to 10% of the straylight radiance. Especially the new topography data can differ from the old data by as much as several hundred meters, whereby a error of 100 m translates to a surface emissivity error of about 5% at mid-level emissivities. The use of unsuitable binning schemes can lead to a high variability of the radiances within the individual bins and thus an increased measurement error and therefore retrieval error. While atmospheric targets allow for a simple 'regular' binning, based on the detector geometry, the repeated observation of surface targets calls for a surface coordinate based binning.

The improved retrieval algorithm provides a better regularization of the ill-posed retrieval problem, noticeable by an increased stability of the retrieved results and the better avoidance of subsidiary solutions. Aside from the incorporation of *a priori* mean values and standard deviations for the parameters, whether known

⁶Corrected: In the published paper, the radiance was mistakenly described to decrease in the outer region of the detector in most spectral ranges due to the homogenization, see footnote on page 76.

or estimated as reasonable, this is accomplished by the introduction of correlation lengths and times in a simultaneous coupled retrieval of several spectra. The capability of the multi-spectrum retrieval algorithm to determine parameters common to all utilized spectra allows for a systematic approach to determine wavelength resolved CO₂ continua compatible with the measurements and the forward model. But systematic measurement and simulation errors are also common to the spectra. For instance imperfections in the CO₂ spectral line data base can cause flawed simulations. Thus, the retrieved common parameters have to be interpreted carefully. Still, wavelength resolved CO₂ opacity corrections can be regarded as wavelength resolved corrections to errors in the forward model. This has the side effect of improved convergence properties of the retrieval algorithm by a better avoidance of subsidiary solutions.

Systematic impacts on the retrieved parameters can be stated here primarily as examples only. This is a consequence of the complex natures of both the radiative transfer in Venus' atmosphere and the modifications in the calibration and preprocessing pipeline and in the retrieval algorithm. The continuum parameters changed mainly due to the gradual nature of the adjustment of the ITF in the range 1.0–1.3 μm. Retrieved cloud densities increased on average due to the predominantly decreased radiances resulting from the sample homogenization.⁷ In one example orbit, the CO and SO₂ column densities underwent a systematic change in the order of 10% mainly due to the different continuum parameters. The surface emissivity at 1.02 μm for that orbit was determined to be generally higher mainly due to the, relatively to the other spectral windows, higher radiances in that window, caused by the adjustment of the ITF in the range 1.0–1.3 μm. A possible surface elevation trend of that emissivity for all studied orbits apparently vanished due to the change in the continuum parameters. The fine structure in the surface emissivity changed mainly due to the differently determined cloud modal composition and the updated topography. In absolute numbers, the surface emissivity changed in the order of about 0.2 and up to 0.36 for one example orbit.

The VIRTIS-M-IR data archive proves extremely valuable due to the unique spectral, spatial, and temporal coverage of Venus. The highly diverse measurements that were recorded under all kinds of observational and environmental conditions during the course of the long and successful mission can be complemented with a multi-spectrum retrieval algorithm to exploit the limits of what can be achieved with the available data.

Many calibrational issues have been resolved or improved, and the presented approaches are of general interest for onboard calibration of spaceborne imaging spectrometers. Still, it should be kept in mind, that even slight nonlinearities in the responsivity can lead, through relative differences in the deviation from linearity, to artifacts like the even-odd effect, although the deviations from linearity themselves lie well within the calibration uncertainty. The detector characteristics can change due to stresses in the launch, cruise, and orbit insertion phases, and ideally, some means to monitor the radiometric calibration should be available. The capability of the determination of straylight spectra from outside the field of view is desirable, as it is for the spectral and spatial in-frame straylight.

Future work will use the calibration and preprocessing updates in conjunction with the new multi-spectrum retrieval algorithm, since this ensures an enhanced reliability for the analysis of surface and deep atmosphere features. The next step in the data analysis of the VIRTIS-M-IR measurements will be a selective retrieval and mapping of parameters on the southern hemisphere. Here, the high measurement repetition rate can be utilized to analyze localized and small surface areas and observe the compatibilities with respect to the surface data. In this context, it is possible to treat the surface emissivity of a small area as common parameter of all measurements covering this area, thereby further improving the reliability of the retrieved values.

A subsequent paper will describe the mathematical framework of the multi-spectrum retrieval algorithm, and its application to the VIRTIS-M-IR nightside measurements will be discussed in detail. This topic was beyond the scope of the present paper due to its complexity.

⁷Correction: The radiances actually increase on average in most spectral ranges due to the homogenization, see footnote on page 76. The total cloud column factors in this constellation increased possibly rather as a consequence of the accordingly also changed continua. For the single cloud mode column factors, there was no clear trend.

Acknowledgements

Nikolay Ignatiev noticed the responsivity issue at 1.0–1.3 μm and the sample inhomogeneity. Nils Müller made the authors aware of the problems and the solutions in connection with the surface topography except for the motion blurring.

This work is funded by the German Research Foundation. We acknowledge the work of the VIRTIS/VEX team and also the entire Venus Express team of ESA and Astrium, who allowed the measurement data used in this investigation to be obtained. We acknowledge ASI and CNES supporting the VIRTIS development and the Venus Express mission as well as DLR supporting the VIRTIS hardware activities.

The authors would like to thank the reviewers for their valuable suggestions to improve this paper.

Chapter IV

MSR, a multi-spectrum retrieval technique for spatially-temporally correlated or common Venus surface and atmosphere parameters

David Kappel¹

¹German Aerospace Center (DLR), Institute of Planetary Research, Rutherfordstrasse 2, 12489 Berlin, Germany

A copyedited version of this article was published in:
Journal of Quantitative Spectroscopy and Radiative Transfer, 133:153–176, 2014.
Received 28.05.2013; received in revised form 26.07.2013; accepted 30.07.2013.
Available online 05.08.2013. [10.1016/j.jqsrt.2013.07.025](https://doi.org/10.1016/j.jqsrt.2013.07.025)

Copyright: 2013 Elsevier Ltd. All rights reserved.

Abstract

A common way to regularize mathematical ill-posed retrieval problems in atmospheric remote sensing is the incorporation of single-spectrum Bayesian *a priori* mean values and standard deviations for the parameters to be retrieved, along with measurement and simulation error information. This decreases the probability to obtain unlikely parameter values. For a reliable evaluation of measurements with sparse spectral information content, like Venus' nightside emissions in the infrared as acquired by the VIRTIS-M-IR instrument aboard ESA's Venus Express spacecraft, it can help to consider further *a priori* knowledge.

A new multi-spectrum retrieval technique (MSR) is presented that allows to incorporate expected correlation lengths and times for the retrieval parameters used to describe several spectra. It is demonstrated by examples that this decreases the probability to retrieve spatial-temporal state vector distributions that are incompatible with these *a priori* spatial-temporal correlations. Also, *a priori* correlations between the parameters used to describe a single spectrum and exhibiting similar *a priori* spatial-temporal behavior, act to rule out unlikely single-spectrum state vectors. Parameters with infinite correlation length or time and identic single-spectrum *a priori* data are spatially or temporally constant and can be retrieved as parameters that are common to a certain selection of measurements. This is shown to be especially useful to retrieve surface emissivity in the infrared as parameter that is common to several measurements that repeatedly cover the same target, and to determine deep atmospheric CO₂ opacity corrections, which are common to all Venus nightside spectra. Also this way, all considered measurements can be parameterized by a fully consistent set of atmospheric, surface, and instrumental parameters that respects all available *a priori* data as well as the measurement and simulation error distributions and that does not neglect the context between adjacent measurements. MSR is demonstrated to enhance the retrieval reliability and accuracy and pushes the VIRTIS-M-IR data evaluation to its limits.

IV.1 Introduction

The geology and composition of Venus' surface are topics of active research. There are only a few *in situ* measurements, performed by the VENERA probes (Avduevskii et al., 1983). Most areas appear to consist of basaltic material, but it is poorly classified. Knowledge of surface emissivity in the infrared can provide constraints for surface composition and weathering affected texture. Global surface emissivity maps can only be acquired by applying remote sensing techniques. A global topography, reflectivity, and emissivity data base, referred to 2.385 GHz, has been obtained by the Magellan mission (Pettengill et al., 1991). However, a detailed analysis of Venus' geology requires input from spectral ranges that are more diagnostic to surface composition, like the infrared.

Venus' surface can not be directly observed in the visible and infrared. The hot surface (735 K at 0 km altitude when assumed to be in thermodynamic equilibrium with the bottom of the atmosphere according to the Venus International Reference Atmosphere VIRA (Seiff et al., 1985; Zasova et al., 2006b)) emits altitude dependent thermal radiation, as it does the hot deep atmosphere. This radiation is absorbed and multiply scattered by the gaseous and particulate components of the atmosphere, thereby strongly affecting the signals of the surface emissions that carry information about surface temperature and emissivity. The atmosphere is opaque with the exception of a few transparency windows between 0.8 and 1.3 μm that probe down to the surface. Additional windows between 1.3 and 2.6 μm are affected by the deep atmospheric temperature field and composition (Pollack et al., 1993; Meadows and Crisp, 1996). Reflected sunlight strongly outweighs these emissions, thereby limiting the data usable for surface emissivity extraction in the infrared to nightside measurements.

ESA's planetary probe Venus Express (VEX) orbits the planet since 2006. The Mapping channel in the InfraRed of the Visible and InfraRed Thermal Imaging Spectrometer (VIRTIS-M-IR) aboard VEX acquires spectrally resolved (432 spectral bands uniformly dividing the range 1.0–5.2 μm) two-dimensional images of targets on Venus (Drossart et al., 2007; Arnold et al., 2011, 2012c). The carefully calibrated and preprocessed measurements (Cardesin-Moinelo et al., 2010; Kappel et al., 2012b) provide the data base where the surface information shall be extracted from.

Hyper-spectral data can be quantitatively evaluated by using a retrieval algorithm in conjunction with a detailed radiative transfer simulation model ('forward model'). The radiance spectrum that is detected by the space-borne measuring instrument, can be simulated by the forward model that numerically solves the radiative transfer equation. The result depends on the state parameters of atmosphere (altitude profiles of temperature and of gaseous and particulate constituents, absorption and scattering properties of the constituents), surface (elevation, temperature, emissivity), instrument (band-to-wavelength-mapping, full width at half maximum (FWHM) of the instrumental response function), and others (observational and illuminational geometry, O_2 nightglow, etc.). The parameters that shall be retrieved are compiled into the so-called 'state vector'. The retrieval algorithm compares the state-vector dependent simulation to the measurement and iteratively varies the state vector until the simulation well fits the measurement. The corresponding state vector then adequately parameterizes the measurement and is interpreted to represent the physical states of the atmosphere, surface, instrument, and others, that led to the measured spectrum. Herefore, a forward model is used, similar to that described by Haus and Arnold (2010). It is a plane-parallel, LTE¹, line-by-line code taking into account thermal emissions by surface and atmosphere, and absorption and multiple scattering by gases and clouds. Some additional noteworthy details are presented in Section IV.4.1 (p. 116).

But depending on spectral resolution and information content of the measurement and on complexity of the forward model, different state vectors can parameterize the same measurement equally well. Thus, this inversion of the radiative transfer equation is mathematically an ill-posed problem. The usual way to treat such problems is a regularization (Tikhonov, 1995), for instance by defining *a priori* probability distributions, which the state vectors are assumed to follow. A convenient distribution is a Gaussian with certain mean value vector and covariance matrix. The *a priori* mean vector is defined to be the physically expected value of the state vector and the *a priori* covariance matrix its expected covariance matrix. The utilized *a priori* data for VIRTIS-M-IR retrievals is based on former observational *in situ* results gathered during the VENERA missions (Avduevskii et al., 1983) and on the analysis of earlier ground based high-resolution data (Marcq

¹Corrected: In the published paper, the code was mistakenly stated to be a non-LTE code.

et al., 2006; de Bergh et al., 1995; Pollack et al., 1993; Meadows and Crisp, 1996) as well as on other space-borne experiments (limb observations, de Kok et al., 2011, radio science, Tellmann et al., 2009). The spectra also suffer from measurement and calibration errors on the one hand and from simulation errors on the other hand. This information can also be incorporated into the retrieval algorithm in order to arrive at a Bayesian interpretation (Rodgers, 2000) of the regularization. Here, the measurements and simulations, along with the *a priori* and error information, lead to an *a posteriori* probability distribution. The location of its maximum represents the best estimate of the state vector and has to be iteratively determined by the retrieval algorithm. The standard deviations of, and the correlations between, the retrieved parameters can be estimated through an approximation of the Hessian of this *a posteriori* probability distribution at the best estimate of the state vector. They are measures for the retrieval uncertainties and interferences. This single-spectrum regularization decreases the probability to obtain unlikely parameter values.

However, influence of noise, the presence of parameters with very similar impacts on spectra, as well as the possible existence of subsidiary solutions due to the complex non-linear dependence of radiance on the state vector may cause unexpected discontinuities in the spatial and temporal distribution of the retrieved parameters. Especially for measurements with sparse spectral information content, like the VIRTIS-M-IR measurements of Venus' nightside emissions, this may seriously degrade the reliability of retrieved single-spectrum parameters.

To overcome this problem, a multi-spectrum retrieval algorithm (MSR) is presented (Section IV.2) that allows for the utilization of additional *a priori* knowledge such as *a priori* spatial-temporal correlations. These are usually neglected but nevertheless always present, since contiguous measurements are unlikely to originate from completely unrelated state vectors. One pivotal aspect is the design of a suitable *a priori* covariance matrix (Section IV.3 (p. 107)) that is positive definite by construction and allows for the encoding of the single-spectrum parameters' *a priori* standard deviations, spatial-temporal correlations, and local correlations (for instance as required for single-spectrum temperature profile regularization). In the limit of infinite correlation lengths or times for certain parameters, this covariance matrix will degenerate. Then, a special-case treatment can be derived that corresponds to the concept of retrieving parameters common to a selection of measurements (Section IV.3.5 (p. 116)). Details of the forward model as well as retrieval parameters relevant for VIRTIS-M-IR measurements of Venus' nightside are presented in Section IV.4 (p. 116). Section IV.5 (p. 120) demonstrates by corresponding examples that MSR decreases the probability to retrieve unlikely parameter distributions, helps to avoid subsidiary solutions and to disentangle parameters with strongly differing spatial-temporal *a priori* correlations, compensates for noise effects, and allows to combine the information content of several spectra to determine hard-to-retrieve parameters that are common to a selection of measurements. A selection of mathematical details is presented in Appendix IV.A (p. 126), as well as some notes on the implementation of MSR. First results have been presented by Kappel et al. (2010a,b, 2012c,b), and the present paper develops the corresponding mathematical background.

IV.2 Multi-spectrum retrieval algorithm (MSR)

This section recites the basics of Bayesian regularization as presented by Rodgers (2000, Sections 2.3 and 5.2), but already in a generalized multi-spectrum retrieval formulation, and the involved quantities are defined. The required *a priori* covariance matrix will be constructed in Section IV.3 (p. 107).

Let $\mathbf{y}_i \in \mathbb{R}^{m_i}$, $i \in \{1, \dots, r\}$ be the column vector representing the measured spectrum number i out of r measurements. The entry number $j \in \{1, \dots, m_i\}$ of \mathbf{y}_i shall be denoted as $(\mathbf{y}_i)_j$ and is the radiance acquired by measurement i at a certain wavelength or wavenumber. The dimensions m_i of the \mathbf{y}_i may differ, to allow for the utilization of spectra from different data sources at varying spectral resolution and different spectral intervals. This also allows for the proper treatment of *NaN* ('Not a Number') values at certain wavelengths by simply ignoring these data points. Then let the 'extended measurement vector' \mathbf{Y} be the concatenation $\mathbf{Y} = (\mathbf{y}_1^T, \dots, \mathbf{y}_r^T)^T \in \mathbb{R}^M$, forming an element of the 'extended measurement space' of dimension $M = \sum_{i=1}^r m_i$, which is the direct sum of single-spectrum measurement spaces. For notational convenience, column vectors like $(\mathbf{y}_1^T, \dots, \mathbf{y}_r^T)^T$ will be abbreviated as $(\mathbf{y}_1, \dots, \mathbf{y}_r)$ in the following.

\mathbf{X} shall denote the 'extended state vector' used to compute the 'extended simulation outcome vector' $\mathbf{F}(\mathbf{X})$. The iterative algorithm has to fit $\mathbf{F}(\mathbf{X})$ to \mathbf{Y} by varying \mathbf{X} . \mathbf{X} is the concatenation of r single-spectrum state

vectors $(\mathbf{x}_1, \dots, \mathbf{x}_r)$. In anticipation of Section IV.3.5 (p. 116) that introduces the concept of the retrieval of a parameter vector $\mathbf{x}_C \in \mathbb{R}^c$ common to r spectra, the extended state vector may also assume the form $\mathbf{X} = (\mathbf{x}_C, \mathbf{x}_1, \dots, \mathbf{x}_r) \in \mathbb{R}^N$. All single-spectrum state vectors \mathbf{x}_i are assumed to have the same dimension, $\mathbf{x}_i \in \mathbb{R}^n$, and thus $N = c + rn$, but generalization is straightforward. When the m_i -dependent single-spectrum simulation outcome for spectrum i is denoted as the column vector $\mathbf{f}_i \in \mathbb{R}^{m_i}$, then $\mathbf{F}(\mathbf{X}) \in \mathbb{R}^M$ can be written as $(\mathbf{f}_1(\mathbf{x}_C, \mathbf{x}_1), \dots, \mathbf{f}_r(\mathbf{x}_C, \mathbf{x}_r))$. In the following, for convenience, the adjective 'extended' will not be explicitly written anymore, except when it is not clear from context, whether a single-spectrum or a multi-spectrum object is referred to.

Similar to Rodgers (2000), it may be assumed that the measurement, calibration, and simulation error distribution can be characterized by a Gaussian distribution in the residual $\mathbf{Y} - \mathbf{F}(\mathbf{X})$ between measurement \mathbf{Y} and simulation $\mathbf{F}(\mathbf{X})$ of the measurement given the state vector \mathbf{X} . The corresponding error covariance matrix \mathbf{S}_E is of dimension $M \times M$. A Gaussian distribution is usually a good approximation for real world errors (central limit theorem) and simple enough to derive useful formulas. Also, the probability distribution function with the least information content (meaning without implying further knowledge) that is consistent with the parameterization by a mean value vector and a covariance matrix, is the corresponding Gaussian (Rodgers, 2000). Then the conditional probability distribution function for measurement \mathbf{Y} , provided that the state vector is \mathbf{X} , is given by

$$P_m(\mathbf{Y}|\mathbf{X}) = \frac{1}{N_1} \exp\left(-\frac{1}{2}(\mathbf{Y} - \mathbf{F}(\mathbf{X}))^T \mathbf{S}_E^{-1}(\mathbf{Y} - \mathbf{F}(\mathbf{X}))\right),$$

with normalization factor N_1 . Due to the only limited knowledge on measurement errors and their relations across several measurements, \mathbf{S}_E is assumed to be of block diagonal shape, such that the errors of different measurements are treated as independent. The individual blocks on the diagonal will be denoted as \mathbf{S}_{ϵ_i} for the corresponding spectrum number i . Also, the \mathbf{S}_{ϵ_i} are all assumed to be diagonal, such that the errors at different wavelengths are treated as independent of each other. The values on the diagonal are the variances of the errors (squares of the standard deviations) and shall be independent of \mathbf{X} . However, the \mathbf{S}_{ϵ_i} may depend on i and the wavelengths of the corresponding measurements y_i . For VIRTIS measurements, twice the spectrally resolved standard deviation of deep space observations is thereby a first estimation of the random error. Further errors may also enter the error covariance matrix, like those due to data calibration and preprocessing (Kappel et al., 2012b) as well as simulation.

The *a priori* probability distribution function the state vector \mathbf{X} is assumed to follow, i.e. the probability density of \mathbf{X} before knowledge of the outcome of the measurement, is analogously written as

$$P_P(\mathbf{X}) = \frac{1}{N_2} \exp\left(-\frac{1}{2}(\mathbf{X} - \mathbf{A})^T \mathbf{S}_A^{-1}(\mathbf{X} - \mathbf{A})\right).$$

N_2 is the normalization factor and \mathbf{S}_A the extended *a priori* covariance matrix of dimension $N \times N$. If \mathbf{S}_A is assumed to be a diagonal matrix, neither coupling between entries corresponding to the same single-spectrum state vector, nor between different single-spectrum state vectors, nor between common parameters is expected. In this case, the diagonal entries denote the individual *a priori* variances of the retrieval parameters. The better the knowledge of a certain parameter is, the smaller should the corresponding variance be set. For a detailed discussion of non-trivial *a priori* covariance matrices, see Section IV.3. $\mathbf{A} = (\mathbf{a}_C, \mathbf{a}_1, \dots, \mathbf{a}_r) \in \mathbb{R}^N$ is the extended *a priori* mean value vector of the extended state vector $\mathbf{X} \in \mathbb{R}^N$. The *a priori* data is not very well known for retrieval problems related to Venus. For all practical purposes concerning the VIRTIS measurements, it is therefore not possible to set *a priori* data dependent on the measurement situation. Thus, \mathbf{S}_A will not depend on \mathbf{X} , nor will \mathbf{A} , and $\mathbf{a}_i \in \mathbb{R}^n$ will not depend on i and will simply be denoted by \mathbf{a} .

Let P_M denote the probability distribution function of the extended measurement before it is made. It is not dependent on \mathbf{X} , but on \mathbf{Y} only.

The *a posteriori* probability distribution function of \mathbf{X} is the conditional probability distribution function $P_p(\mathbf{X}|\mathbf{Y})$ of the extended state vector \mathbf{X} , provided that the extended measurement vector is found to be \mathbf{Y} .

It follows from Bayes' theorem (Rodgers, 2000) that $P_p(\mathbf{X}|\mathbf{Y}) = P_m(\mathbf{Y}|\mathbf{X})P_P(\mathbf{X})/P_M(\mathbf{Y})$. With the abbreviation $F_c(\mathbf{X}) := -2 \log P_p(\mathbf{X}|\mathbf{Y}) - 2 \log N_3$, the term $F_c(\mathbf{X})$ reads

$$(\mathbf{X} - \mathbf{A})^T \mathbf{S}_A^{-1} (\mathbf{X} - \mathbf{A}) + (\mathbf{Y} - \mathbf{F}(\mathbf{X}))^T \mathbf{S}_E^{-1} (\mathbf{Y} - \mathbf{F}(\mathbf{X})), \quad (\text{IV.1})$$

where the normalization terms and \mathbf{X} -independent terms are all absorbed into N_3 and are unimportant for the retrieval.

Note that both \mathbf{S}_E and \mathbf{S}_A as covariance matrices have to be real, symmetric, and positive semi-definite. They even have to be positive definite to allow for the proper definition of the various probability distribution functions. Also note that $0 \leq F_c(\mathbf{X}) \in \mathbb{R}$, since \mathbf{S}_E^{-1} and \mathbf{S}_A^{-1} are consequently also positive definite.

The information on \mathbf{X} is improved from $P_P(\mathbf{X})$ before measurement to $P_p(\mathbf{X}|\mathbf{Y})$ after measurement. Knowledge of $P_p(\mathbf{X}|\mathbf{Y})$ corresponds to the solution of the retrieval problem. It is useful to approximate $P_p(\mathbf{X}|\mathbf{Y})$ as function of \mathbf{X} by a function parameterizable by a few characteristic parameters. Again, this suggests a Gaussian, the least-information-content function with mean value vector and covariance matrix, now to be derived from $P_p(\mathbf{X}|\mathbf{Y})$.

The mean value vector is approximated by the location of the (global) maximum $\hat{\mathbf{X}}$ of $P_p(\mathbf{X}|\mathbf{Y})$. \mathbf{F} can be assumed to be a continuously differentiable function of \mathbf{X} , provided that the basic input of the radiative transfer equation solver (altitude profiles of optical depth, single scattering albedo, Legendre moments of the scattering phase function, and temperature; some boundary conditions) depends differentially on the retrieval parameters (Spurr, 2008). Also, \mathbf{F} should be bounded for finite arguments to be physically reasonable. Thus, a necessary condition for $\hat{\mathbf{X}}$ to be the location of a local maximum of $P_p(\mathbf{X}|\mathbf{Y})$ is its zeroing of the derivative of $P_p(\mathbf{X}|\mathbf{Y})$, or equivalently of F_c , with respect to \mathbf{X} . Since a local maximum of $P_p(\mathbf{X}|\mathbf{Y})$ corresponds to a local minimum of F_c , F_c is called the cost function of the retrieval problem, the function to be minimized. It must be kept in mind that due to the possibly complex nature of \mathbf{F} as non-linear function on a high-dimensional state space, there may be more than one local maximum of $P_p(\mathbf{X}|\mathbf{Y})$, but the global maximum is the best estimate of the state vector. In $P_p(\mathbf{X}|\mathbf{Y})$, Gaussian damping by the *a priori* information $P_P(\mathbf{X})$ mathematically somewhat improves the identification of the best estimate. If the *a priori* covariances are small enough, this leads to the elimination of subsidiary solutions, at least in the extreme case where the standard deviations tend to 0. In this case, the solution is forced to attain the vector of the *a priori* mean values. But in practice, it must be kept in mind that a determined local maximum could be just a subsidiary maximum. In absence of a fast and reliable global minimizer, the retrieval algorithm will determine local minima of $F_c(\mathbf{X})$, see Appendix IV.A.1 (p. 126), and as a rough test, it should be checked whether different initial guesses and *a priori* data lead to the same or a similar solution.

An expression for the width of $P_p(\mathbf{X}|\mathbf{Y})$ can be obtained by using the quadratic term in the Taylor expansion of F_c at $\hat{\mathbf{X}}$. By neglecting the derivative of the Jacobian in comparison to the other terms, one arrives at

$$\hat{\mathbf{S}}^{-1} = \mathbf{S}_A^{-1} + \mathbf{K}(\hat{\mathbf{X}})^T \mathbf{S}_E^{-1} \mathbf{K}(\hat{\mathbf{X}}) \quad (\text{IV.2})$$

of dimension $N \times N$, where $\nabla \mathbf{F}(\mathbf{X}) =: \mathbf{K}(\mathbf{X})$ is the Jacobian of dimension $M \times N$ of the forward model at \mathbf{X} . $\hat{\mathbf{S}}$ will be interpreted as the covariance matrix of the *a posteriori* probability distribution function of the state vector \mathbf{X} at the retrieved solution $\hat{\mathbf{X}}$ (Rodgers, 2000). The diagonal entries provide a measure of the uncertainty of the retrieved parameters, and the off-diagonal entries bear information on the interdependence of the parameters. However, it is still necessary to perform a detailed retrieval error characterization (Kappel et al., 2012a), as will be presented in a subsequent paper.

Appendix IV.A (p. 126) discusses some details of the implementation of MSR.

IV.3 *A priori covariance matrix*

In this section, an *a priori* covariance matrix \mathbf{S}_A is constructed that is suitable for use in MSR.

First, the retrieval of common parameters shall not be considered. Let there be n single-spectrum retrieval parameters $(\mathbf{x}_i)_k$ for each of the r measurements ($i \in \{1, \dots, r\}$ and $k \in \{1, \dots, n\}$).

Let the number i of the spectrum be fixed. Then for the measured spectrum \mathbf{y}_i , \mathbf{S}_A shall encode (diagonal entries) the *a priori* variance of the corresponding single-spectrum state vector \mathbf{x}_i that parameterizes the corresponding forward model simulation $\mathbf{f}_i(\mathbf{x}_i)$. Also, \mathbf{S}_A shall encode expected correlations between the n entries $(\mathbf{x}_i)_k$ of single-spectrum state vector \mathbf{x}_i (*a priori* 'local correlations'). Such correlations can be accomplished by a non-diagonal covariance matrix for the single-spectrum retrieval problem.

Now let k be fixed and i vary. Then \mathbf{S}_A shall encode expected correlations between the r parameters $(\mathbf{x}_i)_k$. These will be called *a priori* 'spatial-temporal correlations', as they describe the correlation behavior of the entries number k of the single-spectrum state vectors in space and time. These exist due to a certain continuity of the physical state of the atmosphere, caused by the inertia of matter and the drive to compensate thermodynamic disequilibria.

Finally, \mathbf{S}_A shall allow to treat parameters with infinite spatial or temporal *a priori* correlation. As will be seen (Appendix IV.A.3 (p. 129)), such parameters are spatially or temporally constant, i.e. they are common to certain sets of spectra.

\mathbf{S}_A shall be constructed as an easily parameterizable covariance matrix that can transparently encode both *a priori* local and spatial-temporal correlations as special cases. Also, it shall encode the standard deviations of all parameters of all single-spectrum state vectors, and shall allow to retrieve common parameters. It must be positive definite and ideally so already by construction. In the following, the terms '*a priori* correlation' and 'coupling' will be used synonymously.

Section IV.3.1 reduces the construction of the covariance matrix \mathbf{S}_A to the construction of a correlation matrix \mathbf{C}_A . Also, for multi-spectrum problems without common parameters, the general structure of \mathbf{C}_A is presented. As a first step in the construction of such a \mathbf{C}_A , the single-parameter problem for several spectra with arbitrary spatial-temporal data point distribution is discussed in Section IV.3.2. Next, single-spectrum correlation matrices for several parameters are discussed in Section IV.3.3 (p. 113). Then, for given single-parameter spatial-temporal correlation data and local single-spectrum correlation data, the Kronecker product is the key to construct correlation matrices for several parameters and several spectra in Section IV.3.4 (p. 113). The treatment of common parameters is discussed in Section IV.3.5 (p. 116).

IV.3.1 *A priori* correlation matrix

A finite dimensional covariance matrix is a matrix containing the covariances between finitely many random variables. It is therefore real, symmetric, and positive semi-definite. Conversely, each finite dimensional, real, symmetric, positive semi-definite matrix is a covariance matrix (Anderson, 1958, Theorem 2.3.1).

A positive semi-definite matrix has exclusively non-negative eigenvalues. But for a covariance matrix, a zero eigenvalue corresponds to a parameter which is exactly known (zero uncertainty) or perfectly coupled to a linear combination of other parameters. Such a parameter does not need to be retrieved or must be treated in a different way (Appendix IV.A.3 (p. 129)), respectively. Therefore, only real, symmetric, positive definite matrices (positive eigenvalues) will be considered in the following. This also ensures the existence of the inverse, which is needed in Section IV.2 (p. 105).

To make the construction of a *covariance* matrix \mathbf{S}_A more transparent, a normalized form is defined, the *correlation* matrix \mathbf{C}_A with entries

$$(\mathbf{C}_A)_{ij} := \frac{(\mathbf{S}_A)_{ij}}{\sigma_i \sigma_j}, \quad \text{or} \quad \mathbf{C}_A = \mathbf{B}^T \mathbf{S}_A \mathbf{B}, \quad (\text{IV.3})$$

and with the *a priori* standard deviations $\sigma_i := \sqrt{(\mathbf{S}_A)_{ii}}$ and the diagonal matrix \mathbf{B} that has the entries $B_{ii} = 1/\sigma_i$. \mathbf{C}_A is well defined, since the diagonal entries of a positive definite matrix are positive. All entries of \mathbf{C}_A must be in the (closed) real interval $[-1, 1]$ (a consequence of Cauchy-Schwarz inequality (Horn and Johnson, 1990, p. 0.6.3) when applied to vectors $\mathbf{v}_i := \sqrt{\mathbf{S}_A} \mathbf{e}_i$. Here, $\sqrt{\mathbf{S}_A}$ is defined by spectral decomposition (Horn and Johnson, 1990, p. 4.1.5), and \mathbf{e}_i is the i -th standard vector). According to Eq. (IV.3), each diagonal entry equals 1 (each parameter is perfectly correlated to itself), \mathbf{C}_A is symmetric, and it is positive definite since \mathbf{B} is (Horn and Johnson, 1990, p. 7.1.6).

For an easy construction and parameterization of \mathbf{S}_A , first \mathbf{C}_A will be constructed, and then \mathbf{S}_A is obtained by scaling \mathbf{C}_A with the *a priori* standard deviations σ_i according to Eq. (IV.3). For ease of use, not the variances σ_i^2 , but 2 times the standard deviations ($2\sigma_i$) are used as the input variables in the computer implementation, encoding the typical lengths of the expected variation intervals of the parameters.

Not considering the retrieval of common parameters (Section IV.3.5 (p. 116)), in the notation of Section IV.2 (p. 105), the structure of the nr -dimensional extended parameter vector \mathbf{X} (with $c = 0$) implies the structure of \mathbf{S}_A . The correlation matrix \mathbf{C}_A inherits the same structure. As \mathbf{X} consists of r sub-vectors of length n , \mathbf{C}_A has to be a symmetric $nr \times nr$ matrix composed of $r \times r$ blocks of size $n \times n$. For $i, j \in \{1, \dots, r\}$ and $k, l \in \{1, \dots, n\}$, $(\mathbf{b}_{ij})_{kl}$, the entry (k, l) of block (i, j) , encodes the *a priori* correlation between parameter k corresponding to measurement i and parameter l corresponding to measurement j . It should not be different from the coupling between the l -th parameter of measurement i and the k -th parameter of measurement j , because neither of the measurements i or j shall be distinguished from the other, i.e. $(\mathbf{b}_{ij})^T = \mathbf{b}_{ij} = (\mathbf{b}_{ji})^T$, where the latter equality follows from symmetry of \mathbf{C}_A . In particular, the blocks \mathbf{b}_{ii} on the diagonal of \mathbf{C}_A are symmetric, and they are positive definite and all identically, as they are the couplings between the parameters of the same measurement and no measurement shall be distinguished from the other. This single-spectrum correlation matrix $\mathbf{b}_{ii} =: \mathbf{h}$ will be constructed in Section IV.3.3 (p. 113).

IV.3.2 Single-parameter problem for several spectra

As a first step in constructing \mathbf{C}_A , a correlated retrieval problem for several measurements with arbitrary distribution of distinct footprints in space and time is considered, where each of the spectra is described by only one single parameter. This could be a total cloud column factor, for instance. Therefore, all blocks \mathbf{b}_{ij} (Section IV.3.1) of \mathbf{C}_A are just real numbers, with $\mathbf{b}_{ij} =: (g_{ij}) \in \mathbb{R}^1$ and all $g_{ii} := 1$. Assume that correlation between any two measurements only depends on distance between their footprints. Here, distance is initially defined by an abstract metric $d(\cdot, \cdot)$ and will be specified later. It could be Euclidean distance in \mathbb{R}^2 (planetary surface treated as plane), \mathbb{R}^3 (as surface in \mathbb{R}^3), or \mathbb{R}^4 (including temporal separation). The 'distance matrix'² $\mathbf{d} \in \mathbb{R}^{r \times r}$ with entries $d_{ij} := d(\mathbf{x}_i, \mathbf{x}_j)$ is defined as the matrix of distances between the measurement footprints at locations \mathbf{x}_i , $i \in \{1, \dots, r\}$ of r measurements.

For an easy and transparent parameterization and interpretation of \mathbf{C}_A for the single-parameter problem, only correlation length and correlation time shall determine the strengths of the *a priori* correlations for a fixed footprint distribution. A long correlation length $\lambda \gg \pi R_{\text{Venus}}$, with the maximum spatial distance πR_{Venus} for footprints on Venus and Venus radius R_{Venus} , corresponds to a strong coupling close to 1, and similar with correlation time τ and reference time scale of four Earth days (time scale of atmospheric super-rotation). The correlation matrix for the case where any coupling is absent is defined as $\mathbf{C}_A := \mathbb{1}$, which should also be the limit of \mathbf{C}_A for $\lambda \downarrow 0$ and $\tau \downarrow 0$.

In the following, it will be discussed, how a proper correlation matrix \mathbf{C}_A can be yielded from \mathbf{d} . The difficulty lies in the requirement that for *arbitrary* distinct footprints, \mathbf{C}_A will turn out positive definite by construction. The occurrence of some measurements with coinciding footprint space-time coordinates is not treated here. That case is only possible by using more than one measuring instrument.

IV.3.2.1 Positive definite functions

Before a proper treatment of general spatial-temporal separations between measurement footprints will be established in Section IV.3.2.3 (p. 112), only spatial separations are considered for now.

The key to yield \mathbf{C}_A from \mathbf{d} , is the concept of positive definite functions, see [Schoenberg and De Boor \(1988\)](#) for a collection of a series of the original papers from 1938, and [Baxter \(2003\)](#) for the notation and definitions adopted for this work.

²Corrected: In the published paper, this was mistakenly written as $\mathbf{d} \in \mathbb{R}^r$.

Let \mathcal{H} be a real (possibly infinite dimensional) separable Hilbert space with norm $\|\cdot\|_2$ and $f : \mathbb{R}_+ \rightarrow \mathbb{R}$ be a function for which the quadratic form

$$\sum_{i=1}^r \sum_{j=1}^r a_i a_j f(\|\mathbf{x}_i - \mathbf{x}_j\|_2^2) \quad (\text{IV.4})$$

is non-negative for any $r \in \mathbb{N}^*$, any real $\mathbf{a} = (a_1, \dots, a_r)^T \in \mathbb{R}^r$, and any points $\mathbf{x}_1, \dots, \mathbf{x}_r \in \mathcal{H}$, then f is called *positive definite on \mathcal{H}* . f is positive definite on \mathcal{H} , if and only if f is *completely monotonic* (Schoenberg and De Boor, 1988), i.e. f is continuous in 0 and

$$(-1)^k f^{(k)}(x) \geq 0, \quad \forall k \in \mathbb{N} \cup \{0\}, \text{ and for } 0 < x < \infty. \quad (\text{IV.5})$$

This can be applied to $\mathcal{H} = \mathbb{R}^n$ with Euclidean norm $\|\cdot\|_2$, to see that for $\mathbf{x}_1, \dots, \mathbf{x}_r \in \mathcal{H}$ and for $d(\mathbf{x}_i, \mathbf{x}_j) := \|\mathbf{x}_i - \mathbf{x}_j\|_2 = d_{ij}$, the real symmetric $r \times r$ matrix \mathbf{C}_A with entries $(\mathbf{C}_A)_{ij} := f((d_{ij})^2)$ is positive semi-definite, and it is even positive definite for non-constant f (note that then $f(0) > 0$) and distinct points in Euclidean \mathbb{R}^n (Baxter, 2003). Hence, \mathbf{C}_A is a valid correlation matrix, when f is non-constant and normalized such that $f(0) = 1$.

According to Miller and Samko (2001, Eq. 1.13), the function defined by $f(x) := \exp(-\sqrt{x})$ is completely monotonic. Measuring physical distances d_p in terms of a characteristic length scale λ to get rid of physical units, i.e. $x := d_p/\lambda$, it follows that for arbitrary distinct points in Euclidean \mathbb{R}^n , the matrix with entries $\exp(-d_{ij}/\lambda)$ is a correlation matrix.

However, this is not the most suited choice. Define the 'correlation function' $f_d(x) := f(x^2)$. It takes the (normalized) distances as arguments and reads for this choice $f_d^1(x) := \exp(-x) = \exp(-d_p/\lambda)$ with the physical distance d_p . Its non-zero derivative at $x = 0$ means that observations that are only slightly separated, are modeled to perceive fast changing correlations for varying distances. $f_d^1(x)$ is associated with a first order Gauss-Markov-process, a 'memory-less' system describing an atmosphere where only *location* is of importance (Daley, 1991, Section 4.3) and (Balgovind et al., 1983). For many physical processes, it is more realistic to consider systems which respect certain inertial properties. This includes atmospheric physics with its inert atmospheric molecules and the fast balancing of thermodynamic disequilibria. These systems are more suitably modeled by a second order Gauss-Markov-process where *location* and *momentum* are considered (Gelb, 1974, pp. 44–45, and example 3.9-1). Balgovind et al. (1983) derive³ $f_d^2(x) := (1+x)\exp(-x)$, which has a derivative of 0 at $x = 0$, i.e. observations that are only slightly separated, are modeled to perceive slowly changing correlations. f_d^2 is also given by other investigations on Earth's atmosphere (Daley, 1991; Gelb, 1974; Gaspari and Cohn, 1999). Note that the derivative of $f_d^2(\sqrt{x})$ is $-\exp(-\sqrt{x})/2$. Since $\exp(-\sqrt{x})$ has already been established as completely monotonic, $f_d^2(\sqrt{x})$ satisfies Eq. (IV.5) and is therefore positive definite.

But widely separated measurements have non-vanishing correlations for both f_d^1 and f_d^2 . This is on the one hand not realistic, see discussion by Gaspari and Cohn (1999, Section 4.d) and references therein on forecast error correlations for Earth's troposphere. On the other hand, the largest structure in MSR, the Jacobian (Eq. (IV.A.2) (p. 126)), would have many small non-zero entries which are unimportant for the retrieval. To not waste computational resources, the Jacobian should possess many zero entries (see sparse matrix formulation in Appendix IV.A.4 (p. 133)), and the correlation function should thus have compact support, i.e. it should be zero outside of a compact (closed and bounded in Euclidean space) set. Even for the very well probed terrestrial atmosphere, the empirically substantiated correlation is quite ambiguous and there is no unique 'best' model (Daley, 1991, Fig. 4.5), and Venus correlations are much less known. Thus for simplicity it seems best, to choose a single appropriate correlation function that is compatible with the considerations above and will be utilized with suitable scaling for different retrieval parameters, and to test robustness against reasonable *a priori* data variations.

Therefore, a third class of correlation functions with compact support, vanishing derivative at $x = 0$, and satisfying Eq. (IV.4) is used. Gaspari and Cohn (1999) construct such a function as self-convolution $c := g * g$ of a continuous real function g with compact support. Herefore, observe that $\mu := \mathcal{F}[c] =$

³Note: This is not to be read as the square of f_d , but as the second example of a correlation function.

$(2\pi)^{n/2} \mathcal{F}[g] \cdot \mathcal{F}[g] \geq 0$, where $*$ denotes convolution, \mathcal{F} the Fourier transform in n dimensions such that $\mathcal{F}[g](\mathbf{k}) := \int g(\mathbf{x}) \exp(-i\langle \mathbf{k}, \mathbf{x} \rangle) d\mathbf{x}$, $d\mathbf{x} = d\mathbf{x}^n / (2\pi)^{n/2}$, $\langle \cdot, \cdot \rangle$ the Euclidean standard scalar product, and μ the Fourier transform of a correlation function c with $c(\mathbf{x}_i - \mathbf{x}_j) := f(\|\mathbf{x}_i - \mathbf{x}_j\|_2^2)$ as in Eq. (IV.4). Then for any vector $\mathbf{a} = (a_1, \dots, a_r)^T \in \mathbb{R}^r$, the quadratic form

$$\begin{aligned} \sum_{i,j=1}^r a_i a_j c(\mathbf{x}_i - \mathbf{x}_j) &= \sum_{i,j=1}^r a_i a_j \mathcal{F}^{-1}[\mu](\mathbf{x}_i - \mathbf{x}_j) = \sum_{i,j=1}^r a_i a_j \int \mu(\mathbf{k}) \exp(i\langle \mathbf{k}, \mathbf{x}_i - \mathbf{x}_j \rangle) d\mathbf{k} \\ &= \int \left| \sum_{i=1}^r a_i \exp(i\langle \mathbf{k}, \mathbf{x}_i \rangle) \right|^2 \mu(\mathbf{k}) d\mathbf{k} \geq 0 \end{aligned}$$

will be non-negative. Hence, the matrix with entries $c(\mathbf{x}_i - \mathbf{x}_j)$ will be positive semi-definite. See [Reed and Simon \(1975, Chapters IX.1 and IX.2\)](#) and [Gaspari and Cohn \(1999, Theorems 2.10 and 3.a.3\)](#) for a more complete discussion.

[Gaspari and Cohn \(1999\)](#) use the real function $g(\mathbf{z}) := (1 - |\mathbf{z}|/\nu)I_\nu(|\mathbf{z}|)$ on $\mathbb{R}^3 \ni \mathbf{z}$, where

$$I_\nu(|\mathbf{z}|) = \begin{cases} 1 & |\mathbf{z}| \leq \nu \\ 0 & |\mathbf{z}| > \nu \end{cases}.$$

The radial dependence of the resulting homogeneous and isotropic correlation function on \mathbb{R}^3 is a fifth-order piecewise rational function f_d^3 ([Gaspari and Cohn, 1999, Eq. 4.10](#))

$$f_d^3(x) = \begin{cases} -\frac{x^5}{4} + \frac{x^4}{2} + \frac{5x^3}{8} - \frac{5x^2}{3} + 1 & 0 \leq x < 1 \\ \frac{x^5}{12} - \frac{x^4}{2} + \frac{5x^3}{8} + \frac{5x^2}{3} - 5x + 4 - \frac{2}{3x} & 1 \leq x < 2 \\ 0 & x \geq 2 \end{cases} \quad (\text{IV.6})$$

with $x = |\mathbf{z}|/\nu = d_p/\nu$. f_d^3 is continuous and twice continuously differentiable on \mathbb{R} . It is a proper correlation function by construction ([Gaspari and Cohn, 1999](#)). Thus, the non-constant $f_d^3(\sqrt{y})$ is completely monotonic as function of y , and f_d^3 is therefore a valid correlation function in any dimension. f_d^3 has derivative 0 at $x = 0$ and is explicitly of compact support since it is set to 0 for $d_p \geq 2\nu$.

The correlation length λ is defined as the physical distance where the correlation function attains the value e^{-1} . For f_d^3 this is the case at $d_p = \lambda = n_3\nu$ with the normalization factor $n_3 \approx 0.808768$. For comparison, $n_1 = 1$ for f_d^1 , and $n_2 \approx 2.14691$ for f_d^2 , such that $f_d^i(n_i d_p/\lambda) = e^{-1}$ at $d_p = \lambda$. Fig. IV.1 compares f_d^3 and f_d^2 with f_d^1 . Note that f_d^3 vanishes for $d_p \geq 2\lambda/n_3 \approx 2.47\lambda$. Also note its zero derivative at $d_p = 0$ and its stronger relative weighting of the correlation of nearby measurements ($d_p < \lambda$) which better represents the inertial properties of the physical system.

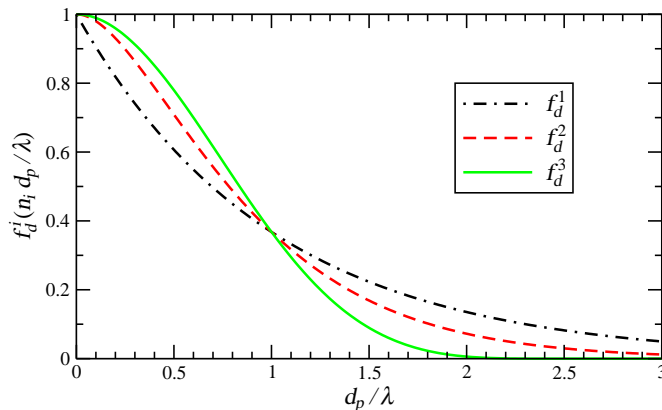


FIGURE IV.1: Comparison of the correlation functions f_d^1 , f_d^2 , and f_d^3 .

IV.3.2.2 Spherical planetary surface

The measurement footprints can be approximated to be located on a spherical surface $S^2 \subset \mathbb{R}^3$ (planetary surface or top of cloud deck). A positive definite function on S^2 can be induced by restricting a positive definite function on \mathbb{R}^3 to S^2 . Therefore substitute the physical distance d_p , measured in \mathbb{R}^3 , of points on the spherical surface, by the chordal distance $d_p = 2R \sin \frac{\vartheta}{2}$ (Gaspari and Cohn, 1999, Section 2.3). For a sphere with fixed radius R , this distance depends only on the geodetic angle of separation $\vartheta \in [0, \pi]$ between the two points on the sphere, and the induced correlation function is invariant under isotropic transformations of S^2 (Gaspari and Cohn, 1999, Section 2.2). ϑ follows directly from the Euclidean standard scalar product between any two considered vectors \mathbf{v}_i and \mathbf{v}_j on the unit sphere: $\cos \vartheta_{ij} = \langle \mathbf{v}_i, \mathbf{v}_j \rangle$. In terms of geographic longitude ϕ and latitude ψ , such a vector reads $\mathbf{v}_j = (\cos \phi_j \cos \psi_j, \sin \phi_j \cos \psi_j, \sin \psi_j)^T$. For a set of r distinct points on the sphere, f_d^3 then leads to the wanted positive definite $r \times r$ a priori correlation matrix with entries $(\mathbf{C}_A)_{ij} = f_d^3(n_3 \frac{2R}{\lambda} \sin \frac{\vartheta_{ij}}{2})$. \mathbf{C}_A is symmetric and its diagonal entries are manifestly 1, and thus only the $r(r-1)/2$ entries below the diagonal have to be computed.

IV.3.2.3 Spatial-temporal and other separations

By measuring temporal separation $d_{t,ij}$ between measurements i and j in terms of a correlation time τ , points on the planetary surface (or cloud top) with arbitrary distinct space-time footprints ('observation movies') and with Euclidean distance measured on the space $\mathbb{R}_s^3 \times \mathbb{R}_t^1 \cong \mathbb{R}^4$ comprising the three-dimensional spatial space \mathbb{R}_s^3 and the temporal space \mathbb{R}_t^1 , lead to the correlation matrix with entries

$$(\mathbf{C}_A)_{ij} = f_d^3 \left(n_3 \sqrt{\left(\frac{2R}{\lambda} \sin \frac{\vartheta_{ij}}{2} \right)^2 + \left(\frac{d_{t,ij}}{\tau} \right)^2} \right). \quad (\text{IV.7})$$

This includes as special cases the purely spatial ($d_t = 0$) version discussed in Section IV.3.2.2 as well as measurements that were acquired at the same spatial coordinates but at different times, like in time series observations of a certain surface spot ('target tracking mode', $d_p = 0$). \mathbf{C}_A is positive definite, because f_d^3 is a correlation function on any Euclidean \mathbb{R}^n , and it is associated to a second order Gauss-Markov-process, reflecting the inertial properties of the system. Measurements with a wide (compared to λ and τ) spatial-temporal separation are not correlated. A hyper-surface of constant positive correlation is an ellipsoid ($|\Delta \mathbf{x}/\lambda|^2 + |\Delta t/\tau|^2 = K^2$).

However, current knowledge is not sufficient to single out the best approximation to reality. It is also conceivable to define the space-time distance as $|d_p/\lambda| + |d_t/\tau|$ or similar. But then the argument with the Euclidean structure does not carry over, and so Eq. (IV.7) will be adopted.

There are also parameters that experience inter-measurement a priori correlations, but not with respect to the measurement target coordinates (Section IV.4 (p. 116)). These include detector related parameters like full width at half maximum (FWHM) of the instrumental response function of VIRTIS-M-IR which are related to the location on the detector and to time. Small changes in these coordinates are unlikely to yield abrupt changes in the parameters, and the a priori correlations can be defined by

$$(\mathbf{C}_A)_{ij} = f_d^3 \left(n_3 \sqrt{\left(\frac{|s_i - s_j|}{\sigma} \right)^2 + \left(\frac{d_{t,ij}}{\tau} \right)^2} \right), \quad (\text{IV.8})$$

where s_i is the sample coordinate on the detector associated with the measurement i . σ is the correlation strength in sample direction.

Finally, there are parameters that will be treated as temporally constant, like local surface emissivity when it is retrieved as parameter common to measurements covering the same surface spot, or the deep atmosphere temperature profile as parameter common to measurements associated to a fixed latitude. In these cases, the purely spatial correlation matrix discussed in Section IV.3.2.2 is used, corresponding to Eq. (IV.7) with $\tau = \infty$ (compare Appendix IV.A.3 (p. 129)).

For easier use, all correlation types discussed in this section will be referred to as spatial-temporal correlations, in contrast to local correlations.

IV.3.3 Single-spectrum problem for several parameters

As the next step in constructing \mathbf{C}_A , this section discusses, how valid single-spectrum *a priori* correlation matrices \mathbf{h} with entries h_{ij} (Section IV.3.1 (p. 108)) for several parameters can be constructed.

h_{ij} encodes the strength of the coupling between single-spectrum parameters x_i and x_j . Let c_i ($|c_i| < 1$) denote the 'nearest neighbor coupling' between the 'neighboring' parameters x_i and x_{i+1} . $c_i = 0$ translates to vanishing correlation and $c_i < 0$ to anti-correlation. Define coupling between parameters x_i and x_{i+2} as a function of the nearest neighbor couplings c_i and c_{i+1} . The modulus of 'next-to-nearest neighbor coupling' shall be smaller than either of the nearest neighbor couplings moduli. If one of the nearest neighbor couplings is zero, the next-to-nearest neighbor coupling shall be zero. If one of the nearest neighbor couplings is positive while the other is negative, then the next-to-nearest neighbor coupling shall be negative. The simplest way to implement these requirements is, to define the next-to-nearest neighbor coupling as the product of the nearest neighbor couplings. Analogously, this can be done with the coupling to the third neighbors, and so on. Therefore \mathbf{h} shall be defined as

$$\mathbf{h} = \begin{pmatrix} 1 & c_1 & \cdots & c_1 c_2 \cdots c_{n-1} \\ c_1 & 1 & \cdots & c_2 \cdots c_{n-1} \\ \vdots & \vdots & \ddots & \vdots \\ c_1 c_2 \cdots c_{n-1} & c_2 \cdots c_{n-1} & \cdots & 1 \end{pmatrix}, \quad (\text{IV.9})$$

an easy-to-implement matrix, which is parameterized by just the $n - 1$ nearest neighbor couplings of n parameters.

To show that \mathbf{h} is a valid correlation matrix, recall that any $n \times n$ matrix $\tilde{\mathbf{h}}$ with entries $\tilde{h}_{ij} := |h_{ij}| := \exp(-\|\mathbf{x}_i - \mathbf{x}_j\|_2/\lambda)$ is a correlation matrix for distinct vectors \mathbf{x}_i and $\mathbf{x}_j \in \mathbb{R}^m$ and $0 < \lambda \in \mathbb{R}$ (f_d^1 in Section IV.3.2.1 (p. 109), $\lambda := 1$, $m := 1$, the n vectors \mathbf{x}_i are points on the real line with nearest-neighbor distances $-\log |c_k|$). Define \mathbf{V}_l as a diagonal $n \times n$ matrix with the first l entries on the diagonal -1 and the remaining 1 . $\mathbf{V}_l^T \mathbf{h} \mathbf{V}_l$ changes signs of h_{ij} in the blocks $(i \leq l, j > l)$ and $(i > l, j \leq l)$. Then $\mathbf{V}_l^T \tilde{\mathbf{h}} \mathbf{V}_l$ is positive definite (Horn and Johnson, 1990, p. 7.1.6). Since all of its diagonal entries are still 1 , it is a correlation matrix. This can be reformulated by allowing $-1 < c_l < 0$ in addition to $0 \leq c_k < 1$, $k \in \{1, \dots, n-1\}$ for \mathbf{h} in Eq. (IV.9) to still qualify as correlation matrix. Similarly, this independently follows for all $l \in \{1, \dots, n-1\}$. Hence, \mathbf{h} in Eq. (IV.9) is a correlation matrix for $|c_k| < 1$, $k \in \{1, \dots, n-1\}$.

\mathbf{h} can describe local *a priori* correlations for a single spectrum, like between column factors (minor gases, cloud modes) that may have correlations or anti-correlations. It can also describe inter-level correlations of atmospheric profiles ($c_k := \exp(-|z_k - z_{k+1}|/\lambda)$ with z_k the altitude of level k and λ the inter-level correlation length, an obvious generalization of Rodgers (2000, Eq. 2.83)). Also, *a priori* correlations between common parameters (Sections IV.3.5 (p. 116) and IV.4.3 (p. 119)) can be modeled this way. Note that, properly taking into account the signs (see $\mathbf{V}_l^T(\cdot)\mathbf{V}_l$), other correlation functions than f_d^1 from Section IV.3.2.1 (p. 109) still lead to proper single-spectrum correlation matrices.

IV.3.4 Full covariance matrix for correlated retrievals

This section discusses the construction of the full covariance matrix for several parameters and several spectra for given single-parameter spatial-temporal correlation data (Section IV.3.2 (p. 109)) and local single-spectrum correlation data (Section IV.3.3). While there seems to be no simple solution for arbitrary local couplings, it is possible to provide correlation matrices sufficiently general for VIRTIS data retrieval.

First, a correlation matrix is constructed for a group of several locally coupled parameters that experience identical fixed correlation length and time. For example, temperature altitude profiles have local inter-level-correlations and may be described by the same horizontal spatial-temporal correlation data. The Kronecker product (Horn and Johnson, 1991, Section 4.2) is well suited to treat this case.

The Kronecker product $\mathbf{A} \otimes \mathbf{B}$ (Horn and Johnson, 1991, Definition 4.2.1) of an $m \times n$ -matrix \mathbf{A} with entries A_{ij} and a $p \times q$ -matrix \mathbf{B} is defined to be the $mp \times nq$ -dimensional block matrix

$$\mathbf{A} \otimes \mathbf{B} := \begin{pmatrix} A_{11}\mathbf{B} & \cdots & A_{1n}\mathbf{B} \\ \vdots & \ddots & \vdots \\ A_{m1}\mathbf{B} & \cdots & A_{mn}\mathbf{B} \end{pmatrix} \quad (\text{IV.10})$$

and is not commutative in general. According to Horn and Johnson (1991, 4.2.4 and 4.2.13), the result of the Kronecker product of symmetric positive definite matrices is symmetric positive definite.

Let there be G groups of parameters with group-specific correlation length λ_g and time τ_g for each group $g \in \{1, \dots, G\}$. Then let \mathbf{h}_g be the positive definite $n_g \times n_g$ matrix of the single-spectrum correlations between the n_g parameters of group g (constructed as \mathbf{h} in Section IV.3.3). The total count n of single-spectrum parameters over all groups amounts to $n = \sum_{g=1}^G n_g$. The spatial-temporal $r \times r$ correlation matrix for a single parameter from this group g shall be denoted by $\boldsymbol{\varrho}_g$. By using λ_g , τ_g , and f_d^3 , it is computed according to Section IV.3.2.3 (p. 112) from the space-time coordinates of the r measurement footprints. It is the same for all parameters of group g .

The matrix $\boldsymbol{\varrho}_g \otimes \mathbf{h}_g$ is then the correlation matrix \mathbf{C}_A^g for group g (note that $(\boldsymbol{\varrho}_g)_{ii} = 1$).

$$\boldsymbol{\varrho}_g \otimes \mathbf{h}_g = \begin{pmatrix} \mathbf{h}_g & (\boldsymbol{\varrho}_g)_{12}\mathbf{h}_g & \cdots & (\boldsymbol{\varrho}_g)_{1r}\mathbf{h}_g \\ (\boldsymbol{\varrho}_g)_{12}\mathbf{h}_g & \mathbf{h}_g & \cdots & (\boldsymbol{\varrho}_g)_{2r}\mathbf{h}_g \\ \vdots & \vdots & \ddots & \vdots \\ (\boldsymbol{\varrho}_g)_{1r}\mathbf{h}_g & (\boldsymbol{\varrho}_g)_{2r}\mathbf{h}_g & \cdots & (\boldsymbol{\varrho}_g)_{rr}\mathbf{h}_g \end{pmatrix} =: \mathbf{C}_A^g \quad (\text{IV.11})$$

\mathbf{C}_A^g satisfies all necessary conditions for the correlations of parameters belonging to group g . It includes spatial-temporal coupling for single parameters as well as local coupling for single spectra as special cases. \mathbf{C}_A^g is symmetric positive definite with all diagonal entries 1, and the single blocks are symmetric, compare Section IV.3.1 (p. 108).

Next, groups of parameters with different spatial-temporal correlations are combined. For example, temperature vs. cloud altitude profiles with different inter-level-correlations may have different horizontal spatial-temporal correlations.

Let $(\mathbf{x}_i)_k$ denote the k -th single-spectrum parameter of spectrum i . The concatenated list \mathbf{X} (as in Section IV.2 (p. 105)) of the n parameters for each of the r measurements

$$\mathbf{X} = \left(\underbrace{(\mathbf{x}_1)_1, \dots, (\mathbf{x}_1)_n}_{\text{measurement 1}}, \dots, \underbrace{(\mathbf{x}_r)_1, \dots, (\mathbf{x}_r)_n}_{\text{measurement r}} \right)^T \quad (\text{IV.12})$$

is a permutation of the list $\overline{\mathbf{X}}$ of the r measurements for each of the n single-spectrum parameters

$$\overline{\mathbf{X}} = \left(\underbrace{(\mathbf{x}_1)_1, \dots, (\mathbf{x}_r)_1}_{\text{parameter 1}}, \dots, \underbrace{(\mathbf{x}_1)_n, \dots, (\mathbf{x}_r)_n}_{\text{parameter n}} \right)^T. \quad (\text{IV.13})$$

The associated permutation $\mathbf{\Pi}_n^r$ with $\overline{\mathbf{X}} = \mathbf{\Pi}_n^r \mathbf{X}$ acts for all $i \in \{1, \dots, r\}$ and for all $k \in \{1, \dots, n\}$ as

$$(\mathbf{X})_{n(i-1)+k} = (\mathbf{x}_i)_k = (\overline{\mathbf{X}})_{r(k-1)+i} =: (\overline{\mathbf{x}}_k)_i.$$

The permutation $\mathbf{\Pi}_{n_g}^r$ can be used to permute \mathbf{C}_A^g to obtain $\mathbf{\Pi}_{n_g}^r (\boldsymbol{\varrho}_g \otimes \mathbf{h}_g) (\mathbf{\Pi}_{n_g}^r)^T =: \overline{\mathbf{C}}_A^g$.

$$\overline{\mathbf{C}}_A^g = \begin{pmatrix} \boldsymbol{\varrho}_g & (\mathbf{h}_g)_{12}\boldsymbol{\varrho}_g & \cdots & (\mathbf{h}_g)_{1n_g}\boldsymbol{\varrho}_g \\ (\mathbf{h}_g)_{12}\boldsymbol{\varrho}_g & \boldsymbol{\varrho}_g & \cdots & (\mathbf{h}_g)_{2n_g}\boldsymbol{\varrho}_g \\ \vdots & \vdots & \ddots & \vdots \\ (\mathbf{h}_g)_{1n_g}\boldsymbol{\varrho}_g & (\mathbf{h}_g)_{2n_g}\boldsymbol{\varrho}_g & \cdots & (\mathbf{h}_g)_{n_g n_g}\boldsymbol{\varrho}_g \end{pmatrix} \quad (\text{IV.14})$$

This is the same as $\mathbf{h}_g \otimes \boldsymbol{\varrho}_g$ and hence positive definite.

Now a block diagonal matrix $\overline{\mathbf{C}}_A$ can be formed with all $\overline{\mathbf{C}}_A^g$ as the G positive definite blocks on the diagonal.

$$\overline{\mathbf{C}}_A := \begin{pmatrix} \mathbf{h}_1 \otimes \boldsymbol{\varrho}_1 & 0 & \cdots & 0 \\ 0 & \mathbf{h}_2 \otimes \boldsymbol{\varrho}_2 & \ddots & \vdots \\ \vdots & \ddots & \ddots & 0 \\ 0 & \cdots & 0 & \mathbf{h}_G \otimes \boldsymbol{\varrho}_G \end{pmatrix} \quad (\text{IV.15})$$

As a direct sum of positive definite matrices, $\overline{\mathbf{C}}_A$ is positive definite (for a correspondingly partitioned $\mathbf{v} = (\mathbf{v}_1, \dots, \mathbf{v}_G) \neq 0$, the quadratic form $\langle \mathbf{v}, \overline{\mathbf{C}}_A \mathbf{v} \rangle = \langle \mathbf{v}_1, \overline{\mathbf{C}}_A^1 \mathbf{v}_1 \rangle + \dots + \langle \mathbf{v}_G, \overline{\mathbf{C}}_A^G \mathbf{v}_G \rangle$ is positive). In general, $\overline{\mathbf{C}}_A$ can not be represented as Kronecker product.

Each of the G blocks on the diagonal corresponds to the permuted correlation matrix of one of the G parameter groups, encoding local as well as spatial-temporal correlations. The correlation lengths and times are allowed to differ from block to block but must be constant within each block. Parameters belonging to a certain group may locally be arbitrarily coupled among each other. However, no local coupling between the different groups can be implemented this way.

In order to recover the sorting associated to \mathbf{X} (Eq. (IV.12)), the inverse permutation has to be applied to $\overline{\mathbf{C}}_A$ to obtain $\mathbf{C}_A := (\mathbf{\Pi}_n^r)^T \overline{\mathbf{C}}_A \mathbf{\Pi}_n^r$. Although the dimensions $n_{gr} \times n_{gr}$ of $\overline{\mathbf{C}}_A^g$ depend on g , this is the correct permutation, since it is associated to r measurements and n parameters, which is the underlying structure of $\overline{\mathbf{C}}_A$. As $\overline{\mathbf{C}}_A$ is positive definite and a permutation matrix has full rank, \mathbf{C}_A is positive definite (Horn and Johnson, 1990, p. 7.1.6). It is symmetric with all diagonal entries 1, because $\overline{\mathbf{C}}_A$ is.

The full covariance matrix \mathbf{S}_A is computed according to Eq. (IV.3) (p. 108), by scaling \mathbf{C}_A with the single-spectrum standard deviations σ_k of the single-spectrum parameters k .

$$(\mathbf{S}_A)_{n(i-1)+k, n(j-1)+l} = \sigma_k \sigma_l (\mathbf{C}_A)_{n(i-1)+k, n(j-1)+l} \quad (\text{IV.16})$$

This is done for all measurements $i, j \in \{1, \dots, r\}$ and for all parameters $k, l \in \{1, \dots, n\}$.

The $nr \times nr$ matrix \mathbf{S}_A satisfies all requirements, except for a possible inter-group coupling. As can explicitly be shown for the case of two measurements, each described by two locally coupled single-spectrum parameters that have different *a priori* correlation lengths, \mathbf{C}_A can fail to be positive definite for too strong inter-group coupling. The underlying reason is that strong local coupling between the parameters forces the retrieved values to have strongly correlated spatial-temporal behavior, which is not consistent when strongly differing correlation lengths are chosen. This manifests itself by the failure to construct a proper correlation matrix, unless the local coupling is relaxed or the spatial-temporal correlations are equalized. This explains, why all correlation data can be chosen freely and independently as long as inter-group coupling is disregarded.

Thus, in order to allow arbitrary space-time distributions of the measurement footprints for problems with many measurements and parameters, either arbitrary spatial-temporal correlation data can be set for the different parameters, or arbitrary local coupling may be required. For the first case, these parameters have to be assigned to different parameter groups and no local coupling is allowed between them. For the second case, these parameters have to be assigned to the same parameter group and spatial-temporal correlation data must coincide.

In general, however, a correlation matrix is not unique for given local and spatial-temporal correlation data. For instance, the distance matrix approach (Section IV.3.2 (p. 109)) could be applied to a suitable point distribution on the Cartesian product space of the spatial-temporal and the local parameter dimensions. But then, local and spatial-temporal correlations for the full multi-spectrum problem would not be independent anymore in their impacts, and the advantages of the Kronecker product construction would get lost: It is ideally suited to the computation of the scaled residual (Appendix IV.A.2 (p. 127)) and the sparse matrix formulation of the retrieval algorithm (Appendix IV.A.4 (p. 133)). It also enables a clean derivation of the retrieval of common parameter vectors (Appendix IV.A.3 (p. 129)). In addition, inter-group coupling is not necessary for Venus retrieval problems, as is demonstrated by Section IV.4.2 (p. 118), which presents a basic categorization of the relevant parameter groups herefore.

IV.3.5 Retrieval of common parameters

This section discusses the *a priori* covariance matrix for retrieval problems involving parameters with perfect spatial or temporal coupling (spatial or temporal *a priori* correlation equal to 1, corresponding to infinite correlation length or time, leading to parameters being affinely linear functions of each other) and identic single-spectrum *a priori* data (affinely linear functions are then the identity function, Appendix IV.A.3 (p. 129)). Such parameters can not spatially or temporally vary for a certain set of r considered measurements. To avoid a degenerated *a priori* covariance matrix, such a parameter will not be treated as r individual parameters that are perfectly coupled, but as a single parameter that is common to the involved measurements. Also, this helps to save computer resources. To verbally distinguish common parameters from spatially-temporally varying parameters, the latter are cited as 'local parameters'. This should not be confused with 'local coupling between parameters' as opposed to 'spatial-temporal coupling'.

The retrieved value of a common parameter can be defined as the limit of the retrieved values of the corresponding r local parameters for ever stronger spatial or temporal coupling. In Appendix IV.A.3 (p. 129) it is shown that computing this limit is equivalent to retrieving a common parameter in the sense of Section IV.2 (p. 105) while uniquely defining the corresponding *a priori* covariance matrix. A statistical \sqrt{r} -like relative weighting factor between common and local parameters is conceivable that reflects the influence of a common parameter on r spectra. Appendix IV.A.3 (p. 129) clarifies that the weighting is exactly equal.

The *a priori* covariance matrix \mathbf{S}_A follows as block diagonal with \mathbf{S}_C and \mathbf{S}_L as the blocks on its diagonal. \mathbf{S}_C encodes the *a priori* correlations between the various common parameters and their *a priori* standard deviations. It can be constructed by defining a suitable correlation matrix \mathbf{C}_C by nearest-neighbor-coupling (Section IV.3.3 (p. 113)) or by a distance matrix (Section IV.3.2.3 (p. 112)), and by scaling \mathbf{C}_C with the *a priori* standard deviations σ_k of the common parameters (Eq. (IV.3) (p. 108)). \mathbf{S}_L can be constructed according to Section IV.3.4 (p. 113) and encodes the *a priori* local and spatial-temporal correlations as well as standard deviations of the local parameters. \mathbf{S}_A is a proper covariance matrix when \mathbf{S}_C and \mathbf{S}_L are.

For VIRTIS-M-IR measurements of Venus, some relevant common parameters along with a suitable \mathbf{C}_C are discussed in Section IV.4.3 (p. 119).

IV.4 Parameters for Venus retrieval problems

This section presents a basic categorization of relevant parameters for Venus retrieval problems. Compare also Haus and Arnold (2010); Kappel et al. (2012b) for a discussion of these parameters in context of the radiative transfer forward model. Section IV.4.1 summarizes the most important properties of the forward model. The categorization of the parameters also demonstrates that it suffices here to construct correlation matrices without considering inter-group coupling. Local parameters are treated by an *a priori* correlation matrix according to Section IV.3.4 (p. 113), common parameters according to Section IV.3.5.

IV.4.1 Forward model

A radiative transfer forward model is utilized to simulate the observable radiances. It is a plane-parallel, LTE⁴, line-by-line code taking into account thermal emissions by surface and atmosphere, and absorption and multiple scattering by gases and clouds. It is similar to the forward model described by Haus and Arnold (2010), but the underlying radiative transfer equation solver DISORT (Stamnes et al., 1988) is replaced by LIDORT (Spurr, 2001, 2008). This way, the forward model is capable of providing analytic derivatives of the simulated radiances with respect to a number of atmospheric, surface, and instrumental parameters. Jacobians with respect to the remaining parameters (mainly temperature variables) can be evaluated perturbatively (slower and possibly affected by numerical noise). To increase numerical efficiency, uninteresting wavelength ranges can be blacked out automatically (initial radiances or Jacobians below certain thresholds) or manually.

From the VIRTIS-M-IR spectral range (1.0–5.2 μm), only 1.0–2.5 μm shall be utilized for this study. Venus' nightside emissions in this range mainly originate from altitudes below 40 km (Haus and Arnold, 2010, Fig. 4)

⁴Corrected: In the published paper, the code was mistakenly stated to be a non-LTE code.

where temperature is quite stable with time, and they are thus nearly unaffected by the strong mesospheric temperature variations above 59 km (Tellmann et al., 2009). Also, details of the cloud altitude distribution have almost no impact here, since the main cloud deck (≥ 48 km, Marov et al., 1980) resides above the line forming altitude region. In contrast, spectral signatures longward of $3 \mu\text{m}$ are strongly influenced by variations of temperature and cloud altitude distributions above 48 km.

Temperature and pressure altitude profiles are taken from the Venus International Reference Atmosphere (VIRA, Seiff et al., 1985; Zasova et al., 2006b) at the equator (midnight). The surface is assumed to be in thermodynamic equilibrium with the bottom of the atmosphere, and therefore, the surface temperature equals the VIRA temperature at the respective surface elevation. Surface emissivity must lie in the interval $[0, 1]$.

The main constituent of Venus' atmosphere is CO_2 (96.5% by volume). Considered minor gaseous constituents are H_2O , CO , SO_2 , OCS , HCl , and HF . Altitude profiles of their volume mixing ratios are given by Haus and Arnold (2010) and are based on the profiles by Pollack et al. (1993). Quasi-monochromatic absorption cross sections due to their allowed molecular transitions are computed from the spectral line databases CDSD (CO_2 , Tashkun et al., 2003), HITEMP (CO_2 , Pollack et al., 1993, CO , H_2O isotopes 1–3, Rothman et al., 1995; to be in line with Haus and Arnold, 2010, the more recent HITEMP2010, Rothman et al., 2010, is not yet considered here), and HITRAN08 (H_2O isotopes 4–6, SO_2 , OCS , HCl , HF , Rothman et al., 2009) by using spectral line shapes listed by Haus and Arnold (2010). Molecular Rayleigh scattering is treated according to Hansen and Travis (1974). Non-LTE O_2 emissions (' O_2 nightglow') at $1.27 \mu\text{m}$ from an altitude region around 100 km (Piccioni et al., 2009) are not considered, and therefore, the $1.28 \mu\text{m}$ window will be blacked out in practice due to its contamination by O_2 nightglow.

The high pressure and high temperature environment of Venus' deep atmosphere makes it difficult to characterize the absorption properties of its main constituent CO_2 . Neither the line shapes of the allowed transitions, nor other effects contributing to the absorption cross-section (continuum, collisional induced absorption, line mixing) are sufficiently well constrained through laboratory or theory in order to satisfactorily reproduce observed spectra in the infrared. Also, the line data bases utilized for computing the absorption cross-sections of the allowed transitions are not perfect (Haus and Arnold, 2010; Bézard et al., 2011). They are based on theoretical models and numerical computations, and not on laboratory measurements (Tashkun et al., 2003). Good knowledge of the CO_2 opacity is important for a reliable retrieval of parameters like surface emissivity. Wavelength dependent corrections to the CO_2 opacity as given by the allowed transitions, are in the following shortly referred to as 'continuum'. The continuum depends on the utilized line databases and line shapes but is independent of the measurement. For this study, continuum is treated as spectrally constant throughout the range of an atmospheric transparency window, but it can depend on the window. These window-specific scalars for the spectral windows at 1.02, 1.10, 1.18, 1.28, 1.31, 1.74, $2.3 \mu\text{m}$ are set to 0, 2, 0.35, 3, 4, 15, 120 in units of 10^{-29}cm^2 , respectively. These values are inspired by preliminary results from application of MSR to actual VIRTIS-M-IR nightside spectra.

The clouds of Venus are modeled to comprise the four modes 1, 2, 2', and 3. Each mode consists of spherical droplets of 75% sulfuric acid (refractive indices taken from Palmer and Williams (1975); Carlson and Anderson (2011)). Cloud particle radii are log-normally distributed with modal radii of 0.3, 1.0, 1.4, $3.65 \mu\text{m}$ and unitless dispersions of 1.56, 1.29, 1.23, 1.28 for the four modes, respectively (Pollack et al., 1993). Mode specific initial altitude profiles of particle number densities are taken from Haus et al. (2013). Actual cloud modal abundances are defined by 'cloud mode factors' that scale the number densities of these four initial altitude profiles. The mode factors may strongly vary, and no detailed *a priori* knowledge is available. Wavelength dependent scattering and absorption properties of the clouds are computed by using Mie theory (Wiscombe, 1980).

Fig. IV.2 (offset 0.0) displays a typical synthetic spectrum ('reference spectrum'). The Jacobians of several retrieval parameters that shall be considered in the following and are relevant for actual measurements, are shown with various offsets. The values that led to Fig. IV.2 are: FWHM of instrumental response function 17 nm, surface emissivity 0.65, surface elevation 0 km, no O_2 nightglow, cloud mode factors all set to 1, nadir-looking observational geometry, no noise. The figure illustrates that surface emissivity is observable in the spectral windows at 1.02, 1.10, and $1.18 \mu\text{m}$ ('surface windows'), continua affect all considered windows, the abundances of the different cloud modes affect the spectrum in a very similar way and in all windows, and the impact of the FWHM is quite distinct. Minor gases do not affect the short-wavelength flank of the

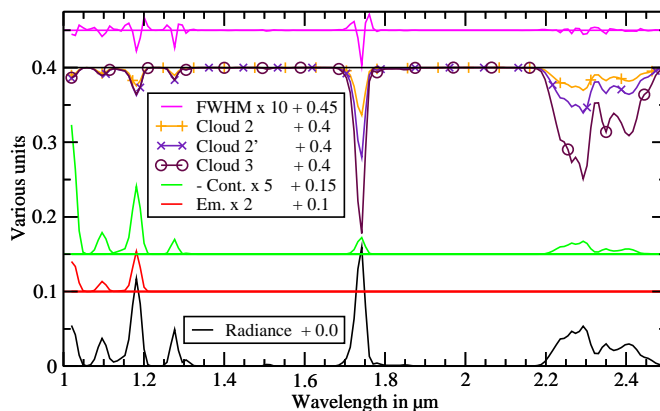


FIGURE IV.2: [From bottom to top] Offset 0: synthetic radiance spectrum in $W/(m^2 \text{ sr } \mu\text{m})$, various positive offsets: scaled Jacobians with respect to surface emissivity ('Em.', unit $W/(m^2 \text{ sr } \mu\text{m})$), continuum ('Cont.', between 2.1 and $2.5 \mu\text{m}$ scaled by factor of 10 relative to remaining range for better representation, unit $W/(m^2 \text{ sr } \mu\text{m}) \cdot 10^{29} \text{ cm}^{-2}$), cloud mode column factors ('Cloud', unit $W/(m^2 \text{ sr } \mu\text{m})$), and FWHM of VIRTIS-M-IR instrumental response function ('FWHM', unit $W/(m^2 \text{ sr } \mu\text{m nm})$).

$2.3 \mu\text{m}$ window ($2.15\text{--}2.30 \mu\text{m}$), but strongly affect the long-wavelength flank which thus shall not be used for retrievals of cloud parameters. Even so, minor gas variations shall not be considered in this study, despite their (moderate) impact on the $1.74 \mu\text{m}$ peak and the range $1.10\text{--}1.18 \mu\text{m}$. As cloud parameters should not be retrieved from the surface windows, and the $1.28 \mu\text{m}$ window shall be blacked out due to its O_2 nightglow contamination, the range $1.295\text{--}2.300 \mu\text{m}$ is left to retrieve cloud parameters from.

IV.4.2 Local parameters

First, the atmospheric parameters may be divided into the cloud group, the minor gases group, the atmospheric temperature group, and O_2 nightglow.

Horizontally, the cloud opacity exhibits a rather short correlation length of the order of several hundred kilometers and correlation times of a few hours. This can be checked by analyzing the auto-correlation function of nightside radiance observation movies in the short wavelength flank of the $2.3 \mu\text{m}$ window as proxy. This correlation data will be carried over to the column densities of the individual cloud modes 1, 2, 2', and 3.

Minor gas column density variations seem to be better represented by longer correlation lengths of the order of more than thousand kilometers. This can be estimated for CO by observing the spatial variation in the results by Tsang et al. (2009) and is also applied to the other minor gases as first estimate. Similarly, the correlation time is likely larger than the cloud correlation time. The spatial-temporal scales of atmospheric super-rotation and convection can serve as a motivation herefor.

For cloud or minor gases altitude density profiles, it is reasonable to assign the spatial-temporal properties of the column densities to the horizontal variability of the profiles as well and to treat the vertical variability as locally coupled parameters.

Thus, the cloud parameter group comprises the total cloud column factor, the column factors of the individual cloud modes, and the parameters describing the corresponding cloud mode profiles. Similarly, the minor gases parameter group includes the column factors and profiles of all minor gases. *A priori* couplings between gases and clouds are neglected, but the parameters of either group can be coupled to other parameters within their group. This includes the vertical variability of the respective altitude profiles. Also, for instance, cloud modes 2' and 3 may well be slightly anti-correlated, as might be OCS and SO_2 , but this is not considered in practice.

Atmospheric temperatures in the mesosphere are treated to have correlation properties similar to the minor gases and thus could well be assigned to the minor gases group. But couplings with the minor gases are not expected, and so they will be regarded as a distinct group. O_2 nightglow is also treated as one separate parameter group.

Auxiliary instrumental parameters like the FWHM of the instrumental response function and the slope and intercept of the band-to-wavelength mapping are not sufficiently well predictable by the calibration pipeline at the moment and thus have to be retrieved as auxiliary parameters needed to adequately simulate the observed spectra (Kappel et al., 2012b, Section 4.4). They are not coupled to atmospheric or surface parameters, but may be coupled among themselves. Therefore, they are assigned to one separate parameter group and treated according to Eq. (IV.8) (p. 112).

All these different groups can safely be treated as independent from each other, and inter-group coupling is not necessary to describe the parameter correlations as long as *a priori* knowledge is as limited as presently.

IV.4.3 Common parameters

As discussed in Section IV.4.1 (p. 116), the CO₂ continuum is not sufficiently well known. However, the observed VIRTIS-M-IR spectra themselves can be regarded as measurements thereof, but now with the locally varying parameters as interfering factors. Although for this study modeled as window-specific and spectrally constant throughout the range of an atmospheric transparency window, the continuum may freely vary in wavelength direction and is treated as a parameter vector. It is clearly common to all measurements of Venus' atmosphere and will be retrieved as parameter that is common to a selection of as many as possible spectra under as many as possible environmental and observational conditions. This way, it shall be ensured that it is compatible with all measurements and as reliable as possible. The continuum has to be determined only once and will thereafter be used as fixed value for subsequent retrievals of atmospheric and surface parameters. It can be regularized by only allowing for limited variation in wavelength direction. This can be achieved by a nearest-neighbor coupling in wavelength direction (Section IV.3.2 (p. 109)) or also by a distance matrix with respect to distances in wavelength direction (Section IV.3.3 (p. 113)), but both ways are purely heuristically, since not much is known about the wavelength dependence of the continuum. First results that are based on MSR have been presented by Kappel et al. (2012b).

Surface properties should be quite unrelated to variations in the atmosphere, except for a possible coupling of surface temperature and atmospheric temperature at the surface, which will be neglected. When the occurrence of volcanic activity (as observable⁵ by VIRTIS-M-IR in the nightside NIR surface windows at 1.02, 1.10, and 1.18 μm) is neglected (Müller et al., 2012a), the spectral surface emissivity can be regarded as common to all measurements that repeatedly cover the same target bin on the surface. Or in other words, the entire surface emissivity map of the planet is common to all measurements targeting the planet. Note that a measurement is only sensitive (i.e. non-zero entry in the Jacobian) to surface emissivity at surface bins that are actually covered by the measurement. Retrieving surface emissivity as parameter common to measurements repeatedly covering a target, yields a fully consistent parameter set describing all considered measurements (Kappel et al., 2012c). In contrast, the corresponding single-spectrum retrievals yield different emissivity values for each of these measurements in most cases. This implies an inconsistent parameter set describing the full set of utilized measurements, implicitly also allowing for inconsistent atmospheric parameter values. The emissivities at nearby spots are possibly correlated. This purely spatial situation can be treated by using the correlation matrix from Eq. (IV.7) (p. 112) with $\tau = \infty$. The typical correlation length is 100 km, i.e. the expected surface resolution as it is limited by atmospheric blurring (Moroz, 2002).

The deep atmospheric temperature field is not yet sufficiently well known for a reliable surface emissivity retrieval. The corresponding Jacobians are quite similar to cloud Jacobians, and disentanglement is not feasible for single-spectrum retrievals. A general circulation model (Lebonnois et al., 2010a, personal communication) and measurements (Tellmann et al., 2009; Avduevskii et al., 1983) are compatible with a temporally rather constant tropospheric temperature field that is altitude and latitude dependent, probably a consequence of high thermal inertia and thermodynamic stable layering in the deep atmosphere. This is not the case for the highly variable mesosphere. Thus, a deep atmospheric temperature altitude profile is essentially a parameter vector common to measurements covering a given latitude. The latitudinal dependencies of the temperature profiles can be coupled by using a correlation matrix similar to that for the surface emissivity

⁵Note: This does not mean that it was observed. The formulation rather refers to the principle observability using VIRTIS-M-IR.

map, but spatial separation is only measured in latitude direction, i.e. $(\mathbf{C}_C)_{ij} = f_d^3 (n_3 |\vartheta_i - \vartheta_j| / \Theta)$, compare Section IV.3.2.3 (p. 112). The latitude corresponding to measurement i is hereby ϑ_i , and the correlation strength Θ in latitude direction can be set to 45° .

Finally, while it is possible to couple the different mentioned common parameter types, this seems not to be useful. Any coupling to local parameters is also not needed.

IV.5 Examples and discussion

Since MSR determines locations of local minima of the cost function F_c , a non-negative real function on a possibly high dimensional parameter space (Eq. (IV.1) (p. 107), also applicable for single-spectrum retrievals by setting inter-measurement couplings to zero), it is easy to find local subsidiary minima, which are potentially far from the global minimum, especially in presence of measurement noise. This section discusses by two examples, how this situation can be improved by using MSR (Section IV.2 (p. 105), with *a priori* covariance matrix \mathbf{S}_A from Section IV.3 (p. 107)) by not only incorporating information on expected parameter values, but also expected relations between parameters. The more actually available *a priori* knowledge is utilized, the better certain solutions being incompatible with the *a priori* data can be ruled out from the outset. Some resulting improvements in the data analysis of Venus nightside spectra acquired by VIRTIS-M-IR have already been published by Kappel et al. (2012b, Section 5.1). The retrieval algorithm has been sketched there only shortly, and the full description has been announced to be published in a subsequent (the present) paper.

To test MSR, a set of synthetic VIRTIS-M-IR radiance spectra of Venus' nightside emissions in the range 1.0–2.5 μm is generated by using the radiative transfer forward model. The utilized 'true' atmospheric, surface, and instrumental parameters underlying these spectra are thus exactly known by definition. Gaussian noise with a certain standard deviation σ is added to the simulated spectra to emulate the loss of the spectra's information content caused by random measurement imperfections. Systematic measurement and calibration errors will be considered in a subsequent paper (set parameters that are not retrieved to values different from their assumed values, distort shapes of the radiance peaks). By using different regularization schemes, the relevant parameters are then retrieved from the synthetic spectra and compared to their 'true' values.

Example (A) studies a swath of 30 concurrent synthetic spectra covering the equator at longitudes from 1–30 $^\circ\text{E}$. Fig. IV.3 depicts the 'true' cloud column factors 2, 2', and 3. The remaining parameters are as for

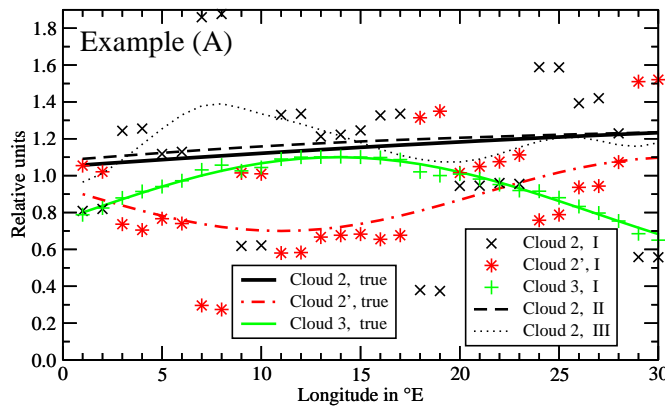


FIGURE IV.3: Comparison of 'true' cloud mode column factors (left key) of longitudinal synthetic measurement swath with corresponding retrieved values (right key) for different models of *a priori* correlation lengths λ_i for cloud mode i . I: $\lambda_2 = 0 \text{ km} = \lambda_{2'} = \lambda_3$, II: $\lambda_2 = 20000 \text{ km}$, $\lambda_{2'} = \lambda_3 = 500 \text{ km}$, III: $\lambda_2 = 2000 \text{ km} = \lambda_{2'} = \lambda_3$.

the reference spectrum (Fig. IV.2 (p. 118)), and Gaussian noise with the unrealistically small double standard deviation $2\sigma = 2 \cdot 10^{-4} \text{ W}/(\text{m}^2 \text{ sr } \mu\text{m})$ is added to the synthetic spectra. MSR is used to retrieve the cloud mode factors from the radiance spectra for three different regularization models from the spectral range 1.295–2.300 μm (1.31, 1.74, and 2.3 μm peaks). *A priori* mean values and double standard deviations are set to 1.0 and 2.0, respectively, to allow for a sufficiently wide range the retrieved cloud mode factors may vary in. Note that 1 $^\circ$ longitude at the equator corresponds to about 107 km referred to the cloud top level.

Model I sets all *a priori* correlation lengths to zero and corresponds to single-spectrum retrievals. While cloud mode 3 abundance can be retrieved quite reliably, modes 2 and 2' are difficult to disentangle and strongly deviate from their true values. This is a consequence of the smallness of one of the three available peaks ($1.31 \mu\text{m}$ -peak radiance $\approx 10^{-2} \text{ W}/(\text{m}^2 \text{ sr } \mu\text{m})$) that are used to determine the three unknown cloud mode factors, the presence of noise, and the similarity of the Jacobians especially of the cloud mode factors 2 and 2'. Note that for zero noise, the true values can be retrieved exactly.

Model II sets *a priori* correlation lengths that approximate the true parameter distributions. The dependence on correlation length modifications by factors of 0.5 or 2 has been verified to be relatively small. Mode 3 factors are not depicted as they almost exactly coincide with their true values. Mode 2' factors are not shown because deviations from their true values are opposite and of a similar magnitude (but smaller) as deviations for mode 2 (compare model I results in the figure). Retrieved mode 2 factors deviate less than 10% from their true values.

Model III sets for all cloud modes identical *a priori* correlation lengths that approximate the geometric mean of the three correlation lengths from model II. Retrieved mode 3 factors match the true values well. Modes 2 and 3 can not be disentangled (only mode 2 shown). Setting all *a priori* correlation lengths to 20000 km, or to 500 km, respectively, leads to worse results.

Averaged least-squares norms of residuals between synthetic and fitted radiances are least for model II and largest for model I. Within model III, the geometric-mean-case leads to the smallest residuals.

In Example (A), as in many real-world atmospheric remote sensing problems, measurements are not isolated soundings in space and time, but each measurement is accompanied by adjacent measurements. If they are nevertheless treated as independent from other soundings, then spatial or temporal continuity in the measurements may not translate to a certain expected continuity in retrieved parameters like cloud column densities. This is due to the ill-posed nature of the retrieval problem and the existence of subsidiary minima of the cost function. Actually, contiguous real-world measurements are unlikely to originate from completely unrelated state vectors, since the physical state of the atmosphere should obey a certain continuity. This follows from the inertia of matter and the drive to compensate thermodynamic disequilibria and results in a certain continuity of the observable radiance. Therefore, it can help to reduce the effective size of the parameter space by not only incorporating *a priori* mean values and standard deviations as usual, but by also taking *a priori* spatial-temporal correlations into account. This decreases the number of potential solutions and could be expected to produce larger residuals between measurements and fits. But for Example (A), as for actual retrievals of VIRTIS spectra (Kappel et al., 2012b), the residuals in fact decrease on average. This indicates avoided subsidiary solutions of F_c , justifying this correlated retrieval. However, when the imposed correlations are too strong, translating to an overly reduction of the effective size of the parameter space, residuals turn out to become larger again, since the global minimum itself is overly affected.

In addition, Example (A) illustrates that parameters with strongly differing correlation lengths can be better disentangled by using multi- than by using single-spectrum regularization. But the more similar any two parameters' Jacobians are (smaller Euclidean angle), the worse they can be disentangled (modes 2 and 2'). Note that for parameters with equal Jacobians, the distribution of the retrieved parameters is determined by *a priori* correlation data only, and disentanglement is not based on measurements anymore. This case must be avoided and underlines the necessity to check robustness of the retrieved results against reasonable *a priori* data and initial guess modifications. In Example (A), noise is sufficiently small to just disentangle cloud modes 2 and 2' by using MSR, but stronger noise destroys more information. In practice (noise with $2\sigma = 2 \cdot 10^{-3} \text{ W}/(\text{m}^2 \text{ sr } \mu\text{m})$ and systematic errors), modes 2 and 2' can not be disentangled from the considered spectral range, and only mode 2' and 3 variations are considered in the following. Resulting real-world retrieval errors will be studied elsewhere.

Note that, when a smooth behavior of the retrieved result is expected, it is far better to increase the probability to find a smooth parameter set as retrieval solution, than to smooth results from uncorrelated retrievals. Due to the non-linear nature of the forward model, smoothing of parameters will in general not lead to a consistent parameter set describing the measurements, especially when jumps between different subsidiary minima are involved, or parameters close to their domain boundaries.

In conclusion of Example (A), *a priori* spatial-temporal correlations can be regarded as 'elastic bands' forcing the parameters to stay close to self-establishing general spatial-temporal trends. This increases the

probability of convergence to spatial-temporal parameter distributions compatible with the expectations on continuity and distribution of the true atmospheric state, attenuates the impact of noise, and decreases the probability of running into subsidiary minima of the cost function.

As discussed, parameters with strongly differing spatial-temporal correlations can be better disentangled. The extreme case hereof is that of infinite spatial or temporal coupling, translating to spatial or temporal constancy of the respective parameters when *a priori* mean values and standard deviations are identical. But as that causes S_A to degenerate, this case must be treated in a different way (Appendix IV.A.3 (p. 129)), by retrieving parameters that are common to certain sets of spectra (Section IV.3.5 (p. 116)).

To illustrate this case, **Example (B)** studies a synthetic observation movie with 30 repetitions (1 h intervals) of 30 surface bins that evenly cover the equator from 1–30 °E (Figs. IV.4 and IV.5). The spectra are

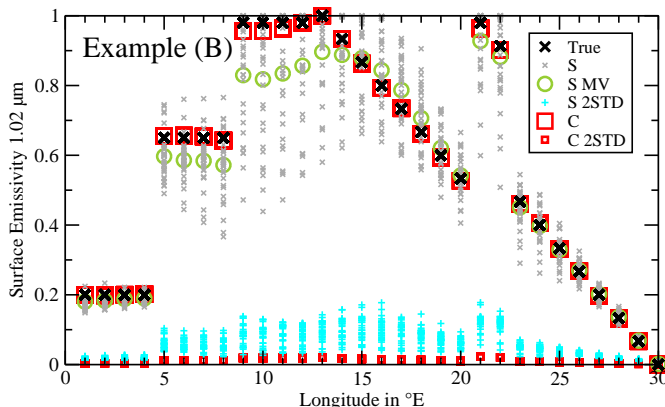


FIGURE IV.4: Comparison of 1.02 μm -surface emissivities of synthetic cube ('True') with corresponding retrieved values for different regularization models. S: single-spectrum results, S MV: their mean values for the respective longitude bins, S 2STD: twice their *a posteriori* standard deviations. C: surface emissivities as parameters common to their respective surface bins, C 2STD: twice their *a posteriori* standard deviations.

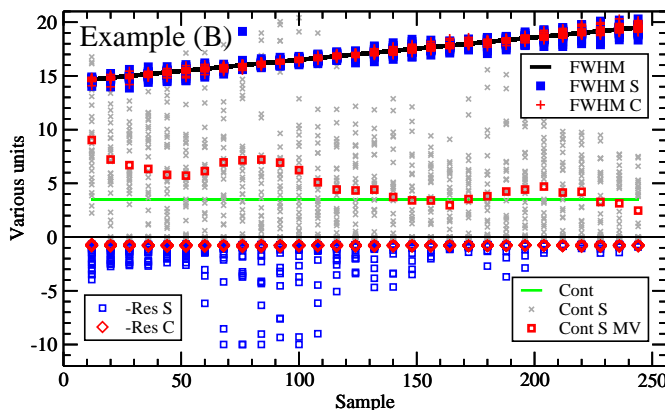


FIGURE IV.5: Detector sample dependence of various parameters. FWHM: 'true' FWHM of instrumental response function in nm, FWHM S: retrieved single-spectrum results, FWHM C: results of correlated retrievals. Cont: 'true' continuum parameter ($3.5 \cdot 10^{-30} \text{ cm}^2$) for 1.18 μm window, Cont S: retrieved continuum parameters (single-spectrum results, same unit), Cont S MV: their mean values for the respective detector sample bins. Retrieved continuum as parameter common to all spectra is 3.32 ± 0.24 in the same unit. Res S: least-squares norms in $10^{-4} \text{ W}/(\text{m}^2 \text{ sr } \mu\text{m})$ of residuals between synthetic and fitted radiances, divided by number of utilized spectral bands (single-spectrum results), Res C: the same for multi-spectrum results.

generated as being acquired by the VIRTIS-M-IR detector that has 256 spatial samples in a row, by the samples with numbers $s = 4 + 8 \cdot \text{Longitude}/^\circ\text{E}$. Cloud modes 2' and 3 are independently varied according to a pseudo-random spatial-temporal pattern with 1000 km correlation length, 10 h correlation time, mean value ≈ 1.0 , and double standard deviation ≈ 0.6 . Along the sample direction, the FWHM of the instrumental response function is varied according to $(17 + (s - 124)/48) \text{ nm}$ which is inspired by test retrievals from actual measurements. Surface emissivities in the spectral transparency windows at 1.02, 1.10, and 1.18 μm

are common to all spectra covering the same respective surface bin. 1.02 μm -surface-emissivity is modeled to span the whole range 0–1 and to have three four-bin plateaus at emissivity levels 0.2, 0.65, and 0.98, as well as an abrupt anomaly around 21.5 °E. Emissivities in the other two surface windows are all set to 0.65. The remaining parameters are as for the reference spectrum (Fig. IV.2 (p. 118)). In particular, the continuum is common to all spectra. Gaussian noise with double standard deviation $2\sigma = 2 \cdot 10^{-3} \text{ W}/(\text{m}^2 \text{ sr } \mu\text{m})$ is added to the synthetic spectra.

In a first stage of the retrieval pipeline, cloud mode factors 2' and 3 (1 ± 20 , 1000 km, 10 h), FWHM ((17 ± 30) nm, 75 samples, 5 h), and continua at 1.31, 1.74, and 2.3 μm ($(1 \pm 10^3) \cdot 10^{-29} \text{ cm}^2$, 0 km, 0 h) are retrieved from 1.295–2.300 μm , where the values in parentheses list *a priori* mean value \pm double standard deviation, correlation length and time of the respective parameter. The second stage retrieves 1.02 μm -surface-emissivity (0.5 ± 20 , 0 km, 0 h), and 1.10 μm - and 1.18 μm -surface-emissivity and -continuum from their respective peaks. The *a priori* standard deviations are set very wide to largely exclude their and the mean values' impact. Results from single- (no common parameters, no *a priori* correlations) and multi-spectrum regularization (continuum common to all spectra, surface emissivities common to all spectra covering the same surface bin, *a priori* correlation lengths and times as given except for common parameters) are compared to true values in Figs. IV.4 and IV.5.

Retrieved single-spectrum continua (only depicted for 1.18 μm) have a large scatter. Their mean values \pm their double standard deviations are $(1.8 \pm 1.2, 0.50 \pm 0.90, 4.8 \pm 7.6, 15.8 \pm 4.2, 124 \pm 50) \cdot 10^{-29} \text{ cm}^2$ for the spectral windows at 1.10, 1.18, 1.31, 1.74, 2.3 μm (note missing 1.02 and 1.28 μm windows). Continua as common parameters \pm their double *a posteriori* standard deviations are $(2.00 \pm 0.09, 0.33 \pm 0.03, 4.2 \pm 0.3, 15.02 \pm 0.07, 119.5 \pm 0.5) \cdot 10^{-29} \text{ cm}^2$ (same windows). The single-spectrum mean values and the multi-spectrum values agree with the true values within the given margins, but the margins for the single-spectrum results are considerably wider. Note that the 95%-confidence intervals for the 900 single-spectrum results (multiply double standard deviations by $1.96/(2 \cdot \sqrt{900})$ according to Student's t-distribution) are in the order of magnitude of the multi-spectrum *a posteriori* double standard deviations, meaning that single-spectrum retrieval has statistically failed to retrieve the continuum.

Retrieved cloud mode 2' factors (mode 3 factors) have a root-mean-square deviation (RMSD) of 0.28 and 0.053 (0.15 and 0.027) to their true values for single- and multi-spectrum results, respectively. As the true modes 2' and 3 have the same mean value and standard deviation, this shows that cloud mode 3 can be retrieved more reliably than mode 2'. MSR results are more reliable than single-spectrum results.

The FWHM can be retrieved quite reliably already for single-spectrum regularization (RMSD 0.31 nm), although MSR results (RMSD 0.19 nm) are more reliable.

Retrieved single-spectrum surface emissivities (only depicted for 1.02 μm , RMSD 0.11) have a large scatter and large *a posteriori* double standard deviations. Their bin-wise mean values do not match very well to the true values. Especially the larger emissivities are difficult to retrieve, since the radiance response to emissivity changes near 1.0 is small compared with changes in the lower emissivity range. This effect amplifies noise impacts at higher emissivities. An additional contribution to the degree of the emissivity underestimation is the presence of the upper emissivity domain boundary. This can be seen in the extreme case where true emissivity is 1 and scattered retrieved values are only allowed to extend to values ≤ 1 such that the mean value must be strictly < 1 for non-zero scatter. Still, the spatial fine structure (plateaus, jumps, anomaly) is resolved to a certain degree. MSR results (RMSD 0.0086) agree well with the true values and have very small *a posteriori* double standard deviations, representing the increased information content per spectrum due to the restriction of the effective size of the parameter space by incorporating finite and infinite *a priori* correlations. As the 1.02 μm -continuum is not retrieved, but set to its true value, wrong single-spectrum 1.02 μm -emissivity mean values are here not related to a wrong continuum in this window, but to wrong cloud modal abundances partly caused by wrong continua between 1.295–2.300 μm , and by convergence to subsidiary minima.

For the not depicted surface emissivities at 1.10 and 1.18 μm , the true values are 0.65 and 0.65 for each of the bins. The retrieved values are scattered according to 0.49 ± 0.8 and 0.69 ± 0.5 with RMSD 0.40 and 0.21 (single-spectrum), and 0.65 ± 0.04 and 0.63 ± 0.02 with RMSD 0.016 and 0.024 (multi-spectrum bins). This shows that MSR results are more reliable than single-spectrum results. Also, emissivities at 1.10 and 1.18 μm are more difficult to retrieve than those at 1.02 μm , in part a consequence of the lower surface radiance contribution in these peaks (Haus and Arnold, 2010, Fig. 5). But it is also due to the utilization of the

'true' 1.02 μm -continuum, and thus, neglect of its retrieval error.

Example (B) underlines that retrieved common parameters (continuum, emissivity) are not just mean values of single-spectrum results. This can be explained by observing the least-squares norms of residuals between synthetic and fitted radiances. While they are very close to the artificial noise level for MSR fits, they are about 60% larger on average for single-spectrum fits. About 30% of the single-spectrum fits are significantly worse than the corresponding MSR fits. As in Example (A), this demonstrates the superiority of MSR in avoiding subsidiary minima of the cost function. Example (B) also illustrates improved disentanglement between parameters with similar Jacobians in two examples for extreme cases of strongly differing *a priori* correlation behavior. The first example is the disentanglement of continua (infinite correlation length and time) from clouds (finite correlation lengths and times) in the first stage of the retrieval pipeline (1.295–2.300 μm). The second example is the disentanglement of surface emissivities (correlation length 0, correlation time ∞) from continua (correlation length ∞ , correlation time ∞) in the second stage of the retrieval pipeline (1.000–1.235 μm).

An example to illustrate the retrieval of locally coupled parameters in presence of spatial-temporal couplings (e.g. temperature altitude profiles with vertical coupling of level temperatures and horizontal spatial-temporal coupling of temperatures from contiguous measurements, preventing arbitrarily large retrieved temperature fluctuations between contiguous levels and footprint locations) will be studied in a subsequent paper.

IV.6 Conclusions and outlook

Currently, VIRTIS-M-IR spectra of Venus' nightside emissions establish the only data source in the infrared with high repetition and spatial resolution, where Venus' surface emissivity can be extracted from on a global scale. A radiative transfer forward model is required to simulate spectra in dependence on surface, atmospheric, and instrumental parameters. A retrieval algorithm iteratively varies these parameters until the simulated well fit the measured spectra. The so-retrieved parameters are interpreted as the surface, atmospheric, and instrumental state that led to the measurements. But single VIRTIS-M-IR spectra have a comparatively low information content, and different parameter combinations can describe the same measurement equally well. Hence, the inversion of the forward model is mathematically an ill-posed problem and must be regularized. A common approach is the minimization of a non-negative retrieval cost function that arises from the incorporation of Bayesian *a priori* mean values, standard deviations, and correlations the retrieval parameters are to respect, as well as measurement and simulation error information. This essentially rules out unlikely state vectors. Still, this cost function is a non-linear function on a possibly high-dimensional space, and it is easy to run into subsidiary local minima far away from the global minimum.

It was exemplarily shown that the multi-spectrum regularization presented in this paper (MSR) can considerably improve the data analysis of contiguous measurements with sparse spectral information content by minimizing a retrieval cost function on a parameter space that encompasses several measurements and that incorporates *a priori* spatial-temporal correlations between the state vectors of the different measurements. This naturally arising regularization decreases the probability to retrieve unlikely spatial-temporal parameter distributions. Uninteresting subsidiary minima of the retrieval cost function and unphysical jumps between them can be better avoided, and the impact of noise can be attenuated.

A detailed error analysis of the single-spectrum retrieval of local surface emissivity at 1.02, 1.10, and 1.18 μm on Venus shows that this parameter is difficult and error-prone to retrieve (Kappel et al., 2012a), as will be presented in a subsequent paper. But neglecting VIRTIS-observable geologic activity on Venus⁶, surface emissivity is common to measurements that repeatedly cover the same surface spot on Venus. In the same way, corrections to the CO₂ opacity in the extreme environmental conditions in the deep atmosphere of Venus ('continuum') are common to all measurements of Venus' nightside emissions. Knowledge gain from single-spectrum retrieval of these hard-to-determine parameters is very limited due to interfering atmospheric variations. As it was shown, their single-spectrum retrieval thus statistically fails, although the spectra are sensible to these parameters.

⁶Note: This does not mean that geologic activity was observed. The formulation rather refers to the principle observability using VIRTIS-M-IR.

But MSR is especially useful to disentangle retrieval parameters with similar Jacobians and strongly differing correlation lengths or times. The extreme case for parameters with infinite correlation lengths or times and identic single-spectrum *a priori* data corresponds to the retrieval of parameters common to certain selections of measurements, so for instance for surface emissivity (correlation length 0, correlation time ∞) and continuum (infinite correlation length and time). It was demonstrated that this approach leads to a better disentanglement of continua from spatially-temporally varying atmospheric parameters and of emissivities from continua, to smaller residuals between measurements and fits, and thus to more reliable retrieval results than corresponding single-spectrum retrievals.

The *a posteriori* retrieval uncertainties are lower for MSR compared to single-spectrum retrievals, as it was shown (see also [Kappel et al., 2012b](#), for real-world examples). This results from the incorporation of the context of adjacent measurements, making more information available that contributes to the determination of the parameters describing a certain spectrum. Especially when single-spectrum information content is low, this is important to improve the quality of the retrieved information. Single-spectrum retrieval, on the other hand, can be regarded as an only very rough approximation of reality, since the presence of spatial-temporal correlations is rather the regular case.

It was verified that a simple smoothing or averaging of retrieved single-spectrum results does in general not lead to correct results or to a consistent parameter set describing the measurements, especially when there are unphysical jumps between different subsidiary minima or parameters close to their domain boundaries. By using MSR, all considered measurements can be parameterized by a fully consistent set of atmospheric, surface, and instrumental parameters that respects all available single- and multi-spectrum *a priori* data as well as the measurement and simulation error distributions. But as always, when regularizing an ill-posed problem, it must be checked that retrieved results do not significantly change for *a priori* and initial guess modifications.

Section IV.5 (p. 120) demonstrated that MSR allows to retrieve continua and surface emissivities from VIRTIS-M-IR measurements, when random measurement errors are assumed to be the only error sources. Note that common parameters retrieved from real-world measured spectra have to be carefully interpreted, since systematic measurement and simulation errors are also common to the spectra. The impact of systematic errors will be discussed in a subsequent paper. First tests revealed that in their presence, knowledge of continua is crucial to reliably retrieve emissivities, and it may be necessary to first assume mean surface emissivities in order to determine surface window continua. The constraint that emissivities globally must be non-negative and must not exceed unity then helps to constrain valid continua. On the other hand, it may be sufficient to utilize more diverse measurements (particularly with respect to topography) to disentangle emissivities and continua, but further studies are required.

[Kappel et al. \(2012b\)](#) already applied MSR to actual VIRTIS-M-IR spectra of Venus' nightside in order to disentangle continua from spatial-temporal atmospheric variations. As shall be presented in a subsequent paper, it will also be applied to retrieve surface emissivity maps of Venus as parameter vectors that are common to measurements that repeatedly cover the same surface bins. Compared to single-spectrum retrieval, this approach also has a higher chance of success, because relative changes in the spatial distribution of surface emissivity may be easier to detect than absolute values. This is a consequence of the underlying physical continuity in spatial-temporal variations of interfering parameters like minor gas and cloud modal distributions, temperature variations, and others. The presented multi-spectrum retrieval algorithm is ideally suited for this task, since it allows to incorporate all these continuity and consistency constraints. In conjunction with a refined consistent data calibration and preprocessing ([Kappel et al., 2012b](#)), retrieval reliability and accuracy can thus be pushed to their limits. However, while the processing time overhead of MSR compared to corresponding single-spectrum retrievals is negligible for up to a few thousand spectra, any retrieval based on full radiative transfer forward model simulations requires considerable computational resources. Thus, MSR will be selectively applied at first to localized targets that were beforehand identified to be of special geological interest ([Arnold et al., 2008](#); [Müller et al., 2008](#); [Smrekar et al., 2010](#)).

IV.A Appendix

Some mathematical derivations and details on the implementation of MSR are presented here.

IV.A.1 Cost function as least squares norm

This appendix reformulates the cost function in terms of a least-squares norm and discusses MSR's inputs, i.e. residual and Jacobian of the extended forward model simulations, as well as its outputs, i.e. the best estimate of the state vector and the corresponding *a posteriori* covariance matrix.

The best estimate of the state vector that is compatible with the *a priori* and error knowledge and adequately parameterizes the measurements, is the global minimum of the cost function F_c from Eq. (IV.1) (p. 107). An iterative algorithm is used to identify local minima of F_c . When a cost function has the form of a least-squares residual norm $\|\mathbf{R}(\mathbf{X})\|_2$, this special structure can be exploited to improve numerical efficiency, like it is done by the numerically quite robust trust region formulation of the Levenberg-Marquardt algorithm (Moré, 1978). Here, an \mathbf{X} is determined that locally minimizes the least-squares norm, or equivalently $\|\mathbf{R}(\mathbf{X})\|_2^2$. To see that F_c has this structure, define the 'scaled residual' in the notation of Section IV.2 (p. 105)

$$\mathbf{R}(\mathbf{X}) := \begin{pmatrix} \mathbf{S}_A^{-1/2}(\mathbf{X} - \mathbf{A}) \\ \mathbf{S}_E^{-1/2}(\mathbf{Y} - \mathbf{F}(\mathbf{X})) \end{pmatrix} \in \mathbb{R}^{N+M}, \quad (\text{IV.A.1})$$

which implies $\|\mathbf{R}(\mathbf{X})\|_2^2 = \mathbf{R}(\mathbf{X})^T \mathbf{R}(\mathbf{X}) = F_c(\mathbf{X})$. \mathbf{R} is a mapping from \mathbb{R}^N to \mathbb{R}^{N+M} . $\mathbf{S}_A^{-1/2}$ is such that $(\mathbf{S}_A^{-1/2})^T \mathbf{S}_A^{-1/2} = \mathbf{S}_A^{-1}$, and analogously with \mathbf{S}_E . $\mathbf{S}_A^{-1/2}$ is the inverse square root of the positive definite symmetric matrix \mathbf{S}_A and is here not computed by using spectral decomposition, but by the numerically fast and stable Cholesky decomposition. Any real, symmetric, positive definite $N \times N$ matrix \mathbf{S}_A can be Cholesky decomposed into the product $\mathbf{S}_A = \mathbf{U}^T \mathbf{U}$ of the transpose of an upper triangular matrix \mathbf{U} and \mathbf{U} itself by using asymptotically $N^3/3$ (Golub and van Loan, 1996, Section 4.2) arithmetical operations, compared to $9N^3$ arithmetical operations for diagonalization by the symmetric QR algorithm (Golub and van Loan, 1996, Section 8.3). $(\mathbf{U}^T)^{-1} =: \mathbf{U}^{-T} =: \mathbf{S}_A^{-1/2}$ is then an inverse matrix square root of \mathbf{S}_A in the required sense. See Appendix IV.A.2 for an efficient computation for matrices \mathbf{S}_A with a structure as presented in Section IV.3 (p. 107). The difference to the matrix square root, if defined by matrix diagonalization, is just an orthogonal transformation of $\mathbf{R}(\mathbf{X})$ that is consequently not observable when minimizing the least-squares norm of $\mathbf{R}(\mathbf{X})$. The inverse square root of \mathbf{S}_E , when assumed to be a diagonal matrix, is just the matrix \mathbf{S}_E with its diagonal entries replaced by their inverse square roots.

The Jacobian \mathbf{J} of \mathbf{R} is needed as input to the iterative algorithm (Moré, 1978) and follows from Eq. (IV.A.1) as

$$\mathbf{J}(\mathbf{X}) = \nabla \mathbf{R}(\mathbf{X}) = \begin{pmatrix} \mathbf{S}_A^{-1/2} \\ -\mathbf{S}_E^{-1/2} \mathbf{K}(\mathbf{X}) \end{pmatrix} \in \mathbb{R}^{N+M} \times \mathbb{R}^N, \quad (\text{IV.A.2})$$

with the Jacobian \mathbf{K} of the forward model \mathbf{F} . $\mathbf{J}(\mathbf{X})$ is the largest data structure in MSR and determines the problem size still manageable on a given computer hardware. Sparse matrix formulation of $\mathbf{J}(\mathbf{X})$, and thereby of the entire retrieval algorithm, considerably increases that limit and is discussed in Appendix IV.A.4 (p. 133).

When the best estimate of \mathbf{X} is denoted by $\hat{\mathbf{X}}$ (the retrieved solution), the $N \times N$ -dimensional *a posteriori* covariance matrix $\hat{\mathbf{S}}$ at the retrieved solution follows from (compare Eq. (IV.2) (p. 107))

$$\hat{\mathbf{S}}^{-1} = (\mathbf{J}(\hat{\mathbf{X}}))^T \mathbf{J}(\hat{\mathbf{X}}). \quad (\text{IV.A.3})$$

The corresponding correlation matrix $\hat{\mathbf{C}}$ follows from Eq. (IV.3) (p. 108). The block structures of $\hat{\mathbf{S}}$ and $\hat{\mathbf{C}}$ are inherited from the structure of $\hat{\mathbf{X}}$. The diagonal entries $(\hat{\mathbf{S}})_{ii}$ of $\hat{\mathbf{S}}$ are the variances σ_i^2 of the retrieved parameters according to the *a posteriori* probability distribution. $2\sigma_i$ provides a first measure for the retrieval uncertainty, but a detailed retrieval error analysis should be performed in addition, as will be presented in a subsequent paper. The off-diagonal entries of $\hat{\mathbf{C}}$ provide an estimate on how well a retrieved parameter is disentangled from the influences of other parameters. An absolute value close to 1 indicates bad disentanglement.

$\widehat{\mathbf{C}}$ may be costly to compute and to store, and often, it is sufficient to compute the blocks corresponding to a few measurements and the related common-parameter-blocks. This already provides a good impression on the disentanglement of common from local parameters, the correlations between parameters associated to different measurements, between common parameters, and between local parameters belonging to one measurement. For an efficient computation of the diagonal entries of $\widehat{\mathbf{S}}$ and a few representative off-diagonal entries of $\widehat{\mathbf{C}}$, see Appendix IV.A.4 (p. 133). Note that the correct weighting of the common parameters (Appendix IV.A.3 (p. 129)) affects both $\widehat{\mathbf{X}}$ and $\widehat{\mathbf{S}}$.

Violations of the retrieval parameters' physical domain boundaries are prevented by the logarithmic barrier method (Nocedal and Wright, 1999, Section 17.2), but with slight modifications to match the presented least-squares-norm formulation. The barrier function B^2 is added to the cost function F_c as a penalty for each parameter $(\mathbf{X})_i$ that approaches one of its domain boundaries (e.g. 0 or 1 for the 1.02 μm -surface-emissivity of a certain spectrum), where⁷ $B(\mathbf{X}) := -\mu \sum_{i=1}^N \log(c_i[(\mathbf{X})_i])$. B^2 is chosen as barrier function instead of B , to allow better incorporation into the least-squares formulation of F_c by introducing an additional dimension to $\mathbf{R}(\mathbf{X})$ with the entry $B(\mathbf{X})$, such that $\mathbf{R}(\mathbf{X})^T \mathbf{R}(\mathbf{X})$ corresponds to the original $F_c(\mathbf{X})$ plus $(B(\mathbf{X}))^2$. c_i is continuous, piecewise differentiable, positive when $(\mathbf{X})_i$ is inside its domain, and linearly approaches 0 at the boundaries. As an additional modification, to minimize impact of the barrier function, $\log(c_i)$ shall be 0 outside a certain small boundary region within the domain. To remove the influence of B on the retrieved result, μ is decreased by a factor of 10 each time a certain number of iterations is completed, until $B(\mathbf{X})$ is neglectable compared to the original⁸ $F_c(\mathbf{X})$. When an iteration step would lead a number of parameters to violate a domain boundary, they are set back into their domain, close (dependent on μ) to the boundary. This prevents the trust region radius to contract to zero too early and still leads to correct results. The Jacobian of \mathbf{R} including the barrier dimension follows immediately by differentiation. For μ small enough, $\widehat{\mathbf{S}}$ is unaffected by B .

IV.A.2 Inverse square root of a priori covariance matrix

This appendix discusses the efficient computation of the inverse square root $\mathbf{S}_A^{-1/2}$ of the covariance matrix \mathbf{S}_A as needed in Appendix IV.A.1. As \mathbf{S}_A is block diagonal with \mathbf{S}_C and \mathbf{S}_L on its diagonal (Section IV.3.5 (p. 116)), the inverse square roots of \mathbf{S}_C and \mathbf{S}_L can be computed independently. Even for larger retrieval problems, \mathbf{S}_C is of rather low dimension (see example in Appendix IV.A.4 (p. 133)), and it is already efficient to Cholesky decompose $\mathbf{S}_C =: \mathbf{U}^T \mathbf{U}$ and to compute $\mathbf{S}_C^{-1/2} := \mathbf{U}^{-T}$. But \mathbf{S}_L , for instance for thousands of measurements and ten retrieval parameters per measurement, is of the order of dimension $10,000 \times 10,000$ and costly to Cholesky decompose. However, the Kronecker product structure of \mathbf{S}_L (Section IV.3.4 (p. 113)) allows for a computational shortcut. Without loss of generality, retrieval of common parameters is not considered here, i.e. \mathbf{S}_A is assumed to only comprise \mathbf{S}_L to share notation with Section IV.3.4 (p. 113).

According to Golub and van Loan (1996, Section 4.5.5), Cholesky decomposition and Kronecker multiplication commute in the sense that

$$\mathbf{U}_S^T \mathbf{U}_S = \mathbf{S} := \mathbf{H} \otimes \mathbf{G} = (\mathbf{U}_H^T \mathbf{U}_H) \otimes (\mathbf{U}_G^T \mathbf{U}_G) = (\mathbf{U}_H \otimes \mathbf{U}_G)^T (\mathbf{U}_H \otimes \mathbf{U}_G)$$

with obvious notation. This is due to the relations $(\mathbf{A} \otimes \mathbf{B})^T = \mathbf{A}^T \otimes \mathbf{B}^T$ and $(\mathbf{A} \otimes \mathbf{B})(\mathbf{C} \otimes \mathbf{D}) = (\mathbf{AC}) \otimes (\mathbf{BD})$ (which also implies $(\mathbf{A} \otimes \mathbf{B})^{-1} = \mathbf{A}^{-1} \otimes \mathbf{B}^{-1}$) (Horn and Johnson, 1991, Section 4.2), and the fact that the Kronecker product of upper triangular matrices is upper triangular, all following immediately from definition. This can be used to rearrange the computation of $\mathbf{S}_A^{-1/2}$ as follows.

\mathbf{S}_A is defined as $\mathbf{C}_A := (\mathbf{\Pi}_n^r)^T \overline{\mathbf{C}}_A \mathbf{\Pi}_n^r$ (Section IV.3.4 (p. 113)) scaled with respect to the *a priori* standard deviations σ_k of the retrieval parameters (Eq. (IV.3) (p. 108)) with $\overline{\mathbf{C}}_A$ from Eq. (IV.15) (p. 115).

As a first step, it can be verified that \mathbf{S}_A may also be computed by first scaling the \mathbf{h}_g in Eq. (IV.15) (p. 115) with the *a priori* standard deviations, and only then to perform the Kronecker products, form the large block

⁷Corrected: In the published paper, the sum mistakenly extended from $i = 0$ to N . Note that, according to the subsequent definition of the c_i , the penalty is zero for a parameter not close to a boundary (this includes parameters where there is no boundary), and thus, the sum can extend over all N retrieval parameters including the ones not close to a boundary.

⁸Corrected: In the published paper, the term 'the original' was mistakenly omitted.

diagonal matrix, and finally permute. Herefore, observe that

$$(\mathbf{S}_A)_{n(i-1)+k, n(j-1)+l} = \sigma_k \sigma_l (\overline{\mathbf{C}}_A)_{r(k-1)+i, r(l-1)+j}, \quad (\text{IV.A.4})$$

for all measurements $i, j \in \{1, \dots, r\}$ and for all parameters $k, l \in \{1, \dots, n\}$, corresponding to Eq. (IV.16) (p. 115) and considering the permutation in the definition of \mathbf{C}_A .

Let \mathbf{h} be the block diagonal matrix with the matrices $\mathbf{h}_1, \dots, \mathbf{h}_G$ on its diagonal and entries h_{kl} . \mathbf{H} shall be the covariance matrix that arises from \mathbf{h} , i.e. $H_{kl} = \sigma_k \sigma_l h_{kl}$, and the blocks on the diagonal of the block matrix \mathbf{H} are denoted by $\mathbf{H}_1, \dots, \mathbf{H}_G$. According to Eqs. (IV.15) (p. 115) and (IV.10) (p. 114), Eq. (IV.A.4) can then be written as

$$(\mathbf{S}_A)_{n(i-1)+k, n(j-1)+l} = \sigma_k \sigma_l h_{kl}(\boldsymbol{\varrho}_g)_{ij} = H_{kl}(\boldsymbol{\varrho}_g)_{ij},$$

where $g \in \{1, \dots, G\}$ depends on the partitioning of \mathbf{h} . Hence, $\mathbf{S}_A = (\mathbf{\Pi}_n^r)^T \overline{\mathbf{S}}_A \mathbf{\Pi}_n^r$, with

$$\overline{\mathbf{S}}_A := \begin{pmatrix} \mathbf{H}_1 \otimes \boldsymbol{\varrho}_1 & \cdots & 0 \\ \vdots & \ddots & \vdots \\ 0 & \cdots & \mathbf{H}_G \otimes \boldsymbol{\varrho}_G \end{pmatrix}. \quad (\text{IV.A.5})$$

Incidentally, this requires fewer multiplications for the scaling, since \mathbf{h} has to be scaled just once (n^2 multiplications), whereas for the scaling of \mathbf{C}_A , each of the r^2 blocks of size $n \times n$ has to be scaled.

Next, observe that the block diagonal structure of $\overline{\mathbf{S}}_A$ and the uniqueness of Cholesky decomposition ensure that the upper triangular Cholesky factor $\overline{\mathbf{U}}$ of $\overline{\mathbf{S}}_A = \overline{\mathbf{U}}^T \overline{\mathbf{U}}$ is block diagonal with the upper triangular Cholesky factors \mathbf{U}_g of the single blocks $\mathbf{H}_g \otimes \boldsymbol{\varrho}_g = \mathbf{U}_g^T \mathbf{U}_g$ as the blocks on its diagonal.

$$\overline{\mathbf{S}}_A = \overline{\mathbf{U}}^T \overline{\mathbf{U}} = \begin{pmatrix} \mathbf{U}_1^T & \cdots & 0 \\ \vdots & \ddots & \vdots \\ 0 & \cdots & \mathbf{U}_G^T \end{pmatrix} \begin{pmatrix} \mathbf{U}_1 & \cdots & 0 \\ \vdots & \ddots & \vdots \\ 0 & \cdots & \mathbf{U}_G \end{pmatrix}$$

Clearly, $\overline{\mathbf{U}}$ is upper triangular. Since Cholesky decomposition and Kronecker multiplication commute, each \mathbf{U}_g can be computed as $\mathbf{U}_g = \mathbf{U}_{\mathbf{H}_g} \otimes \mathbf{U}_{\boldsymbol{\varrho}_g}$ with obvious notation. Note that the \mathbf{U}_g are possibly all of different dimension $n_g r \times n_g r$.

Consider the permutation $(\mathbf{\Pi}_n^r)^T(\cdot)\mathbf{\Pi}_n^r$ that maps the index pair $(r(k-1)+i, r(l-1)+j)$ to $(n(i-1)+k, n(j-1)+l)$. According to the definition of the Kronecker product, each \mathbf{U}_g is a block matrix with blocks of size $r \times r$ that are all upper triangular. Thus, $\overline{\mathbf{U}}$ also is an upper triangular block matrix with blocks of size $r \times r$ that are all upper triangular. Hence, the indices of the entries $\overline{U}_{r(k-1)+i, r(l-1)+j}$ that are non-zero, satisfy $k \leq l$ and $i \leq j$. This implies $n(i-1)+k \leq n(j-1)+l$, i.e. that $(\mathbf{\Pi}_n^r)^T \overline{\mathbf{U}} \mathbf{\Pi}_n^r$ is upper triangular. This proves that $((\mathbf{\Pi}_n^r)^T \overline{\mathbf{U}} \mathbf{\Pi}_n^r)^T ((\mathbf{\Pi}_n^r)^T \overline{\mathbf{U}} \mathbf{\Pi}_n^r) = (\mathbf{\Pi}_n^r)^T \overline{\mathbf{S}}_A \mathbf{\Pi}_n^r = \mathbf{S}_A$ is a (i.e. *the*) Cholesky factorization of $\mathbf{S}_A = \mathbf{U}^T \mathbf{U}$, with upper triangular Cholesky factor $\mathbf{U} = (\mathbf{\Pi}_n^r)^T \overline{\mathbf{U}} \mathbf{\Pi}_n^r$, i.e. \mathbf{U} can be computed by permuting $\overline{\mathbf{U}}$.

Finally, observe that

$$\mathbf{S}_A^{-1/2} := \mathbf{U}^{-T} = ((\mathbf{\Pi}_n^r)^T \overline{\mathbf{U}} \mathbf{\Pi}_n^r)^{-T} = (\mathbf{\Pi}_n^r)^T \overline{\mathbf{U}}^{-T} \mathbf{\Pi}_n^r.$$

Note that the transposed inverse of the upper triangular matrix \mathbf{U} is lower triangular. Also, as $\overline{\mathbf{U}}$ is upper triangular, $\overline{\mathbf{U}}^{-T}$ is lower triangular. Due to the block diagonal structure of $\overline{\mathbf{U}}$, its inverse can simply be computed by forming the block diagonal matrix with the \mathbf{U}_g^{-1} as the blocks on its diagonal. Because of $[\mathbf{A} \otimes \mathbf{B}]^{-1} = \mathbf{A}^{-1} \otimes \mathbf{B}^{-1}$ and $[\mathbf{A} \otimes \mathbf{B}]^T = \mathbf{A}^T \otimes \mathbf{B}^T$, it finally follows

$$\mathbf{S}_A^{-1/2} = (\mathbf{\Pi}_n^r)^T \begin{pmatrix} \mathbf{U}_{\mathbf{H}_1}^{-T} \otimes \mathbf{U}_{\boldsymbol{\varrho}_1}^{-T} & \cdots & 0 \\ \vdots & \ddots & \vdots \\ 0 & \cdots & \mathbf{U}_{\mathbf{H}_G}^{-T} \otimes \mathbf{U}_{\boldsymbol{\varrho}_G}^{-T} \end{pmatrix} \mathbf{\Pi}_n^r. \quad (\text{IV.A.6})$$

Thus, direct Cholesky decomposition of $\mathbf{S}_A = \mathbf{U}^T \mathbf{U}$ and inversion of \mathbf{U} can be avoided. Only the $G n_g \times n_g$ -dimensional matrices \mathbf{H}_g and the $G r \times r$ -dimensional matrices $\boldsymbol{\varrho}_g$ need to be Cholesky decomposed and their upper triangular factors inverted. Permutation and Kronecker multiplication are computationally fast operations. Compare for large r the number of arithmetic operations for the resource dominating Cholesky decompositions: $(nr)^3/3$ for \mathbf{S}_A vs. $\sum_{g=1}^G n_g^3/3 + Gr^3/3$ for the Cholesky decompositions involved in Eq. (IV.A.6). For $r \gg n$, $\sum_{g=1}^G n_g^3/3$ can be neglected against $Gr^3/3$, and the speedup is of the order of n^3/G , which exceeds n^2 due to $G \leq n$. Generically, for ten retrieval parameters per measurement, the speedup exceeds 100. Incidentally, this framework is also ideally suited for the sparse matrix formulation of MSR, as will be seen in Appendix IV.A.4 (p. 133).

IV.A.3 Limit for perfect spatial-temporal coupling

In this appendix, the limit of retrieved values for ever stronger spatial or temporal coupling between r measurements for c single-spectrum parameters with identic single-spectrum *a priori* data will be discussed. It will be shown that computing this limit is equivalent to retrieving c parameters common to these measurements in the sense of Section IV.2 (p. 105), with a certain relative weighting between common and not-common ('local', i.e. spatially-temporally varying) parameters. It suffices to show that in both approaches, the *a posteriori* probability distribution (Section IV.2 (p. 105)) yields the same best estimates and uncertainties of the retrieval parameters. The main purpose of this section is the derivation of the proper relative weighting between the common and the local parameters in the *a priori* covariance matrix. From the outset, it is not clear whether there is a statistical \sqrt{r} -like relative weighting factor that reflects the influence of a common parameter on r spectra.

First, the setting will be defined by considering the permuted parameter space (Eq. (IV.13) (p. 114)). The corresponding *a priori* covariance matrix $\bar{\mathbf{S}}_A$ can be written as in Eq. (IV.A.5). Parameters with, in the limit, perfect spatial or temporal coupling ('perfect-coupling-parameters') must be implemented as separate from, and without inter-group coupling to parameter groups describable by constant finite spatial or temporal coupling ('finite-coupling-parameters'), as they obey different spatial-temporal correlation behavior (Section IV.3.4 (p. 113)). To allow coupling between themselves, these perfect-coupling-parameters may well be combined into one single group, since they can be described by identical spatial-temporal correlation behavior. Denote this parameter group by the index P , such that $\bar{\mathbf{S}}_A = \begin{pmatrix} \bar{\mathbf{S}}_P & 0 \\ 0 & \bar{\mathbf{S}}_L \end{pmatrix}$. Here, $\bar{\mathbf{S}}_L$ is the *a priori* covariance matrix for the finite-coupling-parameters (for the permuted parameter space) and can be written as in Eq. (IV.A.5). Because the perfect-coupling-parameters shall all have identic single-spectrum *a priori* data, their *a priori* covariance matrix can be written $\bar{\mathbf{S}}_P := \mathbf{H}_C \otimes \boldsymbol{\varrho}_P$, where the $r \times r$ matrix $\boldsymbol{\varrho}_P$ describes their spatial-temporal coupling, and \mathbf{H}_C is their (for all measurements the same!) $c \times c$ single-spectrum *a priori* covariance matrix. Let the perfect-coupling-group comprise the parameter vector $\bar{\mathbf{p}} = \mathbf{\Pi}_c^r \mathbf{p} = (\bar{\mathbf{p}}_1, \dots, \bar{\mathbf{p}}_c)$ analog to the notation in Eq. (IV.13) (p. 114) for the permuted parameter space. $\bar{\mathbf{p}}_k \in \mathbb{R}^r$ is for each $k \in \{1, \dots, c\}$ a vector describing the spatial-temporal distribution of single-spectrum parameter number k , and $(\bar{\mathbf{p}}_k)_i = (\mathbf{p}_i)_k$ is the parameter number k of measurement $i \in \{1, \dots, r\}$.

For easier notation, the limit will be computed by using the unpermuted parameter spaces (Eq. (IV.12) (p. 114)) separately for the perfect- and for the finite-coupling-parameters, i.e. the permutation $(\mathbf{\Pi}_{c,n}^r)^T$ will be applied to the permuted parameter space, and correspondingly $(\mathbf{\Pi}_{c,n}^r)^T(\cdot)\mathbf{\Pi}_{c,n}^r$ to $\bar{\mathbf{S}}_A$, where $\mathbf{\Pi}_{c,n}^r := \begin{pmatrix} \mathbf{\Pi}_c^r & 0 \\ 0 & \mathbf{\Pi}_n^r \end{pmatrix}$. This has the advantage of being able to work in the respective unpermuted spaces while still transparently separating perfect- from finite-coupling-parameters in the *a priori* covariance matrix. It does not change results, provided it is kept track of the associations of the entries of the matrix to the entries of the parameter space. Hence, $\mathbf{S}_A = \begin{pmatrix} \mathbf{S}_P & 0 \\ 0 & \mathbf{S}_L \end{pmatrix}$ and $(\mathbf{p}_1, \dots, \mathbf{p}_r, \mathbf{x}_1, \dots, \mathbf{x}_r)$ are the basic quantities to work with, where $\mathbf{p}_i \in \mathbb{R}^c$ and $\mathbf{x}_i \in \mathbb{R}^n$, and the i -independent (identic single-spectrum *a priori* data!) *a priori* mean value vector for the \mathbf{p}_i is $\mathbf{a}_P \in \mathbb{R}^c$ and that for the \mathbf{x}_i is $\mathbf{a} \in \mathbb{R}^n$.

It will now be shown that in the limit of perfect spatial or temporal coupling between the \mathbf{p}_i that have identic single-spectrum *a priori* data, the retrieved values of the \mathbf{p}_i all coincide, i.e. that \mathbf{p}_1 is common to the r measurements. Also, it will follow directly from the *a posteriori* probability distribution that the proper relative weighting between the common and the local parameters is exactly 1.

First, some additional notational conventions shall be fixed. Denote $\mathbf{p}_i - \mathbf{a}_P =: \mathbf{z}_i$ and $\mathbf{x}_i - \mathbf{a} =: \mathbf{Z}_i$ with $\mathbf{z} = (\mathbf{z}_1, \dots, \mathbf{z}_r)$ and $\mathbf{Z} = (\mathbf{Z}_1, \dots, \mathbf{Z}_r)$, such that $(\mathbf{z}, \mathbf{Z}) =: \mathbf{W}$ is the partial permutation of the parameter vector \mathbf{X} translated by its *a priori* mean value vector. The *a posteriori* probability distribution $P_p(\mathbf{X}|\mathbf{Y}) = \frac{1}{N} \exp(-\frac{1}{2}F_c(\mathbf{X}))$, compare Eq. (IV.1) (p. 107) with normalization factor N can now be written as

$$-2 \log(N \tilde{P}_p(\mathbf{W}|\mathbf{Y})) = \mathbf{W}^T \mathbf{S}_A^{-1} \mathbf{W} + (\mathbf{Y} - \tilde{\mathbf{F}}(\mathbf{W}))^T \mathbf{S}_E^{-1} (\mathbf{Y} - \tilde{\mathbf{F}}(\mathbf{W}))$$

with correspondingly transformed functions marked by tildes. In particular, $\tilde{\mathbf{F}}(\mathbf{W}) := \mathbf{F}((\mathbf{p}_1, \mathbf{x}_1), \dots, (\mathbf{p}_r, \mathbf{x}_r)) = (\mathbf{f}_1(\mathbf{p}_1, \mathbf{x}_1), \dots, \mathbf{f}_r(\mathbf{p}_r, \mathbf{x}_r))$, compare notation in Section IV.2 (p. 105) not considering \mathbf{x}_C .

Let the strength of the spatial-temporal coupling of the parameters \mathbf{z} be parameterized by ε . In the limit of $\varepsilon \downarrow 0$, it shall continuously approach perfect spatial or temporal coupling ('or' also allows 'spatial and temporal'). Of the two blocks on the diagonal of the block diagonal matrix \mathbf{S}_A , the first block $\mathbf{S}_P(\varepsilon)$ is associated to the parameters \mathbf{z} and depends on ε , and the other block \mathbf{S}_L is associated to the parameters \mathbf{Z} and does not depend on ε . Clearly, $\lim_{\varepsilon \downarrow 0} \mathbf{S}_P(\varepsilon) = \lim_{\varepsilon \downarrow 0} (\boldsymbol{\varrho}_P(\varepsilon) \otimes \mathbf{H}_C) = \mathbf{1}_{r \times r} \otimes \mathbf{H}_C$, where $\mathbf{1}_{r \times r}$ is the $r \times r$ matrix with all entries 1. $\mathbf{1}_{r \times r}$ is degenerate and thus has no inverse. This is the reason, why the *a posteriori* probability distribution for perfect coupling has to be defined by a limit. Note that the normalization factor N depends on ε . For $\varepsilon > 0$, the inverse of \mathbf{S}_A is the block diagonal matrix with the inverses of the blocks of \mathbf{S}_A as its blocks on the diagonal. The *a posteriori* probability distribution⁹ for \mathbf{z} , $P_z(\mathbf{z}, \varepsilon) := \int \tilde{P}_p((\mathbf{z}, \mathbf{Z})|\mathbf{Y}) d\mathbf{Z}$, for finite ε can thus be written

$$P_z(\mathbf{z}, \varepsilon) =: \frac{1}{N_1(\varepsilon)} \exp\left(-\frac{1}{2} \mathbf{z}^T \mathbf{S}_P^{-1}(\varepsilon) \mathbf{z}\right) \frac{1}{N_2(\varepsilon)} G(\mathbf{z}), \quad (\text{IV.A.7})$$

where $G(\mathbf{z}) := \int \exp(-\frac{1}{2} G_0(\mathbf{z}, \mathbf{Z})) d\mathbf{Z}$ with auxiliary term

$$G_0(\mathbf{z}, \mathbf{Z}) := \mathbf{Z}^T \mathbf{S}_L^{-1} \mathbf{Z} + (\mathbf{Y} - \tilde{\mathbf{F}}(\mathbf{W}))^T \mathbf{S}_E^{-1} (\mathbf{Y} - \tilde{\mathbf{F}}(\mathbf{W})). \quad (\text{IV.A.8})$$

Here, $N_1(\varepsilon) := \int \exp(-\frac{1}{2} \mathbf{z}^T \mathbf{S}_P^{-1}(\varepsilon) \mathbf{z}) d\mathbf{z}$ is the normalization factor for the exponential term in Eq. (IV.A.7) that is going to be singular in the limit, and $N_2(\varepsilon)$ is such that $\int P_z(\mathbf{z}, \varepsilon) d\mathbf{z} = 1$. Note that $N_2(\varepsilon)$ does not normalize $G(\mathbf{z})$ in general, and that the normalization is split into two factors $N_1(\varepsilon)$ and $N_2(\varepsilon)$ in order to separate singular from regular terms to properly manage the limit functions.

In order to properly define the *a priori* covariance matrix for the retrieval of common parameters, $\lim_{\varepsilon \downarrow 0} P_z(\mathbf{z}, \varepsilon)$ has to be evaluated. Since $\mathbf{S}_P(\varepsilon)$ degenerates in the limit, $P_z(\cdot, \varepsilon)$ shall be regarded as tempered distribution. See Reed and Simon (1981, Section V.3) for distribution theory. Let test function φ be an element of Schwartz space, the space of rapidly decreasing infinitely differentiable functions. Then $\lim_{\varepsilon \downarrow 0} \int P_z(\mathbf{z}, \varepsilon) \varphi(\mathbf{z}) d\mathbf{z}$ provides the *a posteriori* probability distribution in the sense of distribution theory. This term shall now be rearranged in order to compute the limit.

Let $\varepsilon > 0$. The first factor of $\mathbf{S}_P(\varepsilon) = \boldsymbol{\varrho}_P(\varepsilon) \otimes \mathbf{H}_C$, the matrix $\boldsymbol{\varrho}_P(\varepsilon)$, is real symmetric and can thus be diagonalized by an orthogonal matrix $\mathbf{Q}(\varepsilon)$ that consists of eigenvectors of $\boldsymbol{\varrho}_P(\varepsilon)$ (Horn and Johnson, 1990, Theorem 4.1.5), i.e. $\boldsymbol{\varrho}_P(\varepsilon) = \mathbf{Q}(\varepsilon) \mathbf{D}(\varepsilon) \mathbf{Q}^T(\varepsilon)$, where the diagonal matrix $\mathbf{D}(\varepsilon)$ has the corresponding eigenvalues $D_{ii}(\varepsilon)$ on its diagonal. The eigenvalues are continuous functions of the entries of $\boldsymbol{\varrho}_P(\varepsilon)$ (Serre, 2010, Theorem 5.2). Moreover, an algebraically simple eigenvalue is an analytic function of perturbations of the matrix entries, and so is the corresponding eigenvector (Serre, 2010, Theorem 5.3). For eigenvalues that are not algebraically simple, the eigenvectors need not be continuous. The eigenvalues of $\lim_{\varepsilon \downarrow 0} \boldsymbol{\varrho}_P(\varepsilon) = \mathbf{1}_{r \times r}$ are r and 0 , and r is an algebraically simple eigenvalue with eigenvector $(1, \dots, 1)^T = \mathbf{1}_r$. Here, $\mathbf{1}_r \in \mathbb{R}^r$ is the vector with all entries 1. Therefore, and since $\boldsymbol{\varrho}_P(\varepsilon)$ continuously depends on ε , $\mathbf{D}(\varepsilon)$ and $\mathbf{Q}(\varepsilon)$ can be written as

$$\mathbf{D}(\varepsilon) = \begin{pmatrix} r + d_1(\varepsilon) & 0 & \dots & 0 \\ 0 & d_2(\varepsilon) & \ddots & \vdots \\ \vdots & \ddots & \ddots & 0 \\ 0 & \dots & 0 & d_r(\varepsilon) \end{pmatrix} \quad \text{and} \quad \mathbf{Q}(\varepsilon) = \begin{pmatrix} (1 + q_1(\varepsilon))/v(\varepsilon) \\ (1 + q_2(\varepsilon))/v(\varepsilon) \\ \vdots \\ (1 + q_r(\varepsilon))/v(\varepsilon) \end{pmatrix} \Bigg| \begin{matrix} \\ \\ \\ * \end{matrix}, \quad (\text{IV.A.9})$$

⁹Corrected: In the published paper, $\tilde{P}_p((\mathbf{z}, \mathbf{Z})|\mathbf{Y})$ in the present line was mistakenly written $\tilde{P}_p(\mathbf{z}, \mathbf{Z})|\mathbf{Y}$.

where $D_{ii}(\varepsilon) > 0$ for $\varepsilon > 0$ and $\lim_{\varepsilon \downarrow 0} d_i(\varepsilon) = 0$. Furthermore, $\lim_{\varepsilon \downarrow 0} q_i(\varepsilon) = 0$, and $v(\varepsilon)$ normalizes the first column of $\mathbf{Q}(\varepsilon)$, whence $\lim_{\varepsilon \downarrow 0} v(\varepsilon) = \sqrt{r}$. While v and all d_j and q_i are continuous in ε , the remaining columns $*$ of $\mathbf{Q}(\varepsilon)$ need not be continuous functions of ε . However, the absolute values of their entries are bounded from above by 1, since $\mathbf{Q}(\varepsilon)$ is orthogonal.

Let $\sqrt{\mathbf{D}^{-1}(\varepsilon)}$ be the diagonal matrix with the entries $(D_{ii}(\varepsilon))^{-1/2}$ on its diagonal. Then by using the identity matrix $\mathbb{1}_{c \times c}$ of dimension $c \times c$, the substitution $\boldsymbol{\xi} := [(\sqrt{\mathbf{D}^{-1}(\varepsilon)}\mathbf{Q}^T(\varepsilon)) \otimes \mathbb{1}_{c \times c}]\mathbf{z}$ yields for $\int P_z(\mathbf{z}, \varepsilon)\varphi(\mathbf{z}) d\mathbf{z}$:

$$\int \frac{(\det \mathbf{D}(\varepsilon))^{c/2}}{N_1(\varepsilon)} \exp\left(-\frac{1}{2}\boldsymbol{\xi}^T[\mathbb{1}_{r \times r} \otimes \mathbf{H}_C^{-1}]\boldsymbol{\xi}\right) \cdot \frac{1}{N_2(\varepsilon)} G(\boldsymbol{\psi}(\varepsilon, \boldsymbol{\xi})) \cdot \varphi(\boldsymbol{\psi}(\varepsilon, \boldsymbol{\xi})) d\boldsymbol{\xi}, \quad (\text{IV.A.10})$$

with $\boldsymbol{\psi}(\varepsilon, \boldsymbol{\xi}) = [(\mathbf{Q}(\varepsilon)\sqrt{\mathbf{D}(\varepsilon)}) \otimes \mathbb{1}_{c \times c}]\boldsymbol{\xi}$. This is a consequence of the change-of-variables formula $\int_{\boldsymbol{\psi}(V)} f(\mathbf{z}) d\mathbf{z} = \int_V f(\boldsymbol{\psi}(\boldsymbol{\xi})) |\det \mathbf{J}_{\boldsymbol{\psi}}(\boldsymbol{\xi})| d\boldsymbol{\xi}$ (Rudin, 1974, Theorems 8.26, 8.28) and due to

$$|\det [(\mathbf{Q}(\varepsilon)\sqrt{\mathbf{D}(\varepsilon)}) \otimes \mathbb{1}_{c \times c}]| = |\det (\mathbf{Q}(\varepsilon)\sqrt{\mathbf{D}(\varepsilon)})|^c = (\det \mathbf{D}(\varepsilon))^{c/2},$$

which holds because of $\det (\mathbf{A} \otimes \mathbf{B}) = (\det \mathbf{A})^n (\det \mathbf{B})^m$ for matrices \mathbf{A} of dimension $m \times m$ and \mathbf{B} of dimension $n \times n$ (Graham, 1981, Section 2.3, X) and $\det \mathbf{Q}(\varepsilon) = 1$.

As the $*$ in Eq. (IV.A.9) are bounded, it follows that

$$\lim_{\varepsilon \downarrow 0} \mathbf{Q}(\varepsilon)\sqrt{\mathbf{D}(\varepsilon)} = \begin{pmatrix} 1 & 0 & \cdots & 0 \\ \vdots & \vdots & & \vdots \\ 1 & 0 & \cdots & 0 \end{pmatrix} \in \mathbb{R}^{r \times r},$$

and therefore

$$\lim_{\varepsilon \downarrow 0} \boldsymbol{\psi}(\varepsilon, \boldsymbol{\xi}) = (\boldsymbol{\xi}_1, \dots, \boldsymbol{\xi}_1) = \mathbf{1}_r \otimes \boldsymbol{\xi}_1 \in \mathbb{R}^{rc}.$$

To now compute $\lim_{\varepsilon \downarrow 0} \int P_z(\mathbf{z}, \varepsilon)\varphi(\mathbf{z}) d\mathbf{z}$, Lebesgue's Dominated Convergence Theorem (Rudin, 1974, Theorem 1.34) shall be applied to evaluate $\lim_{\varepsilon \downarrow 0}$ of Eq. (IV.A.10) by interchanging limit and integral. Thereto, it shall be checked whether the Theorem's assumptions apply (i.e. whether for the sequence of functions that point-wise converges to the limit function under the integral, there exists an integrable dominating function).

First, observe that Eq. (IV.A.8) implies that G is bounded, since it can be written as $\int \exp(-\frac{1}{2}\mathbf{Z}^T \mathbf{S}_L^{-1} \mathbf{Z}) K(\mathbf{z}, \mathbf{Z}) d\mathbf{Z}$, with K bounded by 1 and the positive definite \mathbf{S}_L^{-1} providing an exponential damping for the integration. Here, K is bounded and continuous, since \mathbf{S}_E^{-1} is positive definite and the forward model outcome \mathbf{F} is continuous (see Section IV.2 (p. 105)), and therefore also $\tilde{\mathbf{F}}$. Furthermore, $|G(\mathbf{z}) - G(\tilde{\mathbf{z}})| \leq \int \exp(-\frac{1}{2}\mathbf{Z}^T \mathbf{S}_L^{-1} \mathbf{Z}) \cdot 2 d\mathbf{Z}$, providing an integrable dominating function for the verification that G is continuous because K is, by applying Lebesgue's Dominated Convergence Theorem to $|G(\mathbf{z}) - G(\tilde{\mathbf{z}})|$.

Next, the properties of $N_1(\varepsilon)$ and $N_2(\varepsilon)$ as normalizing factors in Eq. (IV.A.7) for small (i.e. Eq. (IV.A.9) holds) $\varepsilon \geq 0$ shall be investigated.

By using the same substitution that was used to arrive at Eq. (IV.A.10), one obtains

$$N_1(\varepsilon) = (2\pi)^{rc/2} (\det \mathbf{H}_C)^{r/2} (\det \mathbf{D}(\varepsilon))^{c/2},$$

since $\int \exp(-\frac{1}{2}\mathbf{x}^T \mathbf{A} \mathbf{x}) d\mathbf{x} = (2\pi)^{n/2} / \sqrt{\det \mathbf{A}}$ for a real symmetric positive definite matrix \mathbf{A} of dimension $n \times n$.

By the same substitution, N_2 can be written as

$$N_2(\varepsilon) = (2\pi)^{-rc/2} (\det \mathbf{H}_C)^{-r/2} \cdot \int \exp\left(-\frac{1}{2}\boldsymbol{\xi}^T[\mathbb{1}_{r \times r} \otimes \mathbf{H}_C^{-1}]\boldsymbol{\xi}\right) G(\boldsymbol{\psi}(\varepsilon, \boldsymbol{\xi})) d\boldsymbol{\xi}. \quad (\text{IV.A.11})$$

The arguments that yielded boundedness and continuity of G , carry over to the verification that N_2 is in ε

continuous at $\varepsilon = 0$, because $\mathbf{Q}(\varepsilon)\sqrt{\mathbf{D}(\varepsilon)}$ and hence $\psi(\varepsilon, \boldsymbol{\xi})$ are. As G is bounded, there exists some finite $\tilde{K} > 0$ such that for all $\varepsilon \geq 0$, $\tilde{K} \exp\left(-\frac{1}{2}\boldsymbol{\xi}^T[\mathbf{1}_{r \times r} \otimes \mathbf{H}_C^{-1}]\boldsymbol{\xi}\right)$ is an integrable dominating function in $\boldsymbol{\xi}$ for the integrand in Eq. (IV.A.11). Thus Lebesgue's Dominated Convergence Theorem can be applied to Eq. (IV.A.11) to obtain $N_2(0) := \lim_{\varepsilon \downarrow 0} N_2(\varepsilon)$.

$$N_2(0) = (2\pi)^{-rc/2} (\det \mathbf{H}_C)^{-r/2} \cdot \int \exp\left(-\frac{1}{2}\boldsymbol{\xi}^T[\mathbf{1}_{r \times r} \otimes \mathbf{H}_C^{-1}]\boldsymbol{\xi}\right) G(\mathbf{1}_r \otimes \boldsymbol{\xi}_1) d\boldsymbol{\xi},$$

as G is continuous and $\psi(\varepsilon, \boldsymbol{\xi})$ converges point-wise to $\mathbf{1}_r \otimes \boldsymbol{\xi}_1$ for $\varepsilon \downarrow 0$. For generic \mathbf{Y} and positive definite \mathbf{S}_L and \mathbf{S}_E , $G(\mathbf{z})$ is positive for finite $\tilde{\mathbf{F}}$, see Eq. (IV.A.8) (p. 130). But for finite arguments, $\tilde{\mathbf{F}}$ should be finite (Section IV.2 (p. 105)). Hence, for small $\varepsilon \geq 0$, $N_2(\varepsilon)$ is some finite positive number.

Lebesgue's Dominated Convergence Theorem can now be applied to evaluate $\lim_{\varepsilon \downarrow 0}$ of Eq. (IV.A.10). As a test function in Schwartz space, φ is continuous and bounded, as is G . $N_2(\varepsilon)$ is positive for small $\varepsilon \geq 0$, finite, and continuous in ε at $\varepsilon = 0$. Thus, for some finite $\bar{K} > 0$, $\bar{K} \exp\left(-\frac{1}{2}\boldsymbol{\xi}^T[\mathbf{1}_{r \times r} \otimes \mathbf{H}_C^{-1}]\boldsymbol{\xi}\right)$ is an integrable dominating function in $\boldsymbol{\xi}$ for the integrand for small $\varepsilon \geq 0$, and by applying the theorem, it follows that $\lim_{\varepsilon \downarrow 0} \int P_z(\mathbf{z}, \varepsilon) \varphi(\mathbf{z}) d\mathbf{z}$ is equal to

$$(2\pi)^{-rc/2} (\det \mathbf{H}_C)^{-r/2} \cdot \frac{1}{N_2(0)} \cdot \int \exp\left(-\frac{1}{2}\boldsymbol{\xi}^T[\mathbf{1}_{r \times r} \otimes \mathbf{H}_C^{-1}]\boldsymbol{\xi}\right) G(\mathbf{1}_r \otimes \boldsymbol{\xi}_1) \varphi(\mathbf{1}_r \otimes \boldsymbol{\xi}_1) d\boldsymbol{\xi}.$$

Since $\boldsymbol{\xi}^T[\mathbf{1}_{r \times r} \otimes \mathbf{H}_C^{-1}]\boldsymbol{\xi} = \sum_{i=1}^r \boldsymbol{\xi}_i^T \mathbf{H}_C^{-1} \boldsymbol{\xi}_i \in \mathbb{R}$, evaluating the integral over $d\boldsymbol{\xi}_2 \cdots d\boldsymbol{\xi}_r$ and absorbing the uninteresting terms into the constant \tilde{N} , yields

$$\frac{1}{\tilde{N}} \int \exp\left(-\frac{1}{2}\boldsymbol{\xi}_1^T \mathbf{H}_C^{-1} \boldsymbol{\xi}_1\right) G(\mathbf{1}_r \otimes \boldsymbol{\xi}_1) \varphi(\mathbf{1}_r \otimes \boldsymbol{\xi}_1) d\boldsymbol{\xi}_1.$$

This term can be rewritten by using the c -dimensional δ -distribution ($\int \delta^c(\mathbf{t}) f(\mathbf{t}) d\mathbf{t} = f(\mathbf{0})$ for $\mathbf{t} \in \mathbb{R}^c$), such that

$$\lim_{\varepsilon \downarrow 0} \int P_z(\mathbf{z}, \varepsilon) \varphi(\mathbf{z}) d\mathbf{z} = \frac{1}{\tilde{N}} \int \delta^c(\mathbf{z}_1 - \mathbf{z}_2) \cdots \delta^c(\mathbf{z}_1 - \mathbf{z}_r) \cdot \exp\left(-\frac{1}{2}\mathbf{z}_1^T \mathbf{H}_C^{-1} \mathbf{z}_1\right) G(\mathbf{1}_r \otimes \mathbf{z}_1) \varphi(\mathbf{z}) d\mathbf{z}.$$

This equation shows that the *a posteriori* probability distribution for \mathbf{z} concentrates to the plane $\mathbf{1}_r \otimes \mathbf{z}_1$ (all \mathbf{z}_i coincide). This means that \mathbf{z}_1 is spatially or temporally constant, i.e. it is common to the r measurements. For the whole space (including the \mathbf{Z} -dimensions), the induced probability distribution on that plane can be written $\frac{1}{\tilde{N}} \exp\left(-\frac{1}{2}\tilde{F}_c\right)$, with cost function $\tilde{F}_c(\mathbf{z}, \mathbf{Z})$ that reads

$$\mathbf{z}_1^T \mathbf{H}_C^{-1} \mathbf{z}_1 + \mathbf{Z}^T \mathbf{S}_L^{-1} \mathbf{Z} + (\mathbf{Y} - \tilde{\mathbf{F}}(\mathbf{1}_r \otimes \mathbf{z}_1, \mathbf{Z}))^T \mathbf{S}_E^{-1} (\mathbf{Y} - \tilde{\mathbf{F}}(\mathbf{1}_r \otimes \mathbf{z}_1, \mathbf{Z})). \quad (\text{IV.A.12})$$

Define the new extended parameter space as the dimensionally reduced parameter space on that plane, i.e. $(\mathbf{1}_r \otimes \mathbf{z}_1, \mathbf{Z})$ is dimensionally reduced to obtain $(\mathbf{z}_1, \mathbf{Z})$. Rename the vector of the common parameters $\mathbf{z}_1 := \mathbf{z}_C$ and its *a priori* covariance matrix $\mathbf{H}_C := \mathbf{S}_C$. Here and in the following, the subscript 'C' is intended to flag quantities that involve common parameters. Revert the translational substitutions with respect to the *a priori* mean values at the beginning of this section, and denote the vector of the parameters associated to \mathbf{S}_L by $\mathbf{X}_L := (\mathbf{x}_1, \cdots, \mathbf{x}_r)$, along with its *a priori* mean value vector $\mathbf{A}_L := (\mathbf{a}, \cdots, \mathbf{a})$, such that $\mathbf{Z} = \mathbf{X}_L - \mathbf{A}_L$, and similarly with $\mathbf{z}_C := \mathbf{x}_C - \mathbf{a}_C$, where $\mathbf{a}_C := \mathbf{a}_P$. The extended parameter vector shall be denoted by $\mathbf{X} := (\mathbf{x}_C, \mathbf{X}_L)$, and its *a priori* mean value vector by $\mathbf{A} := (\mathbf{a}_C, \mathbf{A}_L)$, leading to the same notation as in Section IV.2 (p. 105). $\tilde{\mathbf{F}}(\mathbf{1}_r \otimes \mathbf{z}_1, \mathbf{Z})$ can be written as $\mathbf{F}((\mathbf{x}_C, \mathbf{x}_1), \cdots, (\mathbf{x}_C, \mathbf{x}_r)) = (\mathbf{f}_1(\mathbf{x}_C, \mathbf{x}_1), \cdots, \mathbf{f}_r(\mathbf{x}_C, \mathbf{x}_r))$ and will be denoted by $\mathbf{F}_C(\mathbf{X})$.

Thus, finally the *a posteriori* probability distribution can be written $\frac{1}{N} \exp\left(-\frac{1}{2}F_c\right)$, with normalization factor N and cost function $F_c(\mathbf{X})$ that reads

$$(\mathbf{x}_C - \mathbf{a}_C)^T \mathbf{S}_C^{-1} (\mathbf{x}_C - \mathbf{a}_C) + (\mathbf{X}_L - \mathbf{A}_L)^T \mathbf{S}_L^{-1} (\mathbf{X}_L - \mathbf{A}_L) + (\mathbf{Y} - \mathbf{F}_C(\mathbf{X}))^T \mathbf{S}_E^{-1} (\mathbf{Y} - \mathbf{F}_C(\mathbf{X})), \quad (\text{IV.A.13})$$

and which has to be minimized by the retrieval. This shows that the relative weighting between the common and the local parameters is exactly 1, and not some \sqrt{r} -like value. Also, it follows that spatially or temporally perfectly coupled parameters can be treated as common parameters in the sense of Section IV.2 (p. 105), where \mathbf{S}_A is a block diagonal matrix with \mathbf{S}_C and \mathbf{S}_L as its blocks on the diagonal.

For VIRTIS-M-IR measurements of Venus, some relevant common parameters along with a suitable \mathbf{S}_C are discussed in Section IV.4.3 (p. 119).

IV.A.4 Sparse matrix formulation

Most entries of the largest structure in MSR, the Jacobian \mathbf{J} (Eq. (IV.A.2) (p. 126)), are zero. This can be exploited by using sparse matrix storage formats that only store the non-zero entries and their positions (Davis, 2006). The 'coordinate list' format (COO) requires 16 bytes of storage space for each non-zero entry (4 for integer row index, 4 for integer column index, 8 for value in double precision). The 'compressed column' format (CCS) requires about 12 bytes per entry (4 for row index, 8 for value) for matrices with many more non-zero entries than the number of columns (pointer to where in the value list the columns start, is then neglectable). A matrix stored in 'dense' format as $M \times N$ array, requires 8 bytes per entry. Matrix creation is convenient with COO, matrix computations are efficient with CCS. Sparse matrix formulation of MSR saves computer memory (use sparse matrix storage) and processing time (apply sparse matrix operations), and for VIRTIS data, it allows to treat retrieval problems that are larger by one order of magnitude.

Sparse matrices can be manipulated by using SuiteSparse, a suite of sparse matrix routines that include format conversion and QR factorization (Davis, 2011; Davis et al., 2004a,b; Amestoy et al., 2004, 1996; Davis and Hager, 2005, 2001, 1999, 2009; Chen et al., 2008). SuiteSparse relies on METIS (Karypis and Kumar, 1998).

As an example that is on current standard desktop hardware easily treatable in sparse format, let there be $r = 1,000$ spectra of an effective size of 100 wavelengths each, $c = 100$ common retrieval parameters (surface emissivities in a surface patch of 10×10 bins) and $n = 10$ local retrieval parameters per spectrum. Then \mathbf{J} is of size 110, $100 \times 10,000$, corresponding to about 10^9 (dense) entries, and can be compiled as follows, see Eq. (IV.A.2) (p. 126) and Section IV.3.5 (p. 116).

$\mathbf{S}_C^{-1/2}$ as a small dense matrix (100×100 for the example) is created in dense format according to Section IV.4.3 (p. 119) and then converted to CCS.

$\mathbf{S}_L^{-1/2}$ ($10,000 \times 10,000$ for the example) as given by Eq. (IV.A.6) (p. 128) is ideally suited to be directly created in sparse format. First, the dense \mathbf{H}_g (Appendix IV.A.2 (p. 127)) and $\boldsymbol{\rho}_g$ have to be computed (Sections IV.3.3 (p. 113) and IV.3.2.3 (p. 112)) for the G parameter groups g , yielding the dense $\mathbf{U}_{\mathbf{H}_g}^{-T}$ and $\mathbf{U}_{\boldsymbol{\rho}_g}^{-T}$. This is efficient due to the small sizes of these matrices ($n_g \times n_g$ where $\sum_{g=1}^G n_g = n$, and $r \times r$). The Kronecker products $\mathbf{U}_{\mathbf{H}_g}^{-T} \otimes \mathbf{U}_{\boldsymbol{\rho}_g}^{-T}$ are computed to yield COO matrices. These G sub-matrices are combined and permuted according to Eq. (IV.A.6) (p. 128) in COO representation and converted to CCS. At no point, the dense representation of the full matrix is needed. Note that, the sparser the \mathbf{H}_g or $\boldsymbol{\rho}_g$ are, the sparser $\mathbf{S}_L^{-1/2}$ tends to be, but in general the inverse of a sparse matrix needs not to be sparse anymore. The worst case relative population of $\mathbf{S}_L^{-1/2}$ is about $\frac{1}{2} \sum_{g=1}^G n_g^2 / n^2$ for large r and n .

\mathbf{J} in CCS format can now be assembled column-wise by combining $\mathbf{S}_C^{-1/2}$ and $\mathbf{S}_L^{-1/2}$, and by collecting the columns of the sparse $-\mathbf{S}_E^{-1/2} \mathbf{K}$. In the worst case ($G = 1$, maximal population of all single-spectrum Jacobians), \mathbf{J} is about 3.5% populated in the example above, translating to about 5.2% required storage space compared to dense format.

The single most expensive matrix operation in MSR is the QR factorization of \mathbf{J} as needed in the trust region algorithm (Moré, 1978). A sparse $\mathbf{J} = \mathbf{QRP}^T$ can be factorized by SuiteSparse into an orthogonal matrix \mathbf{Q} and an upper triangular matrix \mathbf{R} (Golub and van Loan, 1996, Section 5.2), (Davis, 2011), where \mathbf{P} is a permutation matrix that can lead to fewer non-zero entries of the sparse \mathbf{R} , and \mathbf{Q} needs not to be stored. The actual determination of the Levenberg-Marquardt step (Moré, 1978, Section 3) is performed as an additional sparse QR factorization.

Appendix IV.A.1 (p. 126) discusses the interpretation of the covariance matrix $\hat{\mathbf{S}}$ (Eq. (IV.A.3) (p. 126)) and the correlation matrix $\hat{\mathbf{C}}$ at the retrieved result. Only the diagonal and a few off-diagonal entries \hat{S}_{ij} of $\hat{\mathbf{S}}$ may be needed, and the corresponding entries of $\hat{\mathbf{C}}$ follow from Eq. (IV.3) (p. 108). In the last retrieval iteration, \mathbf{J} is evaluated at $\hat{\mathbf{X}}$ to yield $\hat{\mathbf{J}}$ with sparse QR factorization $\hat{\mathbf{J}} = \hat{\mathbf{Q}}\hat{\mathbf{R}}\hat{\mathbf{P}}^T$. $\hat{\mathbf{J}}^T\hat{\mathbf{J}} = \hat{\mathbf{P}}\hat{\mathbf{R}}^T\hat{\mathbf{R}}\hat{\mathbf{P}}^T$ (neglecting the structurally empty lines to yield a $N \times N$ matrix from $\hat{\mathbf{R}}\hat{\mathbf{P}}^T$) provides a permuted Cholesky decomposition of $\hat{\mathbf{S}}^{-1} = \hat{\mathbf{J}}^T\hat{\mathbf{J}}$ which is needed to efficiently invert $\hat{\mathbf{S}}^{-1}$. But the inverse of a sparse matrix needs not to be sparse, and it may not be possible to store all of its entries. To avoid the costly computation of $\hat{\mathbf{J}}^T\hat{\mathbf{J}}$ and its inversion via Cholesky decomposition, note that

$$\hat{S}_{ij} = \langle \mathbf{e}_i, \hat{\mathbf{S}}\mathbf{e}_j \rangle = \langle \mathbf{e}_i, \hat{\mathbf{P}}\hat{\mathbf{R}}^{-1}\hat{\mathbf{R}}^{-T}\hat{\mathbf{P}}^T\mathbf{e}_j \rangle = \langle \hat{\mathbf{R}}^{-T}\hat{\mathbf{P}}^T\mathbf{e}_i, \hat{\mathbf{R}}^{-T}\hat{\mathbf{P}}^T\mathbf{e}_j \rangle =: \langle \mathbf{z}_i, \mathbf{z}_j \rangle.$$

with the standard basis vectors \mathbf{e}_i and Euclidean standard scalar product $\langle \cdot, \cdot \rangle$. \mathbf{z}_i can be determined by solving the sparse linear equation $\hat{\mathbf{R}}^T\mathbf{z}_i = \hat{\mathbf{P}}^T\mathbf{e}_i$.

IV.A.5 Further notes on implementation

The retrieval of parameters whose impacts on the simulated spectra can be separated, may be arranged into several stages. Each stage corresponds to a complete run of the retrieval algorithm in order to determine the best estimate for the corresponding retrieval parameter subset by considering a suitable stage-specific spectral range. The *a priori* and error covariance matrices have to be newly constructed for each stage, as has the covariance matrix at the retrieved result. The retrieved values from earlier stages can either be used as fixed input values with now known uncertainties, or as initial guesses for a refined determination of parameters from earlier stages. Such refinements might be necessary, since the adjustment of additional parameters and the inclusion of different wavelength ranges can cause previously retrieved parameters to become suboptimal. This partitioning into stages results in Jacobians of smaller dimensions and consequently decreased maximal computer memory usage, and also processing time that tends to increase faster than linear with problem size. A tight choice of parameters and wavelength ranges for each retrieval stage can decide the processable size of the retrieval problem.

In order to take advantage of multi-core computer hardware, the program is parallelized by using the Message Passing Interface (MPI) (Gropp et al., 1999) as implemented, for instance in OpenMPI (Gabriel et al., 2004). As computer memory is a limiting factor for the processable problem size, only one of the parallel processes has all information needed for the retrieval algorithm, including the *a priori* covariance matrix and the Jacobian, and manages and performs the retrieval iterations. The remaining processes act as co-processors that evaluate their share of the single-spectrum simulations and single-spectrum Jacobians and communicate them via MPI to the main process.

Acknowledgements

This work is funded by the German Aerospace Center e.V. (DLR e.V.).

Chapter V

Error analysis for retrieval of Venus' IR surface emissivity from VIRTIS/VEX measurements

David Kappel¹, Rainer Haus², Gabriele Arnold¹

¹German Aerospace Center (DLR), Institute of Planetary Research, Rutherfordstrasse 2, 12489 Berlin, Germany

²Institute for Planetology, Westfälische Wilhelms-Universität Münster, Wilhelm-Klemm-Straße 10, 48149 Münster, Germany

A copyedited version of this article was published in:
Planetary and Space Science, 113–114: 49–65, 2015.

Received 12.02.2014; received in revised form 13.08.2014; accepted 20.01.2015.

Available online 04.02.2015. doi:[10.1016/j.pss.2015.01.014](https://doi.org/10.1016/j.pss.2015.01.014)

Copyright: 2015 Elsevier Ltd. All rights reserved.

Abstract

Venus' surface emissivity data in the infrared can serve to explore the planet's geology. The only global data with high spectral, spatial, and temporal resolution and coverage at present is supplied by nightside emission measurements acquired by the Visible and InfraRed Thermal Imaging Spectrometer VIRTIS-M-IR (1.0–5.1 μm) aboard ESA's Venus Express. A radiative transfer simulation and a retrieval algorithm can be used to determine surface emissivity in the nightside spectral transparency windows located at 1.02, 1.10, and 1.18 μm . To obtain satisfactory fits to measured spectra, the retrieval pipeline also determines auxiliary parameters describing cloud properties from a certain spectral range. But spectral information content is limited, and emissivity is difficult to retrieve due to strong interferences from other parameters.

Based on a selection of representative synthetic VIRTIS-M-IR spectra in the range 1.0–2.3 μm , this paper investigates emissivity retrieval errors that can be caused by interferences of atmospheric and surface parameters, by measurement noise, and by *a priori* data, and which retrieval pipeline leads to minimal errors.

Retrieval of emissivity from a single spectrum is shown to fail due to extremely large errors, although the fits to the reference spectra are very good. Neglecting geologic activity, it is suggested to apply a multi-spectrum retrieval technique to retrieve emissivity relative to an initial value as a parameter that is common to several measured spectra that cover the same surface bin. Retrieved emissivity maps of targets with limited extension (a few thousand km) are then additively renormalized to remove spatially large scale deviations from the true emissivity map that are due to spatially slowly varying interfering parameters. Corresponding multi-spectrum retrieval errors are estimated by a statistical scaling of the single-spectrum retrieval errors and are listed for 25 measurement repetitions. For the best of the studied retrieval pipelines, temporally varying interfering atmospheric parameters (cloud parameters, minor gas abundances) contribute errors in the order of 3%–10% of the true emissivity, depending on the surface window, the reference spectrum, and assuming statistical independence of the parameters. Temporally constant interfering parameters that spatially vary on

a scale of 100 km (surface elevation, interfering emissivities) add 9%–16%. Measurement noise with a standard deviation of 10^{-4} W/(m² sr μm) leads to additional 1%–4%. Reasonable modifications of *a priori* mean values have negligible impacts. Retrieved maps are most reliable at 1.02 μm. There is an overall tendency for better results for cases with small cloud opacity, high surface elevation, high emissivity, and small observation angle, but this depends on the emissivity window, retrieval pipeline, and measurement repetition number. Calibration, preprocessing, and simulation errors can lead to additional errors. Based on the presented results, a subsequent paper will discuss emissivity data retrieval for a selected surface target.

V.1 Introduction

Insight into Venus' surface geology is currently quite limited. It is mainly based on radar data (e.g. topography, slope, reflectivity, emissivity acquired by the Magellan probe, [Pettengill et al., 1991](#)), see [Ivanov and Head \(2011\)](#), ground based infrared observations ([Meadows and Crisp, 1996](#)), gravitational data ([Smrekar et al., 2010](#)), as well as on a few *in situ* measurements ([Abdrakhimov and Basilevsky, 2002](#)). Knowledge of wavelength dependent surface emissivity in the infrared can help to better categorize the surface material, texture, and weathering. Such data can be used to study the surface geology, and thus to learn more about the planet's geologic history, for instance about the global resurfacing event ([Basilevsky et al., 1997](#)).

Neglecting geologic activity and assuming thermodynamic equilibrium between surface and bottom of the atmosphere, surface temperature decreases with increasing surface elevation according to the Venus International Reference Atmosphere VIRA ([Seiff et al., 1985](#)). The hot surface (735 K at 0 km) emits radiation that depends on both surface temperature and surface emissivity. Measured upwelling radiation carries information on surface as well as on emissions from the hot deep atmosphere. But the signals are absorbed and multiply scattered by atmospheric gases and clouds. This also leads to a partial loss of spatial information according to an approximate Gaussian blurring with full-width-at-half-maximum (FWHM) in the order of 100 km ([Moroz, 2002](#)). Surface emissions in the infrared are far outweighed by scattered sunlight and can thus only be evaluated on Venus' nightside. Broad regions of nightside infrared spectra are completely blacked out by the high-density hot carbon dioxide atmosphere and the thick sulfuric acid clouds. In the infrared, only a few narrow atmospheric transparency windows between 0.8 and 1.3 μm remain to sound the surface. But measurable top-of-atmosphere radiances are strongly attenuated and distorted by the overlying atmospheric layers ([Pollack et al., 1993](#); [Meadows and Crisp, 1996](#)). Non-LTE O₂ emissions ('O₂ nightglow') at 1.27 μm from an altitude region around 100 km ([Piccioni et al., 2009](#)) strongly affect the 1.28 μm radiance peak. Additional windows between 1.3 and 2.6 μm probe the deep atmosphere.

The only suitable data on a global scale with high spectral, spatial, and temporal resolution and coverage at present is supplied by Venus nightside emission measurements acquired by the InfraRed Mapping channel of the Visible and InfraRed Thermal Imaging Spectrometer (VIRTIS-M-IR) aboard ESA's Venus Express (VEX) space probe ([Drossart et al., 2007](#); [Piccioni et al., 2007](#); [Arnold et al., 2012c](#)). The instrument maps spectrally resolved (432 spectral bands dividing the range 1.0 – 5.1 μm equidistantly with wavelength) two-dimensional images of targets on Venus. The carefully calibrated and preprocessed measurements ([Cardesin-Moinelo et al., 2010](#); [Kappel et al., 2012b](#)) provide the data base where surface information shall be extracted from. Radiances in the 1.28 μm window are not very sensitive against surface emissivity changes. Therefore, and because the instrument's limited spectral resolution does not allow to disentangle interfering O₂ nightglow from emissivity responses in this window, surface emissivity cannot be determined there. Only three radiance peaks between 1.0 and 1.2 μm remain, where surface emissivity can be derived from (1.02, 1.10, 1.18 μm). Emissivity is not easy to obtain from that data, since spectral information content is comparatively low, and atmospheric influences strongly interfere with surface information.

The radiative transfer in the atmosphere of Venus can be modeled by suitable algorithms (e.g. [Haus and Arnold, 2010](#)). Such a radiative transfer simulation forward model computes the synthetic radiance spectrum for a given state of the surface, atmosphere, measuring instrument, and for given optical properties of the gases and clouds, given observational geometry, and if necessary illuminational geometry and solar spectrum, etc. Starting from an initial guess, a retrieval algorithm iteratively varies the parameters that shall be retrieved from a measured spectrum until the corresponding simulation well fits the measurement in the least-squares sense. The parameter values that yield the best-fit spectrum ('retrieved parameters') then adequately parameterize the

measurement and can be regarded as estimations of the corresponding actual states of atmosphere, surface, and instrument.

However, different parameter combinations may describe the same spectrum equally well. Thus, retrieval is mathematically an ill-posed problem. A usual way to treat such problems is by Bayesian regularization (Rodgers, 2000), where the parameters themselves have to fulfill additional conditions. This is achieved by assuming that, prior to the knowledge of the measurement outcome, the parameters follow an *a priori* probability distribution, a Gaussian with certain mean value vector and standard deviations. Measurement and simulation errors are assumed to follow a Gaussian with zero mean value vector and certain standard deviations. The location $\hat{\mathbf{x}}$ of the global maximum of the Bayesian *a posteriori* probability distribution $\exp(-F_c(\mathbf{x})/2)/N$ of the parameter vector \mathbf{x} , given the measured spectrum, is then the state vector that is the most consistent with the measurement and the *a priori* and error information. F_c is the retrieval cost function that has to be minimized to find that global maximum, N is a normalization factor. An iterative algorithm like the trust region formulation of the Levenberg-Marquardt algorithm (Moré, 1978) can be used to identify local minima of F_c , but note that the algorithm possibly converges to just a subsidiary minimum, especially in the presence of measurement noise. The *a posteriori* covariance matrix (essentially the inverse of the Hessian of $F_c/2$ at $\hat{\mathbf{x}}$) can be regarded as a first measure for statistical uncertainties of, and correlations between the retrieved parameters. Basically, the incorporation of *a priori* data decreases the probability to find unreasonable parameter values. As this regularization considers only independent single spectra, it will be called 'single-spectrum regularization'. However, as will be shown in the present paper, retrieved emissivities turn out to have very high uncertainty margins.

But contiguous measurements are not likely to originate from completely unrelated state vectors. For atmospheric parameters, this follows from the inertia of matter and the balancing of thermodynamic disequilibria. If contiguous measurements are nevertheless treated as independent from each other, then spatial or temporal continuity in the measurements may not translate to a certain expected continuity in retrieved parameters. This is due to the existence of different parameters with very similar impacts on the spectra, the ill-posed nature of the retrieval problem, and the existence of subsidiary minima of the cost function. Therefore, a more sophisticated retrieval regularization was developed that in addition incorporates *a priori* spatial-temporal correlations between state vectors and also allows to retrieve parameters that are common to certain selections of measurements (Kappel, 2014). This 'multi-spectrum retrieval algorithm' (MSR) essentially decreases the probability to find unreasonable spatial-temporal state vector distributions. Although MSR decreases the number of potential solutions and could be expected to produce larger residuals between measurements and fits, the residuals in fact decrease on average, which was demonstrated by Kappel et al. (2012c,b) for real spectra, and by Kappel (2014) for synthetic spectra. This indicates that MSR helps to avoid subsidiary solutions. It was also shown that parameters with more different *a priori* correlation lengths or times can be better disentangled. In particular, it was demonstrated that for repeated measurements of a surface target, emissivity can be reasonably well disentangled from cloud parameters, since emissivity can be regarded as parameter with infinite correlation time. This is, because it is a parameter that is common to several measurements that cover the same surface target, when neglecting geologic activity.

It is always important to know the reliability of retrieved results when physical values are determined from measured data. This is especially true for Venus' surface emissivity that is difficult and error prone to retrieve from VIRTIS-M-IR measurements as will be shown. To begin with, the *a posteriori* covariance matrix encodes, how well the surface emissivity could be determined from the utilized measurements, and how well it could be disentangled from the other retrieved parameters, all within the frame of the utilized forward model and under prerequisite of the assumptions on *a priori* data and measurement noise and the choice of the retrieval parameters.

But there are errors that are not reflected in the *a posteriori* covariance matrix. For instance, the latter is completely local. It does not reflect errors that are caused by finding subsidiary solutions and that are due to the possibly complicated *global* dependency of the least-squares residual between measurement and simulation on the model parameters, especially in the presence of measurement noise. Also, the choice of the retrieval parameters, of the spectral ranges that shall be utilized in the retrieval, and of the *a priori* data can lead to different emissivity retrieval results. Next, there are always atmospheric and surface parameters that are not sufficiently well known to be accurately set in the simulation of a synthetic spectrum and that cannot

be derived from the spectrum itself. They are usually set to reasonable values that are compatible with current knowledge on atmospheric and surface conditions and allow to generate realistic synthetic spectra. But when the true underlying parameter values deviate from these assumptions, this can lead to emissivity retrieval errors. This work will estimate the impacts of all error sources listed in this paragraph. It will turn out that these errors can be large compared with the errors encoded in the *a posteriori* covariance matrix.

Finally, forward model simulation errors can lead to errors in the retrieved emissivities, but this effect is difficult to estimate, because of the insufficient knowledge of the optical properties in Venus' hot dense atmosphere and the lack of *in situ* data to compare with. But when realistic input data are employed, the utilized forward model is capable to generate synthetic spectra that very well match the measured spectra for very different kinds of atmospheric and measurement conditions (Haus and Arnold, 2010). Measurement, calibration, and preprocessing errors and their impacts on retrieved emissivities were already partially discussed by Kappel et al. (2012b).

Section V.2 of the present paper defines the terminology and the algorithm that allows to determine the above listed surface emissivity retrieval errors. A number of error measures are defined that are used to monitor the success of the emissivity retrieval. For the case when the multi-spectrum retrieval algorithm MSR is applied, it is discussed, how multi-spectrum retrieval errors can be roughly estimated by plausibly scaling single-spectrum retrieval errors. Section V.3 (p. 143) recites the properties of the forward model, discusses the various forward model parameters involved in this work, and defines several synthetic reference spectra that are representative for a number of typical key measurement situations. Section V.4 (p. 150) investigates, which spectral ranges should be utilized in the retrieval procedures and which auxiliary parameters should be retrieved in order to minimize the emissivity retrieval errors and the noise impacts. It is also explored, how results depend on the measurement situation. The single-spectrum retrieval errors are scaled to obtain rough measures for the multi-spectrum retrieval errors. First results have been presented by Kappel et al. (2012a).

V.2 Notation and strategy of retrieval error analysis

V.2.1 Basic terminology

The 'primary state vector' $\mathbf{e} \in \mathbb{R}^p$ shall comprise the parameters of primary interest, like surface emissivity (giving rise to the notation \mathbf{e}), that shall be retrieved from a measured spectrum $\mathbf{y} \in \mathbb{R}^m$. The i -th entry of \mathbf{e} , where $i \in \{1, \dots, p\}$, is denoted as $(\mathbf{e})_i := e_i$, and similarly, the entries of \mathbf{y} are the measured radiances y_k at wavelengths λ_k , where $k \in \{1, \dots, m\}$. It may be necessary to retrieve parameters that are not of primary interest but must be retrieved along with \mathbf{e} to obtain useful fits to \mathbf{y} at all, like cloud particle abundances. They shall be called 'auxiliary parameters' and are compiled into the 'auxiliary state vector' $\mathbf{z} \in \mathbb{R}^q$. Together, \mathbf{e} and \mathbf{z} comprise the 'state vector' $\mathbf{x} := (\mathbf{e}^T, \mathbf{z}^T)^T \in \mathbb{R}^{p+q}$. In the following, the concatenation of column vectors shall be shortly written without the superscript sign for transposition, such that $\mathbf{x} := (\mathbf{e}, \mathbf{z})$.

Not every relevant parameter can be retrieved from a measured spectrum due to the limited spectral information content. For instance, parameters with small or unspecific spectral signatures cannot be determined. However, they still may affect the spectrum and must be set to certain values to enable the radiative transfer simulation at all. Deviations of the true from these assumed values can lead to errors in the retrieval of \mathbf{x} . Those parameters shall be called 'external parameters' and are combined into the 'external parameter vector' $\mathbf{t} \in \mathbb{R}^r$. Their impact on the retrieved \mathbf{e} is one of the main subjects of this paper.

Finally, there are parameters that are needed for the radiative transfer simulation but whose possible uncertainties are not considered in this paper, like viewing geometry.

The forward model simulation for the parameter combination (\mathbf{x}, \mathbf{t}) shall be denoted as $\mathbf{f}(\mathbf{x}, \mathbf{t}) \in \mathbb{R}^m$ and is the synthetic spectrum that has to be fitted to \mathbf{y} by iterative variations of \mathbf{x} . The partial derivative of \mathbf{f} with respect to a scalar parameter s is denoted as $(\mathbf{J})_s := \partial \mathbf{f} / \partial s \in \mathbb{R}^m$, and the matrix of all first-order partial derivatives, i.e. the Jacobian, as $\mathbf{J} \in \mathbb{R}^{m \times (p+q+r)}$. It is common to refer to $(\mathbf{J})_s$ also as 'Jacobian'.

For a given spectrum, the 'true' values that actually led to the spectrum, shall be denoted as $\underline{\mathbf{e}}$ with entries \underline{e}_i , and similarly with $\underline{\mathbf{z}}$, $\underline{\mathbf{x}}$, and $\underline{\mathbf{t}}$. When retrieving $\mathbf{x} = (\mathbf{e}, \mathbf{z})$ from the spectrum, the best estimate for \mathbf{e} , i.e. the retrieved primary state vector, shall be denoted as $\hat{\mathbf{e}}$ with entries \hat{e}_i , and similarly with $\hat{\mathbf{z}}$.

In order to determine the impact that wrong assumptions on the external parameters \mathbf{t} may have on $\hat{\mathbf{e}}$, the true parameter values must be known for a studied spectrum. There are only few *in situ* data of surface properties. Also, there are no *in situ* measurements of the interfering atmospheric parameters at all that are simultaneous with VIRTIS-M-IR measurements of Venus' nightside emissions. Thus, only synthetic spectra can serve as spectra with known true underlying parameters. Therefore, a 'true' spectrum \mathbf{y} is now defined as the synthetic spectrum $\mathbf{y} = \mathbf{f}(\mathbf{x}, \mathbf{t})$ using a certain parameter set (\mathbf{x}, \mathbf{t}) (the 'true' parameters for \mathbf{y}).

Now let the primary state vector \mathbf{e} comprise surface emissivities e_i at wavelengths λ_i ($i \in I$) that are sensitive to surface emissivity. Focusing on VIRTIS-M-IR measurements, only three surface windows (at 1.02, 1.10, and 1.18 μm) can be used in practice for emissivity retrieval. The set I may thus be written $I = \{1, 2, 3\}$, or more suggestively $I = \{1.02, 1.10, 1.18\}$, which then leads to the notation $e_{1.02}$ for the emissivity in the 1.02 μm window, etc. Now vary a single external parameter t . To study the impact of variations of t on the retrieved \hat{e}_i , a series of w 'wrong' values t_v ($v \in \{1, \dots, w\}$) is defined. The t_v are chosen to cover the range where t is expected to lie in. Along with \mathbf{z} , \mathbf{e} is then retrieved from always the same \mathbf{y} for each of the t_v , yielding $\hat{\mathbf{e}}(t_v)$. While the $\hat{e}_i(t_v)$ are monitored for further evaluation, the auxiliary parameters are not considered further on. The ranges of the $\hat{e}_i(t_v)$ are then measures for the retrieval errors introduced by wrong assumptions on t . These error measures are determined for the most important external parameters and yield an estimate of the uncertainty of $\hat{\mathbf{e}}$ that is due to the uncertainty of these parameters.

The retrieval error analysis procedure is repeated for several different combinations of auxiliary parameters and spectral ranges utilized for the retrieval (Section V.4 (p. 150)). For each of these retrieval pipelines, the retrieval errors are compared, in order to determine an optimal choice for operational retrievals that yields small retrieval errors. Also, the robustness of retrieved results against modifications of *a priori* data is checked. For the best retrieval pipeline, a number of different reference spectra are studied that represent typical measurement situations (Section V.4.6 (p. 156)).

V.2.2 Error measures for single-spectrum retrieval

Now let the true emissivity e be the same for all λ_i . The retrieved surface emissivities $\hat{e}_i(t)$ may depend on the external parameter t and on λ_i . Note that for simplicity, the parameter name is notationally not distinguished from the value it attains. The corresponding surface emissivity retrieval errors shall be summarized by a few characteristic values. For this purpose, define the characteristic range CR the external parameter t is expected to typically (95% probability) vary in.

A first measure RG_i ('Global eRror') for emissivity retrieval errors for each $i \in I$ is then the maximum relative deviation of the retrieved emissivities from the true emissivity when t varies over CR .

$$RG_i := \max_{t \in CR} \frac{|\hat{e}_i(t) - e|}{e} \quad (\text{V.1})$$

In addition, define a measure CD for the worst case 'Color Dispersion' of the retrieved emissivities, i.e. compute at fixed t the maximum difference between the $\hat{e}_i(t)$, relative to the center of the range of the $\hat{e}_i(t)$, and find the maximum of that value when t varies over CR .

$$CD := \max_{t \in CR} \frac{|\max_{i \in I} [\hat{e}_i(t)] - \min_{i \in I} [\hat{e}_i(t)]|}{\max_{i \in I} [\hat{e}_i(t)] + \min_{i \in I} [\hat{e}_i(t)]} / 2 \quad (\text{V.2})$$

In practice, it may be difficult to retrieve the absolute emissivities, and only relative spatial variations may be accessible. To have a quantitative estimation to describe this situation for simultaneously measured spectra, let the retrieved emissivity at wavelength λ_i and location A be $\hat{e}_i(t_A)$, and analogously for location B . Both t_A and t_B may be uncertain, but when B is close to A , then t_B may not be very different from t_A . The expected spatial resolution of retrieved surface data is in the order of 100 km (Moroz, 2002), so it is useful to consider spatially relative surface emissivity retrieval errors that are due to possible variations between t_A and t_B , when A and B are separated by not more than 100 km.

In order to estimate the typical variation between t_A and t_B on the length scale of 100 km, the correlation function f_d for parameter t is introduced. It describes the statistical correlation between t_A and t_B in dependence on the Euclidean distance $d(A, B)$ between A and B . It is closely related to the *a priori* correlation function that describes statistical correlations of retrieval parameters before knowledge from their measurement is available, see [Kappel \(2014, Section 3.2.1\)](#) for a discussion of the latter in context of a multi-spectrum retrieval algorithm. A reasonable correlation function f_d was given by [Gaspari and Cohn \(1999, Eq. 4.10\)](#) and used by [Kappel \(2014, Eq. \(6\)\)](#), see [Fig. V.1](#).

$$f_d(x) = \begin{cases} -\frac{x^5}{4} + \frac{x^4}{2} + \frac{5x^3}{8} - \frac{5x^2}{3} + 1 & 0 \leq x < 1 \\ \frac{x^5}{12} - \frac{x^4}{2} + \frac{5x^3}{8} + \frac{5x^2}{3} - 5x + 4 - \frac{2}{3x} & 1 \leq x < 2 \\ 0 & x \geq 2 \end{cases} \quad (\text{V.3})$$

Here, $x = 0.808768 \cdot d(A, B)/\lambda_t$. The correlation length λ_t for parameter t is the distance where the correlation function attains the value e^{-1} . f_d is continuous and twice continuously differentiable on \mathbb{R}_+ . It has derivative 0 at $d = 0$ and thus reflects inertial properties of atmospheric molecules and the fast balancing of thermodynamic disequilibria, because observations that are only slightly separated, are modeled to perceive slowly changing correlations, see discussions by [Daley \(1991\)](#); [Gelb \(1974\)](#); [Gaspari and Cohn \(1999\)](#); [Balgovind et al. \(1983\)](#). f_d has compact support (it vanishes outside of a closed bounded set) and thus reflects the effective vanishing of correlations for widely separated A and B , see discussion by [Gaspari and Cohn \(1999, Section 4.d\)](#) and references therein on forecast error correlations for Earth's troposphere.

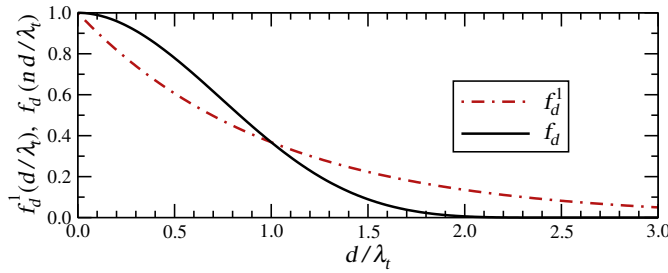


FIGURE V.1: Correlation function f_d in comparison to a simple exponential correlation function f_d^1 with the same correlation length, where $n \approx 0.808768$ such that $f_d(n \cdot 1) = e^{-1} = f_d^1(1)$. f_d vanishes for $d \geq 2.47\lambda_t$. It has zero derivative at $d = 0$ and, compared to f_d^1 , it has a stronger relative weighting of the correlation of nearby measurements ($d < \lambda_t$), which better represents the inertial properties of the physical system.

f_d gives rise to a 2×2 matrix \mathbf{C} with entries $C_{ij} := f_d(0.808768 \cdot d_{ij}/\lambda_t)$, where the d_{ij} are the Euclidean distances that arise for the locations A and B : $d(A, A) =: d_{11} = 0 = d_{22} := d(B, B)$, $d_{21} := d(A, B) =: d_{12}$. Since f_d is a correlation function, \mathbf{C} is positive definite for distinct A and B ([Gaspari and Cohn, 1999](#)). \mathbf{C} is also real, symmetric, and all diagonal entries are 1. Hence, it is a correlation matrix ([Anderson, 1958, Theorem 2.3.1](#))². It describes the statistical correlation between t_A and t_B . Let the probability distributions for t_A and t_B both be Gaussian with mean value \bar{t} and standard deviation σ_t . CR can thus be set to

$$CR := [\bar{t} - 2\sigma_t, \bar{t} + 2\sigma_t]. \quad (\text{V.4})$$

Then the corresponding joint probability distribution for t_A and t_B is $p(t_A, t_B) = \frac{1}{NF} \exp(-\frac{1}{2}\mathbf{v}^T \mathbf{S}^{-1} \mathbf{v})$ with normalization factor NF . Here, $\mathbf{S} := \sigma_t^2 \mathbf{C}$ is the covariance matrix that arises from the correlation matrix \mathbf{C} and the standard deviation σ_t , and $\mathbf{v} := (t_A - \bar{t}, t_B - \bar{t})^T$. Hence, $p(t_A, t_B) = \frac{1}{NF} \exp(-[(t_A - \bar{t})^2 + (t_B - \bar{t})^2 - 2C_{12}(t_A - \bar{t})(t_B - \bar{t})]/[2\sigma_t^2(1 - C_{12}^2)])$. Then the (conditional) probability distribution for t_B for given fixed t_A is a Gaussian with maximum³ $\frac{1}{NF} \exp(-(t_A - \bar{t})^2/(2\sigma_t^2)) \frac{1}{NF_2}$, which is located at $t_B = \bar{t} + C_{12}(t_A - \bar{t})$, the corresponding mean value. The corresponding double standard

¹Corrected: In the published paper, this last clause did not appear. Moreover, the vertical axis of the diagram was just labeled $f_d(0.808768 d/\lambda_t)$, thereby omitting the labeling of f_d^1 . Also compare [Fig. IV.1 \(p. 111\)](#).

²Note: This theorem refers to covariance matrices, but see [Section IV.3.1 \(p. 108\)](#) for the relation between correlation and covariance matrices.

³Corrected: In the published paper, the factor $\frac{1}{NF_2}$ arising from the normalization of the conditional probability distribution for t_B was mistakenly omitted, but this does not affect the subsequent discussion.

deviation is $2\sigma_t\sqrt{1-C_{12}^2}$. Thus, for given t_A , the probability is 95% to find t_B in interval

$$I_{t_A} := \bar{t} + C_{12}(t_A - \bar{t}) + \sqrt{1-C_{12}^2} \cdot [-2\sigma_t, +2\sigma_t]. \quad (\text{V.5})$$

This defines a measure for relative spatial errors RL_i ('reLative eRror') for the retrieved emissivity \hat{e}_i ,

$$RL_i := \frac{1}{2} \max_{t_A \in CR} \left(\max_{t \in I_{t_A} \cap CR} \frac{|\hat{e}_i(t) - \hat{e}_i(t_A)|}{\hat{e}_i(t_A)} \right), \quad (\text{V.6})$$

i.e. the maximum of the ratio is computed for t in a sliding interval $I_{t_A} \cap CR$ around a t_A that varies in CR . The factor $1/2$ is needed, because it is assumed that retrieved emissivities at both locations A and B are affected by errors, and without this factor, RL would indicate the error at B relative to that at A . For strong correlations C_{12} close to 1, the interval I_{t_A} can be approximated by $I_{t_A} = t_A + \sqrt{1-C_{12}^2} \cdot [-2\sigma_t, +2\sigma_t]$. This means that over a sliding interval of length $2I_t$ with

$$I_t := 2\sigma_t\sqrt{1-C_{12}^2}, \quad (\text{V.7})$$

half the maximum relative difference of $\hat{e}_i(t)$ to its value at the center of the interval is wanted. For the computation of RL_i , it is thus sufficient for parameters with C_{12} close to 1 to only state I_t instead of $I_{t_A} = t_A + [-I_t, I_t]$ in the following. On the other hand, when $C_{12} \ll 1$, then I_{t_A} can be approximated by CR (Eq. (V.4)). In this case, RL_i is just the half of the maximal relative difference between any two $\hat{e}_i(t)$ that is possible over the interval CR . This information may be encoded by again using the approximate interval $I_{t_A} = t_A + [-I_t, I_t]$ but now setting $I_t := 4\sigma_t$.

To compute RG_i , CD , and RL_i , the expected mean value \bar{t} , double standard deviation $2\sigma_t$, and correlation length λ_t are given in Section V.3 (p. 143) for each external parameter t . The ideal case would be $RG_i = 0$ for all i , which would imply $CD = 0$ and $RL_i = 0$ for all i . Note that $RL_i = 0$ or $CD = 0$ do not imply $RG_i = 0$.

Random measurement errors destroy some of the spectrum's information content and can lead to a more complicated shape of the graph of the retrieval cost function and thus to an increased number of subsidiary minima and therefore wrong potential retrieval results. To estimate the impact on retrieved emissivities, the retrieval of the $e_i(t)$ at fixed t is repeated N times, where each time a different noise ϵ_n ($n \in \{1, \dots, N\}$) is added to \mathbf{y} , yielding 'noisy true spectra' or 'synthetic measurements' $\mathbf{y}_{\epsilon n} := \mathbf{y} + \epsilon_n$. Only a simple noise model shall be used here, Gaussian noise with zero mean value and a certain wavelength independent standard deviation σ . This way, also the numerical repeatability of the retrieval under slightly altered conditions can be studied. Denoting the emissivity retrieved at wavelength λ_i and at fixed external parameter t from spectrum $\mathbf{y}_{\epsilon n}$ by $\hat{e}_{in}(t)$, then $\bar{e}_i(t)$ shall be the mean value of the $\hat{e}_{in}(t)$ over all N noise repetitions and $\sigma_{Ni}(t)$ the corresponding standard deviation. The corresponding error measures are denoted by \overline{RG}_i , \overline{CD} , and \overline{RL}_i and are computed according to Eqs. (V.1) (p. 139), (V.2) (p. 139), and (V.6), but with $\hat{e}_i(t)$ replaced by $\bar{e}_i(t)$.

When the number N of noise repetitions is large, $\bar{e}_i(t)$ is expected to be very similar to the noiseless result $\hat{e}_i(t)$. Differences are due to both remaining statistical fluctuations and subsidiary solutions. To minimize the impact of statistical fluctuations on \overline{RG}_i , \overline{CD} , and \overline{RL}_i , the number N must be set to a reasonably high value. Note that fluctuation impacts scale with $1/\sqrt{N}$. But to make computational resources easier to handle, the similarity of $\bar{e}_i(t)$ and $\hat{e}_i(t)$ shall be verified with $N := 100$ for only one typical synthetic measurement. In the remaining cases, just the noiseless RG_i , CD , and RL_i shall be determined (Section V.4.6 (p. 156)).

It will turn out that the double standard deviations $2\sigma_{Ni}(t)$ of the retrieved emissivities for the N noise repetitions vary only slightly with the value t (see for instance Fig. V.5 (p. 154)). They are also quite independent from the choice of which external parameter is studied. For each of the wavelengths λ_i , the median $2\sigma_i$ over all those double standard deviations is computed. For better comparison to the error measures, the $2\sigma_i$ are divided by the true emissivity (by analogy with Eq. (V.1) (p. 139)), yielding the 'noise measures'

$$N_i := \frac{2\sigma_i}{e}. \quad (\text{V.8})$$

As a measure QF for monitoring the quality of the fits, define the (unitless) relative deviation of the fit $\mathbf{f}_n(t)$ from the synthetic measurement $\mathbf{y}_{\epsilon n}$ as the Euclidean norm (denoted by $\|\cdot\|_2$) of their difference, divided by the Euclidean norm of the synthetic measurement, $QF_n(t) := \|\mathbf{y}_{\epsilon n} - \mathbf{f}_n(t)\|_2 / \|\mathbf{y}_{\epsilon n}\|_2$. A good fit can be characterized by a small QF in the order of $\|\epsilon_n\|_2 / \|\mathbf{y}_{\epsilon n}\|_2$. For $\mathbf{y} \in \mathbb{R}^m$, this can be approximated by the value $QF_0 := \sigma\sqrt{m} / \|\mathbf{y}\|_2$, because the standard deviation σ of the synthetic measurement noise with zero mean value μ can be estimated by $\sqrt{\frac{1}{m} \sum_{k=1}^m [(\epsilon_n)_k - \mu]^2} = \frac{1}{\sqrt{m}} \|\epsilon_n\|_2$. When QF exceeds a certain threshold value, signaling a failed retrieval run due to a bad fit, the retrieved emissivities will not be taken into account for the error evaluation, and the maximal valid interval for the external parameter is stated. The threshold value is set to 3%, which exceeds QF_0 for the reference spectrum with the smallest $\|\mathbf{y}\|_2$ (0.137 W/(m² sr μ m) for scenario 2 from Section V.3.8 (p. 150), $\sigma = 10^{-4}$ W/(m² sr μ m), $m = 129$ for the range 1.0–2.3 μ m excluding the 1.28 μ m peak, see Section V.3.1 (p. 145)) by half an order of magnitude as safety margin. For real measurements, QF is always monitored and rarely exceeds 6%, and it is typically between 3%–5%. These values even include all measurement and simulation errors, which are not investigated in the present study.

There are three kinds of external parameters that will be studied here. The first kind can vary spatially and temporally and is denoted by 'Atm' as it comprises only atmospheric parameters. The second kind can vary only spatially ('Spa'), and the third kind varies neither spatially nor temporally and is denoted by 'Cnt', since it comprises only so-called 'continuum' parameters, see Section V.3.6 (p. 148). Note that Table V.1 (p. 144) indicates the kinds of all external parameters discussed in Section V.3. Sums of error measures over different external parameters are most useful when these parameters are of the same kind. Assuming the spatially and temporally varying external parameters to vary statistically independently of each other, the global error measures of those parameters can be summarized for each i by a single value $\langle \overline{RG}_i \rangle^{Atm}$. $\langle \overline{RG}_i \rangle^{Atm}$ is the square root of the sum of the squares of those global error measures at wavelength i over the parameters of the first kind (Atm), i.e. these error measures are quadratically added. $\langle \overline{CD} \rangle^{Atm}$ and $\langle \overline{RL}_i \rangle^{Atm}$ are defined analogously. Together, they are denoted as $\langle Atm \rangle$. The summarized values for the parameter kinds Spa and Cnt are similarly defined. All together, $\langle Atm \rangle$, $\langle Spa \rangle$, and $\langle Cnt \rangle$ are called the 'summarized error measures'.

V.2.3 Scaling properties of error measures for multi-spectrum retrieval

It will turn out (Section V.4 (p. 150)) that retrieval errors can be very large when emissivity is retrieved from just one single spectrum. The multi-spectrum retrieval algorithm (MSR) developed by Kappel (2014) allows to retrieve the emissivity of a surface bin as a parameter that is common to N_r measurements that all cover that bin. This approach assumes that geologic activity as observable by VIRTIS-M-IR is negligible, and indeed, corresponding hints on its presence have not been found in the data so far (Müller et al., 2012a). In this sense, emissivity itself has the character of a Spa parameter. Emissivities retrieved with MSR are more reliable. In part, this is due to the fact that for a high measurement repetition number N_r , the impact of fluctuations around the long-term average of an Atm parameter at that surface bin should average out with $1/\sqrt{N_r}$. While a multi- is more complex than a single-spectrum retrieval error analysis, a scaling by this statistical factor yields a rough measure for the order of magnitude of all averaged-out single-spectrum Atm error measures \overline{RG}_i and \overline{CD} , including the corresponding 'summarized' error measures. Note that this scaling approach is based on the assumption that the mean values of the external parameters at that surface bin coincide with the 'true' parameter values discussed in Section V.3. Deviations from this assumption will lead to retrieval errors that may systematically differ from the statistically scaled errors, but these differences can be largely removed as will be discussed in the following paragraphs. A scaling of relative errors in dependence on the repetition number is not considered here. Relative errors were only defined for simultaneous measurements in order to simplify their definitions by only considering correlation lengths and not correlation times. The noise measures N_i (Eq. (V.8)) should scale with $1/\sqrt{N_r}$ as well. In contrast, errors for Spa and Cnt parameters will not average out, since they do not statistically vary with time.

Cnt parameters, the largest sources of error, are fixed for all measurements and should mostly lead to errors that affect retrieved emissivities in the same way. When the ambition to retrieve absolute emissivities is dropped and only spatial emissivity variations shall be studied, one can set an initial emissivity value (e.g. 0.65) and determine compatible Cnt parameters by retrieving them with MSR as parameters that are common to as many and as diverse as possible measurements. For the actual target area, an emissivity map relative

to the initial value can then be retrieved with MSR by using these pre-determined *Cnt* parameters. The *Cnt* error measures are then assumed to be negligible.

But even then, there may remain spatially large scale deviations of the retrieved from the true emissivity map. This is due to spatially slowly (on a scale of thousands of km) varying systematic interferences from other than *Cnt* parameters. These deviations can be removed as follows. Averages of *Atm* parameters over time are not expected to show distinct spatial features on scales below 10° in latitude direction and a few hours in local time direction, respectively (when sufficiently far away from the poles or the terminators), compare Haus et al. (2013, 2014) for cloud parameters. For a surface target not exceeding such dimensions and where only the spatial emissivity fine structure is of interest, the relative emissivity map can be additively 'renormalized' by a constant value, such that the map's new median corresponds to the initial emissivity. The above mentioned systematic differences from the statistically scaled retrieval errors for the cases where the actual mean values of the *Atm* parameters deviate from the assumed values can be largely removed this way. The corresponding summarized *Atm* error measures can then be scaled with $1/\sqrt{N_r}$ (except for the relative errors) and are denoted by ${}^s\langle Atm \rangle$. The scaled noise measures are similarly denoted by ${}^sN_i := N_i/\sqrt{N_r}$. Errors due to uncertainties of spatially slowly varying *Spa* parameters (deep atmospheric temperature field, Section V.3.3 (p. 146)) are spatially slowly varying and are denoted by ${}^s\langle Spa \rangle_S$, even though they are not scaled. For a renormalized relative emissivity map of a target of the mentioned dimensions, they can be neglected as spatially almost constant emissivity offsets that have been removed by the renormalization.

There are *Spa* parameters that are spatially fast varying (on a scale of 100 km), for instance surface elevation (Section V.3.7 (p. 149)). Also, Section V.4.5 (p. 153) investigates a retrieval pipeline where emissivity directly interferes with the auxiliary parameters, because the latter are retrieved from a spectral range that includes the surface windows. For a given surface window, the emissivities from the other windows are then external parameters for the emissivity in the given window and will lead to additional *Spa* errors. In practice, however, clouds have *a priori* correlation lengths (500 km, see Section V.3.5 (p. 147)) and times (a few hours) different from those for emissivity (50 km, ∞ h, see Section V.3.2 (p. 145)). As has been shown by Kappel (2014), incorporation of *a priori* correlation lengths and times improves disentanglement of retrieval parameters, especially when they have very different *a priori* correlation lengths or times. The impact of the better disentanglement of clouds and emissivities on the *Spa* errors may be roughly estimated by scaling the external emissivity errors with the statistical factor $1/\sqrt{N_r}$. This can be motivated by the consideration that more repetitions should result in lesser impacts of interfering external emissivities, since clouds vary in time but the interfering emissivities do not. Even the relative *Spa* errors caused by interfering emissivities can be scaled in the same way, because their *a priori* correlation time is infinite. Note that such a scaling does not apply to surface elevation, because this is not a retrieval parameter. Scaled errors due to spatially fast varying parameters are summarized by quadratically adding the scaled external emissivity contributions and the (unscaled) contributions from other spatially fast varying *Spa* parameters. This 'spatial fine structure' part is denoted by ${}^s\langle Spa \rangle_F$. Note that it is not sufficient to renormalize an emissivity map that is not retrieved relative to an initial emissivity. In this case, the retrieved map can easily become saturated by approaching one of the emissivity bounds 0 or 1, and renormalization yields only a featureless map. A subsequent paper will exemplarily show that a renormalized relative emissivity map retrieved from actual measurements is reasonably independent of the *Cnt* parameters, the initial emissivity, and spatially and temporally constant modifications to *Atm* parameters.

This work studies retrieval errors only. Calibration and preprocessing errors (see Kappel et al., 2012b) of the measured spectra as well as simulation errors and unconsidered external parameters can lead to additional errors for the retrieved emissivities.

V.3 Parameters and reference spectra

Section V.3.1 (p. 145) recites some aspects of the radiative transfer forward model. Then, forward model parameters are discussed that may affect quantitative results of emissivity retrieval from VIRTIS-M-IR spectra of Venus' nightside emissions. For a certain 'default reference spectrum', the 'true' model parameter values are given. Also, for each discussed parameter, the range *CR* (see Eq. (V.4) (p. 140)) is specified over which it is expected to vary. These values are given in form of the expected mean value \bar{t} and double standard deviation

$2\sigma_t$. Also, the interval length I_t (Eq. (V.7) (p. 141)) is given, based on a reasonable correlation length λ_t . The stated information that is discussed in Sections V.3.2 to V.3.7 (p. 149) and needed in Section V.4 (p. 150) is summarized in Table V.1. For the noiseless default reference spectrum, Fig. V.2 displays radiance and Jacobians with respect to the discussed parameters in the range 1.0–2.3 μm . Section V.3.8 (p. 150) introduces a number of additional synthetic reference spectra that cover several important measurement situations.

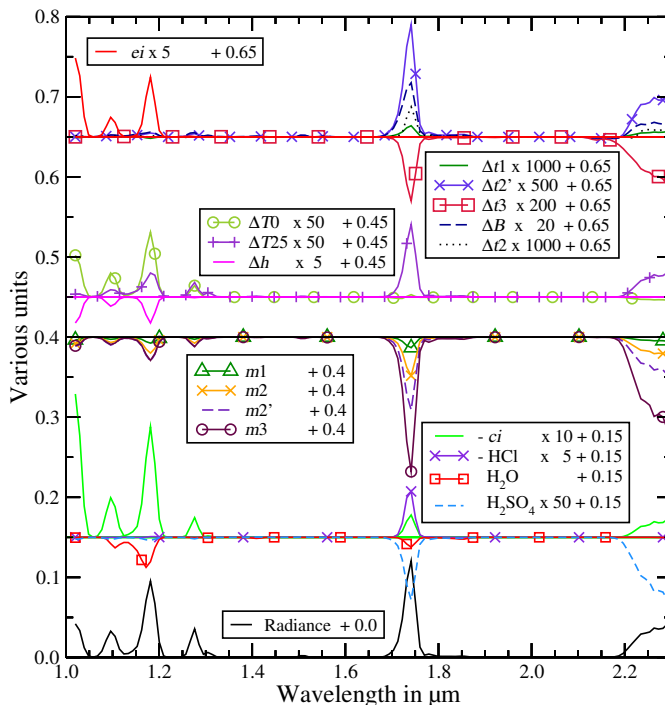


FIGURE V.2: (From bottom to top) Offset +0.0: synthetic radiance spectrum in units of $R:=W/(m^2 \text{ sr } \mu\text{m})$. Various positive offsets: Jacobians with respect to: H_2SO_4 concentration of cloud droplets (H_2SO_4 , unit $R/100\%$), H_2O and HCl column factors (units R), continuum factor in window i (ci , between 2.1 and 2.5 μm scaled by factor of 10 relative to remaining range for better representation, unit $R \cdot 10^{29} \text{ cm}^{-2}$), cloud mode i column factor (mi , unit R), variation of surface elevation (Δh , unit R/km), variation of temperature profile near 0 and 25 km, resp. ($\Delta T25$, $\Delta T0$, unit R/K), cloud altitude profile modifications (ΔB , Δti , units R/km), and surface emissivity in window i (ei , unit R), compare Table V.1. The notation $\times 50$ etc. in the legends indicates by which factor, if any, a Jacobian was scaled for better representation.

t	Description	\bar{t}_t	$2\sigma_t$	I_t
mi	Cloud mode i column factor	1.0	0.5	0.14
$\Delta t1$	Var. of mode 1 top alt.	0 km	3 km	0.85 km
$\Delta t2'$	Var. of mode 2' top alt.	0 km	3 km	0.85 km
$\Delta t3$	Var. of mode 3 top alt.	0 km	3 km	0.85 km
ΔB	Var. of modes 1+2'+3 base alt.	0 km	3 km	0.11 km
$\Delta t2$	Translation of mode 2 profile	0 km	3 km	0.85 km
H_2SO_4	H_2SO_4 conc. of cloud droplets	80.0%	7.5%	2.1%
H_2O	H_2O column factor	1.0	0.25	0.018
HCl	HCl column factor	1.0	0.25	0.018
Δh	Variation of surface elevation	0 km	0.2 km	0.4 km
ei	Surface emissivity, window i	0.65	0.15	0.3
$\Delta T0$	Var. of temp. profile near 0 km	0 K	3 K	0.11 K
$\Delta T25$	Var. of temp. profile near 25 km	0 K	3 K	0.11 K
ci	Continuum factor, window i	1.0	0.25	0

TABLE V.1: Summary of discussed external parameters t . Listed are each parameter's expected mean value \bar{t}_t , double standard deviation $2\sigma_t$, and half length of the sliding interval I_t for the determination of relative error measures, see Section V.2 (p. 138). The three kinds of parameters are grouped by the horizontal lines. The first group comprises *Atm* parameters, the second *Spa*, and the third *Cnt* parameters. Abbreviations: Var. - Variation, alt. - altitude, conc. - concentration, temp. - temperature.

V.3.1 Forward model

In order to numerically simulate observable nightside radiances, a plane-parallel, LTE, line-by-line radiative transfer forward model is utilized that takes into account thermal emissions by surface and atmosphere, and absorption and multiple scattering by gases and clouds. It is similar to the forward model described by Haus and Arnold (2010) with updates by Haus et al. (2013) and was also used by Kappel (2014), where the following summary is based on.

Temperature altitude profiles are taken from the Venus International Reference Atmosphere (VIRA, Seiff et al., 1985) but are optionally modified according to Section V.3.3. Surface temperature is set to the atmospheric temperature at the respective surface elevation. Pressure altitude profiles follow from hydrostaticity and the ideal gas law with VIRA pressure at surface elevation as initial value. CO₂ volume mixing ratio is 96.5%. Considered minor gaseous constituents are H₂O, CO, SO₂, OCS, HCl, and HF. HDO is treated such that for the default reference model, the D/H ratio corresponds to 150 times the corresponding ratio for Earth, compare with literature values of 95 ± 15 at 74 km (Krasnopolsky et al., 2013); 120 ± 40 below the clouds (de Bergh et al., 1991); 157 ± 15 at 72 km (Bjoraker et al., 1992). A HDO/H₂O ratio of 240 ± 25 between 70 and 95 km was reported by Fedorova et al. (2008). Altitude profiles of volume mixing ratios of minor gases are given by Haus and Arnold (2010) and are based on the profiles described by Pollack et al. (1993). Monochromatic absorption cross-sections of gases due to allowed molecular transitions are computed from the spectral line databases CSDS (CO₂, 0.4–0.9 μm and 1.25–1.33 μm , Tashkun et al., 2003), HITEMP (CO₂, Pollack et al., 1993, CO, H₂O isotopologues 161, 181, 171, Rothman et al., 1995), and HITRAN08 (H₂O isotopologues 162, 182, 172, SO₂, OCS, HCl, HF, Rothman et al., 2009) by using spectral line shapes listed by Haus and Arnold (2010). To be in line with Haus and Arnold (2010), the more recent HITEMP2010 (Rothman et al., 2010) is not yet considered here. Molecular Rayleigh scattering is treated according to Hansen and Travis (1974). Spatially and temporally varying non-LTE O₂ emissions ('O₂ nightglow') at 1.27 μm from an altitude region around 100 km (Piccioni et al., 2009) contaminate the 1.28 μm window (1.225–1.295 μm). For retrievals, this window will thus be blacked out, and O₂ nightglow need not be considered. The clouds are modeled according to Haus et al. (2013). As they form a complex source of emissivity retrieval errors, details are presented in Section V.3.5 (p. 147). Wavelength dependent scattering and absorption properties of the clouds are computed according to Mie theory (Wiscombe, 1980).

Resembling an argumentation by Kappel (2014) for a similar situation, from the total VIRTIS-M-IR spectral range (1.0–5.1 μm), only 1.0–2.3 μm shall be utilized for this study. Venus' nightside emissions in this range mainly originate from altitudes below 40 km (Haus and Arnold, 2010, Fig. 4), where temperature is quite stable with time, and they are thus nearly unaffected by the strong mesospheric temperature variations above 58 km that were observed by Haus et al. (2013, 2014); Tellmann et al. (2009). Also, details of the cloud altitude distribution have a minimal impact here, since the main cloud deck (≥ 48 km, Marov et al., 1980) resides above the line forming altitude region. In contrast, spectral signatures longward of 3 μm are strongly influenced by variations of temperature and cloud altitude distributions above 48 km. The range 2.3–2.6 μm is excluded in contrast to Kappel (2014), since the number of interfering parameters shall be kept as low as possible for this study, and in the VIRTIS-M-IR spectral range, most minor gases are active only there (Haus and Arnold, 2010, Fig. 19). Nightside radiances in the range 2.6–3 μm are too small to be useful (Haus and Arnold, 2010, Fig. 2). Note that calibration refinements and preprocessing for VIRTIS-M-IR data as performed by Kappel et al. (2012b) had mainly concentrated on the interval 1.0–2.6 μm .

To be in line with the typical characteristics of VIRTIS-M-IR, the full-width-at-half-maximum (FWHM) of the instrumental response function is set to 17 nm, spectral sampling to 9.49 nm, first spectral band is at 1.02 μm , corresponding to $m = 129$ wavelength bands for the range 1.0–2.3 μm excluding the 1.28 μm peak. For the default reference spectrum, the observation angle is set to zero (nadir-looking).

V.3.2 Surface emissivity

The Jacobians in Fig. V.2 illustrate that in the considered spectral range, spectral surface emissivity is observable in three peaks (1.02, 1.10, and 1.18 μm), which shall be called 'surface window peaks'. The 1.28 μm peak is also slightly affected by surface emissivity but is blacked out here. This gives rise to three parameters of primary interest, $\mathbf{e} =: (e_{1.02}, e_{1.10}, e_{1.18})$. They parameterize the spectral emissivity such that it is constant over

the ranges of the respective windows (1.02–1.055 μm , 1.055–1.125 μm , 1.125–1.225 μm , comprising about four, eight, and ten spectral bands, respectively). Knowledge of all three emissivities can suffice to discriminate between a number of potential surface materials and grain sizes (Haus and Arnold, 2010). Emissivities must lie in the interval $[0, 1]$, and default reference values are all set to 0.65.

In Section V.4.5 (p. 153), emissivities themselves are partially treated as external parameters. For this purpose, it is assumed that for most surface bins, the three corresponding emissivities should not differ much among each other, and the expected double standard deviations are set to $2\sigma_{ei} = 0.15$. With the expected mean values $\bar{t}_{ei} = 0.65$, the CR follow as $[0.5, 0.8]$, corresponding to a variation of 23%. Neglecting geologic activity, emissivities have the character of a *Spa* parameter (and thus have infinite correlation times), and the *a priori* correlation lengths can be set to 50 km (half FWHM of the surface data blurring). According to Eq. (V.3) (p. 140), the correlation coefficient at 100 km footprint separation follows as $C_{12} = 0.0059$. Thus, the approximation of I_{t_A} (Eq. (V.5) (p. 141)) for the case $C_{12} \ll 1$ can be applied, and I_{ei} can be set to 0.3, see paragraph subsequent to Eq. (V.7) (p. 141). Recall that the stated information is summarized in Table V.1 (p. 144).

V.3.3 Deep atmospheric temperature field

A potential source of emissivity retrieval errors is the deep atmospheric temperature field. Below 32 km, it is usually considered to be independent of latitude as described by VIRA. In that range, remote sensing has not yet been performed, and *in situ* measurements were mainly restricted to low latitudes up to about 30° . But altitudinal or latitudinal deviations from VIRA may occur there, and in fact are suggested by a General Circulation Model (Lebonnois et al., 2010a, GCM, personal communication). However, *in situ* measurements and the GCM suggest that the deep atmospheric temperature field is quite constant in time and local time, a consequence of high thermal inertia and thermodynamic stable layering.

Only the equatorial VIRA profile shall be considered here as default reference, and modifications to the VIRA deep atmospheric temperature altitude profile below 50 km are parameterized by the two external parameters $t_{\Delta T0}$ and $t_{\Delta T25}$, see Fig. V.3. $t_{\Delta T0}$ leads to a quadratic offset to VIRA that is zero and has zero

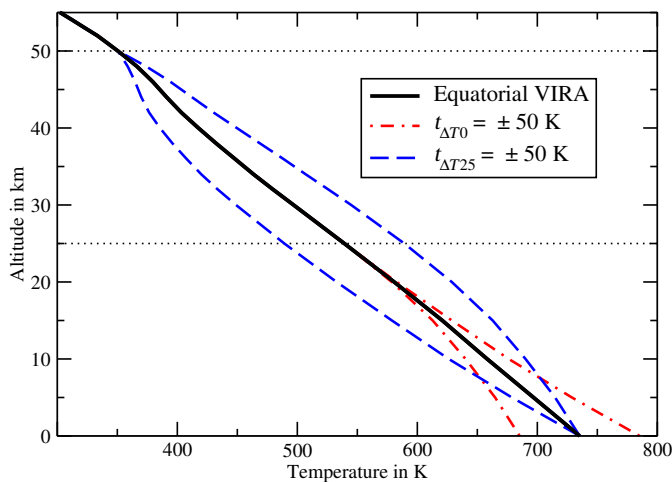


FIGURE V.3: Modified deep atmospheric temperature altitude profiles for values of $t_{\Delta T0}$ and $t_{\Delta T25}$ that are set to exaggerated values for better representation.

derivative at 25 km and is $t_{\Delta T0}$ at 0 km, regardless of the actual surface elevation. $t_{\Delta T25}$ leads to a quadratic offset that is zero at 0 and at 50 km and is $t_{\Delta T25}$ at 25 km. These crude modifications allow to change the temperature in the bulk of the deep atmosphere, and temperature and temperature lapse rate near the surface. $t_{\Delta T0}$ and $t_{\Delta T25}$ are assumed to have expected mean values $\bar{t}_{\Delta T0} = 0 \text{ K} = \bar{t}_{\Delta T25}$. Due to the extremely high atmospheric thermal inertia close to the surface, expected double standard deviations are conceivable to be in the order of $2\sigma_{\Delta T0} = 3 \text{ K} = 2\sigma_{\Delta T25}$ and correlation lengths in the order of $\lambda_{\Delta T0} = 4000 \text{ km} = \lambda_{\Delta T25}$, compare also tropospheric VIRA data above 32 km. The stated mean values correspond to the default reference VIRA temperatures 735.3, 539.2, and 337.0 K at 0, 25, and 50 km, respectively. The stated correlation length corresponds to about 38° latitude difference at the surface and translates to a correlation coefficient

$C_{12} = 0.99932$ at 100 km footprint separation. Thus, the approximation of I_{t_A} (Eq. (V.5) (p. 141)) for the case C_{12} close to 1 can be applied, and it follows that $I_{\Delta T_0} = 0.11 \text{ K} = I_{\Delta T_{25}}$ (Eq. (V.7) (p. 141)).

V.3.4 Minor gases

The only minor gases that provide significant opacity in the studied spectral range (1.0–2.3 μm excluding the 1.28 μm peak) are H_2O (including HDO) and HCl (Haus and Arnold, 2010, Fig. 19). CO influence at the interval boundary (2.28–2.3 μm) is neglected here. Both H_2O and HCl affect the peak at 1.74 μm , and H_2O is in addition observable between 1.10 and 1.20 μm (Fig. V.2 (p. 144)). The profiles from Haus and Arnold (2010, Fig. 6) are used as default reference altitude profiles, but the H_2O column is here scaled such that the concentration at the surface is 25 instead of 32.5 ppmv. The probed altitude regions are located below 25 km (1.10–1.20 μm) and between 20 and 30 km (1.74 μm). H_2O (excluding HDO) and HCl variations shall be parameterized by just total column factors $t_{\text{H}_2\text{O}}$ and t_{HCl} with respect to their default reference altitude profiles that consequently correspond to factors of $t_{\text{H}_2\text{O}} = 1.0 = t_{\text{HCl}}$, translating to 25 or 0.5 ppmv at 25 km, respectively. Recent studies showed that H_2O concentration in the deep atmosphere amounts to a value of 30 ppmv (Bézar et al., 2011), corresponding to $t_{\text{H}_2\text{O}} = 1.2$. This study considers $t_{\text{H}_2\text{O}}$ and t_{HCl} as external parameters with expected mean values $\bar{t}_{\text{H}_2\text{O}} = 1.0 = \bar{t}_{\text{HCl}}$. Expected double standard deviations are set to $2\sigma_{\text{H}_2\text{O}} = 0.25 = 2\sigma_{\text{HCl}}$ and correlation lengths to $\lambda_{\text{H}_2\text{O}} = 2000 \text{ km} = \lambda_{\text{HCl}}$. This can be estimated by observing the spatial variation in the results by Tsang et al. (2009) (for CO) and Haus et al. (2015a) (for CO and H_2O) and is here carried over to other minor gases as first estimate, with the atmospheric convection and its spatial scales as motivation. This leads to $C_{12} = 0.9973$ (Eq. (V.3) (p. 140)) and to $I_{\text{H}_2\text{O}} = 0.018 = I_{\text{HCl}}$ (Eq. (V.7) (p. 141)).

V.3.5 Clouds

The clouds of Venus are usually assumed to comprise four modes (1, 2, 2', and 3). Here, the modes are modeled according to Haus et al. (2013). Each mode consists of spherical droplets of 75% sulfuric acid. Refractive indices are taken from Palmer and Williams (1975) with supplements from Carlson and Anderson (2011). Cloud particle radii are log-normally distributed with modal radii of 0.3, 1.0, 1.4, 3.65 μm and unitless dispersions of 1.56, 1.29, 1.23, 1.28 for the four modes, respectively (Pollack et al., 1993). Default reference profiles of particle number densities N at altitudes h are taken from Haus et al. (2013) and are given by

$$N(h) = \begin{cases} N_0 \exp(- (h - h_t)/s_t) & h > h_t \\ N_0 & h_b \leq h \leq h_t \\ N_0 \exp(- (h_b - h)/s_b) & h < h_b \end{cases} \quad (\text{V.9})$$

Mode-specific values are listed in Table V.2. $N(h)$ is set to zero above 85 km. Actual cloud modal abundances

Cloud mode	1	2	2'	3
Top of peak density, h_t in km	65	66	60	57
Base of peak density, h_b in km	49	65	49	49
Upper scale height, s_t in km	5	3.5	1	1
Lower scale height, s_b in km	1	3	0.1	0.5
PND at h_b , N_0 in cm^{-3}	181	100	50	14

TABLE V.2: Cloud parameters for default reference model as given by Eq. (V.9). PND is the particle number density.

are defined by cloud mode factors $m_1, m_2, m_{2'}$, and m_3 that scale the number densities of the default reference altitude profiles that consequently correspond to cloud mode factors of $m_i = 1.0$. Some of the m_i will be parameterized through auxiliary parameters z_{mi} , while the remaining will be treated as external parameters t_{mi} . Variations of h_b, h_t, s_b , or s_t for cloud mode i rescales N_0 for mode i such that the total number of mode i particles remains constant. This is done in order to disentangle variations of altitude distribution and variations of particle abundance.

The influences of variations of the mode-common H_2SO_4 concentration $t_{\text{H}_2\text{SO}_4}$ of the cloud droplets and of the mode-specific cloud mode factors m_i on surface emissivity retrieval results are investigated in this work. There are studies like that by [Barstow et al. \(2012\)](#) that use or derive values of $t_{\text{H}_2\text{SO}_4}$ of locally up to 95%, which is much higher than the default reference value 75% and values used by other authors. However, the expected mean value $\bar{t}_{\text{H}_2\text{SO}_4}$ is set to 80% and double standard deviation to $2\sigma_{\text{H}_2\text{SO}_4} = 7.5\%$. The m_i may vary strongly, but no detailed knowledge for all modes is available. Expected mean values are all set to 1.0 and double standard deviations to 0.5. Also, some crucial altitude profile variations are studied as external parameters. For physical reasons, deviations of the h_b for modes 1, 2', and 3 from their default reference value 49 km are treated as a joint parameter $t_{\Delta B}$, since below that altitude, the temperature and pressure conditions are thought to force cloud particle numbers to sharply decrease except for possible haze (see *in situ* data described by [Knollenberg and Hunten, 1980](#), and [Marov et al., 1980](#)). The sole considered mode 2 profile variation is modeled to be just a vertical translation by the value $t_{\Delta t2}$. This is sufficient, because mode 2 particles are located well above the line forming altitude region (surface to 40 km) in the considered spectral range. Finally, h_t variations for modes 1, 2', and 3 are studied individually. Deviations from their default reference values are denoted by $t_{\Delta t1}$, $t_{\Delta t2'}$, and $t_{\Delta t3}$, respectively. $t_{\Delta B}$ and the $t_{\Delta ti}$ are all assumed to have expected mean values 0 km and double standard deviations 3 km, compare [Barstow et al. \(2012\)](#); [Haus et al. \(2013, 2014\)](#); [Ignatiev et al. \(2009\)](#) to get an impression of expectable variations of nightside cloud bases, tops, and dayside cloud tops, respectively. Any scale height variations are not considered, as they are of minor importance in the utilized spectral range, compared to h_b and h_t variations.

The expected correlation length for the total cloud opacity is set to $\lambda = 500$ km (with a few hours correlation time), which can be motivated by computing the auto-correlation function of observation movies of $2.3 \mu\text{m}$ nightside radiances as proxy. But note that there is also evidence for smaller scale cloud structures (100–200 km for mottled clouds observed by Venus Express VMC, [Titov et al., 2012](#)), and that small-scale convection in the middle cloud region causes large optical thickness variations ([Imamura and Hashimoto, 2001](#)). The correlation length 500 km is carried over to all other cloud parameters, except for $t_{\Delta B}$, where it is set to a value that is in accordance with the deep atmospheric temperature correlation length of 4000 km. The reason for this is the mentioned temperature related sharp decrease of cloud particle numbers at $t_{\Delta B} = 0$ km.

For $t_{\Delta B}$, it follows that $C_{12} = 0.99932$ (Eq. (V.3) (p. 140)) and $I_{\Delta B} = 0.11$ km (Eq. (V.7) (p. 141)). $t_{\Delta ti}$, t_{mi} , and $t_{\text{H}_2\text{SO}_4}$ all have $C_{12} = 0.9594$ and thus $I_{\Delta ti} = 0.85$ km, $I_{mi} = 0.14$, and $I_{\text{H}_2\text{SO}_4} = 2.1\%$.

V.3.6 CO₂ opacity correction

The atmospheric composition and the physical properties of the atmospheric gases and clouds are not sufficiently well constrained to provide reliable simulations of observable spectra. Especially, the opacity of Venus' atmospheric main gaseous constituent CO₂ is not well predictable for the high-pressure and high-temperature environment of Venus' deep atmosphere. The line databases of the allowed transitions are not based on laboratory measurements, but mostly on theoretical models ([Tashkun et al., 2003](#)) and contain errors ([Haus and Arnold, 2010](#); [Bézar et al., 2011](#)). The line shapes are still under discussion, as are additional opacity effects (continuum, collisional induced absorption, line mixing). The CO₂ opacity due to allowed transitions requires a wavelength dependent correction to produce good fits to real data at all. This correction is in the following shortly referred to as 'continuum'. It depends on the utilized line databases and line shapes but is independent of the measurement. For this study, the continuum is treated as spectrally constant throughout the range of an atmospheric transparency window, but it can depend on the window. These window-specific values are denoted by $c_{1.02}$, $c_{1.10}$, $c_{1.18}$, $c_{1.28}$, $c_{1.31}$, $c_{1.74}$, and $c_{2.3}$, and their default reference values in this study are set to 0.5, 3, 2, 7, 13, 27, 160 in units of 10^{-29} cm^2 , respectively.

These values are inspired by preliminary results of retrieving them with MSR ([Kappel, 2014](#)) as parameters that are common to a large set of highly diverse VIRTIS-M-IR nightside spectra, but they differ from the values used in the cited paper. With the exception of $c_{2.3}$, the continua are difficult to retrieve, even with MSR, since modifications to the retrieval pipeline and the choice of the set of utilized spectra and an initial surface emissivity can (moderately) affect the results. Recall that the here used continuum parameters do not only include the actual continuum contribution, but opacity corrections in general. In addition, they are not well-defined without at the same time stating the utilized line databases and line shapes and are thus not directly comparable to values given by authors who made other choices. Furthermore, a retrieval error analysis analogous to

the present one would be needed to understand the meaning of such retrieved opacity corrections. Therefore, values stated in earlier publications of the present authors should be, as mentioned in those works, regarded as working hypotheses and preliminary values. For better handling in this work, the above stated values are only abstractions of the latest retrieved continua, the latter allowing for extremely well fits to real spectra for a very high diversity of atmospheric and observational conditions. The stated values are rounded and do not include contributions that are not constant throughout the respective window's range. Note that $c_{2.3}$ is here the optimal value for the range 2.1–2.3 μm and differs from the optimal value for the range of the entire 2.3 μm window. It will be shown in Section V.4 that uncertainties in the continua are important sources of retrieval errors when absolute emissivities are retrieved. To avoid the high emissivity retrieval errors implied by the mentioned difficulties, the strategy for the emissivity retrieval will be modified by rather retrieving emissivities relative to an initial emissivity and showing the results to be reasonably independent of the continua (and the initial emissivity).

For the emissivity retrieval analysis, the stated continua are varied according to the external parameters $t_{c1.02}$, $t_{c1.10}$, etc., such that $c_{1.02} \cdot t_{c1.02}$ is the perturbed continuum in the 1.02 μm window, and so on. The expected mean values and double standard deviations are $\bar{t}_{ci} = 1.0$ and $2\sigma_{ci} = 0.25$, respectively. The correlation length of any continuum parameter is necessarily infinite, because it does not spatially vary, see also discussion by Kappel (2014). Thus, there are no relative spatial errors ($RL_i = 0$). This is compatible with Eqs. (V.5) (p. 141) and (V.6) (p. 141) in the limit where C_{12} approaches 1 (Eq. (V.3) (p. 140))⁴.

V.3.7 Surface elevation

The observed radiance depends on the surface elevation of a measurement's footprint. With increasing surface elevation, on the one hand, surface temperature decreases, which leads to lower emissions from the surface. On the other hand, the atmospheric path the emitted radiance has to travel, shortens, leading to less absorption and scattering. For each measurement footprint, surface elevation as fixed input to the radiance simulation is provided according to Kappel et al. (2012b), who use Magellan radar data (Ford and Pettengill, 1992; Rappaport et al., 1999) as basis. Magellan data itself is not perfect and a source of error, as unrealistic small-scale discontinuities in the raw data clearly show. Multiple scattering by gases and clouds cause atmospheric blurring of observable surface information (FWHM 100 km, Moroz, 2002). This is taken into account, as is motion blurring caused by the detector's movement relative to the footprint, but uncertainty in the knowledge of the exact blurring function for instance in dependence on cloud thickness is an additional source of error. Since not the topography itself has to be blurred, but the observed fundamental carrier of the data, the top-of-atmosphere radiance, an effective radiance computed from topographic data is blurred and transformed back to get the blurred surface topography. This procedure introduces further topography uncertainties, since it slightly depends for instance on assumptions on atmospheric gases and clouds, observation angle, and wavelength. Finally, the exact location and size of a measurement's surface footprint depend on the cloud top altitude, as this is roughly the effective source of observed emissions, because scattering strongly decreases only at even higher altitudes. This is also an error source, because this is taken into account for just an initial guess of the cloud top altitude in dependence on latitude based on results by Ignatiev et al. (2009).

The default reference surface elevation is set to 0 km. The deviation of the surface elevation utilized in the radiance simulations from the 'true' surface elevation is parameterized by the external parameter $t_{\Delta h}$ and is expected to amount to the order of 100 m in absolute value for planetary plains and even more for mountainous regions. This is compatible with the order of magnitude of the difference between the 100 and the 65 km FWHM atmospheric blurring of the topography as simple proxy for surface elevation uncertainties. Expected mean value and double standard deviation are set to $\bar{t}_{\Delta h} = 0$ km and $2\sigma_{\Delta h} = 0.2$ km, respectively. The *a priori* correlation length is 50 km (half FWHM of atmospheric blurring), such that $C_{12} = 0.0059$. Thus, the approximation of I_{t_A} (Eq. (V.5) (p. 141)) for the case $C_{12} \ll 1$ can be applied, and $I_{\Delta h}$ can be set to 0.4 km. Recall that Table V.1 (p. 144) summarizes the data for all discussed external parameters.

⁴Note: This assumes the \hat{e}_i in Eq. (V.6) (p. 141) to be continuous functions of t .

V.3.8 Reference spectra

Retrieval errors may depend on environmental and observational conditions. For instance, for all other parameters unchanged, observations of targets with few clouds should lead to smaller surface emissivity retrieval errors than observations of very cloudy regions. Thus, along with the default reference model, additional scenarios shall be investigated, which cover important key situations that may affect the retrieval errors. The scenarios are as follows (also see Fig. V.4).

1. Default reference model.
2. 50% larger abundances of cloud modes 2' and 3.
3. Surface elevation is set to 5000 m.
4. Surface emissivity is set to 0.9.
5. Observation angle is set to 60 degrees.

These descriptions always state the difference to the default reference model. The Euclidean norms $\|\mathbf{y}\|_2$

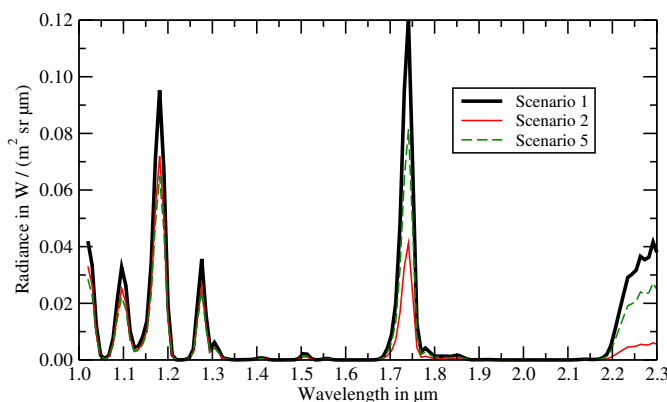


FIGURE V.4: Synthetic reference spectra for scenarios 1, 2, and 5. In comparison with scenario 1 (peak radiances at 1.02, 1.10, 1.18, and 1.28 μm are 0.0420, 0.0327, 0.0952, 0.0357 in units of $\text{W}/(\text{m}^2 \text{sr } \mu\text{m})$), radiances for scenarios 3 (0.0176, 0.0204, 0.0605, 0.0332) and 4 (0.0462, 0.0339, 0.0989, 0.0357) significantly differ only shortward of 1.3 μm and are not depicted.

for the five scenarios in the studied spectral range (1.0–2.3 μm excluding the 1.28 μm peak) are 0.257, 0.137, 0.225, 0.261, and 0.173 $\text{W}/(\text{m}^2 \text{sr } \mu\text{m})$, compare paragraph following Eq. (V.8) (p. 141) in Section V.2 (p. 138). Information losses due to random measurement errors are emulated by adding Gaussian noise with standard deviation $\sigma=10^{-4} \text{W}/(\text{m}^2 \text{sr } \mu\text{m})$ to the respective reference spectrum. For each retrieval run, noise is newly generated. As it can be seen from deep space observations, noise equivalent spectral radiance for actual VIRTIS-M-IR measurements is in the order of $4 \cdot 10^{-4} \text{W}/(\text{m}^2 \text{sr } \mu\text{m})$ for wavelengths shortward of 2.6 μm (256-sample-mode, unbinned, 3 s exposure time). Thus, σ is rather low, but it is a good description for measurements that are binned to match the expected achievable surface resolution (100 km FWHM, equal-area binning (Kappel et al., 2012b) leading to typically 30 spectra per bin for southern hemisphere mapping data at 45 °S). Finally, note that for the emissivity retrieval error analysis, *a priori* mean values and initial guesses for emissivities and cloud mode factors are intentionally set to values (0.5) that are different from their 'true' values, and their double *a priori* standard deviations are set to values (5 and 10, respectively) that are higher than that for operational retrievals, in order to not bind the parameters to their true values from the outset. Dependence on the *a priori* mean values is studied in Section V.4.

V.4 Results

V.4.1 Spectral ranges and auxiliary parameters

Modal abundances of Venus' clouds are parameterized by the cloud mode factors m_1 , m_2 , $m_{2'}$, and m_3 (Section V.3.5 (p. 147)). Due to their similar Jacobians, they are difficult to disentangle, and there is almost no

a priori information known. Also, they are strongly varying with large overall impacts on nightside spectra (Figs. V.2 (p. 144) and V.4). While some of the m_i must thus be retrieved in any case to allow for reasonable fits at all, this already suffices to produce quite good overall fits between 1.0 and 2.3 μm , whereas, technically speaking, surface emissivity is needed to just refine the quality of fits. The auxiliary parameters are selected from the m_i , therefore. Since they are difficult to disentangle, and it may not be possible to retrieve all of them, they will be just treated as auxiliary parameterization of how the cloud modes can possibly affect the shape of the spectra in the frame of a reasonable cloud model. They are not regarded as parameters with well-defined physical meaning, but may still indicate certain trends in the effective cloud particle size (Haus et al., 2013).

It was explained in Section V.3.1 (p. 145) that this study is restricted to the range 1.0–2.3 μm excluding the 1.28 μm window. This range comprises the surface windows at 1.02 μm (1.02–1.055 μm), 1.10 μm (1.055–1.125 μm), and 1.18 μm (1.125–1.225 μm) and the deep atmospheric windows at 1.31 μm (1.295–1.32 μm), 1.74 μm (1.65–1.9 μm), and 2.3 μm (short wavelength flank, 2.15–2.30 μm), see Figs. V.2 (p. 144) and V.4. The parameters of primary interest, the emissivities, can only be retrieved from the surface windows. Different retrieval pipelines can be applied to retrieve the auxiliary parameters along with the emissivities. Each pipeline is specified by a choice of m_i parameters and the spectral range where these m_i are retrieved from. For several different pipelines it is investigated, which one leads to the smallest emissivity retrieval errors. Only results for this pipeline are discussed in detail. The choice of the best pipeline should not strongly depend on details of the reference spectrum. Thus, only the default reference spectrum is considered for this purpose.

V.4.2 Total cloud factor from 1.31 μm peak

The first pipeline retrieves the total cloud factor z_{tc} from the 1.31 μm radiance peak and then the surface emissivities. z_{tc} simultaneously changes all four cloud mode factors in the same way, i.e. $m_i := z_{tc}t_{mi}$ for all external cloud mode scaling parameters t_{mi} . This pipeline emulates the approach by Müller et al. (2008) on the basis of a full radiative transfer simulation. Müller et al. (2008) developed a semi-empirical method to estimate the so-called thermal flux anomaly at 1.02 μm . This is the thermal flux from Venus' surface that is not due to topography related surface temperature. It is correlated to surface emissivity. Along with other semi-empirical data preprocessings, the authors de-cloud the 1.02 μm data with the surface-unaffected 1.31 μm peak as reference for cloud thickness. In doing so, they implicitly assume that there is no cloud induced color dispersion between 1.02 and 1.31 μm ('clouds are gray'). Their method has the advantage of being computationally very fast, and the authors can utilize all suitable VIRTIS-M-IR nightside spectra to generate a southern-hemisphere map of the time-averaged thermal flux anomaly. However, they utilize only two spectral bands, and especially the small 1.31 μm radiance is very susceptible to measurement noise and data calibration and preprocessing errors for instance due to imperfect straylight removal (Kappel et al., 2012b). Note that the 1.31 μm peak is sometimes affected by 1.27 μm O₂ nightglow. In contrast, Haus and Arnold (2010); Kappel et al. (2012b); Kappel (2014) apply a detailed radiative transfer simulation model and a retrieval algorithm and utilize the full spectral range 1.0–2.3 μm excluding the 1.28 μm peak to quantitatively determine surface emissivity. In addition, this approach enables a retrieval error analysis (the present paper). But the required computational resources are considerably larger, and only a selection of spectra can be studied that covers targets that were beforehand identified to be of special geological interest, for instance by using the results by Müller et al. (2008); Smrekar et al. (2010), or geologic maps (Ivanov and Head, 2006) derived from Magellan radar data (Pettengill et al., 1991; Ford and Pettengill, 1992), or the radiance ratio based quick-look method by Arnold et al. (2008). Note that always the full ranges of the respective spectral windows are utilized here and in the following. Exemplary tests show that noise impact on retrieved emissivities is 10–20% higher, when for each window only the single spectral band with the maximum radiance value is utilized, as should be done to achieve a direct comparison to Müller et al. (2008).

The emissivities e_i ($e_{1.02}$, $e_{1.10}$, and $e_{1.18}$) are now retrieved for the default reference model (scenario 1, Section V.3.8) and for 100 noise repetitions. The global error measures \overline{RG}_i , color dispersions \overline{CD} , relative error measures \overline{RL}_i (noisy versions of Eqs. (V.1) (p. 139), (V.2) (p. 139), (V.6) (p. 141)), and noise measures N_i (Eq. (V.8) (p. 141)) can then be computed. The summarized error measures follow immediately. Results are listed in Table V.3, where the values are rounded to the nearest whole percent. Note that t_{HCl} , $t_{e1.74}$, and $t_{e2.3}$ do not affect the relevant radiance peaks here. Also, emissivities need not be considered as

external parameters. Note that the relative error measures for continuum parameters are zero by construction

t	\overline{RG}_i			\overline{CD}	\overline{RL}_i		
$m1$	4	12	8	8	1	2	1
$m2$	4	14	10	8	1	2	2
$m2'$	3	4	2	2	0	1	0
$m3$	8	25	16	21	1	5	3
$\Delta t1$	1	2	2	2	0	1	1
$\Delta t2'$	1	3	3	2	0	1	1
$\Delta t3$	0	1	1	1	0	1	1
ΔB	7	20	22	17	0	1	1
$\Delta t2$	1	3	2	2	0	2	2
H_2SO_4	1	7	5	9	0	1	1
H_2O	5	66	72	115	0	7	8
Δh	12	18	16	7	12	20	18
$\Delta T0$	27	51	46	48	0	2	2
$\Delta T25$	18	36	43	32	0	1	1
$c1.02$	18	1	1	17		/	
$c1.10$	0	86	1	150		/	
$c1.18$	1	2	61	88		/	
$c1.31$	26	66	70	92		/	
$\langle Atm \rangle$	14	76	78	119	2	9	9
$\langle Spa \rangle$	35	65	65	58	12	20	18
$\langle Cnt \rangle$	32	108	93	198		/	
N_i	7	24	23				

TABLE V.3: Surface emissivity retrieval error and noise measures in percent, when the total cloud factor is retrieved as auxiliary parameter from the 1.31 μm peak. Scenario 1, 100 noise repetitions. The three kinds of parameters are grouped by the horizontal lines. The first group comprises *Atm* parameters, the second *Spa*, and the third *Cnt* parameters. The corresponding summarized error measures are given below the double horizontal line. The noise measures $N_{1.02}$, $N_{1.10}$, and $N_{1.18}$ are given in the last row in the respective \overline{RG}_i columns. The largest of the values at the different wavelengths is always typed in bold.

(Section V.3.6 (p. 148), indicated by '/' in the table).

The error measures are quite large and much worse at 1.10 and 1.18 μm than at 1.02 μm . Global and \overline{CD} *Atm* errors are dominated by t_{H_2O} at 1.10 and 1.18 μm , a consequence of the direct influence of H_2O in these peaks (Fig. V.2 (p. 144)). $t_{\Delta T0}$ and $t_{\Delta T25}$ errors dominate the global and \overline{CD} *Spa* error measures, but not the relative ones that are dominated by surface elevation uncertainties. Note that relative errors due to $t_{\Delta h}$ uncertainties are very similar to the corresponding global errors. This is in accordance with the expectation that over a distance (100 km for definition of relative errors) that exceeds the correlation length (50 km for $t_{\Delta h}$), relative spatial errors should not provide other information than the global errors already do. This also justifies the factor 1/2 in definition of the relative error measures (Eq. (V.6) (p. 141)). *Cnt* errors are worst at 1.10 μm . Noise impact is also quite large, and at 1.10 and 1.18 μm , it is three times as large as at 1.02 μm . This is mainly a consequence of the lower surface information content of those peaks, not just of the signal-to-noise ratio, which is for the 1.18 μm peak twice as large as for 1.10 μm (Fig. V.4 (p. 150)). The summarized error and noise measures show that single-spectrum retrieval of emissivities is not possible for this retrieval pipeline (but note that Müller et al. (2008) average over many spectra). Still, apart from impacts due to surface elevation uncertainties, spatial fine structure can be determined quite reliably as can be seen from the \overline{RL}_i -columns.

While the utilization of a wider spectral range than here allows to roughly estimate continuum parameters by applying MSR (shown by Kappel, 2014), this is not possible when only including the 1.31 μm radiance peak in addition to the surface window peaks. Also, for real spectra, the FWHM of the VIRTIS-M-IR instrumental response function varies with detector temperature and location on detector and is currently not sufficiently well predictable in the calibration procedure, as is the spectral band-to-wavelength mapping (Cardesin-Moinelo et al., 2010; Kappel et al., 2012b). By utilizing the spectral range 1.0–2.3 μm , it is possible to retrieve these instrumental parameters from the spectra themselves (shown for FWHM by Kappel, 2014), which is not well possible with the present pipeline.

V.4.3 Three cloud modes from 1.295–2.300 μm

A wider spectral range shall now be utilized. This also increases the available spectral information content and allows to retrieve more auxiliary parameters. When using the full spectral range considered in this work, information can be retrieved from six radiance peaks at most, three of which are carrying surface information. It is thus natural to assume that at most three auxiliary parameters can be retrieved. These comprise three of the four cloud mode factors m_i , and the remaining one has to be treated as external parameter.

When three cloud mode factors are retrieved from the 1.31, 1.74, and 2.3 μm peaks and then the emissivities, it turns out that the lowest overall error measures for emissivity retrieval are achieved when m_1 or m_2 are external parameters, whereas the lowest noise measures result for the external parameters $m_{2'}$ or m_3 . However, the error and noise measures are in all these cases not better and for some external parameters even slightly worse than for the pipeline in Section V.4.2 (p. 151). The reason is that three auxiliary parameters with Jacobians that are very similar longward of 1.295 μm (Fig. V.2 (p. 144)) are retrieved from three radiance peaks, where one of the peaks is small (1.31 μm peak radiance $\approx 10^{-2} \text{ W}/(\text{m}^2 \text{ sr } \mu\text{m})$, Fig. V.2 (p. 144)) and has a small signal-to-noise ratio, compare also Kappel (2014, Section 5). In the best pipeline (external m_2), the retrieved cloud mode factors m_1 , $m_{2'}$, and m_3 typically scatter with double standard deviations of respectively 1.6 (!), 0.4, and 0.1 for the 100 noise repetitions, indicating a bad disentanglement and leading to the high emissivity errors.

V.4.4 Cloud modes 2' and 3 as auxiliary parameters

To overcome this problem, only two cloud mode factors are now retrieved as auxiliary parameters from the range 1.295–2.300 μm and then the emissivities. The lowest error and noise measures result, when both m_1 and m_2 are treated as external, and $m_{2'}$ and m_3 are retrieved as auxiliary parameters. However, when for the same parameter setup only the radiance peaks at 1.74 and 2.3 μm are utilized, results are virtually identical: nearly all error and noise measures differ by 1 percentage point at most, and differences are evenly distributed in both directions, indicating a negligible information loss when discarding the 1.31 μm peak.

The most important difference to the results in Sections V.4.2 (p. 151) and V.4.3 is that the resulting noise measures are now much smaller (by 80%–90%). This can be explained by the much smaller scatter of the retrieved cloud mode factors $m_{2'}$ (double standard deviation of scatter 0.01) and m_3 (0.005) for the 100 noise repetitions. Compared to Section V.4.2 (p. 151), summarized global and \overline{CD} *Atm* error measures are slightly improved, whereas relative *Atm* errors are worse. Summarized *Spa* measures are slightly improved. Summarized *Cnt* measures are larger, because the radiance peaks at 1.74 and 2.3 μm are now included, resulting in $t_{c1.74}$ and $t_{c2.3}$ errors that naturally do not occur in Section V.4.2 (p. 151). Compared to Section V.4.3 (best case), summarized global *Atm* error measures are smaller, but color dispersion as well as most relative errors are slightly worse. Summarized *Spa* errors are slightly better except for $\overline{RG}_{1,10}$ and \overline{CD} . Relative error measures are almost the same, and summarized *Cnt* measures are slightly larger. The retrieval of $m_{2'}$ and m_3 as auxiliary parameters from the 1.74 and 2.3 μm peaks is preferable to the pipelines in Sections V.4.2 (p. 151) and V.4.3, mainly because of the now vastly better noise behavior that leads to much better defined retrieved parameters.

V.4.5 Cloud modes 2, 2', and 3 from 1.00–2.30 μm

Finally, the case is studied, where, along with emissivities, cloud mode factors m_2 , $m_{2'}$, and m_3 are retrieved from the range 1.0–2.3 μm excluding the 1.28 μm peak. This retrieval pipeline leads to the best overall results and is now discussed in more detail. Note that the emissivities do not affect the range longward of 1.295 μm , while the cloud modes affect the whole range. Emissivities directly interfere with the cloud modes, therefore, but the cloud modes are mainly determined from the spectral information content in the range longward of 1.295 μm with the added information that they have to be compatible with a realistic emissivity. This avoids cloud mode factors that allow a good fit longward of 1.295 μm but not in the surface windows. Note that, when m_2 instead of m_1 is treated as external parameter, most error and noise measures slightly worsen. When the 1.31 μm radiance peak is excluded, results do not significantly change, except that the $c1.31$ measures naturally

vanish and that the global H₂O error measure gets worse at 1.02 μm and improves at 1.10 μm, both by about ten percentage points.

Figure V.5 displays retrieved emissivities for a number of external parameters that lead to large error measures. For each depicted parameter, results are shown at least for the wavelength that leads to the worst case

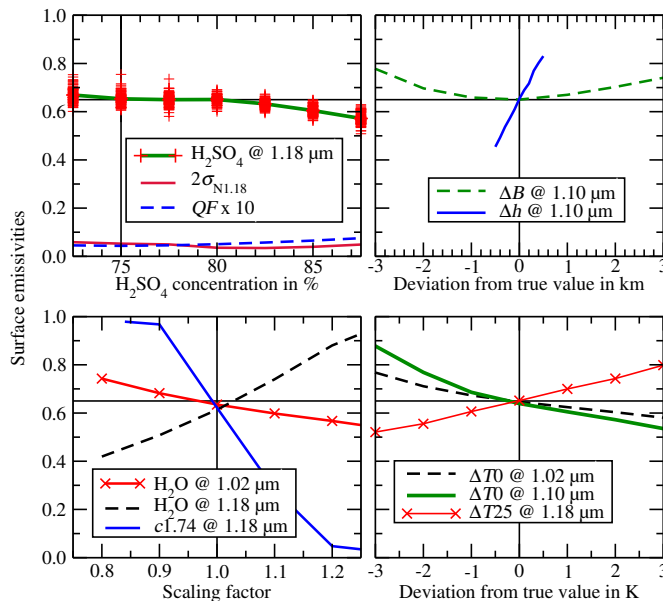


FIGURE V.5: Retrieved surface emissivities for variation of selected external parameters (compare Tables V.1 (p. 144) and V.4) for the pipeline in Section V.4.5. Parameter names and wavelengths of retrieved emissivities are given in the legends. All values are mean values over the 100 noise repetitions, except for top left display where the scattered symbols also show retrieved 1.18 μm emissivities for all noise repetitions. Top left display also shows quality of fit QF (averaged over noise repetitions and scaled by factor of 10 for better representation) and double standard deviation $2\sigma_{N1.18}$ of retrieved 1.18 μm emissivities. Only results for the valid intervals ($QF \leq 3\%$) are shown. True emissivities (0.65) and parameter values are indicated by continuous black lines.

global error measure. The emergence of the error measures can be qualitatively comprehended from such graphs. The deviation of retrieved emissivities from their true values 0.65 depends on wavelength and typically increases with increasing deviation of the external parameter from its true value. Since some of the graphs are not monotonic, the error measures in Section V.2 (p. 138) were not defined by using the deviations of retrieved from true emissivities at the CR boundaries, but by computing the maxima over the entire respective CR intervals (Eqs. (V.1) (p. 139), (V.2) (p. 139), and (V.6) (p. 141)). Large color dispersions occur where the retrieved emissivities at the three surface windows strongly disagree (in the figure for H₂O and to a lesser degree for $\Delta T0$). The relative error measure for a parameter is closely related to the product of I_t and the maximal slope in the graph (Eq. (V.6) (p. 141)). The top left display exemplarily demonstrates that the double standard deviations of the retrieved emissivities for the 100 noise repetitions vary only slightly with the external parameter, see discussion for Eq. (V.8) (p. 141). It also shows a case where the entire parameter interval $CR = [72.5\%, 87.5\%]$ over which the respective external parameter is expected to vary (Table V.1 (p. 144)) yields valid retrievals ($QF \leq 0.8\% \leq 3\%$).

Table V.4 lists the error and noise measures. The rows m_2 , m_2' , m_3 , and ei do not represent the error measures for external parameter variations, but for their *a priori* mean value variations over the range CR . This is indicated by a '+' in the first column. These entries are not taken into account when computing the summarized error measures, but they are negligibly small anyway. t_{H_2O} and $t_{c1.74}$ variations (for both $CR = [0.75, 1.25]$) outside of the intervals $[0.79, 1.25]$ and $[0.84, 1.24]$, respectively, lead to qualities of fits QF that on average over the noise repetitions exceed the threshold of 3% above which a retrieval is not regarded as valid and no error and noise measures are calculated (Section V.2.2 (p. 139)). Row $e1.02$ shows the 1.10 and 1.18 μm emissivity errors, when the 1.02 μm emissivity is treated as external parameter. Since a parameter that is treated as external parameter cannot be retrieved, the entries for $\overline{RG}_{1.02}$ and $\overline{RL}_{1.02}$ are flagged by '/'. The rows $e1.10$ and $e1.18$ show analogous results for external 1.10 and 1.18 μm emissivity

t		\overline{RG}_i		\overline{CD}	\overline{RL}_i		
$m1$		1	2	1	2	0	0 0
$m2$	+	0	1	0	1	0	0 0
$m2'$	+	0	0	0	0	0	0 0
$m3$	+	0	1	1	1	0	0 0
$\Delta t1$		0	1	1	1	0	0 0
$\Delta t2'$		1	2	1	1	0	1 0
$\Delta t3$		1	2	1	1	0	1 0
ΔB		5	20	14	13	0	1 0
$\Delta t2$		0	1	1	1	0	0 0
H_2SO_4		2	3	12	14	1	1 2
H_2O		15	26	43	58	1	1 2
HCl		2	3	8	9	0	1 1
Δh		9	12	12	3	10	13 12
ei	+	0	1	1	0	0	1 1
$e1.02$		/	26	22	5	/	30 24
$e1.10$		6	/	15	10	7	/ 18
$e1.18$		7	22	/	18	7	27 /
$\Delta T0$		18	35	35	13	0	1 1
$\Delta T25$		12	21	23	12	0	0 1
$c1.02$		18	1	1	17		/
$c1.10$		7	85	18	150		/
$c1.18$		14	42	49	75		/
$c1.31$		3	9	8	6		/
$c1.74$		24	83	94	171		/
$c2.3$		17	71	73	101		/
$\langle Atm \rangle$		17	33	48	62	1	2 3
$\langle Spa \rangle$		25	54	51	28	14	43 32
$\langle Cnt \rangle$		38	145	130	260		/
N_i		4	11	8			
${}^s\langle Atm \rangle$		3	7	10	12	1	2 3
${}^s\langle Spa \rangle_F$		9	14	13	5	10	15 13
${}^s\langle Spa \rangle_S$		22	41	42	18	0	1 1
sN_i		1	2	2			

TABLE V.4: Surface emissivity error and noise measures in percent for the pipeline in Section V.4.5 (p. 153), also compare Fig. V.5. Scenario 1, 100 noise repetitions. Values below the last double horizontal line are exemplarily scaled (flagged by superscript ‘ s ’ in ‘ t ’ column) to emulate MSR retrieval of emissivity relative to the initial emissivity 0.65 for $N_r = 25$ measurement repetitions. The largest of the values at the different wavelengths is always typed in bold.

variations, respectively. The entries in the rows $e1.02$, $e1.10$, and $e1.18$ contribute to the summarized Spa errors.

Compared to Section V.4.4 (p. 153), summarized Atm and Cnt errors have reduced. In particular, the relative Atm errors are much smaller. They show that the retrieval errors in the spatial fine structure of a retrieved emissivity map are here essentially not due to Atm parameters. The summarized Spa errors are smaller than in Section V.4.4 (p. 153), except for the relative error measures, where external emissivity variations now contribute. Noise measures have become worse (by a factor of 3) but are still much lower than for any of the other pipelines. The retrieved cloud mode factors m_2 , $m_{2'}$, and m_3 typically scatter with double standard deviations of respectively 0.2, 0.1, and 0.01 for the 100 noise repetitions. The error measures are still very large even for this pipeline. It thus seems to be impossible to obtain reliable emissivity data from single spectra.

However, if a surface bin is covered by several measurements, some error and the noise measures can be improved. This can be done by applying MSR, and by not retrieving absolute emissivities but emissivity maps relative to an initial emissivity and, when appropriate, a subsequent renormalization for targets with limited spatial extension. This was discussed in Section V.2.3 (p. 142), where also the corresponding scaling properties for the error and noise measures were given. Table V.4 illustrates this by showing the scaled summarized error and noise measures for $N_r = 25$ measurement repetitions, excluding the Cnt impacts that are assumed to be negligible. The spatial fine structure part of the Spa errors, ${}^s\langle Spa \rangle_F$, includes the contributions from

$t_{\Delta h}$, $t_{e1.02}$, $t_{e1.10}$, and $t_{e1.18}$. The spatially slowly varying part ${}^s\langle Spa \rangle_S$ comprises the impacts of $t_{\Delta T0}$ and $t_{\Delta T25}$. While noise measures are negligible now, the other errors are still quite large. Scaled global and \overline{CD} *Atm* errors are dominated by t_{H_2O} and $t_{\Delta B}$ uncertainties. Scaled global and \overline{CD} *Spa* errors are very large and are dominated by the temperature uncertainties. The large \overline{CD} ${}^s\langle Spa \rangle_S$ error indicates that the value by which a retrieved emissivity map is corrected in a renormalization may differ for the three surface windows. Spatial fine structure errors are completely dominated by $t_{\Delta h}$ uncertainties, as can be seen from the relative errors.

Spatial $t_{\Delta T0}$ and $t_{\Delta T25}$ variations should not depend on longitude (or local time) but may quite weakly depend only on latitude. The additive renormalization of the retrieved relative emissivity map can remove their error contributions for surface targets with limited latitudinal extension. Then, the retrieval errors due to *Spa* parameters effectively comprise only the spatial fine structure part ${}^s\langle Spa \rangle_F$. Not much can be done with respect to $t_{\Delta h}$ interferences that dominate ${}^s\langle Spa \rangle_F$, except that areas with more rugged mountains should be avoided to keep the elevation uncertainties small. Note that for areas with a wide latitudinal extension, consistent unreasonable large-scale latitudinal trends of retrieved emissivities may hint at a corresponding deviation of the deep atmospheric temperature from VIRA. To be able to recognize the significance of such a deviation and its order of magnitude, ${}^s\langle Spa \rangle_S$ is kept in the table.

Finally, note that for any two different sets of spectra that cover the same surface bin, *Spa* parameters and their uncertainty impacts are identical (at least up to first order in perturbations by the other external parameters). When the repeatability of MSR retrievals with different sets of spectra is tested, differences in the results should thus be mainly explainable with *Atm* errors and noise. The large t_{H_2O} dominated \overline{CD} ${}^s\langle Atm \rangle$ error indicates that errors of the retrieved emissivity maps can spatially differ for the three surface windows but not on the fine structure scale, see relative ${}^s\langle Atm \rangle$ errors and the correlation length for t_{H_2O} (Section V.3.4 (p. 147)). Note that there may be unsystematic calibration or preprocessing errors. For instance, an imperfection in the removal of straylight (Kappel et al., 2012b) can introduce unsystematic additional emissivity errors, and repeatability of MSR retrievals with different sets of spectra may not be given anymore. Furthermore, multi-spectrum retrieval errors are here only roughly estimated by scaling single-spectrum error and noise measures according to plausible rules. This may not sufficiently well describe the true multi-spectrum retrieval errors. Running into subsidiary multi-spectrum retrieval solutions, for example, can increase retrieval errors, and inclusion of information from adjacent measurements can strongly decrease retrieval errors. But the presented scaling should at least provide a rough guideline.

V.4.6 Other reference spectra

Until now, only the default reference spectrum (scenario 1) has been studied. This section presents for the pipeline from Section V.4.5 (p. 153) the error and noise measures for the other reference spectra that were introduced in Section V.3.8 (p. 150). Results are shown in Table V.5. However, considerable computer resources are required to generate a single table like Table V.4. Therefore, no noise repetitions are performed now, and only the noiseless cases are analyzed. To still get an exemplary estimate on noise measures, one single parameter ($m_{2'}$), while its *a priori* mean value is varied to cover its *CR*, is additionally studied for all 100 noise repetitions as before. Both the reduced parameter intervals ensuring valid *QF*'s and the RL_i values do not differ much from the corresponding values for noisy scenario 1 and are not shown here. The RL_i values for rows *e1.02*, *e1.10*, and *e1.18* are not much different from the respective RG_i values.

The noisy results from Table V.4 (S0 columns in Table V.5) agree well with the noiseless error measures, respectively the 'exemplary' noise measures for scenario 1 (S1). Only t_{H_2O} ($RG_{1.02}$, $RG_{1.10}$), $t_{e1.10}$ ($RG_{1.02}$, $RG_{1.18}$), $t_{e1.74}$ ($RG_{1.10}$, *CD*), and $t_{e2.3}$ ($RG_{1.10}$, $RG_{1.18}$, *CD*) have larger differences in their impacts. These can be explained, for instance, by the convergence to different subsidiary minima of the retrieval cost function. But in general, the noiseless results seem to be usable as guidelines for the noisy error measures (see also the summarized error measures), and the noise measures can be reasonably approximated by the exemplary noise measures. The standard deviations of the retrieved emissivities over the 100 noise repetitions are very similar to the averages over the *a posteriori* standard deviations of the individual retrieval runs.

While the larger cloud opacity in scenario 2 leads to a significant degradation of the retrieved emissivities for the pipeline in Section V.4.4 (p. 153), it does not consistently lead to worse error measures for the present

t	$RG_{1.02}$						$RG_{1.10}$						$RG_{1.18}$						CD					
	S0	S1	S2	S3	S4	S5	S0	S1	S2	S3	S4	S5	S0	S1	S2	S3	S4	S5	S0	S1	S2	S3	S4	S5
$m1$	1	1	1	1	1	<i>1</i>	2	1	1	1	1	<i>1</i>	1	1	1	0	1	1	2	2	2	<i>1</i>	2	2
$\Delta t2'$	1	<i>1</i>	1	1	1	1	2	1	1	1	<i>1</i>	1	1	0	1	0	0	0	1	1	2	<i>1</i>	1	1
$\Delta t3$	1	0	2	2	0	1	2	2	4	3	2	2	1	2	4	2	1	<i>1</i>	1	2	5	<i>1</i>	1	1
ΔB	5	5	6	16	6	5	20	20	15	25	<i>11</i>	20	14	14	17	20	<i>11</i>	13	13	13	13	7	5	13
H_2SO_4	2	<i>1</i>	7	2	1	2	3	2	19	4	2	2	12	12	6	10	10	13	14	14	24	8	11	15
H_2O	15	31	22	41	<i>16</i>	28	26	17	21	14	<i>10</i>	22	43	42	6	11	20	44	58	51	<i>19</i>	28	32	52
HCl	2	3	2	3	4	6	3	5	4	3	4	14	8	9	6	5	6	10	9	10	7	6	6	11
Δh	9	10	10	11	10	9	12	12	12	9	8	12	12	11	11	9	8	11	3	3	3	2	2	3
$e1.02$	/	/	/	/	/	/	26	22	43	8	14	22	22	19	40	7	12	18	5	4	5	<i>1</i>	2	4
$e1.10$	6	6	5	6	4	5	/	/	/	/	/	/	15	15	14	7	8	11	10	10	9	<i>1</i>	4	7
$e1.18$	7	7	7	9	6	7	22	22	24	<i>14</i>	14	21	/	/	/	/	/	/	18	17	20	6	9	17
$\Delta T0$	18	17	16	12	<i>11</i>	18	35	34	30	<i>12</i>	14	40	35	33	28	<i>12</i>	14	40	13	14	11	<i>1</i>	4	17
$\Delta T25$	12	12	13	7	11	12	21	21	22	7	15	21	23	23	23	8	17	23	12	12	12	<i>1</i>	7	12
$c1.02$	18	18	19	<i>11</i>	16	18	1	1	1	0	0	1	1	1	1	0	0	1	17	17	18	<i>11</i>	18	17
$c1.10$	7	3	3	2	3	3	85	84	84	43	70	84	18	8	8	2	6	8	150	148	149	38	112	148
$c1.18$	14	16	17	9	11	25	42	46	46	<i>12</i>	21	54	49	50	48	<i>18</i>	28	52	75	72	71	26	43	65
$c1.31$	3	3	3	7	3	3	9	9	9	10	7	9	8	8	8	9	6	7	6	6	6	3	4	6
$c1.74$	24	27	22	39	27	27	83	94	72	<i>54</i>	83	94	94	96	76	<i>54</i>	85	96	171	180	108	47	130	181
$c2.3$	17	16	9	17	16	18	71	62	39	33	51	70	73	65	41	36	52	72	101	84	33	24	55	99
$\langle Atm \rangle$	17	32	24	44	<i>18</i>	29	33	27	33	29	<i>16</i>	33	48	47	<i>21</i>	25	25	49	62	56	34	<i>31</i>	35	57
$\langle Spa \rangle$	25	25	25	21	<i>20</i>	25	54	52	63	23	30	55	51	48	57	20	27	52	28	28	28	7	13	29
$\langle Cnt \rangle$	38	40	35	45	37	45	145	148	126	78	122	154	130	127	99	68	104	131	260	259	201	<i>71</i>	186	262
N_i	4	3	7	6	4	5	11	11	18	8	8	16	8	8	15	6	6	12	8	8	15	6	7	11
$^s \langle Atm \rangle$	3	6	5	9	4	6	7	5	7	6	3	7	10	9	4	5	5	10	12	11	7	6	7	11
$^s \langle Spa \rangle_F$	9	10	10	11	10	9	14	14	16	10	9	13	13	12	14	9	9	12	5	5	5	2	3	5
$^s \langle Spa \rangle_S$	22	21	21	<i>14</i>	16	22	41	40	37	<i>14</i>	21	45	42	40	36	<i>14</i>	22	46	18	18	16	<i>1</i>	8	21
$^s N_i$	1	<i>1</i>	1	1	1	1	2	2	4	2	2	3	2	2	3	1	<i>1</i>	2	2	2	3	1	1	2

TABLE V.5: Emissivity error and noise measures in percent for the pipeline in Section V.4.5 (p. 153). S1–S5: noiseless error measures and exemplary noise measures for scenarios 1–5. S0: noisy results for scenario 1, for comparison to S1 carried over from Table V.4 (p. 155). Largest value out of S1–S5: bold, smallest: italic. Rows with just a few entries 1 and otherwise zero are omitted ($\Delta t1$, $\Delta t2$, and *a priori* data modification results for $m2$, $m2'$, $m3$, ei). Other notation as in Table V.4 (p. 155), but initial emissivity for S4 is 0.9.

pipeline. For instance, $RG_{1.10}$ improves even for $t_{\Delta B}$, and while $RG_{1.02}$ and $RG_{1.10}$ significantly increase for $t_{H_2SO_4}$, $RG_{1.18}$ improves significantly. Also note that for t_{H_2O} , S2 leads to a much smaller $RG_{1.18}$. Spa errors are predominantly unaffected by the larger cloud opacity, except for external $t_{e1.02}$ variations where retrieved emissivities at 1.10 and 1.18 μm significantly worsen. Cnt error measures improve for $t_{c1.74}$ and $t_{c2.3}$ and are unaffected elsewhere. The generally smaller radiances for S2 (Fig. V.4 (p. 150)) lead to a decreased signal-to-noise ratio, which results in accordingly increased noise measures. Except for a few parameters that lead to higher error measures at 1.02 μm , the error measures for S3 mostly decrease compared to S1, partially strongly. Apparently, in spite of the smaller radiances in the surface windows (Fig. V.4 (p. 150)), the increased surface elevation of 5 km leads for S3 to a better sounding of surface properties. This is because at this high elevation, the surface contributes a higher fraction to the observable surface window radiances, as can be checked by simulations, see also Haus and Arnold (2010, Fig. 9). For S4, most error measures are better than for S1. This is likely a result of the higher surface window radiances that follow from the higher true emissivities of 0.9, and of the correspondingly increased fraction of surface information in those radiance peaks. The noise measures for S3 and S4 are mostly slightly improved compared to S1, probably due to the increased surface information content, except for $N_{1.02}$, where for S3 the decreased signal-to-noise ratio following from the smaller surface window radiances (Fig. V.4 (p. 150)) apparently outweighs this effect. S5 exhibits larger t_{HCl} , $t_{\Delta T0}$, $t_{c1.18}$, and $t_{c2.3}$ impacts than S1, whereas most other error measures are unaffected. Most summarized error measures slightly increase. The smaller radiances for S5 that are due to the larger observation angle (Fig. V.4 (p. 150)) lead to a decreased signal-to-noise ratio and increased noise measures.

The scaled summarized error and noise measures for the renormalized MSR retrieval of relative emissivity with $N_r = 25$ repetitions (Section V.2.3 (p. 142)) exhibit higher noise measures compared to those for Section V.4.4 (p. 153), but they are still small. While $^s \langle Atm \rangle$ error measures have become slightly worse

at 1.02 μm , they have become significantly smaller in the other two surface windows. ${}^s\langle Spa \rangle_F$ and ${}^s\langle Spa \rangle_S$ errors have reduced.

The renormalized global errors are dominated by ${}^s\langle Spa \rangle_F$. Mostly, the error and noise measures are larger at 1.10 and 1.18 than at 1.02 μm . There is an overall tendency for better results at low cloud opacity, low observation angle, higher surface elevation, or true emissivity, but differences are not large. This can be seen from the quadratic means over the three wavelengths of the quadratically added global error and noise measures, which read 13%, 14%, 12%, 10%, 14% for S1–S5. The analogous results for the pipeline in Section V.4.4 (p. 153) read 18%, 19%, 13%, 13%, 18% and show slightly more pronounced differences between the five scenarios. They are also slightly larger, which underlines the preference of the present pipeline. The ${}^s\langle Atm \rangle$ error measures alone show no clear tendency except that S4 leads to best results. For a significantly higher measurement repetition number than $N_r = 25$, essentially only $t_{\Delta h}$ errors remain. The just discussed overall tendencies are still valid in this case, except at 1.02 μm where the influence of the scenario is negligible.

Without the renormalization for targets with limited latitudinal extension, ${}^s\langle Spa \rangle_S$ errors are unacceptably large, especially at 1.10 and 1.18 μm . Systematic latitudinal deep atmospheric temperature deviations from VIRA in the order of 3 K should be easily recognizable.

Since the FWHM of the VIRTIS-M-IR instrumental response function is currently not sufficiently well predictable in the calibration procedure (Kappel et al., 2012b), it shall be noted that spectra with a smaller FWHM (for instance 10 instead of 17 nm) tend to yield somewhat smaller (typically by a few percent) error and noise measures. Note that a tenfold increase of the spectral resolution (1.7 nm FWHM, 0.949 nm spectral sampling), does not lead, for instance in case of the retrieval pipeline from Section V.4.2 (p. 151), to large improvements compared to VIRTIS-M-IR resolution. However, at this high spectral resolution it is possible, for instance for the retrieval of $e_{1.02}$, to largely eliminate the interferences of the *Atm* parameters (unscaled summarized global 1.02 μm *Atm* error measure $\leq 2\%$) by retrieving only a total cloud factor along with $e_{1.02}$ from the 1.02 μm peak alone. The spectral range has to be restricted to 1.01–1.05 μm to exclude H_2O interferences at shorter wavelengths. This improvement underlines the importance of the interfering parameters' color dispersion effects that are still present in the first case but largely vanish over the narrow spectral range utilized in the second case. But even for the second case, a number of parameters ($t_{\Delta h}$, $t_{\Delta T0}$, $t_{\Delta T25}$, $t_{c1.02}$) with Jacobians that are very similar to the emissivity Jacobian in the 1.02 μm window lead to retrieval errors that are still large (noiseless $RG_{1.02}$ 10%, 12%, 10%, 24%). They could be removed by a renormalized relative emissivity retrieval, but errors due to topography uncertainties cannot be improved this way.

V.5 Summary and conclusion

The impacts were investigated that a number of interfering parameters and measurement noise can have on 1.02, 1.10, and 1.18 μm surface emissivities that are retrieved from VIRTIS-M-IR spectra of Venus' nightside emissions in the range 1.0–2.3 μm . Spectral information content is limited, and a number of parameters required for the numerical simulation of spectra cannot be uniquely derived from the measured spectra. These parameters are usually set to certain reasonable values that are compatible with current knowledge on atmospheric and surface conditions and allow to generate realistic synthetic spectra. When the true physical values deviate from these assumptions, this may cause surface emissivity retrieval errors.

Synthetic spectra were used as reference spectra where all underlying parameters are known by construction, and Gaussian noise was added to emulate measurement noise. Along with the emissivities, auxiliary parameters had to be retrieved from these synthetic measurements to allow for useful fits at all. The retrieved emissivities were compared to their true values. This was repeated for several different realizations of the Gaussian noise and with each studied interfering parameter set to a series of reasonable values. A number of emissivity retrieval error and noise measures were monitored to allow a categorization of the success of the emissivity retrieval. Global error measures represent for each studied interfering parameter the maximum relative impact on the retrieved emissivities when the interfering parameter is varied over the range it is expected to typically cover. A further characteristic error measure is the color dispersion between the emissivities at the three accessible wavelengths. The third error measure estimates relative errors between two simultaneously measured surface bins that are separated by 100 km, the order of the expected achievable spatial resolution of surface data. The noise measure represents typical retrieval errors due to measurement noise.

Several retrieval pipelines were tested to find out, which auxiliary parameters should be retrieved along with the emissivities from which spectral range in order to achieve the lowest retrieval errors. The best pipeline retrieves cloud mode factors m_2 , $m_{2'}$, and m_3 as auxiliary parameters from the spectral range 1.0–2.3 μm excluding the 1.28 μm peak that is in practice contaminated by non-LTE O_2 nightglow. It was found that even for this pipeline, error and noise measures are so large that emissivity cannot be derived within reasonable error margins from a single VIRTIS-M-IR spectrum, even though the fits well match the synthetic measurements in each case.

This situation can be improved by retrieving the emissivity of a surface bin as a parameter that is common to several measurements that cover this bin by applying the MSR multi-spectrum retrieval algorithm (Kappel, 2014). This assumes negligible geologic activity. MSR can also incorporate correlation lengths and times of the retrieval parameters and thus leads to more reliable results. But even with MSR, absolute emissivity values are difficult to obtain. To minimize errors that are due to CO_2 opacity uncertainties, it can be useful to set an initial emissivity value (e.g. 0.65) and to pre-determine wavelength dependent CO_2 opacity corrections as parameters that are compatible with as many and diverse as possible observed spectra by applying MSR. Using these pre-determined parameters, a surface emissivity map relative to the initial emissivity can be retrieved with MSR for the actual surface target. Moreover, spatially slowly varying systematic interferences from other parameters than the opacity corrections can lead to spatially large scale deviations of the retrieved from the true emissivity map. When only the spatial emissivity fine structure (100 km scale) of a target with limited spatial extensions (a few thousand km) is of interest, the retrieved relative emissivity map can be additively renormalized such that its new median value corresponds to the initial emissivity. Then the spatially slowly varying interferences can be neglected as spatially almost constant emissivity offsets that have been removed by the renormalization. On the other hand, for areas with a wide latitudinal extension, consistent unreasonable large-scale latitudinal trends of retrieved emissivities may hint at a corresponding deep atmospheric temperature deviation from VIRA (Seiff et al., 1985) in latitude direction.

A full multi-spectrum retrieval error analysis is very complex and requires considerable computer resources. But the retrieval error and noise measures can be roughly estimated by plausible scaling rules that emulate the statistical impact when each surface bin is covered by N_r repeated measurements. This was exemplarily done for $N_r = 25$ and five different reference spectra that represent various typical environmental and observational conditions (Table V.5 (p. 157)). Renormalized relative emissivity retrieval errors due to uncertainties of statistically independent temporally varying interfering parameters like cloud properties and minor gas abundances can add up to 3%–10% of the true emissivity value with color dispersions between 6% and 12%, depending on surface window and spectrum. Temporally constant interfering parameters with a spatial fine structure on a scale of 100 km (surface elevation, interfering emissivities from other surface windows) contribute another 9%–16% with color dispersions between 2% and 5%. Measurement noise with a standard deviation of $10^{-4} \text{ W}/(\text{m}^2 \text{ sr } \mu\text{m})$ leads to additional 1%–4%. Reasonable *a priori* data modifications were checked to have negligible impacts. Spatial fine structure errors can add up to 10%, 15%, and 13% for the three wavelengths and are completely dominated by the impacts of assumed surface elevation uncertainties of 200 m (Table V.4 (p. 155)). Useful results are thus possible, but the errors are still not small. Retrieved emissivities are most reliable at 1.02 μm . The most suitable spectra for emissivity retrieval tend to be those with a small cloud opacity, high surface elevation, high emissivity, and small observation angle, but this depends on the emissivity window, retrieval pipeline, and measurement repetition number.

It may be possible that utilization of a wider spectral range of VIRTIS-M-IR could help to reduce errors (but not those due to surface elevation uncertainties). In particular, the cloud mode abundances can probably be better disentangled by additionally using the range around the 4.3 μm CO_2 absorption band, compare Haus et al. (2013). But then, the strong spatial and temporal variations of the mesospheric temperature altitude profiles must be considered by treating them as additional auxiliary parameter vector. A further approach could be to choose more or different auxiliary parameters or to pre-estimate some parameters by other means (ratio based estimation of cloud bottom altitude or H_2SO_4 concentration of cloud droplets, Barstow et al., 2012), but note that this does not concern the parameters that are the most problematic for emissivity retrieval. Also note that even a tenfold spectral resolution does not help to avoid errors due to topography uncertainties. Geologic input and the ranges of the retrieved renormalized relative emissivities and the quality of the fits may help to constrain realistic initial emissivities.

Haus and Arnold (2010) showed $1.02\ \mu\text{m}$ emissivities retrieved from many VIRTIS-M-IR spectra. The authors noted that these emissivities decreased⁵ for increasing topography. It was mentioned that the results were preliminary and had to be interpreted with much care due to interferences from other parameters. In fact, they applied a single-spectrum retrieval. Even though the fits had been very good, it follows from the present work that these results were probably not reliable due to precisely such interferences.

This work has studied retrieval errors only. Calibration, preprocessing, and forward model errors can lead to additional emissivity errors. But calibration and preprocessing were improved by Kappel et al. (2012b), and the forward model is capable of simulating spectra that extremely well fit the measurements for a large variety of physical and observational conditions. Calibration and preprocessing and functional descriptions of the simulated spectra are not expected to be severely wrong, therefore. Even if they were wrong, renormalized relative emissivities would not be strongly affected by that. Interfering parameters that were not studied here can also introduce further errors, for instance varying cloud mode particle size distributions or chemical compositions, further details of the cloud mode altitude distributions, unknown absorbers like possible haze close to the surface (Grieger et al., 2004), etc. But impacts of quasi-random time variations of these parameters should disappear with the inverse square root of the repetition number, and impacts of systematically wrong assumptions should be greatly diminished through the renormalized relative emissivity retrieval. Overall, the potential additional errors mentioned in this paragraph are expected to be not large compared to the already determined MSR retrieval errors, and the results of this paper should give good advice on the typical errors that may occur.

A subsequent paper is planned by the present authors, where, based on the current results, a renormalized relative emissivity map will be retrieved with MSR, and where retrieval errors and reproducibility of results for modified external parameters and initial emissivity will be discussed. It will also be checked, whether maps retrieved from different selections of measurements reasonably agree. For this kind of test, surface elevation and the other temporally constant interfering parameters and their uncertainty impacts are identical (at least up to first order in perturbations by the remaining interfering parameters). Only temporally varying parameters can lead to significant differences. Disagreements that are too large to be explained by the presented results may be due to calibration and preprocessing errors or may indicate that there are temporally varying interfering parameters that have not been considered here.

Acknowledgements

This work is funded by the German Aerospace Center (DLR) e.V. The authors would like to thank the reviewers for their valuable suggestions to improve this paper.

⁵Corrected: In the published paper, it was mistakenly stated that these emissivities increased for increasing topography.

Chapter VI

Multi-spectrum retrieval of Venus IR surface emissivity maps from VIRTIS/VEX nightside measurements at Themis Regio[†]

David Kappel^{1,2}, Gabriele Arnold¹, Rainer Haus³

¹German Aerospace Center (DLR), Institute of Planetary Research, Rutherfordstrasse 2, 12489 Berlin, Germany

²University of Potsdam, Institute of Physics and Astronomy, Karl-Liebknecht-Straße 24/25, 14476 Potsdam-Golm, Germany

³Westfälische Wilhelms-Universität Münster, Institute for Planetology, Wilhelm-Klemm-Straße 10, 48149 Münster, Germany

A copyedited version of this article was published in:
Icarus, 265:42–62, 2016.

Received 08.05.2015; received in revised form 07.10.2015; accepted 14.10.2015.

Available online 23.10.2015. doi:[10.1016/j.icarus.2015.10.014](https://doi.org/10.1016/j.icarus.2015.10.014)

Copyright: 2015 Elsevier Ltd. All rights reserved.

Abstract

Surface emissivity maps in the infrared can contribute to explore Venus' geology. Nightside radiance spectra at Themis Regio acquired by the IR mapping channel of the Visible and InfraRed Thermal Imaging Spectrometer (VIRTIS-M-IR) aboard Venus EXpress (VEX) are used to derive emissivity data from the three accessible spectral surface windows at 1.02, 1.10, and 1.18 μm . The measured spectra are simulated by applying a full radiative transfer model. Neglecting geologic activity, a multi-spectrum retrieval algorithm is utilized to determine the emissivity maps of the surface target as parameter vectors that are common to many spectrally resolved images that cover this target.

Absolute emissivity values are difficult to obtain due to strong interferences from other parameters. The true emissivity mean of the target cannot be retrieved, nor can the emissivity mean of a retrieved map be strictly preset. The retrieved map can exhibit trends with latitude and topography that are probably artificial. Once the trends have been removed in a post-processing step, it can be observed that the magnitude of the resulting spatial emissivity fluctuations around their mean value increases with increasing mean value. A linear transformation is applied that converts the de-trended map to exhibit a defined emissivity mean value called reference emissivity, here 0.5, yielding the 'renormalized emissivity map' with accordingly transformed fluctuations. It is verified that renormalized emissivity maps are largely independent of the emissivity mean before renormalization, of modifications to interfering atmospheric, surface, and instrumental parameters, and of selected details of the retrieval pipeline and data calibration and preprocessing. Extremely large emissivity

[†]When this thesis was submitted for examination (27.05.2015), it contained this article in the form it was initially submitted to *Icarus* (08.05.2015). Here, the article is updated to its revised form in which it was published in *Icarus*. Apart from minor corrections and clarifications, the revised version is slightly re-ordered and contains new figures and the new Appendices A.3 and A.4. Results are unchanged. The appendix is published online-only as supplementary material.

retrieval errors due to imperfect or unconsidered forward model parameters are effectively avoided. If the absolute emissivity at a given bin of the target were known, the absolute emissivity map of the entire target could be computed according to the mentioned transformation, assuming absent true trends with latitude and topography. Until then, the renormalized emissivities are interpreted as spatial variations relative to the reference emissivity. They represent an important step toward the retrieval of absolute emissivities.

Renormalized emissivity maps of Themis Regio at the three surface windows are determined from 64 measurement repetitions. Retrieval errors are estimated by a statistical evaluation of maps derived from various disjoint selections of spectra and using different assumptions on the interfering parameters. Double standard deviation errors for the three surface windows amount to 3%, 8%, and 4%, respectively, allowing geologic interpretation. A comparison to results from an earlier error analysis based on synthetic spectra shows that unconsidered time variations of interfering atmospheric parameters are a major error source. Spatial variations of the 1.02 μm surface emissivity of 20% that correspond to the difference between unweathered granitic and basaltic rocks would be easily detectable, but such variations are ruled out for the studied target area. Emissivity anomalies of up to 8% are detected at both 1.02 and 1.18 μm . At present sensitivity, no anomalies are identified at 1.10 μm , but anomalies exceeding the determined error level can be excluded. With single standard deviation significance, all three maps show interesting spatial emissivity variations.

VI.1 Introduction

Near-infrared (NIR) spectroscopy is a powerful tool to study composition, texture, and grain size of the surface material of planetary objects. Venus is a geologically interesting target, but little is known about the global surface composition, since the hot dense atmosphere complicates NIR remote sensing. On Venus' dayside, the surface is not observable at NIR wavelengths. The available radar data acquired by the Magellan mission (global maps of topography, slope, reflectivity, and emissivity, [Pettengill et al., 1991](#); [Ford and Pettengill, 1992](#)) are less diagnostic for surface composition analyses.

Due to the high surface temperatures, thermal radiation from the surface and low atmosphere dominates NIR spectra of Venus' nightside. Compositional information about the surface is given by its emissivity. Numerous diagnostic absorption bands for minerals and rocks appear within the NIR. Spectra of rock-forming iron-rich mafic minerals like olivine and pyroxenes display characteristic bands at 1 and between 2 and 2.5 μm . Generally, these features tend to increase the spectral emissivity at these wavelengths compared to the spectral continuum. Bright felsic minerals have mostly featureless spectra and low NIR emissivities. In contrast, weathering products like iron oxides or iron sulfides are characterized by featureless spectra of high emissivity. Thus, maps of NIR emissivity data can provide useful information about the nature of Venusian surface material on a global scale. The present work discusses the remote sensing of such maps.

Radiance in the infrared originating from Venus' surface on the dayside is far outweighed (typically by more than three orders of magnitude) by sunlight scattered back from the cloud tops, and surface information cannot be obtained there. The present work focuses on the nightside, therefore. The surface emits radiation that depends on surface temperature (and thus topography) and emissivity. As it propagates upward, it gets mixed with radiation resulting from thermal emissions by the atmospheric gases. In the dense atmosphere of Venus, radiation is multiply scattered and mostly absorbed by atmospheric gases and clouds, and partly reflected back from the surface. Much of the radiation's surface information is destroyed by these processes. Multiple scattering also leads to a spatial blurring of the surface information on a horizontal scale of 100 km ([Moroz, 2002](#)). Only a few narrow spectral transparency windows allow strongly modulated surface radiation to escape into space. This radiation was recorded by the InfraRed Mapping channel of the Visible and InfraRed Thermal Imaging Spectrometer (VIRTIS-M-IR) aboard Venus EXpress (VEX) ([Drossart et al., 2007](#); [Piccioni et al., 2007](#); [Arnold et al., 2012c](#)). VIRTIS-M-IR acquired spectrally resolved images in the range 1.02–5.1 μm . Each spatial pixel provided a radiance spectrum sampling this range with 432 spectral bands. These measurements are currently the only hyperspectral data that allow for a reliable derivation of IR surface emissivity information on global scales. In the VIRTIS-M-IR spectral range, the only parts of the acquired radiance spectra that carry surface information are the spectral peaks at 1.02, 1.10, and 1.18 μm , therefore called the surface window peaks. The fraction of radiance that originates from the surface is smaller in the

latter two peaks (Haus and Arnold, 2010, Fig. 5), which are consequently less sensitive to surface information than the first one.

It has been demonstrated by Helbert et al. (2008) and Müller et al. (2008) that surface information at $1.02\ \mu\text{m}$ can be extracted from VIRTIS-M-IR measurements to some extent in the form of the time-averaged so-called thermal flux anomaly. This is the thermal flux from Venus' surface that is not due to topography-related surface temperature. It is correlated to surface emissivity. The cited authors applied semi-empirical approaches to de-cloud the $1.02\ \mu\text{m}$ VIRTIS-M-IR radiances, with the small surface-unaffected $1.31\ \mu\text{m}$ radiance peak as reference for cloud absorption, and to remove the influence of surface topography. This method utilizes only two spectral bands and is computationally very fast. The authors were therefore able to process all suitable VIRTIS-M-IR nightside spectra. Based on these results and on gravity field data, Smrekar et al. (2010) were able to identify candidates for recent hotspot volcanism. By correlating the thermal flux anomalies and topography data, Müller et al. (2012b) have also identified a possible variation in Venus' rotation period that may be due to long-term changes in the atmospheric circulation. Furthermore, constraints on the planet's volcanism rate (Müller et al., 2012a) were derived based on the semi-empirical approach to evaluate VIRTIS-M-IR data.

A disadvantage of the method of Helbert et al. (2008) and Müller et al. (2008) is that the small $1.31\ \mu\text{m}$ radiance is very susceptible to measurement noise and data calibration and preprocessing errors. Moreover, the varying characteristics of the spectral instrumental response function and spectral band-to-wavelength mapping cannot be taken into account, and the meaning of the flux anomaly map with respect to emissivity and its reliability are not entirely clear in this otherwise very successful approach. Based on these difficulties, it was an open question, whether surface emissivity data can be obtained from the $1.02\ \mu\text{m}$ window on the basis of a full radiative transfer simulation that takes into account the extreme environmental conditions in Venus' deep atmosphere in combination with a retrieval algorithm that respects available *a priori* information. The present work demonstrates that this is possible. In addition, emissivity data from the other two surface windows are determined. Moreover, the reliability of the determined emissivity data from all three windows is quantified.

Starting with an initial parameter set describing defined states of atmosphere, surface, and instrument, it is possible to simulate VIRTIS-M-IR spectra by numerically solving the radiative transfer equation, taking into account thermal emissions by surface and atmosphere, and absorption and multiple scattering by gases and clouds (Haus and Arnold, 2010). Some of the initial parameters can be iteratively modified to improve the fit of the simulated to a given measured spectrum. The parameters that result in the best fit (i.e. the 'retrieved parameters') can be interpreted to describe the actual atmospheric, surface, and instrumental states that led to the measured spectrum. In the present work, the spectral range $1.02\text{--}2.3\ \mu\text{m}$ is utilized to determine in addition to emissivity a number of auxiliary parameters like the cloud abundance that are required to obtain meaningful emissivity values.

This inversion of the radiative transfer equation is mathematically ill-posed, since different surface and atmospheric parameters can describe the same spectrum equally well. The retrieval has to be regularized, therefore. Moreover, the emissivity retrieval error analysis by Kappel et al. (2015) that was based on synthetic spectra showed that the retrieval of emissivity from a single spectrum must fail, even when taking into account Bayesian *a priori* information in the form of expected mean values and standard deviations for the parameters to be retrieved, along with measurement and simulation error information. The reason is that there are interfering parameters like the cloud bottom altitude that cannot be sufficiently reliably derived from the measured spectrum itself but have to be set to certain assumed values to enable the radiative transfer simulation.

Since the single-spectrum information content is thus obviously too low, several spectra have to be utilized to derive surface data. This can be done by applying the recently developed Multi-Spectrum Retrieval algorithm MSR (Kappel, 2014). MSR allows for the additional incorporation of expected correlation lengths and times as *a priori* information for the retrieval parameters of several spectra. It can also retrieve surface emissivity as parameter that is common to several spectra that cover the same surface spot. This way, the probability of retrieving unreasonable parameter values and unlikely spatial-temporal parameter distributions is decreased, and the reliability of retrieved surface emissivity can be enhanced.

Kappel et al. (2015) also showed that the retrieval of absolute emissivity values produces extremely large errors even when applying MSR. The authors proposed to rather determine emissivity maps relative to a certain initial emissivity value. This way, large emissivity errors, for example due to differences between the spatial distributions of time-averaged assumed and true interfering parameters, can be avoided. However, it

must then be clarified, how the relative emissivity maps have to be interpreted. The present work refines the concept of relative emissivity maps.

The question now is, whether the magnitude of the relative emissivities' errors is finally small enough to allow for a geologic interpretation of the derived maps. Or in other words, how well do the retrieved maps represent the true ones? No ground truth within the surface coverage suitable for MSR is available so far. To answer this question, the first main objective of the present work is the exemplary determination of emissivity data maps at 1.02, 1.10, and 1.18 μm of a selected surface target, and the second one is an estimate of the reliability of these maps. It will be shown that the relative maps are reasonably independent of the selection of the measurement data set, the initial emissivity value as well as of other interfering parameters. A geologic interpretation of the determined maps is beyond the scope of the present work. It would require additional information to be taken into account like the Magellan radar reflectivity, emissivity, and slope data, geologic maps derived from the Magellan data, as well as context from relative infrared emissivity maps of further target areas to study large-scale trends. A detailed geologic discussion will be given in a follow-up paper.

In contrast to the very fast semi-empirical method by Müller et al. (2008), the present approach, as any retrieval based on full radiative transfer simulations, requires considerable computer resources and is first selectively applied to targets that are beforehand identified to be of special geological interest. Since the estimate of the reliability of the determined maps in this work is partly based on the comparison of maps derived from disjoint measurement data sets, it is also important that the target is located in an area that exhibits as many as possible suitable VIRTIS-M-IR measurements. Both conditions are fulfilled at Themis Regio, the western part of which is selected as target area (35–47 °S, 270–288 °E) to demonstrate the present approach.

Themis Regio is a highland with a diameter of about 2000 km, located in the southern hemisphere of Venus. It is covered by the USGS quadrangle V-53 extending from 25–50 °S and from 270–300 °E (Stofan and Brian, 2012). Themis Regio has an average height of about 500 m. It is characterized by a corona-dominated hotspot rise related to a long-duration, non-simultaneous, small-scale upwelling (Stofan et al., 1995). Themis Regio contains significant extensional deformation (Stofan and Brian, 2012). Gravity data and the topographic swell suggest that this region is likely underlain by an active plume with ongoing surface deformation due to growth of the rise (Smrekar and Stofan, 1999). The target area used for this paper includes geologic structures like the Shiwanokia Corona (42.0 °S, 279.8 °E, see Hayward (2015) for the nomenclature and Fig. VI.3 (p. 176)d for a topography map of the target area) with steep sided domes, Shulamite Corona (38.8 °S, 284.3 °E), Abeona Mons (44.8 °S, 273.1 °E), Mertseger Mons (38.1 °S, 270.3 °E), impact craters like Kenny (44.4 °S, 271.1 °E), Aksentyeva (42.0 °S, 271.9 °E), and Sabin (38.5 °S, 274.7 °E) with a dark parabola, and wrinkle ridges. Former work suggests that some edifice fields in Themis Regio correlate with high thermal flux anomalies at 1.02 μm extracted from VIRTIS-M-IR/VEX measurements (Müller et al., 2008) and attributed to relatively stratigraphically young units of volcanic origin (Stofan et al., 2010). Therefore, Themis Regio is a geologically interesting target area, and the cited thermal flux data can be compared to real emissivity values derived here at 1.02, 1.10, and 1.18 μm .

The present paper is a direct continuation of a research line that aims at the determination of emissivity data from VIRTIS-M-IR measurements based on radiative transfer simulations. This line was started by Arnold et al. (2008) who developed a quick-look method to identify emissivity anomalies. This method was corroborated by first radiative transfer simulations. The next contribution was a detailed description of a radiative transfer simulation model developed for Venus studies (Haus and Arnold, 2010). A number of refinements in the VIRTIS-M-IR data calibration and preprocessing required for the determination of surface emissivity were presented by Kappel et al. (2012b). Since the derivation of surface information from single spectra is prone to extremely large errors, the multi-spectrum retrieval algorithm MSR was developed that allows for taking the spectral information content of many VIRTIS-M-IR measurements into account. An early version of MSR and corresponding impacts on the data analysis were already presented by Kappel et al. (2012b). The full version of MSR that allows for the retrieval of the emissivity map of a surface target as a parameter vector that is common to several spectrally resolved images covering this target was described at a later time (Kappel, 2014). The expectable single- and multi-spectrum emissivity retrieval errors were then estimated by Kappel et al. (2015) on the basis of synthetic spectra. Even when applying MSR, the retrieval errors were predicted to be too large to obtain useful emissivity data from real VIRTIS-M-IR measurements. It was proposed to rather retrieve relative emissivity maps to achieve a reasonable reliability.

Section VI.2 of the present paper describes important prerequisites for the retrieval of emissivity maps. First, the VIRTIS-M-IR measurements are selected that are the most suitable for the derivation of emissivity data from the target area (high signal-to-noise ratio, thin to moderate cloud cover, few straylight, high measurement repetition number), and the necessary calibration and preprocessing steps are cited (Section VI.2.1). Next, the radiative transfer forward model required to simulate VIRTIS-M-IR spectra is explained (Section VI.2.2 (p. 167)). Then, Section VI.2.3 (p. 169) summarizes the capabilities of the multi-spectrum retrieval algorithm MSR, and it is discussed, why and how the raw retrieved emissivity maps have to be renormalized to obtain well-defined relative emissivity maps. The full MSR retrieval pipeline, which has to anticipate this post-processing, is described in Section VI.2.4 (p. 172), along with the retrieval parameters and their *a priori* data. Section VI.3 (p. 174) presents the raw retrieved emissivity maps of Themis Regio, illustrates the post-processing, and resolves the first major objective of this work by showing the final renormalized emissivity maps at 1.02, 1.10, and 1.18 μm . The second objective, the determination of the maps' reliabilities, is addressed in Section VI.4 (p. 176). For this purpose, results from an earlier retrieval error analysis based on synthetic spectra are first recited (Section VI.4.1 (p. 176)). It is then explained that a statistical analysis of maps retrieved under different conditions from real measurements yields an improved error estimate (Section VI.4.2 (p. 178)). The 'Measurement Selection Tests' (MSTs) detailed in Section VI.4.3 (p. 179) alter these conditions by retrieving maps from different disjoint selections of measurements, whereas for the 'Parameter Modification Tests' (PMTs, Section VI.4.4 (p. 180)), maps are determined from always the same measurement data set but many important interfering parameters are modified. Based on results from these tests, it is discussed, how retrieved maps can be referred to a given reference emissivity (Section VI.4.5 (p. 184)), and how retrieval errors correspondingly transform. Section VI.5 (p. 186) discusses the results of the previous sections, provides the double standard deviation uncertainties of the renormalized emissivity maps, and gives a preliminary discussion of the geologic relevance of the determined maps. Summary and conclusion are presented in Section VI.6 (p. 189).

Appendix VI.A (p. 192), published as online supplementary material, provides additional information. The utilized spectrally resolved VIRTIS-M-IR images are listed in Appendix VI.A.1 (p. 192). Next, Appendix VI.A.2 (p. 192) presents the mathematical background of the renormalization, its effect on the retrieval errors, and how the MSTs and PMTs can be used to estimate the latter. Detector-related trends of the VIRTIS-M-IR spectral registration retrieved from the measurements themselves are reported in Appendix VI.A.3 (p. 199). Finally, Appendix VI.A.4 (p. 200) shows figures that illustrate at 1.10 and 1.18 μm the post-processing of the retrieved maps and the MSTs and PMTs, complementing the corresponding figures at 1.02 μm given in the main text.

VI.2 Data selection, forward model, and multi-spectrum retrieval

This section discusses important prerequisites for the retrieval of emissivity maps. First, the selection of the utilized VIRTIS-M-IR measurements is described (Section VI.2.1). The forward model (Section VI.2.2 (p. 167)) is needed to simulate VIRTIS-M-IR spectra. Parameters can be retrieved from the measurements by applying a multi-spectrum retrieval algorithm (Section VI.2.4 (p. 172)), but the algorithm has to anticipate a suitable post-processing of retrieved emissivity maps to enable meaningful results (Section VI.2.3 (p. 169)).

VI.2.1 Data selection, calibration, and preprocessing

Each Venus Express orbit corresponds to 24 (Earth-)hours (when VIRTIS-M-IR still acquired data). VIRTIS-M-IR data from each orbit are divided into a number of sessions, depending on the science objectives. The data acquired during a session are stored as 'data cube'. Depending on the acquisition mode, the instrument recorded at each exposure at 256 spatial samples a spectrum of 432 bands uniformly dividing the approximate range 1.02–5.1 μm , forming a 'frame'. A data cube is composed of a series of several frames scanning a certain target and thus provides a spectrally resolved two-dimensional spatial image.

Multi-spectrum retrieval of emissivity as parameter common to N_r measurements that cover the same surface bin relies on a self-consistent calibration and data preprocessing. The VIRTIS-M-IR data are calibrated according to Cardesin-Moinelo et al. (2010). Refinements of the calibration in view of the multi-spectrum

emissivity retrieval and based on a detailed detector responsivity analysis are applied according to [Kappel et al. \(2012b\)](#). They include an improvement of the spatial homogeneity of the detector responsivity leading to a wavelength dependent change of the calibrated radiance in the outer region of the detector in sample direction in the order of about 15%. The refinements also include an adjustment of the responsivity in the spectral dimension resulting in an increase of the calibrated radiance between 0% at 1.3 μm and 35% at 1.0 μm . The detector responsivity analysis also revealed a temperature and spatial sample dependent possible nonlinearity of the detector-count-to-radiance mapping that differently affects the even and the odd spectral bands. This leads to the so-called even-odd effect where a sawtooth-like pattern seems to be superimposed on the spectra. For night spectra in the range 1.0–2.6 μm , this effect can be partially removed. At 3.3 s (≥ 8 s) detector exposure time, this correction can amount to 5% ($\leq 1\%$) of the radiance in the nightside peaks. Note that some but not all of these issues are by now (partially) resolved in the most recent data archive as of 2015 at PSA ([Drossart et al., 2013](#)).

[Kappel et al. \(2012b\)](#) also described a data preprocessing of the newly calibrated spectra that is required for emissivity retrieval and includes the removal of straylight and the blurring of the topography data. The latter shall emulate the atmospheric blurring of observable surface information caused by the multiple scattering of radiation by gases and clouds. Note that not topography itself is blurred but the fundamental carrier of the observed information, the radiance. An effective radiance in dependence on topography is therefore computed and blurred with respect to a Gaussian with 100 km FWHM. This corresponds to the expected achievable spatial surface resolution in the infrared ([Moroz, 2002](#)). The effective blurred topography is computed from the blurred effective radiance ([Müller et al., 2008](#)). For a description of the current implementation see [Kappel et al. \(2012b\)](#). In order to reflect this limited achievable surface resolution in the emissivity retrieval, to increase the signal-to-noise ratio, to decrease the amount of data to be analyzed by the retrieval procedure, and to obtain spectra that are referred to always the same surface portion, Venus' surface is binned with respect to Lambert equal-area map projections ([Bugayevskiy and Snyder, 1995](#)), and the data of each cube are binned accordingly. The surface bins' aspect ratios shall not deviate too much from unity, and thus Lambert cylindrical projection (with standard parallel 30°; no local distortion due to the map projection at this latitude) is used equatorward of 38.68° latitude, and Lambert north/south pole azimuthal projection elsewhere. To match the mentioned surface resolution, each bin covers a surface area of about 100×100 km² (91.5×91.5 km² to be exact, allowing for 360 bins in longitude direction in the cylindrical projection). In the following, the term 'measurement' refers to the binned data.

In order to exemplarily demonstrate the intended emissivity retrieval, a target area is selected where as many as possible usable VIRTIS-M-IR measurement repetitions are available. A measurement is said to be usable for this work when the following conditions are fulfilled:

1. surface elevation data is available to avoid the gaps in the Magellan radar topography data ([Ford and Pettengill, 1992](#); [Rappaport et al., 1999](#)),
2. the zenith-sun angle is $\geq 98^\circ$ to exclude dayside and twilight measurements,
3. the observation angle is $\leq 60^\circ$ to avoid significant spherical effects in the radiative transfer,
4. the detector exposure time is ≥ 3 s to exclude spectra with very low signal-to-noise ratios in the surface windows,
5. the number of individual spectra contributing to a binned measurement is ≥ 10 to ensure a sufficient statistical weight and high signal-to-noise ratio,
6. the full spatial resolution of 256 spatial samples per image is available to avoid a coarse assignment of the individual spectra to the bins,
7. the spectrally averaged radiance in the range 2.15–2.30 μm is ≥ 3 mW/(m² sr μm) to exclude measurements with very thick clouds,
8. the removed straylight plus the even-odd-effect correction are ≤ 4 mW/(m² sr μm) on spectral average in the range 1.0–2.6 μm to avoid spectra with very large corrections and thus possibly large uncertainties.

Themis Regio (western part) is selected as target area, since it is geologically interesting and is located in an area that exhibits the largest number of usable VIRTIS-M-IR measurements on the planet. The target comprises all surface bins whose bin center coordinates are located between 35 and 47°S and 270 and 288°E, resulting in $B = 219$ surface bins with ≥ 80 usable measurements each. A measurement data set with 64

repetitions for each bin is selected to be used in most cases in this work. 14,016 binned spectra constitute this selection that will be referred to as $N_r^0 = 64$ repetition data set in the following. Appendix VI.A.1 (p. 192) lists the VIRTIS-M-IR data cubes utilized for the present work.

VI.2.2 Forward model

In order to numerically simulate observable nightside radiances, a plane-parallel, LTE (local thermodynamic equilibrium), line-by-line radiative transfer simulation forward model is utilized that takes into account thermal emissions by surface and atmosphere, and absorption and multiple scattering by gases and clouds. It is similar to the forward model described by Haus and Arnold (2010) with updates by Haus et al. (2013), but the underlying radiative transfer equation solver DISORT (Stamnes et al., 1988) is replaced by LIDORT (Spurr, 2001, 2008). This way, the forward model is capable of providing analytic derivatives of the simulated radiances with respect to a number of atmospheric, surface, and instrumental parameters. The forward model was also used by Kappel (2014) and Kappel et al. (2015) where the following summary is based on.

From the total VIRTIS-M-IR spectral range ($\approx 1.0\text{--}5.1\ \mu\text{m}$), only the interval $1.0\text{--}2.3\ \mu\text{m}$ is utilized here excluding the $1.28\ \mu\text{m}$ window range ($1.225\text{--}1.295\ \mu\text{m}$) that is often contaminated by O_2 nightglow (see below). The line-forming altitude region for the specified range is located below $40\ \text{km}$ (Haus and Arnold, 2010, Fig. 4). Venus' nightside emissions in this spectral range are thus nearly unaffected by strong mesospheric temperature variations above $58\ \text{km}$ that were observed by Tellmann et al. (2009) and Haus et al. (2013, 2014). The temperature below $40\ \text{km}$ is quite stable with time (Seiff et al., 1985). Furthermore, details of the cloud altitude distribution have a minimal impact in this range, since the main cloud deck resides above $48\ \text{km}$ (Marov et al., 1980). In contrast, spectral signatures longward of $3\ \mu\text{m}$ are, according to the cited figure, strongly influenced by variations of temperature and cloud altitude distributions above $48\ \text{km}$. The range $2.3\text{--}2.6\ \mu\text{m}$ is excluded, since the number of interfering parameters for emissivity retrieval shall be kept as low as possible, and in the VIRTIS-M-IR spectral range, most minor gases are active only there (Haus and Arnold, 2010, Fig. 19). Nightside radiances in the range $2.6\text{--}3.0\ \mu\text{m}$ are too small to be useful (Haus and Arnold, 2010, Fig. 2). Spatially and temporally varying non-LTE O_2 emissions (' O_2 nightglow') at $1.27\ \mu\text{m}$ from an altitude region around $100\ \text{km}$ (Piccioni et al., 2009) contaminate the $1.28\ \mu\text{m}$ window. For retrievals, this window will thus be blacked out, and O_2 nightglow need not be considered. Note that calibration refinements and preprocessing for VIRTIS-M-IR data as performed by Kappel et al. (2012b) had mainly concentrated on the range $1.0\text{--}2.6\ \mu\text{m}$.

In the considered spectral range, spectral surface emissivity is observable in the three 'surface window peaks' (1.02 , 1.10 , and $1.18\ \mu\text{m}$). The three parameters $e_{1.02}$, $e_{1.10}$, and $e_{1.18}$ parameterize the spectral emissivity such that it is constant over the ranges of the respective windows ($1.000\text{--}1.055\ \mu\text{m}$, $1.055\text{--}1.125\ \mu\text{m}$, $1.125\text{--}1.225\ \mu\text{m}$, comprising about four, eight, and ten spectral bands, respectively). Knowledge of all three emissivities can suffice to discriminate between a number of potential surface materials and grain sizes (Haus and Arnold, 2010). Emissivities must lie in the interval $[0, 1]$, and initial values are all set to 0.5 .

Temperature altitude profiles are taken from the Venus International Reference Atmosphere (VIRA, Seiff et al., 1985). For studies of nightside spectra in the utilized spectral range, essentially only the tropospheric temperature field is important. Below $32\ \text{km}$, it is usually considered to be independent of latitude as described by VIRA. In that range, remote sensing has not yet been performed, and *in situ* measurements were mainly restricted to low latitudes up to about 30° . But altitudinal or latitudinal deviations from VIRA may occur there, and in fact are suggested by a General Circulation Model (GCM, Lebonnois et al., 2010b, personal communication). However, *in situ* measurements and the GCM suggest that the deep atmospheric temperature field is quite constant in time and local time, a consequence of high thermal inertia and thermodynamic stable layering. Deviations from the VIRA temperature profile shall be parameterized by two parameters. ΔT_0 leads to a quadratic offset to VIRA below $25\ \text{km}$ that is zero and has zero derivative at $25\ \text{km}$ and is ΔT_0 at $0\ \text{km}$, regardless of the actual surface elevation. ΔT_{25} leads to a quadratic offset below $50\ \text{km}$ that is zero at 0 and at $50\ \text{km}$ and is ΔT_{25} at $25\ \text{km}$. This allows for a modification of the temperature in the bulk of the deep atmosphere, and temperature and temperature lapse rate near the surface (see Kappel et al., 2015, Fig. 3). Surface temperature is set to the atmospheric temperature at the respective surface elevation. Pressure altitude profiles follow from hydrostaticity and the ideal gas law with VIRA pressure at the respective surface elevation as initial value. The elevation of a surface bin is provided according to Kappel et al. (2012b), who

use Magellan radar data (Ford and Pettengill, 1992; Rappaport et al., 1999) as basis. The elevation uncertainty of a $91.5 \times 91.5 \text{ km}^2$ surface bin (see Section VI.2.1 (p. 165)) is assumed as 0.2 km (see Kappel et al., 2015).

The CO_2 volume mixing ratio is 96.5%. The only minor gases that provide significant opacity in the studied spectral range are H_2O (including HDO, which is treated such that the initial D/H ratio corresponds to 150 times the corresponding ratio for Earth) and HCl (Haus and Arnold, 2010, Fig. 19). A small CO influence at the interval boundary (2.28–2.30 μm) is neglected here. Initial altitude profiles of volume mixing ratios of minor gases are taken from Haus and Arnold (2010) and are based on the profiles described by Pollack et al. (1993). Note that in contrast to the present work, Kappel et al. (2015) scaled the H_2O column such that the concentration at the surface was 25 instead of 32.5 ppmv. Both H_2O and HCl affect the peak at 1.74 μm (probed altitudes 20–30 km), and H_2O is in addition observable between 1.10 and 1.20 μm ($\leq 26 \text{ km}$). H_2O (excluding HDO) and HCl model variations shall be parameterized by total column factors $t_{\text{H}_2\text{O}}$ and t_{HCl} that scale the respective initial altitude profiles which translate to 32.5 or 0.5 ppmv at 25 km, respectively. Recent studies showed that H_2O concentration in the deep atmosphere amounts to a value of 30_{-5}^{+10} ppmv (Bézar et al., 2011), corresponding to $t_{\text{H}_2\text{O}} \sim 0.92_{-0.15}^{+0.31}$. Monochromatic absorption cross-sections of gases due to allowed molecular transitions are computed from the spectral line databases CDSD (CO_2 , 0.4–0.9 μm and 1.25–1.33 μm , Tashkun et al., 2003), HITEMP (CO_2 , Pollack et al., 1993, H_2O isotopologues 161, 181, 171, Rothman et al., 1995), and HITRAN08 (H_2O isotopologues 162, 182, 172, HCl, Rothman et al., 2009) by using spectral line shapes listed by Haus and Arnold (2010). To be in accordance with the composite line database used by Haus and Arnold (2010) that was extensively validated for radiative transfer in Venus' atmosphere, the more recent HITEMP2010 (Rothman et al., 2010) is not yet considered here. Molecular Rayleigh scattering is treated according to Hansen and Travis (1974).

The opacity of the main gaseous constituent CO_2 for the high-pressure and high-temperature environment of Venus' deep atmosphere is not sufficiently well predictable to provide reliable simulations of observable spectra. The line databases of the allowed transitions are not based on laboratory measurements, but mostly on theoretical models (Tashkun et al., 2003) and contain errors (Haus and Arnold, 2010; Bézar et al., 2011). The line shapes are still under discussion, as are additional opacity effects (continuum, collisional induced absorption, line mixing). The CO_2 opacity due to allowed transitions requires a wavelength dependent correction to produce good fits to real data at all. This correction is in the following shortly referred to as 'continuum'. For this work, it does not only include the actual continuum contribution, but opacity corrections in general. It is independent of the measurement but depends on the utilized line databases and line shapes and is thus not directly comparable to continua given by authors who made other choices. The continuum is treated here as a spectrally constant value throughout the range of an atmospheric transparency window, except for the 1.10 and the 2.3 μm windows. The spectral fine structure fluctuations of the latter around the value $c_{2.3} = 160 \cdot 10^{-29} \text{ cm}^2$ are relatively easy to retrieve and can be found in Kappel et al. (2012b, Fig. 11). To allow for satisfactory fits to the 1.10 μm peak, its continuum is modeled as a (wavenumber-) linear function that connects the values $c_{1.056} = 22 \cdot 10^{-29} \text{ cm}^2$ and $c_{1.124} = -6.9 \cdot 10^{-29} \text{ cm}^2$ at wavelengths 1.056 and 1.124 μm . The other continua are denoted by $c_{1.02}$, $c_{1.18}$, $c_{1.31}$, and $c_{1.74}$, where the subscripts indicate the wavelengths of the respective windows, and are set to 0.39, 1.9, 9.6, and 26 in units of 10^{-29} cm^2 , respectively. These values are the most recent continuum results of the present authors and were retrieved with MSR (Kappel, 2014) as parameters that are common to a large set of highly diverse VIRTIS-M-IR nightside spectra and assuming a fixed surface emissivity of 0.5 (the initial emissivity). Modifications to the retrieval pipeline and the choice of the set of utilized spectra and the initial emissivity can affect the results (order of 10%–20%, depending on the window). However, a retrieval error analysis analogous to the one performed by Kappel et al. (2015) for surface emissivity would be needed to understand their significance, but these values are not the primary target of this work. Therefore, values stated in this and in earlier publications of the present authors should be, as mentioned in those works, regarded as working hypotheses and preliminary values. Note that in this work, the surface window continua are treated as fine-tuning parameters that shall prevent the retrieved emissivities to systematically approach the boundaries 0 or 1, as will be explained in Section VI.2.3. It was shown by Kappel et al. (2015) that uncertainties in the continua are important sources of retrieval errors for absolute emissivities. To avoid high emissivity retrieval errors due to continuum uncertainties, the strategy for the emissivity retrieval is modified by rather retrieving relative emissivities and showing the results to be reasonably independent of the continua, the initial emissivity, and other parameters.

The clouds are assumed to comprise four modes (1, 2, 2', and 3) and are modeled according to [Haus et al. \(2013\)](#). Each mode consists of spherical droplets of 75% sulfuric acid. Refractive indices are taken from [Palmer and Williams \(1975\)](#) with supplements from [Carlson and Anderson \(2011\)](#). Cloud particle radii are log-normally distributed with modal radii of 0.3, 1.0, 1.4, 3.65 μm and unitless dispersions of 1.56, 1.29, 1.23, 1.28 for the four modes, respectively ([Pollack et al., 1993](#)). Initial profiles of particle number densities N at altitudes h are taken from [Haus et al. \(2013\)](#) and are given by

$$N(h) = \begin{cases} N_0 \exp(- (h - h_t)/s_t) & h > h_t \\ N_0 & h_b \leq h \leq h_t \\ N_0 \exp(- (h_b - h)/s_b) & h < h_b \end{cases} \quad (\text{VI.1})$$

Mode-specific values are listed in Table VI.1. $N(h)$ is set to zero above 85 km. Actual cloud modal abun-

Cloud mode	1	2	2'	3
Top of peak density, h_t in km	65	66	60	57
Base of peak density, h_b in km	49	65	49	49
Upper scale height, s_t in km	5	3.5	1	1
Lower scale height, s_b in km	1	3	0.1	0.5
PND at h_b , N_0 in cm^{-3}	181	100	50	14

TABLE VI.1: Initial cloud parameters for Eq. (VI.1). PND is the particle number density.

dances are defined by cloud mode factors m_1 , m_2 , $m_{2'}$, and m_3 that scale the number densities of the initial altitude profiles. Variations of h_b , h_t , s_b , or s_t for cloud mode i rescale N_0 for mode i such that the total number of mode i particles per horizontal unit area remains constant. This is done in order to disentangle variations of altitude distribution and variations of particle abundance. Deviations of the h_b for modes 1, 2', and 3 from their initial value 49 km are treated as a joint parameter, since below that altitude, the temperature and pressure conditions are thought to force cloud particle numbers to sharply decrease except for possible haze (see *in situ* data described by [Knollenberg and Hunten, 1980](#), and [Marov et al., 1980](#)). The cloud top altitude is defined as the altitude where the cloud optical depth at 1.0 μm attains unity. [Haus et al. \(2013, 2014\)](#) described a slow decrease of the local-time- and time-averaged nighttime cloud top altitudes from ~ 71 km at the equator to ~ 70 km at mid latitudes and then to ~ 61 km at polar latitudes. Here, this is implemented in an abstracted form as a linear decrease of h_b and h_t for cloud mode 2 and h_t for cloud mode 1 by 10 km (referred to Table VI.1) between 55° and 80° latitude. Wavelength dependent scattering and absorption properties of the clouds are computed according to Mie theory ([Wiscombe, 1980](#)).

VI.2.3 General remarks on multi-spectrum retrieval and renormalization

Since spectral information content is limited, there are always atmospheric and surface parameters required for the numerical simulation of spectra that cannot be uniquely derived from the measured spectra. These parameters interfere with emissivity data and are usually set to certain reasonable values that are compatible with current knowledge on atmospheric and surface conditions and allow for the generation of realistic synthetic spectra. When these assumptions deviate from the true physical values, this may cause surface emissivity retrieval errors, even though the fits well match the measured spectra. Compared to this effect, the impact of measurement noise is of secondary importance. It was shown by [Kappel et al. \(2015\)](#) that these errors are too large to obtain reliable absolute emissivities from single VIRTIS-M-IR measurements. However, it was proposed to apply the multi-spectrum retrieval algorithm MSR developed by [Kappel \(2014\)](#) to retrieve emissivity as a parameter that is common to several measured spectra that cover the same surface bin. This assumes that geologic activity (and thus time variations of emissivity) is negligible. This seems to be indeed the case, as [Müller et al. \(2012a\)](#) have argued on the basis of the VIRTIS-M-IR data. MSR allows for the retrieval of parameters that are common to a certain selection of measurements and to incorporate expected mean values, standard deviations, and correlation lengths and times as Bayesian *a priori* information for the retrieval parameters, along with measurement and simulation error information. This decreases the probability of retrieving unreasonable values and spatial-temporal distributions of the parameters, allows for

taking the context of adjacent measurements into account, and thus enhances the reliability of the retrieved results. All considered measurements can be parameterized by a fully consistent set of atmospheric, surface, and instrumental parameters.

Even with MSR, absolute emissivity values are difficult to obtain. Given a certain surface bin that is covered by N_r measurements, the impact of fluctuations around the long-term average of a temporally varying parameter at that surface bin should statistically average out with $1/\sqrt{N_r}$. Examples of such temporally varying interfering parameters are the column abundances m_i of the cloud modes, top and bottom altitudes of the vertical cloud mode particle distributions, the H_2SO_4 concentration of the cloud droplets, and atmospheric trace gas abundances. Since the spatial distributions of the long-term averages of these interfering parameters are not exactly known, they cannot be considered in the radiative transfer simulations, and retrieved emissivity maps may therefore systematically deviate from the true emissivity map. However, as long as the measurements of the surface target are not in the vicinity of the terminators or the polar regions, the long-term average of the interfering parameters should not spatially vary on scales smaller than a few thousand km. This can be motivated by the symmetries and spatial scales of the global atmospheric circulation. Uncertainties of constant interfering parameters like the continuum parameters can lead to additional large emissivity errors.

It was proposed by [Kappel et al. \(2015\)](#) to remove these errors as follows. First, to minimize emissivity errors that are due to continuum parameter uncertainties, wavelength dependent continua are pre-determined with MSR as common parameters that are compatible with as many and diverse as possible observed spectra. An initial emissivity value has to be defined for this purpose to complete the parameter set required to solve this retrieval problem without too strongly underconstraining it. The pre-determined continua do not necessarily coincide with the true ones but have proved to be compatible with almost all VIRTIS-M-IR nightside spectra analyzed so far. Using them, a surface emissivity map, quasi 'relative to the initial emissivity', can be retrieved with MSR from a suitable measurement data set that repeatedly covers the actual surface target. This map is henceforth also called the 'raw retrieved emissivity map'. The mean value of this map can differ from the initial emissivity, since the measurement data sets utilized to determine the continua and the map (and therefore the corresponding time-averaged interfering true parameters) do not necessarily coincide. It was proposed to add a constant value to the retrieved relative emissivity map such that its new median value corresponds to the initial emissivity. This way, the impacts of uncertainties in the mentioned interfering parameters were predicted to be largely removed. In the present work, this addition is not performed at this point. Note that the present work does not use median values but mean values, because additional statistical parameters like standard deviation have to be analyzed here. The median's advantage of robustness against statistical outliers was verified to be not really necessary here.

Additional effects have to be taken into account. For instance, the relative emissivity maps can exhibit spatially slowly varying trends in latitude direction that are probably unrealistic from the geologic point of view. Such trends were assumed to be negligible by [Kappel et al. \(2015\)](#) who utilized synthetic spectra to develop the retrieval of relative emissivities. The relevance of these trends was only recognized when real measurements were analyzed in the frame of the present work. The occurrence of these latitudinal trends can be explained with the spatial distributions of the time-averaged true values of interfering parameters. Again motivated by the symmetries and spatial scales of the global atmospheric circulation, and provided that the measurements of the surface target are not in the vicinity of the terminators or the polar regions, these parameter distributions are expected to be spatially slowly varying, and only in latitude direction. Moreover, they can depend on the utilized measurement data set. The respective parameters used in the forward model simulation are, in absence of detailed knowledge, mostly set to constant values. These spatially slowly varying deviations between time-averaged true and assumed parameters lead to corresponding artificial latitudinal trends in the retrieved emissivity map.

It also turned out that, for not too high surface elevations, the retrieved emissivities can exhibit a trend with surface elevation that is approximately linear. This trend seems to be unrealistic from a geologic point of view, at least if it should turn out as a global phenomenon that occurs regardless of geologic context. If not real, it might be explained by unexpected extinction properties close to the surface in the low-lying regions of the planet, for instance due to errors in the CO_2 absorption or to a kind of haze close to the surface, compare also [Grieger et al. \(2004\)](#); [Erard et al. \(2009\)](#). But such a conclusion would require a detailed retrieval analysis of a much larger portion of Venus' surface than is currently possible with the available computer resources.

Therefore, the origins of such trends are not further discussed here. It is assumed until the emergence of convincing arguments to the contrary that these are not real emissivity trends, but retrieval artifacts due to imperfect or unconsidered forward model parameters. Note that this is just an assumption at the moment, and it should be kept in mind that actual trends with surface elevation (due to trends in the distribution of dust, surface composition, or weathering) might exist.

At each surface window, the trends of the raw retrieved emissivity map with both latitude and surface elevation are jointly removed ('de-trended') by a multiple linear regression (see Appendix VI.A.2.1 (p. 192) for details), but in a way that does not change the emissivity mean value. For an illustration, see Fig. VI.1 (p. 175)a that depicts a raw retrieved emissivity map at 1.02 μm , and Fig. VI.2 (p. 175) that shows the resulting trends with latitude and topography. In Fig. VI.1 (p. 175)b, the topography trend is removed, and in Fig. VI.1 (p. 175)c both the topography and the latitude trends. These figures are explained later in Section VI.3 (p. 174), since the retrieval pipeline required to derive these maps can only be introduced after the discussions in the present subsection.

However, the spatial fluctuations of the de-trended emissivities around their mean tend to increase in magnitude for increasing emissivity mean, because the radiance response to small emissivity perturbations around an emissivity base value decreases for increasing emissivity base value. The fluctuations are small compared to the emissivity mean. This effect is detailed in Section VI.4.5 (p. 184). It is shown there that it can be quantified according to an (affinely) linear transformation with respect to the mean values of the raw retrieved emissivities. To remove the impact on the derived emissivity maps, this linear transformation is used to refer the de-trended maps to a certain reference emissivity value, here 0.5. The result is called the 'renormalized emissivity map referred to the reference emissivity 0.5'. In the following, the maps will always be referred to 0.5, except when stated otherwise, and the result is shortly called 'renormalized emissivity map'. The emissivity mean of this renormalized map coincides with the reference emissivity, i.e. the emissivities now spatially fluctuate around the reference emissivity. If the reference emissivity coincided with the (unknown) true absolute mean emissivity of the target area, the amplitude of the derived fluctuations would coincide with the amplitude of the true fluctuations, assuming that there are no real emissivity trends with latitude and topography. The described linear transformation replaces the plain addition operation proposed by Kappel et al. (2015) to make the emissivity mean value coincide with the initial emissivity. Using the linear transformation, the renormalized emissivity map can easily be referred to other reference emissivities if needed. The dependence of the fluctuation amplitude on the assumed mean emissivity of the target area is an important effect for the quantification of spatial emissivity variations and cannot be neglected. This effect is most pronounced at 1.02 μm .

By applying the entire renormalization procedure described in the last paragraphs, the extremely high emissivity retrieval errors due to systematically wrong assumptions on interfering parameters can be largely avoided. In return, it has to be verified that the renormalized retrieved maps do not significantly change when the initial emissivity, the continua, slowly varying latitudinal deviations of the utilized from the actual deep atmospheric temperature field, and other interfering parameters are modified. The selected surface target should not exceed spatial dimensions of a few thousand km, a scale on which the interfering parameter trends and thus the systematic deviations of the retrieved from the true emissivity map can be thought to be approximately linear functions of latitude, allowing for a corresponding renormalization. In the same way, the surface elevation range of the target should not be exceedingly wide to ensure approximate linearity of the trend with topography and its successful renormalization.

The regression coefficients for each map are listed in addition to the mean emissivity before renormalization (Table VI.4 (p. 181)). The interplay between unexpected extinction properties close to the surface, an unconsidered latitudinal trend of the deep atmospheric temperature field, the utilized continua, and mean and latitudinal trends of time-averaged cloud abundances, cloud bottom altitudes, and H_2O abundances, as well as other discrepancies between utilized and true parameters, depending on the selection of spectra, can lead to different emissivity means and regression coefficients.

In practice, this means that the raw retrieved emissivities may approach their domain boundaries, i.e. the boundaries of the set of physically valid values attainable by the respective parameter (0 or 1 for emissivity), or are even cut off at these boundaries. This may occur even for fixed continua and deep atmospheric temperature field, in particular when comparing target areas at different latitudes. Note that violations of these boundaries

are prevented in the retrieval process by a modification (Kappel, 2014, Appendix A.1) of the logarithmic barrier method (Nocedal and Wright, 1999, Section 17.2). In the extreme case, the raw retrieved emissivities of all surface bins may thus become 1, for instance, in which case renormalization would lead to a featureless map where all emissivities would correspond to the reference emissivity. On the one hand, this is the reason, in particular in presence of trends of the raw retrieved emissivities with topography or latitude, for choosing the initial emissivity 0.5 as the value that is farthest away from the emissivity domain boundaries. On the other hand, renormalization alone turns out to be insufficient to make the determination of useful emissivity maps fail-safe. As a workaround, the current approach for operational retrievals is to retrieve the surface window continua each time anew along with the emissivity maps. The resulting continua differ only slightly, but now they take on the character of fine-tuning parameters that shall prevent the emissivity maps to approach the boundaries 0 or 1 from the outset. Renormalization is still needed to ensure an exact coincidence of the emissivity mean with the reference emissivity and to remove the mentioned latitude and topography trends. Note that after renormalization, the emissivity mean corresponds to the reference emissivity 0.5, and the slopes of linear trends with latitude and surface elevation are zero, such that an additional subsequent renormalization would not change results anymore. In the following, the term 'renormalized emissivity' is to be understood to include the fine-tuning step. It will be verified that no further modifications to this approach are required to obtain reasonably reliable emissivity data maps.

Note that the retrieval error analysis by Kappel et al. (2015) did not consider measurement errors. Moreover, the shapes of simulated and measured spectral peaks can slightly differ, in which case the parameters can more easily converge to subsidiary solutions. For instance, when the spatially slowly varying time-averaged cloud abundance for the utilized set of measurements exceeds the long-term average, the retrieval algorithm may converge to a solution where the decreased radiance average is explained by a modified cloud mode abundance in conjunction with a decreased emissivity. This may lead to retrieval errors that exceed those listed by Kappel et al. (2015) and amplify the emissivity domain boundary problem. Application of the approach described in this section, however, should largely remove such errors.

All these subtleties necessitate a verification of the applicability of the synthetic retrieval error analysis results by Kappel et al. (2015) to real renormalized emissivity maps. This is discussed in Section VI.4 (p. 176).

VI.2.4 Retrieval pipeline

Studying synthetic spectra, Kappel et al. (2015) have compared several single-spectrum retrieval pipelines for surface emissivity retrieval. For the pipeline that yielded the smallest retrieval errors, the auxiliary parameters that have to be retrieved to allow for useful fits at all comprise the cloud mode 2, 2', and 3 factors. Along with the emissivities, these parameters are determined from the spectral range 1.0–2.3 μm excluding the blacked out 1.28 μm window. This pipeline is used as a baseline for a suitable multi-spectrum retrieval pipeline. To be applicable to real, not synthetic measurements, the new pipeline has to be more elaborate. The main reason is that three parameters that describe the spectral registration and that are crucial for emissivity retrieval are not sufficiently predictable by the calibration pipeline: the spectral sampling $\delta\lambda^s$, the wavelength λ_1^s of first spectral band, and the full-width-at-half-maximum $FWHM^s$ of the spectral instrumental response function (Kappel et al., 2012b). An $FWHM^s$ that is wavelength independent can be checked to allow for satisfactory fits, but $FWHM^s$ and λ_1^s turn out to vary with spatial sample on the detector and detector temperature. $\delta\lambda^s$ seems to be generally constant, and an optimal value of 9.49 nm per spectral band can thus be determined with MSR as parameter that is common to many (thousands) and diverse VIRTIS-M-IR spectra. $FWHM^s$ and λ_1^s , on the other hand, must be individually determined for each spectrum. It was shown by Kappel (2014) that $FWHM^s$ can be retrieved quite reliably already for single-spectrum retrieval, although MSR results taking into account the context of adjacent measurements are more accurate. λ_1^s can be retrieved very reliably, since it well disentangles from any other considered retrieval parameter due to its distinct Jacobian. Appendix VI.A.3 (p. 199) depicts and describes the detector-related trends for retrieved λ_1^s and $FWHM^s$.

In the following, it is to be understood that the retrieval parameters are always determined for the entire set of utilized measurements by applying MSR and using the *a priori* data listed in Table VI.2. The initial guess for the retrieval iterations is always set to the corresponding *a priori* mean value a , except for λ_1^s where it is set to the value predicted by the calibration pipeline. The *a priori* standard deviations are here set to values that are larger than is realistic, to not constrain the effective parameter ranges too much, thereby focusing more on

Parameter	a	σ	λ	τ
λ_1^s	1.02 μm	0.03 μm	0.3×256	0.2 h
$FWHM^s$	17 nm	5 nm	0.5×256	0.2 h
m_1, m_2, m_2', m_3	1	5	500 km	3.6 h
H_2O^b	1	0.5	2000 km	8 h
Continua	10^{-29} cm^2	10^{-27} cm^2	/	/
$e_{1.02}, e_{1.10}, e_{1.18}$	0.5	2	50 km	/

TABLE VI.2: *A priori* mean values a , standard deviations σ , correlation lengths λ , and correlation times τ for retrieval parameters. λ_1^s : wavelength of first spectral band, $FWHM^s$: FWHM of spectral instrumental response function, m_i : column scaling factor for cloud mode i , H_2O^b : factor for H_2O column below 26 km, e_j : emissivity at surface window j . λ for λ_1^s ($FWHM^s$) is set to 30% (50%) of the spatial width of the detector of 256 samples. Retrieval of common parameters (infinite correlation lengths or times) is indicated by '/'.

the spatial-temporal relations. In the future, it will be tested, whether it is safe to set them to smaller values. Single-spectrum retrieval results show that both $FWHM^s$ and λ_1^s have a quite smooth detector sample and temperature dependence. Due to the properties of the VEX orbit, detector temperature with the spacecraft close to an eclipse boundary can vary with time on a scale of a few minutes. It improves disentanglement from other parameters, in particular for $FWHM^s$, when correlation lengths and times are set as *a priori* data for MSR according to Table VI.2. As discussed by Kappel et al. (2015, Section 3.5), the expected correlation lengths for the cloud mode factors are set to $\lambda = 500$ km (with a few hours correlation time), which can be motivated by computing the auto-correlation function of observation movies of 2.3 μm nightside radiances as proxy. But there is also evidence for smaller scale cloud structures (100–200 km for mottled clouds observed by VMC/VEX, Titov et al., 2012), and small-scale convection in the middle cloud region causes large optical thickness variations (Imamura and Hashimoto, 2001). It can be shown by computing the corresponding Jacobian that the parameter H_2O^b , which is defined to scale the H_2O column only below 26 km, mostly affects the range 1.10–1.20 μm and only slightly influences the 1.74 μm peak. In contrast (see Fig. 2 by Kappel et al., 2015, for a selection of relevant Jacobians), a factor for the entire H_2O column significantly affects both ranges and thus leads to a stronger interference with clouds than H_2O^b does. Since the number of interferences between retrieval parameters should be kept as low as possible, usage of H_2O^b is preferred here over a factor for the entire H_2O column. Note that, according to the respective Jacobians, H_2O variations at higher altitudes can be compensated in the 1.74 μm peak by slightly different cloud mode abundances. The correlation length for H_2O^b is chosen to be compatible with data for minor gases by Tsang et al. (2009) and Haus et al. (2015a), with the atmospheric convection and its spatial scales as motivation. Correlation time is such that a distance corresponding to half of the correlation length is covered by gases at wind speeds of ≈ 35 m/s that prevail at 26 km altitude (Schubert, 1983, Fig. 9). For surface emissivities, the *a priori* correlation length can be set to 50 km, which corresponds to the half FWHM of the expected achievable spatial surface resolution in the IR (100 km, Moroz, 2002).

It can be seen from deep space observations that noise equivalent spectral radiance for actual VIRTIS-M-IR measurements is in the order of $4 \cdot 10^{-4} \text{ W}/(\text{m}^2 \text{ sr } \mu\text{m})$ for wavelengths shortward of 2.6 μm (256-sample-mode, unbinned, 3 s exposure time). As discussed in Section VI.2.1 (p. 166), each VIRTIS-M-IR cube is binned to match the 100 km FWHM of the surface data blurring. For a given data cube, typically 30 spectra contribute to each bin for southern hemisphere mapping data at 45 °S (Kappel et al., 2015). It is thus reasonable to assume a Gaussian with standard deviation $\sigma_N = 10^{-4} \text{ W}/(\text{m}^2 \text{ sr } \mu\text{m})$ as first guess for the measurement and simulation error distribution for binned data.

The retrieval pipeline is arranged into several stages that shall ensure a steady convergence and a minimal use of resources. If all retrieval parameters were determined in a single stage from the entire wavelength range, not only unnecessarily large computer memory usage and processing time had to be used (faster than linearly increasing with problem size (Kappel, 2014)), but the parameters could more easily converge to subsidiary minima far away from the global minimum of the retrieval cost function.

The first stage retrieves λ_1^s from the 1.74 μm peak. Note that the result is not final, since later stages will refine this value, based on the ever-increasing improvement of the fit for an ever-wider wavelength range. The second stage determines λ_1^s and $FWHM^s$ in addition to cloud mode factors m_2' and m_3 from the 1.74 and 2.3 μm peaks. In the later stages, λ_1^s and $FWHM^s$ are both determined with ever-improving refinements, but

this will not be mentioned anymore. The third stage estimates the surface window continua (as fine-tuning parameters as explained), while the fourth stage repeats the second stage but also determines m_2 and utilizes the surface windows in addition. At this point, the retrieved values quite well parameterize the measured spectra for most of the relevant wavelength range, and it is unlikely that in the later stages, the retrieval parameters lock to subsidiary solutions that are farther away from the global minimum of the retrieval cost function than at this stage. The emissivities are technically only needed to refine the fit and are determined later. Note that the $1.31\ \mu\text{m}$ peak is not included yet, since it does not yield significant additional information (Kappel et al., 2015) and that the $1.31\ \mu\text{m}$ continuum is not determined yet. The fifth stage repeats the third to refine the surface windows continua, and the sixth stage repeats the fourth, but (optionally omitted) retrieves m_1 and H_2O^b in addition. The seventh stage retrieves a first version of the surface emissivities, and the eighth and ninth stages repeat stages six and seven for a final refinement. Optionally, a last stage retrieves the $1.31\ \mu\text{m}$ continuum for completeness. The resulting maps are renormalized as described above.

VI.3 Renormalized emissivity maps at Themis Regio

The raw emissivity map at $1.02\ \mu\text{m}$ retrieved according to Section VI.2.4 (p. 172) from the $N_r^0 = 64$ repetition data set introduced in Section VI.2.1 (p. 165) is shown in Fig. VI.1a. The emissivity average over all bins of the target area is 0.48 (compare Table VI.4 (p. 181), row ' $N_r^0 = 64$ ', column 'Mean', first value). To enable a better comparison to all subsequent map representations, a constant value of (0.5-0.48) is added to the raw emissivity of each bin leading to a 'shifted' map with average 0.5. This map is interpolated (using thin plate splines, Williams et al., 2014) between the shifted emissivity values at the bin centers and represented according to the depicted color bar. An equirectangular map projection is used with the center of the shown latitude range as standard parallel, i.e. there is no local distortion due to the map projection at this latitude. The longitude range $270.5\text{--}287.8^\circ\text{E}$ covered by the bin centers corresponds to a distance of 1373 km measured along the standard parallel, the latitudinal extension -46.99 to -35.63°N corresponds to 1200 km. The '+' symbols indicate the centers of the surface bins. The switch between Lambert cylindrical and Lambert south pole azimuthal projections at -38.68°N for the equal area surface binning (Section VI.2.1 (p. 165)) is clearly discernible from the distribution of the bin centers. Fig. VI.1d depicts the blurred Magellan topography (see Section VI.2.1 (p. 165), for the unblurred map see Fig. VI.3 (p. 176)d) of the target area.

As it was explained in Section VI.2.3 (p. 169), the raw emissivity maps can exhibit (probably artificial) trends with topography and latitude. This is illustrated in Fig. VI.2 for the raw emissivities at 1.02 , 1.10 , and $1.18\ \mu\text{m}$ derived from the $N_r^0 = 64$ data set. For a better representation, the trends are shown separately (trend with topography left, trend with latitude right). There is an obvious correlation between raw emissivity and topography. The latitudinal trend is less pronounced, but its removal is still important for quantitative comparisons between different maps of the same target. Moreover, the latitude range is quite small here, and additional maps with wider latitude ranges are needed to assess this trend's global relevance. The slopes of both trends are listed in row ' $N_r^0 = 64$ ' of Table VI.4 (p. 181). It will be shown in Section VI.4 (p. 176) that for the same target area, the slopes depend on interfering parameters and the selection of the measurements (compare Table VI.4 (p. 181)), which leads to large differences between raw maps of the same target. On the other hand, the renormalized maps, where both trends have been removed, are very similar among each other as will be shown. This indicates that the trends are artificial indeed. The unrealistic systematic divergence between the raw emissivities at different surface windows for increasing surface elevation points to the same conclusion. It was already explained that the trends are probably due to imperfect forward modeling. If the trends are artificial, their magnitudes are so large that their occurrence cannot be neglected and they have to be removed to obtain useful maps. Fig. VI.1b depicts the map from Fig. VI.1a with the topography trend removed, and in Fig. VI.1c, both the trends with topography and latitude are removed.

It was discussed in Section VI.2.3 (p. 169) that the spatial fluctuations of the de-trended emissivities around their mean value tend to increase in magnitude for increasing emissivity mean. To finally obtain the renormalized maps, the de-trended maps have to be referred to the reference emissivity 0.5 according to a linear transformation that is detailed in Section VI.4.5 (p. 184). The renormalized emissivity maps derived from the $N_r^0 = 64$ repetition data set and referred to the reference emissivity 0.5 are shown in Fig. VI.3 (p. 176). This

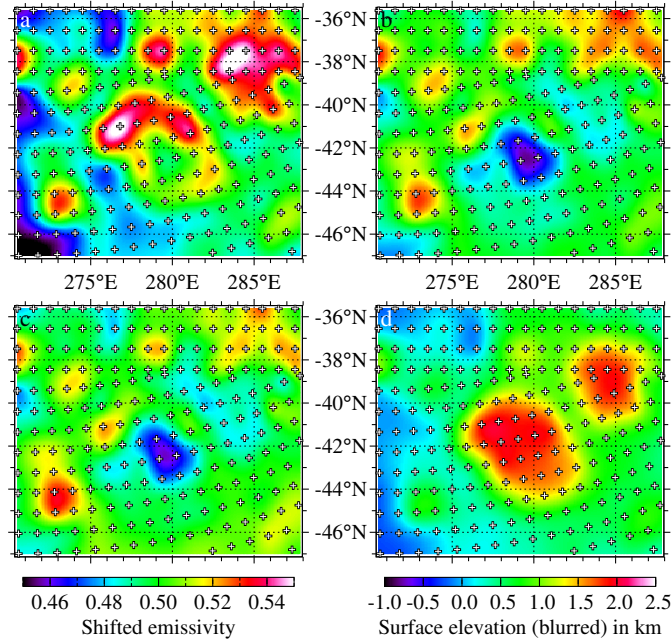


FIGURE VI.1: Removal of trends with topography and latitude for the $1.02\ \mu\text{m}$ emissivity map of Themis Regio retrieved from the $N_r^0 = 64$ measurement repetition data set. (a) Raw map, (b) trend with topography removed, (c) trends with topography and latitude removed, (d) utilized surface elevation (blurred Magellan topography). Suitable constants were added to the emissivity maps such that the map averages are always 0.5 for better representation. The corresponding results at 1.10 and $1.18\ \mu\text{m}$ are given in Figs. VI.A.3 (p. 200) and VI.A.4 (p. 201) in the supplementary material. Horizontal axes: longitudes, vertical axes: latitudes. 1° latitude corresponds to $105.62\ \text{km}$ at the surface. For color representations of the figures in this work, the reader is referred to the online version of this article.

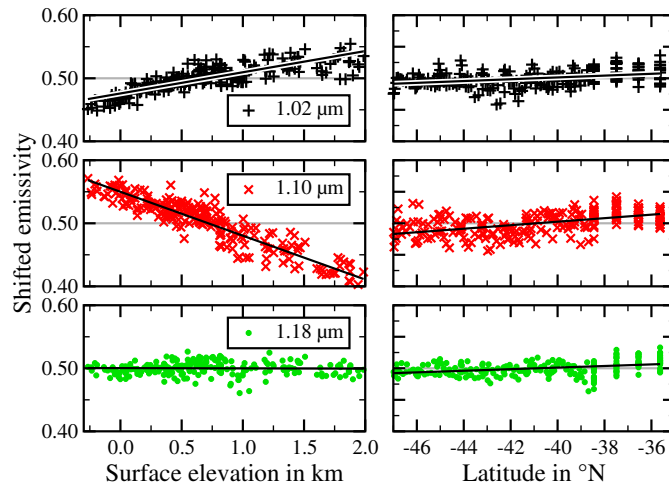


FIGURE VI.2: Scatterplots (symbols) and linear trends (black lines, for slopes see row ' $N_r^0 = 64$ ' of Table VI.4 (p. 181)) illustrating the trends with topography and latitude in the raw retrieved emissivity maps of Themis Regio. Left: trend with blurred Magellan topography when trend with latitude is removed. Right: trend with latitude when trend with topography is removed. Suitable constants were added to the emissivities such that the map averages are always 0.5 for better representation.

is the first main result of this work. The second main objective, the reliability of these results, is addressed in Section VI.4. Recall that the maps represent not absolute but relative emissivity values.

The $1.02\ \mu\text{m}$ renormalized emissivity map shows distinct spatial variations. They indicate heterogeneous surface properties. Pronounced anomalies occur relative to the average 0.5 (green) of the renormalized emissivity map. Two major trends characterize the studied area. Low emissivity is centered over Shivanokia Corona (42.0°S , 279.8°E , see Section VI.1 (p. 162)), whereas a positive emissivity anomaly appears in association with Abeona Mons (44.8°S , 273.1°E). These results cannot be explained by spatial topography

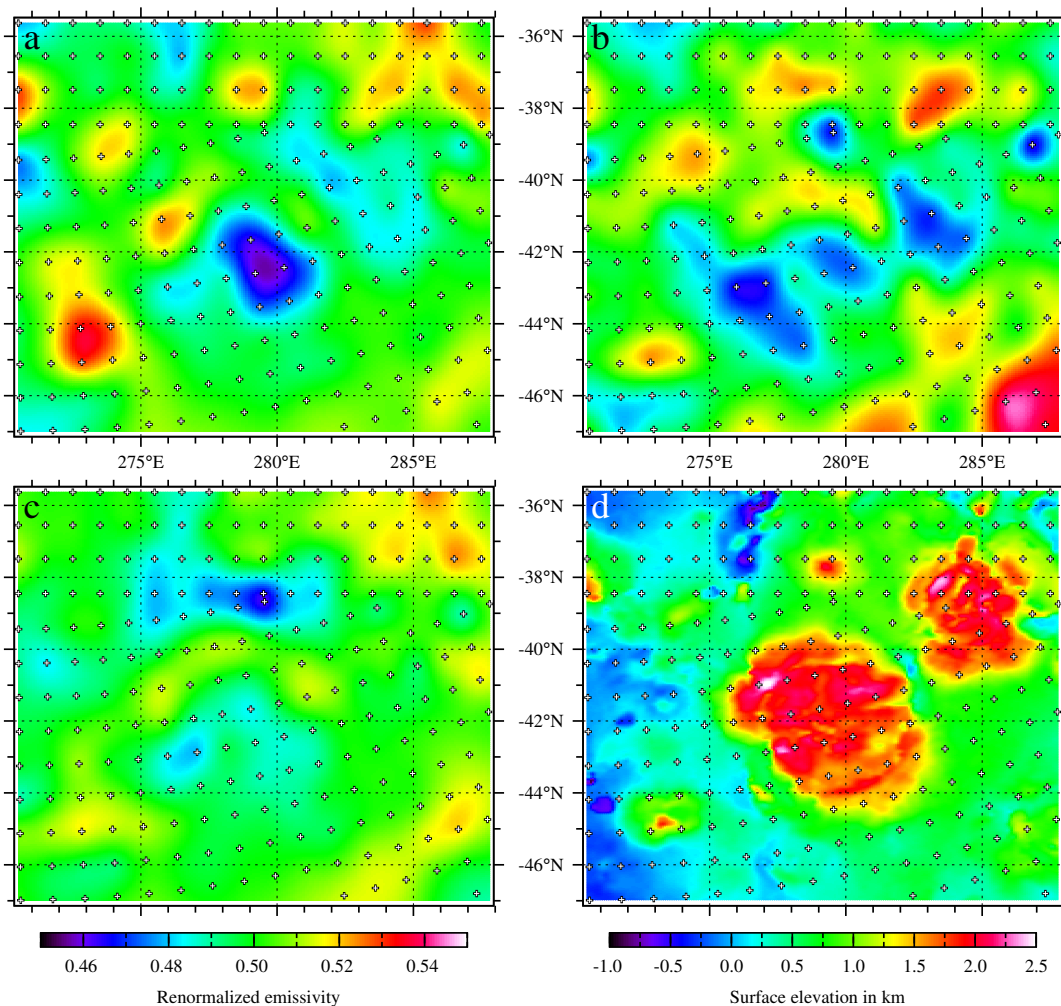


FIGURE VI.3: Renormalized emissivity maps ($N_r^0 = 64$ measurement repetition data set) of Themis Regio referred to reference emissivity 0.5 at (a) $1.02\ \mu\text{m}$, (b) $1.10\ \mu\text{m}$, and (c) $1.18\ \mu\text{m}$, and (d) surface elevation (unblurred Magellan topography). Axes as in Fig. VI.1.

variations, since both these areas exhibit higher surface elevations than their respective surroundings. Rather, the emissivity variations clearly correspond to relevant geologic surface patterns. A detailed discussion of emissivity correlation at all three wavelengths with geomorphologic surface features will be given in a follow-up paper.

VI.4 Retrieval errors and reference emissivity

No measured value makes sense without knowledge about its reliability. This is particularly true for the emissivity maps derived in this work. Section VI.4.1 recites predictions regarding their reliability gained from an earlier study with synthetic spectra. A statistical analysis of maps retrieved from real measurements is used for an improved error estimation (Sections VI.4.2 (p. 178), VI.4.3 (p. 179), and VI.4.4 (p. 180)). Based on results from Section VI.4.4 (p. 180), it is discussed, how retrieved maps can be referred to a given reference emissivity (Section VI.4.5 (p. 184)).

VI.4.1 Retrieval errors determined from synthetic spectra

Kappel et al. (2015) have performed an error analysis for the single-spectrum retrieval of surface emissivity from synthetic VIRTIS-M-IR spectra. Corresponding multi-spectrum retrieval errors for a renormalized emissivity map were estimated from the respective single-spectrum errors by plausible scaling rules that emulate the statistical impact when each surface bin is covered by N_r repeated measurements. Appendix VI.A.2 (p. 192)

of the present work justifies that these rules are approximately valid, also discussing the assumptions required to derive them. The case $N_r = 25$ was used by Kappel et al. (2015) to illustrate the order of magnitude of the various contributions to the retrieval errors of the renormalized emissivity maps. The present work focuses on the case of $N_r = 64 =: N_r^0$, and in the following, retrieval errors are given that are scaled to N_r^0 , based on the values given by Kappel et al. (2015, Table 5) where five different reference spectra were studied.

Errors due to uncertainties of temporally varying interfering parameters (cloud parameters, minor gas abundances) scale with $1/\sqrt{N_r}$, compare Eq. (VI.A.3) (p. 195). Double standard deviation errors are in the order of 2%–6% of the true emissivity, depending on the surface window and the utilized spectrum, and assuming statistical independence of the interferences. The main contributors for this case are uncertainties of the cloud bottom altitude and the H₂O content of the atmosphere.

Time independent interfering parameters that are spatially constant (continua) or vary on a scale $\gg 100$ km (deep atmospheric temperature field uncertainties) theoretically do not contribute to retrieval errors (Eq. (VI.A.3) (p. 195)). Those parameters that spatially vary on a scale of 100 km (surface elevation, interfering emissivities) have been excluded from the discussions in Appendix VI.A.2 (p. 192). They cannot be removed by the renormalization procedure since they are not spatially slowly varying. Largest error contributor in this category is the surface elevation uncertainty. For smooth surface regions, surface elevation uncertainties for bins with an area of roughly $100 \times 100 \text{ km}^2$ are assumed to be in the order of 100 m, and for more rugged mountainous areas even higher. Generally, an uncertainty of 200 m is assumed here. Corresponding emissivity errors do not improve for an increased N_r , because uncertainties do not average out over time. The errors at a given surface window due to (25%-) uncertainties of the emissivity parameters of the respective other surface windows are assumed to statistically scale with $1/\sqrt{N_r}$ (Kappel et al., 2015, Section 2.3). Together, the temporally constant and spatially fast varying interfering parameters lead to corresponding errors in the order of 9–13% for the three windows.

Measurement noise with a standard deviation of $10^{-4} \text{ W}/(\text{m}^2 \text{ sr } \mu\text{m})$ leads to additional 1%–2%. Reasonable modifications of *a priori* mean values have negligible impacts. Retrieved maps are most reliable at $1.02 \mu\text{m}$. There is an overall tendency for better results for cases with small cloud opacity, high surface elevation, high true emissivity, and small observation angle, but this depends on the emissivity window, retrieval pipeline, and measurement repetition number. Spatial fine structure is more reliable than large-scale spatial trends are.

Table VI.3 summarizes the renormalized emissivity errors referred to a typical synthetic VIRTIS-M-IR spectrum, the default reference spectrum from Kappel et al. (2015, Section 3 and Table 4). Note that these values slightly differ from the errors just stated that are based on five different reference spectra. Also note that these errors are referred to a surface emissivity of 0.65. The column R_1 shows the (not renormalized) single-spectrum retrieval errors. Note that the statistically scaled errors for the case $N_r = 64$ (column R_{64}) only apply when the emissivity maps are renormalized according to Section VI.2.3 (p. 169). The rows with '✓' in the R_{64} -column show the error contributions that are largely removed when using renormalized multi-spectrum retrieval and that would not decrease for increasing N_r without renormalization.

Calibration, preprocessing, and simulation errors can lead to additional emissivity errors. But calibration and preprocessing were improved by Kappel et al. (2012b), and the forward model is capable of simulating spectra that extremely well fit the measurements for a large variety of physical and observational conditions. Calibration, preprocessing, and functional descriptions of the simulated spectra are not expected to be severely wrong, therefore. Even if they were wrong, renormalized emissivities would not be strongly affected by that. Interfering parameters that were not studied by Kappel et al. (2015) can also introduce further errors, for instance varying cloud mode particle size distributions or chemical compositions, further details of the cloud mode altitude distributions, unknown absorbers like possible haze close to the surface (Grieger et al., 2004; Erard et al., 2009), etc. But impacts of systematically wrong assumptions on these parameters should be greatly diminished through the renormalized emissivity retrieval, and impacts of quasi-random time variations around the long-term averages should disappear with the inverse square root of the repetition number.

One can try to reduce the emissivity errors by retrieving one of the interfering parameters whose uncertainty causes large emissivity errors (like H₂O) as a further parameter. But this can only succeed, when the parameter can be reliably determined. A retrieval error analysis like that reported by Kappel et al. (2015) would be required to decide this. Haus et al. (2015a) performed such an analysis for the retrieval of minor gas

Uncertain parameters	2σ	R_1			R_{64}		
t		17	35	49	2	4	6
Cloud bottom	3 km	5	20	14	1	3	2
H ₂ SO ₄	10%	2	3	12	0	0	2
H ₂ O	25%	15	26	43	2	3	5
HCl	25%	2	3	8	0	0	1
Measurement noise	$2\sigma_N$	4	11	8	0	1	1
Interfering emissivities	25%	9	34	27	1	4	3
Surface elevation	200 m	9	12	12	9	12	12
ΔT_0	3 K	18	35	35	/	/	/
ΔT_{25}	3 K	12	21	23	/	/	/
Continua	25%	38	145	130	/	/	/
$c_{1.74}$	25%	24	83	94	/	/	/
$c_{2.3}$	25%	17	71	73	/	/	/

TABLE VI.3: Quadratically added errors R_{N_r} of 1.02, 1.10, and 1.18 μm emissivities (renormalized in case of $N_r = 64$) that were retrieved from a synthetic spectrum, in %, for 2σ -uncertainties of the listed parameters and N_r measurement repetitions. The row ' t ' represents quadratically added (root of sum of squares) errors due to many temporally and spatially varying parameters and measurement noise with $\sigma_N=10^{-4} \text{ W}/(\text{m}^2 \text{ sr } \mu\text{m})$, see Kappel et al. (2015, Table 4), but only the largest contributors are listed here in the sub-rows. 'Cloud bottom': base altitude for cloud modes 1, 2', 3; 'H₂SO₄': H₂SO₄ concentration of cloud droplets; 'H₂O' and 'HCl': column factors for these minor gases; ' ΔT_0 ', ' ΔT_{25} ': deep atmospheric temperature profile near 0 or 25 km; 'Continua': quadratically added contributions from the continua of all considered windows, among them from the 1.74 and the 2.3 μm continua. Impact of reasonable *a priori* mean value modifications: $\leq 1\%$.

abundances from VIRTIS-M-IR measurements at the long wavelength flank of the 2.3 μm nightside peak with the result that H₂O can be determined with a moderate accuracy. This was a different wavelength range than used for the present work, and results cannot be carried over. But nevertheless, this is used as an opportunity to optionally include the H₂O abundance as a retrieval parameter here (see Section VI.2.4 (p. 172)) in contrast to Kappel et al. (2015), with the aim to slightly improve emissivity results.

VI.4.2 Measurement Selection Tests and Parameter Modification Tests

According to Table VI.3, the renormalization approach is thus predicted to enable much more useful results at $N_r = 64$ than at $N_r = 1$, but it involves a number of subtleties, and errors are still not negligible. Moreover, the errors listed in Table VI.3 were estimated from synthetic spectra. Thus, it is advisable to verify their applicability to real data. To examine the reliability of actual renormalized emissivity maps, two types of tests are designed, in the following called 'Measurement Selection Test' (MST) and 'Parameter Modification Test' (PMT).

The VIRTIS-M-IR data can be regarded as measurements of surface emissivity maps. The MSTs shall explore, whether these measurements are repeatable within the frame of a certain (acceptable) measurement uncertainty, provided that geologic activity as would be observable by VIRTIS-M-IR is negligible. For this purpose, maps are determined from S disjoint data sets ('batches') with N_r repetitions each, using the same retrieval pipeline as for N_r^0 . These sets should lead to maps that are reasonably similar among each other. At a fixed bin, the scatter of the renormalized emissivities around their mean value provides a measure of the emissivity accuracy that is achievable at N_r repetitions. This measure can be scaled to estimate the uncertainty of the N_r^0 map. This is discussed in detail in Appendix VI.A.2.3 (p. 195). Since the resulting raw emissivity mean values may differ for the different maps, it is particularly important at this point to refer all the maps to the same reference emissivity in view of the mean value dependence of the amplitude of spatial emissivity fluctuations around their mean value. To facilitate a direct comparison of the various error measures used in the present work, all of them are represented in terms of double standard deviations in percent of the reference emissivity 0.5 (which is at the same time the mean renormalized emissivity), referred to $N_r^0 = 64$ repetitions. For the MSTs, surface elevation and the other temporally constant interfering parameters and their uncertainty impacts are identical (at least up to first order in perturbations by the remaining interfering parameters). Only temporally varying parameters can lead to significant differences. Disagreements between the maps that are

too large to be explained by the values in Table VI.3 may be due to calibration and preprocessing errors, may indicate that there are temporally varying interfering parameters that have not been considered here, may hint at an underestimation of the probable range the interfering parameters are assumed to cover, may be due to actual time variations of the emissivities, etc. In order to verify the statistical properties, MSTs are performed with the combinations $N_r = 32$ & $S = 2$, $N_r = 16$ & $S = 4$, and $N_r = 8$ & $S = 8$, such that always $N_r S = N_r^0$.

With the PMTs, it shall be checked, whether the renormalized emissivity maps are reasonably independent with respect to modifications of the most important interfering parameters. These include parameters that have to be set to assumed values to allow for the generation of realistic synthetic spectra and that yield the majority of the errors listed in Table VI.3. The dependence of the maps on the choice of the initial emissivity and the continua is also examined. In addition, a number of modifications to the details of the retrieval pipeline as well as the calibration and preprocessing will be studied. Since even the computation of a single map requires considerable computer resources, not the full 64 repetition data set is utilized, but a data set leading to 25 repetitions. The results are statistically scaled to allow for uncertainty interpretations of the $N_r = 64$ case. The mathematical background of the PMTs and their relation to the MSTs are discussed in Appendix VI.A.2.4 (p. 197).

Both reliability tests are complementary in the sense that for the MSTs, the parameters that are not retrieved stay constant between batches in the forward model simulations whereas their true underlying values vary, and vice versa for the PMTs. The MSTs can be regarded to yield a measure for the random errors, and the PMTs for the systematic errors. Results of both tests are presented in Sections VI.4.3 and VI.4.4.

Each of these tests requires one or more full retrieval runs ('scenarios'). Each scenario is based on a certain measurement data set comprising N_r measurement repetitions, the configuration of the retrieval pipeline, the choice of the forward model parameters, and the details of the calibration and preprocessing. An abbreviation (in **bold**) and a description are given in the following for each scenario. The abbreviations are used in Table VI.4 (p. 181) (column 'Scenario'). This table lists for each of the three surface windows the renormalization coefficients of the emissivity maps, as well as a statistical comparison measure. The latter can be found in the column 'SRMSD' (scaled root-mean-square-deviation, see comment before Eq. (VI.A.3) (p. 195)) and quantifies the deviation of the respective scenario's renormalized emissivity map from a reference map, in a reasonable sense scaled to be directly comparable to the N_r^0 scenario, and represented as double standard deviations in percent of the reference emissivity 0.5. In case of an MST with S batches, the reference map is the average over the batches, and for the PMTs, it is scenario $N_r = 25$ **base** which is completely analogous to scenario ' $N_r^0 = 64$ ', except that the data set has only 25 repetitions. For details, see Appendix VI.A.2 (p. 192). The VIRTIS-M-IR cubes utilized for these tests are listed in Appendix VI.A.1 (p. 192).

VI.4.3 Measurement Selection Tests

Three MSTs are performed and are used to estimate the retrieval uncertainty with respect to the selection of the measurement data set, see Appendix VI.A.2.3 (p. 195).

$N_r = 32$, batch 1 / batch 2: Renormalized emissivity maps are determined for two disjoint data sets (batches 1 and 2) with 32 repetitions each. The maps at $1.02 \mu\text{m}$ are depicted in Figs. VI.4a & b. Although there are differences, the magnitudes and spatial distributions of the deviations from the respective map averages 0.5 (green) are very similar between both maps. As it was discussed, the difference between the maps is a measure for the uncertainty of the results. Also compare to Fig. VI.3 (p. 176)a showing the more reliable corresponding map determined from the $N_r^0 = 64$ data set, which is very similar to both Figs. VI.4a & b.

$N_r = 16$, batches 1–4: The $N_r^0 = 64$ data set is divided into four disjoint $N_r = 16$ data sets.

$N_r = 8$, batches 1–8: The $N_r^0 = 64$ data set is divided into eight disjoint $N_r = 8$ data sets. Results of the three tests are divided by single horizontal lines in Table VI.4 (p. 181). The quadratically averaged SRMSDs of the S batches of a given MST yield an estimate of the uncertainty of the renormalized emissivity map at N_r^0 (see discussion below Eq. (VI.A.4) (p. 196)). Table VI.5 (p. 185) summarizes these estimates for the three MSTs and gives a rough estimate of these measures' uncertainties (according to Appendix VI.A.2.1 (p. 192)).

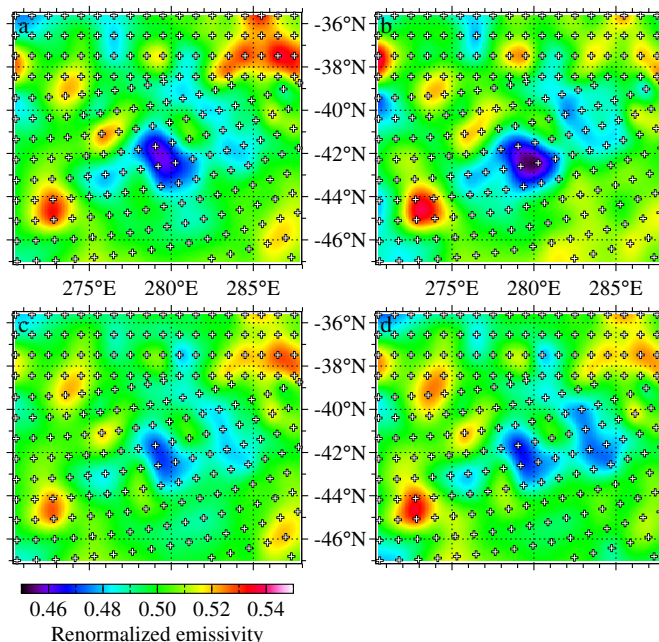


FIGURE VI.4: Examples for MSTs and PMTs showing renormalized $1.02\ \mu\text{m}$ emissivity maps of Themis Regio referred to reference emissivity 0.5. (a) MST ' $N_r = 32$, batch 1', (b) MST ' $N_r = 32$, batch 2', (c) PMT ' $N_r = 25$ base', (d) PMT 'Continuum $1.74\ \mu\text{m}$ '. Axes as in Fig. VI.1 (p. 175). The corresponding results at $1.10\ \mu\text{m}$ and $1.18\ \mu\text{m}$ are given in Figs. VI.A.5 (p. 201) and VI.A.6 (p. 202) in the supplementary material.

VI.4.4 Parameter Modification Tests

Based on $N_r = 25$ base (see Fig. VI.4c showing the renormalized $1.02\ \mu\text{m}$ map), it is now investigated, whether renormalized emissivity maps are reasonably independent with respect to modifications of the most important interfering parameters that are not sufficiently well known. For each PMT, one of the interfering parameters is modified by setting it to a value that differs by a reasonable amount from the value utilized for the retrieval of the map $N_r = 25$ base. The corresponding renormalized emissivity map is determined and compared to the base map (root-mean-square-deviation, scaled to N_r^0 and represented as double standard deviations in percent of the reference emissivity, see Appendix VI.A.2.4 (p. 197)).

The studied parameters can be in principle temporally varying (indicated by uppercase letter ' T ' on the right of the 'Scenario' column in Table VI.4), spatially varying but time independent (' L '), or constant in time and space (' C '). However, in the tests, the modifications can have a different character. For instance, the cloud bottom altitude can in principle vary with time (' T '), but the modification in the test is constant in time and space. This is indicated by a lowercase ' c ' in the table. In the same way, parameter modifications that vary with time are indicated by ' t ', and those that are time independent but vary in space by ' l '. The lowercase letters coincide with the categorization into t -, l -, and c -parameters in Appendix VI.A.2 (p. 192) and decide the scaling behavior of the renormalized emissivity errors. Parameter modifications that theoretically (see Eq. (VI.A.6) (p. 198) and also Eq. (VI.A.3) (p. 195)) do not lead to renormalized emissivity retrieval errors, because their impact is annihilated by the renormalization procedure (c - and spatially slowly varying l -parameters), are indicated by '0' on the right of the 'Scenario' column, the others by '1'.

The scaled PMT error results can be used to roughly estimate the impact that such modifications would have on the N_r^0 -case. This can be done by quadratically adding them to the MST estimates, see Appendix VI.A.2.4 (p. 197). However, some of the PMTs study the same parameter but in different ways, other PMTs have been performed just for general interest. Thus, only the PMT errors indicated by superscript '*' in the 'Scenario'-column of Table VI.4 are added to the MST error estimate. The quadratically added errors of the flagged PMTs are shown in Table VI.5 (p. 185) in the 'PMTs'-row. The quadratic sum of the latter and the largest of the three MST estimates is represented for each of the three surface windows in the 'Total'-row of this table. These values provide an estimate for the total error of the N_r^0 -maps in Fig. VI.3 (p. 176), represented as double standard deviations in percent of the reference emissivity.

The PMT results are listed below the double horizontal line in Table VI.4. The modified parameters fall into three groups, forward model parameters, modifications to the characteristics of the retrieval pipeline, and modifications to calibration and preprocessing. Results for these groups are divided by single horizontal lines in the table.

Scenario		Mean	100×Slope/°lat	10×Slope/km	SRMSD
$N_r^0 = 64$		0.48 0.67 0.62	0.14 0.28 0.13	0.34 -0.70 -0.00	
$N_r = 32$, batch 1		0.49 0.64 0.66	0.10 0.65 0.14	0.29 -0.62 -0.08	1.56 4.87 2.55
$N_r = 32$, batch 2		0.46 0.70 0.59	0.20 -0.15 0.23	0.29 -0.70 -0.01	1.56 4.87 2.55
$N_r = 16$, batch 1		0.49 0.65 0.61	0.06 1.07 0.04	0.36 -0.75 0.04	1.91 6.27 2.02
$N_r = 16$, batch 2		0.48 0.67 0.60	0.08 0.34 0.09	0.37 -0.48 0.04	1.92 7.35 2.56
$N_r = 16$, batch 3		0.49 0.71 0.66	0.09 -0.09 -0.19	0.35 -0.77 0.03	3.15 9.08 3.61
$N_r = 16$, batch 4		0.48 0.72 0.65	0.22 0.48 0.51	0.38 -0.60 -0.00	2.56 8.13 2.85
$N_r = 8$, batch 1		0.49 0.67 0.62	-0.04 0.71 0.10	0.39 -0.70 -0.07	1.75 3.38 2.39
$N_r = 8$, batch 2		0.49 0.64 0.59	0.11 1.50 -0.06	0.29 -0.82 0.13	1.52 8.09 2.57
$N_r = 8$, batch 3		0.49 0.64 0.59	-0.09 0.35 0.23	0.24 -0.72 0.01	1.83 6.19 2.14
$N_r = 8$, batch 4		0.48 0.68 0.61	0.18 0.29 -0.04	0.46 -0.27 0.06	2.55 6.89 2.21
$N_r = 8$, batch 5		0.49 0.72 0.66	-0.21 -1.03 -0.74	0.43 -0.54 0.16	3.22 9.10 4.65
$N_r = 8$, batch 6		0.49 0.70 0.66	0.34 0.91 0.37	0.26 -0.99 -0.09	2.47 7.81 2.90
$N_r = 8$, batch 7		0.48 0.70 0.65	0.28 1.12 0.68	0.35 -0.89 -0.24	3.00 9.72 3.68
$N_r = 8$, batch 8		0.48 0.72 0.64	0.14 -0.16 0.28	0.38 -0.35 0.22	2.40 7.95 4.24
$N_r = 25$ base		0.48 0.64 0.59	0.08 0.43 0.02	0.22 -0.74 -0.02	0 0 0
Init. emiss. 0.625	<i>Cc0</i>	0.60 0.77 0.72	0.10 0.48 0.03	0.23 -0.81 -0.08	0.11 0.15 0.10
Init. emiss. 0.750	* <i>Cc0</i>	0.71 0.90 0.85	0.10 0.52 0.04	0.25 -0.88 -0.15	0.19 0.39 0.17
Init. emiss. 0.875	<i>Cc0</i>	0.83 0.99 0.97	0.11 0.12 0.04	0.27 -0.34 -0.20	0.25 3.65 0.40
Continuum 1.74 μm	* <i>Cc0</i>	0.48 0.65 0.59	0.16 0.71 0.17	0.23 -0.98 -0.23	0.73 1.17 1.49
Continuum 2.3 μm	* <i>Cc0</i>	0.48 0.62 0.57	0.08 0.40 0.02	0.23 -0.62 0.06	0.14 0.39 0.26
Temp. 0 km	<i>Lc0</i>	0.48 0.63 0.59	0.08 0.46 0.01	0.24 -0.66 0.01	0.17 0.24 0.11
Temp. 25 km	<i>Lc0</i>	0.48 0.63 0.59	0.08 0.50 0.02	0.24 -0.71 0.01	0.08 0.16 0.11
Temp. 25 km -0.3 K	<i>Lc0</i>	0.48 0.64 0.59	0.07 0.49 0.00	0.22 -0.75 -0.02	0.04 0.10 0.06
Temp. 0 km trend	* <i>Ll0</i>	0.47 0.65 0.60	-0.23 0.56 -0.34	0.20 -0.81 -0.05	0.34 0.52 0.36
Temp. 25 km trend	* <i>Ll0</i>	0.48 0.65 0.60	0.17 0.60 0.07	0.20 -0.78 -0.04	0.08 0.15 0.11
Cloud bottom	* <i>Tc0</i>	0.47 0.67 0.61	0.05 0.48 -0.05	0.21 -0.82 -0.07	0.10 0.26 0.24
H ₂ SO ₄	* <i>Tc0</i>	0.48 0.65 0.60	0.14 0.63 0.11	0.28 -0.70 -0.03	0.55 0.70 0.93
H ₂ SO ₄ alt. gradient	<i>Tc0</i>	0.48 0.68 0.61	0.08 0.58 0.01	0.23 -0.88 -0.16	0.22 0.64 0.76
H ₂ O	* <i>Tc0</i>	0.52 0.60 0.58	0.05 0.97 0.31	0.38 -0.86 -0.04	0.89 1.07 0.64
HCl	* <i>Tc0</i>	0.48 0.63 0.59	0.07 0.47 0.00	0.22 -0.70 0.02	0.08 0.18 0.15
Surface haze	<i>Tc0</i>	0.46 0.69 0.62	0.14 0.63 0.04	0.57 -1.28 -0.23	1.53 1.75 0.69
No m_1 retrieval	<i>Tt1</i>	0.50 0.72 0.72	0.14 0.65 0.21	0.28 -0.81 -0.15	0.36 0.71 0.78
No H ₂ O ^b retrieval	<i>Tt1</i>	0.50 0.62 0.65	0.10 0.55 0.17	0.24 -0.51 -0.00	0.33 1.03 0.82
Pipeline II	<i>Tt1</i>	0.52 0.55 0.53	0.08 0.99 0.37	0.31 -0.58 0.05	0.52 0.83 0.55
Pipeline II, normal noise	<i>Tt1</i>	0.52 0.55 0.53	0.08 0.99 0.37	0.31 -0.58 0.04	0.51 0.82 0.54
Pipeline II+ m_1 +H ₂ O ^b	* <i>Cc0</i>	0.48 0.63 0.58	0.07 0.55 0.03	0.22 -0.82 -0.02	0.16 0.44 0.25
Wavel. dep. FWHM	* <i>Cc0</i>	0.49 0.59 0.56	0.05 0.48 0.06	0.21 -0.67 0.02	0.15 0.53 0.32
Detector responsivity	* <i>Cc0</i>	0.47 0.70 0.62	0.08 0.54 0.04	0.16 -1.13 -0.06	0.28 0.88 0.41
Unsmoothed straylight	* <i>Tt1</i>	0.48 0.64 0.59	0.07 0.26 0.10	0.24 -0.55 -0.08	0.65 1.86 0.61
Topo. 65 km	<i>Ll1</i>	0.48 0.64 0.59	0.06 0.43 0.02	0.25 -0.72 -0.00	0.58 0.52 0.33
Topo. 65 km R100	<i>Ll1</i>	0.48 0.64 0.59	0.06 0.43 0.02	0.25 -0.75 -0.01	0.80 0.34 0.32
Topo. 30 km	<i>Ll1</i>	0.48 0.64 0.59	0.07 0.51 0.01	0.29 -0.68 0.02	1.16 1.29 0.65
Topo. 30 km R100	* <i>Ll1</i>	0.48 0.64 0.59	0.08 0.51 0.02	0.28 -0.75 0.01	1.60 0.49 0.67

TABLE VI.4: Results of MSTs and PMTs. Detailed explanations can be found in Section VI.4 (p. 176). The entries in column 'Scenario' correspond to the bold-typed shortcuts used in the descriptions in Sections VI.4.3 (p. 179) and VI.4.4. Renormalization coefficients and SRMSDs are given in the next four blocks of columns. Each block shows the data for the surface windows at 1.02, 1.10, and 1.18 μm next to each other. Mean values of the retrieved emissivity maps before renormalization are listed in the 'Mean' columns, the slopes of linear trends with latitude, scaled with a factor 100 for better representation, in the columns '100 × Slope/°lat', and the scaled slopes of linear trends with surface elevation in the columns '10 × Slope/km'. The SRMSDs are comparison measures referred to $N_r^0 = 64$ repetitions and are represented as double standard deviations in percent of the reference emissivity 0.5.

Forward model parameters

Init. emiss. 0.625 / 0.750 / 0.875: The initial emissivity e_{init} is set to 0.625 / 0.750 / 0.875, respectively, instead of 0.500. The results listed in Table VI.4 demonstrate for the PMTs 'Init. emiss. 0.625' and 'Init. emiss. 0.750' that the choice of the initial emissivity does not significantly affect renormalized emissivity maps referred to 0.5, SRMSDs are smaller than 0.4%. Note that this would not be the case without reference emissivity transformation. The best choice for the initial emissivity (or rather the raw emissivity mean value) would be the surface emissivity average of the planet. Fegley et al. (1997) reviewed that weathering products like iron oxides could be widely present on Venus' surface. This corresponds with the argumentation by Smrekar et al. (2010) that the background emissivity of Venus' southern hemisphere is 0.5-0.6 at $1 \mu\text{m}$, a value consistent with fine-grained hematite (Baldrige et al., 2009). Moreover, it is important to use an initial emissivity value as far away from the emissivity domain boundaries 0 and 1 as possible, in particular when the presence of trends with latitude and topography in the raw retrieved emissivities cannot be excluded, as it was explained in Section VI.2.3 (p. 169). The results for the value 0.875 illustrate this point, as the SRMSD at $1.10 \mu\text{m}$ is the largest of all PMT results. A detailed inspection reveals that the raw emissivities for many bins are cut off at the upper emissivity domain boundary 1 (raw emissivity mean value 0.99 !). The initial emissivity that otherwise leads to the largest SRMSDs (0.750) is selected to contribute to the total error in Table VI.5 (p. 185).

Continuum 1.74 μm / 2.3 μm : The continuum parameters $c_{1.74}$ and $c_{2.3}$, respectively, are increased by 25%. SRMSDs contribute to the total error. Uncertainties of these continua potentially cause large errors without renormalization (Table VI.3 (p. 178)), but these PMTs demonstrate that renormalized emissivities are only moderately affected. This is illustrated for 'Continuum 1.74 μm ' when comparing the resulting renormalized map at $1.02 \mu\text{m}$ represented in Fig. VI.4 (p. 180)d to Fig. VI.4 (p. 180)c showing the map for ' $N_r = 25$ base'. The respective SRMSD is among the largest of those that contribute to the total error at $1.02 \mu\text{m}$. Recall that the surface window continua are retrieved as fine-tuning parameters (Section VI.2.3 (p. 169)), and that the $1.31 \mu\text{m}$ peak is not used here for emissivity retrieval.

Temp. 0 / 25 km: ΔT_0 and ΔT_{25} , respectively, are decreased by 3 K to modify the deep atmospheric temperature profile close to the surface and around 25 km altitude. These modifications hardly affect the renormalized maps. To estimate the impact that an even smaller modification has, **Temp. 25 km -0.3 K** decreases the temperature around 25 km by only 0.3 K. Even though the magnitude of this modification is a tenth of the one for the preceding test, the SRMSDs are only about halved. The difference to the base case seems not to fast converge to zero. This indicates a limited numerical repeatability of the retrieval under slightly altered conditions, but the effect is not large compared to the other PMTs. **Temp. 0 / 25 km trend:** ΔT_0 and ΔT_{25} , respectively, are set to exhibit a $\cos(\text{latitude})$ -trend with a range of 3 K over the latitude range $[\theta_1, \theta_2] = [-46.99^\circ, -35.63^\circ]$ of the target area, $(\cos \theta - \cos \theta_1) / (\cos \theta_2 - \cos \theta_1) \cdot 3 \text{ K}$. The magnitude of this trend is exaggerated as it would correspond to a range of 23 K between equator and pole, whereas the order of a few K seems to be more realistic. Note the strong impact on the latitude trend renormalization coefficient for $1.02 \mu\text{m}$ in case of the ΔT_0 test. Nevertheless, the effect on the renormalized emissivity maps is surprisingly small, in particular for ΔT_{25} , even though the renormalization not exactly annihilates this only approximately linear trend of the parameters (see Appendix VI.A.2.2 (p. 194)). SRMSDs contribute to the total error.

Cloud bottom: The h_b for cloud modes 1, 2', 3 are jointly decreased by 3 km. According to Kappel et al. (2015) (see Table VI.3 (p. 178) of the present work), this is expected to be one of the largest error contributors for parameters that can temporally vary, along with the H_2SO_4 concentration of the cloud droplets and the abundances of H_2O and HCl . But this test demonstrates that a constant misplacement of the cloud bottom hardly affects the renormalized emissivities. SRMSDs contribute to the total error.

H_2SO_4 / H_2SO_4 alt. gradient: The H_2SO_4 concentration of the cloud droplets is set in the first test to 87.5% instead of 75.0%. For the other test, the concentration is set to change with altitude according to an abstracted form of the profile shown by James et al. (1997) (linear function with slope $-2.5 \text{ \%}/\text{km}$, attaining 88% at 55 km, cutoff at 50% and 95.6%). These modifications yield much larger errors than the cloud bottom modifications. SRMSDs of the H_2SO_4 test with the larger errors (the first one) are selected to contribute to the total error.

H_2O / HCl : The H_2O and the HCl column factors, respectively, are decreased by 25%. While the HCl

concentration change has almost no impact, H₂O has a larger response. Note that H₂O^{*b*} is not retrieved for the H₂O test (see Section VI.2.4 (p. 172)), so it really constitutes a change of the retrieval pipeline as well. SRMSDs of both tests contribute to the total error.

Surface haze: An additional absorber is considered below 2000 m altitude, for simplicity modeled as gas (0.1 ppmv) with wavelength independent molecular absorption cross-section 10⁻²⁰ cm². This test is performed to illustrate the impact of this hypothetical parameter that is normally not included in the forward model. It has a quite strong effect on the topography trend renormalization coefficients, and the error contribution is among the largest of all PMTs. Note that the bins whose surface elevation reaches above this haze yield the largest errors. But as a parameter whose role is not clear yet, its SRMSDs are excluded from the total error. Since this haze can in principle change with time, it is categorized as a *T*-parameter, but the PMT only changes the abundance by a constant value and has *c*-character, therefore.

Retrieval pipeline

No *m*₁ retrieval: The retrieval of cloud mode factor 1 in stages six and eight of the pipeline is omitted. The character of this PMT is difficult to specify. On the one hand, the difference of *m*₁ to the retrieval result from the base case is naturally time dependent. On the other hand, this is the case for all the other PMTs, too, since the retrieved *m*₁ values are not likely to always exactly agree. However, for this PMT, *m*₁ differs as a matter of principle. This PMT is thus set to have *T*- and *t*-character. This is corroborated by the consideration that the renormalized emissivity retrieval errors due to *m*₁ uncertainties should average out more efficiently with increasing *N_r*. **No H₂O^{*b*} retrieval:** Here, the retrieval of H₂O^{*b*} in stages six and eight of the pipeline is omitted. Again, this leads to a *T*- and *t*-character. The error contribution is quite large in the 1.10 and 1.18 μm windows.

Pipeline II: This is a test, where several characteristics of the retrieval pipeline are modified. The *a priori* correlation data is slightly modified, the standard deviation σ_N of the measurement and simulation error distribution is doubled, and, as in the two preceding tests, *m*₁ and H₂O^{*b*} are not retrieved. Thus, it has *T*- and *t*-character. The error contribution is smaller than could be expected from all these changes. **Pipeline II, normal noise:** This PMT is the same as the one before, except that σ_N is set to the usual value. The impact compared to 'Pipeline II' is marginal. **Pipeline II+*m*₁+H₂O^{*b*}:** Here, the retrieval of *m*₁ and H₂O^{*b*} is reintroduced compared to 'Pipeline II'. The PMT has therefore *C*- and *c*-character. The only differences to the base case are the modified *a priori* correlation data and the doubled σ_N . Since operational retrievals in the present work always include *m*₁ and H₂O^{*b*} retrieval, but the correlation data and σ_N were chosen somewhat arbitrarily, the resulting SRMSDs contribute to the total error. However, this PMT demonstrates that certain details of the retrieval pipeline can be less important than the choice of the value for some of the interfering forward model parameters.

Calibration and preprocessing

Wavel. dep. FWHM: The FWHM of the spectral instrumental response function is not sufficiently well predictable by the calibration pipeline. In this work, it is normally retrieved for each spectrum as a value that is assumed to be constant with wavelength. For this PMT, it is modeled to change in dependence on wavelength according to a quadratic function of the spectral bands *b*. The offset to the retrieved wavelength constant value amounts to 0 nm at the first (*b* = 1, ≈ 1.02 μm) and the last (*b* = 432, ≈ 5.1 μm) spectral bands and to +3 nm in the middle (*b* = 216.5, ≈ 3.1 μm). This is a PMT that is parameterized by a single constant value and has thus *C*- and *c*-character. The error impact is not large. SRMSDs contribute to the total error.

Detector responsivity: One of the calibration refinement issues discussed by Kappel et al. (2012b) constitutes an adjustment of the detector responsivity in the spectral dimension resulting in an increase of the calibrated radiance between 0% at 1.3 μm and 35% at 1.0 μm. To examine the effect of possible errors of this adjustment, the amount of the correction is halved for this *C*- and *c*-PMT. Surprisingly, this has only a small effect on the SRMSD for the surface window with the largest responsivity modification, the one at 1.02 μm. At 1.10 and 1.18 μm, the impact is larger. SRMSDs contribute to the total error. Note that the impact of a spatial detector inhomogeneity as it was present before the calibration refinement is not studied here. But error

contributions are expected to be large and not well reproducible, because they would depend on details like which part of the surface target is probed by which part of the detector. However, they would not be included in the total errors, since the inhomogeneity is corrected quite well.

Unsmoothed straylight: Normally, the straylight is assumed in this work to show no spatial fine structure over the spatial dimensions, but only instrument-related general trends that vary slowly compared to the spatial extension of a single VIRTIS-M-IR image. This can be justified by the nature of the most relevant straylight source where Venus' dayside is outside but close to the VIRTIS-M-IR field of view (Kappel et al., 2012b, Section 4.1.1, issue 3). Therefore, the straylight, which is computed for each (unbinned) spectrum of a VIRTIS-M-IR cube, is normally median-smoothed over the cube's spatial dimensions before being subtracted from the measured spectra. The size of the two-dimensional neighborhood used for smoothing is 64×64 pixels for the utilized 256-sample-mode cubes. For this PMT, the smoothing is not performed. The result is not very realistic but can serve to estimate the impact of errors in the determination of the straylight spectra. The difference between smoothed and unsmoothed straylight statistically varies with time and should more efficiently average out for increased N_r . This PMT has T - and t -character, therefore. Note that the amount of straylight is clearly correlated with the distance of the field of view to the terminator. However, most of this correlation is removed for the difference between smoothed and unsmoothed straylight. SRMSDs contribute to the total error and are very large at $1.10 \mu\text{m}$ ($\approx 2\%$). This is because this radiance peak is the smallest of the surface window peaks and thus the most affected by errors in the straylight removal.

Topo. 65 km: The emulation of the atmospheric blurring of the surface topography normally assumes a FWHM of 100 km. Now, the FWHM is set to 65 km. This can still be regarded as a realistic value and is probably valid for observations with few clouds. This test can also serve to emulate the effect of slight errors in the underlying Magellan topography and the blurring approach just in the most critical areas, the mountainous terrains, where the topography is spatially particularly fast varying and topography errors are more likely. For the target area, the topographies for the 65 km- and the 100 km-blurring differ by up to about 125 m (root-mean-square-deviation 35 m). This PMT has L - and l -character, but the impact is not annihilated by the renormalization, because the topography difference is spatially fast varying. However, this PMT is explicitly excluded in the discussions in Appendix VI.A.2 (p. 192) and must be treated separately, because the renormalization operator itself depends on topography. For this PMT, the renormalization is performed using the 65 km-blurring, whereas the base case renormalization naturally relies on the 100 km-blurring. For comparison, **Topo. 65 km R100**, which otherwise coincides with 'Topo. 65 km', is renormalized based on the 100 km-blurring. While the SRMSD increases at $1.02 \mu\text{m}$ because of the modified renormalization, it surprisingly decreases at the other two surface windows. **Topo. 30 km / Topo. 30 km R100:** These PMTs are completely analogous to the two preceding cases, but the FWHM is even reduced to 30 km. This is probably not realistic anymore but helps to further quantify emissivity errors due to topography errors. The topographies for the 30 km- and the 100 km-blurring differ by up to about 250 m (RMSD 63 m). Of the topography PMTs, the largest SRMSDs for each window are selected to contribute to the total error ('Topo. 30 km' at $1.10 \mu\text{m}$, 'Topo. 30 km R100' otherwise, but only the latter is indicated with superscript '**' in the 'Scenario'-column of Table VI.4 (p. 181)).

VI.4.5 Reference emissivity

As discussed in Section VI.2.3 (p. 169), when trends of a raw retrieved emissivity map with latitude and topography are removed such that the emissivity mean value M is not changed, the thus de-trended emissivities spatially fluctuate around M with a higher amplitude for cases with higher M . This effect can be observed by comparing emissivities computed with respect to different initial emissivities e_{init} as it was done in the frame of the PMTs 'Init. emiss. 0.625 / 0.750 / 0.875' in Section VI.4.4 (p. 180). M can differ from e_{init} as explained earlier and is listed for different cases in the 'Mean' columns in Table VI.4 (p. 181) in the rows ' $N_r = 25$ base' ($e_{\text{init}} = 0.500$), 'Init. emiss. 0.625', 'Init. emiss. 0.750', and 'Init. emiss. 0.875'. M_0 refers to the case with $e_{\text{init}} = 0.500$ (e.g. $M_0 = 0.48$ at $1.02 \mu\text{m}$ according to the table). To avoid the dependence of fluctuation amplitudes on an uncontrollable M when performing quantitative comparisons between different emissivity maps, for instance in the frame of the retrieval error estimations, the emissivities have to be referred to a certain fixed reference emissivity, here 0.5, with then directly comparable fluctuation amplitudes. The results can be later transformed to other reference emissivities if needed.

N_r	S	R_{64}			Δ
32	2	1.6	4.9	2.6	10
16	4	2.4	7.8	2.8	6
8	8	2.4	7.6	3.2	4
PMTs		2.2	3.2	2.2	
Total		3.3	8.4	4.0	
Synthetic		2.4	6.1	7.0	
Synth. rev.		1.9	5.8	6.2	

TABLE VI.5: Summary of MST and PMT results. The three MST rows below the first horizontal line show for the surface windows at 1.02, 1.10, and 1.18 μm the quadratically averaged SRMSDs from Table VI.4 (p. 181) and represent the uncertainty of renormalized emissivities with respect to the selection of the measurement data set, determined from the MSTs ' $N_r = 32$, batches 1–2', ' $N_r = 16$, batches 1–4', and ' $N_r = 8$, batches 1–8'. They coincide with the statistical error estimate for the deviation of the N_r^0 -map from the true renormalized emissivity map (see $\delta^{N_r, S}$ from Appendix VI.A.2.3 (p. 195)). 'PMTs': quadratic sum of SRMSDs from '**'-indicated PMTs in Table VI.4 (p. 181). 'Total': quadratic sum of PMT estimate and maximum of the MST estimates. 'Synthetic': quadratic sum of errors from Table VI.3 (p. 178), but excluding those due to surface elevation uncertainties. 'Synth. rev.': revised synthetic errors, see Section VI.5. Values are double standard deviation errors in percent of the reference emissivity referred to 64 repetitions. Δ : double standard deviation errors of MST estimates in percent according to Appendix VI.A.2.1 (p. 192).

The transformation between different reference emissivities, and therefore different values of M , will now be derived. For this purpose, the trends of a given raw retrieved emissivity map at a fixed surface window with latitude and topography are removed by multiple linear regression in such a way that the mean emissivity M is unchanged. The resulting values at the different surface bins are compiled into the vector \mathbf{r}_M .

The scatterplots of $\mathbf{r}_M - M$ for the case $e_{\text{init}} = 0.750$ in dependence on $\mathbf{r}_{M_0} - M_0$ are shown in Fig. VI.5 (left). Note that the mean value of $\mathbf{r}_M - M$ is zero for each surface window, as it is the case with $\mathbf{r}_{M_0} - M_0$. The fluctuations are small compared to the emissivity mean, giving rise to a first order model. The scatterplots

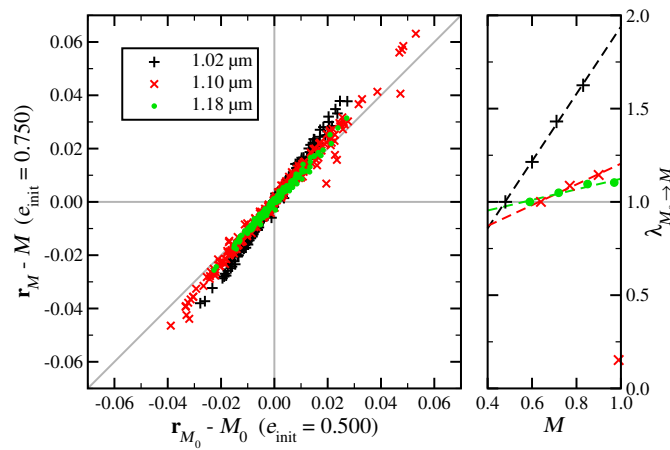


FIGURE VI.5: Dependence of emissivity fluctuations on their raw mean value M for the three surface windows. Left: Scatterplots between $\mathbf{r}_M - M$ for the case $e_{\text{init}} = 0.750$ and $\mathbf{r}_{M_0} - M_0$ ($e_{\text{init}} = 0.500$). Right: Slopes $\lambda_{M_0 \rightarrow M}$ of the scatterplots for different M (symbols) and corresponding linear regression functions (dashed), see text for explanations.

approximately follow the regression function $(\mathbf{r}_M - M) = \lambda_{M_0 \rightarrow M} \cdot (\mathbf{r}_{M_0} - M_0)$ with the slope $\lambda_{M_0 \rightarrow M}$ that transforms results for cases with mean value M_0 into those with mean value M . This slope depends on M_0 and M (see Fig. VI.5, right) with regression function $\lambda_{M_0 \rightarrow M} = 0.137 + 1.802 \cdot M$ at 1.02 μm , $\lambda_{M_0 \rightarrow M} = 0.649 + 0.556 \cdot M$ at 1.10 μm , and $\lambda_{M_0 \rightarrow M} = 0.840 + 0.283 \cdot M$ at 1.18 μm . These regressions are regarded as valid for M larger than ≈ 0.5 and not close to 1 to avoid extrapolation and stay in the linear regime. Note that the case $e_{\text{init}} = 0.875$ at 1.10 μm is unreliable as explained, because $M = 0.99$ is too close to 1. It is therefore excluded from the regression. Since $(\mathbf{r}_{0.5} - 0.5) = \lambda_{M_0 \rightarrow 0.5} \cdot (\mathbf{r}_{M_0} - M_0)$, the 'renormalized emissivity map referred to the reference emissivity 0.5' as it was introduced in Section VI.2.3 (p. 169) follows for a given surface window as $\mathbf{r}_{0.5} = 0.5 + \lambda_{M_0 \rightarrow 0.5} / \lambda_{M_0 \rightarrow M} \cdot (\mathbf{r}_M - M)$. As already mentioned, the

maps will here always be referred to 0.5, except when stated otherwise, and $\mathbf{r}_{0.5}$ is shortly called 'renormalized emissivity map'.

A renormalized emissivity map already referred to 0.5 can be referred to another reference emissivity M according to $\mathbf{r}_M = M + \lambda_{0.5 \rightarrow M} \cdot (\mathbf{r}_{0.5} - 0.5)$, where $\lambda_{M' \rightarrow M} := \lambda_{M_0 \rightarrow M} / \lambda_{M_0 \rightarrow M'}$. Note that the dividing of $\lambda_{M_0 \rightarrow M}$ by $\lambda_{M_0 \rightarrow 0.5}$ ensures the scaling factor to attain the value 1 at $M = 0.5$. The impact of such a reference emissivity change on the first main result of this work represented in Fig. VI.3 (p. 176) can be estimated by simply scaling the tick labels of the color bar for the renormalized emissivities according to this transformation. As an example, for the reference emissivity $M = 0.75$, the color bar range is transformed from $[0.450, 0.550]$ to the interval $0.250 + [0.428, 0.572]$ at $1.02 \mu\text{m}$, to $0.250 + [0.443, 0.557]$ at $1.10 \mu\text{m}$, and to $0.250 + [0.446, 0.554]$ at $1.18 \mu\text{m}$. When the true absolute emissivity \hat{A} of just a single surface bin b of the target with renormalized retrieved emissivity $\mathbf{r}_{0.5}(b)$ were known, for instance by ground truth, the absolute emissivity map of the entire target could be computed according to the mentioned transformation, assuming absent trends of the true emissivity map with latitude and topography. For this purpose, only a suitable M has to be found. Writing $\lambda_{0.5 \rightarrow M} = p + q \cdot M$, it follows $M = (\hat{A} - p \cdot (\mathbf{r}_{0.5}(b) - 0.5)) / (1 + q \cdot (\mathbf{r}_{0.5}(b) - 0.5))$.

As a consequence of the mentioned linear transformation, a small emissivity perturbation $\delta_{0.5}$ in the renormalized emissivity map referred to the reference emissivity 0.5 scales according to $\delta_M = \lambda_{0.5 \rightarrow M} \cdot \delta_{0.5}$ when the reference emissivity is changed from 0.5 to M . Hence, a relative emissivity error $\varepsilon_{0.5}$ (e.g. $\delta_{0.5}$ divided by the reference emissivity) scales according to $\varepsilon_M = \lambda_{0.5 \rightarrow M} \cdot 0.5 / M \cdot \varepsilon_{0.5}$. In the example for the reference emissivity 0.750, the relative errors are multiplied by 0.96 at $1.02 \mu\text{m}$, by 0.77 at $1.10 \mu\text{m}$, and by 0.71 at $1.18 \mu\text{m}$. This does not mean that the errors decrease, but rather that the reference value increases. The color relations in Fig. VI.3 (p. 176) with respect to (absolute, i.e. not relative) emissivity retrieval errors are not affected by a change of the reference emissivity, i.e. an emissivity anomaly exceeding the error levels stays an anomaly regardless of the reference emissivity transformation (this will later be illustrated by Fig. VI.6 (p. 188)). In this respect, the renormalized emissivity maps and absolute errors are well-defined with respect to the reference emissivity.

VI.5 Discussion

The variation of the renormalization coefficients for the different scenarios is not unexpected (Section VI.2.3 (p. 169)) and necessitates the renormalization procedure. According to the MSTs and PMTs, the renormalized maps statistically agree within tolerances listed in Table VI.4 (p. 181), taking into account the different N_r . The spatially slowly (or not) varying time independent interfering parameters studied by Kappel et al. (2015) (continuum parameters, deep atmospheric temperature field modifications) lead to very large unrenormalized emissivity retrieval errors (up to an order of 100%) that do not statistically scale with $1/\sqrt{N_r}$, because they do not average out over time. However, it was argued that these errors are largely removed by the renormalization. The PMTs of the present work support this conclusion. The same applies with respect to unconsidered systematic latitude trends of the cloud or minor gas parameters (Appendix VI.A.2 (p. 192)). Furthermore, renormalized emissivity maps were shown to be reasonably independent of the choice of the initial emissivity, as long as the latter is not close to 0 or 1. Slight modification to the retrieval pipeline and calibration and preprocessing are not critical as well.

The (unscaled with respect to N_r) retrieval errors for the MST with $N_r = 32$ (2.2%, 6.9%, 3.6%) are clearly smaller than for $N_r = 16$ results (4.9%, 15.6%, 5.6%), and those are clearly smaller than for $N_r = 8$ (6.8%, 21.6%, 9.1%), which can be found by backscaling the MST errors from Table VI.5 from N_r^0 to the respective N_r . Moreover, the N_r^0 -referred MST errors in Table VI.5 do not differ much for different N_r and even have the tendency to decrease with increasing N_r . The error scaling rules thus seem to apply, and the estimation of the N_r^0 -errors using these rules seems to be valid. However, it should be expected that even the N_r^0 -referred MST errors decrease with increasing N_r due to MSR's usage of more context data from measurements adjacent in time or space. This is the case for $N_r = 32$, but $N_r = 16$ -errors are not consistently smaller than those for $N_r = 8$. Also note the high errors Δ for the MST estimates of 4%–10%, so no conclusion regarding decreasing N_r^0 -errors with increasing N_r is possible yet based on present results. This must be studied with further surface targets and, if possible, with higher N_r^0 by relaxing the demands on 'usable measurements' (Section VI.2.1 (p. 165)).

Next, the compatibility of present results with the retrieval errors estimated by Kappel et al. (2015) from synthetic spectra ('synthetic errors') is examined, see comparison in Table VI.5 (p. 185). Since the MST estimates are not strictly monotonically decreasing with increasing N_r , not the result from the MST with $N_r = 32$ that is closest to N_r^0 is used as estimate for N_r^0 , but the maximum value from the three MSTs. MST errors are interpreted to be mainly due to actual variations of those interfering parameters that can vary with time. This is just what the synthetic errors describe, and thus, these two estimates are compared. The synthetic errors well agree with the MST estimate at $1.02\ \mu\text{m}$ but are underestimated at $1.10\ \mu\text{m}$ and overestimated at $1.18\ \mu\text{m}$. The synthetic errors are based on assumptions for the effective range (double standard deviation) the interfering parameters are thought to statistically cover, while the MSTs do not rely on such assumptions. These parameter ranges are obvious candidates for the disagreements, therefore. Table VI.3 (p. 178) shows that H_2O might be responsible for the synthetic overestimate at $1.18\ \mu\text{m}$. Indeed, the utilized spectral range is mainly sensitive to tropospheric properties, which are thought to be quite stable with time and spatially slowly varying. The assumed 25%-range for the H_2O abundance is therefore probably too high. Moreover, the H_2O^b abundance is retrieved here in contrast to Kappel et al. (2015), admittedly probably with low accuracy, but this could also help to reduce the impact of H_2O variations. The double standard deviation range is now assumed as 5% instead of 25%. The response of the retrieved emissivity to H_2O is quite linear in the discussed range (Kappel et al., 2015, Fig. 5), and thus the error contribution approximately scales with the assumed range. In the same way, the contribution from 25%-uncertainties of emissivities from the other respective surface windows should be reduced to 9%-uncertainties, which is more realistic in view of the 'Total'-row in Table VI.5 (p. 185). The effective variability of the cloud bottom altitude is likely smaller than the assumed 3 km, since this altitude is related to the probably spatially slowly varying (thereby annihilated by renormalization) and temporally almost not varying tropospheric temperature and pressure conditions, see discussion by Kappel et al. (2015, Section 3.5) based on data by Knollenberg and Hunten (1980) and Marov et al. (1980). It is now set to 1 km. Although the response to the retrieved emissivity is not linear (Kappel et al., 2015, Fig. 5), a linear downscaling leads to a valid upper boundary for the error contribution in this case. Next, even though it is a PMT result, errors in the straylight removal have to be taken into account by quadratically adding the 'Unsmoothed straylight' SRMSDs, to make the synthetic errors better comparable to what the MST errors represent. Finally, the errors listed in Table VI.3 (p. 178) were based on a reference spectrum with surface emissivity 0.65 and have to be referred to the reference emissivity 0.5 to be comparable to the error measures in the present work (see Section VI.4.5 (p. 184) for a discussion on the reference emissivity transformation of relative errors). In conclusion, this yields 1.9%, 5.8%, and 6.2% as revised synthetic estimate for the three surface windows, see Table VI.5 (p. 185). Even though the information content of the $1.10\ \mu\text{m}$ peak is comparable to that of the $1.18\ \mu\text{m}$ peak (Haus and Arnold, 2010, Fig. 5), the $1.10\ \mu\text{m}$ MST errors are probably so large, because this radiance peak is much smaller than the $1.18\ \mu\text{m}$ peak (Haus and Arnold, 2010, Fig. 21) and real measurement errors and simulation errors thus have a much larger impact there. Also note that errors in the straylight removal have the largest impact there. The remaining disagreements might be explained by impacts of calibration, preprocessing, measurement, and simulation errors, unconsidered interfering parameters, subsidiary retrieval solutions, or higher order terms and side effects from other assumptions in Appendix VI.A.2.2 (p. 194) that were used to justify the error adding and scaling rules that led to Table VI.3 (p. 178). Moreover, this table shows errors based on just a single reference spectrum. Kappel et al. (2015, Table 5) have shown that the errors for other reference spectra can be quite different. But in general, it seems plausible that the MST errors mainly originate from interfering parameters that vary with time. MSTs do not suggest time variations of the true surface emissivities of the target, but note that for some reason, the MST errors are slightly higher for the chronological second half of the utilized VIRTIS-M-IR data than for the first half (Table VI.4 (p. 181)). Maybe atmospheric motions were increased or the straylight situation was different.

The choice of smaller FWHMs for the topography blurring does not lead to as large impacts as could be expected. The renormalized emissivity errors determined by Kappel et al. (2015) due to topography uncertainties might be overestimated, therefore. Spatially small-scale topography errors average out due to the blurring. The 65 km- and the 30 km- differ from the 100 km-blurred topography of the bins by up to about 125 m and 250 m, respectively, with double root-mean-square-deviations of 70 m and 126 m. As mentioned, these differences can serve to study the effect of slight errors in the underlying Magellan topography just in the areas where the topography is spatially fastest varying and errors are most likely. They also illustrate

that the assumed uncertainty of the surface elevation of 200 m is not completely wrong. However, the statistical impact is rather connected to the double root-mean-square-deviations between the topography maps. The synthetic emissivity errors due to topography uncertainties should therefore be scaled from 9%, 12%, and 12% (Table VI.3 (p. 178)) for the three surface windows down to 6%, 8%, and 8%, based on the double root-mean-square-deviation between the 100 km- and the 30 km-blurred topography. But this can only partly explain the small SRMSDs in Table VI.4 (p. 181). The main reason is probably the renormalization, which itself depends on topography and naturally attenuates its influences, even for the PMTs 'Topo. 65 km R100' and 'Topo. 30 km R100'. Therefore, the synthetic error estimates in Table VI.5 (p. 185) exclude topography impacts, which are difficult to determine in view of the renormalization, and which are not present in the MST estimates anyway. However, they are included in the PMT error contributions as mentioned.

Apart from the PMT 'Init. emiss. 0.875' (unrenormalized emissivities are clearly cut off at the upper emissivity domain boundary 1 as noted), the largest SRMSDs occur for the PMTs, 'Continuum 1.74 μm ', 'H₂O', 'Surface haze', 'Unsmoothed straylight', and for topography uncertainties. Special care must be given to these parameters, in order to improve retrieval results.

Fig. VI.6 shows for the three surface windows the renormalized retrieved emissivities from the $N_r^0 = 64$ repetition case (see Fig. VI.3 (p. 176)) for the bin with center coordinates at 280.26 °E, 42.44 °S (located at Shiwanokia Corona). The error bars represent the double standard deviations summarized in Table VI.5 (p. 185).

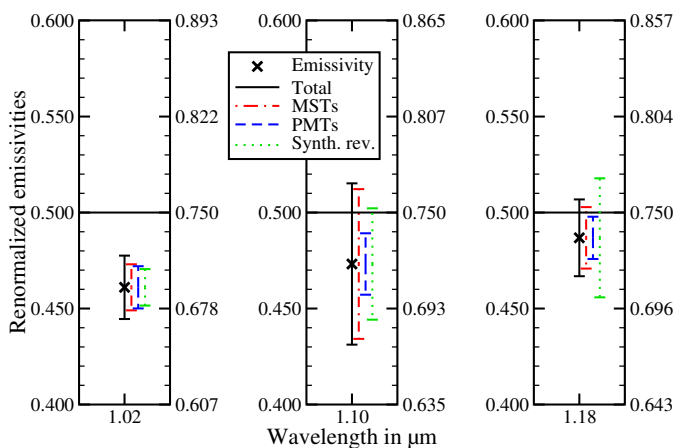


FIGURE VI.6: Renormalized emissivities from Fig. VI.3 (p. 176) at 280.26 °E, 42.44 °S for the 1.02, 1.10, and 1.18 μm windows (0.461, 0.473, and 0.487 referred to reference emissivity 0.500). The error bars (wavelength offsets for better representation) illustrate the double standard deviation errors listed in Table VI.5 (p. 185). Respective left axes: reference emissivity 0.500, right: 0.750.

Two cases for the reference emissivity are illustrated, 0.5 and 0.75. 'MSTs' corresponds to the maximum value of the three MST rows in this table. 'Total' is now the valid estimate of the multi-spectrum retrieval errors at $N_r^0 = 64$ measurement repetitions and is the quadratic sum of 'MSTs' and 'PMTs' in the figure. For the represented surface bin, the deviation of the renormalized emissivity at 1.02 μm from the reference emissivity is statistically significant (double standard deviation) according to both 'Total' and synthetic error measures. At 1.10 and 1.18 μm , neither of both errors indicates a significant deviation. From now on, only the 'Total' errors will be used. Recall that the shown emissivities are not absolute emissivities. Rather, they represent deviations from the reference emissivity and are only valid as absolute emissivities when the reference emissivity coincides with the true emissivity mean of the target area. A true emissivity mean different from the reference emissivity requires a transformation as discussed. This figure illustrates that these deviations can be statistically double-standard-deviation-significant or not. However, true emissivities may exhibit real trends with topography or latitude, which are not reflected by renormalized retrieved emissivities. According to the 'Total' errors, only bins where the renormalized emissivity deviations from the spatial mean value 0.5 exceed 0.017, 0.042, and 0.020, respectively, for the three surface windows, have significant emissivity anomalies. Referred to the 1.02 μm -map in Fig. VI.3 (p. 176), this is the case for areas with deviations from green that are at least orange or light blue. For 1.10 μm , only white and black are significant, and for 1.18 μm red and blue. These color criteria still apply, when the reference emissivity is changed and the color bar is accordingly

transformed as discussed in Section VI.4.5 (p. 184) (compare also the two reference emissivity cases illustrated in Fig. VI.6). When the demand on the statistical significance is relaxed to one standard deviation, the criteria change correspondingly.

Based on the MST and PMT results, it is possible to roughly extrapolate the expectable renormalized emissivity errors referred to the reference emissivity 0.5 for larger N_r . About 400 repetitions would be needed for MST errors at 1.02 μm to fall below 1%, in which case the errors for the other windows would amount to 3.1% and 1.3%, respectively. At $N_r = 1000$, MST errors would read 0.6%, 2.0%, and 0.8%, and it would take about 4000 repetitions for the errors in all surface windows to fall below 1% (0.3%, 0.99%, 0.4%). PMT errors, on the other hand, hardly decrease with increasing N_r . Even at 10000 repetitions, they would still amount to 2.1%, 2.6%, and 2.2%. This is because many PMT errors do not scale with $1/\sqrt{N_r}$, since the parameter modifications are constant with time. However, the extrapolation from $N_r = 25$ to such large repetition numbers is certainly not valid. In addition, the resources needed for MSR retrieval would be enormous, and VIRTIS-M-IR did not acquire so many usable measurement repetitions for any target on Venus.

On the other hand, spatial variations of surface emissivity of 20% that would correspond to the difference between unweathered granitic and basaltic rocks (Hashimoto and Sugita, 2003) would be easily detectable already at $N_r = 8$ in case of the 1.02 μm window. The present work suggests that such large variations do not occur in the studied target area, but note that contrasts for weathered material might be smaller, see discussions by Haus and Arnold (2010) and Arnold et al. (2012c).

Present results show relevant variations that indicate the heterogeneity of Venus' surface emissivity. High emissivity signatures correlate with edifices like Abeona Mons and other volcanic structures. Shivanokia Corona has areas of lower emissivity. The complexity in this region might suggest long histories and an apparently older corona (Stofan and Smrekar, 1998). In general, these anomalies can be caused by local changes in composition, age, and/or textural differences of the surface (Arnold et al., 2015). Compared to the thermal flux data at 1.02 μm obtained by Müller et al. (2008), the new relative emissivity maps at 1.02, 1.10, and 1.18 μm enable a more direct and more quantitative interpretation. Moreover, the removal of topographic, atmospheric, and other interferences is improved. Thus, the new maps will allow for a more precise disentanglement of the different sources causing the observed surface emissivity variations. A detailed geologic discussion of these results is under preparation for a follow-up publication.

VI.6 Summary and conclusion

Maps of surface emissivity data at 1.02, 1.10, and 1.18 μm are determined from VIRTIS-M-IR/VEX measurements of Venus' nightside emissions. The surface target at Themis Regio is located between 35 and 47 °S and 270 and 288 °E. The usable measurements most suitable for emissivity retrieval are selected (high signal-to-noise ratio, thin to moderate cloud cover, few straylight, etc.). The radiance spectra are carefully calibrated and preprocessed (Kappel et al., 2012b). A full radiative transfer forward model with special consideration of the extreme environmental conditions in Venus' deep atmosphere is used for the simulation of radiance spectra, taking into account thermal emissions by surface and atmosphere, and absorption and multiple scattering by gases and clouds (Haus and Arnold, 2010). Since spectral information content is limited, there are always parameters that cannot be uniquely derived from the measured spectra. They are set to reasonable values that allow for the generation of realistic synthetic spectra. When these assumptions deviate from the true physical values, this may cause surface emissivity retrieval errors, even though the fits well match the measured spectra. To improve this, a multi-spectrum retrieval algorithm (MSR, Kappel, 2014) is applied to the measured spectra. MSR can retrieve parameters that are common to a set of spectra and takes into account expected mean values, standard deviations, and correlation lengths and times as Bayesian *a priori* information for the retrieval parameters, along with measurement and simulation error information. This decreases the probability of retrieving unreasonable values and spatial-temporal distributions of the parameters, allows for taking the context of adjacent measurements into account, and thus enhances the reliability of the retrieved results. All considered measurements can be parameterized by a fully consistent set of atmospheric, surface, and instrumental parameters. Assuming geologic activity as would be observable by VIRTIS-M-IR to be negligible, the emissivity map of a surface target can be retrieved at each surface window as a parameter vector that is common to spectrally resolved VIRTIS-M-IR images that cover this target N_r times.

In spite of MSR's advantages, absolute emissivity values are difficult to obtain, and an emissivity map has to be retrieved by first setting a certain fixed initial emissivity value and retrieving the map relative to this value. However, the mean value of the retrieved emissivity map does not necessarily coincide with the initial emissivity due to technical reasons. Moreover, the retrieved map can exhibit approximately linear trends with latitude and topography that are likely due to imperfect forward model properties. When these trends are removed for a sufficiently small target by multiple linear regression, it can be observed that the magnitude of the resulting spatial emissivity fluctuations around their mean value increases with increasing mean value. This is because the radiance response to small emissivity perturbations around an emissivity base value decreases for increasing emissivity base value. The fluctuations are small compared to the emissivity mean. To still obtain a well-defined quantitative emissivity map, a linear transformation is applied that converts the map to have an emissivity mean value that attains a fixed reference emissivity, here 0.5. The accordingly changed fluctuation amplitudes are then directly comparable to those of other maps that are referred to the same reference emissivity. The process of retrieving the map relative to an initial emissivity, removing the trends with latitude and topography, and transforming the map to the reference emissivity is called renormalized retrieval, and the result is the renormalized emissivity map. The results can be later transformed to other reference emissivities if needed. This is particularly useful, since the true emissivity mean value of the target is not known and cannot be determined from the VIRTIS-M-IR spectra with current techniques, and geologic interpretations may have to take the magnitude of the fluctuations into account. If the absolute emissivity at a given bin of the target were known, for instance in the form of ground truth data, the absolute emissivity map of the entire target could be computed according to the mentioned transformation, even if the emissivity of the given bin were not the mean emissivity of the target.

An appendix explains the mathematical background of error origination and renormalization and justifies approximate error adding and scaling rules. [Kappel et al. \(2015\)](#) have estimated renormalized emissivity errors based on synthetic spectra. Independently from that, the present work estimates errors based on a statistical evaluation of retrieval results derived from real measurements and compares results from both analyses.

The maps are retrieved and renormalized from a data set with $N_r^0 = 64$ measurement repetitions, which is close to the maximum of the available usable data. Measurement Selection Tests (MSTs) retrieve renormalized emissivity maps from different disjoint selections of spectra with $N_r \in \{8, 16, 32\}$. Double standard deviation error estimates for N_r^0 are derived from these results and amount to 2.4%, 7.8%, and 3.2% for the three surface windows, respectively. This is compared to the synthetic error analysis, but a new evaluation is performed that better matches the conditions of the present work and predicts synthetic errors of 1.9%, 5.8%, and 6.2%. This is compatible with the hypothesis that MST errors are mainly caused by unconsidered time variations of interfering atmospheric parameters. Disagreements might be explained by impacts of calibration, preprocessing, measurement, and simulation errors, unconsidered interfering parameters, subsidiary retrieval solutions, higher order terms and side effects from other assumptions that were used to justify the error adding and scaling rules, and the dependence of the synthetic errors on their reference spectrum. MSTs do not suggest time variations of the true surface emissivities of the target.

Parameter Modification Tests (PMTs) at $N_r = 25$ verify that renormalized emissivity maps are reasonably independent of the choice of the initial emissivity, of modifications to interfering atmospheric, surface, and instrumental parameters, and of some details of the retrieval pipeline and data calibration and preprocessing. Scaled PMT results are used to further quantify the retrieval errors for the N_r^0 -maps. The PMT errors that are taken to contribute to the total renormalized emissivity errors at 64 repetitions amount to 2.2%, 3.2%, and 2.2%, respectively, for the three surface windows. The combined scaled MST and PMT results estimate total double standard deviation errors for the three surface windows of 3.3%, 8.4%, and 4.0%. The results of the MSTs and PMTs suggest that no further modifications to the present approach of the renormalized retrieval are required to obtain reasonably reliable emissivity data maps. MSTs and PMTs also verify that the error scaling rules approximately apply, and that emissivity errors due to unconsidered time dependent latitudinal trends or offsets of underlying atmospheric parameters are effectively removed by the renormalization. The synthetic errors (9%, 12%, 12%) determined by [Kappel et al. \(2015\)](#) due to topography uncertainties are probably overestimated, and the PMTs show that they are more likely below 2%. On the one hand, the assumed 200 m uncertainty was chosen too high. Effects from spatially small-scale topography errors largely average out due to atmospheric blurring on the scale of 100 km. On the other hand, the renormalization itself depends on topography and naturally attenuates its influences. The PMTs demonstrate that the initial emissivity must

be chosen far from 0 and 1, because otherwise, unrenormalized emissivities can be cut off at these emissivity domain boundaries. Significant error sources (1%–2% for at least one surface window) are uncertainties in the 1.74 μm CO_2 continuum absorption, H_2O abundance, topography, and in the removal of straylight. Special care must be given to these parameters for optimal retrieval results.

Significant errors can also be produced by an additional absorber close to the surface (surface haze) that could explain certain (unrenormalized) emissivity trends with surface elevation in interplay with unconsidered latitudinal trends of the deep atmospheric temperature field, the utilized continua, and latitudinal trends of time-averaged atmospheric parameters. Although actual trends with surface elevation (due to trends in the distribution of dust, surface composition, or weathering) may exist, they seem to be unrealistic. It is reasonable, therefore, to regard the trends in the retrieved emissivities, in particular if they should turn out as a global phenomenon that occurs regardless of geologic context, as artifacts due to imperfect or unconsidered forward model parameters, and to remove them by the renormalization. The planned analysis of further surface targets can help to find the correct procedure. Until then, the renormalized emissivities must be interpreted as spatial variations relative to the reference emissivity. However, possible real trends of the true emissivities with topography or latitude cannot be reflected by renormalized retrieved emissivities. Nevertheless, the latter have a well-defined quantitative meaning and represent an important step toward the retrieval of absolute emissivities. Future analyses will aim at the systematic avoidance of trends with latitude and topography and of deviations between the mean of the raw retrieved emissivity map and the initial emissivity from the outset by a suitable regularization of the retrieval, such that trends in the interfering atmospheric parameters and surface haze can be retrieved as parameters common to many diverse spectra with a wide latitude and topography coverage. Then it may be feasible to estimate absolute emissivity maps by looking for the initial emissivity that leads to the smallest residuals between measured and simulated spectra, which is currently not possible due to the trends with latitude and topography in the raw retrieved maps.

Fig. VI.3 (p. 176) depicts the renormalized emissivity maps determined from 64 measurement repetitions. At 1.02 μm , areas with deviations from green that are at least orange or light blue differ statistically significantly (double standard deviation) from the mean of the target area. For 1.10 μm , only white and black are significant, and for 1.18 μm red and blue. Referred to the reference emissivity 0.5, emissivity deviations from the mean of the target of up to 8.1%, 8.4%, and 7.6% are detected at 1.02, 1.10, and 1.18 μm , respectively. When statistically significant emissivity anomalies are defined as deviations exceeding the determined double standard deviation error levels at present $N_r = 64$ -sensitivity (3.3%, 8.4%, 4.0%), anomalies were found at both 1.02 and 1.18 μm . Anomalies $\geq 9\%$ can be ruled out at 1.10 μm . With single standard deviation significance, all three maps show interesting spatial emissivity variations. The retrieval errors of the determined relative emissivity maps are sufficiently small to allow geologic interpretation. A detailed geologic discussion of the results is under preparation for a follow-up publication.

Spatial variations of surface emissivity of 20% that would correspond to the difference between unweathered granitic and basaltic rocks would be easily detectable already at $N_r = 8$ in case of the 1.02 μm window. The present work suggests that such large variations do not occur in the studied target area, but note that contrasts for weathered material might be smaller. According to present results, about 400 repetitions would be needed for MST errors at 1.02 μm to fall below 1%. For all surface windows this would happen only at 4000 repetitions. The combined PMT errors only slightly improve with increasing N_r .

VI.A Appendix - Supplementary material¹

The spectrally resolved VIRTIS-M-IR images utilized for this work are listed in Appendix VI.A.1. Appendix VI.A.2 presents the mathematical background of the renormalization. Detector-related trends of the VIRTIS-M-IR spectral registration retrieved from the measurements themselves are reported in Appendix VI.A.3 (p. 199). Appendix VI.A.4 (p. 200) shows figures that illustrate at 1.10 and 1.18 μm the post-processing of the retrieved maps and the MSTs and PMTs, complementing the corresponding figures at 1.02 μm given in the main text.

VI.A.1 Utilized data cubes

This appendix lists the VIRTIS-M-IR spectrally resolved images ('data cubes') utilized for this work. Each Venus Express orbit corresponds to 24 (Earth-)hours (when VIRTIS-M-IR still acquired data). VIRTIS-M-IR data from each orbit are divided into a number of sessions, depending on the science objectives. For each VIRTIS-M-IR cube name, the number preceding the underscore denotes the orbit number, the number succeeding the underscore denotes the session. Each cube comprises a spectrally resolved (432 spectral bands uniformly dividing the approximate range 1.02–5.1 μm) two-dimensional spatial image (here only cubes used with 256 spatial samples and a number of spatial lines). The following 103 cubes contribute to the $N_r^0 = 64$ repetition data set. Note that the single cubes only partially cover the target area, and more than 64 cubes are needed, therefore, to achieve 64 repetitions for each surface bin.

108_00, 112_01, 121_01, 228_01, 229_01, 331_03, 331_04, 331_05, 332_01, 332_02, 332_03, 332_04, 332_05, 333_00, 333_01, 333_02, 333_03, 333_04, 333_05, 334_01, 342_00, 343_00, 344_00, 344_01, 344_02, 345_00, 345_01, 345_03, 347_00, 347_01, 347_03, 347_05, 349_01, 349_05, 351_01, 351_05, 359_02, 365_02, 365_05, 366_00, 366_01, 366_03, 366_04, 366_06, 366_07, 367_02, 367_05, 368_00, 368_01, 368_03, 368_04, 565_05, 565_07, 565_09, 565_11, 567_05, 567_07, 567_09, 567_11, 567_13, 569_05, 569_07, 569_09, 569_11, 569_13, 569_15, 571_05, 571_07, 571_09, 571_11, 571_13, 574_03, 577_06, 579_06, 579_08, 586_01, 586_04, 588_01, 588_04, 594_01, 594_04, 594_05, 594_08, 596_05, 598_05, 599_01, 599_02, 599_05, 601_01, 601_02, 601_05, 603_02, 603_05, 607_07, 609_05, 609_06, 812_02, 812_06, 818_02, 818_06, 818_10, 824_06, 834_06

For the MSTs, the first 51 cubes (ending with 368_04) from the N_r^0 data set list contribute to batch 1 of the $N_r = 32$ data set. The 50 cubes that contribute to batch 2 of the $N_r = 32$ data set comprise the cubes from the N_r^0 data set list starting with 565_05 but excluding the last three and including 812_10. The $N_r = 16$ and $N_r = 8$ data sets evenly and chronologically divide the repetitions from the N_r^0 data sets among their batches. The 45 cubes from the N_r^0 data set list starting with 331_03 and ending with 368_03 contribute to the $N_r = 25$ data set for the PMTs.

VI.A.2 Mathematical model

This appendix clarifies the role of the renormalization and how it affects the retrieval errors. It motivates the error scaling properties (so far only assumed, see Section VI.4.1 (p. 176) and Kappel et al., 2015) and the underlying mechanisms of error origination. Certain simplifications are formulated that enable these discussions. Suitable comparison measures for results from different batches of the MSTs and for scenarios of the PMTs are defined.

VI.A.2.1 Renormalization and variance

First of all, the removal of emissivity trends with latitude and topography (i.e. the 'de-trending') is introduced in terms of a linear operator. For this purpose, the raw retrieved emissivities from a given scenario and at a given wavelength index (that are momentarily not indicated here for simpler notation) are sorted into a column vector \mathbf{e}_M with entries $e_M(b)$, where $b \in \{1, \dots, B\}$ indicates the surface bin and the subscript M the emissivity mean value, $M = \sum_{b=1}^B e_M(b)/B$. The multiple linear regression model of \mathbf{e}_M with respect to latitudes $\theta(b)$ (compiled into the vector $\boldsymbol{\theta}$) and surface elevations $\mathbf{h}(b)$ (forming the vector \mathbf{h}) can be written

¹This appendix was published online-only as supplementary material to this paper.

$\mathbf{e}_M = \beta^1 + \beta^2 \boldsymbol{\theta} + \beta^3 \mathbf{h} + \boldsymbol{\varepsilon}$, where $\boldsymbol{\varepsilon}$ is the vector of the residuals $\varepsilon(b)$ from the regression. The $\varepsilon(b)$ are later regarded as deviations of the de-trended emissivities from their emissivity mean value M , provided β^1 is such that $\sum_{b=1}^B \varepsilon(b) = 0$. Using the matrix $\mathbf{X} := (\mathbf{1}, \boldsymbol{\theta}, \mathbf{h})$ and the vector $\boldsymbol{\beta} := (\beta^1, \beta^2, \beta^3)^T$, this can be arranged into the equation $\mathbf{e}_M = \mathbf{X}\boldsymbol{\beta} + \boldsymbol{\varepsilon}$, where $\mathbf{1}$ is the B -dimensional column vector with all entries 1. The regression coefficients (β^1 is the intercept) can be found by minimizing the residual sum of squares $\boldsymbol{\varepsilon}^T \boldsymbol{\varepsilon} = (\mathbf{e}_M - \mathbf{X}\boldsymbol{\beta})^T (\mathbf{e}_M - \mathbf{X}\boldsymbol{\beta})$. The best estimate of $\boldsymbol{\beta}$ reads $\hat{\boldsymbol{\beta}} = (\mathbf{X}^T \mathbf{X})^{-1} \mathbf{X}^T \mathbf{e}_M$, which follows from zeroing the derivative of $\boldsymbol{\varepsilon}^T \boldsymbol{\varepsilon}$ with respect to $\boldsymbol{\beta}$. This gives rise to the 'residual matrix' $\mathbf{R} := \mathbf{1} - \mathbf{X}(\mathbf{X}^T \mathbf{X})^{-1} \mathbf{X}^T$ that allows for the computation of the residual of the regression $\hat{\boldsymbol{\varepsilon}} := \mathbf{e}_M - \mathbf{X}\hat{\boldsymbol{\beta}} = \mathbf{R}\mathbf{e}_M$, a vector with entries $\hat{\varepsilon}(b)$. It can be immediately verified that the linear operator \mathbf{R} is an orthogonal projector, i.e. $\mathbf{R}^2 = \mathbf{R}$ and $\mathbf{R}^T = \mathbf{R}$, and that $\mathbf{R}\mathbf{X} = \mathbf{0}$. See also Hogben (2006, Section 52.4) for a summary of multiple linear regression using the residual matrix. It now follows that $\mathbf{X}^T \hat{\boldsymbol{\varepsilon}} = \mathbf{X}^T \mathbf{R}\mathbf{e}_M = (\mathbf{R}\mathbf{X})^T \mathbf{e}_M = \mathbf{0}$, which implies $\sum_{b=1}^B \hat{\varepsilon}(b) = 0$ (since first entry of vector $\mathbf{X}^T \hat{\boldsymbol{\varepsilon}}$ equals zero), and thus that the mean value of the residuals $\hat{\varepsilon}(b)$ over the bins is zero. The de-trended emissivities are therefore written as $\mathbf{r}_M(b) = (\mathbf{R}\mathbf{e}_M)(b) + M$, or short $\mathbf{R}\mathbf{e}_M(b) + M$. \mathbf{r}_M has the mean value M (as indicated by the subscript) and does not exhibit a trend with latitude and topography anymore. A de-trending of \mathbf{r}_M yields \mathbf{r}_M again, since \mathbf{R} is a projector. Note that de-trending does not introduce topography features for constant raw emissivity maps. Moreover, raw emissivity maps that are perfectly correlated with topography do not exhibit topography features after de-trending, since $\mathbf{R}\mathbf{X} = \mathbf{0}$.

As it was discussed in Section VI.2.3 (p. 169) and quantified in Section VI.4.5 (p. 184), the de-trended emissivities spatially fluctuate around their mean value M with a higher amplitude for cases with higher M . A linear transformation was given that refers a de-trended map \mathbf{r}_M to another, defined mean value called 'reference emissivity' e_{ref} , here mostly 0.5. In the appendix, this linear transformation shall be defined also for not de-trended maps \mathbf{e}_M . In the notation of Section VI.4.5 (p. 184), it can then be written $\mathbf{e}_{e_{\text{ref}}} = \lambda_{M \rightarrow e_{\text{ref}}} \cdot (\mathbf{e}_M - M) + e_{\text{ref}}$. Obviously, $\mathbf{e}_{e_{\text{ref}}}$ has the mean value e_{ref} . It is called the 'raw emissivity map referred to the reference emissivity e_{ref} '.

The de-trended emissivity map referred to e_{ref} can be written $\mathbf{r}_{e_{\text{ref}}} = \lambda_{M \rightarrow e_{\text{ref}}} \cdot (\mathbf{r}_M - M) + e_{\text{ref}}$. It has the mean value e_{ref} . Since \mathbf{R} is a projector, $\mathbf{r}_{e_{\text{ref}}}$ is indeed a de-trended map, because $\mathbf{R}\mathbf{r}_{e_{\text{ref}}} = \lambda_{M \rightarrow e_{\text{ref}}} \mathbf{R}\mathbf{r}_M = \lambda_{M \rightarrow e_{\text{ref}}} \mathbf{R}\mathbf{e}_M = \lambda_{M \rightarrow e_{\text{ref}}} (\mathbf{r}_M - M) = \mathbf{r}_{e_{\text{ref}}} - e_{\text{ref}}$. Moreover, de-trending and transforming to another reference emissivity can be interchanged, since $\mathbf{R}(\lambda_{M \rightarrow e_{\text{ref}}} (\mathbf{e}_M - M) + e_{\text{ref}}) + e_{\text{ref}} = \mathbf{r}_{e_{\text{ref}}}$. The vector $\mathbf{r}_{e_{\text{ref}}}$ is called the 'renormalized emissivity map referred to reference emissivity e_{ref} '. Note that an additional renormalization of renormalized emissivities has no effect. \mathbf{R} can act not only on emissivities but also on the parameters the emissivities depend on (it just acts by a matrix multiplication). To avoid an additional denotation, the results are also called 'renormalized' in the latter case, even if there is no referring to a reference emissivity involved.

In the following, e_{ref} is always 0.5, and all maps are referred to 0.5. The subscripts of $\mathbf{e}_{e_{\text{ref}}}$ and $\mathbf{r}_{e_{\text{ref}}}$ are dropped for convenience, such that $\mathbf{e}_{0.5} =: \mathbf{e}$ and $\mathbf{r}_{0.5} =: \mathbf{r}$, and a new subscript utilization can be employed. Now, the raw retrieved maps from retrieval scenario s (referred to the reference emissivity 0.5) are denoted by \mathbf{e}_s . The renormalized map reads $\mathbf{r}_s = \mathbf{R}\mathbf{e}_s + 0.5$, since de-trending and transforming to another reference emissivity can be interchanged. Each scenario is characterized by a selection of measurements that N_r times cover the specified surface target of B surface bins, the retrieval pipeline, assumptions on interfering forward model parameters, the choice of the initial emissivity, data calibration and preprocessing, etc. Note that \mathbf{R} does not depend on scenario s since \mathbf{X} does not. This neglects that the topography of a surface bin can slightly vary for the binned measurements as a result of motion blurring (Kappel et al., 2012b) and because it is a weighted average that respects the surface areas the unbinned measurements actually cover, which can differ for different measurement repetitions. This does not change results of the present discussion. It is also assumed that there are no uncertainties in latitude and topography of each bin, such that \mathbf{R} is the proper renormalization operator also for true emissivities. There are two cases ('Topo. 30/65 km²') where \mathbf{h} indeed differs to allow for the exploration of topography uncertainties. They are excluded here and evaluated separately.

Statistical properties of a random variable X are often described in terms of mean value μ and standard deviation σ . Given only these characteristics, the probability distribution on \mathbb{R} (the real numbers) that has the least information content (i.e. requires no further parameters for description) is a Gaussian. Usage of the standard deviation has some disadvantages. Most importantly, it is not additive for uncorrelated random

variables. This can be overcome by using the variance σ^2 for the characterization of a probability distribution. When μ and σ^2 are not known, they have to be estimated from S random samples x_s of the random variable X . Unbiased estimates of μ and σ^2 , respectively, are the sample mean value $\bar{x} := \sum_{s=1}^S x_s/S$ and the sample variance $\text{Var}^s[x_s] := \sum_{s=1}^S (x_s - \bar{x})^2/(S-1)$ (DeGroot and Schervish, 2012, Section 8.7). The denominator $S-1$ for $\text{Var}^s[x_s]$ is used instead of S , since the mean value is not known and has to be estimated itself. An estimate is unbiased when its statistical expectation value coincides with the true value, in this case when the averages of the \bar{x} and the $\text{Var}^s[x_s]$, respectively, computed from many repetitions with always S samples approach μ and σ^2 . Note that the sample standard deviation $\sqrt{\text{Var}^s[x_s]}$ is a biased estimate of σ (Shao, 2003, for a correction factor in case of Gaussians see Example 3.4). Therefore, only after averaging (over bins), variances are expressed as double standard deviations in percent of the reference emissivity, and then also scaled to $N_r = 64$ repetitions to enable direct comparison to results in Section VI.3 (p. 174). The variance of the sample mean \bar{x} is σ^2/S (DeGroot and Schervish, 2012, Theorem 6.2.3) and can be estimated by $\text{Var}^s[x_s]/S$. The standard deviation of $\text{Var}^s[x_s] - \sigma^2$ in case of Gaussians is $\sqrt{2/(S-1)}\sigma^2$ (DeGroot and Schervish, 2012, Eq. 8.7.8). When averaging over B repetitions of computing $\text{Var}^s[x_s]$ with different choices of samples (i.e. over B bins), the standard deviation of $(\sqrt{\langle \text{Var}^s[x_s] \rangle} - \sigma)(\sqrt{\langle \text{Var}^s[x_s] \rangle} + \sigma) \approx (\sqrt{\langle \text{Var}^s[x_s] \rangle} - \sigma) \cdot 2\sigma$ follows as $\sigma^2\sqrt{2}/\sqrt{BS-B}$, where the angular brackets denote the averaging over the B repetitions. The double standard deviation relative error for the estimate of σ by $\sqrt{\langle \text{Var}^s[x_s] \rangle}$ can thus be estimated as about $\Delta := \sqrt{2}/\sqrt{BS-B}$. Note that the inverse of the square root exists for $S \geq 2$. Finally, the variance of the sum of uncorrelated random variables is the sum of the variances (DeGroot and Schervish, 2012, Theorem 4.6.6), and $\text{Var}^s[\zeta x_s] = \zeta^2 \text{Var}^s[x_s]$ and $\text{Var}^s[x_s + a] = \text{Var}^s[x_s]$ for constants ζ and a .

VI.A.2.2 First order model

Recall that at a given surface window, the retrieved emissivity map \mathbf{e}_s of the target is referred to the reference emissivity 0.5. The true emissivity map $\hat{\mathbf{e}}$ is also to be understood as being referred to 0.5 (according to the mentioned transformation). To enable the following analysis of the error sources and the approximate statistical scaling properties, a number of simplifications are required. At bin b , $\mathbf{e}_s(b)$ is written in terms of deviations from the true emissivity $\hat{\mathbf{e}}(b)$ that originate in the failure to exactly know the true quantities that led to the radiances recorded by VIRTIS-M-IR. The 'hat' accent is used in the following to indicate those true quantities.

$$\mathbf{e}_s(b) \approx \hat{\mathbf{e}}(b) + \sum_{k=1}^{N_r} \sum_{p=1}^{P_t} \frac{\partial \hat{\mathbf{e}}(b)}{\partial \hat{\mathbf{t}}_{s,k}^p(b)} (\mathbf{t}_{s,k}^p(b) - \hat{\mathbf{t}}_{s,k}^p(b)) + \sum_{p=1}^{P_l} \frac{\partial \hat{\mathbf{e}}(b)}{\partial \hat{\mathbf{l}}^p(b)} (\mathbf{l}_s^p(b) - \hat{\mathbf{l}}^p(b)) + \sum_{p=1}^{P_c} \frac{\partial \hat{\mathbf{e}}(b)}{\partial \hat{\mathbf{c}}_s^p} (c_s^p - \hat{\mathbf{c}}^p) \quad (\text{VI.A.1})$$

The ' \approx ' shall indicate that only a first order model is used here, which also neglects the impacts of noise, subsidiary retrieval solutions, numerical repeatability under slightly altered conditions, etc. There are P_t parameters $\hat{\mathbf{t}}_{s,k}^p(b)$ like the cloud bottom altitude or H₂O abundance that can vary with time (and location), where k denotes, which value this parameter has at the k -th of the N_r repetitions that form scenario s . The P_l parameters $\hat{\mathbf{l}}^p(b)$ (e.g. parameterization of offset to true deep atmospheric temperature field) can only vary with location (and thus do not depend on k or s). The P_c parameters $\hat{\mathbf{c}}^p$ are spatially and temporally constant (e.g. continuum parameters, initial emissivity) and therefore do neither depend on bin b nor on k nor s . The corresponding parameters without 'hat' denote the values that are assumed during the forward model simulations. To allow for the exploration of responses to modifications of certain parameters in the frame of the PMTs, $\mathbf{l}_s^p(b)$ and c_s^p can also depend on s . The retrieved parameters except for the emissivities themselves are all assumed to attain their true values, such that only the interfering parameters are considered as error contributors in this first order model. Even though there exist spatial-temporal correlations between the true parameters, all statistical correlations whatsoever are assumed to be negligibly small for this appendix. The renormalized true t -parameters are assumed to be normally distributed around their renormalized assumed counterparts, with estimated variances (either with respect to location or to time) that can be approximated by their underlying (long-term) variances that are assumed to not depend on time, location, or retrieval scenario s . Furthermore, underlying variances over time at fixed location and variances over space at fixed time shall coincide with the underlying variance over time and location of the respective parameter. Finally, the partial derivatives $\partial \hat{\mathbf{e}}(b)/\partial \hat{\mathbf{t}}_{s,k}^p(b)$ etc. are approximated to not depend on the values the parameters attain and to

coincide with the simulated emissivity derivatives (without 'hat'). They are thus written as $1/N_r \cdot \partial e/\partial t^p$, $\partial e/\partial l^p$, and $\partial e/\partial c^p$, respectively. Note that modification of $\mathbf{t}_{s,k}^p(b)$ at just the k -th of the N_r repetitions only slightly affects $\mathbf{e}_s(b)$ (notice absence of index k compared to $\mathbf{t}_{s,k}^p(b)$) and ever less so with increasing N_r , whereas modification of temporally constant parameters concerns all N_r repetitions and has a larger effect on $\mathbf{e}_s(b)$ in the same magnitude as a single-spectrum derivative. This can be described by the factor $1/N_r$ in front of $\partial e/\partial t^p$. Then Eq. (VI.A.1) implies

$$\mathbf{R}\mathbf{e}_s(b) \approx \mathbf{R}\widehat{\mathbf{e}}(b) + \sum_{p=1}^{P_t} \frac{\partial e}{\partial t^p} \frac{1}{N_r} \sum_{k=1}^{N_r} \mathbf{R}(\mathbf{t}_{s,k}^p(b) - \widehat{\mathbf{t}}_{s,k}^p(b)). \quad (\text{VI.A.2})$$

The c -terms vanish, since \mathbf{R} applied to the b -independent c -parameters yields zero. The only true and assumed l -parameters considered for the present analysis (topography uncertainties have been excluded for now) are spatially slowly varying with latitude, and the spatial extension of the target has been chosen to allow for a good approximation of this variation by a function linear with latitude, compare $l0$ -parameters in Table VI.4 (p. 181). Hence, they are nearly annihilated by \mathbf{R} , and the l -terms are not considered furthermore.

The main objective of this appendix is a statistical characterization of $\mathbf{r}_s(b) - \widehat{\mathbf{r}}(b)$, the deviation of the renormalized retrieved emissivities $\mathbf{r}_s(b) = \mathbf{R}\mathbf{e}_s(b) + 0.5$ from renormalized true emissivities $\widehat{\mathbf{r}}(b) := \mathbf{R}\widehat{\mathbf{e}}(b) + 0.5$, i.e. the renormalized emissivity retrieval errors. The variance of $\mathbf{r}_s(b) - \widehat{\mathbf{r}}(b)$ over the bins is estimated by $\text{Var}_b[\mathbf{r}_s(b) - \widehat{\mathbf{r}}(b)] = \text{Var}_b[\mathbf{R}\mathbf{e}_s(b) - \mathbf{R}\widehat{\mathbf{e}}(b)] = \sum_{b=1}^B (\mathbf{R}\mathbf{e}_s(b) - \mathbf{R}\widehat{\mathbf{e}}(b))^2/B$, since the mean over the bins of $\mathbf{R}\mathbf{e}_s(b) - \mathbf{R}\widehat{\mathbf{e}}(b)$ is exactly zero and does not need to be estimated (therefore not $B - 1$ but B as denominator). Note that this corresponds to the square of $\text{RMSD}[\mathbf{r}_s, \widehat{\mathbf{r}}] := \sqrt{\sum_{b=1}^B (\mathbf{r}_s(b) - \widehat{\mathbf{r}}(b))^2/B}$, the root-mean-square-deviation (RMSD) between \mathbf{r}_s and $\widehat{\mathbf{r}}$. Then Eq. (VI.A.2) implies

$$\begin{aligned} \text{Var}_b[\mathbf{r}_s(b) - \widehat{\mathbf{r}}(b)] &\approx \text{Var}_b \left[\sum_{p=1}^{P_t} \frac{\partial e}{\partial t^p} \frac{1}{N_r} \sum_{k=1}^{N_r} \mathbf{R}(\mathbf{t}_{s,k}^p(b) - \widehat{\mathbf{t}}_{s,k}^p(b)) \right] \\ &\approx \sum_{p=1}^{P_t} \left(\frac{\partial e}{\partial t^p} \right)^2 \frac{1}{N_r^2} \sum_{k=1}^{N_r} \text{Var}_b[\mathbf{R}(\mathbf{t}_{s,k}^p(b) - \widehat{\mathbf{t}}_{s,k}^p(b))] \approx \frac{1}{N_r} \sum_{p=1}^{P_t} \left(\frac{\partial e}{\partial t^p} \right)^2 \text{Var}[\mathbf{R}(\mathbf{t}^p - \widehat{\mathbf{t}}^p)]. \end{aligned} \quad (\text{VI.A.3})$$

The second approximation is valid, because all statistical correlations between the parameters were assumed to be negligibly small. The last approximation applies, since $\text{Var}_b[\mathbf{R}(\mathbf{t}_{s,k}^p(b) - \widehat{\mathbf{t}}_{s,k}^p(b))] \approx \text{Var}[\mathbf{R}(\mathbf{t}^p - \widehat{\mathbf{t}}^p)]$, where Var in the last term indicates the underlying variance over time and location of the term in the square brackets. The latter was assumed to have variances that are independent of time and location, and variances over time and those over location were assumed to coincide with the variance over time and location.

Note that, according to Eq. (VI.A.3), modifications of assumed t -parameters by a constant offset or by a trend with latitude and topography do not change the renormalized emissivity errors in this simplified model, except for impacts of noise, subsidiary solutions, numerical repeatability under slightly altered conditions, etc., compare for instance $T0$ -parameters in Table VI.4 (p. 181).

VI.A.2.3 Measurement Selection Tests

Each MST utilizes of a series of S batches with indices $s \in \{1, \dots, S\}$ that all have the same N_r such that $SN_r = N_r^0 = 64$, which is the measurement repetition number of the data set used for the results in Section VI.3 (p. 174). The scatter of the renormalized emissivities $\mathbf{r}_s(b)$ over the different batches provides a measure of their uncertainty at N_r repetitions. In this section, this measure is determined and compared with results from Appendix VI.A.2.2.

Focusing on a single surface bin center b and unindicated wavelength index, the $\mathbf{r}_s(b)$ are distributed according to a certain underlying probability distribution, here assumed to be the normal distribution. Mean value $\mathbf{r}(b)$ (the underlying renormalized emissivity) and variance $\mathbf{V}(b)$ (the accuracy achievable for the renormalized emissivity derived from one batch with N_r repetitions) of the underlying Gaussian are not known and have to be estimated from the $\mathbf{r}_s(b)$. The latter can be regarded as (quasi-)random sample of size S of the underlying probability distribution. The sample mean is estimated as $\bar{\mathbf{r}}(b) := \sum_{s=1}^S \mathbf{r}_s(b)/S$, sample variance

as $\overline{\mathbf{V}}(b) := \text{Var}^s[\mathbf{r}_s(b)] = \sum_{s=1}^S (\mathbf{r}_s(b) - \overline{\mathbf{r}}(b))^2 / (S - 1)$. Note that it can be checked for the retrieved MST results that $\overline{\mathbf{V}}(b)$ does not significantly change with b .

The average value of $\mathbf{V}(b)$ is denoted as V . $\langle \overline{\mathbf{V}} \rangle := \sum_{b=1}^B \overline{\mathbf{V}}(b) / B$ is an (unbiased) estimate of V . Note that overlining of variables is associated with operations that involve batch indices s , whereas angular brackets involve bins b . $\langle \overline{\mathbf{V}} \rangle$ can be written

$$\langle \overline{\mathbf{V}} \rangle = \frac{1}{B} \sum_{b=1}^B \frac{1}{S-1} \sum_{s=1}^S (\mathbf{R}\mathbf{e}_s(b) - \mathbf{R}\overline{\mathbf{e}}(b))^2 = \frac{1}{S-1} \sum_{s=1}^S D_s^2, \quad (\text{VI.A.4})$$

where $\overline{\mathbf{e}}(b) = \sum_{s=1}^S \mathbf{e}_s(b) / S$, and $D_s := \text{RMSD}[\mathbf{r}_s, \overline{\mathbf{r}}] = \text{RMSD}[\mathbf{R}\mathbf{e}_s, \mathbf{R}\overline{\mathbf{e}}]$. This close link between $\langle \overline{\mathbf{V}} \rangle$ and the D_s suggests to use D_s to describe the dissimilarity of the renormalized emissivity maps \mathbf{r}_s determined from the different batches s (in particular when observing the structural similarity to the identity $\text{Var}_b[\mathbf{r}_s(b) - \widehat{\mathbf{r}}(b)] = (\text{RMSD}[\mathbf{r}_s, \widehat{\mathbf{r}}])^2$, see comment before Eq. (VI.A.3), that measures the renormalized retrieval errors in terms of a root-mean-square-deviation). Observation of the D_s can be used to explore the variability of the retrieval results with respect to data selection. For a selection of MSTs (with given N_r), the D_s for each s and the three wavelength indices are listed in Table VI.4 (p. 181) in the columns SRMSD ('scaled' RMSD) in a scaled form, $2D_s / \sqrt{S-1}$ in percent of the reference emissivity 0.5. With denominator \sqrt{S} instead of $\sqrt{S-1}$, they would in a reasonable sense be scaled to $N_r = 64$ repetitions as will be seen. But at this point it seems more natural to use denominator $\sqrt{S-1}$, because then, the scaled D_s need only be quadratically averaged to obtain $2\sqrt{\langle \overline{\mathbf{V}} \rangle} / \sqrt{S}$ in percent of the reference emissivity, a value that will be shown below to estimate the percental double standard deviation error of the $N_r^0 = 64$ -map. This scaling of D_s therefore enables a direct comparison to the other error measures in this work. Note that the denominator $\sqrt{S-1}$ relatively increases the SRMSDs with small S (i.e. large N_r) with respect to those with large S (small N_r) in Table VI.4 (p. 181).

According to Eq. (VI.A.2), $\langle \overline{\mathbf{V}} \rangle = \sum_{b=1}^B \text{Var}^s[\mathbf{R}\mathbf{e}_s(b)] / B$ can be approximated by

$$\begin{aligned} \langle \overline{\mathbf{V}} \rangle &\approx \frac{1}{B} \sum_{b=1}^B \text{Var}^s \left[\sum_{p=1}^{P_t} \frac{\partial e}{\partial t^p} \frac{1}{N_r} \sum_{k=1}^{N_r} \mathbf{R}(\mathbf{t}_{s,k}^p(b) - \widehat{\mathbf{t}}_{s,k}^p(b)) \right] \\ &\approx \frac{1}{B} \sum_{b=1}^B \sum_{p=1}^{P_t} \left(\frac{\partial e}{\partial t^p} \right)^2 \frac{1}{N_r^2} \sum_{k=1}^{N_r} \text{Var}^s[\mathbf{R}(\mathbf{t}_{s,k}^p(b) - \widehat{\mathbf{t}}_{s,k}^p(b))], \end{aligned}$$

because $\widehat{\mathbf{e}}(b)$ is independent of batch s and hence a constant with respect to variance estimation over s , and all statistical correlations between the parameters were assumed to be negligibly small. In the same way as for Eq. (VI.A.3), one has $\text{Var}^s[\mathbf{R}(\mathbf{t}_{s,k}^p(b) - \widehat{\mathbf{t}}_{s,k}^p(b))] \approx \text{Var}[\mathbf{R}(\mathbf{t}^p - \widehat{\mathbf{t}}^p)]$, which is independent of k and b . The averaging over bins can be omitted, therefore. Note that, to obtain a more stable statistics, this averaging is still performed when estimating $\langle \overline{\mathbf{V}} \rangle$ from the renormalized emissivity maps determined from the S batches. Finally, using Eq. (VI.A.3),

$$\langle \overline{\mathbf{V}} \rangle = \frac{1}{B} \sum_{b=1}^B \text{Var}^s[\mathbf{r}_s(b)] \approx \frac{1}{N_r} \sum_{p=1}^{P_t} \left(\frac{\partial e}{\partial t^p} \right)^2 \text{Var}[\mathbf{R}(\mathbf{t}^p - \widehat{\mathbf{t}}^p)] \approx \text{Var}_b[\mathbf{r}_{s_0}(b) - \widehat{\mathbf{r}}(b)], \quad (\text{VI.A.5})$$

which explicitly shows the independence of $\langle \overline{\mathbf{V}} \rangle$ from S (as it should be).

Hence, $\text{Var}_b[\mathbf{r}_{s_0}(b) - \widehat{\mathbf{r}}(b)]$, the measure for the renormalized emissivity retrieval errors (at a given wavelength index) for a certain retrieval scenario s_0 with N_r repetitions, can be approximately estimated by $\langle \overline{\mathbf{V}} \rangle = \sum_{b=1}^B \text{Var}^s[\mathbf{r}_s(b)] / B$, the measure for the scatter and thus the statistical uncertainty (with respect to data selection but otherwise under the same scenario) of the renormalized emissivities determined from single batches with N_r repetitions. This is not too surprising, given the various simplifications that led to this result. But it can serve to discuss a number of important properties.

The error estimation for the results from Section VI.3 (p. 174) at $N_r^0 = 64$ repetitions cannot be directly performed by computing $\langle \overline{\mathbf{V}} \rangle$ with $N_r = 64$, since the N_r^0 retrieval run cannot be repeated using one or even several additional disjoint data sets due to lacking coverage of the target area with usable measurements

as defined in Section VI.2.1 (p. 165). But the error scaling properties with N_r should be compatible with Eq. (VI.A.5). This can be used to estimate the N_r^0 -error with an MST by dividing the N_r^0 data set into S disjoint sets (batches) that always cover the target $N_r^0/S = N_r^{\text{MST}}$ times and computing the corresponding $\langle \bar{V} \rangle$. Taking the $(\partial e / \partial t^p)^2 \text{Var}[\mathbf{R}(t^p - \hat{t}^p)]$ to be unchanged, the error for N_r^0 (one standard deviation) can then be extrapolated as $\sqrt{\langle \bar{V} \rangle} \cdot \sqrt{N_r^{\text{MST}}/N_r^0} = \sqrt{\langle \bar{V} \rangle} / \sqrt{S}$. Since the $\bar{V}(b)$ are averaged over $B = 219 \gg 1$ bins (Section VI.2.1 (p. 165)) before taking the square root, the standard deviation bias nearly vanishes even for $S = 2$. Note that the 'sample standard deviation of the mean' over all S batches, referred to $\bar{\mathbf{r}}(b)$, is an intuitive scatter error estimation for the N_r^0 -result at b , because it is a measure for the scatter error of the average value over all S batches of the renormalized emissivities. It reads $\sqrt{\bar{\mathbf{V}}(b)} / \sqrt{S}$, and the average over all bins (performed in terms of variances to avoid bias) results as $\sqrt{\langle \bar{V} \rangle} / \sqrt{S}$, which coincides with the extrapolated N_r^0 -error. To enable direct comparison to the other error measures in the present work, $\langle \bar{V} \rangle$ for an MST with N_r repetitions and S batches is represented in terms of double standard deviations referred to $N_r^0 = 64$ repetitions, $\delta^{N_r, S} := 2\sqrt{\langle \bar{V} \rangle} / \sqrt{S}$, in percent of the reference emissivity 0.5. This discussion also justifies the scaled form of the D_s from Eq. (VI.A.4) as $2D_s / \sqrt{S}$ in percent of the reference emissivity, but recall that the denominator $\sqrt{S-1}$ is used for representation in Table VI.4 (p. 181) to enable a more direct comparison to N_r^0 . For the present work, $\delta^{32,2}$, $\delta^{16,4}$, and $\delta^{8,8}$ are determined (see Table VI.5 (p. 185)), which will be used to estimate the uncertainty of the $N_r^0 = 64$ -maps shown in Fig. VI.3 (p. 176).

Retrospectively, Eq. (VI.A.5) also justifies the assumed multi-spectrum retrieval error scaling rules proposed by Kappel et al. (2015) (see Section VI.4.1 (p. 176) of the present work). Namely, of the considered parameters only t -parameters contribute in the first order to the double standard deviation renormalized emissivity retrieval errors, errors from different parameters are quadratically added (square root of sum of squares), and errors scale with $1/\sqrt{N_r}$ and correspond to single-spectrum retrieval errors for $N_r = 1$. It can now be clarified in which way the errors listed by these authors (determined from single-spectrum retrievals with synthetic spectra, summarized in Table VI.3 (p. 178) of the present work) are to be understood. They describe the spatially averaged scatter with respect to data selection and are only first order approximations under the condition of the various assumptions formulated in Appendix VI.A.2.2 (p. 194). The first order contribution from a single parameter at $N_r = 1$ to the double standard deviation renormalized emissivity error is the derivative of the emissivity with respect to this parameter, multiplied by the expected double standard deviation of the renormalized parameter variation. This is the same as the first order emissivity variation resulting from a parameter change corresponding to the double standard deviation of the parameter. This is exactly the way, how errors were estimated by Kappel et al. (2015). But note that some of the emissivity responses in that paper were already in the non-linear regime. The reasons for disagreements between errors listed there and in the present work lie in violations of the assumptions, in particular, the first order-assumption, the independence of the emissivity derivatives from the parameter values, insufficient assumptions on the expected ranges of the interfering parameters, the simplified correlation and variance properties, and the increased information content taken into account with multi-spectrum retrieval.

Eq. (VI.A.5) also states that any errors on the parameter assumptions that are annihilated by \mathbf{R} have no first order impact on the renormalized emissivity maps. In particular, the renormalized emissivity maps are not affected when the spatial distribution of the long-term average of an interfering parameter (e.g. cloud bottom altitude) exhibits a slowly varying latitudinal trend that is not reflected in the assumed parameter values used in the retrievals. A constant offset does also not change the renormalized emissivity maps under the assumptions stated in Appendix VI.A.2.2 (p. 194). In the same way, modifications to c -parameters (continua, initial emissivity) and latitudinal l -parameter trends (deep atmospheric temperature profile) have no impact. However, real-world responses to such parameter modifications are non-zero even for theoretically vanishing error contributions ($c0$ - and $l0$ -PMTs in Table VI.4 (p. 181); there are no $t0$ -parameters). This is due to higher order terms etc.

VI.A.2.4 Parameter Modification Tests

The PMTs serve to study the impact of modifications to a number of assumed parameters and to characteristics of retrieval pipeline, calibration, and preprocessing on the renormalized emissivity maps. To save resources, the maps are determined from only $N_r = 25$ repetitions, and results are scaled to $N_r^0 = 64$. The base map \mathbf{r}_0 , with respect to which the modified maps \mathbf{r}_P are compared, is determined from scenario ' $N_r = 25$ base'

and denoted by the index '0'. The index 'P' runs through the other different bold-typed shortcuts used in the PMT descriptions in Section VI.4.4 (p. 180).

In analogy to the definition of D_s from Eq. (VI.A.4) (p. 196), the dissimilarity of \mathbf{r}_P from \mathbf{r}_0 is measured as $D_{P,0} := \text{RMSD}[\mathbf{r}_P, \mathbf{r}_0] = \sqrt{\text{Var}_b[\mathbf{r}_P(b) - \mathbf{r}_0(b)]}$ (last equation in the same way as comment before Eq. (VI.A.3) (p. 195)). Using Eq. (VI.A.2) (p. 195), this leads to

$$(D_{P,0})^2 \approx \text{Var}_b \left[\frac{\partial e}{\partial t} \frac{1}{N_r} \sum_{k=1}^{N_r} \mathbf{R}(\mathbf{t}_{P,k}(b) - \mathbf{t}_{0,k}(b)) \right] \approx \frac{1}{N_r} \left(\frac{\partial e}{\partial t} \right)^2 \text{Var}[\mathbf{R}(\mathbf{t}_P - \mathbf{t}_0)], \quad (\text{VI.A.6})$$

because $\mathbf{R}\hat{\mathbf{e}}(b)$ and the true parameters do not differ between a PMT and the ' $N_r = 25$ base'-case. Since only one parameter is modified between each 'P'- and the '0'-case, the superscript ' P ' is omitted for the t -variables. (Again, none of the considered c - or l -parameters contributes, since their differences between the 'P'- and the '0'-case are annihilated by \mathbf{R} .) Regarding the second approximation, note that the considered assumed t -parameters are either 'under control', because they are set to constant values and have really the character of l - or c -parameters (like cloud parameters, minor gases). Or, the difference between the 'P'- and '0'-parameters statistically varies in the same way as for a true parameter (e.g. difference of residuals from different straylight removal procedures). Hence, the second approximation applies, in the former case trivially so, because the parameters are annihilated by \mathbf{R} , and in the second case for reasons analogous to those given for Eq. (VI.A.3) (p. 195).

Eq. (VI.A.6) states that any modifications to the parameter assumptions that are annihilated by \mathbf{R} have no impact on the renormalized emissivity maps. But corresponding real-world responses are non-zero even for theoretically vanishing error contributions ($c0$ - and $l0$ -PMTs in Table VI.4 (p. 181)). This is due to higher order terms and other assumptions that do not fully apply. For each PMT and the three wavelength indices, the $D_{P,0}$ are listed in Table VI.4 (p. 181) in the columns SRMSD in a scaled form, $D_{P,0} \cdot F$ in percent of the reference emissivity 0.5. The scaling factor F is set to $\sqrt{25/64}$ for t -parameters ('t' on the right in the 'Scenario'-column) and to 1 elsewhere. The former cases profit from an increase of N_r due to an averaging-out effect, because at fixed bin they statistically vary with time, see Eq. (VI.A.6), the latter not. This way, the $D_{P,0}$ are in a reasonable sense scaled to $N_r^0 = 64$ repetitions. Note that they are already without a factor of 2 comparable (see Eq. (VI.A.6) for t -parameters) to percental double standard deviation errors by way of the choice of their perturbations' magnitudes as expected double standard deviations, compare Kappel et al. (2015, Table 1).

Parameter modifications (in the way of the PMTs) to the N_r^0 -case itself lead to additional errors to the MST error estimate for the N_r^0 -map. This impact cannot be directly determined due to the huge computational resources this would require. To still obtain a rough estimate of this effect, the squared PMT errors $(D_{P,0})^2$ are scaled to N_r^0 repetitions (then denoted as $(D_{P',s_0})^2$) and added to the squared MST error estimate $\text{Var}_b[\mathbf{r}_{s_0}(b) - \hat{\mathbf{r}}(b)]$. This can be motivated by

$$\text{Var}_b[\mathbf{r}_{P'}(b) - \hat{\mathbf{r}}(b)] = \text{Var}_b[\mathbf{r}_{s_0}(b) - \hat{\mathbf{r}}(b) + \mathbf{r}_{P'}(b) - \mathbf{r}_{s_0}(b)] = \text{Var}_b[\mathbf{r}_{s_0}(b) - \hat{\mathbf{r}}(b)] + (D_{P',s_0})^2 + \xi, \quad (\text{VI.A.7})$$

with the covariance $\xi = 2 \text{Cov}_b[\mathbf{r}_{s_0}(b) - \hat{\mathbf{r}}(b), \mathbf{r}_{P'}(b) - \mathbf{r}_{s_0}(b)]$ (DeGroot and Schervish, 2012, Theorem 4.6.6). \mathbf{r}_{s_0} is the renormalized retrieved emissivity map for the N_r^0 -case and $\mathbf{r}_{P'}$ the result from a hypothetical PMT at N_r^0 repetitions. ξ is possibly not negligible, but it should be small compared to the other terms on the right hand side of Eq. (VI.A.7). Note that it is theoretically (according to Eq. (VI.A.6)) zero for the PMTs where the parameters are 'under control' as above, since the square of the covariance does not exceed the product of the variances of its two input variables (DeGroot and Schervish, 2012, Theorem 4.6.3). Some of the PMTs study the same parameter but in different ways (different initial emissivities, different deep atmospheric temperature field perturbations, etc.), other PMTs have been performed just for general interest (e.g. 'Surface haze', 'H₂SO₄ alt. gradient'). Thus, only the PMT errors indicated by '*' in the 'Scenario'-column of Table VI.4 (p. 181) are added to the MST error estimate, see Table VI.5 (p. 185).

VI.A.3 Wavelength of first spectral band and spectral FWHM

This section gives additional retrieval results that are less relevant for the conclusions of the present paper but are still interesting on their own. It is discussed in Section VI.2.4 (p. 172) that there are parameters describing the spectral registration that are not sufficiently predictable by the current calibration pipeline and that are crucial for emissivity retrieval. The wavelength λ_1^s of the first spectral band and the full-width-at-half-maximum $FWHM^s$ of the spectral instrumental response function have to be retrieved from the spectra themselves as additional parameters. They are found to vary with spatial sample on the detector and detector temperature. Note that the other, not detector-related, retrieved parameters (clouds, gases) cover only a small part of the global latitude–longitude or latitude–local-time space, respectively, and are therefore less representative of any potential global trends.

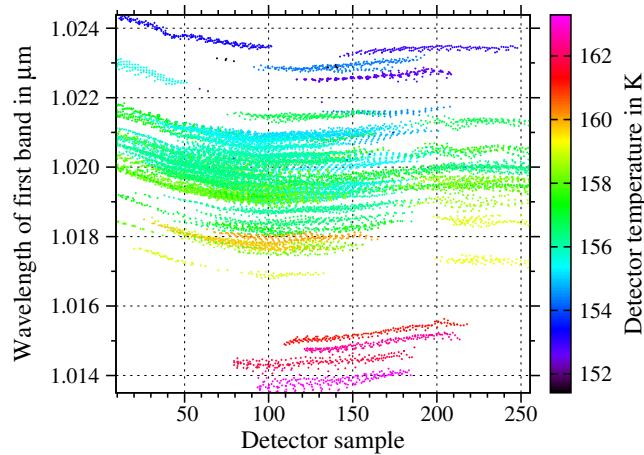


FIGURE VI.A.1: Dependence of wavelength λ_1^s of first spectral band on detector sample and temperature.

The scatterplot in Fig. VI.A.1 depicts this dependence for λ_1^s as retrieved from the ' $N_r^0 = 64$ ' data set comprising 14,016 spectra (after binning). Note that the detector sample in the figure is the average over the sample values of the VIRTIS-M-IR pixels contributing to the respective binned spectrum (see Section VI.2.1 (p. 165)). There is a trend of lower λ_1^s with higher detector temperature (order of 0.8 nm/K). This trend is not strict indicating secondary dependencies on further parameters. For a fixed VIRTIS-M-IR frame (and hence at fixed temperature), λ_1^s tends to drop by about 1 nm from sample 1 at the left edge of the detector to about sample 100 where a local minimum occurs. It then rises by about 0.5 nm over the next 100 samples and roughly stays at this level up to sample 256 at the right edge. At average temperatures, 1.020 μm is a representative value for λ_1^s at the detector center. Measurements at higher detector temperatures are better suited to sample the low-wavelength flank of the nightside surface window peak at 1.02 μm that is only partially covered by VIRTIS-M-IR.

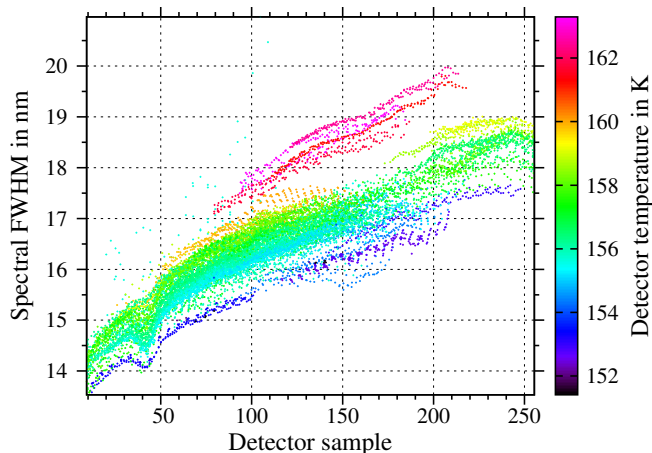


FIGURE VI.A.2: Dependence of spectral FWHM on detector sample and temperature.

Fig. VI.A.2 depicts the dependence of $FWHM^s$ as retrieved from the same measurement data set. This time, there is a (not strict) trend of higher $FWHM^s$ with higher detector temperature (order of 0.25 nm/K). For a fixed VIRTIS-M-IR frame, $FWHM^s$ tends to increase by about 4 nm from the left edge of the detector to the right edge. This increase is more pronounced for the 75 leftmost samples. At average temperatures, 17 nm is a representative value for $FWHM^s$ at the detector center. Measurements at lower detector temperatures and on the left part of the detector are better suited to resolve spectral features. Note that both λ_1^s and $FWHM^s$ are derived from the wavelength range 1.0–2.3 μm utilized for this work and may not be valid for the remaining VIRTIS-M-IR range up to 5.1 μm .

VI.A.4 Additional figures

This section presents figures analogous to Figs. VI.1 (p. 175) and VI.4 (p. 180) but for the 1.10 and 1.18 μm surface windows instead of the 1.02 μm window.

Fig. VI.A.3 illustrates the de-trending at 1.10 μm . The impact of the trend with topography is larger than at 1.02 μm . Also, the effect of the removal of the latitudinal trend is more pronounced than at 1.02 μm . In contrast, the trends at 1.18 μm are of a much smaller magnitude, see Fig. VI.A.4. Recall that the transformation to the reference emissivity 0.5 still has to be performed in order to obtain Figs. VI.3 (p. 176)b and c.

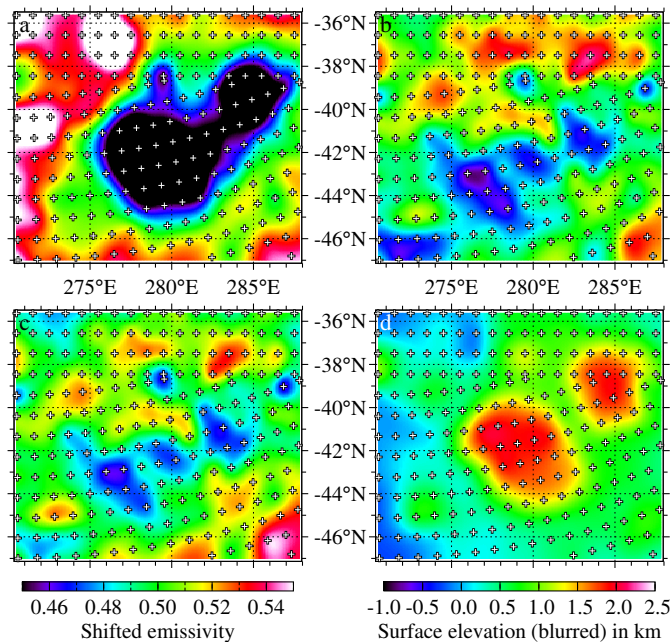


FIGURE VI.A.3: Removal of trends with topography and latitude for the 1.10 μm emissivity map of Themis Regio retrieved from the $N_r^0 = 64$ measurement repetition data set. (a) Raw map, (b) trend with topography removed, (c) trends with topography and latitude removed, (d) utilized surface elevation (blurred Magellan topography). Representation as in Fig. VI.1 (p. 175).

One of the main results of this work is the estimate for the reliability of the renormalized emissivity maps. It was found that the double standard deviation uncertainties for the 1.02, 1.10, and 1.18 μm maps derived from 64 measurement repetitions are given by 3.3%, 8.4%, 4.0%, respectively, of the reference emissivity 0.5. Fig. VI.A.5 illustrates that the 1.10 μm map is quite unreliable compared to the map at 1.02 μm . The PMT 'Continuum 1.74 μm ', which leads to almost the largest SRMSD contributing to the total error at 1.10 μm (see Table VI.4 (p. 181)), still yields quite similar patterns between Figs. VI.A.5c and d. However, the most direct and demonstrative test, the MST where maps are determined from two disjoint data sets, shows that the spatial patterns disagree between Figs. VI.A.5a and b. This measurement repeatability failure of the maps corresponds to the finding that no statistically significant emissivity anomaly is found at 1.10 μm at present $N_r = 64$ -sensitivity. In contrast, the MST illustrated in Fig. VI.A.6 (p. 202) shows a much better agreement between the fine-structures of the patterns, although the general appearances are not nearly as similar as for

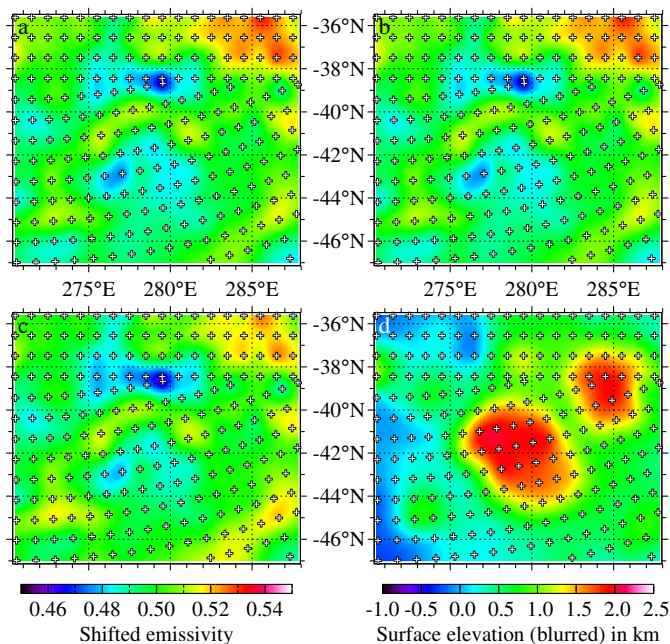


FIGURE VI.A.4: Removal of trends with topography and latitude for the $1.18\ \mu\text{m}$ emissivity map of Themis Regio retrieved from the $N_r^0 = 64$ measurement repetition data set. (a) Raw map, (b) trend with topography removed, (c) trends with topography and latitude removed, (d) utilized surface elevation (blurred Magellan topography). Representation as in Fig. VI.1 (p. 175).

the analogous maps at $1.02\ \mu\text{m}$. The PMT depicted in Figs. VI.A.6c and d contributes the largest SRMSD to the total error at $1.18\ \mu\text{m}$.

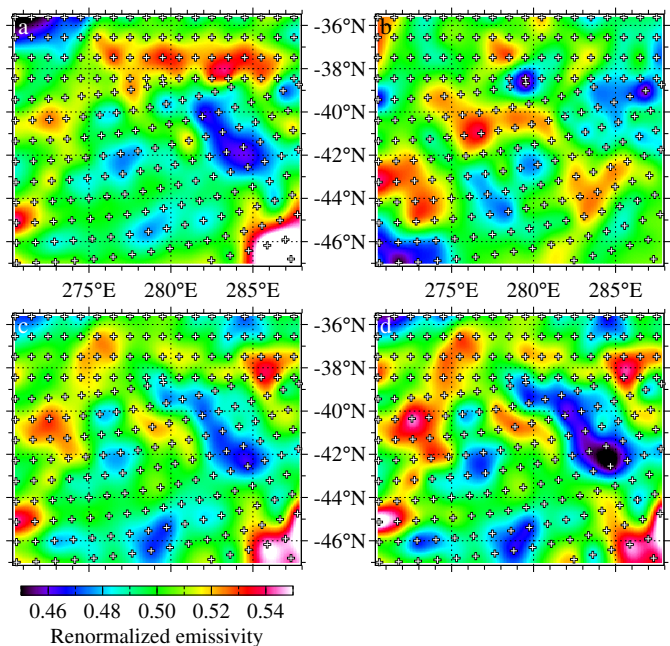


FIGURE VI.A.5: Examples for MSTs and PMTs showing renormalized $1.10\ \mu\text{m}$ emissivity maps of Themis Regio referred to reference emissivity 0.5. (a) MST ' $N_r = 32$, batch 1', (b) MST ' $N_r = 32$, batch 2', (c) PMT ' $N_r = 25$ base', (d) PMT 'Continuum $1.74\ \mu\text{m}$ '. Representation as in Fig. VI.4 (p. 180).

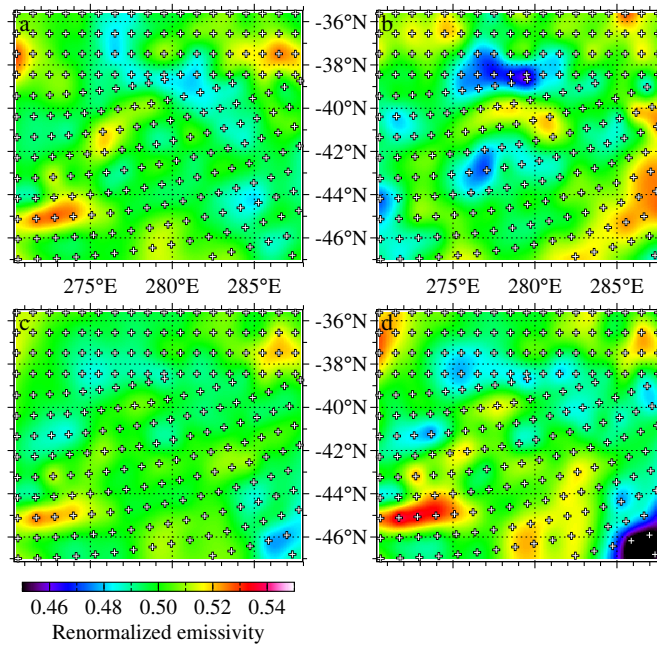


FIGURE VI.A.6: Examples for MSTs and PMTs showing renormalized $1.18\ \mu\text{m}$ emissivity maps of Themis Regio referred to reference emissivity 0.5. (a) MST ' $N_r = 32$, batch 1', (b) MST ' $N_r = 32$, batch 2', (c) PMT ' $N_r = 25$ base', (d) PMT 'Continuum $1.74\ \mu\text{m}$ '. Representation as in Fig. VI.4 (p. 180).

Acknowledgements

This work is funded by the German Aerospace Center e.V. (DLR e.V.). We acknowledge the work of the VIRTIS/VEX PIs Pierre Drossart (CNRS/LESIA, Paris) and Giuseppe Piccioni (INAF-IAPS, Rome), the VIRTIS/VEX team, and also the entire Venus Express team of ESA and Astrium, who made the measurement data available that were used in this study. The authors would like to thank the reviewers for their valuable suggestions to improve this paper.

Chapter VII

Discussion, summary, and outlook

VII.1 Discussion

The main goal of the present thesis was the derivation of IR surface emissivity data maps at the three accessible spectral transparency windows located at 1.02, 1.10, and 1.18 μm from Venus nightside radiance spectra acquired by VIRTIS-M-IR.

It was found that this task necessitated many different steps that mostly aimed at the best possible reliability of the derived data. The first step was the development of a radiative transfer simulation model that allowed the computation of a synthetic radiance spectrum for a given state of the atmosphere, surface, and measuring instrument (Chapter II (p. 25)). This model had to be very accurate in order to enable satisfying retrieval results. For this purpose, it had to take into account many relevant radiative processes that are experienced by photons before they are registered by the measuring instrument. This included the thermal emission of the photons by surface and atmosphere, the influence of phenomena such as multiple scattering and absorption by atmospheric gases and clouds and backreflection at the surface, the observation geometry, and finally the spectral registration by the instrument. This radiative transfer simulation was developed in close cooperation with Haus and Arnold (2010) and was thus partly based on previously existing know-how. Nevertheless, it was implemented by the present author from scratch to qualify him to understand the principles and the details of radiative transfer, to suitably optimize it, and to prepare it for Bayesian retrieval and the computation of analytic Jacobians. In fact, this collaborative effort led to mutual improvements in terms of both accuracy and efficiency. Section I.2.1 (p. 3) discussed major recent contributions to the field of radiative transfer in Venus' atmosphere. Along with the contents of Section II.2 (p. 27), the results and techniques described in these papers were taken into account as marked by respective citations. This radiative transfer simulation model represented one of the baselines of this thesis.

The other baseline was formed by the VIRTIS-M-IR measurements. Thus, the next step that was required to achieve the main goal of this work was a thorough analysis and subsequent preprocessing of the acquired radiation spectra (Chapter III (p. 67)). The VIRTIS-M-IR measurements were unique for this goal, and, although they were available in already very good quality, a number of calibration refinement steps were needed with regard to surface emissivity retrieval to ensure the best possible accuracy of the derived data. The spectra had to be preprocessed by a number of special algorithms to make them suitable for a direct utilization in the retrieval process. For use with the multi-spectrum retrieval algorithm MSR, the self-consistency of the measurements was one of the most important aspects that was achieved with these data preparations. It was not tested whether the calibration refinements and preprocessings are strictly required also for retrieval targets other than surface data, but since the surface information is encoded in the data as a mere second order effect, at least any derived surface data would probably be of a doubtful quality without these refinements. However, the detector responsivity adjustment at 1.0–1.3 μm (Section III.3.2.3 (p. 77)) led to smaller changes in the renormalized retrieved emissivity maps than might have been expected (compare Table VI.4 (p. 181), row 'Detector responsivity' showing the effect of halving the adjustment's magnitude). The reason is that, in contrast to the other calibration refinements and preprocessings, this adjustment affected all spectra in the same (self-consistent) way, and the renormalization largely removed resulting impacts. The retrieval of absolute emissivities, on the other hand, would have been much more affected, see for instance the renormalization

coefficients with respect to emissivity trends with surface elevation.

Both the refined measured spectra as well as the radiative transfer simulation program can be regarded to have state-of-the-art status, because on the one hand, the radiative transfer simulation algorithm takes into account all known processes that are relevant for the main goal of this work. On the other hand, it is possible to generate synthetic measurements that fit the refined measured VIRTIS-M-IR spectra in the spectral range 1.0–2.6 μm for a large variety of physical and observational conditions with a quality that, to the author's knowledge, could not be achieved before. This can be recognized by comparing the (representative) fits in Fig. II.24 (p. 66) or any other recent fit by the authors of the fourth paper with any fit to VIRTIS-M-IR spectra presented in the recent literature. Therefore, although residual calibration, preprocessing, and simulation errors can never be completely ruled out, calibration, preprocessing and functional descriptions of the simulated spectra are not expected to exhibit substantial errors. This gives good reason to believe that the derived surface data have the best quality that is possible when analyzing VIRTIS-M-IR measurements with current techniques.

Proceeding from these firm baselines, the next step was the development of a suitable retrieval algorithm. It was shown that single-spectrum retrieval algorithms fail to extract reliable surface information from VIRTIS-M-IR spectra (Chapter V (p. 135)). This is, for instance, the reason why the surface emissivities retrieved by Haus and Arnold (2010) at 1.02 μm cannot be regarded as sufficiently reliable for geologic interpretation. The multi-spectrum retrieval algorithm MSR was developed to overcome this problem (Chapter IV (p. 103); Kappel et al., 2010a,b, 2012b,c; Arnold et al., 2012a,b, 2013; Kappel, 2014; Kappel et al., 2015, 2016, announced by Haus and Arnold, 2010). Although certain forms of a multi-spectrum retrieval have been described in the literature (see Section I.2.4 (p. 8)), this was done with other aims and capabilities. To the best of the present author's knowledge, multi-spectrum retrieval has never been applied to Venus problems before. In addition, the capabilities of MSR are optimally suited for Venus problems, and none of the other multi-spectrum retrieval approaches, although certainly very successful in the respective fields they are intended for, would sufficiently satisfy the demands of the present work. In fact, most of the other approaches can be regarded as special cases of MSR from the point of view of the regularization capabilities as it was discussed in Section I.2.4 (p. 8). Even the sophisticated algorithm of Ungermann et al. (2010a,b, 2011) that seems to have been developed at about the same time as the early version of MSR has only one aspect by which MSR could be improved, the extremely large problem size that can be treated in the regularization. But this aspect is currently not relevant to the present work, because the treatable problem size is limited by the resource-intensive radiative transfer simulations in Venus' atmosphere rather than by the regularization, see discussion in Section I.2.4 (p. 8). In other respects, for instance concerning the suitability and the flexibility of the *a priori* covariance matrix based on the Kronecker product in the present work, the algorithm of Ungermann that has been developed for tomographic retrieval problems in Earth's atmosphere would have disadvantages when it would be applied instead of MSR to determine Venus surface emissivity maps. The development of MSR was therefore absolutely required for this thesis. In addition to the usual single-spectrum *a priori* information, that is, mean values and standard deviations of the retrieval parameters and correlations between them, MSR can take into account the context of adjacent measurements by incorporating *a priori* spatial-temporal correlations for the parameters of different spectra. Moreover, MSR is able to retrieve parameter vectors that are common to several measurements. Exploiting the Kronecker product structure of the *a priori* covariance matrix, this was shown in Appendix IV.A.3 (p. 129) to be equivalent to the retrieval of parameters with infinite *a priori* correlation length or time and spatially or temporally constant single-spectrum *a priori* data. The weighting between common and other parameters was shown to be exactly unity. Using MSR, the probability to retrieve unreasonable parameter values and spatial-temporal parameter distributions can be decreased. It was shown that MSR leads to more reliable results than single-spectrum retrieval algorithms do, in particular, when retrieving parameters with similar Jacobians and strongly differing correlation data, like cloud parameters, CO₂ opacity corrections, and surface emissivity maps. It is beneficial, therefore, to apply MSR to retrieve surface emissivity maps at the three accessible wavelengths as parameter vectors that are common to a set of spectrally resolved VIRTIS-M-IR images that cover the same surface target. From a mathematical point of view, MSR allows the parameterization of all considered measurements by a fully consistent set of atmospheric, surface, and instrumental parameters that respects all available *a priori* data as well as the measurement and simulation error distributions and that does not neglect the context between adjacent measurements. Note, however,

that the full consistency of the MSR retrieval parameter set is partially lost as a result of the renormalization post-processing described in Chapter VI (p. 161).

But even with MSR it turned out to be difficult to determine surface emissivity data. This was realized, when emissivity maps for the same target area derived from different sets of measurements had very different structures, i.e. the results were not repeatable. Note that such a repeatability test had not been performed in the papers by other authors that worked on Venus IR emissivity determination (see Section 1.2.2 (p. 4)). To understand this repeatability failure, a detailed multi-spectrum retrieval error analysis would have been useful, but it would have been very difficult to perform due to the high-dimensional and non-linear nature of the retrieval problem. To still uncover the causes that prevented the repeatability of the retrieval results and to avoid them if possible, a detailed retrieval error analysis based on single synthetic spectra was carried out (Chapter V (p. 135)). To estimate the corresponding multi-spectrum retrieval errors, the determined single-spectrum retrieval errors were scaled according to scaling rules that were justified in Appendix VI.A (p. 192) with a simple mathematical error origination model using a number of simplifications.

This error analysis revealed several different problems. The information content of a single VIRTIS-M-IR spectrum is limited, and not all parameters that are not sufficiently well known in advance and that are needed in the radiative transfer simulation can be determined from the measured spectrum itself. Such interfering parameters have to be set to defined reasonable values compatible with current knowledge on atmospheric and surface conditions and that allow the generation of realistic synthetic spectra. When the true parameter values deviate from these assumptions, this can lead to emissivity retrieval errors, even though the fit well matches the measurement. Based on different synthetic measurements typical for Venus' nightside and where the true parameters leading to these spectra are known by construction, this effect was explored and quantified according to a few characteristic error measures. Several retrieval pipelines were investigated, and the one that yielded the smallest error measures was selected for the subsequent studies and formed the basis of the MSR retrieval pipeline.

After also performing a retrieval error analysis using real measurements (Chapter VI (p. 161)) and a corresponding mathematical motivation (Appendix VI.A (p. 192)), it can be summarized that MSR emissivity retrieval errors mostly originate from differences between assumed and true underlying parameters, where these differences can be decomposed into a part (A) that has a spatially slowly (typical length scale 1000 km) varying time average, a part (B) that comprises the time dependent fluctuations around part (A), as well as a part (C) containing spatially fast (typical length scale 100 km) varying time independent interfering parameters.

The differences from part (A) mostly vary in latitudinal direction only, motivated by the symmetries and spatial scales of the global atmospheric circulation. This category also comprises the wavelength dependent CO₂ opacity that is constant in time and space, as well as the deep atmospheric temperature field that is (almost) constant in time and spatially slowly varying with latitude. The emissivity retrieval errors due to this part can be largely avoided by the renormalized MSR retrieval of the emissivity maps as it was described in Section VI.2.3 (p. 169). Here, corrections to the wavelength dependent CO₂ opacity are pre-determined with MSR as parameters that are common to many and diverse VIRTIS-M-IR measurements to minimize emissivity retrieval errors due to CO₂ opacity uncertainties. An initial emissivity value (in the present work 0.5) has to be defined for this purpose to complete the parameter set required to solve this retrieval problem without too strongly underconstraining it. Using the pre-determined opacity corrections, a surface emissivity map relative to the initial emissivity can be retrieved with MSR from a suitable measurement data set that repeatedly covers the actual surface target. The mean value of this map can differ from the initial emissivity, since the measurement data sets utilized to determine the opacity corrections and the map (and therefore the corresponding time averaged interfering true parameters) do not necessarily coincide. For the retrieval of the relative surface emissivity map, the opacity corrections in the surface windows are treated as fine-tuning parameters that are slightly modified to avoid that the emissivities come close to their domain boundaries 0 and 1. The relative emissivity maps exhibit approximately linear trends with latitude and topography that are unrealistic from a geologic point of view and are probably due to simulation errors. These trends are removed with the help of multiple linear regression without changing the emissivity mean of the map. Finally, it can be observed that the spatial fluctuations of the de-trended emissivities around their mean tend to increase in magnitude for increasing emissivity mean, because the radiance response to small emissivity perturbations

around an emissivity base value decreases for increasing emissivity base value. Since the emissivity mean of the de-trended map does not have a controlled value, different de-trended maps cannot be directly compared at this stage. An affinely linear transformation is applied that converts the de-trended emissivity map to have an emissivity mean value that coincides with a defined reference emissivity. The result of this procedure is called renormalized emissivity map, referred to the reference emissivity.

Errors due to part (B) statistically average out with $1/\sqrt{N_r}$, where N_r is the number of measurements covering a surface bin in the multi-spectrum retrieval. This was motivated in Appendix VI.A.2.3 (p. 195) and was demonstrated to apply using the measurement selection tests in Section VI.4.3 (p. 179). At a given surface window, part (C) contributes emissivity errors due to uncertainties of emissivities in the respective other surface windows and of the surface elevation. It was argued in Section V.2.3 (p. 142) that the interfering emissivities and other parameters better disentangle for higher N_r when using MSR. The impact of surface elevation uncertainties on renormalized emissivity maps was demonstrated to be moderate (see Section VI.4.4 (p. 180), Subsection 'Calibration and preprocessing').

Most emissivity retrieval errors can be avoided by the renormalized retrieval. The remaining errors can be mainly attributed to part (B) and part (C) contributions and to higher-order effects. In Chapter VI (p. 161), renormalized emissivity maps of a target in the Themis Regio were determined at 1.02, 1.10, and 1.18 μm , and corresponding emissivity errors were estimated by a statistical evaluation of maps derived from various disjoint selections of spectra and using different assumptions on the interfering parameters. The errors decrease when N_r is increased, and they were shown at $N_r = 64$ to be sufficiently small to allow the geologic interpretation of the determined maps. It was verified that the renormalized emissivity maps are largely (i.e. in the frame of the derived error levels) independent of the utilized measurement data set, of the initial emissivity, of modifications to interfering atmospheric, surface, and instrumental parameters, and of selected details of the retrieval pipeline and data calibration and preprocessing. The double standard deviation errors determined with the synthetic spectra (2%, 6%, and 6% at 1.02, 1.10, and 1.18 μm , respectively, referred to $N_r = 64$ and reference emissivity 0.5) and those based on real measurements (3%, 8%, 4%) are largely compatible. It is reasonable, therefore, to ascribe the 'real' errors mainly to causes revealed through the 'synthetic' error analysis. The 'real' errors are used to describe the error levels of the determined renormalized emissivity maps of Themis Regio.

Such a thorough emissivity retrieval error analysis has not yet been performed by other authors that worked on the determination of Venus surface emissivity data. Essentially only simple guesses or rough estimates had been given, if at all.

Since the spatial fluctuations of renormalized emissivity maps around their mean value, the reference emissivity, increase in magnitude for increasing reference emissivity, it is necessary to convert the renormalized maps according to a transformation quantified in Section VI.3 (p. 174), when the emissivity mean value of the map shall attain a given value, for instance a value dictated by possible future ground truth data. In the same way, if the absolute emissivity at a given bin of the target were known, the absolute emissivity map of the entire target could be computed according to the mentioned transformation, assuming absent true trends with latitude and topography. This effect has not yet been quantified before by other authors, but it cannot be neglected, and it may be important for a more quantitative geologic interpretation.

The largest deviations from the reference emissivity found in the renormalized Themis Regio maps amount to about 8% at either surface window. Emissivity anomalies (i.e. deviations exceeding the determined error level) were therefore found at 1.02 and 1.18 μm , whereas anomalies exceeding 8% (or 9%, to be on the safe side) can be ruled out at 1.10 μm . It was clarified in Section VI.3 (p. 174), how the emissivity errors transform when the reference emissivity is changed. It is important to note that an emissivity anomaly exceeding the determined error level still exceeds the error level when the reference emissivity is changed. In this sense, the occurrence of emissivity anomalies is well-defined (i.e. independent of the reference emissivity).

The renormalized emissivities are interpreted as spatial variations relative to the reference emissivity. They represent an important step toward the retrieval of absolute emissivities. However, true emissivities may exhibit, even if they are implausible from the current point of view, real trends with topography or latitude, which are not reflected by renormalized maps.

Section I.2.2 (p. 4) cited other authors that worked on the determination of Venus surface emissivity information in the infrared. Compared to these works, the present thesis constitutes the first time that surface

emissivity data were derived using full radiative transfer and a retrieval algorithm respecting *a priori* information, and where emissivity is treated as an intrinsic retrieval parameter, as it is discussed in the following.

The multivariate statistical analysis by [Erard et al. \(2009\)](#) as a purely descriptive method did not consider the radiative transfer in Venus' atmosphere. Moreover, only the topography related surface temperature effects could be isolated, no emissivity information. However, the authors also reported about indications of a high opacity layer close to the surface in the low lying regions of the planet. The occurrence of such a layer is one factor for a possible explanation for the existence of the emissivity trends with topography before renormalization, as it was discussed in Chapter VI (p. 161).

Surface emissivity data at 1.02 μm were derived by [Helbert et al. \(2008\)](#); [Müller et al. \(2008\)](#) using VIRTIS-M-IR measurements. Based on a semi-empirical approach, these authors determined a map of the time averaged thermal flux anomaly, i.e. the thermal flux from Venus' surface that is not due to topography related surface temperature, and which is correlated with surface emissivity. The 1.02 μm radiances were de-clouded with the small surface-unaffected 1.31 μm radiance peak as reference for cloud absorption. Many issues have been identified and solved in the four articles accumulated in the present thesis that are absolutely essential for the present work but not relevant to the semi-empirical approach. These issues revealed many important underlying mechanisms that explain, why some information can be extracted and other can not. In contrast to the work of [Helbert et al. \(2008\)](#); [Müller et al. \(2008\)](#), the present approach is based on a full radiative transfer simulation and a retrieval algorithm taking into account *a priori* data, considers the refined data calibration and preprocessing, and exploits the spectral information content in the range 1.0–2.3 μm excluding the 1.28 μm peak. The flux anomaly was determined only at 1.02 μm , and its meaning with respect to emissivity and its reliability are not entirely clear in the otherwise very successful approach by the cited authors. In the present thesis, emissivity data were determined at all three surface windows, their relation to absolute surface emissivities was precisely clarified, and their reliability was thoroughly quantified. However, the semi-empirical method includes only two spectral bands and is computationally very fast, which is why the authors were able to utilize all suitable VIRTIS-M-IR nightside spectra. As pointed out in Chapter V (p. 135), the required computational resources for the present work are considerably larger than for the semi-empirical approach, and with the currently available resources, only a selection of spectra can be studied that covers targets that were beforehand identified to be of special geological interest, for instance by using the results by [Helbert et al. \(2008\)](#); [Müller et al. \(2008\)](#); [Smrekar et al. \(2010\)](#), or geologic maps ([Ivanov and Head, 2006, 2011](#); [Stofan and Brian, 2012](#)) derived from Magellan radar data ([Pettengill et al., 1991](#); [Ford and Pettengill, 1992](#)), or the radiance ratio based quick-look method by [Arnold et al. \(2008\)](#).

Using ratios between VMC/VEX ([Markiewicz et al., 2007](#)) images at 1 μm that are relatively free from cloud opacity variations, [Shalygin et al. \(2012\)](#); [Basilevsky et al. \(2012\)](#) searched for surface emissivity anomalies. They applied a two-stream approximation to estimate emissivity data from the radiance ratios. They did not consider the full radiative transfer in Venus' atmosphere, nor did they treat emissivity as intrinsic retrieval parameter. The emissivity error of 10%-20% given by these authors was not based on a detailed retrieval error analysis but on the scaling of observed cloud opacity variations of about 10% in the frame of the two-stream approximation.

[Meadows and Crisp \(1996\)](#) de-clouded ground based radiance images at 1.18 μm by dividing them by corresponding 1.31 μm radiance images. At fixed cloud properties, they applied a full radiative transfer simulation model to compute synthetic radiance images at 1.18 μm , taking into account the surface topography and assuming a constant surface emissivity of 0.85. Then the authors investigated the ratio of the de-clouded measured images and the synthetic ones, in order to infer possible spatial surface emissivity variations. Like [Shalygin et al. \(2012\)](#); [Basilevsky et al. \(2012\)](#), they did not treat emissivity as intrinsic retrieval parameter, nor did they consider *a priori* data. The authors did not comment on errors in the determined emissivity data but stated that they did not succeed in detecting emissivity variations in excess of 10%.

Using preprocessed Galileo NIMS ([Carlson et al., 1991](#)) data, [Hashimoto et al. \(2008\)](#) presented the, until then, most sophisticated approach to determine emissivity information. First, they determined cloud mode 2' and 3 abundances using the 1.74 and 2.3 μm peaks. Then, using a full radiative transfer simulation model, they computed synthetic 1.18 μm radiances for a series of emissivity values taking these cloud data into account. Emissivities were determined from the preprocessed measured radiances according to this synthetic 'look-up table'. Again, this approach did not treat emissivity as intrinsic retrieval parameter, and no *a priori* data were

taken into account. Moreover, the physical emissivity domain boundaries 0 and 1 were not respected, as it is evident from many determined emissivity values outside these bounds. Furthermore, the preprocessing of the measured spectra involved the manual removal of the radiances' limb darkening according to the radiance dependence on the emission angle that was determined with a series of synthetic spectra and corroborated by a scatterplot of the measured data. Such a step was not required in the present work, since observation geometry was fully taken into account at the radiative transfer simulations used in the retrieval process. Hashimoto et al. (2008) pointed out that their method is prone to large errors and discussed several potential error sources that alternatively could explain the determined spatial emissivity variations. However, they did not give an emissivity error margin.

Haus and Arnold (2010) went a step further insofar as they treated 1.02 μm surface emissivity as an intrinsic retrieval parameter. They also used a full radiative transfer model, even taking the observational geometry into account, which is why they did not need a limb-darkening correction in their data preprocessing. But they did not take *a priori* information into account. In this respect, the present work is a continuation of the work of these authors, the more so, since the radiative transfer simulation program of the present work was developed in close cooperation with them, and they were co-authors for most of the papers accumulated in this thesis. The authors pointed out that their results were preliminary and discussed several error sources but did not give a strict emissivity error margin. It follows from the present thesis that these retrieved 1.02 μm emissivities were not sufficiently reliable to allow geologic interpretation due to strong interferences from other parameters.

The four articles that constitute the present thesis demonstrated that it is possible to determine reliable emissivity data at all three surface windows covered by VIRTIS-M-IR using a full radiative transfer simulation model and a retrieval algorithm that exploits a large part of the VIRTIS-M-IR spectra's information content, treats emissivities as intrinsic retrieval parameters, and respects *a priori* information and physical constraints. However, this problem was not easy to solve. A sophisticated multi-spectrum retrieval algorithm and a refined data calibration and preprocessing were required, and only detailed retrieval error analyses pointed the way toward reliable results. With the current techniques, it is not yet possible to determine absolute emissivity values, but the obtained emissivity maps relative to a reference emissivity are important steps toward absolute emissivity maps. Strict error margins were given that turned out to be sufficiently small to allow geologic interpretation, which is planned for future work. Apart from the fact that the determined emissivity maps are relative to a reference emissivity and not absolute, the presented approach allowed the achievement of the main goal of this thesis and pushes the VIRTIS-M-IR data evaluation and Venus IR surface emissivity determination in general to their (current) limits.

The determined renormalized emissivity maps of a target in the Themis Regio (see Section VI.1 (p. 162)) shown in Section VI.3 (p. 174) were shortly discussed in Section VI.5 (p. 186). Themis Regio is characterized by a corona-dominated hotspot rise related to a long duration, non-simultaneous, small-scale upwelling (Stofan et al., 1995). Themis Regio contains significant extensional deformation (Stofan and Brian, 2012). Gravity data and the topographic swell suggest that this region is likely underlain by an active plume with ongoing surface deformation due to growth of the rise (Smrekar and Stofan, 1999). Magellan radar data (Pettengill et al., 1991; Ford and Pettengill, 1992; Rappaport et al., 1999) are not very specific to surface composition. *In situ* surface data (see Sections I.1 (p. 2) and I.2.3 (p. 6)) were only sampled at seven landing sites so far, none of which is covered by the Themis Regio target, and a global overview of the surface composition is difficult to infer from these data. The thermal flux anomaly map at 1.02 μm determined by Müller et al. (2008) constituted a successful step to globally derive surface properties based on the infrared surface emissivity that is more diagnostic to surface composition than radar data are. Some edifice fields in Themis Regio correlate with positive thermal flux anomalies and may be attributed to relatively stratigraphically young units of volcanic origin (Stofan et al., 2010). The present work qualitatively improves the flux anomaly data by Müller et al. (2008) and provides maps at all three surface windows that are quantitatively directly related to absolute emissivity data. These results enable a much more detailed geologic interpretation of the Themis Regio target, which is planned for the near future. It was discussed in Section VI.5 (p. 186) that high emissivity signatures correlate with edifices like Abeona Mons and other volcanic structures. Shiwanokia Corona has areas of lower emissivity. The complexity in this region might suggest long histories and an apparently older corona (Stofan and Smrekar, 1998). In general, these anomalies can be caused by local changes in composition, age, and/or textural differences of the surface (Arnold et al., 2015).

VII.2 Summary

The main goal of the present thesis was the determination of surface emissivity data maps in the infrared from VIRTIS-M-IR radiance spectra of Venus' nightside emissions. A full radiative transfer simulation model and a retrieval algorithm were used for this purpose. Achieving this goal proved to be much more difficult than expected. The radiative transfer simulation had to take into account multiple scattering by atmospheric gases and clouds as well as the extreme environmental conditions in Venus' deep atmosphere that lead to partly not well known optical properties. The required computer resources were quite high, and the radiative transfer simulation had to be continuously improved with respect to both the underlying physics and the numerical efficiency.

To enable the determination of reliable emissivity data, the utilized VIRTIS-M-IR spectra had to be as self-consistent and as faithful to reality as possible. This necessitated a number of calibration refinements based on a detailed detector responsivity analysis as well as the development of a suitable data preprocessing.

The relatively low spectral information content of the measured spectra and the accordingly difficult determination of surface emissivity data led to the idea to utilize several spectra to derive a single quantity like the emissivity of a surface bin and to incorporate the context of adjacent measurements. The multi-spectrum retrieval algorithm MSR was developed and heavily optimized to properly and efficiently address this approach.

But even with MSR, early retrieved emissivity maps turned out to be unreliable. In order to overcome this problem, its cause had to be identified using a detailed emissivity retrieval error analysis based on synthetic spectra. The largest errors were found to be due to interferences from parameters that had to be set to assumed values to enable the radiative transfer simulation but could not be derived from the spectra themselves.

The original ambition to derive absolute emissivities had to be dropped to still obtain useful emissivity data. This led to the concept of a retrieval of emissivity maps relative to a certain reference emissivity. In conjunction with MSR, this was implemented as a combination of the retrieval of auxiliary fine-tuning parameters and of some post-processing steps to remove apparently artificial emissivity trends with latitude and topography and to transform the de-trended maps to have a mean value that coincided with the reference emissivity. The resulting 'renormalized emissivity maps' were interpreted as spatial variations relative to the reference emissivity. However, true emissivities may exhibit real trends with latitude and topography, even if this seems to be unlikely from a geologic point of view.

Finally, renormalized emissivity maps referred to the reference emissivity 0.5 were derived at the accessible surface windows (1.02, 1.10, and 1.18 μm) from VIRTIS-M-IR measurements in the spectral range 1.0–2.3 μm that covered a surface target of 219 surface bins at Themis Regio 64 times. A sophisticated retrieval pipeline and the renormalization approach were used, both of them being the result of numerous trial-and-error improvements. The double standard deviation errors of these maps were quantified as about 3%, 8%, and 4% for the three surface windows according to several tests where both the utilized measurement data set and many interfering parameters were modified. These renormalized emissivity maps will be used for geologic interpretations.

The sacrifice of (unreliable) absolute emissivity data in favor of (reliable) relative emissivity data is acceptable with respect to a first geologic interpretation, since the latter can mainly rely on just spatial emissivity variations. However, if the absolute emissivity at a given bin of the target were known, for instance in the form of ground truth data, the absolute emissivity map of the entire target could be computed according to the above mentioned transformation. In this sense, the renormalized emissivity maps are as close to absolute emissivity maps as is possible with current techniques. These are the first Venus IR emissivity results from consequent application of a full radiative transfer simulation program and a retrieval algorithm respecting the available *a priori* information and treating emissivity as intrinsic retrieval parameter. Apart from the fact that the determined emissivity maps are relative to a reference emissivity and not absolute, the main goal of this thesis was achieved with the derivation of the maps at Themis Regio. These maps are the first ones that consider all three surface windows covered by VIRTIS-M-IR. Their reliability was quantified according to two complementary methods, and their relation to absolute emissivities was precisely clarified. This approach pushes the VIRTIS-M-IR data evaluation to its limits.

Starting with the development of a suitable radiative transfer simulation program and the calibration refinements and data preprocessing, proceeding with the development of a powerful new multi-spectrum retrieval

algorithm, a retrieval error analysis with synthetic spectra, and concluding with the application to a geologically interesting surface target, the determination of useful surface emissivity data for this target along with a retrieval reliability verification and error estimation, the present thesis covered many important remote sensing topics.

VII.3 Outlook

Naturally, the present work cannot provide final answers, and improvements are always possible. The next logical step is the geologic interpretation of the Themis Regio target based on the new renormalized emissivity maps in combination with a surface morphology based geologic map of the region (Stofan and Brian, 2012) and the radar topography, emissivity, reflectivity, and slope data acquired by Magellan (Ford and Pettingill, 1992; Rappaport et al., 1999). This way, the relevance of the identified emissivity anomalies can be assessed. Moreover, the relevance of the general spatial variations of the maps for all three surface windows at double and possibly even at single standard deviation significance can be evaluated. The 1.02 μm map will be compared to the thermal flux anomaly map of Müller et al. (2008) in context with the interpretation of certain anomalies thereof as candidates for recent hotspot volcanism as described by Smrekar et al. (2010). This will be addressed in a follow-up paper.

It is also planned to analyze other geologically interesting surface targets. But also conceptually interesting targets that cover wide latitude or longitude ranges and those that cover wide or narrow topography ranges have to be studied. Note that absolute emissivity must globally never violate its domain boundaries 0 and 1, and it should not exhibit consistent latitudinal trends. Such requirements could help to further constrain details of the retrieval procedure and to identify the most realistic reference emissivity.

One of the most pressing issues is a better and more systematic treatment of the currently retrieved emissivity trends with latitude and topography before renormalization. The first algorithmic improvement beyond the present work will therefore be the implementation of additional constraints in the retrieval regularization that force the retrieved emissivity maps to not exhibit trends with latitude and topography from the outset. Moreover, the emissivity average over the target shall be forced to attain the reference emissivity value from the outset. This can be accomplished by introducing for the 'scaled residual' \mathbf{R} a few additional dimensions that encode these constraints in terms of logarithmic barrier functions (see Section IV.A.1 (p. 126)). This way, the renormalization post-processing steps shall be systematically avoided, and the full consistency of the MSR retrieval parameter set that is partially lost as a result of the post-processing can be preserved. The causes that lead to the current (presumably artificial) emissivity trends with latitude and topography before renormalization can then be ascribed to trends in atmospheric parameters (e.g. so far unconsidered trends in the deep atmospheric temperature field or the cloud mode abundances, bottom altitudes, and droplet compositions) and to surface haze, depending on the magnitude and spatial and temporal consistency of this effect, by retrieving some of them as parameters that are common to many diverse spectra with a wide latitude and topography coverage. If it should turn out to be impossible to avoid the retrieved emissivity trends with latitude and topography this way simultaneously for all three surface windows, this would be an argument for the actual presence of such trends in the true emissivity maps.

If the avoidance of the emissivity trends before renormalization proves successful, it is possible to retrieve maps while systematically modifying the choice of the reference emissivity. The reference emissivity that leads to the smallest residual between measurements and best fits is then a good candidate for a more realistic absolute emissivity mean of the target. This gives a chance to finally retrieve absolute emissivity maps. This approach is neither sensible nor feasible in presence of artificial emissivity trends that have to be removed in a post-processing step, for instance because of the potential cutoff at the emissivity domain boundaries. Nevertheless, the residuals slightly (order of 1.0%) decreased on average in the PMTs in Section VI.4.4 (p. 180), when the initial emissivity was changed from 0.500 to 0.625 or to 0.750 (1.7%) and even 0.875 (2.1%). However, the latter case is already affected by severe cutoffs at the emissivity domain boundary 1, as it was discussed in the cited section. Also, this does not prove a systematic trend, as there might, for instance, exist a minimum between the 0.750 and the 0.875 cases. Moreover, the residuals could be quite different in absence of trends with latitude and topography. Also note that the initial emissivity does not coincide with the mean emissivity in these cases. However, this decrease could indicate that the mean emissivity of the Themis Regio target

is possibly larger than 0.5, but in presence of the emissivity trends with latitude and topography, this effect should not be overrated and was therefore not mentioned by [Kappel et al. \(2016\)](#).

One open question is the expected decrease of MST errors that are scaled to a fixed measurement repetition number N_r^0 with increasing N_r due to MSR's usage of more *a priori* data (see Chapter VI (p. 161)). This decrease was so far observed to be not consistent.¹ This must be studied with further surface targets and, if possible, with higher N_r by relaxing the demands on the usability of VIRTIS-M-IR measurements for emissivity retrieval.

The capability of MSR to retrieve parameters that are common to a selection of spectra can be used to retrieve emissivity data at a spatial resolution that is finer than the atmospheric blurring limit (FWHM in the order of 100 km, [Moroz, 2002](#)). Possible high-resolution surface bins can be chosen to subsample the current bins. Then, a high-resolution emissivity map can be retrieved as parameter vector that is common to many spectra that are binned according to the high-resolution surface bins. This exploits the variability of the surface footprints of the different single-spectrum measurements (before binning) and is essentially a deconvolution of the atmospheric blurring. The feasibility of this approach depends on the number of usable measurements that cover the target.

Finally, the number of usable measurement repetitions proved to be a deciding factor for emissivity retrieval. The earlier mentioned Akatsuki mission will hopefully provide new Venus nightside data (radiance measurements at 0.90, 0.97, 1.01, 1.73, 2.26, and 2.32 μm from the IR1 and IR2 cameras, [Nakamura et al., 2007](#), are useful for nightside studies), and it remains to be assessed, whether these data can be used for emissivity retrieval. Other factors that can help to improve emissivity results, in particular with respect to absolute emissivities, are better CO_2 opacity data as they are currently being measured by [Tran et al. \(2011\)](#); [Stefani et al. \(2013\)](#); [Snels et al. \(2014\)](#). Concerning the more distant future, radiance measurements at higher spectral resolution are desirable ([Kappel et al., 2015](#)) as well as additional *in situ* data of atmosphere and surface, and improved topography data. Measured emissivities of analog materials with different composition, grain size, and texture at Venus surface temperatures are important prerequisites for a better interpretation of retrieved emissivity data. Such measurements are currently performed by [Maturilli et al. \(2008\)](#).

¹Note: One reason might be the long time separation between many of the VIRTIS-M-IR cubes utilized for the determination of the renormalized emissivity maps. These cubes were listed in Section VI.A.1 (p. 192). For a given cube, the number of the VEX orbit on which it was acquired is indicated by the number preceding the underscore in the cube name. The duration of one VEX orbit was 24 h, whereas the *a priori* correlation times for the atmospheric parameters listed in Table VI.2 (p. 173) do not exceed 8 h. Thus, the *a priori* information on the retrieval parameters was in many cases not increased by the incorporation of *a priori* time correlations.

Bibliography

- [**Abdrakhimov and Basilevsky, 2002**] A. M. Abdrakhimov and A. T. Basilevsky. “Geology of the Venera and Vega Landing-Site Regions”. *Solar Syst. Res.* 36.2 (2002), pp. 136–159. doi: [10.1023/A:1015222316518](https://doi.org/10.1023/A:1015222316518) (cit. on pp. [2](#), [136](#)).
- [**Abramowitz and Stegun, 1972**] M. Abramowitz and I. A. Stegun. *Handbook of Mathematical Functions: With Formulas, Graphs, and Mathematical Tables*. Applied mathematics series. U.S. Department of Commerce, National Bureau of Standards, 1972. ISBN: 978-0-486-61272-0 (cit. on p. [32](#)).
- [**Allen, 1963**] C. W. Allen. *Astrophysical quantities, 2nd Edition*. University of London, Athlone Press, 1963 (cit. on p. [53](#)).
- [**Allen, 1987**] D. A. Allen. “The dark side of Venus”. *Icarus* 69.2 (1987), pp. 221–229. doi: [10.1016/0019-1035\(87\)90101-1](https://doi.org/10.1016/0019-1035(87)90101-1) (cit. on pp. [2](#), [3](#)).
- [**Allen and Crawford, 1984**] D. A. Allen and J. W. Crawford. “Cloud structure on the dark side of Venus”. *Nature* 307.5948 (1984), pp. 222–224. doi: [10.1038/307222a0](https://doi.org/10.1038/307222a0) (cit. on pp. [2](#), [3](#)).
- [**Amestoy et al., 1996**] P. R. Amestoy, T. A. Davis, and I. S. Duff. “An Approximate Minimum Degree Ordering Algorithm”. *SIAM J. Matrix Anal. & Appl.* 17.4 (1996), pp. 886–905. doi: [10.1137/S0895479894278952](https://doi.org/10.1137/S0895479894278952) (cit. on p. [133](#)).
- [**Amestoy et al., 2004**] P. R. Amestoy, T. A. Davis, and I. S. Duff. “Algorithm 837: AMD, an approximate minimum degree ordering algorithm”. *ACM Trans. Math. Softw.* 30.3 (2004), pp. 381–388. doi: [10.1145/1024074.1024081](https://doi.org/10.1145/1024074.1024081) (cit. on p. [133](#)).
- [**Anderson, 1958**] T. W. Anderson. *An introduction to multivariate statistical analysis*. Wiley publications in statistics. New York, NY, USA: Wiley, 1958 (cit. on pp. [108](#), [140](#)).
- [**Arnold et al., 2015**] G. Arnold, D. Kappel, R. Haus, M. Ivanov, and L. T. Pedroza. “Retrieval and study of near-infrared surface emissivity maps of Themis Regio on Venus with VIRTIS-M (Venus Express)”. In: *EPSC Abstracts Vol. 10, European Planetary Science Congress 2015*. EPSC2015-160. 2015 (cit. on pp. [189](#), [208](#)).
- [**Arnold et al., 2000**] G. Arnold, R. Haus, and H. Hirsch. “The Planetary Fourier Spectrometer (PFS): studies of the Martian atmosphere and surface”. *Forschungsbericht-Deutsches Zentrum für Luft und Raumfahrt* 18 (2000) (cit. on p. [35](#)).
- [**Arnold et al., 2008**] G. Arnold, R. Haus, D. Kappel, P. Drossart, and G. Piccioni. “Venus surface data extraction from VIRTIS/Venus Express measurements: Estimation of a quantitative approach”. *J. Geophys. Res.* 113.E5 (2008), E00B10. doi: [10.1029/2008JE003087](https://doi.org/10.1029/2008JE003087) (cit. on pp. [6](#), [68](#), [71](#), [91](#), [94](#), [96](#), [99](#), [125](#), [151](#), [164](#), [207](#)).
- [**Arnold et al., 2012a**] G. Arnold, R. Haus, and D. Kappel. “Construction of global maps of atmospheric and surface features of Venus based on new retrieval methods”. In: *EGU General Assembly 2012*. Vol. 14. 2012, pp. 11417–11417 (cit. on pp. [8](#), [204](#)).
- [**Arnold et al., 2012b**] G. Arnold, R. Haus, and D. Kappel. “Retrieval of surface properties in the NIR nightside windows of Venus”. In: *The Third Moscow Solar System Symposium*. 2012, pp. 50–51 (cit. on pp. [8](#), [204](#)).
- [**Arnold et al., 2013**] G. Arnold, D. Kappel, R. Haus, and S. Ebert. “Surface emissivity retrieval from VIRTIS/VEX data in the Quetzalpetlatl quadrangle on Venus based on the new MSR multi-spectrum retrieval technique”. In: *The Fourth Moscow Solar System Symposium*. 2013, pp. 106–107 (cit. on pp. [8](#), [204](#)).
- [**Arnold et al., 2011**] G. E. Arnold, P. Drossart, G. Piccioni, and R. Haus. “Venus atmospheric and surface studies from VIRTIS on Venus Express”. In: *Proc. SPIE 8154, Infrared Remote Sensing and Instrumentation XIX*. 2011, 81540W–81540W–17. doi: [10.1117/12.892895](https://doi.org/10.1117/12.892895) (cit. on p. [104](#)).
- [**Arnold et al., 2012c**] G. E. Arnold, R. Haus, D. Kappel, G. Piccioni, and P. Drossart. “VIRTIS/VEX observations of Venus: overview of selected scientific results”. *J. Appl. Remote Sens.* 6.1 (2012), pp. 063580–1–063580–20. doi: [10.1117/1.JRS.6.063580](https://doi.org/10.1117/1.JRS.6.063580) (cit. on pp. [3](#), [25](#), [104](#), [136](#), [162](#), [189](#)).
- [**Avduevskii et al., 1983**] V. S. Avduevskii, M. I. Marov, I. N. Kulikov, V. P. Shari, A. I. Gorbachevskii, G. R. Uspenskii, and Z. P. Cheremukhina. “Structure and parameters of the Venus atmosphere according to Venera probe

- data". In: *Venus*. Ed. by D. M. Hunten, L. Colin, T. M. Donahue, and V. I. Moroz. University of Arizona Press, 1983, pp. 280–298 (cit. on pp. 69, 104, 119).
- [Baines et al., 2000] K. H. Baines, G. Bellucci, J.-P. Bibring, R. H. Brown, B. J. Buratti, E. Bussoletti, F. Capaccioni, P. Cerroni, R. N. Clark, A. Coradini, D. P. Cruikshank, P. Drossart, V. Formisano, R. Jaumann, Y. Langevin, D. L. Matson, T. B. McCord, V. Mennella, R. M. Nelson, P. D. Nicholson, B. Sicardy, C. Sotin, G. B. Hansen, J. J. Aiello, and S. Amici. "Detection of Sub-Micron Radiation from the Surface of Venus by Cassini/VIMS". *Icarus* 148.1 (2000), pp. 307–311. doi: 10.1006/icar.2000.6519 (cit. on pp. 2, 4).
- [Baldrige et al., 2009] A. M. Baldrige, S. J. Hook, C. I. Grove, and G. Rivera. "The ASTER spectral library version 2.0". *Remote Sens. Environ.* 113.4 (2009), pp. 711–715. doi: 10.1016/j.rse.2008.11.007 (cit. on pp. 7, 182).
- [Balgovind et al., 1983] R. Balgovind, A. Dalcher, M. Ghil, and E. Kalnay. "A stochastic-dynamic model for the spectral structure of forecast errors". *Mon. Weather Rev.* 111.4 (1983). doi:10.1175/1520-0493(1983)111<0701:ASDMFT>2.0.CO;2, pp. 701–721 (cit. on pp. 110, 140).
- [Barichello et al., 1996] L. B. Barichello, R. D. M. Garcia, and C. E. Siewert. "The Fourier decomposition for a radiative-transfer problem with an asymmetrically reflecting ground". *J. Quant. Spectrosc. Rad.* 56.3 (1996), pp. 363–371. doi: 10.1016/0022-4073(96)84526-2 (cit. on p. 32).
- [Barstow et al., 2012] J. K. Barstow, C. C. C. Tsang, C. F. Wilson, P. G. J. Irwin, F. W. Taylor, K. McGouldrick, P. Drossart, G. Piccioni, and S. Tellmann. "Models of the global cloud structure on Venus derived from Venus Express observations". *Icarus* 217.2 (2012). In: *Advances in Venus Science*, pp. 542–560. doi: 10.1016/j.icarus.2011.05.018 (cit. on pp. 4, 47, 49, 148, 159).
- [Barsukov et al., 1986] V. L. Barsukov, A. T. Basilevsky, G. A. Burba, N. N. Bobinna, V. P. Kryuchkov, R. O. Kuzmin, O. V. Nikolaeva, A. A. Pronin, L. B. Ronca, I. M. Chernaya, V. P. Shashkina, A. V. Garanin, E. R. Kushky, M. S. Markov, A. L. Sukhanov, V. A. Kotelnikov, O. N. Rzhiga, G. M. Petrov, Y. N. Alexandrov, A. I. Sidorenko, A. F. Bogomolov, G. I. Skrypnik, M. Y. Bergman, L. V. Kudrin, I. M. Bokshtein, M. A. Krondrod, P. A. Chochia, Y. S. Tyuflin, S. A. Kadnichansky, and E. L. Akim. "The Geology and Geomorphology of the Venus Surface as Revealed by the Radar Images Obtained by Veneras 15 and 16". In: *Lunar and Planetary Science Conference Proceedings*. Vol. 16. Lunar and Planetary Science Conference Proceedings. 1986, pp. D378–D398 (cit. on p. 7).
- [Barsukov et al., 1992] V. L. Barsukov, A. T. Basilevsky, V. P. Volkov, and V. N. Zharkov, eds. *Venus Geology, Geochemistry, and Geophysics - Research results from the USSR*. University of Arizona Press, Tucson, 1992, p. 165 (cit. on p. 7).
- [Basilevsky et al., 1997] A. T. Basilevsky, J. W. Head, G. G. Schaber, and R. G. Strom. "The Resurfacing History of Venus". In: *Venus II: Geology, Geophysics, Atmosphere, and Solar Wind Environment*. Ed. by S. W. Bougher, D. M. Hunten, and R. J. Phillips. Space science series. University of Arizona Press, Tucson, 1997, pp. 1047–1086. ISBN: 9780816518302 (cit. on pp. 1, 6, 136).
- [Basilevsky et al., 2012] A. T. Basilevsky, E. V. Shalygin, D. V. Titov, W. J. Markiewicz, F. Scholten, T. Roatsch, M. A. Kreslavsky, L. V. Moroz, N. I. Ignatiev, B. Fiethe, B. Osterloh, and H. Michalik. "Geologic interpretation of the near-infrared images of the surface taken by the Venus Monitoring Camera, Venus Express". *Icarus* 217.2 (2012). In: *Advances in Venus Science*, pp. 434–450. doi: 10.1016/j.icarus.2011.11.003 (cit. on pp. 4, 5, 7, 207).
- [Basilevsky and Head, 1998] A. T. Basilevsky and J. W. Head. "The geologic history of Venus: A stratigraphic view". *J. Geophys. Res.: Planets* 103.E4 (1998), pp. 8531–8544. doi: 10.1029/98JE00487 (cit. on p. 6).
- [Basilevsky and Head, 2000] A. T. Basilevsky and J. W. Head. "Geologic units on Venus: evidence for their global correlation". *Planet. Space Sci.* 48.1 (2000), pp. 75–111. doi: 10.1016/S0032-0633(99)00083-5 (cit. on p. 6).
- [Basilevsky and Head, 2003] A. T. Basilevsky and J. W. Head. "The surface of Venus". *Rep. Prog. Phys.* 66.10 (2003), pp. 1699–1734. doi: 10.1088/0034-4885/66/10/R04 (cit. on p. 6).
- [Baxter, 2003] B. J. C. Baxter. *Positive definite functions on Hilbert space*. Tech. rep. University of Cambridge, Department of Applied Mathematics and Theoretical Physics, Numerical Analysis Group. 2003 (cit. on pp. 109, 110).
- [Benner et al., 1995] D. C. Benner, C. P. Rinsland, V. M. Devi, M. A. H. Smith, and D. Atkins. "A multispectrum nonlinear least squares fitting technique". *J. Quant. Spectrosc. Rad.* 53.6 (1995), pp. 705–721. doi: 10.1016/0022-4073(95)00015-D (cit. on p. 8).
- [Bézar et al., 1990] B. Bézar, C. de Bergh, D. Crisp, and J.-P. Maillard. "The deep atmosphere of Venus revealed by high-resolution nightside spectra". *Nature* 345.6275 (1990). doi:10.1038/345508a0, pp. 508–511. doi: 10.1038/345508a0 (cit. on p. 3).
- [Bézar et al., 2009] B. Bézar, C. C. C. Tsang, R. W. Carlson, G. Piccioni, E. Marcq, and P. Drossart. "Water vapor abundance near the surface of Venus from Venus Express/VIRTIS observations". *J. Geophys. Res.* 114.E5 (2009), E00B39. doi: 10.1029/2008JE003251 (cit. on pp. 4, 39, 99).

- [Bézar et al., 2011] B. Bézar, A. Fedorova, J.-L. Bertaux, A. Rodin, and O. Korablev. “The 1.10- and 1.18- μm nightside windows of Venus observed by SPICAV-IR aboard Venus Express”. *Icarus* 216.1 (2011), pp. 173–183. doi: [10.1016/j.icarus.2011.08.025](https://doi.org/10.1016/j.icarus.2011.08.025) (cit. on pp. 4, 41, 117, 147, 148, 168).
- [Bjoraker et al., 1992] G. L. Bjoraker, H. P. Larson, M. J. Mumma, R. Timmermann, and J. L. Montani. “Airborne Observations of the Gas Composition of Venus Above the Cloud Tops: measurements of H_2O , HDO, HF, and the D/H and $^{18}\text{O}/^{16}\text{O}$ Isotopic Ratios”. In: *AAS/Division for Planetary Sciences Meeting Abstracts*. Vol. 24. Bulletin of the American Astronomical Society. 1992, p. 995 (cit. on pp. 41, 145).
- [Brodbeck et al., 1991] C. Brodbeck, N. Van-Thanh, J.-P. Bouanich, C. Boulet, A. Jean-Louis, B. Bézar, and C. de Bergh. “Measurements of Pure CO_2 Absorption at High Densities Near 2.3 μm ”. *J. Geophys. Res.* 96.E2 (1991), pp. 17497–17500. doi: [10.1029/91JE01680](https://doi.org/10.1029/91JE01680) (cit. on p. 93).
- [Bugayevskiy and Snyder, 1995] L. M. Bugayevskiy and J. Snyder. *Map Projections: A Reference Manual*. Taylor & Francis, 1995. ISBN: 9780748403042 (cit. on pp. 56, 166).
- [Cardesin-Moinelo et al., 2010] A. Cardesin-Moinelo, G. Piccioni, E. Ammannito, G. Filacchione, and P. Drossart. “Calibration of Hyperspectral Imaging Data: VIRTIS-M Onboard Venus Express”. *IEEE Trans. Geosci. Remote* 48 (2010), pp. 3941–3950. doi: [10.1109/TGRS.2010.2064325](https://doi.org/10.1109/TGRS.2010.2064325) (cit. on pp. 12, 25, 68, 71, 78, 84, 104, 136, 152, 165).
- [Carlotti, 1988] M. Carlotti. “Global-fit approach to the analysis of limb-scanning atmospheric measurements”. *Appl. Opt.* 27.15 (1988), pp. 3250–3254. doi: [10.1364/AO.27.003250](https://doi.org/10.1364/AO.27.003250) (cit. on p. 8).
- [Carlotti and Carli, 1994] M. Carlotti and B. Carli. “Approach to the design and data analysis of a limb-scanning experiment”. *Appl. Opt.* 33.15 (1994), pp. 3237–3249. doi: [10.1364/AO.33.003237](https://doi.org/10.1364/AO.33.003237) (cit. on p. 8).
- [Carlotti et al., 2006] M. Carlotti, G. Brizzi, E. Papandrea, M. Prevedelli, M. Ridolfi, B. M. Dinelli, and L. Magnani. “GMTR: Two-dimensional geo-fit multitarget retrieval model for Michelson Interferometer for Passive Atmospheric Sounding/Environmental Satellite observations”. *Appl. Opt.* 45.4 (2006), pp. 716–727. doi: [10.1364/AO.45.000716](https://doi.org/10.1364/AO.45.000716) (cit. on p. 8).
- [Carlson and Anderson, 2011] R. Carlson and M. Anderson. “Absorption properties of sulfuric acid in Venus’s infrared spectral windows region”. In: *EPSC-DPS Joint Meeting 2011*. 2011, p. 1171 (cit. on pp. 46, 50, 117, 147, 169).
- [Carlson et al., 1991] R. W. Carlson, K. H. Baines, T. Encrenaz, F. W. Taylor, P. Drossart, L. W. Kamp, J. B. Pollack, E. Lellouch, A. D. Collard, S. B. Calcutt, D. Grinspoon, P. R. Weissman, W. D. Smythe, A. C. Ocampo, G. E. Danielson, F. P. Fanale, T. V. Johnson, H. H. Kieffer, D. L. Matson, T. B. McCord, and L. A. Soderblom. “Galileo Infrared Imaging Spectroscopy Measurements at Venus”. *Science* 253.5027 (1991), pp. 1541–1548. doi: [10.1126/science.253.5027.1541](https://doi.org/10.1126/science.253.5027.1541) (cit. on pp. 2, 4, 5, 207).
- [Chandrasekhar, 1950] S. Chandrasekhar. *Radiative transfer*. International series of monographs on physics. Clarendon Press, 1950 (cit. on p. 31).
- [Chen et al., 2008] Y. Chen, T. A. Davis, W. W. Hager, and S. Rajamanickam. “Algorithm 887: CHOLMOD, Supernodal Sparse Cholesky Factorization and Update/Downdate”. *ACM Trans. Math. Softw.* 35.3 (2008), 22:1–22:14. doi: [10.1145/1391989.1391995](https://doi.org/10.1145/1391989.1391995) (cit. on p. 133).
- [Clough et al., 1989] S. A. Clough, F. X. Kneizys, and R. W. Davies. “Line shape and the water vapor continuum”. *Atmos. Res.* 23.3–4 (1989), pp. 229–241. doi: [10.1016/0169-8095\(89\)90020-3](https://doi.org/10.1016/0169-8095(89)90020-3) (cit. on p. 40).
- [Clough et al., 2005] S. A. Clough, M. W. Shephard, E. J. Mlawer, J. S. Delamere, M. J. Iacono, K. Cady-Pereira, S. Boukabara, and P. D. Brown. “Atmospheric radiative transfer modeling: a summary of the AER codes”. *J. Quant. Spectrosc. Rad.* 91.2 (2005), pp. 233–244. doi: [10.1016/j.jqsrt.2004.05.058](https://doi.org/10.1016/j.jqsrt.2004.05.058) (cit. on p. 40).
- [Crisp et al., 1991] D. Crisp, D. A. Allen, D. H. Grinspoon, and J. B. Pollack. “The dark side of Venus: near-infrared images and spectra from the Anglo-Australian observatory”. *Science* 253.5025 (1991), pp. 1263–1266. doi: [10.1126/science.11538493](https://doi.org/10.1126/science.11538493) (cit. on pp. 2, 3).
- [Crisp, 1986] D. Crisp. “Radiative forcing of the Venus mesosphere: I. Solar fluxes and heating rates”. *Icarus* 67.3 (1986), pp. 484–514. doi: [10.1016/0019-1035\(86\)90126-0](https://doi.org/10.1016/0019-1035(86)90126-0) (cit. on p. 47).
- [Daley, 1991] R. Daley. *Atmospheric Data Analysis (Cambridge Atmospheric and Space Science Series)*. Cambridge, UK: Cambridge University Press, 1991. ISBN: 0521 382157 (cit. on pp. 110, 140).
- [Davies et al., 1986] M. E. Davies, V. K. Abalakin, M. Bursa, T. Lederle, and J. H. Lieske. “Report of the IAU/IAG-COSPAR working group on cartographic coordinates and rotational elements of the planets and satellites - 1985”. *Celestial Mech.* 39 (1986), pp. 103–113. doi: [10.1007/BF01232291](https://doi.org/10.1007/BF01232291) (cit. on p. 88).
- [Davies et al., 1992] M. E. Davies, V. K. Abalakin, A. Brahic, M. Bursa, B. H. Chovitz, J. H. Lieske, P. K. Seidelmann, A. T. Sinclair, and I. S. Tiufin. “Report of the IAU/IAG-COSPAR Working Group on Cartographic Coordinates and Rotational Elements of the Planets and Satellites - 1991”. *Celest. Mech. Dyn. Astr.* 53 (1992), pp. 377–397. doi: [10.1007/BF00051818](https://doi.org/10.1007/BF00051818) (cit. on p. 88).

- [Davis, 2006] T. A. Davis. *Direct methods for sparse linear systems*. Fundamentals of algorithms. Society for Industrial and Applied Mathematics, 2006. ISBN: 978-0-89871-613-9. DOI: [10.1137/1.9780898718881](https://doi.org/10.1137/1.9780898718881) (cit. on p. 133).
- [Davis, 2011] T. A. Davis. “Algorithm 915, SuiteSparseQR: Multifrontal multithreaded rank-revealing sparse QR factorization”. *ACM Trans. Math. Softw.* 38.1 (2011), 8:1–8:22. DOI: [10.1145/2049662.2049670](https://doi.org/10.1145/2049662.2049670) (cit. on p. 133).
- [Davis and Hager, 1999] T. A. Davis and W. W. Hager. “Modifying a Sparse Cholesky Factorization”. *SIAM J. Matrix Anal. & Appl.* 20.3 (1999), pp. 606–627. DOI: [10.1137/S0895479897321076](https://doi.org/10.1137/S0895479897321076) (cit. on p. 133).
- [Davis and Hager, 2001] T. A. Davis and W. W. Hager. “Multiple-rank modifications of a sparse Cholesky factorization”. *SIAM J. Matrix Anal. & Appl.* 22.4 (2001), pp. 997–1013. DOI: [10.1137/S0895479899357346](https://doi.org/10.1137/S0895479899357346) (cit. on p. 133).
- [Davis and Hager, 2005] T. A. Davis and W. W. Hager. “Row modifications of a sparse Cholesky factorization”. *SIAM J. Matrix Anal. & Appl.* 26.3 (2005), pp. 621–639. DOI: [10.1137/S089547980343641X](https://doi.org/10.1137/S089547980343641X) (cit. on p. 133).
- [Davis and Hager, 2009] T. A. Davis and W. W. Hager. “Dynamic Supernodes in Sparse Cholesky Update/Downdate and Triangular Solves”. *ACM Trans. Math. Softw.* 35.4 (2009), 27:1–27:23. DOI: [10.1145/1462173.1462176](https://doi.org/10.1145/1462173.1462176) (cit. on p. 133).
- [Davis et al., 2004a] T. A. Davis, J. R. Gilbert, S. I. Larimore, and E. G. Ng. “A column approximate minimum degree ordering algorithm”. *ACM Trans. Math. Softw.* 30.3 (2004), pp. 353–376. DOI: [10.1145/1024074.1024079](https://doi.org/10.1145/1024074.1024079) (cit. on p. 133).
- [Davis et al., 2004b] T. A. Davis, J. R. Gilbert, S. I. Larimore, and E. G. Ng. “Algorithm 836: COLAMD, a column approximate minimum degree ordering algorithm”. *ACM Trans. Math. Softw.* 30.3 (2004), pp. 377–380. DOI: [10.1145/1024074.1024080](https://doi.org/10.1145/1024074.1024080) (cit. on p. 133).
- [De Bergh et al., 1995] C. de Bergh, B. Bézard, D. Crisp, J. P. Maillard, T. Owen, J. Pollack, and D. Grinspoon. “Water in the deep atmosphere of Venus from high-resolution spectra of the night side”. *Adv. Space Res.* 15.4 (1995), pp. 79–88. DOI: [10.1016/0273-1177\(94\)00067-B](https://doi.org/10.1016/0273-1177(94)00067-B) (cit. on pp. 69, 93, 105).
- [De Bergh et al., 1991] C. de Bergh, B. Bézard, T. Owen, D. Crisp, J.-P. Maillard, and B. L. Lutz. “Deuterium on Venus: observations from Earth”. *Science* 251.4993 (1991), pp. 547–549. DOI: [10.1126/science.251.4993.547](https://doi.org/10.1126/science.251.4993.547) (cit. on pp. 41, 145).
- [De Kok et al., 2011] R. de Kok, P. G. J. Irwin, C. C. C. Tsang, G. Piccioni, and P. Drossart. “Scattering particles in nightside limb observations of Venus’ upper atmosphere by Venus Express VIRTIS”. *Icarus* 211.1 (2011), pp. 51–57. DOI: [10.1016/j.icarus.2010.08.023](https://doi.org/10.1016/j.icarus.2010.08.023) (cit. on pp. 69, 105).
- [De Souza-Machado et al., 2002] S. De Souza-Machado, L. L. Strow, D. Tobin, H. Motteler, and S. Hannon. *UMBC-LBL: An algorithm to compute line-by-line spectra*. Tech. rep. http://as1.umbc.edu/pub/sergio/CLASSES/UMBC/P721_Fall2012/lbl.pdf. University of Maryland Baltimore County, Department of Physics, 2002 (cit. on pp. 39, 40).
- [DeGroot and Schervish, 2012] M. H. DeGroot and M. J. Schervish. *Probability and Statistics, Fourth Edition*. Addison-Wesley series in statistics. Addison-Wesley, 2012. ISBN: 9780321500465 (cit. on pp. 194, 198).
- [Delaye et al., 1989] C. Delaye, J.-M. Hartmann, and J. Taine. “Calculated tabulations of H₂O line broadening by H₂O, N₂, O₂, and CO₂ at high temperature”. *Appl. Opt.* 28.23 (1989), pp. 5080–5087. DOI: [10.1364/AO.28.005080](https://doi.org/10.1364/AO.28.005080) (cit. on p. 37).
- [Dinelli et al., 2004] B. M. Dinelli, D. Alpaslan, M. Carlotti, L. Magnani, and M. Ridolfi. “Multi-target retrieval (MTR): the simultaneous retrieval of pressure, temperature and volume mixing ratio profiles from limb-scanning atmospheric measurements”. *J. Quant. Spectrosc. Rad.* 84.2 (2004), pp. 141–157. DOI: [10.1016/S0022-4073\(03\)00137-7](https://doi.org/10.1016/S0022-4073(03)00137-7) (cit. on p. 8).
- [Donahue et al., 1982] T. M. Donahue, J. H. Hoffman, R. R. Hodges, and A. J. Watson. “Venus Was Wet: A Measurement of the Ratio of Deuterium to Hydrogen”. *Science* 216.4546 (1982), pp. 630–633. DOI: [10.1126/science.216.4546.630](https://doi.org/10.1126/science.216.4546.630) (cit. on p. 1).
- [Drossart et al., 2007] P. Drossart, G. Piccioni, A. Adriani, F. Angrilli, G. Arnold, K. H. Baines, G. Bellucci, J. Benkhoff, B. Bézard, J.-P. Bibring, A. Blanco, M. I. Blecka, R. W. Carlson, A. Coradini, A. D. Lellis, T. Encrenaz, S. Erard, S. Fonti, V. Formisano, T. Fouchet, R. Garcia, R. Haus, J. Helbert, N. I. Ignatiev, P. G. J. Irwin, Y. Langevin, S. Lebonnois, M. A. Lopez-Valverde, D. Luz, L. Marinangeli, V. Orofino, A. V. Rodin, M. C. Roos-Serote, B. Saggini, A. Sanchez-Lavega, D. M. Stam, F. W. Taylor, D. Titov, G. Visconti, M. Zambelli, R. Hueso, C. C. C. Tsang, C. F. Wilson, and T. Z. Afanasenko. “Scientific goals for the observation of Venus by VIRTIS on ESA/Venus Express mission”. *Planet. Space Sci.* 55.12 (2007), pp. 1653–1672. DOI: [10.1016/j.pss.2007.01.003](https://doi.org/10.1016/j.pss.2007.01.003) (cit. on pp. 3, 25, 68, 104, 136, 162).
- [Drossart et al., 2013] P. Drossart, G. Piccioni, and ESA. *FTP access to data by Visible and InfraRed Thermal Imaging Spectrometer (VIRTIS)/Venus Express at the Planetary Science Archive (PSA)*. <ftp://psa.esac.esa.int/pub/mirror/VENUS-EXPRESS/VIRTIS/>. 2013 (cit. on pp. 25, 166).

- [Erard and Garceran, 2008] S. Erard and K. Garceran. *VIRTIS VEX geometry files formatting*. LESIA document VVX-LES-SW-2268. Issue 1.2. 2008 (cit. on pp. 14, 71, 87, 88).
- [Erard et al., 2009] S. Erard, P. Drossart, and G. Piccioni. “Multivariate analysis of Visible and Infrared Thermal Imaging Spectrometer (VIRTIS) Venus Express nightside and limb observations”. *J. Geophys. Res.* 114.E9 (2009). E00B27, pp. 1–20. DOI: [10.1029/2008JE003116](https://doi.org/10.1029/2008JE003116) (cit. on pp. 4, 170, 177, 207).
- [Fedorova et al., 2008] A. Fedorova, O. Korablev, A.-C. Vandaele, J.-L. Bertaux, D. Belyaev, A. Mahieux, E. Neefs, W. V. Wilquet, R. Drummond, F. Montmessin, and E. Villard. “HDO and H₂O vertical distributions and isotopic ratio in the Venus mesosphere by Solar Occultation at Infrared spectrometer on board Venus Express”. *J. Geophys. Res.: Planets* 113.E5 (2008). DOI: [10.1029/2008JE003146](https://doi.org/10.1029/2008JE003146) (cit. on pp. 41, 145).
- [Fegley et al., 1997] B. Fegley, G. Klingelhöfer, K. Lodders, and T. Widemann. “Geochemistry of Surface–Atmosphere Interactions on Venus”. In: *Venus II: Geology, Geophysics, Atmosphere, and Solar Wind Environment*. Ed. by S. W. Bougher, D. M. Hunten, and R. J. Phillips. Space science series. University of Arizona Press, Tucson, 1997, pp. 591–636. ISBN: 9780816518302 (cit. on pp. 7, 182).
- [Ford and Pettengill, 1992] P. G. Ford and G. H. Pettengill. “Venus Topography and Kilometer-Scale Slopes”. *J. Geophys. Res.: Planets* 97.E8 (1992), pp. 13103–13114. DOI: [10.1029/92JE01085](https://doi.org/10.1029/92JE01085) (cit. on pp. 2, 21, 56, 88, 149, 151, 162, 166, 168, 207, 208, 210).
- [Gabriel et al., 2004] E. Gabriel, G. E. Fagg, G. Bosilca, T. Angskun, J. J. Dongarra, J. M. Squyres, V. Sahay, P. Kambadur, B. Barrett, A. Lumsdaine, R. H. Castain, D. J. Daniel, R. L. Graham, and T. S. Woodall. “Open MPI: Goals, Concept, and Design of a Next Generation MPI Implementation”. In: *Proceedings, 11th European PVM/MPI Users’ Group Meeting*. Budapest, Hungary, 2004, pp. 97–104 (cit. on p. 134).
- [Gaspari and Cohn, 1999] G. Gaspari and S. E. Cohn. “Construction of correlation functions in two and three dimensions”. *Q. J. Roy. Meteor. Soc.* 125.554 (1999), pp. 723–757. DOI: [10.1002/qj.49712555417](https://doi.org/10.1002/qj.49712555417) (cit. on pp. 110–112, 140).
- [Gelb, 1974] A. Gelb. *Applied Optimal Estimation*. Cambridge, MA., USA: MIT Press, 1974. ISBN: 9780262570480 (cit. on pp. 110, 140).
- [Germogenova, 1986] T. A. Germogenova. “Local properties of solutions to the transport equation”. *Moscow Izdatel'stvo Nauka* (1986). In Russian (cit. on p. 31).
- [Gilmore et al., 2011] M. S. Gilmore, N. Müller, and J. Helbert. “VIRTIS Emissivity of Alpha Regio Tessera, Venus”. In: *Lunar and Planetary Science Conference*. Vol. 42. Lunar and Planetary Science Conference. 2011, p. 1498 (cit. on p. 7).
- [Golub and van Loan, 1996] G. H. Golub and C. F. van Loan. *Matrix computations*. Johns Hopkins studies in the mathematical sciences. Johns Hopkins University Press, 1996. ISBN: 9780801854149 (cit. on pp. 126, 127, 133).
- [Goody and Yung, 1989] R. M. Goody and Y. L. Yung. *Atmospheric Radiation: Theoretical Basis, 2nd Edition*. Oxford University Press, 1989. ISBN: 9780195051343 (cit. on pp. 28–32, 35, 37, 38).
- [Graham, 1981] A. Graham. *Kronecker products and matrix calculus: with applications*. Ellis Horwood series in mathematics and its applications. Horwood, 1981. ISBN: 9780470273005 (cit. on p. 131).
- [Grassi et al., 2010] D. Grassi, A. Migliorini, L. Montabone, S. Lebonnois, A. Cardesin-Moinelo, G. Piccioni, P. Drossart, and L. V. Zasova. “Thermal structure of Venusian nighttime mesosphere as observed by VIRTIS-Venus Express”. *J. Geophys. Res.* 115.E9 (2010). E09007, pp. 1–11. DOI: [10.1029/2009JE003553](https://doi.org/10.1029/2009JE003553) (cit. on p. 4).
- [Grassi et al., 2014] D. Grassi, R. Politi, N. I. Ignatiev, C. Plainaki, S. Lebonnois, P. Wolkenberg, L. Montabone, A. Migliorini, G. Piccioni, and P. Drossart. “The Venus nighttime atmosphere as observed by the VIRTIS-M instrument. Average fields from the complete infrared data set”. *J. Geophys. Res.* 119.4 (2014). 2013JE004586, pp. 837–849. DOI: [10.1002/2013JE004586](https://doi.org/10.1002/2013JE004586) (cit. on p. 4).
- [Grassi et al., 2008] D. Grassi, P. Drossart, G. Piccioni, N. I. Ignatiev, L. V. Zasova, A. Adriani, M. L. Moriconi, P. G. J. Irwin, A. Negrao, and A. Migliorini. “Retrieval of air temperature profiles in the Venusian mesosphere from VIRTIS-M data: Description and validation of algorithms”. *J. Geophys. Res.* 113.E9 (2008). E00B09, pp. 1–12. DOI: [10.1029/2008JE003075](https://doi.org/10.1029/2008JE003075) (cit. on p. 4).
- [Grieger et al., 2004] B. Grieger, N. I. Ignatiev, N. M. Hoekzema, and H. U. Keller. “Indication of a near surface cloud layer on Venus from reanalysis of Venera 13/14 spectrophotometer data”. In: *Planetary Probe Atmospheric Entry and Descent Trajectory Analysis and Science*. Ed. by A. Wilson. Vol. 544. ESA Special Publication. 2004, pp. 63–70. ISBN: 92-9092-855-7 (cit. on pp. 4, 160, 170, 177).
- [Grinspoon and Bullock, 2003] D. H. Grinspoon and M. A. Bullock. “Did Venus Experience One Great Transition or Two?” In: *AAS/Division for Planetary Sciences Meeting Abstracts*. Vol. 35. Bulletin of the American Astronomical Society. 2003, p. 1007 (cit. on p. 7).
- [Gropp et al., 1999] W. Gropp, E. Lusk, and A. Skjellum. *Using MPI: portable parallel programming with the message-passing interface*. Scientific and engineering computation. MIT Press, 1999. ISBN: 9780262571326 (cit. on p. 134).

- [Guest and Stofan, 1999] J. E. Guest and E. R. Stofan. “A New View of the Stratigraphic History of Venus”. *Icarus* 139.1 (1999), pp. 55–66. doi: [10.1006/icar.1999.6091](https://doi.org/10.1006/icar.1999.6091) (cit. on p. 6).
- [Hansen and Hovenier, 1974] J. E. Hansen and J. W. Hovenier. “Interpretation of the Polarization of Venus”. *J. Atmos. Sci.* 31.4 (1974). doi:[10.1175/1520-0469\(1974\)031<1137:IOTPOV>2.0.CO;2](https://doi.org/10.1175/1520-0469(1974)031<1137:IOTPOV>2.0.CO;2), pp. 1137–1160 (cit. on p. 47).
- [Hansen and Travis, 1974] J. E. Hansen and L. D. Travis. “Light scattering in planetary atmospheres”. English. *Space Sci. Rev.* 16.4 (1974), pp. 527–610. doi: [10.1007/BF00168069](https://doi.org/10.1007/BF00168069) (cit. on pp. 51–53, 117, 145, 168).
- [Hartmann et al., 1988] J. M. Hartmann, L. Rosenmann, M. Y. Perrin, and J. Taine. “Accurate calculated tabulations of CO line broadening by H₂O, N₂, O₂, and CO₂ in the 200–3000-K temperature range”. *Appl. Opt.* 27.15 (1988), pp. 3063–3065. doi: [10.1364/AO.27.003063](https://doi.org/10.1364/AO.27.003063) (cit. on p. 37).
- [Hartmann et al., 2008] J. M. Hartmann, C. Boulet, and D. Robert. *Collisional Effects on Molecular Spectra: Laboratory experiments and models, consequences for applications*. Elsevier Science, 2008. ISBN: 9780080569949 (cit. on pp. 39, 40).
- [Hashimoto and Imamura, 2001] G. L. Hashimoto and T. Imamura. “Elucidating the Rate of Volcanism on Venus: Detection of Lava Eruptions Using Near-Infrared Observations”. *Icarus* 154.2 (2001), pp. 239–243. doi: [10.1006/icar.2001.6713](https://doi.org/10.1006/icar.2001.6713) (cit. on p. 4).
- [Hashimoto and Sugita, 2003] G. L. Hashimoto and S. Sugita. “On observing the compositional variability of the surface of Venus using nightside near-infrared thermal radiation”. *J. Geophys. Res.: Planets* 108.E9 (2003), p. 5109. doi: [10.1029/2003JE002082](https://doi.org/10.1029/2003JE002082) (cit. on pp. 5, 189).
- [Hashimoto et al., 2008] G. L. Hashimoto, M. Roos-Serote, S. Sugita, M. S. Gilmore, L. W. Kamp, R. W. Carlson, and K. H. Baines. “Felsic highland crust on Venus suggested by Galileo Near-Infrared Mapping Spectrometer data”. *J. Geophys. Res.* 113.E5 (2008), pp. 1–10. doi: [10.1029/2008JE003134](https://doi.org/10.1029/2008JE003134) (cit. on pp. 5–7, 207, 208).
- [Haus and Titov, 2000] R. Haus and D. V. Titov. “PFS on Mars Express: preparing the analysis of infrared spectra to be measured by the Planetary Fourier Spectrometer”. *Planet. Space Sci.* 48.12–14 (2000). Mars Exploration Program, pp. 1357–1376. doi: [10.1016/S0032-0633\(00\)00116-1](https://doi.org/10.1016/S0032-0633(00)00116-1) (cit. on p. 35).
- [Haus and Arnold, 2010] R. Haus and G. Arnold. “Radiative transfer in the atmosphere of Venus and application to surface emissivity retrieval from VIRTIS/VEX measurements”. *Planet. Space Sci.* 58.12 (2010), pp. 1578–1598. doi: [10.1016/j.pss.2010.08.001](https://doi.org/10.1016/j.pss.2010.08.001) (cit. on pp. 2, 4, 6, 8, 35, 39, 41, 43, 55, 57, 68, 69, 91, 93–99, 104, 116, 117, 123, 136, 138, 145–148, 151, 157, 160, 163, 164, 167, 168, 187, 189, 203, 204, 208).
- [Haus et al., 2013] R. Haus, D. Kappel, and G. Arnold. “Self-consistent retrieval of temperature profiles and cloud structure in the northern hemisphere of Venus using VIRTIS/VEX and PMV/VENERA-15 radiation measurements”. *Planet. Space Sci.* 89 (2013), pp. 77–101. doi: [10.1016/j.pss.2013.09.020](https://doi.org/10.1016/j.pss.2013.09.020) (cit. on pp. 4, 14, 26, 39–42, 46–49, 53, 117, 143, 145, 147, 148, 151, 159, 167, 169).
- [Haus et al., 2014] R. Haus, D. Kappel, and G. Arnold. “Atmospheric thermal structure and cloud features in the southern hemisphere of Venus as retrieved from VIRTIS/VEX radiation measurements”. *Icarus* 232 (2014), pp. 232–248. doi: [10.1016/j.icarus.2014.01.020](https://doi.org/10.1016/j.icarus.2014.01.020) (cit. on pp. 4, 14, 26, 42, 47–49, 53, 143, 145, 148, 167, 169).
- [Haus et al., 2015a] R. Haus, D. Kappel, and G. Arnold. “Lower atmosphere minor gas abundances as retrieved from Venus Express VIRTIS-M-IR data at 2.3 μm”. *Planet. Space Sci.* 105 (2015), pp. 159–174. doi: [10.1016/j.pss.2014.11.020](https://doi.org/10.1016/j.pss.2014.11.020) (cit. on pp. 4, 147, 173, 177).
- [Haus et al., 2015b] R. Haus, D. Kappel, and G. Arnold. “Radiative heating and cooling in the middle and lower atmosphere of Venus and responses to atmospheric and spectroscopic parameter variations”. *Planet. Space Sci.* 117 (2015), pp. 262–294. doi: [10.1016/j.pss.2015.06.024](https://doi.org/10.1016/j.pss.2015.06.024) (cit. on p. 4).
- [Hayward, 2015] R. Hayward. *Gazetteer of Planetary Nomenclature, International Astronomical Union (IAU) Working Group for Planetary System Nomenclature (WGPSN)*. <http://planetarynames.wr.usgs.gov/Page/VENUS/target>. 2015 (cit. on p. 164).
- [Helbert et al., 2008] J. Helbert, N. Müller, P. Kostama, L. Marinangeli, G. Piccioni, and P. Drossart. “Surface brightness variations seen by VIRTIS on Venus Express and implications for the evolution of the Lada Terra region, Venus”. *Geophys. Res. Lett.* 35.11 (2008). L11201, pp. 1–5. doi: [10.1029/2008GL033609](https://doi.org/10.1029/2008GL033609) (cit. on pp. 5, 7, 163, 207).
- [Herrick et al., 1997] R. R. Herrick, V. L. Sharpton, M. C. Malin, S. N. Lyons, and K. Feely. “Morphology and Morphometry of Impact Craters”. In: *Venus II: Geology, Geophysics, Atmosphere, and Solar Wind Environment*. Ed. by S. W. Bougher, D. M. Hunten, and R. J. Phillips. Space science series. University of Arizona Press, Tucson, 1997, pp. 1015–1046. ISBN: 9780816518302 (cit. on p. 7).
- [Hogben, 2006] L. Hogben. *Handbook of Linear Algebra*. Discrete Mathematics and Its Applications. CRC Press, 2006. ISBN: 9781420010572 (cit. on p. 193).
- [Horn and Johnson, 1990] R. A. Horn and C. R. Johnson. *Matrix Analysis*. Cambridge University Press, 1990. ISBN: 0521386322 (cit. on pp. 108, 113, 115, 130).

- [Horn and Johnson, 1991] R. A. Horn and C. R. Johnson. *Topics in Matrix Analysis*. Cambridge: Cambridge University Press, 1991. ISBN: 0-521-30587-X (cit. on pp. 113, 114, 127).
- [Humlíček, 1982] J. Humlíček. “Optimized computation of the Voigt and complex probability functions”. *J. Quant. Spectrosc. Rad.* 27.4 (1982), pp. 437–444. doi: 10.1016/0022-4073(82)90078-4 (cit. on p. 38).
- [Ignatiev et al., 2009] N. I. Ignatiev, D. V. Titov, G. Piccioni, P. Drossart, W. J. Markiewicz, V. Cottini, T. Roatsch, M. Almeida, and N. Manoel. “Altimetry of the Venus cloud tops from the Venus Express observations”. *J. Geophys. Res.* 114.E9 (2009), E00B43. doi: 10.1029/2008JE003320 (cit. on pp. 4, 47, 48, 87, 148, 149).
- [Imamura and Hashimoto, 2001] T. Imamura and G. L. Hashimoto. “Microphysics of Venusian Clouds in Rising Tropical Air”. *J. Atmos. Sci.* 58.23 (2001). doi:10.1175/1520-0469(2001)058<3597:MOVCI>2.0.CO;2, pp. 3597–3612 (cit. on pp. 148, 173).
- [Ivanov and Head, 2006] M. A. Ivanov and J. W. Head. *Geologic map of the Mylitta Fluctus Quadrangle (V-61), Venus*. <http://pubs.usgs.gov/sim/2006/2920/>. US Geological Survey Scientific Investigations Map 2920, 2006 (cit. on pp. 151, 207).
- [Ivanov and Head, 2011] M. A. Ivanov and J. W. Head. “Global geological map of Venus”. *Planet. Space Sci.* 59.13 (2011), pp. 1559–1600. doi: 10.1016/j.pss.2011.07.008 (cit. on pp. 6, 136, 207).
- [Jackson, 1975] J. D. Jackson. *Classical electrodynamics*. Wiley, 1975. ISBN: 9780471431329 (cit. on p. 45).
- [James et al., 1997] E. P. James, O. B. Toon, and G. Schubert. “A Numerical Microphysical Model of the Condensational Venus Cloud”. *Icarus* 129.1 (1997), pp. 147–171. doi: 10.1006/icar.1997.5763 (cit. on pp. 45, 49, 50, 182).
- [Jolliffe, 2002] I. T. Jolliffe. *Principal Component Analysis*. 2nd. Springer, 2002. ISBN: 0387954422 (cit. on p. 86).
- [Kamp and Taylor, 1990] L. W. Kamp and F. W. Taylor. “Radiative-transfer models of the night side of Venus”. *Icarus* 86.2 (1990), pp. 510–529. doi: 10.1016/0019-1035(90)90231-W (cit. on p. 3).
- [Kappel et al., 2010a] D. Kappel, G. Arnold, and R. Haus. “Multispectrum retrieval techniques applied to Venus deep atmosphere and surface problems”. In: *38th COSPAR Scientific Assembly*. C33-0008-10. 2010 (cit. on pp. 8, 69, 105, 204).
- [Kappel et al., 2010b] D. Kappel, G. Arnold, R. Haus, G. Piccioni, and P. Drossart. “Results from multispectrum retrieval of VIRTIS-M-IR measurements of Venus’ nightside”. In: *EPSC Abstracts Vol. 5, European Planetary Science Congress 2010*. EPSC2010-390. 2010 (cit. on pp. 8, 69, 105, 204).
- [Kappel et al., 2012a] D. Kappel, G. Arnold, and R. Haus. “Sensitivity of Venus surface emissivity retrieval to model variations of CO₂ opacity, cloud features, and deep atmosphere temperature field”. In: *39th COSPAR Scientific Assembly*. B0.8-0008-12. 2012 (cit. on pp. 107, 124, 138).
- [Kappel et al., 2012b] D. Kappel, G. Arnold, R. Haus, G. Piccioni, and P. Drossart. “Refinements in the data analysis of VIRTIS-M-IR Venus nightside spectra”. *Adv. Space Res.* 50.2 (2012), pp. 228–255. doi: 10.1016/j.asr.2012.03.029 (cit. on pp. 8, 11–14, 16, 17, 25–27, 40, 64, 104–106, 116, 119–121, 125, 136–138, 143, 145, 149–152, 156, 158, 160, 164, 166–168, 172, 177, 183, 184, 189, 193, 204).
- [Kappel et al., 2012c] D. Kappel, G. Arnold, and R. Haus. “Retrieval of Surface Emissivity in a Venus Coordinate Patch as Parameter Common to Repeated Measurements by VIRTIS/VEX”. In: *EGU General Assembly 2012*. Vol. 14. 2012, p. 9708 (cit. on pp. 8, 105, 119, 137, 204).
- [Kappel, 2014] D. Kappel. “MSR, a multi-spectrum retrieval technique for spatially-temporally correlated or common Venus surface and atmosphere parameters”. *J. Quant. Spectrosc. Rad.* 133 (2014), pp. 153–176. doi: 10.1016/j.jqsrt.2013.07.025 (cit. on pp. 8, 11, 12, 14, 15, 40, 61, 65, 137, 140, 142, 143, 145, 148, 149, 151–153, 159, 163, 164, 167–169, 172, 173, 189, 204).
- [Kappel et al., 2015] D. Kappel, R. Haus, and G. Arnold. “Error analysis for retrieval of Venus’ IR surface emissivity from VIRTIS/VEX measurements”. *Planet. Space Sci.* 113–114 (2015). SI:Exploration of Venus, pp. 49–65. doi: 10.1016/j.pss.2015.01.014 (cit. on pp. 8, 11, 12, 14, 17, 20, 21, 41, 66, 163, 164, 167–174, 176–178, 182, 186, 187, 190, 192, 197, 198, 204, 211).
- [Kappel et al., 2016] D. Kappel, G. Arnold, and R. Haus. “Multi-spectrum retrieval of Venus IR surface emissivity maps from VIRTIS/VEX nightside measurements at Themis Regio”. *Icarus* 265 (2016), pp. 42–62. doi: 10.1016/j.icarus.2015.10.014 (cit. on pp. 5, 8, 14, 19, 20, 23, 41, 54, 55, 66, 204, 211).
- [Karypis and Kumar, 1998] G. Karypis and V. Kumar. “A Fast and High Quality Multilevel Scheme for Partitioning Irregular Graphs”. *SIAM J. Sci. Comput.* 20.1 (1998), pp. 359–392. doi: 10.1137/S1064827595287997 (cit. on p. 133).
- [Kasting, 1988] J. F. Kasting. “Runaway and moist greenhouse atmospheres and the evolution of Earth and Venus”. *Icarus* 74.3 (1988), pp. 472–494. doi: 10.1016/0019-1035(88)90116-9 (cit. on p. 7).
- [Kasting et al., 1984] J. F. Kasting, J. B. Pollack, and T. P. Ackerman. “Response of Earth’s atmosphere to increases in solar flux and implications for loss of water from Venus”. *Icarus* 57.3 (1984), pp. 335–355. doi: 10.1016/0019-1035(84)90122-2 (cit. on p. 7).

- [Knollenberg and Hunten, 1980] R. G. Knollenberg and D. M. Hunten. “The microphysics of the clouds of Venus: Results of the Pioneer Venus Particle Size Spectrometer Experiment”. *J. Geophys. Res.: Space Physics* 85.A13 (1980), pp. 8039–8058. doi: [10.1029/JA085iA13p08039](https://doi.org/10.1029/JA085iA13p08039) (cit. on pp. 46, 148, 169, 187).
- [Knyazikhin and Myneni, 2004] Y. Knyazikhin and R. B. Myneni. *Physical models in remote sensing. Lecture Notes GG 645, Climate and Vegetation Research Group, Dept. of Geography, Boston University*. <http://cliveg.bu.edu/courses/gg645fall104/chap01/chap01.pdf>. 2004 (cit. on p. 31).
- [Konopliv et al., 1999] A. S. Konopliv, W. B. Banerdt, and W. L. Sjogren. “Venus Gravity: 180th Degree and Order Model”. *Icarus* 139.1 (1999), pp. 3–18. doi: [10.1006/icar.1999.6086](https://doi.org/10.1006/icar.1999.6086) (cit. on p. 2).
- [Krasnopolsky et al., 2013] V. A. Krasnopolsky, D. A. Belyaev, I. E. Gordon, G. Li, and L. S. Rothman. “Observations of D/H ratios in H₂O, HCl, and HF on Venus and new DCl and DF line strengths”. *Icarus* 224 (2013), pp. 57–65. doi: [10.1016/j.icarus.2013.02.010](https://doi.org/10.1016/j.icarus.2013.02.010) (cit. on pp. 41, 145).
- [Kurucz, 1995] R. L. Kurucz. “The Solar Irradiance by Computation”. In: *Proceedings of the 17th Annual Review Conference on Atmospheric Transmission Models, 8-9 June 1994*. Air Force Geophys. Lab., Hanscom AFB, MA 01731. <http://kurucz.harvard.edu/papers/irradiance/solarirr.tab>. 1995 (cit. on p. 31).
- [Lebonnois et al., 2010a] S. Lebonnois, F. Hourdin, F. Forget, V. Eymet, and R. Fournier. “The LMD Venus General Circulation Model: Improvements and Questions”. In: *International Venus Conference, Aussois, France 20–26 June 2010*. http://lesia.obspm.fr/venus2010/sites/venus2010/IMG/pdf/04-04_Lebonnois.pdf. 2010 (cit. on pp. 119, 146).
- [Lebonnois et al., 2010b] S. Lebonnois, F. Hourdin, V. Eymet, A. Cresspin, R. Fournier, and F. Forget. “Superrotation of Venus’ atmosphere analyzed with a full general circulation model”. *J. Geophys. Res.* 115.E6 (2010). E06006, pp. 1–23. doi: [10.1029/2009JE003458](https://doi.org/10.1029/2009JE003458) (cit. on pp. 1, 4, 167).
- [Lecacheux et al., 1993] J. Lecacheux, P. Drossart, P. Laques, F. Deladerriere, and F. Colas. “Detection of the surface of Venus at 1.0 μm from ground-based observations”. *Planet. Space Sci.* 41.7 (1993). Special Issue: The Galileo Venus Encounter: NIMS Results, pp. 543–549. doi: [10.1016/0032-0633\(93\)90035-Z](https://doi.org/10.1016/0032-0633(93)90035-Z) (cit. on p. 3).
- [Lee et al., 2012] Y. J. Lee, D. V. Titov, S. Tellmann, A. Piccialli, N. Ignatiev, M. Pätzold, B. Häusler, G. Piccioni, and P. Drossart. “Vertical structure of the Venus cloud top from the VeRa and VIRTIS observations onboard Venus Express”. *Icarus* 217.2 (2012). Advances in Venus Science, pp. 599–609. doi: [10.1016/j.icarus.2011.07.001](https://doi.org/10.1016/j.icarus.2011.07.001) (cit. on p. 48).
- [Letchworth and Benner, 2007] K. L. Letchworth and D. C. Benner. “Rapid and accurate calculation of the Voigt function”. *J. Quant. Spectrosc. Rad.* 107.1 (2007), pp. 173–192. doi: [10.1016/j.jqsrt.2007.01.052](https://doi.org/10.1016/j.jqsrt.2007.01.052) (cit. on p. 41).
- [Limaye and Smrekar, 2010] S. Limaye and S. Smrekar. “Venus Exploration Analysis Group (VEXAG)”. In: *EGU General Assembly Conference Abstracts*. Vol. 12. EGU General Assembly Conference Abstracts. 2010, p. 7597 (cit. on p. 19).
- [Liou, 2002] K. N. Liou. *An Introduction to Atmospheric Radiation, 2nd Edition*. International Geophysics Series. Academic Press, 2002. ISBN: 9780124514515 (cit. on pp. 4, 27, 31, 32, 35, 44, 49–52).
- [Marcq et al., 2006] E. Marcq, T. Encrenaz, B. Bézard, and M. Birlan. “Remote sensing of Venus’ lower atmosphere from ground-based IR spectroscopy: Latitudinal and vertical distribution of minor species”. *Planet. Space Sci.* 54.13–14 (2006), pp. 1360–1370. doi: [10.1016/j.pss.2006.04.024](https://doi.org/10.1016/j.pss.2006.04.024) (cit. on pp. 4, 69, 104).
- [Marcq et al., 2008] E. Marcq, B. Bézard, P. Drossart, G. Piccioni, J. M. Reess, and F. Henry. “A latitudinal survey of CO, OCS, H₂O, and SO₂ in the lower atmosphere of Venus: Spectroscopic studies using VIRTIS-H”. *J. Geophys. Res.* 113.E5 (2008). E00B07, pp. 1–9. doi: [10.1029/2008JE003074](https://doi.org/10.1029/2008JE003074) (cit. on p. 4).
- [Marcq et al., 2005] E. Marcq, B. Bézard, T. Encrenaz, and M. Birlan. “Latitudinal variations of CO and OCS in the lower atmosphere of Venus from near-infrared nightside spectro-imaging”. *Icarus* 179.2 (2005), pp. 375–386. doi: [10.1016/j.icarus.2005.06.018](https://doi.org/10.1016/j.icarus.2005.06.018) (cit. on p. 4).
- [Markiewicz et al., 2007] W. J. Markiewicz, D. V. Titov, N. Ignatiev, H. U. Keller, D. Crisp, S. S. Limaye, R. Jaumann, R. Moissl, N. Thomas, L. Esposito, S. Watanabe, B. Fiethe, T. Behnke, I. Szemerey, H. Michalik, H. Perplies, M. Wedemeier, I. Sebastian, W. Boogaerts, S. F. Hviid, C. Dierker, B. Osterloh, W. Böker, M. Koch, H. Michaelis, D. Belyaev, A. Dannenberg, M. Tschimmel, P. Russo, T. Roatsch, and K. D. Matz. “Venus Monitoring Camera for Venus Express”. *Planet. Space Sci.* 55.12 (2007). In: *The Planet Venus and the Venus Express Mission, Part 2*, pp. 1701–1711. doi: [10.1016/j.pss.2007.01.004](https://doi.org/10.1016/j.pss.2007.01.004) (cit. on pp. 5, 207).
- [Markiewicz et al., 2014] W. J. Markiewicz, E. Petrova, O. Shalygina, M. Almeida, D. V. Titov, S. S. Limaye, N. Ignatiev, T. Roatsch, and K. D. Matz. “Glory on Venus cloud tops and the unknown UV absorber”. *Icarus* 234.0 (2014), pp. 200–203. doi: [10.1016/j.icarus.2014.01.030](https://doi.org/10.1016/j.icarus.2014.01.030) (cit. on pp. 1, 47).
- [Marov et al., 1980] M. Y. Marov, V. E. Lystsev, V. N. Lebedev, N. L. Lukashevich, and V. P. Shari. “The structure and microphysical properties of the Venus clouds: Venera 9, 10, and 11 data”. *Icarus* 44.3 (1980), pp. 608–639. doi: [10.1016/0019-1035\(80\)90131-1](https://doi.org/10.1016/0019-1035(80)90131-1) (cit. on pp. 117, 145, 148, 167, 169, 187).

- [Marquardt, 1963] D. W. Marquardt. “An Algorithm for Least-Squares Estimation of Nonlinear Parameters”. *J. Soc. Ind. Appl. Math.* 11.2 (1963), pp. 431–441. doi: [10.2307/2098941](https://doi.org/10.2307/2098941) (cit. on p. 63).
- [Maturilli et al., 2008] A. Maturilli, J. Helbert, and L. Moroz. “The Berlin emissivity database (BED)”. *Planet. Space Sci.* 56.3–4 (2008), pp. 420–425. doi: [10.1016/j.pss.2007.11.015](https://doi.org/10.1016/j.pss.2007.11.015) (cit. on p. 211).
- [McKinnon et al., 1997] W. B. McKinnon, K. J. Zahnle, B. A. Ivanov, and H. J. Melosh. “Cratering on Venus: models and observations”. In: *Venus II: Geology, Geophysics, Atmosphere, and Solar Wind Environment*. Ed. by S. W. Bougher, D. M. Hunten, and R. J. Phillips. Space science series. University of Arizona Press, Tucson, 1997, pp. 969–1014. ISBN: 9780816518302 (cit. on p. 7).
- [Meadows and Crisp, 1996] V. S. Meadows and D. Crisp. “Ground-based near-infrared observations of the Venus nightside: The thermal structure and water abundance near the surface”. *J. Geophys. Res.* 101.E2 (1996), pp. 4595–4622. doi: [10.1029/95JE03567](https://doi.org/10.1029/95JE03567) (cit. on pp. 5, 10, 69, 104, 105, 136, 207).
- [Miller and Samko, 2001] K. S. Miller and S. G. Samko. “Completely monotonic functions”. *Integr. Transf. Spec. F.* 12.4 (2001), pp. 389–402. doi: [10.1080/10652460108819360](https://doi.org/10.1080/10652460108819360) (cit. on p. 110).
- [Mlawer et al., 2003] E. J. Mlawer, D. C. Tobin, and S. A. Clough. “A new water vapor continuum model: MT_CKD_1.0”. In: *Proceedings of the Thirteenth Atmospheric Radiation Measurement (ARM) Science Team Meeting*. http://www.arm.gov/publications/proceedings/conf13/poster_abs/P00225. 2003 (cit. on p. 40).
- [Moré, 1978] J. Moré. “The Levenberg-Marquardt algorithm: Implementation and theory”. In: *Numerical Analysis*. Ed. by G. A. Watson. Vol. 630. Lecture Notes in Mathematics. Springer Berlin Heidelberg, 1978. Chap. 10, pp. 105–116. ISBN: 978-3-540-08538-6. doi: [10.1007/BFb0067700](https://doi.org/10.1007/BFb0067700) (cit. on pp. 11, 16, 63, 126, 133, 137).
- [Moroz, 2002] V. I. Moroz. “Estimates of visibility of the surface of Venus from descent probes and balloons”. *Planet. Space Sci.* 50.3 (2002), pp. 287–297. doi: [10.1016/S0032-0633\(01\)00128-3](https://doi.org/10.1016/S0032-0633(01)00128-3) (cit. on pp. 4, 5, 10, 56, 87, 88, 90, 119, 136, 139, 149, 162, 166, 173, 211).
- [Moroz et al., 1985] V. I. Moroz, V. M. Linkin, and D. Oertel. “The results of an infrared experiment on Venera-15 and -16”. *Sov. Phys. Usp.* 28.6 (1985), pp. 524–525. doi: [10.1070/PU1985v028n06ABEH005208](https://doi.org/10.1070/PU1985v028n06ABEH005208) (cit. on p. 4).
- [Müller et al., 2008] N. Müller, J. Helbert, G. L. Hashimoto, C. C. C. Tsang, S. Erard, G. Piccioni, and P. Drossart. “Venus surface thermal emission at 1 μm in VIRTIS imaging observations: Evidence for variation of crust and mantle differentiation conditions”. *J. Geophys. Res.* 113.E5 (2008), E00B17. doi: [10.1029/2008JE003118](https://doi.org/10.1029/2008JE003118) (cit. on pp. 5, 7, 14, 17, 87–89, 125, 151, 152, 163, 164, 166, 189, 207, 208, 210).
- [Müller et al., 2012a] N. Müller, J. Helbert, E. R. Stofan, S. E. Smrekar, G. Piccioni, and P. Drossart. “Search for active lava flows with VIRTIS on Venus Express”. In: *American Geophysical Union, 45th Fall Meeting*. 2012, P24B–02 (cit. on pp. 5, 119, 142, 163, 169).
- [Müller et al., 2012b] N. T. Müller, J. Helbert, S. Erard, G. Piccioni, and P. Drossart. “Rotation period of Venus estimated from Venus Express VIRTIS images and Magellan altimetry”. *Icarus* 217.2 (2012). In: *Advances in Venus Science*, pp. 474–483. doi: [10.1016/j.icarus.2011.09.026](https://doi.org/10.1016/j.icarus.2011.09.026) (cit. on pp. 5, 87, 88, 163).
- [Nakamura et al., 2007] M. Nakamura, T. Imamura, M. Ueno, N. Iwagami, T. Satoh, S. Watanabe, M. Taguchi, Y. Takahashi, M. Suzuki, T. Abe, G. L. Hashimoto, T. Sakanoi, S. Okano, Y. Kasaba, J. Yoshida, M. Yamada, N. Ishii, T. Yamada, K. Uemizu, T. Fukuhara, and K. Oyama. “Planet-C: Venus Climate Orbiter mission of Japan”. *Planet. Space Sci.* 55.12 (2007). In: *The Planet Venus and the Venus Express Mission, Part 2*, pp. 1831–1842. doi: [10.1016/j.pss.2007.01.009](https://doi.org/10.1016/j.pss.2007.01.009) (cit. on pp. 3, 19, 211).
- [Nikolaeva et al., 1992] O. V. Nikolaeva, M. A. Ivanov, and V. K. Borozdin. “Evidence on the crustal dichotomy [of Venus]”. In: *Venus Geology, Geochemistry, and Geophysics - Research results from the USSR (A 92-39726 16-91)*. Ed. by V. L. Barsukov, A. T. Basilevsky, V. P. Volkov, and V. N. Zharkov. University of Arizona Press, Tucson, 1992, pp. 129–139 (cit. on p. 7).
- [Niro et al., 2007] F. Niro, G. Brizzi, M. Carlotti, E. Papandrea, and M. Ridolfi. “Precision improvements in the geofit retrieval of pressure and temperature from MIPAS limb observations by modeling CO₂ line-mixing”. *J. Quant. Spectrosc. Rad.* 103.1 (2007), pp. 14–26. doi: [10.1016/j.jqsrt.2006.07.012](https://doi.org/10.1016/j.jqsrt.2006.07.012) (cit. on p. 8).
- [Nocedal and Wright, 1999] J. Nocedal and S. J. Wright. *Numerical Optimization*. Springer Series in Operations Research. Springer, 1999. ISBN: 9780387987934 (cit. on pp. 127, 172).
- [Olivero and Longbothum, 1977] J. J. Olivero and R. L. Longbothum. “Empirical fits to the Voigt line width: A brief review”. *J. Quant. Spectrosc. Rad.* 17.2 (1977), pp. 233–236. doi: [10.1016/0022-4073\(77\)90161-3](https://doi.org/10.1016/0022-4073(77)90161-3) (cit. on p. 38).
- [Palmer and Williams, 1975] K. F. Palmer and D. Williams. “Optical Constants of Sulfuric Acid; Application to the Clouds of Venus?” *Appl. Opt.* 14.1 (1975), pp. 208–219. doi: [10.1364/AO.14.000208](https://doi.org/10.1364/AO.14.000208) (cit. on pp. 45, 46, 50, 117, 147, 169).
- [Papoulis, 1991] A. Papoulis. *Probability, Random Variables and Stochastic Processes*. 3rd. McGraw-Hill Companies, 1991. ISBN: 0070484775 (cit. on p. 47).

- [Pettengill et al., 1980] G. H. Pettengill, E. Eliason, P. G. Ford, G. B. Lorient, H. Masursky, and G. E. McGill. “Pioneer Venus Radar results altimetry and surface properties”. *J. Geophys. Res.: Space Physics* 85.A13 (1980), pp. 8261–8270. doi: [10.1029/JA085iA13p08261](https://doi.org/10.1029/JA085iA13p08261) (cit. on p. 5).
- [Pettengill et al., 1991] G. H. Pettengill, P. G. Ford, W. T. K. Johnson, R. K. Raney, and L. A. Soderblom. “Magellan: Radar Performance and Data Products”. *Science* 252.5003 (1991), pp. 260–265. doi: [10.1126/science.252.5003.260](https://doi.org/10.1126/science.252.5003.260) (cit. on pp. 2, 56, 104, 136, 151, 162, 207, 208).
- [Pettengill et al., 1992] G. H. Pettengill, P. G. Ford, and R. J. Wilt. “Venus surface radiothermal emission as observed by Magellan”. *J. Geophys. Res.: Planets* 97.E8 (1992), pp. 13091–13102. doi: [10.1029/92JE01356](https://doi.org/10.1029/92JE01356) (cit. on p. 2).
- [Piccioni et al., 2007] G. Piccioni, P. Drossart, A. Sanchez-Lavega, R. Hueso, F. W. Taylor, C. F. Wilson, D. Grassi, L. Zasova, M. Moriconi, A. Adriani, S. Lebonnois, A. Coradini, B. Bézard, F. Angrilli, G. Arnold, K. H. Baines, G. Bellucci, J. Benkhoff, J. P. Bibring, A. Blanco, M. I. Blecka, R. W. Carlson, A. Di Lellis, T. Encrenaz, S. Erard, S. Fonti, V. Formisano, T. Fouchet, R. Garcia, R. Haus, J. Helbert, N. I. Ignatiev, P. G. J. Irwin, Y. Langevin, M. A. Lopez-Valverde, D. Luz, L. Marinangeli, V. Orofino, A. V. Rodin, M. C. Roos-Serote, B. Saggin, D. M. Stam, D. Titov, G. Visconti, and M. Zambelli. “South-polar features on Venus similar to those near the north pole”. *Nature* 450.7170 (2007), pp. 637–640. doi: [10.1038/nature06209](https://doi.org/10.1038/nature06209) (cit. on pp. 3, 136, 162).
- [Piccioni et al., 2009] G. Piccioni, L. Zasova, A. Migliorini, P. Drossart, A. Shakun, A. Garcia Munoz, F. P. Mills, and A. Cardesin-Moinelo. “Near-IR oxygen nightglow observed by VIRTIS in the Venus upper atmosphere”. *J. Geophys. Res.: Planets* 114.E5 (2009). doi: [10.1029/2008JE003133](https://doi.org/10.1029/2008JE003133) (cit. on pp. 30, 55, 117, 136, 145, 167).
- [Pieters et al., 2015] C. M. Pieters, T. Hiroi, and B. Patterson. *RELAB: Keck/NASA Reflectance Experiment Laboratory*. <http://www.planetary.brown.edu/relab/>. 2015 (cit. on p. 7).
- [Plateaux et al., 2001] J.-J. Plateaux, L. Regalia, C. Boussin, and A. Barbe. “Multispectrum fitting technique for data recorded by Fourier transform spectrometer: application to N₂O and CH₃D”. *J. Quant. Spectrosc. Rad.* 68.5 (2001), pp. 507–520. doi: [10.1016/S0022-4073\(00\)00040-6](https://doi.org/10.1016/S0022-4073(00)00040-6) (cit. on p. 8).
- [Plesa, 2008] A.-C. Plesa. “Vergleich der Levenberg-Marquardt-Methode mit der Powell-Dog-Leg-Methode in nicht-linearen Ausgleichsproblemen”. In German. MA thesis. Universität Passau, 2008 (cit. on p. 64).
- [Pollack et al., 1993] J. B. Pollack, J. B. Dalton, D. Grinspoon, R. B. Wattson, R. Freedman, D. Crisp, D. A. Allen, B. Bézard, C. DeBergh, L. P. Giver, Q. Ma, and R. Tipping. “Near-Infrared Light from Venus’ Nightside: A Spectroscopic Analysis”. *Icarus* 103.1 (1993), pp. 1–42. doi: [10.1006/icar.1993.1055](https://doi.org/10.1006/icar.1993.1055) (cit. on pp. 3, 10, 39–41, 43, 47–49, 69, 91, 104, 105, 117, 136, 145, 147, 168, 169).
- [Rappaport et al., 1999] N. J. Rappaport, A. S. Konopliv, A. B. Kucinskas, and P. G. Ford. “An Improved 360 Degree and Order Model of Venus Topography”. *Icarus* 139.1 (1999), pp. 19–31. doi: [10.1006/icar.1999.6081](https://doi.org/10.1006/icar.1999.6081) (cit. on pp. 2, 21, 27, 56, 88, 149, 166, 168, 208, 210).
- [Reed and Simon, 1975] M. Reed and B. Simon. *II: Fourier analysis, self-adjointness*. Methods of Modern Mathematical Physics. Academic Press, 1975. ISBN: 9780125850025 (cit. on p. 111).
- [Reed and Simon, 1981] M. Reed and B. Simon. *I: Functional Analysis*. Methods of Modern Mathematical Physics. Academic Press, 1981. ISBN: 0125850506 (cit. on p. 130).
- [Rodgers, 2000] C. D. Rodgers. *Inverse Methods for Atmospheric Sounding: Theory and Practice (Series on Atmospheric, Oceanic and Planetary Physics)*. Singapore: World Scientific Publishing Company, 2000. ISBN: 981022740X (cit. on pp. 11, 63, 64, 66, 69, 105–107, 113, 137).
- [Rothman et al., 2009] L. S. Rothman, I. E. Gordon, A. Barbe, D. C. Benner, P. F. Bernath, M. Birk, V. Boudon, L. R. Brown, A. Campargue, J.-P. Champion, K. Chance, L. H. Coudert, V. Dana, V. M. Devi, S. Fally, J.-M. Flaud, R. R. Gamache, A. Goldman, D. Jacquemart, I. Kleiner, N. Lacome, W. J. Lafferty, J.-Y. Mandin, S. T. Massie, S. N. Mikhailenko, C. E. Miller, N. Moazzen-Ahmadi, O. V. Naumenko, A. V. Nikitin, J. Orphal, V. I. Perevalov, A. Perrin, A. Predoi-Cross, C. P. Rinsland, M. Rotger, M. Simeckova, M. A. H. Smith, K. Sung, S. A. Tashkun, J. Tennyson, R. A. Toth, A. C. Vandaele, and J. V. Auwera. “The HITRAN 2008 molecular spectroscopic database”. *J. Quant. Spectrosc. Rad.* 110.9–10 (2009), pp. 533–572. doi: [10.1016/j.jqsrt.2009.02.013](https://doi.org/10.1016/j.jqsrt.2009.02.013) (cit. on pp. 36, 37, 41, 117, 145, 168).
- [Rothman et al., 2010] L. S. Rothman, I. E. Gordon, R. J. Barber, H. Dothe, R. R. Gamache, A. Goldman, V. I. Perevalov, S. A. Tashkun, and J. Tennyson. “HITEMP, the high-temperature molecular spectroscopic database”. *J. Quant. Spectrosc. Rad.* 111.15 (2010), pp. 2139–2150. doi: [10.1016/j.jqsrt.2010.05.001](https://doi.org/10.1016/j.jqsrt.2010.05.001) (cit. on pp. 41, 117, 145, 168).
- [Rothman et al., 1995] L. S. Rothman, R. B. Wattson, R. Gamache, J. W. Schroeder, and A. McCann. “HITRAN HAWKS and HITEMP: high-temperature molecular database”. In: *Proc. SPIE 2471, Atmospheric Propagation and Remote Sensing IV, 105 (June 15, 1995)*. 1995, pp. 105–111. doi: [10.1117/12.211919](https://doi.org/10.1117/12.211919) (cit. on pp. 41, 117, 145, 168).
- [Rudin, 1974] W. Rudin. *Real and complex analysis*. McGraw-Hill series in higher mathematics. McGraw-Hill, 1974. ISBN: 9780070542334 (cit. on p. 131).

- [Russell et al., 1980] C. T. Russell, R. C. Elphic, and J. A. Slavin. “Limits on the possible intrinsic magnetic field of Venus”. *J. Geophys. Res.: Space Physics* 85.A13 (1980), pp. 8319–8332. doi: [10.1029/JA085iA13p08319](https://doi.org/10.1029/JA085iA13p08319) (cit. on p. 1).
- [Schaber et al., 1992] G. G. Schaber, R. G. Strom, H. J. Moore, L. A. Soderblom, R. L. Kirk, D. J. Chadwick, D. D. Dawson, L. R. Gaddis, J. M. Boyce, and J. Russell. “Geology and distribution of impact craters on Venus: What are they telling us?” *J. Geophys. Res.: Planets* 97.E8 (1992), pp. 13257–13301. doi: [10.1029/92JE01246](https://doi.org/10.1029/92JE01246) (cit. on p. 7).
- [Schoenberg and De Boor, 1988] I. J. Schoenberg and C. De Boor. *I. J. Schoenberg: selected papers. Volume 1*. Ed. by Carl de Boor. Contemporary Mathematicians. Birkhäuser, 1988. ISBN: 9780817634045 (cit. on pp. 109, 110).
- [Schubert, 1983] G. Schubert. “General Circulation and the Dynamical State of the Venus Atmosphere”. In: *Venus*. Ed. by D. M. Hunten, L. Colin, T. M. Donahue, and V. I. Moroz. Space science series. University of Arizona Press, Tucson, 1983, pp. 681–765. ISBN: 9780816507887 (cit. on p. 173).
- [Seidelmann et al., 2002] P. K. Seidelmann, V. K. Abalakin, M. Bursa, M. E. Davies, C. de Bergh, J. H. Lieske, J. Oberst, J. L. Simon, E. M. Standish, P. Stooke, and P. C. Thomas. “Report of the IAU/IAG Working Group on Cartographic Coordinates and Rotational Elements of the Planets and Satellites: 2000”. *Celest. Mech. Dyn. Astr.* 82.1 (2002), pp. 83–111. doi: [10.1023/A:1013939327465](https://doi.org/10.1023/A:1013939327465) (cit. on p. 88).
- [Seiff et al., 1985] A. Seiff, J. T. Schofield, A. J. Kliore, F. W. Taylor, S. S. Limaye, H. E. Revercomb, L. A. Sromovsky, V. V. Kerzhanovich, V. I. Moroz, and M. Y. Marov. “Models of the structure of the atmosphere of Venus from the surface to 100 kilometers altitude”. *Adv. Space Res.* 5.11 (1985), pp. 3–58. doi: [10.1016/0273-1177\(85\)90197-8](https://doi.org/10.1016/0273-1177(85)90197-8) (cit. on pp. 1, 10, 41, 104, 117, 136, 145, 159, 167).
- [Serre, 2010] D. Serre. *Matrices: Theory and Applications*. Graduate Texts in Mathematics. Springer, 2010. ISBN: 9781441976826 (cit. on p. 130).
- [Shalygin et al., 2012] E. V. Shalygin, A. T. Basilevsky, W. J. Markiewicz, D. V. Titov, M. A. Kreslavsky, and T. Roatsch. “Search for ongoing volcanic activity on Venus: Case study of Maat Mons, Sapas Mons and Ozza Mons volcanoes”. *Planet. Space Sci.* 73.1 (2012). In: *Solar System science before and after Gaia*, pp. 294–301. doi: [10.1016/j.pss.2012.08.018](https://doi.org/10.1016/j.pss.2012.08.018) (cit. on pp. 5, 207).
- [Shao, 2003] J. Shao. *Mathematical Statistics*. Springer Texts in Statistics. Springer, 2003. ISBN: 9780387953823 (cit. on p. 194).
- [Sharpton and Head, 1985] V. L. Sharpton and J. W. Head. “Analysis of regional slope characteristics on Venus and Earth”. *J. Geophys. Res.: Solid Earth* 90.B5 (1985), pp. 3733–3740. doi: [10.1029/JB090iB05p03733](https://doi.org/10.1029/JB090iB05p03733) (cit. on p. 6).
- [Smrekar and Stofan, 1999] S. E. Smrekar and E. R. Stofan. “Origin of Corona-Dominated Topographic Rises on Venus”. *Icarus* 139.1 (1999), pp. 100–115. doi: [10.1006/icar.1999.6090](https://doi.org/10.1006/icar.1999.6090) (cit. on pp. 164, 208).
- [Smrekar et al., 2010] S. E. Smrekar, E. R. Stofan, N. Müller, A. Treiman, L. Elkins-Tanton, J. Helbert, G. Piccioni, and P. Drossart. “Recent Hotspot Volcanism on Venus from VIRTIS Emissivity Data”. *Science* 328.5978 (2010), pp. 605–608. doi: [10.1126/science.1186785](https://doi.org/10.1126/science.1186785). eprint: <http://www.sciencemag.org/content/328/5978/605.full.pdf> (cit. on pp. 1, 5, 7, 125, 136, 151, 163, 182, 207, 210).
- [Snels et al., 2014] M. Snels, S. Stefani, G. Piccioni, and B. Bézard. “Carbon dioxide absorption at high densities in the nightside transparency window of Venus”. *J. Quant. Spectrosc. Rad.* 133 (2014), pp. 464–471. doi: [10.1016/j.jqsrt.2013.09.009](https://doi.org/10.1016/j.jqsrt.2013.09.009) (cit. on pp. 4, 211).
- [Söderlund et al., 1998] J. Söderlund, L. B. Kiss, G. A. Niklasson, and C. G. Granqvist. “Lognormal Size Distributions in Particle Growth Processes without Coagulation”. *Phys. Rev. Lett.* 80 (11 1998), pp. 2386–2388. doi: [10.1103/PhysRevLett.80.2386](https://doi.org/10.1103/PhysRevLett.80.2386) (cit. on p. 47).
- [Spurr, 2001] R. Spurr. “Linearized radiative transfer theory: a general discrete ordinate approach to the calculation of radiances and analytic weighting functions, with application to atmospheric remote sensing”. PhD thesis. OAI Repository of the Technische Universiteit Eindhoven (TU/e) [<http://cache.libr.tue.nl:1972/csp/dare/DARE.Repository.cls>] (Netherlands): Technische Universiteit Eindhoven, 2001. doi: [10.6100/IR545442](https://doi.org/10.6100/IR545442) (cit. on pp. 31–33, 116, 167).
- [Spurr, 2008] R. Spurr. “LIDORT and VLIDORT: Linearized pseudo-spherical scalar and vector discrete ordinate radiative transfer models for use in remote sensing retrieval problems”. In: *Light Scattering Reviews 3*. Ed. by A. A. Kokhanovsky. Springer Praxis Books. Springer Berlin Heidelberg, 2008, pp. 229–275. ISBN: 978-3-540-48305-2. doi: [10.1007/978-3-540-48546-9_7](https://doi.org/10.1007/978-3-540-48546-9_7) (cit. on pp. 31, 33, 107, 116, 167).
- [Stamnes, 1982] K. Stamnes. “On the computation of angular distributions of radiation in planetary atmospheres”. *J. Quant. Spectrosc. Rad.* 28.1 (1982), pp. 47–51. doi: [10.1016/0022-4073\(82\)90096-6](https://doi.org/10.1016/0022-4073(82)90096-6) (cit. on p. 33).
- [Stamnes et al., 1988] K. Stamnes, S.-C. Tsay, W. Wiscombe, and K. Jayaweera. “Numerically stable algorithm for discrete-ordinate-method radiative transfer in multiple scattering and emitting layered media”. *Appl. Opt.* 27.12 (1988), pp. 2502–2509. doi: [10.1364/AO.27.002502](https://doi.org/10.1364/AO.27.002502) (cit. on pp. 31, 32, 116, 167).

- [Stamnes et al., 2000] K. Stamnes, S.-C. Tsay, W. Wiscombe, and I. Laszlo. “DISORT, a general-purpose Fortran program for discrete-ordinate-method radiative transfer in scattering and emitting layered media: documentation of methodology”. *Goddard Space Flight Center, NASA* (2000). http://www.met.reading.ac.uk/~qb717363/adiant/rfm-disort/DISORT_documentation.pdf (cit. on pp. 31–33).
- [Stefani et al., 2013] S. Stefani, G. Piccioni, M. Snels, D. Grassi, and A. Adriani. “Experimental CO₂ absorption coefficients at high pressure and high temperature”. *J. Quant. Spectrosc. Rad.* 117 (2013), pp. 21–28. DOI: 10.1016/j.jqsrt.2012.11.019 (cit. on pp. 4, 211).
- [Stoer and Bulirsch, 1993] J. Stoer and R. A. Bulirsch. *Introduction to Numerical Analysis, 2nd Edition*. Texts in Applied Mathematics. Springer, 1993. ISBN: 978038797878X (cit. on p. 32).
- [Stofan and Brian, 2012] E. R. Stofan and A. W. Brian. *Geologic map of the Themis Regio quadrangle (V-53), Venus*. <http://pubs.usgs.gov/sim/3165/>. US Geological Survey Scientific Investigations Map 3165, 2012 (cit. on pp. 164, 207, 208, 210).
- [Stofan and Smrekar, 1998] E. R. Stofan and S. E. Smrekar. “Coronae at Large Topographic Rises on Venus: Implications for Plume Evolution and Delamination”. In: *Lunar and Planetary Science Conference LPSC XXIX*. Vol. 29. 1998, p. 1502 (cit. on pp. 189, 208).
- [Stofan et al., 1997] E. R. Stofan, V. E. Hamilton, D. M. Janes, and S. E. Smrekar. “Coronae on Venus: Morphology and origin”. In: *Venus II: Geology, Geophysics, Atmosphere, and Solar Wind Environment*. Ed. by S. W. Bougher, D. M. Hunten, and R. J. Phillips. Space science series. University of Arizona Press, Tucson, 1997, pp. 931–965. ISBN: 9780816518302 (cit. on p. 7).
- [Stofan et al., 2010] E. R. Stofan, S. E. Smrekar, J. Helbert, and N. Müller. “Themis Regio, Venus: Emissivity Signatures in VIRTIS-Venus Express Data”. In: *2010 VEXAG International Workshop, Madison, Wisconsin, USA*. http://www.ssec.wisc.edu/venus-workshop-submission/files/stofan_ellen-22.pdf. 2010 (cit. on pp. 164, 208).
- [Stofan et al., 1995] E. R. Stofan, S. E. Smrekar, D. L. Bindschadler, and D. A. Senske. “Large topographic rises on Venus: Implications for mantle upwelling”. *J. Geophys. Res.: Planets* 100.E11 (1995), pp. 23317–23327. DOI: 10.1029/95JE01834 (cit. on pp. 164, 208).
- [Surkov, 1997] Y. Surkov. *Exploration of Terrestrial Planets from Spacecraft: Instrumentation, Investigation, Interpretation, 2nd Edition*. Astronomy and Astrophysics Series. Wiley, 1997. ISBN: 9780471964292 (cit. on p. 7).
- [Svedhem et al., 2007] H. Svedhem, D. V. Titov, D. McCoy, J.-P. Lebreton, S. Barabash, J.-L. Bertaux, P. Drossart, V. Formisano, B. Häusler, O. Korablev, W. J. Markiewicz, D. Nevejans, M. Pätzold, G. Piccioni, T. L. Zhang, F. W. Taylor, E. Lellouch, D. Koschny, O. Witasse, H. Eggel, M. Warhaut, A. Accomazzo, J. Rodriguez-Canabal, J. Fabrega, T. Schirmann, A. Clochet, and M. Coradini. “Venus Express—The first European mission to Venus”. *Planet. Space Sci.* 55.12 (2007). The Planet Venus and the Venus Express Mission, Part 2, pp. 1636–1652. DOI: 10.1016/j.pss.2007.01.013 (cit. on pp. 2, 25).
- [Tashkun and Perevalov, 2008] S. A. Tashkun and V. I. Perevalov. *CDSD-VENUS: Carbon Dioxide Spectroscopic Databank version for studying of Venus atmosphere*. <ftp://ftp.iao.ru/pub/CDSD-2008/Venus/>. 2008 (cit. on pp. 4, 36).
- [Tashkun et al., 2003] S. A. Tashkun, V. I. Perevalov, J.-L. Teffo, A. D. Bykov, and N. N. Lavrentieva. “CDSD-1000, the high-temperature carbon dioxide spectroscopic databank”. *J. Quant. Spectrosc. Rad.* 82.1–4 (2003), pp. 165–196. DOI: 10.1016/S0022-4073(03)00152-3 (cit. on pp. 36, 41, 93, 117, 145, 148, 168).
- [Tellmann et al., 2009] S. Tellmann, M. Pätzold, B. Häusler, M. K. Bird, and G. L. Tyler. “Structure of the Venus neutral atmosphere as observed by the Radio Science experiment VeRa on Venus Express”. *J. Geophys. Res.* 114.E9 (2009), E00B36. DOI: 10.1029/2008JE003204 (cit. on pp. 69, 105, 117, 119, 145, 167).
- [Thomas and Stamnes, 2002] G. E. Thomas and K. Stamnes. *Radiative Transfer in the Atmosphere and Ocean*. Atmospheric and space science. Cambridge University Press, 2002. ISBN: 9780521890618 (cit. on p. 37).
- [Tikhonov, 1995] A. N. Tikhonov. *Numerical Methods for the Solution of Ill-Posed Problems*. Mathematics and Its Applications. Kluwer Academic Publishers, 1995. ISBN: 9780792335832 (cit. on pp. 11, 104).
- [Titov et al., 2006] D. V. Titov, H. Svedhem, D. Koschny, R. Hoofs, S. Barabash, J.-L. Bertaux, P. Drossart, V. Formisano, B. Häusler, O. Korablev, W. J. Markiewicz, D. Nevejans, M. Pätzold, G. Piccioni, T. L. Zhang, D. Merritt, O. Witasse, J. Zender, A. Accomazzo, M. Sweeney, D. Trillard, M. Janvier, and A. Clochet. “Venus Express science planning”. *Planet. Space Sci.* 54.13–14 (2006). The Planet Venus and the Venus Express Mission, pp. 1279–1297. DOI: 10.1016/j.pss.2006.04.017 (cit. on pp. 2, 25).
- [Titov et al., 2012] D. V. Titov, W. J. Markiewicz, N. I. Ignatiev, L. Song, S. S. Limaye, A. Sanchez-Lavega, J. Hessemann, M. Almeida, T. Roatsch, K.-D. Matz, F. Scholten, D. Crisp, L. W. Esposito, S. F. Hviid, R. Jaumann, H. U. Keller, and R. Moissl. “Morphology of the cloud tops as observed by the Venus Express Monitoring Camera”. *Icarus* 217.2 (2012). Advances in Venus Science, pp. 682–701. DOI: 10.1016/j.icarus.2011.06.020 (cit. on pp. 148, 173).

- [Titov et al., 2008] D. V. Titov, F. W. Taylor, H. Svedhem, N. I. Ignatiev, W. J. Markiewicz, G. Piccioni, and P. Drossart. “Atmospheric structure and dynamics as the cause of ultraviolet markings in the clouds of Venus”. *Nature* 456.7222 (2008), pp. 620–623. doi: [10.1038/nature07466](https://doi.org/10.1038/nature07466) (cit. on p. 48).
- [Tonkov et al., 1996] M. V. Tonkov, N. N. Filippov, V. V. Bertsev, J. P. Bouanich, N. Van-Thanh, C. Brodbeck, J. M. Hartmann, C. Boulet, F. Thibault, and R. L. Doucen. “Measurements and empirical modeling of pure CO₂ absorption in the 2.3 μm region at room temperature: far wings, allowed and collision-induced bands”. *Appl. Opt.* 35.24 (1996), pp. 4863–4870. doi: [10.1364/AO.35.004863](https://doi.org/10.1364/AO.35.004863) (cit. on pp. 39, 41, 93).
- [Tran et al., 2011] H. Tran, C. Boulet, S. Stefani, M. Snels, and G. Piccioni. “Measurements and modelling of high pressure pure CO₂ spectra from 750 to 8500 cm⁻¹. I—central and wing regions of the allowed vibrational bands”. *J. Quant. Spectrosc. Rad.* 112.6 (2011), pp. 925–936. doi: [10.1016/j.jqsrt.2010.11.021](https://doi.org/10.1016/j.jqsrt.2010.11.021) (cit. on pp. 4, 93, 211).
- [Tsang et al., 2008a] C. C. C. Tsang, P. G. J. Irwin, F. W. Taylor, and C. F. Wilson. “A correlated-k model of radiative transfer in the near-infrared windows of Venus”. *J. Quant. Spectrosc. Rad.* 109.6 (2008). Spectroscopy and Radiative Transfer in Planetary Atmospheres, pp. 1118–1135. doi: [10.1016/j.jqsrt.2007.12.008](https://doi.org/10.1016/j.jqsrt.2007.12.008) (cit. on p. 4).
- [Tsang et al., 2009] C. C. C. Tsang, F. W. Taylor, C. F. Wilson, S. J. Liddell, P. G. J. Irwin, G. Piccioni, P. Drossart, and S. B. Calcutt. “Variability of CO concentrations in the Venus troposphere from Venus Express/VIRTIS using a Band Ratio Technique”. *Icarus* 201.2 (2009), pp. 432–443. doi: [10.1016/j.icarus.2009.01.001](https://doi.org/10.1016/j.icarus.2009.01.001) (cit. on pp. 4, 118, 147, 173).
- [Tsang et al., 2008b] C. C. C. Tsang, P. G. J. Irwin, C. F. Wilson, F. W. Taylor, C. Lee, R. de Kok, P. Drossart, G. Piccioni, B. Bézard, and S. Calcutt. “Tropospheric carbon monoxide concentrations and variability on Venus from Venus Express/VIRTIS-M observations”. *J. Geophys. Res.: Planets* 113.E5 (2008), E00B08–1–E00B08–13. doi: [10.1029/2008JE003089](https://doi.org/10.1029/2008JE003089) (cit. on p. 4).
- [Tsang et al., 2010] C. C. C. Tsang, C. F. Wilson, J. K. Barstow, P. G. J. Irwin, F. W. Taylor, K. McGouldrick, G. Piccioni, P. Drossart, and H. Svedhem. “Correlations between cloud thickness and sub-cloud water abundance on Venus”. *Geophys. Res. Lett.* 37.2 (2010). L02202, pp. 1–5. doi: [10.1029/2009GL041770](https://doi.org/10.1029/2009GL041770) (cit. on p. 4).
- [Twomey et al., 1977] S. Twomey, B. Herman, and R. Rabinoff. “An Extension to the Chahine Method of Inverting the Radiative Transfer Equation”. *J. Atmos. Sci.* 34.7 (1977). doi:[10.1175/1520-0469\(1977\)034<1085:AETTCM>2.0.CO;2](https://doi.org/10.1175/1520-0469(1977)034<1085:AETTCM>2.0.CO;2), pp. 1085–1090 (cit. on p. 4).
- [Ungermann et al., 2010a] J. Ungermann, L. Hoffmann, P. Preusse, M. Kaufmann, and M. Riese. “Tomographic retrieval approach for mesoscale gravity wave observations by the PREMIER Infrared Limb-Sounder”. *Atmos. Meas. Tech.* 3.2 (2010), pp. 339–354. doi: [10.5194/amt-3-339-2010](https://doi.org/10.5194/amt-3-339-2010) (cit. on pp. 8, 204).
- [Ungermann et al., 2010b] J. Ungermann, M. Kaufmann, L. Hoffmann, P. Preusse, H. Oelhaf, F. Friedl-Vallon, and M. Riese. “Towards a 3-D tomographic retrieval for the air-borne limb-imager GLORIA”. *Atmos. Meas. Tech.* 3.6 (2010), pp. 1647–1665. doi: [10.5194/amt-3-1647-2010](https://doi.org/10.5194/amt-3-1647-2010) (cit. on pp. 8, 204).
- [Ungermann et al., 2011] J. Ungermann, J. Blank, J. Lotz, K. Leppkes, L. Hoffmann, T. Guggenmoser, M. Kaufmann, P. Preusse, U. Naumann, and M. Riese. “A 3-D tomographic retrieval approach with advection compensation for the air-borne limb-imager GLORIA”. *Atmos. Meas. Tech.* 4.11 (2011), pp. 2509–2529. doi: [10.5194/amt-4-2509-2011](https://doi.org/10.5194/amt-4-2509-2011) (cit. on pp. 8, 204).
- [Vandevender and Haskell, 1982] W. H. Vandevender and K. H. Haskell. “The SLATEC mathematical subroutine library”. *SIGNUM Newsl.* 17.3 (1982), pp. 16–21. doi: [10.1145/1057594.1057595](https://doi.org/10.1145/1057594.1057595) (cit. on p. 64).
- [Wang and Sirota, 2002] W. F. Wang and J. M. Sirota. “Perturbative study of spectral line shapes involving line-mixing and collision-duration asymmetry”. *J. Chem. Phys.* 116.2 (2002), pp. 532–537. doi: [10.1063/1.1425826](https://doi.org/10.1063/1.1425826) (cit. on p. 39).
- [Williams, 2013] D. R. Williams. *Venus Fact Sheet from The National Space Science Data Center, NASA Goddard Space Flight Center*. <http://nssdc.gsfc.nasa.gov/planetary/factsheet/venusfact.html>. 2013 (cit. on p. 1).
- [Williams, 2015] D. R. Williams. *Chronology of Venus Exploration*. http://nssdc.gsfc.nasa.gov/planetary/chronology_venus.html. 2015 (cit. on p. 2).
- [Williams et al., 2014] T. Williams, C. Kelley, and many others. *Gnuplot 4.6: an interactive plotting program*. <http://gnuplot.sourceforge.net/>. 2014 (cit. on p. 174).
- [Wilson et al., 2008] C. F. Wilson, S. Guerlet, P. G. J. Irwin, C. C. C. Tsang, F. W. Taylor, R. W. Carlson, P. Drossart, and G. Piccioni. “Evidence for anomalous cloud particles at the poles of Venus”. *J. Geophys. Res.* 113.E9 (2008), E00B13. doi: [10.1029/2008JE003108](https://doi.org/10.1029/2008JE003108) (cit. on pp. 4, 41).
- [Wilson et al., 2009] C. F. Wilson, C. C. C. Tsang, P. G. J. Irwin, F. W. Taylor, B. Bézard, S. Erard, R. W. Carlson, P. Drossart, G. Piccioni, and R. C. Holmes. “Analysis of thermal emission from the nightside of Venus at 1.51 and 1.55 μm”. *Icarus* 201.2 (2009), pp. 814–817. doi: [10.1016/j.icarus.2009.03.010](https://doi.org/10.1016/j.icarus.2009.03.010) (cit. on p. 4).

- [Wiscombe, 1980] W. J. Wiscombe. “Improved Mie scattering algorithms”. *Appl. Opt.* 19.9 (1980), pp. 1505–1509. doi: [10.1364/AO.19.001505](https://doi.org/10.1364/AO.19.001505) (cit. on pp. 32, 44, 45, 117, 145, 169).
- [Zasova, 2012] L. V. Zasova. “Venus investigations after Venus Express: mission Venera-D”. In: *Tenth meeting of the Venus Exploration and Analysis Group (VEXAG)*. http://www.lpi.usra.edu/vexag/Nov2012/presentations/13_VeneraD_Zasova.pdf. 2012 (cit. on p. 19).
- [Zasova et al., 1999] L. V. Zasova, I. A. Khatountsev, V. I. Moroz, and N. I. Ignatiev. “Structure of the Venus middle atmosphere: Venera 15 Fourier spectrometry data revisited”. *Adv. Space Res.* 23.9 (1999), pp. 1559–1568. doi: [10.1016/S0273-1177\(99\)00169-6](https://doi.org/10.1016/S0273-1177(99)00169-6) (cit. on p. 48).
- [Zasova et al., 2006a] L. V. Zasova, V. I. Moroz, V. Formisano, N. I. Ignatiev, and I. V. Khatuntsev. “Exploration of Venus with the Venera-15 IR Fourier spectrometer and the Venus Express planetary Fourier spectrometer”. English. *Cosm. Res.* 44.4 (2006), pp. 349–363. doi: [10.1134/S0010952506040083](https://doi.org/10.1134/S0010952506040083) (cit. on p. 48).
- [Zasova et al., 2006b] L. V. Zasova, V. I. Moroz, V. M. Linkin, I. V. Khatuntsev, and B. S. Maiorov. “Structure of the Venusian atmosphere from surface up to 100 km”. English. *Cosm. Res.* 44.4 (2006), pp. 364–383. doi: [10.1134/S0010952506040095](https://doi.org/10.1134/S0010952506040095) (cit. on pp. 41, 89, 104, 117).
- [Zasova et al., 2007] L. V. Zasova, N. Ignatiev, I. Khatuntsev, and V. Linkin. “Structure of the Venus atmosphere”. *Planet. Space Sci.* 55.12 (2007). *The Planet Venus and the Venus Express Mission, Part 2*, pp. 1712–1728. doi: [10.1016/j.pss.2007.01.011](https://doi.org/10.1016/j.pss.2007.01.011) (cit. on p. 48).
- [Zolotov and Volkov, 1992] M. I. Zolotov and V. P. Volkov. “Chemical processes on the planetary surface”. In: *Venus Geology, Geochemistry, and Geophysics - Research results from the USSR*. Ed. by V. L. Barsukov, A. T. Basilevsky, V. P. Volkov, and V. N. Zharkov. University of Arizona Press, Tucson, 1992, pp. 177–199 (cit. on p. 7).

Selbstständigkeitserklärung

Hiermit erkläre ich, dass diese Arbeit an keiner anderen Hochschule eingereicht sowie selbständig von mir und ausschließlich mit den angegebenen Mitteln angefertigt wurde.

Potsdam, den 27.05.2015

David Kappel